Imaging with the VLTI

Nuno Gomes

Supervisor: Paulo J. V. Garcia

Co-Supervisor: Françoise Delplancke

Programa Doutoral em Astronomia

U.PORTO

FACULDADE DE CIÊNCIAS
UNIVERSIDADE DO PORTO

July 2014 (amended in July 2016)

The work in this thesis is based on research carried out at the department of *Physics and Astronomy* of *Faculdade de Ciências da Universidade do Porto*, Portugal. No part of this thesis has been submitted elsewhere for any other degree or qualification and it is all my own work unless referenced to the contrary in the text.

© **Nuno Gomes: July 2014 (amended in July 2016)**
"The copyright of this thesis rests with the author. No quotations from it should be published without the author's prior written consent, and information derived from it should be acknowledged".

Faculdade de Ciências da Universidade do Porto

Imaging with the VLTI

Nuno Gomes

Dissertation submitted to Faculdade de Ciências da Universidade do Porto
to obtain the degree of

Philosophiae Doctor in Astronomy

President: Doutor Orfeu Bertolami
Referee: Doutor Jean-Baptiste Le Bouquin
Referee: Doutor Damien Segransan
Referee: Doutor Carlos Manuel Correia da Silva
[Referee]: Doutor Paulo Jorge Valente Garcia

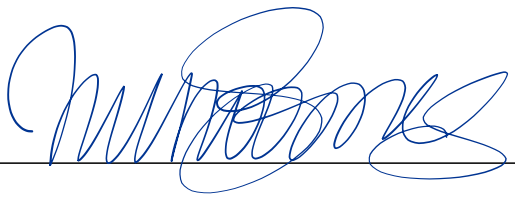

July 2014 (amended in July 2016)

To my mother and sister.

Abstract

PHASE REFERENCING AND IMAGE RECONSTRUCTION are two fundamental areas for the scientific success of optical interferometry. This is attested by the effort in building instruments such as PIONIER, MIRC, and the PRIMA facility, as well as the second generation VLTI instrumentation (GRAVITY and MATISSE). The work developed under the framework of this thesis can be divided into two distinct although interrelated areas: (*a*) *instrumentation*, associated to phase referencing interferometry and the commissioning runs of PRIMA, the Phase Referenced Imaging and Micro-Arcsecond Astrometry dual-feed facility of ESO, and (*b*) *data simulation and analysis* with a study on interferometric image reconstruction.

With respect to optical interferometric observations, imaging became a reality in the last three decades. It is a common practice in current facilities and it lies at the heart of the *Planet Formation Imager* (PFI) concept. In order to achieve a good quality image, the visibility phase has to be measured by an interferometer. However, due to the turbulence in the atmosphere, the stabilisation of the fringes in the laboratory is usually a challenging and complex task. Two approaches have been used to tackle this problem: the partial measurement of the phase by means of *closure phases*, *i.e.*, by measuring the combined phase of a triplet of telescopes, and the use of *phase referencing* to obtain the full phase information. In the latter, an unresolved source, or, at least, a centre-symmetrical one, needs to be close enough to the object of interest, in order to reference the phase and get its full information. Whilst instruments measuring closure phases deliver limited phase information, they are cheaper and less technically demanding. Consequently, they have been widespread amongst interferometers, such as VLTI and CHARA, and are planned to be used for forthcoming facilities, such as MROI. Notwithstanding, new instruments have been devised aiming at phase referencing, of which PRIMA is the first at the VLTI, combining two telescopes at a time. GRAVITY will soon be implemented at Paranal, and it will be able to combine four telescopes using the phase referencing technique.

Detailed studies of the imaging capacity of *phase closure versus phase referencing* are not available and were object of this thesis. Three objects of distinct apparent sizes and morphologies (a stellar cluster, a young stellar object, and a stellar photosphere) have been mock observed with the VLTI. The *Simple* noise model was developed in order to estimate the statistics of the observables, and its performance was compared to other previously published models, which account for more variables affecting the error bars of the visibility quantities, such as the detector's readout noise or the Strehl ratio. The *Simple* noise model was devised having in mind simplicity and the correct reproduction of the dependence of the complex visibility phase with the visibility amplitude. The results indicate that it is able to reproduce this expected theoretical behaviour, and that it behaves

fairly regarding the remainder of the visibility quantities, such as the power-spectrum and the bi-spectrum. In addition, the *accuracy function* was designed, a quality function aiming at the unbiased quantification of a restored image's quality when compared to a true image.

Firstly, *phase referencing* and *closure phase* images were compared when they were produced by the same observational scenarios. Using *accuracy* and other published quality functions, such as the *RMS of the imaging beauty contest*, or the *fidelity* function of ALMA, the results show that for a poorly paved (u,v)-space, phase referencing images are of better quality than closure phase ones. For a well-filled *uv*-coverage, both cases yield images of similar quality.

Secondly, *phase referencing* and *closure phase* cases were compared under different observational scenarios mounted over the same number of nights. The compared set-ups consisted in: (*a*) two telescopes phase referencing *vs* three telescopes closure phase (resembling PRIMA *vs* AMBER); (*b*) three telescopes phase referencing *vs* four telescopes closure phase ("super PRIMA" or GRAVITY like *vs* PIONIER); (*c*) four telescopes phase referencing *vs* six telescopes closure phase (GRAVITY *vs* VSI). Because phase referencing data acquisition was always performed using less telescopes than closure phase, the (u,v)-space presented less sampled spatial frequencies. Phase referenced images produced with the *standard* set-ups were typically of poor quality, as classified by the aforementioned quality functions, and were easily surpassed by images produced from closure phase configurations. The overall picture changed, though, when a better pavement of the (u,v)-space was implemented. (u,v)-points selection was performed while keeping the total number of sampled spatial frequencies fixed. In this case, phase referencing and closure phase images became of comparable quality.

In the scope of PRIMA, a study was carried out with the aim of understanding the effects of angular anisoplanatism in the determination of visibility amplitudes. This work is of major importance for phase referencing, because visibility measurements are expected to be affected by the position of the fainter object relative to the fringe tracking star, when the latter is placed in the optical axis. Initially, an algorithm to compute visibility amplitudes from PRIMA's Fringe Sensor Units (FSUs) data was developed and tested against previously published data, acquired during PRIMA's commissioning run #2. The sources consisted of two unresolved stars, HD15520 and HD18829. The resulting visibility amplitudes, respectively equal to 1.2 ± 0.3 and 1.3 ± 0.3, are compliant with point-like objects and agree with the published results.

Then, the so-called *faint-object science mode* was analysed. In this mode, PRIMA is combined with AMBER. The light emitted by a bright reference object is sent to one of the FSUs, while light coming from a faint science object, *i.e.*, a source with such a high magnitude that cannot be tracked by PRIMA's infra-red camera IRIS, is sent directly to AMBER. The star separator corrects the slow drifts of the beams between the telescopes and the laboratory and, therefore, AMBER is able to measure the visibility amplitude for longer integration times. In order for it to work, it is fundamental that the position offsets of both beams (one from the bright reference star, the other from the faint "scientific" object) are correlated. This problem was addressed by measuring the coordinates of the centroids of both beams at IRIS. It was found that apart from the defocus on AT3, there is a strong correlation between the centroids, demonstrating as such that this mode is feasible.

Keywords: Astronomical optical interferometry. Phase referencing. Phase closure. PRIMA. Image reconstruction. Image quality assessment.

Resumo

REFERÊNCIA DE FASE E RECONSTRUÇÃO DE IMAGEM são duas áreas fundamentais para o sucesso científico da interferometria no ótico. Este facto é atestado pelo esforço na construção de instrumentos, tais como o PIONIER e o MIRC, e com a instalação do PRIMA, bem como pela segunda geração de instrumentação do VLTI (GRAVITY e MATISSE). O trabalho desenvolvido no âmbito desta tese pode ser dividido em duas áreas distintas, não obstante interrelacionadas: (*a*) *instrumentação*, associado à interferometria de referência de fase e às missões de teste do PRIMA, a unidade de alimentação-dupla denominada Phase Referenced Imaging and Micro-arcsecond Astrometry do ESO, e (*b*) *simulação e análise de dados* com um estudo acerca da reconstrução de imagem em interferometria.

No que diz respeito às observações interferométricas no óptico, a obtenção de imagens tornou-se uma realidade nas últimas três décadas. É uma prática comum nas atuais instalações e uma peça fundamental do conceito *Planet Formation Imager* (PFI). A fim de se alcançar uma imagem de boa qualidade, a fase da visibilidade tem de ser medida por um interferómetro. No entanto, devido à turbulência na atmosfera, a estabilização das franjas no laboratório é geralmente uma tarefa difícil e complexa. São duas as abordagens usadas para resolver este problema: a medição parcial da fase por meio de *fases de clausura*, ou seja, através da medição da fase combinada de um trio de telescópios, e o uso de *referência de fase* para obter a sua informação na plenitude. Nesta última, torna-se necessário que uma fonte não resolvida, ou, pelo menos, uma fonte centrosimétrica se localize perto o suficiente do objeto de interesse, de modo a se referenciar a fase e, assim, a obtê-la totalmente. Embora os instrumentos capazes de medir fases de clausura oferecem uma informação limitada da fase, são mais baratos e menos exigentes sob o ponto de vista técnico. Consequentemente, têm sido largamente usados em interferómetros como o VLTI e o CHARA, e estão projetados para serem usados em futuras instalações, como o MROI. Não obstante, novos instrumentos foram concebidos com o objetivo de executarem referência de fase, dos quais o primeiro é o PRIMA no VLTI, combinando dois telescópios simultaneamente. O GRAVITY será em breve implementado no Paranal, sendo capaz de combinar quatro telescópios usando a técnica de referência de fase.

Estudos detalhados sobre a capacidade de produzir imagens em *clausura* ou *confinamento de fase versus referência de fase* não estão disponíveis e foram um dos objetivos principais desta tese. Três objetos de diferentes tamanhos aparentes e morfologias distintas (um enxame estelar, um objeto estelar jovem, e uma fotosfera estelar) foram virtualmente observados com o VLTI. O *modelo de ruído simples* foi desenvolvido de modo a estimar as estatísticas das observáveis, e o seu desempenho foi comparado com outros modelos previamente publicados, que levam em

consideração mais variáveis que afetam as barras de erro das diversas quantidades associadas à visibilidade, tais como o ruído de leitura do detetor ou a razão de Strehl. O *modelo de ruído simples* foi concebido tendo em vista a simplicidade e a reprodução correta da dependência da fase da visibilidade complexa com a amplitude da visibilidade. Os resultados indicam que este modelo é capaz de reproduzir este comportamento teórico esperado, e que se comporta de forma razoável relativamente às restantes quantidades da visibilidade, tais como o espetro de potência e o biespectro. Além disso, foi desenvolvida a *função de acuidade*, uma função de qualidade que tem por objetivo a quantificação imparcial da qualidade de uma imagem restaurada quando comparada com uma imagem verdadeira.

Em primeiro lugar, a *referência de fase* e o *confinamento de fase* foram comparados mediante cenários observacionais distintos, quando produzidos durante o mesmo número de noites. Usando a *função de acuidade* e outras funções de qualidade já publicadas, como o *RMS do concurso de beleza de imagem*, ou a *função de fidelidade* do ALMA, os resultados mostram que para um espaço-(u,v) mal pavimentado, as imagens em referência de fase são de melhor qualidade do que as de clausura de fase. Para uma cobertura do espaço-(u,v) bem preenchida, ambos os casos originam imagens de qualidade semelhante.

Em segundo lugar, a *referência de fase* e a *clausura de fase* foram comparadas usando diferentes cenários de observação, criados com o mesmo número de noites. As configurações de comparação foram as seguintes: (a) dois telescópios em referência de fase *vs* três telescópios em clausura de fase (que se assemelha ao PRIMA *vs* o AMBER); (b) três telescópios em referência de fase *vs* quatro telescópios em confinamento de fase ("super-PRIMA" ou tipo GRAVITY *vs* PIONIER); (c) quatro telescópios em referência de fase *vs* seis telescópios em clausura de fase (GRAVITY *vs* VSI). Uma vez que a aquisição de dados em referência de fase foi sempre realizada utilizando menos telescópios do que no confinamento de fase, o espaço-(u,v) caracteriza-se por um menor número de frequências espaciais amostradas no primeiro do que no segundo casos. Imagens obtidas a partir de configurações padrão em referência de fase foram tipicamente de má qualidade, tal como atestado pelas funções de qualidade anteriormente mencionadas, e foram facilmente superadas por imagens produzidas a partir de configurações em clausura de fase. Porém, o quadro geral mudou quando foi implentada uma melhor cobertura do espaço-(u,v). Foi realizada uma seleção dos pontos-(u,v) mantendo-se fixo o número total de frequências espaciais amostradas. Neste caso, as imagens em referência de fase e em clausura de fase passaram a ser de qualidade semelhante.

No âmbito do PRIMA, foi realizado um estudo com o objetivo de compreender os efeitos do anisoplanatismo angular na determinação das amplitudes da visibilidade. Este trabalho é de grande importância para a referência de fase, porque é esperado que as medições de visibilidade sejam afetadas pela posição do objeto menos brilhante em relação à estrela usada para seguir as franjas, quando esta é colocada no eixo ótico. Inicialmente, foi desenvolvido um algoritmo para calcular as amplitudes de visibilidade a partir de dados da Unidade Sensora de Franjas (FSU, em inglês) do PRIMA. O algoritmo foi testado com dados publicados anteriormente, adquiridos durante a missão de implementação e teste #2 do PRIMA. As fontes consistiram de duas estrelas não resolvidas, HD15520 e HD18829. As amplitudes de visibilidade resultantes, respetivamente iguais a 1.2 ± 0.3 e 1.3 ± 0.3, são compatíveis com objetos pontuais e concordam com os resultados publicados.

Seguidamente, o chamado *modo de ciência de objetos ténues* foi analisado. Neste modo, o PRIMA é combinado com o AMBER. A luz emitida por um objeto de referência brilhante é enviada para uma das FSUs, enquanto a luz proveniente de um objeto científico ténue, ou seja, uma fonte com uma magnitude tal que não pode ser rastreado pela câmara de infra-vermelhos IRIS do PRIMA, é enviada diretamente para o AMBER. O separador de estrelas corrige os desvios lentos dos feixes de luz entre os telescópios e o laboratório e, portanto, o AMBER é capaz de medir a amplitude da visibilidade para tempos de integração mais longos. Para que esta técnica

funcione, é fundamental que os deslocamentos das posição dos dois feixes de luz (um proveniente da estrela de referência brilhante, o outro do objeto "científico" ténue) estejam correlacionadas. Este problema foi abordado através da medição das coordenadas dos centróides de ambas os feixes no IRIS. Verificou-se que para além da desfocagem no AT3, há uma forte correlação entre os centróides, provando, assim, que este modo é viável.

Palavras chave: Interferometria astronómica no óptico. Referência de fase. Clausura de fase. Confinamento de fase. PRIMA. Reconstrução de imagem. Avaliação da qualidade de imagem.

Acknowledgments

I would like to gratefully thank my Ph.D. supervisor Doctor Paulo Jorge Valente Garcia for his guidance and suggestions, that motivated me and made this work a reality, and for his help and advice that allowed me to get an FCT grant. My acknowledgement also to my Ph.D. co-supervisor, Doctor Françoise Delplancke, for her guidance and suggestions, specially on the instrumentation framework of this thesis. Heartfelt thanks also go to Doctor Éric Thiébaut, for his interest, support, counselling and dedication to this work, which he provided whenever he could.

I also would like to gratefully thank my friends Inês Ínsua, Víctor Granados, Vanessa Agra-Amboage and Ana Palmero for their support, and specially my family, without whose unconditional support and help this thesis would not have been possible.

Nuno Gomes

Publications

Gomes, Nuno; Garcia, Paulo J. V.; Thiébaut, Éric. *Assessing the quality of restored images in optical long-baseline interferometry*. Monthly Notices of the Royal Astronomical Society, 465(4), 16 pp. (November 2016).

Gomes, Nuno; Garcia, Paulo J. V.; Thiébaut, Éric. *Two, three, four, or six telescopes with phase referencing or closure phase relations: the best tactics for interferometric image reconstruction*. In Optical and Infrared Interferometry IV. Proceedings of SPIE, Volume 9146, article id. 91462M, 10 pp. (July 24, 2014). Montréal, Canada, June 23, 2014.

Gomes, Nuno; Schmid, Christian; Sahlmann, Johannes; Ménardi, Sérge; Abuter, Roberto; Mérand, Antoine; Delplancke, Françoise. *Estimating visibility amplitudes with the PRIMA fringe trackers*. In Optical and Infrared Interferometry III. Proceedings of SPIE, Volume 8445, article id. 844522, 9 pp. (September 12, 2012). Amsterdam, Netherlands, July 01, 2012.

Gomes, Nuno; Garcia, Paulo J. V.; Thiébaut, Éric M.; Renard, Stéphanie; Filho, Mercedes. *Comparison between closure phase and phase referenced interferometric image reconstructions*. In Proceedings of SPIE, Volume 7734, id. 773438, 13 pp. (July 21, 2010). San Diego, California, USA, June 27, 2010.

Schmid, Christian; Abuter, Roberto; Mérand, Antoine; Sahlmann, Johannes; Alonso, Jaime; Andolfato, Luigi; van Belle, Gerard T.; Delplancke, Françoise; Derie, Frédéric; Di Lieto, Nicola; Frahm, Robert; Gitton, Philippe B.; **Gomes, Nuno**; Justen, B.; Ramirez,;res; Schuhler, Nicolas. *Status of PRIMA for the VLTI – heading to astrometry*. In Optical and Infrared Interferometry III. Proceedings of SPIE, Volume 8445, article id. 84450F (2012). Amsterdam, Netherlands, July 01, 2012.

Sahlmann, Johannes; Abuter, Roberto; Ménardi, Serge; Schmid, Christian; Di Lieto, Nicola; Delplancke, Françoise; Frahm, Robert; **Gomes, Nuno**; Haguenauer, Pierre; Lévêque, Samuel; Morel, Sebastian; Müller, André; Phan Duc, Tan; Schuhler, Nicolas; van Belle, Gerard. *First results from fringe tracking with the PRIMA fringe sensor unit*. In Optical and Infrared Interferometry II. Proceedings of SPIE, Volume 7734, article id. 773422 (July 21, 2010). San Diego, California, USA, June 27, 2010.

Schmid, Christina; Abuter, Roberto; Ménardi, Serge; Andolfato, Luigi; Delplancke, Françoise; Dérie, Frédéric; Di Lieto, Nicola; Frahm, Robert; Gitton, Philippe; **Gomes, Nuno**; Haguenauer, Pierre; Lévêque, Samuel; Morel, Sebastian; Müller, André; Phan Duc, Tan; Pozna, Eszter; Sahlmann, Johannes; Schuhler, Nicolas; van Belle, Gerard. *Status of PRIMA for the VLTI or the*

quest for user-friendly fringe tracking. In Optical and Infrared Interferometry II. Proceedings of SPIE, Volume 7734, article id. 77340F (July 22, 2010). San Diego, California, USA, June 27, 2010.

"I do not know what I may appear to the world, but to myself I seem to have been only like a boy playing on the sea-shore, and diverting myself in now and then finding a smoother pebble or a prettier shell than ordinary, whilst the great ocean of truth lay all undiscovered before me."

Sir Isaac Newton

Contents

List of Figures

List of Tables

List of Abbreviations

ACU	**A**lignment and **C**ompensation **U**nit
ADU	**A**nalogue-to-**D**igital **U**nit
AGB	**A**symptotic **G**iant **B**ranch
AGN	**A**ctive **G**alactic **N**ucleus
AIPS	**A**stronomical **I**mage **P**rocessing **S**ystem
ALMA	**A**tacama **L**arge **M**illimeter **A**rray
AMBER	**A**stronomical **M**ulti-**BE**am combine**R**
AO	**A**daptive **O**ptics
ARAL	**AR**tificial Source and **AL**ignment Unit
AT	**A**uxiliary **T**elescope
BBM	**B**uilding **B**lock **M**ethod
BC	**B**eam **C**ombiner
BOB	**B**roker for **O**bservation **B**locks
BS	**B**eam **S**plitter
BSMEM	**BiS**ectrum **M**aximum **E**ntropy **M**ethod
CCD	**C**harge-**C**oupled **D**evice
CGS	**C**entimetre-**G**ram-**S**econd
CHAMP	**CHA**RA **M**ichigan **P**hase-tracker
CHARA	**C**enter for **H**igh Angular **R**esolution **A**stronomy
CMOS	**C**omplementary **M**etal-**O**xide **S**emiconductor
COAST	**C**ambridge **O**ptical **A**perture **S**ynthesis **T**elescope
DDL	**D**ifferential **D**elay **L**ine
DL	**D**elay **L**ine
DEC	**DEC**lination
DF	**D**ual **F**eed
DFT	**D**iscrete **F**ourier **T**ransform
DIT	**D**etector **I**ntegration **T**ime

DOPDC	**D**ifferential **OPDC**
E-ELT	**E**uropean **E**uropean **E**xtremely **L**arge **T**elescope
ESO	European Organisation for Astronomical Research in the Southern Hemisphere, formerly know as **E**uropean **S**outhern **O**bservatory
FCUP	**F**aculdade de **C**iências da **U**niversidade do **P**orto
FFT	**F**ast **F**ourier **T**ransform
FINITO	**F**ringe tracking **I**nstrument of **NI**ce and **TO**rino
FIR	**F**ar **I**nfra **R**ed
FITS	**F**lexible **I**mage **T**ransport **S**ystem
FOV	**F**ield **O**f **V**iew
FSM	**F**ield **S**elector **M**irror
FSU	**F**ringe **S**ensor **U**nit
FT	**F**ourier **T**ransform
FTK	**F**ringe **T**rac**K**ing
FWHM	**F**ull **W**idth at **H**alf **M**aximum
GMT	**G**iant **M**agellan **T**elescope
GRAVITY	**G**eneral **R**elativity **A**nalysis via **V**LT **I**nterferome**T**r**Y**
GUI	**G**raphical **U**ser **I**nterface
IFG	**I**RIS **F**ast **G**uiding
IFOA	**I**RIS **F**eeding **O**ptics to **A**MBER
ILG	**I**RIS **L**ab **G**uiding
IOTA	**I**nfrared-**O**ptial **T**elescope **A**rray
IR	**I**nfra-**R**ed
IRIS	**I**nfra**R**ed **I**mage **S**ensor
ISG	**I**RIS **S**low **G**uiding
ISS	**I**nterferometer **S**upervisor **S**oftware
JD	**J**ulian **D**ate
LBOI	**L**ong **B**aseline **O**ptical **I**nterferometry
LBT	**L**arge **B**inocular **T**elescope
LCU	**L**ocal **C**ontrol **U**nit
LMOT	**L**inear **MOT**or
MACIM	**MA**rkov **C**hain **IM**ager
MARCEL	Artificial beam generator of the VLTI
MATISSE	**M**ulti **A**per**T**ure mid-**I**nfrared **S**pectro**S**copic **E**xperiment
MCM	**M**onte-**C**arlo **M**arkov

MET	PRIMA **MET**rology System
MIDI	**MID**-Infrared **I**nterferometric Instrument
MIR	**M**id **I**nfra-**R**ed
MiRA	**M**ulti-aperture **i**mage **R**econstruction **A**lgorithm
MIRC	**M**ichigan **I**nfra**R**ed **C**ombiner
MCF	**M**utual **C**oherence **F**unction
MCM	**M**onte-**C**arlo **M**arkov
MEM	**M**aximum **E**ntropy **M**ethod
MROI	**M**agdalena **R**idge **O**bservatory **I**nterferometer
MSDF	**M**utual **S**pectral **D**ensity **F**unction
MTF	**M**odulation **T**ransfer **F**unction
NIR	**N**ear **I**nfra-**R**ed
NPOI	**N**avy **P**recision **O**ptical **I**nterferometer, formerly known as Navy Prototype Optical Interferometer and temporarily as Navy Optical Interferometer
NSR	**N**oise to **S**ignal **R**atio
OB	**O**bservation **B**lock
OIFITS	**O**ptical **I**nterferometry **FITS** Exchange Format
OPD	**O**ptical **P**ath **D**ifference
OPDC	**OPD C**ontroller
OPDZ	**O**ptical **P**ath **D**ifference **Z**ero
OPL	**O**ptical **P**ath **L**ength
OTF	**O**ptical **T**ransfer **F**unction
P2PP	**P**hase **II P**roposal **P**reparation
PACMAN	**P**RIMA **A**strometric **C**amera for **M**icro-arcsecond **A**stro**N**omy
PBS	**P**olarising **B**eam **S**plitter
PFCSGUI	**P**RIMA **F**SU **C**ontrol **S**oftware **GUI**
PFI	**P**lanet **F**ormation **I**mager
PIONIER	**P**recision **I**ntegrated **O**ptics **N**ear-infrared **I**maging **E**xpe**R**iment
PM	**P**roper **M**otion
PRIMA	**P**hase **R**eferenced **I**maging and **M**icro-Arcsecond **A**strometry
PRIMET	**PRI**MA **MET**rology
PSD	**P**ower **S**pectral **D**ensity
PTV	**P**eak **T**o **V**alley
PSF	**P**oint **S**pread **F**unction
RA	**R**ight **A**scension
RMN	**R**eflective **M**emory **N**etwork

RMS	**R**oot **M**ean **S**quare
RON	**R**ead **O**ut **N**oise
RTD Scope	**R**eal **T**ime **D**isplay **SCOP**e **GUI**
SCF	**S**elf **C**oherence **F**unction
SF	**S**ingle **F**eed
SI	**S**ystème **I**nternacional d'Unités or International System of Units
SNR	**S**ignal to **N**oise **R**atio
STRAP	**S**ystem for **T**ip-tilt **R**emoval with **A**valanche **P**hotodiodes
STS	**ST**ar **S**eparator
TMT	**T**hirty **M**eter **T**elescope
TRK	**TR**a**K**ing
UT	**U**nit **T**elescope
UV	**U**ltra-**V**iolet
VCM	**V**ariable **C**urvature **M**irror
VLBI	**V**ery-**L**ong-**B**aseline **I**nterferometry
VLT	**V**ery **L**arge **T**elescope
VLTI	**V**ery **L**arge **T**elescope **I**nterferometer
WISARD	**W**eak-phase **I**nterferometric **S**ample **A**lternating **R**econstruction **D**evice
WR	**W**olf-**R**ayet
WHT	**W**illiam **H**erschel **T**elescope
YSO	**Y**oung **S**tellar **O**bject
ZOPD	**Z**ero **O**ptical **P**ath **D**ifference

List of Symbols

A
ACU **A**lignment **C**ontrol **U**nit.
ADU **A**nalogue-to-**D**igital **U**nit.
AMBER **A**stronomical **M**ulti-**BE**am Combine**R**.
A Amplitude of a wave.
Å ångström.
ARAL **AR**tificial Source and **AL**ignment Unit.
$\mathscr{A}$ Effective area of a telescope.

B
BOB **B**roker for **O**bservation **B**locks.
$\vec{B}$ Baseline vector.

C
* Complex conjugate.

D
D Diameter of an aperture.
$\mathscr{D}$ Domain in space.
DDL **D**ifferential **D**elay **L**ine.
δ Optical path difference.
δ_{A} Atmospheric optical path difference.
$\delta_{\odot}$ Zero optical path difference.
δ_{int} Internal (instrumental) optical path difference.
$\Delta\nu$ Bandwidth or spectral width.
DL **D**elay **L**ine.
DOPDC **d**ifferential **O**ptical **P**ath **D**ifference **C**ontroller.

E
$\mathscr{E}$ Total efficiency or throughput.
E_0 Energy of a photon.
$\langle\cdot\rangle\,\mathscr{E}\{\cdot\}$ Ensemble average.
ESO **E**uropean **S**outhern **O**bservatory.

F
f Spatial frequency.
FITS **F**lexible **I**mage **T**ransport **S**ystem.

$\widehat{I}$ Fourier transform of I.
$\mathscr{F}\{\cdot\}$ Fourier transform operator.
$\mathscr{F}^{-1}\{\cdot\}$ Inverse Fourier transform operator.
$\mathscr{F}$ Fresnel number.
FSU **F**ringe **S**ensor **U**nit.
FTK **F**ringe **T**rac**K**ing.

G
$\mathscr{G}$ Grid of angular directions.
$g_i(t)$ Transmission gain *or* complex throughput in telescope i.
$\tilde{\Gamma}(\Delta t)$ Time autocorrelation function.
$\Gamma(\vec{r}, \tau)$ Self coherence function.
$\Gamma(\vec{r}_1, \vec{r}_2, \tau)$ Mutual coherence function.
$\widehat{\Gamma}(\vec{r}_1, \vec{r}_2, \nu)$ Mutual spectral density function.
$\gamma(\vec{r}, \tau)$ Complex degree of self coherence.
$\gamma(\vec{r}_1, \vec{r}_2, \tau)$ Complex degree of (mutual) coherence.
GUI **G**raphical **U**ser **I**nterface.

I
I Intensity of light.
$\mathbf{I}^+$ Generalised inverse of matrix **I**.
IRIS **I**nfra**R**ed **I**mage **S**ensor.
ISS **I**nterferometer **S**upervisor **S**oftware.

K
k Wave number.

L
L Optical path length.
ℓ_c Coherence length.
λ Wavelength.
LCU **L**ocal **C**ontrol **U**nit.
LMOT **L**inear **MOT**or.

M
MARCEL **M**ulti-beam **A**lignment **R**eference and **C**alibration IR **E**mitter for the VLTI **L**aboratory.
MIDI **MID**-Infrared **I**nterferometric Instrument.
m_K Apparent magnitude in the K band.

N
$\mathbb{N}$ Set of all integer numbers.
ν Frequency.

O
OB **O**bservation **B**lock.
OPD **O**ptical **P**ath **D**ifference.
OPDC **O**ptical **P**ath **D**ifference **C**ontroller.
OPDC GUI **O**ptical **P**ath **D**ifference **C**ontroller **GUI**.
OPDC GUI DL **OPDC GUI D**elay **L**ine.

OPL **O**ptical **P**ath **L**ength.

P

P2PP **P**hase **II** **P**roposal **P**reparation.
PACMAN **P**RIMA **A**strometric **C**amera for **M**icro-arcsecond **A**stro**N**omy.
pfcsGui **P**RIMA **F**SU **C**ontrol **S**oftware **GUI**.
ϕ Visibility phase.
ϕ_i Phase of the gain in telescope i.
PRIMA **P**hase **R**eferenced **I**maging and **M**icro **A**rcsecond **A**strometry.
PRIMET **PRI**MA **MET**rology.

Q

$\mathbb{Q}^+$ Set of all positive rational numbers.

R

r_0 Fried parameter.
$\vec{\rho}$ Position vector in the plane of observation.
$\vec{\rho'}$ Position vector in the aperture plane.
$\vec{\rho''}$ Position vector in the source plane.
$\mathbb{R}$ Set of all real numbers.
$\mathbb{R}_0^+$ Set of all non-negative real numbers.
RTD Scope **R**eal **T**ime **D**isplay **SCOP**e **GUI**.
$\vec{r} = (x, y, z)$ Position vector in space.

S

$\mathscr{S}(\vec{\rho}')$ Aperture function.
σ Standard deviation.
σ^2 Variance.
SNR **S**ignal to **N**oise **R**atio.
STS **ST**ar **S**eparator.

T

t Time.
τ Time delay.
τ_0 Atmospheric coherence time.
τ_c Coherence time.
τ_i Amplitude of the gain in telescope i.
$\mathbf{I}^T$ Transpose of matrix $\mathbf{I}$.
TRK **TR**a**K**ing.

V

$\mathscr{V}$ Fringe visibility.
V Visibility amplitude.
VLTI **V**ery **L**arge **T**elescope **I**nterferometer.
$\tilde{V} = V\,e^{i\phi}$ Complex visibility.

W

$\wp$ Set of possible telescope gains.

Y

$\upsilon(\vec{r},t)$ Optical disturbance.

Z

ZPD **Z**ero **P**ath **D**ifference.

$\mathbb{Z}$ Set of all integer numbers.

Chapter 1

Introduction

"All men have stars, but they are not the same things for different people. For some, who are travelers, the stars are guides. For others they are no more than little lights in the sky. For others, who are scholars, they are problems..."

— ANTOINE DE SAINT-EXUPÉRY (1900-1944)

Contents

STARS are one of the main subjects of interest to astronomers. They act as freely available laboratories, where physical phenomena, otherwise very difficult to reproduce on Earth, such us nuclear fusion, strong and large-scale magnetic interactions, mass ejection and planet formation (to name a few), take place. Moreover, they play an essential role as factories, producing heavy elements which are released to the interstellar medium when they die, after leaving the relatively stable *main sequence* phase.

All information known about stars comes from the electromagnetic radiation they emit. It was found that young stars are surrounded by *discs*, flattened ring-shaped masses of gas, dust and debris, from which astronomers believe planets are formed. Understanding the physical conditions and phenomena interplaying at these discs is fundamental to comprehend the formation of planets and ultimately the genesis of our own solar system. To achieve this goal, it is essential to produce sharp images of the environments surrounding young stellar objects (YSOs) from neighbouring giant molecular clouds, such as Orion and Tauri. However, this is not an easy task, even with current and forthcoming top class instruments, and special techniques ought to be developed to overcome this problem.

The need for stellar interferometry

One of the biggest challenges that astronomers have to face is the production of detailed images of faint small objects. Telescopes are characterised, amongst others, by two important parameters that limit observations: their capacity to collect light and their sharpness. The former is expressed by the telescope's *sensitivity*, while the latter is translated by its *resolution*. Both of them scale with the size of the main mirror of the telescope. The *theoretical angular resolving power* or ultimate *angular resolution* of an optical system with aperture D is given by the *Rayleigh criterion* (Roy and Clarke, 2003):

$$\theta_D \simeq 1.22\frac{\lambda}{D}, \tag{1.1}$$

where λ is the wavelength of the observed radiation.

The Earth's atmosphere is composed of several layers and cells of different refraction indices, in relative motion. The structure of the turbulence above a telescope, characterised by physical quantities such as temperature, flow velocity and humidity, is continually changing. As a result, the path followed by the light coming from a celestial body through the atmosphere takes several detours until reaching the detector, and the wavefronts associated with the progression of radiation become corrugated. Due to this turbulence, images wander randomly in the focal plane, coming in and out of focus, at a rate of about 100 times a second, thus becoming blurred. This effect, referred as *seeing*, is commonly measured by the full width at half maximum (FWHM) of the intensity across the *seeing disc*, the image of a point-like object (ibid.). The commonly referred good sites, such as Paranal, rarely report nights during the year when the seeing disc is below $0.5''$. Hence, from the resolution point of view, it would not be considered logical to build telescopes with apertures larger than a few tens of centimetres.

Adaptive optics (AO) systems allow for the partially correction of the deformations of the wavefronts, introduced by the turbulent atmosphere. By combining wavefront sensors, deformable mirrors and fast actuators, it is possible to sense the deformations and apply compensating tilts, so that wavefronts reacquire an almost planar shape again. Large telescopes of the 10 m class, using modern AO systems, have been built during the last two decades, improving both their sensitivity and effective resolution. These systems routinely allow the production of diffraction-limited imaging in the infra-red (IR), which closely match the limits set by optical theory. Examples are the twin 8 m Gemini at Mauna Kea, Hawaii, and Cerro Pachon, Chile; the Very Large Telescope (VLT) at Cerro Paranal, Chile, with four 8.2 m telescopes; the Large Binocular Telescope (LBT) on Mount Graham, USA, with two 8.4 m main mirrors; and the twin Keck 10 m telescopes on Mauna Kea, Hawaii. Optical telescopes of the 30–40 m class — the international Giant Magellan Telescope (GMT), the American Thirty Meter Telescope (TMT), and the European Extreme Large Telescope (E-ELT) — are expected to be ready by the beginning of the third decade of the current century, all employing top quality AO systems, aiming at better resolutions and much higher sensitivities than that of space telescopes.

However, the distances to stars are so great, that even with the next generation telescopes

it will be very difficult to resolve them, as well as their circumstellar environments, and make measurements of their apparent diameters out of conventional images. This limitation is overcome with the techniques of *aperture synthesis* and *stellar interferometry*, whose principles are based in Young's double slit experiment. In the former, a mask fits the telescope aperture, so that only some small areas of the main mirror collect light. The outcome is a fringe pattern formed at the focal plane. In the latter, light collected by independent telescopes separated by a distance larger than their apertures is brought together and coherently combined in a detector. If the *optical path difference* (OPD) of the beams is less than the light's coherence length, an interference pattern is produced in the detector.[1] The resolution of the information contained in the fringes is characterised not by the diameter of the telescopes, but rather by the separation between them, called the *baseline*, B:

$$\theta_B \simeq \frac{\lambda}{2B}. \tag{1.2}$$

Therefore, from eq. (1.1), the resolution given by two telescopes separated by a distance B is better than the resolution of a single telescope of diameter B (this result supports the implementation of the aperture synthesis technique). When the array is composed of large mirror telescopes separated by long baselines, the increase in resolution is matched by a corresponding gain in sensitivity. These properties make stellar interferometry an unique tool for high angular resolution astronomy.

Current facilities, such as the VLTI and CHARA, feature baselines in the range of 100 m or more, providing these interferometers with greater resolutions than the forthcoming state-of-the-art ground-based telescopes.

The origins of astronomical interferometry

The fundamental principles in the field of interferometry were mainly established by the work of Sir Thomas Young in the beginning of the 19$^{\text{th}}$ century. From his famous *Double Slit Experiment*, performed in 1802, he proved that light propagates as a wave, being thus able to interfere with itself. He also demonstrated the *Principles of Superposition* and *Coherence* (T. Young, 1804), and the *Wave Theory of Light* came to be.

In 1851, Hippolyte Fizeau designed a special interferometric device to measure the relative speed of light in moving water (Fizeau, 1851), suggesting it could be used to measure the speed of the Earth through the *luminiferous aether*. In his report on the contribution of the year 1867, he suggested that an interferometer could be used to measure the angular diameters of stars (Fizeau, 1868).

In 1887, Michelson and Morley performed the most famous "failed experiment" in the history of Physics, when, using a special interferometer arrangement, they unsuccessfully attempted to detect the relative motion of matter through the stationary luminiferous aether. The outcome of

[1] Assuming that the beams are temporarily coherent, their polarisation properties are compatible, and the relative irradiances are close in magnitude, conditions usually automatically verified in stellar interferometry.

this experiment paved the way to the theory of special relativity by Albert Einstein. By then, interferometers were already common instruments within the optical experimental framework.

The first astronomical interferometers came to life soon after the proposal by Fizeau, firstly by Edouard Stéphan in 1872, and then by Albert Michelson in 1889. The major motivation behind them was the measurement of stellar diameters. These can be inferred from the visibility of the interference fringes, which is proportional to the spatial extent of the star. The first star to have its diameter measured was the red giant Betelgeuse, in 1920, after measurements on the Mount Wilson Observatory using a Michelson stellar interferometer (Michelson and Pease, 1921). This was the first step to find the solution for one of the most paramount problems in observational astronomy, to wit, to obtain resolved images of neighbouring stars (ten Brummelaar, Tuthill and van Belle, 2013).

Astrophysics at very high angular resolution

Interesting structures and objects surrounding young stellar environments, such as planet forming regions and transitional discs, are have scales between 0.1 and 100 au from their parent star. The closest star-forming regions, such as Tauri-Auriga or Rho-Ophiuchi, are about 140 pc away from the Solar System. Therefore, modern interferometers, which can resolve objects with apparent angular sizes scaling a few milliarcseconds (mas) when working in the domain of the near and mid infra-red (respectively NIR and MIR), are able to probe, for example, the inner regions of the circumstellar environments of nearby molecular clouds. Similarly, any bright enough object with an apparent angular size in the scale of mas can be studied by modern interferometric facilities. The classical application of long baseline interferometry is the measurement of stellar diameters, as was referred in section 1.2. Other significant examples are:

- **Binary stars** — several measurements of the visibility amplitudes of a binary system (two stars orbiting around a common point) allow the derivation of the orbital parameters. When combined with spectroscopic observations, these values yield the individual masses of the stars, the inclination angle of the orbit, and the distance to the system. Successful examples illustrating this method are 12 Boötis, at a distance of 37 pc (Boden, Creech-Eakman and Queloz, 2000), β-Centauri, 102 pc from the Solar System (Davis et al., 2005), and 75 Cancri, ω Draconis, HD200077, and ι Pegasi, respectively at 31.2, 23.6, 40.6 and 11.5 pc from the Sun (Konacki et al., 2010).
- **Circumstelar discs** — present in all YSOs, they are strong emitters in the NIR and MIR bands. Spatially resolving circumstellar discs is important to understand their structures. This is traditionally achieved by means of several techniques, such as:
  - *Scattered light imaging* up to the MIR regime (McCabe, Duchêne and Ghez, 2003), which yields the overall geometry of the disc: outer radius (up to 1 000 au from the central star when instruments sensitive enough are used), inclination, surface density profiles, and vertical scale height of the dust component for edge-on discs (S. Wolf et al., 2012);

  - *Thermal emission imaging*. The central star heats the surrounding dust grains, which re-emit as grey bodies in the NIR and MIR up to 10 au, and in the far-IR (FIR) and (sub)millimetre regimes beyond that distance. Thus, high angular resolution observations in the NIR and MIR bands allow one to perceive details in the immediate vicinity of the star (ibid.).
  - *Polycyclic aromatic hydrocarbons* (PAH) observations, that provide information on the large scale structure of discs, such as flaring and vertical height (ibid.).[2]
  - *Photometric time series* in the range from the optical to the MIR, on a time scale of a few days to a few months, which yield spatial information about protoplanetary discs. Some asymmetries existing in the inner regions of the discs are translated into variable flux emitted in the aforementioned wave bands (ibid.).

  Applying baselines 100 to 200 m long, current interferometric facilities are able to spatially resolve the innermost regions (typically up to a few aus) of protoplanetary and debris discs in the optical, NIR and MIR. Some interesting examples observed by means of optical/IR long baseline interferometry are (ibid.): (*a*) Herbig Ae/Be stars (J. D. Monnier, R. Millan-Gabet et al., 2005; Vinković and Jurkić, 2007), (*b*) T Tauri stars (R. L. Akeson et al., 2005; Eisner, Hillenbrand et al., 2007), (*c*) the puffed-up form of the dusty inner rim (J. D. Monnier, J.-P. Berger et al., 2006), (*d*) the hot gas inside the dusty inner rim (Isella et al., 2008; E. Tatulli et al., 2008), (*e*) magnetospheric accretion and outflowing winds/jets with gas line observations (Eisner, J. D. Monnier et al., 2010; S. Kraus et al., 2008), and (*f*) debris discs (Buenzli et al., 2010; Lagrange et al., 2009). Recently (http://www.eso.org/public/news/eso1436/), ALMA, the ESO's Atacama Large Millimeter/submillimeter Array, produced a spectacular high-resolution image at sub-millimetre wavelengths of the circumstellar planet-forming disc around the young star HL Tauri. The disc, seen with unprecedented fine details at a resolution of about 35 mas, exhibits concentric bright rings separated by gaps, the signatures of forming planets.

- **Exoplanets** — High linear resolution images on the order of 0.1 au of the inner regions of protoplanetary discs are fundamental to unambiguously address questions related to the surface density profile and the volumetric dust distribution in the regions closer to the central star of protoplanetary discs before planet formation, and to the asymmetries in the inner few aus induced by planets in any type of discs. The signatures that (proto-)planets leave in discs after formation are easier to detect than the planets themselves and can unequivocally indicate the presence of such bodies around a star. The required high resolution images can only be achieved with long baseline interferometry — the image of HL Tauri recently produced by the Atacama Large Millimetre/sub-millimetre Array (ALMA) is a good example of that (ESO, 2014b). By using a reference star to phase the interferometer, the phase referencing technique allows for longer integration times on fainter objects, and for integrations with increased spectral resolution. This was one of the main objectives of PRIMA (F. Delplancke,

[2] PAH grains existing in the disc can be excited by the ultra-violet (UV) radiation emitted by the central star beyond 100 au in the surface layers of flared discs, common in early-type stars, such as Herbig Ae/Be stars.

2008; S. Wolf et al., 2012), and it will be achieved at the VLTI when GRAVITY is made available to the community (Eisenhauer et al., 2005). MATISSE will complement GRAVITY's observations to the MIR (Lopez et al., 2014), and data from both instruments will be used to constrain the physical conditions within 1 au of a protoplanetary disc. Astrometric detection of exoplanets is also within reach of interferometric observations, *i.e.*, the presence of companions of planetary nature is inferred from the wobbling or reflex motion of the host star due to the gravitational influence of the formers on the latter. The amplitude of the expected reflex motion of a star of mass $M_\star$, at a distance d from the Earth, having a planet of mass M_P with orbital radius R_P, is given by (S. Wolf et al., 2012):

$$\Delta\alpha = 0.33 \left(\frac{R_P}{1\,\mathrm{au}}\right) \left(\frac{M_P}{1\,\mathrm{M}_\oplus}\right) \left(\frac{M_\star}{1\,\mathrm{M}_\odot}\right)^{-1} \left(\frac{d}{10\,\mathrm{pc}}\right)^{-1} \mu\mathrm{as}. \tag{1.3}$$

It was expected that Jupiter mass planets at distances of 1 to 5 au from their parent star would be within reach of PRIMA with a precision of a few tens of uas, and it is hopped that GRAVITY will be able to detect Jupiter and Saturn mass like planets at around 1 au from their host star. Direct imaging of extrasolar planets require sub-mas angular resolutions in the optical and IR. Although challenging, it is within reach of optical interferometers whether to use the phase referencing technique or to apply high-precision differential closure phase measurements (ibid.).

- **Pulsating variable stars** — these stars exhibit periodic fluctuations in their apparent magnitude and spectrum due to expansion and contraction of their atmospheres. Pulsating variables give a great insight about physical processes taking place within stars, including their surroundings, and can be used to determine distances. There are two main intrinsic pulsating stars: *Miras* and *Cepheids*. Their positions in the *Hertzsprung-Russell diagram* (H-R diagram) are illustrated in Figure 1.1. Miras are pulsating red giants belonging to the *asymptotic giant branch* (AGB), with periods longer than 100 days and luminosity amplitudes typically ranging from 2.5 to 11 magnitudes (Ragland et al., 2006). Stellar interferometry allows to test the atmospheric models of Mira stars, by measuring their radial variations and asymmetries, and the pulsation modes. Cepheids are found on the so-called *instability strip* (Gautschy and Saio, 1996), the inclined band of the H-R diagram containing variable stars (RR Lyraes, classical Cepheids, W Virginis, and δ Scuties). These stars undergo pulsations with very regular periods, on the order of days to months. Because of this remarkable regularity, Cepheids play a crucial role in the determination of distances on the extragalactic scale up to several Mpc, acting as standard candles. Their distance can be inferred from the Period-Luminosity relation (*P-L* relation) or *Leavitt's law*, from which other distance indicators (such as super-novae) and the Hubble constant H_0 can be calibrated. The *P-L* relationship, in turn, is traditionally calibrated by the *parallax pulsation technique* or *Baade-Wesselink method* (Mérand, P. Kervella and Gallenne, 2009), in which the angular size and the pulsational velocity of the surface of the star are measured. From them, distances to Cepheids are directly estimated. The accuracy with which these distances are determined are important for

the cosmological distance ladder and for the perception of the whole scale of the Universe. Long baseline optical interferometry can yield measurements of these parameters with great accuracy, as it has been performed to several nearby Cepheids by, for example, P. Kervella, (2006), P. Kervella et al., (2004) and Mérand, P. Kervella, Coudé du Foresto et al., (2005).

Outline of the manuscript

This manuscript is divided into four main parts: the *introduction*, *phase referenced interferometry*, *interferometric image reconstruction* and the *conclusions*.

Chapter 2 focus on fundamental concepts in the realm of optical interferometry. The motivation for astronomical interferometry, the concepts of coherence and complex visibility, and the van Cittert-Zernick theorem are introduced on the basis of Young's double slit experiment.

Parts II and III, respectively related to phase referencing and image reconstruction, are the main blocks of the text, being organised as follows:

- Chapter 3 describes PRIMA, the dual-feed facility of ESO, as well as its main subsystems.
- Chapter 4 explains the concept of angular anisoplanatism, and outlines the estimation of visibility amplitudes by the FSUs, the fringe sensor units of PRIMA.
- Chapter 5 highlights PRIMA's operation modes, with particular emphasis to the faint object science mode.
- Chapter 6 pertains to the principles behind interferometric image reconstruction. Several reconstruction algorithms in the radio and optical domains are described, and the state of the art is presented.
- Chapter 7 introduces the tools needed for interferometric data simulation, with emphasis given to the noise models and the quantification of the quality of restored images.
- Chapter 8 is dedicated to the comparison between two popular and distinct scenarios in the realm of interferometric image reconstruction: *phase referencing* and *closure phase*. The strengths and weaknesses of each scenario are highlighted for different observational configurations.
- Chapter 9 summarises the results collected in the framework of this thesis and the conclusions, both in the domain of PRIMA and of image reconstruction. Future directions, applications and prospects for PRIMA commissioning data and interferometric image reconstruction studies are also discussed.

In the appendices, appendix B demonstrates, by means of mathematical induction, that the total number of linearly independent triangles in an array of n telescopes is equal to $(n-1)(n-2)/2$. Appendix C proves that the phase difference between the two beams of any of the two FSUs which emerge from PRIMA's beam combiner is π. Appendix D illustrates the FSU operation manual, which was written during 5 PRIMA commissioning runs at Paranal — this document provides a compendium of calibration and fringe tracking operation steps of the PRIMA FSUs, both in single- and dual-feed modes. The manuscript is finalised with appendix E, describing GalileoMobile, an international outreach programme.

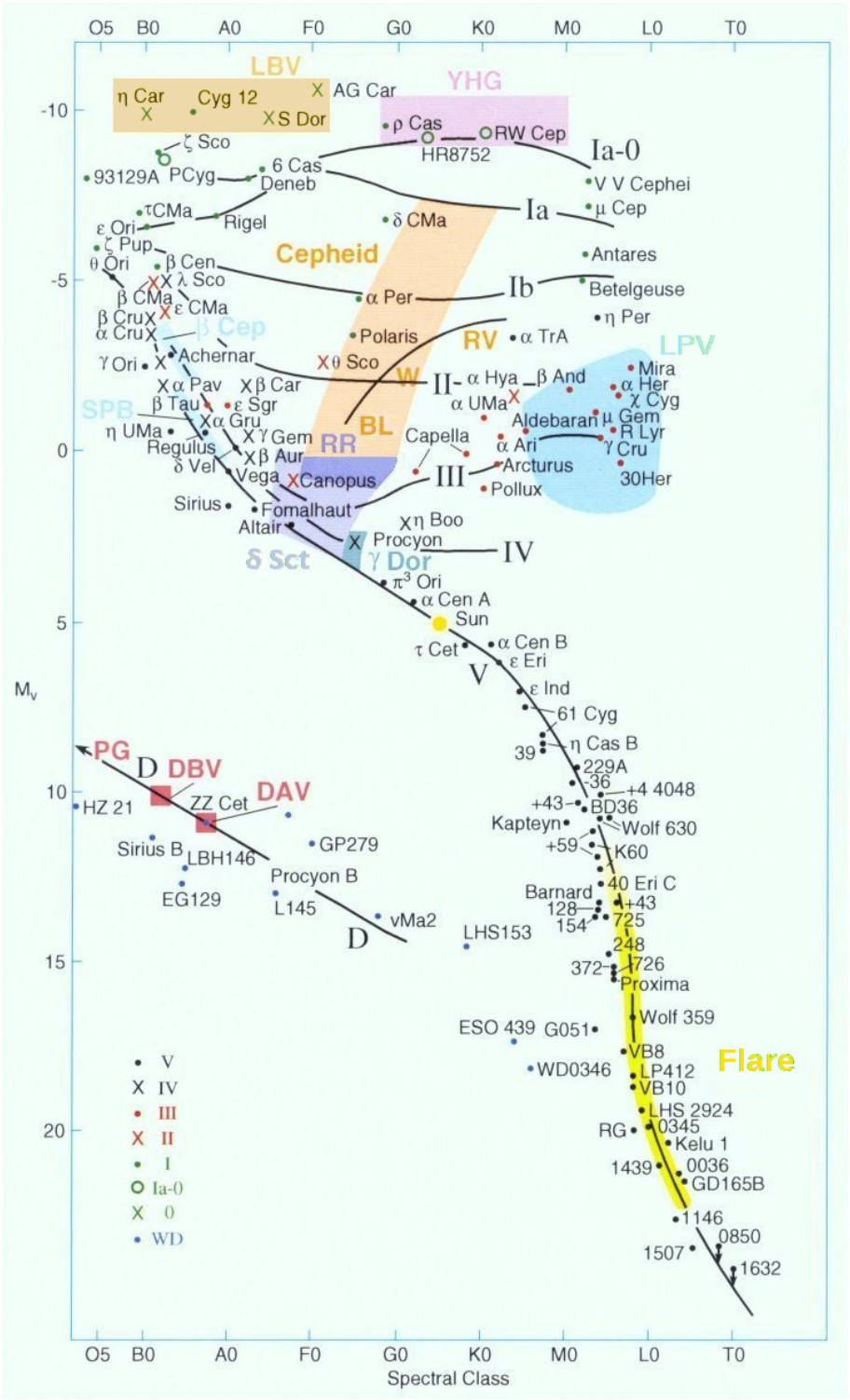

Figure 1.1: Hertzsprung-Russel diagram of variable stars. Stars are graphed according to their absolute visual magnitude and spectral class. The MKK (Morgan-Keenan-Kellman) luminosity classes, designated by a Roman numeral, are the following (Carroll and Ostlie, 2007): Ia-O (*extreme, luminous supergiants or hypergiants*), Ia (*luminous supergiants*), Ib (*less luminous supergiants*), II (*bright giants*), III (*normal giants*), IV (*subgiants*), V (*main-sequence (dwarf) stars*), VI/sd (*subdwarfs*, not represented in the diagram), and D (*white dwarfs, indicated by WD in the figure*). The inclined orange-yellow band above the middle of the figure indicate the *instability strip*, which includes several types of variable stars, such as the *classical Cepheids*. Right to the Cepheids the group of *long period variables* (LPV) is found, which includes *Mira* stars. From the *Cambridge Encyclopedia of Stars* (Kaler, 2006).

Part I

Theoretical Background

Chapter 2

Long Baseline Optical Interferometry

We can imagine that this complicated array of moving things which constitutes "the world" is something like a great chess game being played by the gods, and we are observers of the game. We do not know what the rules of the game are; all we are allowed to do is to watch the playing. Of course, if we watch long enough, we may eventually catch on to a few of the rules.

— RICHARD FEYNMAN, *The Feynman Lectures on Physics*

Contents

THIS CHAPTER pertains to the fundamental concepts about optical (visible/IR) interferometry, which are thoroughly used in the subsequent chapters of the thesis. The motivation behind the usage of astronomical interferometry and basic notions related to the combination of electromagnetic waves are provided in section 2.1. Section 2.2 introduces the ideas of *coherence* and *complex visibility*, leading to the *van Cittert-Zernick theorem*, and having the Young's experiment as a supporting background. Finally, section 2.3 débuts the *coaxial* and *multiaxial combination schemes*, as well as the *ABCD method*, and the importance of photometric calibration.

The adopted approach is highly inspired in the book "Principles of Stellar Interferometry" (A. Glindemann, 2011), and in the school notes "Principles of Long Baseline Stellar Interferometry" (Lawson, 2000), which are excellent self-containing texts for those being introduced to the subject of optical interferometry.

Interference with two apertures

Interferometry is a technique in which light waves are superimposed and recombined — under conditions to be explained in what follows — in order to increase the resolution and, thus, to extract information from the sources that otherwise is inaccessible. The recombination of the sampled wavefronts yield interference *fringes*, that exhibit bright and dark bands, depending on weather the wavefronts constructively add their amplitudes or destructively cancel them. The bands resulting from constructive interference are brighter than the sum of intensities of the individual wavefronts. The interference patterns are fixed by the correlation of the amplitudes of the wavefronts and, hence, this is also called *amplitude interferometry* (A. Glindemann, 2011).[1]

An *astronomical interferometer* is an array of separated apertures (telescopes) — two, at least — that simultaneously observe the same object and redirect its light to the spot where interference fringes are produced. The reason to move from a single aperture to a diluted array of telescopes separated by more than their own sizes is related to the fact that a single (large) telescope is not capable to resolve the disc of most of the stars and other objects of astrophysical interest (Saha, 2011), simply because they are located too far away. This leads to the notion of *angular resolution*, already introduced in eq. (1.1):

$$\theta \approx \frac{\lambda}{L} \tag{2.1}$$

where λ is the wavelength of the observed radiation and L is a characteristic length (diameter of a telescope, distance between two telescopes, size of a turbulent cell in the atmosphere, etc.). The angle θ measures the *spatial resolution* and the smaller it is, the finer the details that can be observed.

In terms of angular resolution, the array performs no worse than a wide telescope of diameter equal to the largest separation between all the apertures. When the interferometric data is used to produce reconstructed images, the technique is called *aperture synthesis*. However, the increase in resolution is achieved at the expense of losing sensitivity because, on the one hand, the array is not able to collect as many photons as a telescope with a diameter encompassing the collection of telescopes and, on the other hand, the multitude of mirrors and lenses needed to "coherently" combine the light and produce the interference pattern dramatically decrease the final flux. Therefore, special instruments and techniques needed to be developed in order to minimise that effect.

[1] There is the *intensity interferometry* as well, measuring the correlation of intensities in each telescope, which is based on the *Hambury Brown and Twiss effect* (Hanbury Brown and Twiss, 1956). Although less challenging in terms of technology and precision, intensity interferometers are less sensitive than their amplitude counterparts.

Preliminary definitions

The electromagnetic waves emitted by astronomical objects encompass an electric field vector $\vec{E}$ and a magnetic field vector $\vec{H}$,[2] perpendicular to each other and both to the direction of propagation of the waves. The external product between both vectors yields the *Poynting vector*, $\vec{S} = \vec{E} \times \vec{H}$, which represents the *energy flux density* and indicates the direction of propagation of light. In Astronomy, the time average of the Poynting vector, $\langle \vec{S} \rangle$, is known as the *flux*, in units of $\mathrm{W\,m^{-2}}$. The signal an optical detector is able to measure is the *power* (in units of W), which corresponds to the integral of the flux over the collecting area of the detector.

For clarity and simplicity, most of the subsequent concepts will be introduced by means of dimensionless quantities. This choice is justified by the fact that the measure of interest is most importantly the spatial distribution of the flux rather than its absolute value.

Considering that the electromagnetic field is propagating along the z-direction, the *monochromatic optical disturbance* $\upsilon(z,t)$ is defined as a dimensionless scalar proportional to one of the two components of the electric or the magnetic field, *e.g.*, E_x:

$$\upsilon \propto E_x. \tag{2.2}$$

The constant of proportionality is chosen in order to make υ dimensionless. The optical disturbance is usually a complex quantity (although only the real part represents the electromagnetic wave), and it is the base scalar from which other quantities are going to be defined. When the optical system is linear, the wave coming out of it is given by the product of the optical disturbance and the complex *transfer function*.[3] For a monochromatic plane wave propagating in the z-axis, the optical disturbance is given by

$$\upsilon_\lambda(z,t) = \upsilon_0\, \mathrm{e}^{-\mathrm{i}(\omega t - kz)}, \tag{2.3}$$

where $\omega = 2\pi\nu$ is the *angular frequency*, ν is the *frequency* of the radiation, t is the time, $k = 2\pi/\lambda$ is the *wave number*, and λ is the *wavelength* of the monochromatic wave.[4]

The *intensity* can be defined as a dimensionless quantity proportional to the flux and, thus, to the detected power:

$$I(z) \equiv \lim_{T\to\infty} \frac{1}{2T} \int_{-T}^{T} \upsilon(z,t)\,\upsilon^*(z,t)\,\mathrm{d}t = \upsilon_0^2. \tag{2.4}$$

The *amplitude* of the wave, $A(\vec{r})$, is defined so that

$$\upsilon(\vec{r},t) = A(\vec{r})\,\mathrm{e}^{-\mathrm{i}\omega t}. \tag{2.5}$$

[2] Throughout this thesis, it is always assumed that media are isotropic.

[3] The transfer function represents the relation between the input and the output of a linear and shift-invariant system with no initial conditions and zero-point equilibrium. It describes the attenuation and the phase shift experienced by the electromagnetic wave in passing through the optical system (Gaskill, 1978).

[4] The subscript λ in υ_λ indicates that the quantity is monochromatic. However, a polychromatic version of the optical disturbance will be defined in what follows. Whether one is talking about the monochromatic or the polychromatic version of the quantity is easily understandable from the context. Therefore, from now on, the subscript will be removed for improved readability.

Hence, from eq. (2.4),

$$I(\vec{r}) = |A(\vec{r})|^2. \tag{2.6}$$

For polychromatic radiation, the principle of superposition allows one firstly to consider the propagation of light in the monochromatic case, and then to integrate over all frequencies of the spectra. This leads to the concepts of *polychromatic optical disturbance*, $\upsilon(\vec{r},t)$, *spectral amplitude*, $A(\vec{r},\nu)$ and *spectral intensity*, $I(\vec{r},\nu)$, respectively defined by

$$\upsilon(\vec{r},t) = \int_0^\infty A(\vec{r},\nu)\,\mathrm{e}^{-\mathrm{i}2\pi\nu t}\,\mathrm{d}\nu \tag{2.7}$$

and

$$I(\vec{r}) = \int_0^\infty I(\vec{r},\nu)\,\mathrm{d}\nu. \tag{2.8}$$

The last equation is only valid because optical detectors measure the power as a time average (A. Glindemann, 2011).

An important concept for the theory of coherence (explored in section 2.2.1) is the one of autocorrelation function. The *time autocorrelation function*, $\tilde{\Gamma}$, of a function $u(t)$ depending only on time (for instance, a sample function of a random process), is defined by (J. W. Goodman, 2000)

$$\tilde{\Gamma}(\Delta t) \doteq \langle u(t+\Delta t)u(t)\rangle = \lim_{T\to\infty}\frac{1}{2T}\int_{-T}^{T} u(t+\Delta t)u(t)\,\mathrm{d}t. \tag{2.9}$$

The physical importance of this function resides on the fact that it measures the structural similarity of the function $u(t)$ at two different times.

Young's interference experiment

In 1801, the English polymath Thomas Young conducted a fundamental experiment in optics demonstrating interference phenomena, that became a cornerstone for the theory supporting the wave nature of light (*e.g.*, D. S. Goodman, 1994; J. W. Goodman, 1996). Young built an apparatus consisting of a pinhole emanating quasi-monochromatic light that illuminated an opaque screen, positioned at a large distance from the light source and containing two very small holes or slits, and a target screen after it, where light interfered and a diffraction pattern was observed (T. Young, 1807). The geometry of the experiment, which is illustrated in fig. 2.1, is very helpful to introduce the concepts that follow. The light source is located at a large distance from the first screen, so that the electromagnetic waves illuminating the *pinholes* can be regarded approximately as plane waves. The two apertures are small enough in order to simulate point sources,[5] producing semi-spherical wavefronts by diffraction, that propagate towards the viewing screen, where they interfere constructively or destructively, depending on the magnitude of the OPD δ between the optical paths

[5]More precisely and in light of the scalar diffraction theory presented in section 2.1.3, a *pinhole* is an aperture so narrow that, for small diffracting angles, the diffracted wave is equivalent to a single spherical wave originated at the aperture (A. Glindemann, 2011).

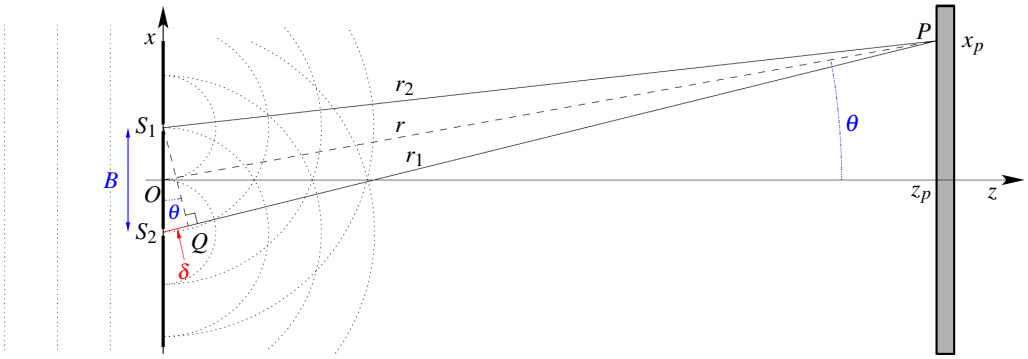

Figure 2.1: The geometry of Young's experiment. The OPD δ is indicated by the red line joining S_2 and Q. The coordinates of P are (x_p, z_p). Because the distance z_p is large when compared to B, the angle $\angle QS_1S_2$ is approximately equal to θ (adapted from ibid.).

from each pinhole source to the observing point.[6] The distance between the two screens, z_p, must be large when compared to the separation between the pinholes, B, which is known as the (geometric) *baseline* (the distance $\overline{S_1Q}$ is known as *projected* or *effective baseline*).

The OPD δ for an observing point P at position x_p or angle θ, indicated by the red line joining the source S_2 and the point Q, is given by

$$\text{OPD} = \delta = \overline{S_2P} - \overline{S_1P}. \tag{2.10}$$

Since z_p is much larger than B, the distances $\overline{S_2P}$ and $\overline{S_1P}$ are approximately equal, and the OPD is

$$\delta \simeq \overline{S_2Q} \simeq B \sin\theta \simeq B\,\theta \simeq B\frac{x_p}{z_p}. \tag{2.11}$$

A bright fringe occurs when there is constructive interference, *i.e.*, when the OPD is a multiple of the wavelength ($\delta_\text{b} = m\lambda$, with $m \in \mathbb{Z}$). Hence, a bright fringe will be visible in every point x_b such that

$$x_\text{b} = m\frac{\lambda\, z_p}{B}. \tag{2.12}$$

A dark fringe, on the other hand, is found when there is destructive interference, which occurs when the path difference between the two waves is a multiple of half the wavelength, *i.e.*, for $\delta_\text{d} = \left(m + \frac{1}{2}\right)\lambda$, with $m \in \mathbb{Z}$. Thus the points of dark fringes have coordinates x_d such that

$$x_\text{d} = \left(m + \frac{1}{2}\right)\frac{\lambda\, z_p}{B}. \tag{2.13}$$

The first dark fringe is found for $m = 0$, *i.e.*, for

$$\delta_\text{min} = \frac{\lambda}{2} = B\theta_\text{min}. \tag{2.14}$$

[6] The idea of adding two light beams to produce darkness under the right conditions was radical and revolutionary by the time of Young, and the matter was settled not before Arago performed a detailed *experimentum crucis* in 1818, where the Poisson-Arago spot could be observed (*e.g.*, Fresnel, 1866; D. S. Goodman, 1994).

Then, for a baseline B, the resolution R of an interferometer is

$$R = \theta_{\min} = \frac{\lambda}{2B}. \tag{2.15}$$

This equation, which lies on the basis of the theory of interferometry, justifies the use of an interferometer of baseline B instead of a monolithic telescope with diameter B for high angular resolution astronomy (*cf.* section 1.1, page 3).

The spectral amplitude A of a spherical wave at a distance $r = |\vec{r}|$ is

$$A(\vec{r}, \nu) = \frac{A_0}{r} \mathrm{e}^{\mathrm{i}kr}. \tag{2.16}$$

By the principle of superposition, the amplitude in a point P is the sum of the amplitudes of the two spherical waves originating at the secondary sources (pinholes):

$$A(x_p, \nu) = \frac{A_0}{r_1} \mathrm{e}^{\mathrm{i}kr_1} + \frac{A_0}{r_2} \mathrm{e}^{\mathrm{i}kr_2}, \tag{2.17}$$

which, taking $r_{1,2} \simeq z_p$ simplifies to

$$A(x_p, \nu) = 2\frac{A_0}{z_p} \mathrm{e}^{\mathrm{i}k\frac{r_1+r_2}{2}} \cos\left(k\frac{r_1 - r_2}{2}\right). \tag{2.18}$$

From eqs. (2.6), (2.10) and (2.11), the spectral intensity is given by

$$I(\theta, \nu) = 2\left(\frac{A_0}{z_p}\right)^2 [1 + \cos(k\,\theta\,B)] \propto [1 + \cos(k\,\theta\,B)]. \tag{2.19}$$

Because the maxima of the cosine function are distributed in the two-dimensional viewing screen, the resulting intensity fringes are also known as the *fringe pattern*. Its contrast can be quantified by the *fringe visibility*, $\mathscr{V}$, a normalised quantity defined by Michelson, (1920) as:

$$\mathscr{V} = \frac{I_{\max} - I_{\min}}{I_{\max} + I_{\min}}. \tag{2.20}$$

The arrival time difference corresponding to the OPD between the light emanating from the two pinholes is called the *time delay*, τ, and it is equal to

$$\tau = \frac{\theta B}{c}, \tag{2.21}$$

where c is the speed of light in vacuum ($c = 2.997\,924\,58 \times 10^8\,\mathrm{m\,s^{-1}}$).

The combination of the three last equations allows one to conclude that the fringe contrast $\mathscr{V}$ is reduced with increasing time delay τ, *i.e.*, with greater OPD $\delta = \theta B$.

Scalar theory of diffraction

The scalar diffraction theory can be directly derived from the Maxwell's equations. In what follows, light is described by classical electrodynamics, and two approximations are assumed: (*i*) polarisation is disregarded and, thus, light is treated as a scalar quantity, and (*ii*) the propagation of the two orthogonal components of the electric field are considered independent. The latter is valid when the wavelength is much smaller then the diffracting aperture and when the plane of observation lies far enough from the aperture, two conditions easily satisfied in astronomical telescopes. For the following analysis, only the space between the aperture and observation planes is of interest, and the incoming wave is assumed plane with amplitude $A(\vec{\rho}\,') = A_0$, where $\vec{\rho}\,'$ is a position vector in the aperture plane.

The *Huygens construction* — the *wavefront*[7] after diffraction in the aperture is the result of the superposition of elementary spherical waves (called *wavelets*) originated in each point of the aperture — was extended by Fresnel in order to account for interference, by postulating that the secondary wavelets mutually interfere. The combination of Huygens' construction with Fresnel's principle on interference is known as the *Huygens–Fresnel principle*, and it is summarised in the *Rayleigh–Sommerfeld diffraction formula*, which describes the propagation of the amplitude A in space after traversing an aperture Ξ (J. W. Goodman, 1996):

$$A(\vec{\rho}) = \frac{1}{\mathrm{i}\lambda} \iint_{\Xi} A(\vec{\rho}\,') \frac{\mathrm{e}^{\mathrm{i}kr}}{r} \mathrm{d}\vec{\rho}\,', \tag{2.22}$$

where $A(\vec{\rho}\,')$ is the amplitude of the incoming wave and $\vec{\rho}$ is a position vector in the plane of observation (*cf.* fig. 2.2). Compared to the incident wave, and due to the diffraction at the aperture

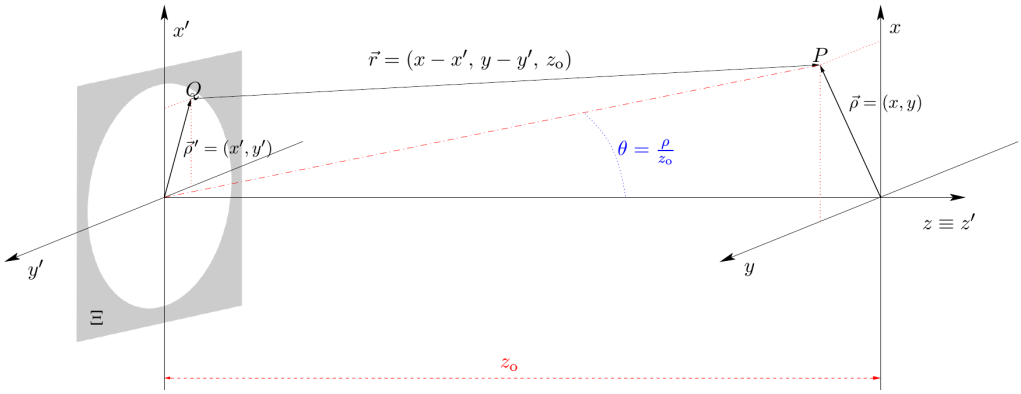

Figure 2.2: The geometry for the diffraction at an aperture Ξ. The axis x' and y' define the *aperture plane*, x and y define the *plane of observation*, $\rho = |\vec{\rho}\,|$, and $z \equiv z'$ is the *optical axis* (adapted from ibid.).

itself, the amplitude of the spherical diffracted wave is reduced by $1/\lambda$ and its phase is shifted by $-\pi/2$.

[7] The locus of points having the same phase as the propagating wave.

Using the *Fresnel approximation*

$$r \simeq z_0 + \frac{|\vec{\rho} - \vec{\rho}\,'|^2}{2z_0}, \tag{2.23}$$

eq. (2.22) reduces to the *Fresnel diffraction integral* for the *near-field* (J. W. Goodman, 1996):

$$A(\vec{\rho}) = \frac{1}{\mathrm{i}\lambda z} \iint_{-\infty}^{+\infty} A_{\mathrm{ap}}(\vec{\rho}\,')\, \mathrm{e}^{\mathrm{i}k\frac{|\vec{\rho}\,'|^2}{2z}}\, \mathrm{e}^{-\mathrm{i}k\frac{\vec{\rho}\cdot\vec{\rho}\,'}{z}}\, \mathrm{d}\vec{\rho}\,', \tag{2.24}$$

where z_0 was replaced by z, $A_{\mathrm{ap}} = \mathscr{S}(\vec{\rho}\,')A(\vec{\rho}\,')$ is the *amplitude in the aperture* and $\mathscr{S}(\vec{\rho}\,')$ is the *aperture function*. The aperture function encompasses the shape of the aperture Ξ in its module and optical aberrations in its phase (A. Glindemann, 2011). When the phase of the aperture function is nil, the optical system is said *diffraction limited*, and it is able to produce images with an angular resolution imposed only by the theoretical limit.

The *field regime* can be specified by the dimensionless parameter

$$\mathscr{F} = \frac{a^2}{\lambda z}, \tag{2.25}$$

known as the *Fresnel number*, where a is the characteristic size (radius) of the aperture. $\mathscr{F} \gtrsim 1$ corresponds to the *near-field regime* (Fresnel diffraction), while $\mathscr{F} \ll 1$ produces the *far-field regime*, for which $|\vec{\rho}\,'|^2/(2z) \ll \lambda$, *i.e.*, when the plane of observation is located at very large distances from the aperture.[8] The latter corresponds to the *Fraunhofer diffraction*, whose diffracted wave's amplitude or diffraction pattern, when viewed at a long distance from the aperture, is given by (J. W. Goodman, 1996)

$$A(\vec{\rho}) = \frac{1}{\mathrm{i}\lambda z} \iint_{-\infty}^{+\infty} A_{\mathrm{ap}}(\vec{\rho}\,')\, \mathrm{e}^{\frac{-\mathrm{i}k\vec{\rho}\cdot\vec{\rho}\,'}{z}}\, \mathrm{d}\vec{\rho}\,', \tag{2.26}$$

known as the *Fraunhofer diffraction integral*.

In the particular case when the observation point is located at the focal plane of a lens, $z = F$ and $\vec{\theta} \simeq \vec{\rho}/F$, yielding a form of eq. (2.26) that describes the situation in a telescope (Born and E. Wolf, 2003):

$$A(\vec{\theta}) = \frac{1}{\mathrm{i}\lambda F} \iint_{-\infty}^{+\infty} A_{\mathrm{ap}}(\vec{\rho}\,')\, \mathrm{e}^{-\mathrm{i}k\vec{\theta}\cdot\vec{\rho}\,'}\, \mathrm{d}\vec{\rho}\,' = \frac{1}{\mathrm{i}\lambda F}\, \mathscr{F}\{A_{\mathrm{ap}}(\vec{\rho}\,')\}, \tag{2.27}$$

where $\mathscr{F}\{\cdot\}$ denotes a Fourier transform. Hence, the application of the Huygens-Fresnel principle to an aperture states that, in the far-field regime, the diffraction pattern is the spatial Fourier transform of the shape of the aperture.

If the optical system can be considered linear, than the diffraction pattern corresponds to the response of the system to an optical impulse. When the source is point like, *i.e.*, *unresolved*, the response of the imaging system is called the *point spread function* (PSF). The PSF is a measure

[8] For $\mathscr{F} \gg 1$, the laws of geometrical optics can be applied.

of the imaging quality of the system, in the sense that it represents the spread of the brightness distribution in the focal plane, and it characterises the interplay between the diffraction of light and the degree of aberrations introduced by the system.

Owing to diffraction, for telescopes with circular apertures the image of an unresolved source, *i.e.*, the brightness distribution of a diffraction limited PSF is not a point but a disc surrounded by bright and dark rings called the *Airy pattern*. Its first minimum happens for $\theta_{\text{min}} \simeq 1.22\lambda/D$, where D is the diameter of the telescope. This angle is often used to estimate the angular resolution of an optical system: two unresolved objects are considered just resolved when the first minimum of the Airy pattern of one coincides with the diffraction maximum of the other. In honour of Lord Rayleigh, who first stated it, this is known as the *Rayleigh criterion* for resolution of a telescope (ibid.).[9]

Two telescopes interferometer

An astronomical interferometer is obtained by *coherently* combining the light collected by at least two telescopes, simultaneously observing the same celestial object. The most common configuration for optical interferometry is the Michelson interferometer (Schöller, 2000), which was used in 1887 by Albert Michelson and Edward Morley in an experiment to attempt the detection of the relative motion of matter through the postulated stationary *luminiferous aether* (or "*aether wind*").[10] This is an interferometer based on amplitude division, commonly used to measure the *temporal coherence* of a source, *i.e.*, the correlation of the light with itself at different moments in time (Saha, 2011). fig. 2.3 illustrates the basic schematics of this interferometer, where it can be seen that coherent light emitted by a source is split in two different paths and later recombined, in order to produce an interference pattern.

The study of the *spatial coherence* of light, *i.e.*, the correlation between two light waves at different points in space, can be done with the Young's experiment, already described in section 2.1.2 (ibid.).

Astronomical interferometers are used to measure both the spatial and temporal characteristics of the electromagnetic radiation emitted by a celestial body. The mirrors M_1 and M_2 in fig. 2.3 correspond to the telescopes or apertures of the array observing one same object, which is represented by the points b and c in the aforementioned figure.

One of the first astronomical interferometers was the *Michelson stellar interferometer*, which is schematically depicted in fig. 2.4. The apparatus was built on the Mount Wilson Observatory's reflector telescope, and it produced the first scientific results in 1920, by measuring the diameter of the red giant star Betelgeuse (α *Orionis*).[11] In order to achieve that goal, the fringe visibility of the source and, thus, the coherence of the star, was inferred from the distance between the siderostats,

[9] Other less conservative resolution criteria, like the *full width at half maximum* (FWHM) one, which defines $\theta_{\text{min}} = \theta_{\text{FWHM}} = \lambda/D$ are also commonly used to determine the minimum resolvable distance of a telescope.

[10] The negative results of the experiment (Michelson and Morley, 1887) destroyed the theory supporting the need of a medium for the propagation of light and ultimately led to the emergence of the special theory of relativity.

[11] The angular diameter of Betelgeuse was found to be equal to $0''.047$ (Michelson and Pease, 1921).

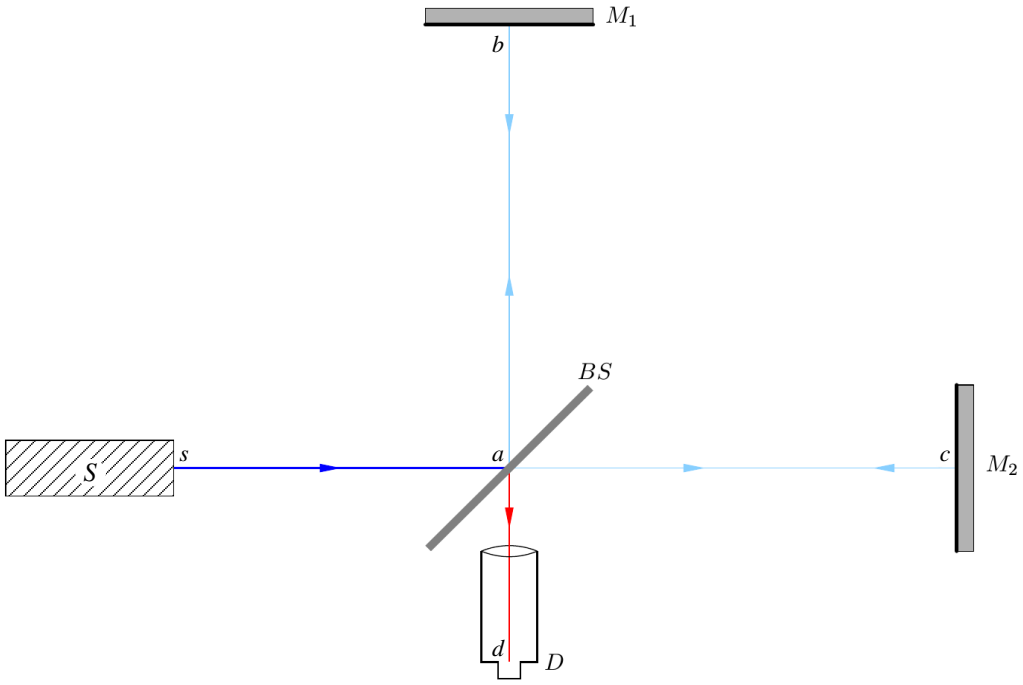

Figure 2.3: Schematics of Michelson's interferometer. The beam of light sa, emitted by the coherent light source S, is partially reflected and partially transmitted in the beam splitter BS. The reflected part ab is reflected by mirror M_1 along the path ba, being partially transmitted along ad, and the transmitted part is returned by mirror M_2 along ca, which in turn is partially reflected along ad. When the paths ab and ac are equal, both beams recombine at a and interfere along ad, producing an interference pattern observable by the detector D (adapted from Michelson and Morley, 1887).

B. Coherence is a central concept in interferometry, and it is going to be explored in the following subsections.

Coherence functions

The notion of *coherence* is intimately related to the interference phenomena, and it can be defined as the property of waves to produce stationary interference, *i.e.*, to create a constant fringe pattern in time and space. Coherent light has the ability to produce fringes, like the ones in Young's experiment, with good contrast. The *coherence function* is a dimensionless mathematical tool that allows one to quantify the coherence of light. It can assume several forms, but it is generally defined as the correlation function of the optical disturbance v, and it can be measured by optical detectors (A. Glindemann, 2011). High values of the coherence function correspond to fringes with good contrast in interference phenomena.

Mutual coherence and self coherence functions

The *mutual coherence function* (MCF), Γ, corresponds to the correlation function or the second order moment of the optical disturbance v at times $t_1 = t$ and $t_2 = t + \Delta t$ and at positions ρ_1 and ρ_2

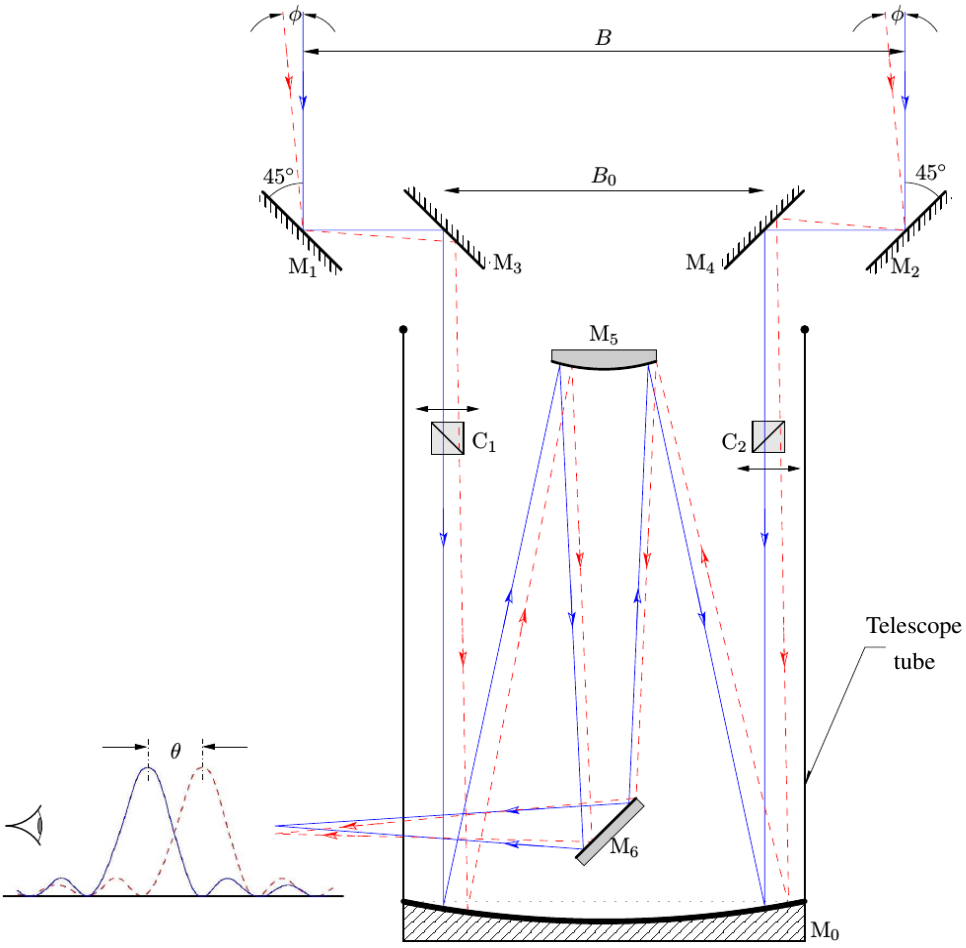

Figure 2.4: Schematics of Michelson stellar interferometer, mounted at the 100-inch (2.54 m, M_0) telescope at Mount Wilson, as per 1920 (adapted from Michelson and Pease, 1921; Saha, 2011). The outer mirrors M_1 and M_2 are siderostats, while M_3 and M_4 are fixed to the structure. The distances between M_1 and M_3, and M_4 and M_2 are kept equal to each other. The fringe visibility of the star is controlled by the distance B between the siderostats, and, thus, from B the coherence of the source can be inferred. The fringe spacing θ is controlled by the smaller separation between M_3 and M_4. The plane parallel glass plate and/or opposite glass wedges C_1 and C_2 can be tilted and/or moved allowing the equalisation of the optical paths between the two beams and effectively making the wavefronts parallel at the entrance pupil (Saha, 2011).

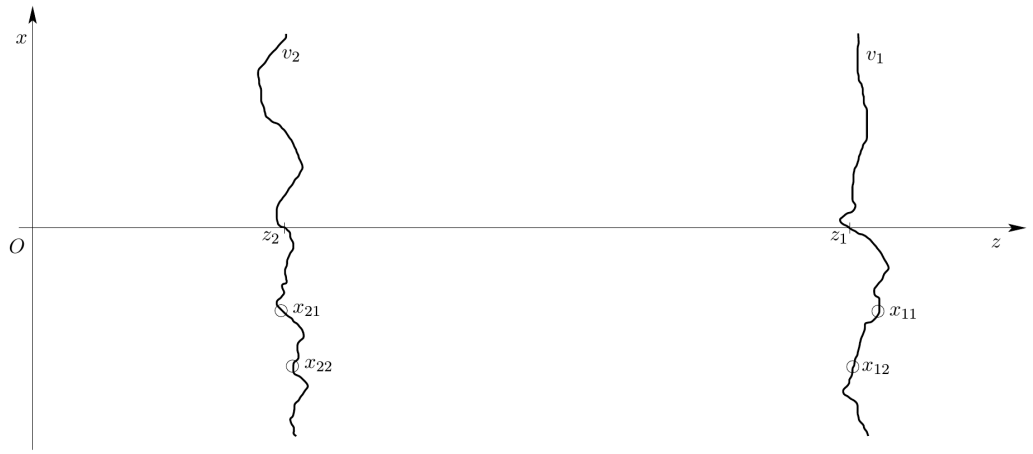

Figure 2.5: Conceptual representation of the propagation of light as an ergodic random process. The two wavefronts were emitted at times t and $t+\Delta t$ from a very distance source, and, therefore, they are viewed at different positions on the z-axis. Each wavefront corresponds to an individual realisation or ensemble member of the random emission process, where the random variable is the optical disturbance v (adapted from ibid.).

in the wavefront (*e.g.*, at the locations of two telescopes):

$$\Gamma(\vec{\rho}_1, \vec{\rho}_2, \Delta t) = \lim_{T\to\infty} \frac{1}{2T} \int_{-T}^{T} v(\vec{\rho}_1, t+\Delta t) v^*(\vec{\rho}_2, t)\, \mathrm{d}t \tag{2.28a}$$

$$= \langle v(\vec{\rho}_1, t+\Delta t) v^*(\vec{\rho}_2, t)\rangle \tag{2.28b}$$

$$= \mathscr{E}\{v(\vec{\rho}_1, t+\Delta t) v^*(\vec{\rho}_2, t)\}, \tag{2.28c}$$

where the integration time T is taken longer than the periodically oscillation of the electromagnetic wave, *i.e.*, $T \gg 1/\nu$,[12] and $\mathscr{E}\{\cdot\}$ denotes an ensemble average. The equality between eqs. (2.28a) to (2.28c) stems from the ergodicity of the propagation of light (A. Glindemann, 2011; J. W. Goodman, 2000), from now on regarded as a random process (*cf.* fig. 2.5).

When $\vec{\rho}_1$ and $\vec{\rho}_2$ coincide in space, the MCF is called the *self coherence function* (SCF, $\tilde{\Gamma}$, J. W. Goodman, 2000; Saha, 2011):

$$\tilde{\Gamma}(\vec{\rho}, \Delta t) = \Gamma(\vec{\rho}, \vec{\rho}, \Delta t) = \langle v(\vec{\rho}, t+\Delta t) v^*(\vec{\rho}, t)\rangle. \tag{2.29}$$

Therefore, from eq. (2.9), the SCF matches the autocorrelation of the optical disturbance when viewed at a fixed point $\vec{\rho}$, and it is a measure of the temporal coherence of the emitting source.

From eq. (2.4), it is straightforward to conclude that the ordinary intensity of light incident on the point $\vec{\rho}$, $I(\vec{\rho})$, corresponds to the MCF calculated at two identical points of space and for a given time, *i.e.*, it is the same as the SCF for $\Delta t = 0$:

$$I(\vec{\rho}) = \Gamma(\vec{\rho}, \vec{\rho}, 0) = \tilde{\Gamma}(\vec{\rho}, 0) = \lim_{T\to\infty} \frac{1}{2T} \int_{-T}^{T} v(\vec{\rho}, t+\Delta t) v^*(\vec{\rho}, t)\, \mathrm{d}t. \tag{2.30}$$

It is normal that the intensity varies for any two different pairs of points in a wavefront, which

[12] This condition is necessary for ergodicity. The other condition that need to be assumed for the process to be ergodic is that it must be stationary in time (J. W. Goodman, 2000).

yields a variable MCF. This fact prevents one to estimate the probability to measure the same value of intensity, *i.e.*, the *pure correlation* of optical disturbances. In order to achieve that, a normalised quantity, the *complex degree of (mutual) coherence* or *complex correlation coefficient* of optical disturbances, γ, is defined as the MCF normalised by the intensities at the locations $\vec{\rho}_1$ and $\vec{\rho}_2$:

$$\gamma(\vec{\rho}_1, \vec{\rho}_2, \Delta t) = \frac{\Gamma(\vec{\rho}_1, \vec{\rho}_2, \Delta t)}{\sqrt{\Gamma(\vec{\rho}_1, \vec{\rho}_1, 0)}\sqrt{\Gamma(\vec{\rho}_2, \vec{\rho}_2, 0)}} = \frac{\Gamma(\vec{\rho}_1, \vec{\rho}_2, \Delta t)}{\sqrt{\tilde{\Gamma}(\vec{\rho}_1, 0)}\sqrt{\tilde{\Gamma}(\vec{\rho}_2, 0)}} = \frac{\Gamma(\vec{\rho}_1, \vec{\rho}_2, \Delta t)}{\sqrt{I(\vec{\rho}_1)}\sqrt{I(\vec{\rho}_2)}}. \tag{2.31}$$

This quantity corresponds to a normalised cross-correlation function of two random processes (J. W. Goodman, 2000). It is a measure of both the temporal and spatial coherence, and its modulus is proportional to the contrast of the interference fringes (Saha, 2011).

Similarly, the *complex degree of self coherence* or *complex autocorrelation coefficient*, $\tilde{\gamma}$, is defined as

$$\tilde{\gamma}(\vec{\rho}, \Delta t) = \frac{\tilde{\Gamma}(\vec{\rho}, \Delta t)}{\tilde{\Gamma}(\vec{\rho}, 0)} = \frac{\tilde{\Gamma}(\vec{\rho}, \Delta t)}{I(\vec{\rho})}. \tag{2.32}$$

It is a measure of the temporal coherence, and it describes the correlation of intensity of light between two points, one of which is fixed in space,

Mutual spectral density function

Equation (2.7) established the relation between the spectral amplitude $A(\vec{r}, \nu)$ and the optical disturbance $v(\vec{r}, t)$ through a Fourier transform. The equivalent in the realm of the coherence functions is done by means of the *mutual spectral density function* (MSDF), also known as the *cross spectral density function*, $\widehat{\Gamma}$, defined as the correlation function of the spectral amplitudes, and linked to the MCF by means of a Fourier transform (A. Glindemann, 2011; J. W. Goodman, 2000):

$$\Gamma(\vec{\rho}_1, \vec{\rho}_2, \Delta t) = \int \widehat{\Gamma}(\vec{\rho}_1, \vec{\rho}_2, \nu)\, \mathrm{e}^{-\mathrm{i}2\pi\Delta t\nu}\, \mathrm{d}\nu. \tag{2.33}$$

The MSDF contains the spectrum of the emitting source and it is useful to describe the propagation of the coherence properties of light through space.

The *spectral intensity*, $I(\vec{\rho}, \nu)$, is defined as the MSDF calculated at some point in space:

$$I(\vec{\rho}, \nu) \doteq \widehat{\Gamma}(\vec{\rho}, \vec{r}, \nu). \tag{2.34}$$

From eq. (2.33), it is found that the (*polychromatic* or *white-light*) *intensity*, $I(\vec{\rho})$, is no more than the integral of the spectral intensity over the frequency band:

$$I(\vec{\rho}) = \Gamma(\vec{\rho}, \vec{\rho}, 0) = \int \widehat{\Gamma}(\vec{\rho}, \vec{\rho}, \nu)\, \mathrm{d}\nu = \int I(\vec{\rho}, \nu)\, \mathrm{d}\nu. \tag{2.35}$$

The combination of eqs. (2.29), (2.33) and (2.34) leads to the conclusion that the SCF, $\tilde{\Gamma}(\vec{\rho}, \Delta t)$, is the Fourier transform of the spectral intensity, $I(\vec{\rho}, \nu)$:

$$\tilde{\Gamma}(\vec{\rho}, \Delta t) = \Gamma(\vec{\rho}, \vec{\rho}, \Delta t) = \int \widehat{\Gamma}(\vec{\rho}, \vec{\rho}, \nu)\, \mathrm{e}^{-\mathrm{i}2\pi\Delta t\nu}\, \mathrm{d}\nu = \int I(\vec{\rho}, \nu)\, \mathrm{e}^{-\mathrm{i}2\pi\Delta t\nu}\, \mathrm{d}\nu. \tag{2.36}$$

Table 2.1: Description of the coherence functions defined in the main text.

Definition	Name	Type of coherence
$\Gamma(\vec{\rho}_1, \vec{\rho}_2, \Delta t) = \langle v(\vec{\rho}_1, t+\Delta t)\, v^*(\vec{\rho}_2, t)\rangle$	Mutual coherence function	Spatial and temporal
$\tilde{\Gamma}(\vec{\rho}, \vec{\rho}, \Delta t) = \langle v(\vec{\rho}, t+\Delta t)\, v^*(\vec{\rho}, t)\rangle$	Self coherence function	Temporal
$\gamma(\vec{\rho}_1, \vec{\rho}_2, \Delta t) = \frac{\Gamma(\vec{\rho}_1, \vec{\rho}_2, \Delta t)}{\sqrt{I(\vec{\rho}_1)}\sqrt{I(\vec{\rho}_2)}}$	Complex degree of (mutual) coherence	Spatial and temporal
$\tilde{\gamma}(\vec{\rho}, \Delta t) = \frac{\tilde{\Gamma}(\vec{\rho}, \Delta t)}{I(\vec{\rho})}$	Complex degree of self coherence	Temporal
$\widehat{\Gamma}(\vec{\rho}_1, \vec{\rho}_2, \nu) = \mathscr{F}^{-1}\{\Gamma(\vec{\rho}_1, \vec{\rho}_2, \Delta t)\}$	Mutual spectral density function	Spatial and temporal

Hence, the narrower the spectral bandwidth, the greater the temporal coherence of the source.

The *coherence time*, Δt_c, is defined as the time difference Δt for which the SCF is notably reduced.[13] Usually, it is taken $\Delta t_c \simeq 1/\Delta\nu$. The fringes produced by Young's interference experiment exhibit a lower contrast (or fringe visibility) when Δt is decreased — *cf.* eqs. (2.20) and (2.21), page 16. Therefore, both the fringe visibility and the SCF evidence the same behaviour towards the spectral bandwidth, *i.e.*, the narrower $\Delta\nu$ the greater the coherence of the wave and the contrast of the fringes.

The equivalent to Δt_c in the space domain is the *coherence length*, ℓ_c, which corresponds to the OPD above which the contrast is severely reduced.[14] It is commonly defined as (A. Glindemann, 2011):

$$\ell_c = c\,\Delta t_c \tag{2.37a}$$

$$\simeq \frac{c}{\Delta\nu} = \frac{\lambda\,\nu}{\Delta\nu} = \frac{\lambda^2}{\Delta\lambda}, \tag{2.37b}$$

where $\Delta\lambda$ is the optical bandwidth used for observations.

Table 2.1 lists all aforementioned coherence functions, indicating the type of coherence (temporal and/or spatial) measured by them.

The *level of coherence* is measured by the modulus of the complex degree of coherence, $\gamma(\vec{\rho}_1, \vec{\rho}_2, \Delta t)$. When $|\gamma(\vec{\rho}_1, \vec{\rho}_2, \Delta t)| = 1$ for all position vectors $\vec{\rho}_1$ and $\vec{\rho}_2$ belonging to a domain $\mathscr{D}$ and all time differences Δt, the light is said to be *perfectly coherent*, and all the optical disturbances inside those space and time domains are totally correlated (A. Glindemann, 2011; J. W. Goodman, 2000).[15] In this case, the fringe visibility (contrast) is equal to 1.

[13] Equivalently, it is the time over which a propagating electromagnetic wave is considered coherent.

[14] When the OPD between all the interfering waves is less than ℓ_c, the interfering phenomena is strong.

[15] All solutions $A(\vec{r})$ of the *Helmholtz equation*

$$\left(\nabla^2 + k^2\right) A(\vec{r}) = 0, \tag{2.38}$$

where $\nabla^2 = \nabla\cdot\nabla = \partial^2/\partial x^2 + \partial^2/\partial y^2 + \partial^2/\partial z^2$ is the Laplacian and $k = 2\pi/\lambda$ is the wave number, like monochromatic plane and spherical waves, represent perfectly coherent light.

Inversely, a source is said *incoherent* when the optical disturbances are completely uncorrelated even if infinity small distances and time intervals are considered, *i.e.*, when the MCF $\Gamma(\vec{\rho}_1, \vec{\rho}_2, \Delta t) = 0, \forall \vec{\rho}_1 \neq \vec{\rho}_2, \forall \Delta t \neq 0$ and, thus, the degree of coherence $|\gamma(\vec{\rho}_1, \vec{\rho}_2, \Delta t)| = 0$, $\forall \vec{\rho}_1 \neq \vec{\rho}_2$ and $\Delta t \neq 0$. In that case, all points of the source radiate independently from each other (A. Glindemann, 2011; J. W. Goodman, 2000). In general, all celestial bodies are considered incoherent sources of light (A. Glindemann, 2011).

The MSDF is very suitable to describe incoherent wave-fields, since for a sufficiently wide spectrum (to which correspond large values of the MSDF), the MCF will be small enough in respect to Δt. Spatially incoherent light with an arbitrary spectrum is adequately specified by the following MSDF (ibid.):

$$\widehat{\Gamma}(\vec{\rho}_1, \vec{\rho}_2, \nu) = \lambda^2 I(\vec{\rho}_1, \nu)\, \delta(\vec{\rho}_1 - \vec{\rho}_2). \tag{2.39}$$

The van Cittert-Zernike theorem

The *van Cittert-Zernike theorem*, firstly derived by Cittert, (1934) and later demonstrated in a simpler way by Zernike, (1938), can be enunciated in two variants: a *generalised* version, which describes the propagation of the coherence function, and a *fundamental* form, specifying the spatial coherence of the field in the observation region.

Generalised form of the theorem

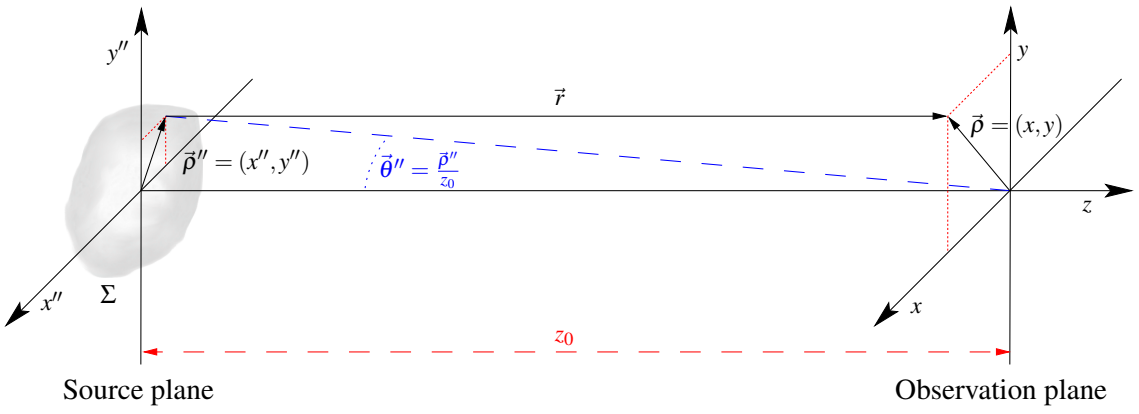

Figure 2.6: The geometry for the propagation of the coherence function of an incoherent source located in the plane Σ, the *source plane*, which is defined by the axis x'' and y''. The *plane of observation* is defined by the axis x and y. Both planes are separated by distance z_0, which is much larger than the size of the source or the area being considered in the observation plane. This allows for the small angle approximations, such as $\vec{\theta}'' = \vec{\rho}''/z_0$. In a stellar interferometer, any celestial body under observation corresponds to the source and the plane of observation corresponds to the aperture plane of the interferometer (adapted from ibid.).

Considering an incoherent emitting source located at a distance z_0 from the observation plane Σ (*cf.* fig. 2.6), the generalised van Cittert-Zernike theorem specifies how the MCF in the observation plane can be estimated from the MCF in the source plane. The propagation of the MSDF in space

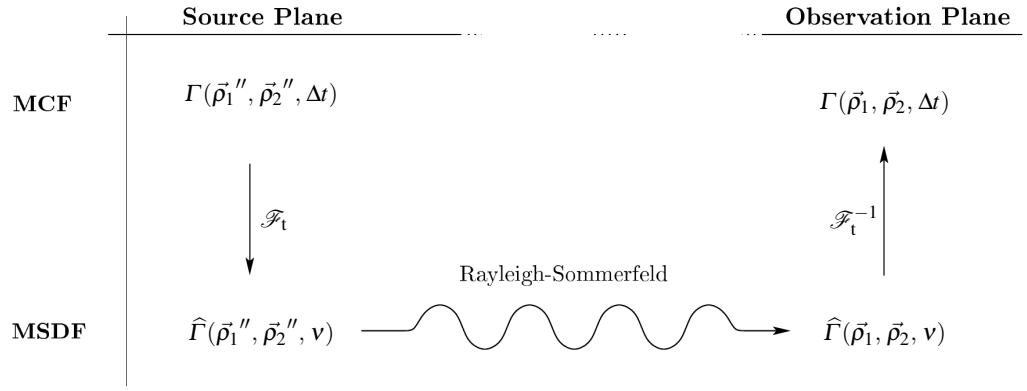

Figure 2.7: Diagram showing the principle behind the generalised van Cittert-Zernike theorem. The MCF in the observation region can be calculated using the following steps: (*i*) the MSDF in the plane of the source is determined by Fourier transforming the MCF; (*ii*) then the MSDF in the observation plane is computed by applying the Rayleigh-Sommerfeld formula (2.22) to the MSDF obtained in the previous step; (*iii*) and, finally, the latter is Fourier back-transformed, providing the MCF in the observation plane (adapted from ibid.).

is described by the equation (J. W. Goodman, 2000):

$$\widehat{\Gamma}(\vec{\rho}_1, \vec{\rho}_2, \nu) = \frac{1}{(\lambda z_0)^2} \iint_{\Sigma} \widehat{\Gamma}(\vec{\rho}_1'', \vec{\rho}_2'', \nu)\, \mathrm{e}^{\mathrm{i}k(\vec{\rho}_1 - \vec{\rho}_2)}\, \mathrm{d}\vec{\rho}_1''\mathrm{d}\vec{\rho}_2'', \tag{2.40}$$

which results from applying the Rayleigh-Sommerfeld diffraction formula (eq. (2.22), page 17) to the MSDF in the source plane, yielding the MSDF in the plane of observation. This formula is valid when the angles involved are small and the distance z_0 is large enough to allow for the Fresnel approximation, conditions easily satisfied in the case of astronomical sources observed by an array of telescopes.

The generalised van Cittert-Zernike theorem is illustrated in fig. 2.7 and can be summarised as follows:

1. The MSDF $\widehat{\Gamma}(\vec{\rho}_1'', \vec{\rho}_2'', \nu)$ in the source plane is calculated from the MCF $\Gamma(\vec{\rho}_1'', \vec{\rho}_2'', \Delta t)$ in the same plane by means of the eq. (2.33);
2. Then, the MSDF $\widehat{\Gamma}(\vec{\rho}_1, \vec{\rho}_2, \nu)$ in the observation plane is computed by applying eq. (2.40) to $\widehat{\Gamma}(\vec{\rho}_1'', \vec{\rho}_2'', \nu)$;
3. Finally, the MCF $\Gamma(\vec{\rho}_1, \vec{\rho}_2, \Delta t)$ in the observation plane is determined by Fourier back-transforming the MSDF $\widehat{\Gamma}(\vec{\rho}_1, \vec{\rho}_2, \nu)$ in the same plane. The coherence properties of the polychromatic light in the plane of observation are completely described by this MCF (A. Glindemann, 2011).

Fundamental form of the theorem

Being thermal emitters, stars are *spatially incoherent sources of light*. Consequently, the radiation they emit is characterised by random changes of phase between the photons. In its simplest form, a star can be shaped as a disc whose diameter is independent of the wavelength over the observed spectrum. Thus, their spectral intensity $I(\vec{\theta}'', \nu)$, eq. (2.34), can be written as the product of two independent variables, to wit, the *source brightness distribution*, $I_b(\vec{\theta}'')$, and $G(\nu)$,

the *source spectrum* (ibid.):

$$I(\vec{\theta}'', \nu) = I_{\mathrm{b}}(\vec{\theta}'')\, G(\nu). \tag{2.41}$$

The source brightness distribution is a dimensionless quantity. It describes the shape of the intensity of the source, which is assumed to be constant over the observed wavelength band. The source spectrum has units of Hz^{-1} and is generally normalised by the condition $\int G(\nu)\mathrm{d}\nu = 1$. It is limited by the observed bandwidth, which typically results from the juxtaposition of the instrument and the Earth's atmosphere spectral windows (case of ground-based observations).

Applying a change from spatial to angular coordinates, and replacing $\vec{r}_i/z_0$ by $\vec{\theta}_i''$ and $\mathrm{d}\vec{r}_i$ by $z_0^2\,\mathrm{d}\vec{\theta}_i''$, the MSDFs of a star in the source plane, eq. (2.39), and in the plane of observation, eq. (2.40), can be respectively written as

$$\widehat{\Gamma}(\vec{\theta}_1'', \vec{\theta}_2'', \nu) = \frac{\lambda^2}{z_0^2} I_{\mathrm{b}}(\vec{\theta}_1'', \nu)\, \delta(\vec{\theta}_1'' - \vec{\theta}_2'')\, G(\nu), \tag{2.42}$$

and

$$\widehat{\Gamma}(\vec{\rho}_1, \vec{\rho}_2, \nu) = G(\nu) \int I_{\mathrm{b}}(\vec{\theta}'')\, \mathrm{e}^{-\mathrm{i}k(\vec{\rho}_1 - \vec{\rho}_2)\cdot\vec{\theta}''}\, \mathrm{d}\vec{\theta}''. \tag{2.43}$$

In the plane of observation, the MSDF at frequency ν, *i.e.*, the spatial coherence is determined by the Fourier transform of the source brightness distribution (the source intensity shape), $I_{\mathrm{b}}(\vec{\theta}'')$. The Fourier transform is a function of $1/\lambda$ (because $k = 2\pi/\lambda$), and it depends on the difference between the individual coordinates, $\vec{\rho}_1 - \vec{\rho}_2$. Therefore, for incoherent sources, the coherence functions in the plane of observation uniquely rely on the coordinate difference:

$$\widehat{\Gamma}(\vec{\rho}_1, \vec{\rho}_2, \nu) = \widehat{\Gamma}(\vec{\rho}_1 - \vec{\rho}_2, \nu) \tag{2.44}$$

and

$$\Gamma(\vec{\rho}_1, \vec{\rho}_2, \Delta t) = \Gamma(\vec{\rho}_1 - \vec{\rho}_2, \Delta t). \tag{2.45}$$

In the case of polychromatic light, the MCF and the MSDF in the plane of observation are related by two entangled Fourier transforms (A. Glindemann, 2011; J. W. Goodman, 2000):

$$\Gamma(\vec{\rho}_1 - \vec{\rho}_2, \Delta t) = \int \widehat{\Gamma}(\vec{\rho}_1 - \vec{\rho}_2, 0)\, \mathrm{e}^{-\mathrm{i}2\pi\nu\Delta t}\, \mathrm{d}\nu \tag{2.46a}$$

$$= \int G(\nu) \int I_{\mathrm{b}}(\vec{\theta}'')\, \mathrm{e}^{-\mathrm{i}k(\vec{\rho}_1 - \vec{\rho}_2)\cdot\vec{\theta}''}\, \mathrm{d}\vec{\theta}'' \mathrm{e}^{-\mathrm{i}2\pi\nu\Delta t}\, \mathrm{d}\nu. \tag{2.46b}$$

This double integral can be simplified by assuming the *quasi-monochromatic approximation*, *i.e.*, by restricting the width of the spectrum and, consequently, the size of the source. This is achieved by assuming a narrow spectrum $G(\nu)$, taking $\Delta\nu \ll \nu_0$ (ν_0 is the average frequency), and by integrating the source over time intervals shorter than the coherence time, $\Delta t \ll 1/\Delta\nu$ (this implies that $\delta \ll \ell_{\mathrm{c}}$, *i.e.*, the OPD must be much smaller than the coherence length). Then,

$$\Gamma_{\mathrm{qm}}(\vec{\rho}_1 - \vec{\rho}_2, \Delta t) = \int I_{\mathrm{b}}(\vec{\theta}'')\, \mathrm{e}^{-\mathrm{i}k_0(\vec{\rho}_1 - \vec{\rho}_2)\cdot\vec{\theta}''}\, \mathrm{d}\vec{\theta}'' \tag{2.47a}$$

$$= \Gamma_{\rm qm}(\vec{\rho}_1 - \vec{\rho}_2, 0)\, \mathrm{e}^{-\mathrm{i}2\pi\nu_0\Delta t}, \tag{2.47b}$$

being k_0 the average wave number. $\Gamma_{\rm qm}(\vec{\rho}_1 - \vec{\rho}_2, 0)$ is the correlation function determined by the Fourier transform of the source shape. Equation (2.47) encloses the fundamental form of the van Cittert-Zernike theorem, which establishes the spatial coherence of light in the plane of observation:

$$\Gamma_{\rm qm}(\vec{\rho}_1 - \vec{\rho}_2, 0) = \int I_{\rm b}(\vec{\theta}'')\, \mathrm{e}^{-\mathrm{i}k_0(\vec{\rho}_1 - \vec{\rho}_2)\cdot\vec{\theta}''}\, \mathrm{d}\vec{\theta}''. \tag{2.48}$$

Therefore, the MCF $\Gamma_{\rm qm}(\vec{\rho}_1 - \vec{\rho}_2, 0)$ of an incoherent source in the observation plane and for time intervals $\Delta t = 0$ is linked to its brightness distribution $I_{\rm b}(\vec{\theta}'')$ by a Fourier transform.

The van Cittert-Zernike theorem is most commonly written as

$$\widetilde{V}(\vec{\rho}_1 - \vec{\rho}_2) = \frac{\Gamma_{\rm qm}(\vec{\rho}_1 - \vec{\rho}_2, 0)}{\sqrt{I(\vec{\rho}_1) I(\vec{\rho}_2)}} = \frac{\int I_{\rm b}(\vec{\theta}'')\, \mathrm{e}^{-\mathrm{i}k_0(\vec{\rho}_1 - \vec{\rho}_2)\cdot\vec{\theta}''}\, \mathrm{d}\vec{\theta}''}{\int I_{\rm b}(\vec{\theta}'')\mathrm{d}\vec{\theta}''}, \tag{2.49}$$

where the MCF $\Gamma_{\rm qm}(\vec{\rho}_1 - \vec{\rho}_2, 0)$ was normalised by the geometric mean of the intensities $I(\vec{r}_i) = \Gamma_{\rm qm}(\vec{r}_i - \vec{r}_i, 0)$ at vector positions $\vec{\rho}_1$ and $\vec{\rho}_2$. This normalised MCF corresponds to the degree of coherence γ at $\Delta t = 0$, as defined by eq. (2.31), and, in the quasi-monochromatic approximation, it is commonly known as the *complex visibility function*, $\widetilde{V}(\vec{\rho}_1 - \vec{\rho}_2)$. The integral over $I_{\rm b}(\vec{\theta}'')$ in the denominator is denoted by $I_0 = \int I_{\rm b}(\vec{\theta}'')\mathrm{d}\vec{\theta}''$, which describes the homogeneous intensity of the source in the plane of observation.[16]

Special attention must be paid to the fact that $\widetilde{V}$ is a function of coordinate difference only, not of the absolute positions of the two points $\vec{\rho}_1$ and $\vec{\rho}_2$. Therefore, for a given object and time of observation, two identical baseline vectors yield the same complex visibility function.

The amplitude of the visibility function, the so-called *visibility amplitude*, $\left|\widetilde{V}(\vec{\rho}_1 - \vec{\rho}_2)\right|$, will henceforth be denoted by V, and its phase, also known as *visibility phase*, $\phi(\vec{\rho}_1 - \vec{\rho}_2)$, which is identical to the phase of the MCF at $\Delta t = 0$, will be designated by ϕ. From (2.49),

$$0 \leqslant V \leqslant 1 \text{ and } \widetilde{V}(0) = 1. \tag{2.50}$$

Moreover, since the source brightness distribution is, by definition, a positive real quantity, V is symmetric and ϕ is antisymmetric, *i.e.*,

$$\left|\widetilde{V}(\vec{\rho}_1 - \vec{\rho}_2)\right| = \left|\widetilde{V}(\vec{\rho}_2 - \vec{\rho}_1)\right|, \tag{2.51}$$

and

$$\phi(\vec{\rho}_1 - \vec{\rho}_2) = -\phi(\vec{\rho}_2 - \vec{\rho}_1). \tag{2.52}$$

V is frequently presented as the ratio between the *correlated flux* and the *total flux* because, from eq. (2.49), the visibility function results from the quotient between the MCF, which is the

[16] This value is constant, but only in the absence of phenomena perturbing the incoming wavefront. For ground based interferometers, however, the intensity of the source fluctuates randomly due to the turbulence introduced by the Earth's atmosphere, and the values of I at $\vec{\rho}_1$ and $\vec{\rho}_2$ need to be individually taken into account and calibrated.

correlation function of the optical disturbances, and the integrated intensity (A. Glindemann, 2011).

Combining Equations (2.43) and (2.49), the MSDF for polychromatic light can be rewritten as

$$\widehat{\Gamma}(\vec{\rho}_1, \vec{\rho}_2, \nu) = G(\nu)\, I_0\, \widetilde{V}(\vec{\rho}_1 - \vec{\rho}_2), \tag{2.53}$$

where the MSDF was split into two terms: one, $G(\nu)$ accounts for the temporal coherence, and the other, $\widetilde{V}(\vec{\rho}_1 - \vec{\rho}_2)$, describes the spatial coherence. Inasmuch as the homogeneous intensity of the source I_0 and the spectrum $G(\nu)$ are real quantities, the phase of the MSDF is identical to the phase of the visibility function.

The van Cittert-Zernike theorem can also be written as a function of the *spatial frequencies* $\vec{f} = (\vec{\rho}_1' - \vec{\rho}_2')/\lambda = \vec{B}/\lambda$, where $\vec{\rho}_i', i = 1,2$, is the position vector in the aperture plane of the aperture i, and $\vec{B}$ is the *baseline vector*. Usually, the spatial frequencies are denoted $f_{x'} = B_{x'}/\lambda = u$ and $f_{y'} = B_{y'}/\lambda = v$. With this notation, the van Cittert-Zernike theorem becomes

$$\widetilde{V}(u,v) = \frac{\iint I_\mathrm{b}(\theta_{x''}, \theta_{y''}) \mathrm{e}^{-\mathrm{i}2\pi(u\theta_{x''} + v\theta_{y''})} \mathrm{d}\theta_{x''} \mathrm{d}\theta_{y''}}{\iint I_\mathrm{b}(\theta_{x''}, \theta_{y''}) \mathrm{d}\theta_{x''} \mathrm{d}\theta_{y''}}. \tag{2.54}$$

Hence, the visibility function corresponds to the Fourier transform of the source brightness distribution divided by I_0, or, equivalently, the complex visibilities are samples of the Fourier spectrum of the source structure at the spatial frequencies (u,v), which are defined by the positions of the interferometer's apertures.

It is important to note that, in this notation, $\vec{B}$ actually corresponds to the *effective baseline*, the projection of the baseline vector onto a plane perpendicular to the line of sight. This plane, where the *spatial frequencies vector* $\vec{f} = (u,v)$ lie, is the so-called *uv-plane* or (u,v)*-plane* of the interferometer.

The intensity distribution of a diffraction pattern

For an incoherent source whose light is subject to interference such as in the Young's double slit experiment, the *spectral intensity* in the plane of observation $I(\vec{\theta}, \nu)$, *i.e.*, the intensity distribution of the diffraction pattern at frequency ν, is given by[17]

$$I(\vec{\theta}, \nu) = 2\, G(\nu)\, I_0' \left[1 + \left|\widetilde{V}(\vec{B})\right| \cos\left(\phi(\vec{B}) - k\vec{\theta}\cdot\vec{B}\right)\right], \tag{2.55}$$

where $\vec{\theta}\cdot\vec{B} = r_2 - r_1$, $I_0' = (\lambda_0/z_0)^2 I_0$, λ_0 is the mean wavelength, and z_0 is the distance between the source and the aperture plane (see fig. 2.2, page 17). The fringe pattern is, thus, proportional to $[1 + \cos\{\cdot\}]$, a result which is similar to eq. (2.19). Since the amplitude of the visibility is always non-negative and less than unity, the contrast of the fringe pattern is determined by V, which

[17] This result stems from the application of the Rayleigh-Sommerfeld diffraction formula, eq. (2.22), to an aperture composed of two pinholes of diameter λ. Alternatively, it can be deduced in a similar way to eq. (2.18), replacing the constant amplitudes A_0 by the variable amplitudes $\lambda^2 A(\vec{\rho}_1, \nu)$ and $\lambda^2 A(\vec{\rho}_2, \nu)$, where λ^2 accounts for the area of the sub-apertures. Refer to A. Glindemann, (2011) for details about the results presented in this subsection.

attenuates the cosine function. The position of the white-light fringe[18] is, in turn, regulated by the visibility phase.

Equation (2.55) is valid when the intensities in both apertures are constant and equal to each other. However, in the presence of turbulence, as it always happens for ground observations, this condition is not verified because the wavefront is corrugated, and the spectral intensity in the plane of observation is

$$I(\vec{\theta},\nu) = G(\nu)\left[I_1 + I_2 + 2\sqrt{I_1 I_2}\,V\cos\left(\phi - k\vec{\theta}\cdot\vec{B}\right)\right], \tag{2.56}$$

where the individual intensities in the apertures are equal to $I(\vec{\rho}_i,\nu) = G(\nu)I_i$, for $i = 1,2$. In this case, the cosine function is still modulated by V, which now comes multiplied by a factor, and the fringe visibility or contrast at zero OPD (*i.e.*, around the white-light fringe) is

$$\mathscr{V} = 2\frac{\sqrt{I_1 I_2}}{I_1 + I_2}\cdot V. \tag{2.57}$$

The quasi-monochromatic approximation (section 2.2.2.2, page 27) is also used to deal with the polychromatic case when the radiation is emitted by a remote extended source. In this scenario, the spectral band must be narrow, that is, $\Delta\nu \ll \nu_0$, which means that the object is small enough in order that the visibility function does not vary over $\Delta\nu$ (A. Glindemann, 2011). The intensity distribution of the diffraction pattern produced by two interfering sources in the quasi-monochromatic approximation is given by

$$I_{\mathrm{qm}}(\vec{\theta},\nu) = 2I_0'\left[1 + g_B(\vec{\theta})\,V\cos\left(\phi - k\vec{\theta}\cdot\vec{B}\right)\right], \tag{2.58}$$

with $\vec{\theta}\cdot\vec{B} = tc$, $k_0\vec{\theta}\cdot\vec{B} = 2\pi\nu_0 t$, and $g_B(\theta) = g(\vec{\theta}\cdot\vec{B}/c) = g(t)$. The latter is the Fourier transform with respect to ν of the *centred spectrum*, $G_{\mathrm{c}}(\nu) = G(\nu+\nu_0)$: $g(t) = \mathscr{F}_\nu\{G_{\mathrm{c}}(\nu)\}$.

The ABCD method

The visibility amplitude and phase can be determined by the *ABCD method*, which was originally proposed by Wyant, (1975) and later described by M. Shao and Staelin, (1977). In the ABCD method, the intensity of the light is measured at four different points of the interferometric pattern, around the white-light fringe, that are separated by $1/4$ of the fringe spacing. Denoting the intensities by I_{A}, I_{B}, I_{C}, and I_{D}, the visibility amplitude and phase are respectively given by

$$V = \left|\widetilde{V}(\vec{B})\right| = \mathscr{V} = C\frac{\sqrt{(I_{\mathrm{A}} - I_{\mathrm{C}})^2 + (I_{\mathrm{B}} - I_{\mathrm{D}})^2}}{I_{\mathrm{tot}}}, \tag{2.59a}$$

$$\phi = \phi(\vec{B}) = \arctan\left(\frac{I_{\mathrm{A}} - I_{\mathrm{C}}}{I_{\mathrm{B}} - I_{\mathrm{D}}}\right), \tag{2.59b}$$

[18] The *white-light fringe* is the fringe formed at OPDZ or OPD-zero ($\vec{\theta} = 0$; see page 37), where all wavelengths reach their intensity maximum (A. Glindemann, 2011; Lawson, 2000).

where C is a constant whose value depends on the measurement method, and $I_{\text{tot}} = I_{\text{A}} + I_{\text{B}} + I_{\text{C}} + I_{\text{D}}$. In practice, the visibility has always to be calibrated, for which typically an unresolved source (with nominal visibility $V = 1$) is used (A. Glindemann, 2011).

In the ABCD method, it is important to use the white-light fringe to determine the visibility amplitude, since that is the fringe that leads to the highest contrast. Nevertheless, this method is very robust when it comes to measure the fringe position, because the phase estimation, as opposed to the fringe visibility, is not affected by the temporal coherence and, thus, by which fringe of the packet is selected for the determination of the phase (ibid.).

An application of the ABCD method within the framework of this thesis can be found in chapter 4, page 61, where visibility amplitudes of stars observed with the fringe sensor units of PRIMA were estimated.

Combination schemes

The characteristics of an interferometer are essentially determined by the layout of telescopes array and by the beam combination scheme used for the instrument.

In the *Fizeau configuration*,[19] the interferometer is similar to a single telescope with a masked aperture, because the images of the apertures of the telescopes are *homothetically* mapped in the beam combining instrument, *i.e.*, they correspond to a downscaled replica of the interferometer array.[20] The *interferometric field of view* (FOV), *i.e.*, the area of the image with fringes, is as large as that of the telescopes that constitute the array, being limited uniquely by the optical design of the interferometer. However, Fizeau configurations are difficult to build because the effective baselines are in constant motion due to the rotation of the Earth. Consequently, the fringe spacing varies during the observation, and a suitable pixel size must be found for the scanning of the fringe pattern for all baselines (A. Glindemann, 2011; J. W. Goodman, 2000).

In the *Michelson configuration* (recall fig. 2.4), the apertures of the telescopes are not homothetically mapped, since their distances in the beam combination instrument are chosen without taking into account the baseline between the two telescopes. As a result, the configuration is more relaxed in terms of optical design, but the interferometric FOV is very limited in size, to less than the Airy disc or the diffraction limit of the individual apertures (A. Glindemann, 2011; J. W. Goodman, 2000).[21]

The constraints are brought to a limit in the *co-axial combination* scheme, where the *exit pupils* are superimposed (*i.e.*, they are projected on top of and parallel to each other) in the detector with the aid of a beam combiner. Consequently, unlike all the other configurations that separate the exit

[19] This configuration is named after Hippolyte Fizeau, who was a pioneer in the domain of stellar interferometry.

[20] In *homothetic mapping*, the exit pupils are imaged in the combination instrument in such a way that the ratio of the distance between the pupils to their diameters is the same as that of the baseline to the telescopes aperture (A. Glindemann, 2011; J. W. Goodman, 2000).

[21] *Sparse aperture masking* can be used to reduce the problems of the Fizeau configuration. In this technique, an aperture mask with holes and fixed baselines is placed in front of a single telescope, therefore ensuring the proper re-imaging of the exit pupil (Tuthill, J. D. Monnier and William C Danchi, 1999).

pupils in the image plane, there is no formation of fringes. The *optical path length* (OPL) in one of the arms of the interferometer is temporally modulated, and an Airy disc without fringes is seen, with an intensity that varies with the OPD: the Airy disc is bright when constructive interference is produced, and dark otherwise. Therefore, a fringe pattern can be extracted as a function of the OPD or of the time difference Δt, but not as a function of the diffraction angle, θ (A. Glindemann, 2011; J. W. Goodman, 2000) — this is the case of PRIMA, which is going to be detailed in chapter 3.

It is current practice to classify all configurations as Michelson ones provided they do not include homothetic mapping of the exit pupils. This way, designs with separated apertures in the exit pupil that are not Fizeau configurations, such as the one Michelson himself used on Mount Wilson in 1920, are classified as Michelson's — the case of non-homothetical separated apertures in the exit pupil is called *multi-axial combination* scheme.

Part II

Phase Referenced Interferometry

Chapter 3

The PRIMA facility

"Neat, don't you think? You've been stumbling around the fringes of this one for ages. Or were you too bored to notice the pattern?"

— MYCROFT, *Sherlock* (2010)

Contents

GROUND-BASED OBSERVATORIES face important physical and technical challenges when trying to produce interferometric data. Above all, circumventing the effects of the atmospheric turbulence is mandatory, because this phenomenon is responsible for corrugating the incoming wavefronts prior to detection by telescopes. Instrumental vibrations introduce additional difficulties to the stabilisation of the fringes and the measurement of both the amplitude and the phase of the visibility.

This chapter is dedicated to the description of PRIMA, the dual-feed facility designed by ESO to address the aforementioned obstacles. It is highly inspired in the work presented by F. Delplancke, Derie et al., (2006), J. Sahlmann et al., (2009) and J. Sahlmann et al., (2013). Section 3.1 discusses the impact of atmospheric turbulence on ground-based observations and describes concepts that have been traditionally used to achieve a desirable performance with an interferometer. Section 3.2 provides a brief functional description of the VLTI, with emphasis on the delay lines and the interferometric laboratory. Finally, section 3.3 introduces PRIMA and outlines the principles behind its operation.[1]

Motivation for fringe tracking and phase referencing

A stellar interferometer uses spatially separated sections of the wavefront to coherently combine light in an interferometric laboratory. The shapes of incoming plane waves emitted by distant stars change when traversing the Earth's atmosphere, due to variations in the column density of the air along different directions. Light is collected by two or more telescopes and travels through unconnected beam trains towards the lab. Consequently, upon arrival to the instrument for combination, the light beams used to create the fringe pattern have travelled different optical path lengths (OPLs), either due to the distinct trajectories they have followed through the turbulent atmosphere, and to the optical path difference (OPD) introduced by the active equipment existent inside the arms of the interferometer.

The random motion of the fringe pattern due to atmospheric turbulence prevents long integration times, but this motion can be frozen by reducing the integrations to the order of magnitude of the jitters' time-scale, a few multiples of 10 ms (at a wavelength of 2 µm). This technique presents the disadvantage of limiting the effective working magnitude of the instrument, determined by the apparent magnitude of the faintest observable object, since only bright sources can be properly detected during such short integration times.

A more satisfactory strategy to circumvent this difficulty, already implemented in modern interferometers, such as the VLTI and CHARA, consists in using short exposures on a sufficiently bright reference star for *fringe tracking*.[2] In this method, the fringe pattern is rapidly scanned, yielding the position of the white-light fringe, which is fed into a servo loop, thus allowing to stabilise the fringe motion to a jitter with order of magnitude ideally smaller than the fringe spacing (A. Glindemann, 2011). Stabilising the fringes on a nearby bright enough object leads to an effective increase of the atmospheric coherence time and, consequently, it grants the possibility of tracking fainter fringes for longer integration times. Consequently, fringe tracking improves the limiting magnitude of an interferometer, provided a referencing object exists close by (Lane and M. M. Colavita, 2003).

[1] Further details about the PRIMA concept can be found in the aforementioned papers and references therein.

[2] CHARA is only able to perform on-axis fringe tracking, *i.e.*, stabilisation of fringes on the object that is being observed. In the US jargon, this technique is known as *self-referencing*.

A *fringe tracker* or *fringe sensor unit* (FSU), is a device consisting of a closed loop control system that is able to measure the position of the fringes, to stabilise them, and to compensate for the OPD. An *OPD sensor* and an *OPD actuator* are placed in the optical delay of both interferometer arms. The former detects the fringes and determines their position relative to a reference in the lab. Afterwords, it sends commands to the OPD actuator in order to compensate the position of the fringe pattern every time it is not centred in the reference point. The actuator has the mission to modify the OPL in the corresponding arm of the interferometer, so as to recentre the fringe packet for *zero OPD* (ZOPD). The problem thus remains to determine the *OPD-zero* (OPDZ), $\delta_{\odot}$, the position for ZOPD, *i.e.*, the default position of the white light fringe for zero phase.[3] Determining this position in absolute terms when using two telescopes requires a relative accuracy of 10^{-11} in the OPD measurement (for a laser metrology accuracy of some nanometres). When the position of the fringes is properly stabilised by a fringe tracker, the limiting magnitude of an instrument is increased given that longer integration times can be applied.

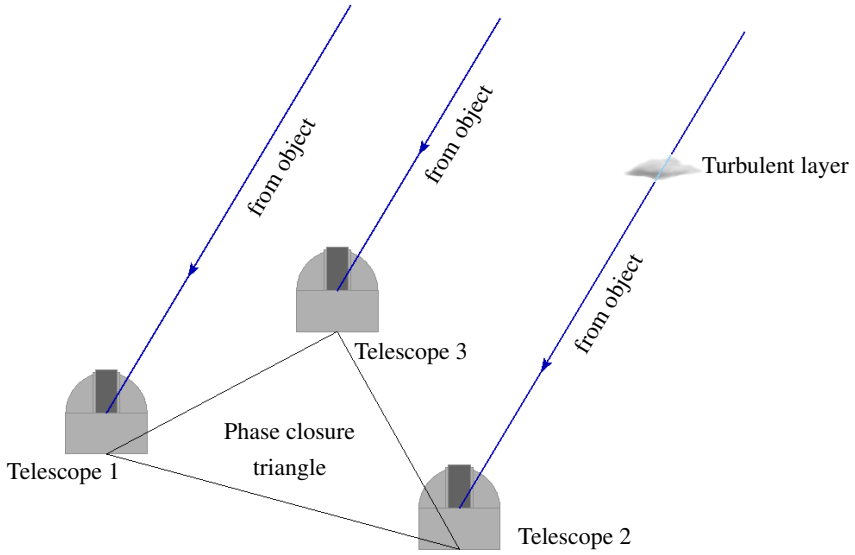

Figure 3.1: Schematic of phase closure technique and principle behind the closure phase interferometric observable. Adapted from ibid.

Another effect of the fringe jitter produced by the turbulence in the atmosphere is the introduction of time delays in the wavefronts, which are translated into phase shifts in the fringes detected in an interferometer. As a consequence, the phase of the fringes cannot be measured accurately. The production of images of non-centre-symmetric objects rely on the Fourier phase of the source brightness distribution, which is encoded in the fringe phase. Therefore, these atmospheric phase delays lead to the loss of an important information about the object and limit the application of the van Cittert-Zernike theorem to simple centre-symmetric sources, such as round stars or discs. Whilst an effective fringe tracker is able to stabilise the position of the fringes in the lab, it is not necessarily sufficient to allow for the measurement of the visibility phase. One can aim at two levels

[3] While the ZOPD is the absence of OPD between the arms of the interferometer, the OPDZ is a virtual line in the laboratory where the photons of both telescopes are simultaneously brought together in order to produce a fringe packet.

of OPD correction: by *coherencing* or by *co-phasing*. The former allows reliable measurements of the visibility amplitude, but not of its phase, because while the OPD is kept below the coherence length ℓ_c of the observed radiation, it is always larger than the wavelength ($\lambda < \mathrm{OPD} < \ell_c$). Measurements of the phase can be achieved, however, using co-phasing, a more changeling technique that permits the control of the OPD error below one wavelength or a small fraction of it ($\mathrm{OPD} < \lambda$). Additionally, adaptive optics systems can be applied to each collected wavefront prior to recombination, in order to provide real-time partial compensation of the phase errors (L. A. Thompson, 1994).

At present, there are two approaches for phase retrieval: *phase closure* and *phase referencing*. Phase closure is a successful method developed by radio interferometrists (Jennison, 1958), which is employed to recover part of the fringe phase information. It consists in coherently combining three telescopes and measuring the joint phase of the triangle of baselines, known as the *closure phase*. The principle behind closure phase can be explained by means of fig. 3.1. Above telescope 2 of the 3-telescope array, there is a turbulent pocket layer in the atmosphere, that introduces a phase delay. The latter produces equal but opposite phase shifts in the fringes between adjoining baselines and, hence, the sum of the fringe phases between telescopes 1–2, 2–3, and 3–1 is insensitive to the phase delay above telescope 2. Since this reasoning holds for arbitrary phase delays above any of the telescopes, the closure phase, *i.e.*, the sum of the three phases around a close triangle of baselines, is not affected by telescope-specific phase errors introduced by the atmosphere (nor induced by the optics). Hence, this combined phase is a good interferometric observable (J. D. Monnier, 2007).

The invariance of the closure phase to telescope-specific phase shifts can be derived from the *bi-spectrum* or *triple product*, $\widetilde{B}_{ijk}$, a complex quantity defined as the product of the three visibilities measured in the baselines of a triangle of apertures:

$$\widetilde{B}_{ijk} = \widetilde{V}_{ij}\widetilde{V}_{jk}\widetilde{V}_{ki}, \tag{3.1}$$

where the indices i, j, and k specify the three apertures located in the pupil of each telescope (J. D. Monnier, 2003). The measured complex visibility $\widetilde{V}^{\mathrm{meas}}$ is written as the product between complex gains $\widetilde{G} = G\mathrm{e}^{\mathrm{i}\psi}$, which represent the errors introduced by a specific telescope, and the true visibility $\widetilde{V}$:

$$\widetilde{V}_{ij}^{\mathrm{meas}} = \widetilde{G}_i\widetilde{G}_j^*\widetilde{V}_{ij}. \tag{3.2}$$

The amplitude G corresponds to a scale factor, representing all beam-specific effects that modify the intensity of the source radiation, such as the local scintillation, the reflectivity of the mirrors, or the sensitivity of the detector. The phase ψ encode all phase shifts specific to the telescope and beam, such as those caused by atmospheric turbulence or unstable optical path lengths along the beam-train (J. D. Monnier, 2007). The measured bi-spectrum can be written as

$$\widetilde{B}_{ijk} = \widetilde{V}_{ij}^{\mathrm{meas}}\widetilde{V}_{jk}^{\mathrm{meas}}\widetilde{V}_{ki}^{\mathrm{meas}} \tag{3.3a}$$

$$= G_iG_j\mathrm{e}^{\mathrm{i}(\psi_i-\psi_j)}\widetilde{V}_{ij}\cdot G_jG_k\mathrm{e}^{\mathrm{i}(\psi_j-\psi_k)}\widetilde{V}_{jk}\cdot G_kG_i\mathrm{e}^{\mathrm{i}(\psi_k-\psi_i)}\widetilde{V}_{ki} \tag{3.3b}$$

$$= G_i^2 G_j^2 G_k^2 V_{ij} V_{jk} V_{ki}\, \mathrm{e}^{\mathrm{i}(\phi_{ij}+\phi_{jk}+\phi_{ki})}. \tag{3.3c}$$

Hence, the phase of the bi-spectrum is equal to the closure phase:

$$\phi_c = \phi_{ijk} = \phi_{ij} + \phi_{jk} + \phi_{ki}. \tag{3.4}$$

The quality of phase closure images is analysed in Chapters 7 and 8.

Phase referencing is another method used to compensate for the phase disturbances introduced by the atmosphere. Fringe tracking is used to fix the position of the fringes of the bright object. Then, the fringe position of the faint object is measured with respect to the position of the fringes of the bright target, using the internal metrology and the phase of the scientific instrument (such as AMBER). This technique is the analogous in interferometry to adaptive optics in single telescopes. The basic idea can be explained by considering two emitting sources close to each other in the sky, which are simultaneously observed by the interferometer. When one of them is centre-symmetric and bright enough, its fringe phase can be used to determine and correct, in real time, the fringe phase of the fainter object (the scientific target). The light from the reference source is fed into a fringe tracker, which stabilises its fringes. If the angular separation between the two targets is inferior to the *isoplanatic angle*,[4] then the correction to the OPD from the reference object can be applied to the scientific source and both fringes become stabilised in the lab. Since for a centre-symmetric object the intrinsic visibility phase is zero, the visibility phase of the scientific target can be inferred from the separation between the fringe packets. The principle of phase referencing is illustrated in fig. 3.6, page 47.

Therefore, by means of phase referencing, interferometers are able to observe faint targets and to measure their visibility phase, provided that there is a suitable reference source nearby inside the FOV. The ability to observe simultaneously two celestial objects is thus an important and highly desirable feature in long-baseline optical interferometry.

Functional description of the VLTI

The Very Large Telescope (VLT), built on top of Cerro Paranal, Chile, at an altitude of 2 635 m, was designed with interferometric observations in mind, *i.e.*, aiming at the coherent combination of telescopes in the Very Large Telescope Interferometer (VLTI). The VLTI comprises four fixed 8.2 m unit telescopes (UTs) and four moveable 1.8 m auxiliary telescopes (ATs). The former can be combined with a maximum baseline of 130 m, and the latter, moving on top of rail tracks, can be relocated to 30 stations, using baselines of up to 200 m (A. Glindemann et al., 2004, see fig. 3.2). The ATs can be placed on any station, provided that there are no more than one per rail track perpendicular to the delay line tunnel. In principle, up to eight ATs can be combined — this number is limited by the available number of *delay lines* (8) in the delay line tunnel —

[4] The *isoplanatic angle* is the angle between two objects on the sky for which the correlation of the fringe motion induced by the atmosphere is sufficiently high. When only the tip-tilt is corrected, the correlation is measured on the image motion alone, and this angle is called the *isokinetic angle* (Wilhelm, Köhler and Gitton, 2002).

but, to date, only six delay lines are in operation and no more than four telescopes have been coherently combined in the VLTI.[5] This gives room for improvements regarding the *uv*-coverage and to properly configure the array aiming at the scientific purposes of the observations — the advantages of combining six beams have already been demonstrated by CHARA (*e.g.*, Richardson et al., 2013).

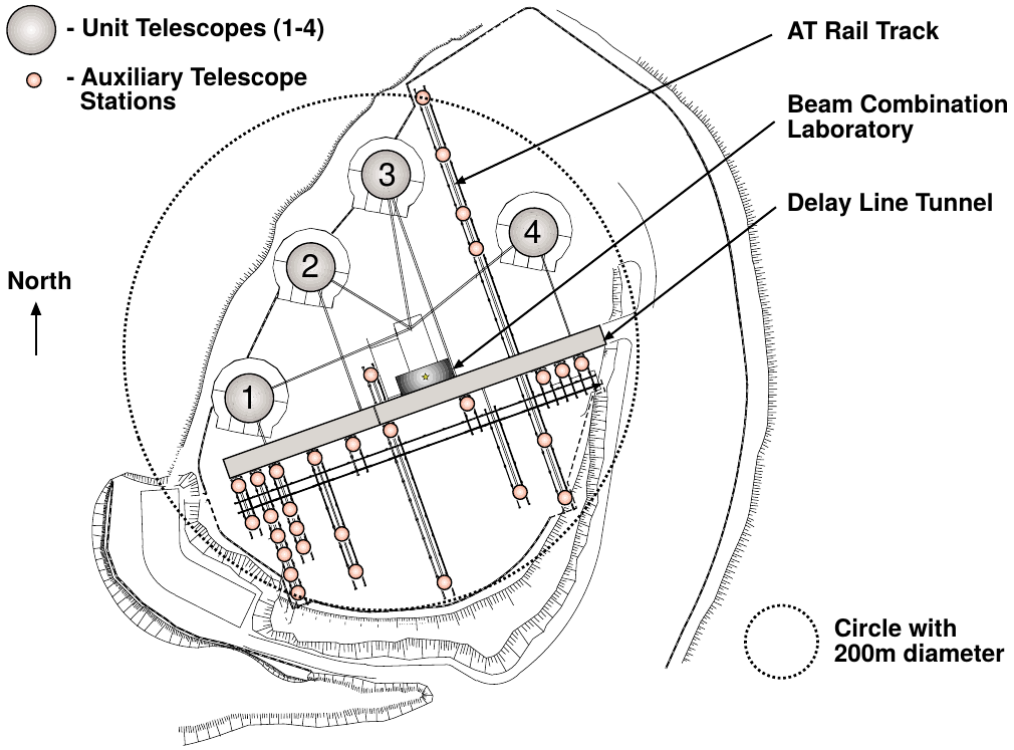

Figure 3.2: Schematic layout of the VLTI on Cerro Paranal (Paranal hill). The 8.2 m UTs are labelled with numbers 1 to 4. The 1.8 m AT stations, indicated by the beige circles, are connected by rail tracks, on which the auxiliary telescopes can be relocated. Currently, there are four ATs in operation. The longest achievable baseline is 130 m and 200 m, respectively with the UTs and the ATs (source: ESO, 2004).

The schematic operating principle of the VLTI is illustrated in fig. 3.3. When the observed star is not located at the zenith, the wavefront is not parallel to the baseline vector. Consequently, a geometrical delay is produced because the wavefront does not reach both telescopes at the same time. Collected light travels through an underground system of mirrors and delay lines, inside ducts and tunnels, and is brought together in the instrument at the interferometric laboratory.

The VLTI delay lines

For ground-based telescopes moving independently from each other, because they are fixed on the Earth's surface, an optical path difference emerges when the observed objects are not located in the zenith (recall fig. 3.3) because, in that case, the effective and geometric baselines do not coincide. Also, due to the rotation of the globe, the geometrical OPL from the object to each telescope evolves

[5]For the definition of *delay line*, refer to page 42.

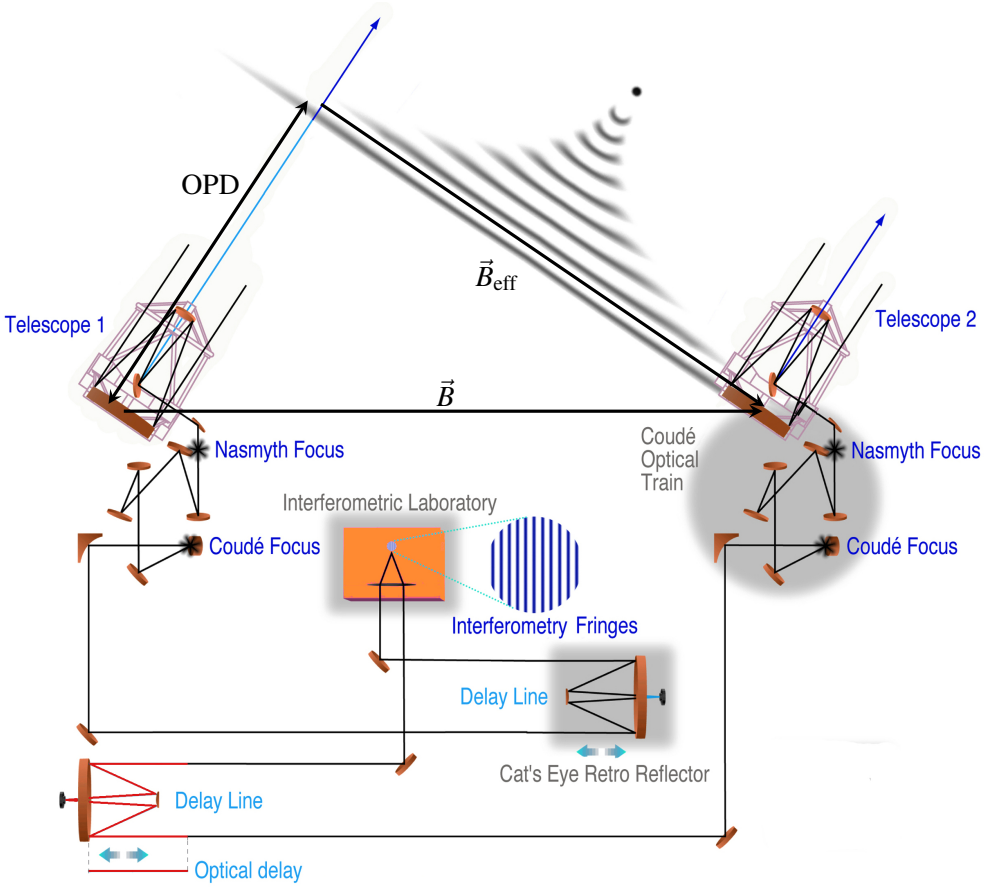

Figure 3.3: Schematic operating principle of the VLTI. Due to the projection of the (geometric) baseline $\vec{B}$ onto the plane of the sky, *i.e.*, onto the plane perpendicular to the line of sight, yielding the effective baseline $\vec{B}_{\rm eff}$, an OPD emerges between both interferometer arms. The *optical delay*, the extra optical path added to one of the arms of the interferometer in order to make the optical paths equal, is adjusted by means of moveable cat's eye retro-reflectors. Source: ESO, 2000 (adapted).

differently and a smooth trajectory arises for the OPD (neglecting atmospheric effects).[6] In addition to this geometrical origin, the OPD usually also has atmospheric and instrumental causes. On the one hand, the Earth's atmosphere acts as a significant barrier to precise interferometric observations because its dynamic perturbations distort the original plane waves and introduce an OPD between the interfering beams. This OPD produces low-frequency perturbations of the fringe position of several coherence lengths within a few seconds. On the other hand, telescopes structural vibrations, thermal gradients, and independent internal vibrations of the opto-mechanical components inside the interferometer arms, produced by micro-seismicity or active equipment such as fans and pumps, introduce high-frequency oscillations of the OPD in the range of several hundreds of nanometres (nms) on time-scales of milliseconds (ms). The atmospheric perturbations combined with this internal OPD produce an overall unstable OPD,[7] which makes the determination of the ZOPD a difficult task (J. M. Beckers, 1990a,b). In order to produce the interference of light and obtain

[6] Extra OPDs can related to the positions of the mirrors in the optical train.

[7] When the light ducts are not evacuated, environmental disturbances along the beam trains (up to beam combination), such as turbulence, humidity and temperature gradients, might introduce extra OPDs.

fringes, this OPD has to be compensated for by the so-called *delay lines*.

A *delay line* (DL) is a retro-reflective optical device (a cat's eye) built on top of a movable carriage, that reflects the light coming from the telescope to an interferometric instrument (see figs. 3.4a and 3.4b). The carriage is guided by precision rails, aligned along the u-direction. The *optical delay* applied to the incoming beam compensates for the OPD between two different arms of the interferometer by continuously maintaining equal path lengths between them during an observation. The optical delay is adjusted by a 2-stage actuation system that combines range with accuracy: on the one hand, by longitudinal shifts of the carriage produced by linear motors, and, on the other hand, by minute displacements of a Variable Curvature Mirror (VCM), one of the cat's eye mirrors that is mounted on a piezoelectric translation stage and that re-images the telescope exit pupil.[8] When the optical paths are equal within a few tens of wavelengths, fringes are produced in the selected instrument at the lab.

A laser metrology subsystem is used to control and measure the position of the delay lines with an accuracy of 5 nm over the full DL stroke of 60 m.

Each of the six VLTI DLs is provided with dual-feed capabilities, applying the same OPD correction to both beams coming from the same telescope.

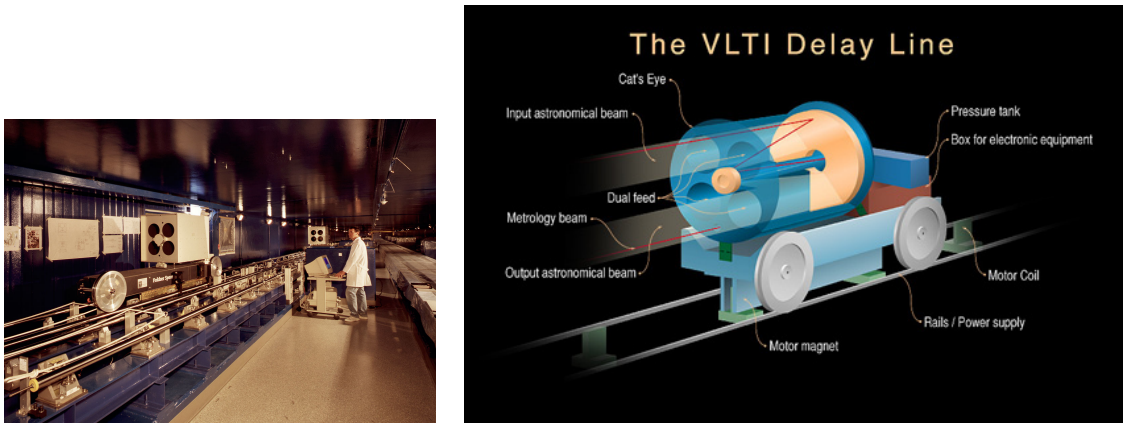

(a) **(b)**

Figure 3.4: A view along the interferometric tunnel, with the rails for two of the VLTI DLs (3.4a), and schematic view of a VLTI DL (3.4b). Source: ESO, 2004.

The interferometric laboratory

The VLTI laboratory is the room where all the interferometric instruments are installed. It is located bellow the platform of the observatory, at the level of the delay line tunnel (see fig. 3.5). Up to 2015, the lab is hosting

(*a*) the two-beam combiner MIDI, which operates in the mid-infrared region of the spectrum (N-band);

[8] The delay lines ought to be moveable systems so as to be able to compensate for the geometric delay, which is constantly varying during the night due to the rotation of the Earth.

(*a*) the three-beam combiner AMBER, working in the near-infrared wavelength bands (J-, H-, and K- bands);

(*a*) PRIMA, the dual-feed facility of ESO, operating in the near-infrared (K band), already decommissioned, and

(*a*) PIONIER, a four-beam combiner working in the near-infrared (H-band).

Also installed in the lab are IRIS, the infrared beam tip-tilt sensor, and FINITO, a three-beam fringe sensor. In 2015, MIDI and PRIMA FSUs are being removed, and PIONIER is being moved to make space for the second generation instruments GRAVITY and MATISSE.

The PRIMA experiment

Large FOVs are technically difficult to implement. A solution to circumvent this obstacle is to split the beam at the telescope so as to separate the primary and the secondary objects, and to obtain smaller FOVs for each of them. For a single baseline, the interferometer has to deal with four beams and to provide two fringe trackers. This kind of facility is known as a *dual-feed* interferometer. It was with the principles of dual-feeding and phase referencing in mind that the Phase Referenced Imaging and Micro-arcsecond Astrometry (PRIMA) experiment was devised at the VLTI.

PRIMA was the planned dual-feed facility of ESO, devised to enable the simultaneous interferometric observation of two emitting sources with two telescopes (either two ATs or two UTs). Each object was expected to have a size of at most $2''$ when using the UTs, and $8.9''$ when using the ATs, and they could be separated by up to 1 arcmin (Wilhelm, Köhler and Gitton, 2002). Due to late completion, lower than expected performance, and arrival of the second generation instruments, the project was decommissioned in June 2014 (ESPRI, 2014).

PRIMA was designed aiming at higher sensitivity — integration time limiting magnitudes around $m_{\mathrm{K}} \simeq 13$ for the UTs and $m_{\mathrm{K}} \simeq 11$ for the ATs — high angular resolution imaging of faint objects — expected spatial resolution around 1 mas — and high precision astrometry — approximately 10 µas over a $10''$ field when operating in the K-band (F. Delplancke, Derie et al., 2006; F. Delplancke, Leveque et al., 2000).

One of the major difficulties that had to be overtaken in order to fulfil these goals was the smearing of the fringe packet caused by the turbulence of the atmosphere. The time scale associated to the dynamic behaviour of the fringe pattern induced by the atmospheric turbulence is wavelength dependent, but it is typically of the order of the millisecond in the infrared. For example, in the K-band, after a few tens of milliseconds, the fringe packet is smeared out, which severely limits the ability to observe faint targets.

The principle of operation relies on finding within the isoplanatic angle — approximately 1 arcmin at 10 µm and $10''$ at 2 µm of the *secondary target* (usually, the *scientific star*) — a sufficiently bright object (the *primary*, or *fringe tracking*, or *guide target*) that can be used as a reference

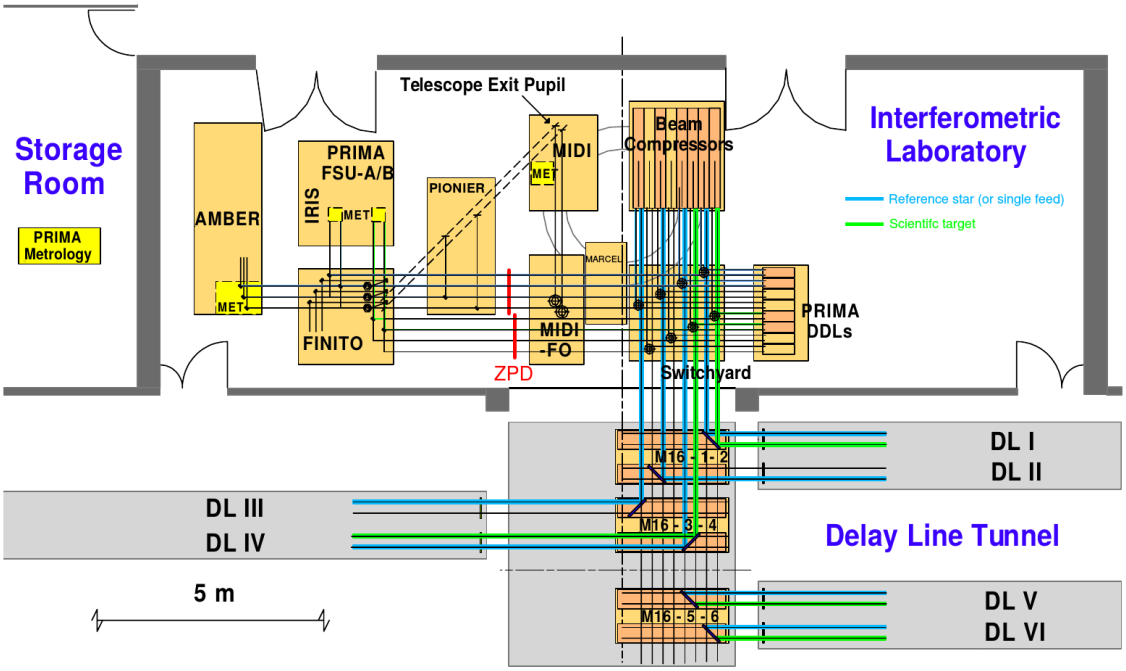

(a)

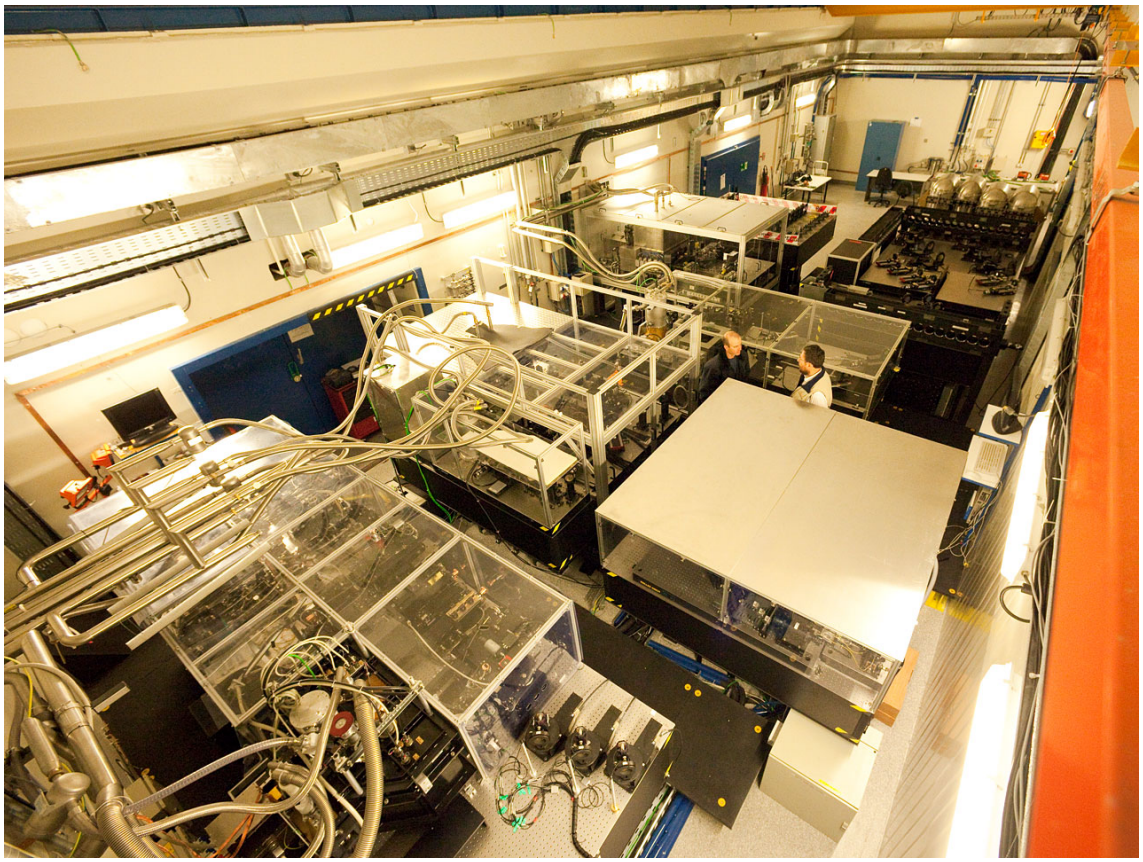

(b)

Figure 3.5: The VLTI laboratory. (*a*) Layout of the lab, where current instruments and beam routing are indicated (adapted from Lévêque, 2003, using information from J.-P. Berger, Zins et al., 2010). (*b*) Image of the lab as seen in March 2009. AMBER is located at the bottom left corner, and the DDLs at the top right corner of the photograph (source: ESO, 2009).

star for the stabilisation of the fringe motion, induced by atmospheric turbulence.[9] Usually, no star is on-axis. Both the primary and the secondary stars can be located anywhere in the FOV, provided they lie within the *isoplanatic patch*.[10]

Measuring the ΔOPD (section 3.3.1) inside the interferometer with a laser metrology system introduces the capability of imaging faint objects and of determining the precise angular separation between the two stars, *i.e.*, *narrow-angle astrometry* becomes possible.

The PRIMA operating principle

Figure 3.6 illustrates the PRIMA operating principle, the so-called *phase referencing* technique, where the OPDZ position of the secondary star is determined with respect to the primary star. Two objects are simultaneously observed with two telescopes, where the *star separators* (STSs) split the light beams coming from the primary and the secondary targets. Upon arrival to the delay line tunnel, two of the four beams (one beam from the primary object and the other from the secondary target) experience a common delay, and are then redirected to the VLTI laboratory. An extra relative delay between the primary and the secondary target beams is introduced by the *differential delay lines* (DDLs) before the final combination of the two beam pairs and detection of the fringe patterns.[11]

A precondition for phase-referenced imaging is the assumption that the fringe tracking star has a radially symmetric angular intensity distribution, *i.e.*, the phase ϕ of its visibility function is zero. The fundamental observable of PRIMA is the *differential* OPD or *differential delay* (ΔOPD or $\Delta\delta$). It corresponds to the shift in OPD of the white light fringe of the secondary star with respect to the white light fringe of the primary star, and it is given by

$$\Delta\delta = \Delta\mathrm{OPD} = \mathrm{OPD_P} - \mathrm{OPD_S} = \Delta\vec{S}\cdot\vec{B} + \frac{\phi}{k} + \Delta\delta_{\mathrm{int}} + \Delta\delta_{\mathrm{Atm}}, \tag{3.5}$$

where $\mathrm{OPD_P}$ and $\mathrm{OPD_S}$ are respectively the OPDs of the primary and the secondary targets (in fig. 3.6, $\mathrm{OPD_P} = \delta_{\mathrm{B}}$ and $\mathrm{OPD_S} = \delta_{\mathrm{A}}$). To the ΔOPD contribute (F. Delplancke et al., 2003):

- The **differential external OPD**, $\Delta\omega = \Delta\vec{S}\cdot\vec{B}$, with $\Delta\vec{S}$ and $\vec{B}$ denoting the *angular separation vector* between the two stars and the *baseline vector*, respectively. $\Delta S = |\widehat{S}_{\mathrm{P}} - \widehat{S}_{\mathrm{S}}|$, where $\widehat{S}_{\mathrm{P}}$ and $\widehat{S}_{\mathrm{S}}$ are versors (unit length), respectively pointing to the primary and secondary star.

[9] The roles of the "reference" and the "science" targets/stars are exchanged between exoplanet search and the other science cases. For this reason, this terminology is avoided in this chapter. Instead, it is always adopted the terms *primary/guide/fringe tracking* star — to denote the brighter star on which the fringes are tracked, and which serves as the zero point for the metrology and phase referencing measurements — and *secondary/fainter* star — to designate the fainter star, which is integrated longer and on which the position of the fringes with respect to the primary star is determined.

[10] The *isoplanatic patch* is the angular region on the sky over which the wavefront correction applied by an adaptive optics system allows for a well-corrected image (Hardy, 1998; M. Shao and Staelin, 1977) — *cf.* definition of page 96.

[11] This section pertains only with the operating principle of PRIMA. For details on how to calibrate and operate the instrument, please consult Appendix D.

- The **object phase** term, ϕ/k, where ϕ is the phase of the complex visibility of the secondary star[12] and k is the *mean wave number* of the observed spectral band ($k = 2\pi/\lambda_0$).
- The **differential internal (instrumental) OPD**, $\Delta\delta_{\text{int}}$, due to slightly different OPLs for the two stars inside the interferometer.
- The **differential atmospheric OPD**, $\Delta\delta_{\text{Atm}}$, introduced by the turbulent atmosphere, due to anisoplanatism, *i.e.*, because the incoming light from both objects follow different paths along the atmosphere — it causes a random differential motion of the fringe patterns (*cf.* chapter 4).

The shift $\Delta\delta$ between the two fringe systems is measured by a metrology system and, depending on the operation mode, by the combination of the two FSUs or by a dedicated FSU and a scientific instrument. In the astrometric mode, one of the FSUs closes the fringe tracking loop on the primary target and returns OPD_P, while the other FSU does the same for the scientific object and yields OPD_S. In the phase referenced imaging mode, $\Delta\delta$ is obtained by combining one of the FSUs with MIDI or AMBER.

The mean of $\Delta\delta_{\text{Atm}}$ is zero and, therefore, this term can be averaged out by successive measurements of $\Delta\delta$. Moreover, the RMS error of $\Delta\delta_{\text{Atm}}$, σ_{Atm} (in arcseconds), is proportional to $B^{-2/3} \cdot \Delta S \cdot t^{-1/2}$, where t is the observing time expressed in hours, S is in radians and B in metres (Lindegren, 1980; M. Shao and M. M. Colavita, 1992). Hence, another way to bring down $\Delta\delta_{\text{Atm}}$ is by increasing t — which strengthens the need for a fringe tracker during observations.[13]

The *internal* OPD, $\Delta\delta_{\text{int}}$, is measured by the dedicated PRIMA metrology system, which monitors the OPLs of the arms of the interferometer up to the Coudé focus of the ATs/UTs,[14] using a Michelson interferometric set-up and laser beams that follow the path of the light coming from both targets.

The first two terms, $\Delta\vec{S} \cdot \vec{B}$ and ϕ, cannot be distinguished with a single measurement. However, in phase referenced imaging mode, by measuring $\Delta\delta$ for many different (known) baseline vectors $\vec{B}$, the (constant) angular separation $\Delta\vec{S}$ can be "extracted" from the measured $\Delta\delta$ to determine ϕ. It is thus important to know $\vec{B}$ with high accuracy, which can be achieved by observing calibrator stars. The extraction of $\Delta\vec{S}$ from the measurement of $\Delta\delta$ is based on the knowledge of the predictable time-dependent behaviour of $\Delta\vec{S} \cdot \vec{B}$.

In the astrometric mode, both object phases ϕ are supposed to be zero (centre-symmetric intensity distribution for primary and secondary stars). Then, the difference $\Delta\delta$ of the white light fringe positions together with the measured $\Delta\delta_{\text{int}}$ yields the exact angular separation of the two objects, ΔS.

[12] Strictly speaking, the object phase term is equal to $\phi_\text{R} + \phi_\text{S}$, the phases of the complex visibility of the primary and the secondary targets, respectively. However, since it is required that the reference object is centre-symmetric, $\phi_\text{R} = 0$.

[13] In order to achieve 10 µas accuracy for an astrometric measurement with two stars separated by $10''$ with a baseline of 200 m, the observing time t must be around 30 min (*e.g.*, F. Delplancke, 2008; Lazorenko et al., 2009).

[14] In 2012, the VLTI team moved the retro-reflector up to the centre of M2.

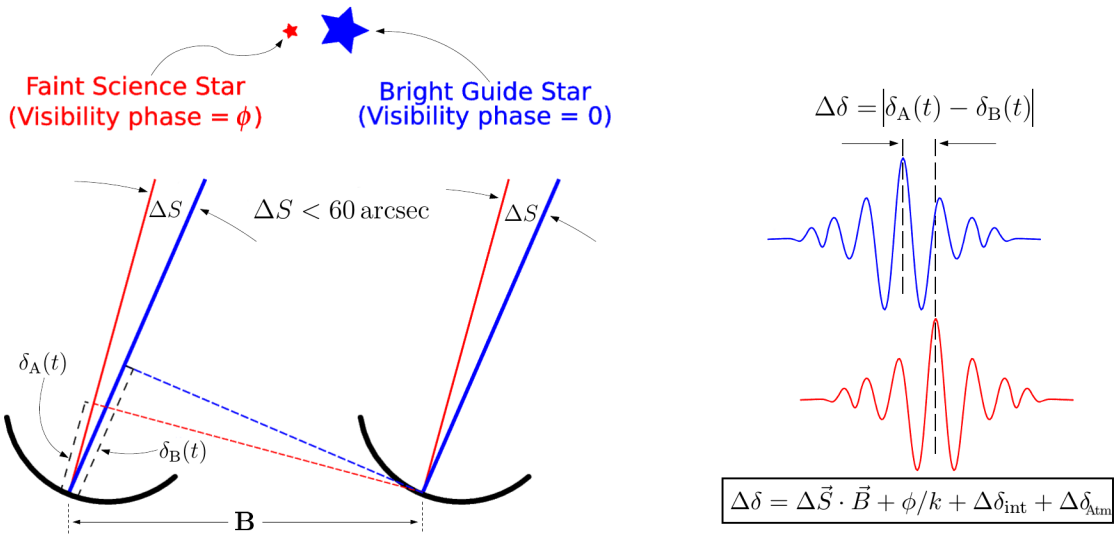

Figure 3.6: Schematic of the process of phase referenced imaging and astrometry. The stabilization of the fringe packet of the secondary object (red line) is accomplished by using a bright guide star (primary star, blue line) as a reference. The difference in the positions of the two fringe packets is determined by the OPD given by the product of $\Delta\vec{S}$ — the angular separation vector of the stars — and $\vec{B}$ — the baseline vector — by the phase ϕ of the visibility function of the secondary object, and by the OPD caused by the atmospheric turbulence and by the internal OPD (adapted from F. Paresce, 2002, and F. Delplancke, 2008).

Faint-object science mode

This would be the most basic operation mode of PRIMA, very similar to the imaging mode. The goal would be to track fringes on a bright guide object, in order to stabilise the fringes of a nearby faint secondary target. The fringe packet of the latter would be sent to instruments such as AMBER or MIDI, that would measure the corresponding visibility amplitude. The major differences between this and the imaging mode are (*a*) the bright guide star does not need to be centre-symmetric, because the visibility phase of the faint object is not measured (only its amplitude is determined by the instrument combined with the operating FSU), and (*b*) since the visibility phase is not an observable, the metrology system is not used.

The *faint science mode* was expected to push the limiting magnitude of the VLTI to fainter objects ($m_K \gtrsim 13$ with the UTs and $m_K \gtrsim 11$ with the ATs). Although it integrated the plans of the current thesis, the mode was never implemented during the commissioning runs. Nevertheless, conceptual studies and data analysis considered essential for the outputs of this thesis were carried out within this framework, being presented in chapter 5.

Imaging mode

The phase referenced *imaging mode* corresponds to an upgraded version of the faint-object science mode, with the addition of measuring the phase of the secondary target. When operating in this mode, PRIMA would be combined with AMBER or MIDI. The incoming light from a primary bright star would be sent to one of the FSUs, serving as a fringe tracking source, while the beam from the fainter secondary object would feed one of the aforementioned instruments.

The differential delay between the bright and faint source fringes would be measured using the metrology system. For each integrating point, the observables would be the visibility amplitude V, measured with AMBER or MIDI, and the visibility phase ϕ, *i.e.*, the position of the fringes with respect to the ZOPD determined by the FSU. As presented in section 2.2.2, to the pair (V,ϕ) corresponds one component of the Fourier transform of the source brightness distribution. Therefore, in principle, measuring the amplitude and phase of the visibility for several spatial frequencies (u,v), *i.e.*, for a number of different baselines, would allow one to recover the intensity distribution of the emitting secondary object with a higher spatial resolution (around 1 mas in the K-band) for fainter objects than phase closure techniques (F. Delplancke, Leveque et al., 2000). For the imaging mode to work, the guide star would have to be centre-symmetric (its visibility phase assumed to be zero), serving as a reference for the science source fringe phase.

Developing the phase referenced imaging mode with AMBER, the so-called PRIMA+AMBER *mode*, was the primary goal of this thesis. It was meant to characterise a set of complex visibility points of pre-main sequence stellar environments, namely the planet forming regions around young stars. Ultimately, if it was possible to sample enough spatial frequencies for a scientific object, a phase referenced image reconstruction would have been attempted. Unfortunately, ESO cancelled the imaging mode of PRIMA in April 2010, and the initial plan of the thesis was changed accordingly.

Astrometric mode

In the narrow-angle astrometric mode, both FSUs are used simultaneously to measure the phase delay. The observable is the angular separation $\Delta S = |\widehat{S_P} - \widehat{S_S}|$ between the primary and the secondary targets. Similarly to the imaging mode, one of the FSUs stabilises both fringe packets by closing the fringe tracking loop on the primary star, and measures $\delta_P = \mathrm{OPD_P}$. The difference is that, in this case, the light from the secondary object is fed into the other FSU, and $\delta_S = \mathrm{OPD_S}$ is precisely measured. Hence, the differential delay $\Delta\delta = |\delta_P - \delta_S|$ is extracted from PRIMA measurements. Both objects are assumed to be unresolved and, thus, their phases ϕ are equal to zero. When $\Delta\delta_{\mathrm{Atm}}$ is brought down to zero, as described in section 3.3.1 (page 45), and $\Delta\delta_{\mathrm{int}}$ is accurately determined, the careful knowledge of $\vec{B}$ yields the angular separation ΔS.[15]

The main scientific objective of the astrometric mode was the discovery of new exoplanets. With a precision of 10 µas over a FOV of $10''$ for operations in the K-band, it was expected that the reflex motion of a solar-type star, induced by a planet with a mass comparable to that of Uranus, was detected. Complementary radial-velocity observations of the system would yield the accurate mass of the planet (J. Sahlmann et al., 2013).[16]

[15] The main difference is that, in the astrometric mode, the needed accuracy on ΔOPD has to be much better than on the imaging mode ($\sim$ 10 mas instead of $\sim$ 200 mas). To achieve this goal, the two FSUs have been combined in replacement of the FSU + AMBER combination, to minimise asymmetries and non-common paths. Thanks to it, there is the possibility to perform swapping and to make differential measurements.

[16] Unfortunately, PRIMA's astrometric precision rarely went below 100 µas during the long commissioning period, and the project was eventually cancelled in June 2014.

PRIMA's subsystems

PRIMA can be subdivided into four subsystems: the *star separator* (STS), the *differential delay lines* (DDLs), the *fringe sensor units* (FSUs) and the *metrology system*.

Star Separator

The STS is an optical system placed at the UTs/ATs Coudé focus. It has two functions (Nijenhuis et al., 2008): (*i*) to pick up two stars in the FOV and to output them as two 80 mm parallel collimated beams that are sent through the light ducts to the DLs, and (*ii*) to provide the retroreflector mirror for the metrology system.[17] The STS comprises a roof shaped mirror with a sharp edge, that splits the incoming beam containing the primary and the secondary objects into two beams, each containing the light from only one object. It allows the transmission of two fields of view up to 1 arcmin apart in the sky. The diameters of these fields can be up to $2''$ and $8.9''$ for UTs and ATs, respectively.

Additionally, the STS allows the control of the pupil lateral and longitudinal positions, and the tip-tilt of the individual beams. It also provides a mode to calibrate the ZOPD, by injecting the *same* (primary) star into both of the output beams (feeds).[18]

Differential Delay Lines

The optical design of the DLs allows the possibility of guiding two beams in parallel from the star separator to the beam combination laboratory. The role of the DLs is to compensate for the varying geometric delay in each target-type beam (primary or secondary object light beam), caused by the rotation of the Earth. Due to the angular separation between the observed targets, a difference in the white light fringe position of the primary and secondary objects can be expressed as a differential OPD $\Delta\delta$ of up to 120 mm. This relative delay is adjusted and introduced by the DDLs with a precision of 5 nm (Pepe et al., 2008). The retroreflection is secured by a cat's eye and the optical delay is introduced by a fast two stage actuation system.

Each of the DDLs installed in the interferometric laboratory are able to delay only one light beam. Since four stellar beams are in interplay during PRIMA operations, four DDLs were installed in the lab (these correspond to the metallic vacuum vessels at the bottom of fig. 3.5b, page 44).

The Fringe Sensor Units

The PRIMA fringe trackers are called *Fringe Sensor Units* (FSUs). Together, they constitute the main subsystem of PRIMA, being responsible for the combination of the two pairs of beams, and for the detection and tracking of the resultant fringes. They consist of two identical units, "A" (FSUA) and "B" (FSUB), whose fringe sensing roles can be interchanged by means of a swapping

[17] In 2012, the retroreflector was moved up to the centre of M2.

[18] $\Delta S = 0, \phi = 0, \Delta\delta_{\mathrm{Atm}} = 0 \Longrightarrow \Delta\delta = \Delta\delta_{\mathrm{int}}$.

operation. The layout of a FSU is illustrated in fig. 3.7 (for more details, see J. Sahlmann et al., 2009).

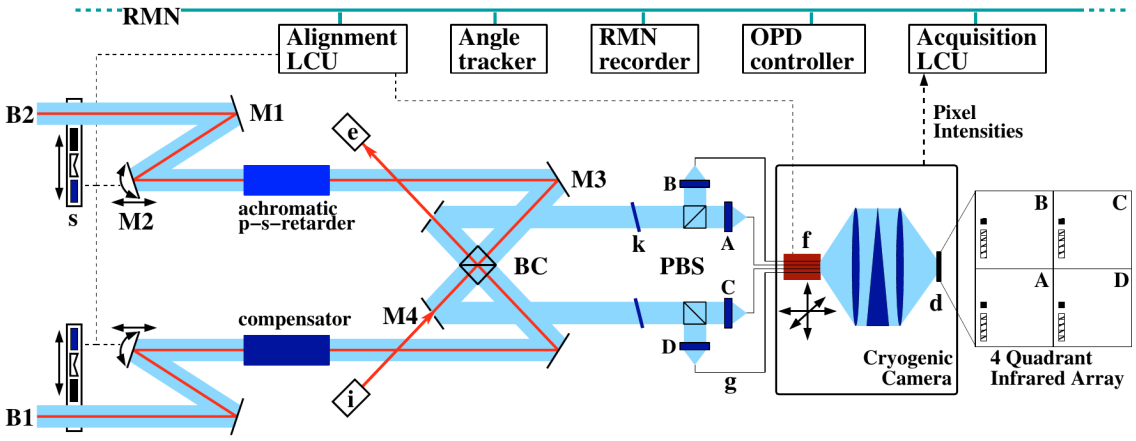

Figure 3.7: The FSU layout, showing the light beams paths, the beam combination and the detection principle. **B1** and **B2**: optical beams coming from the telescope; **s**: shutter system (motorised stages), used to block the beams or to introduce longitudinal atmospheric dispersion compensators; **M1**, **M3** and **M4**: fixed mirrors; **M2**: tip-tilt mirror controlled by a piezoelectric translation stage; **BC**: beam combiner, which superimposes beams B1 and B2; **k**: dichroic mirrors, which deflect the H-band light; **PBS**: polarising beam splitters, which split each combined beam; **A**, **B**, **C**, and **D**: beams generated by the PBSs, which are out of phase by $\pi/2$; **g**: single-mode fibres, to where the beams A, B, C and D are injected by means of coupling doublets; **f**: fibre bundle; **d**: the four-quadrant infrared detector of PRIMA (PICNIC); **LCU**: acquisition local control unit; **i** and **e**: respectively injection and extraction of the laser metrology beams (red) in BC; **RMN**: reflective memory network, which allows the communication between the LCUs and the other VLTI real-time control systems (ibid.).

An IR camera in FSUA measures the position of the white light fringe of the primary star, and the twin unit FSUB measures the position of the fringe packet of the secondary star. Both operate in spectrometric mode, thus providing the error signal for the fringe tracking system (and the difference in white light fringe position between guide and scientific stars). For observation of a $m_K = 11$ star with the UTs, it is necessary to provide an error signal with a measurement noise of 30 nm RMS. In order to achieve a good sky coverage, it is important that both FSUs are sensitive enough — even at the cost of reducing measurement accuracy.

The PRIMA FSU is located in the interferometric laboratory. Both units (A and B) are usable as sensors for the fringe tracking system. In astrometric mode, FSUA and FSUB are used simultaneously for both stars (*cf.* chapter 5, page 81).

Metrology system

A highly accurate metrology system monitors the differential internal OPD fluctuation $\Delta\delta_{\text{int}}$, to ultimately reach an instrumental phase accuracy which is limited by atmospheric piston anisoplanatism only. The metrology system measures the internal differential delay $\Delta\delta_{\text{int}}$ between both stars in the two interferometer arms, with a 5 nm accuracy over a period of typically 30 minutes (F. Delplancke, Derie et al., 2006). This accuracy requirement is driven by the PRIMA astrometric mode. The principle of the PRIMA Laser Metrology System is equivalent to two heterodyne Michelson laser interferometers, operating simultaneously at two different heterodyne frequencies,

and having a common optical path with both stellar channels through the VLTI/PRIMA optical train. The difference between the OPD measured by the two interferometers is directly recorded.

The metrology laser beams were chosen in the infrared ($\lambda = 1\,319\,\mathrm{nm}$), close to the scientific bands to reduce longitudinal dispersion. At the laboratory, they have a diameter equal to 1 mm, which enlarges to about 4.5 mm during the propagation in the tunnels. They have a common path with the stellar beams since they are injected in the telescopes central obscuration created from the secondary mirrors. This way, stray light in the instrument is avoided. The metrology beams are retroreflected at the telescope by the STS. When the returning beams are extracted by the FSU, the instrumental OPD $\Delta\delta_{\mathrm{int}}$ is inferred.

This system is incremental, *i.e.*, the OPD is measured with respect to a reference position, which is needed to be initialised. In case of reference imaging, the bright object beam is split into two identical beams at the level of the star separator. The metrology can be initialised when fringes are detected simultaneously on the FSU and on the instrument, meaning that $\Delta\delta_{\mathrm{int}}$ is equal to zero (ibid.). In the astrometric mode, the two stars in the FSUs are swapped in order to calibrate the zero point of the metrology.

The PRIMA observables

The observables measured with PRIMA depend on the operation mode. They were introduced along the previous subsections and are summarised in table 3.1.

Table 3.1: The PRIMA observables for each operation mode. The *fundamental* observable refers to the differential optical delay, from which all other observables are derived.

PRIMA Observables	
Fundamental:	differential delay, $\Delta\delta = \delta_{\mathrm{P}} - \delta_{\mathrm{S}} = \mathrm{OPD_P} - \mathrm{OPD_S}$
Imaging mode:	complex visibility amplitude, V, and phase, ϕ
Faint science object mode:	complex visibility amplitude, V
Astrometric mode:	angular separation, ΔS

PRIMA scientific goals

In addition to the scientific objectives of PRIMA, enumerated in sections 3.3.2 to 3.3.4, to wit, to probe the planet forming regions around YSOs and the detection of extra-solar planets, a plethora of targets could fit in the astrophysical science accessible with PRIMA. Examples of such are:[19]

- **Phase referenced imaging**: late type stars (star diameters, mass loss, dust-shells, limb darkening, "hot spots", pulsation), circumstellar dust disc and ejecta, binary systems, compact stellar objects (white dwarfs, pulsars and black holes in binary systems), stellar clusters

[19] For a detailed and extensive list of scientific drivers for PRIMA, see, for instance, F. Delplancke, Leveque et al., (2000), F. Paresce et al., (1996) and A. Quirrenbach et al., (1998).

(dynamics of both globular and open clusters), galactic centre (spectral classification of stars and determination of radial velocities); novae and supernovae, solar system (asteroids, dwarf planets, comets and occultations); quasars and active galactic nuclei, Magellanic clouds and neighbouring galaxies.

- **Narrow-angle astrometry**: galactic centre, globular clusters, binary stars, open clusters, brown dwarfs, gravitational micro-lensing events, and parallaxes.
- **Faint science objects**: gravitational microlensing (MACHOs and galactic centre black holes).

Some of these scientific objectives are technically demanding, and would require the originals expected precision of 10 µas and sensitivity for tracking ($m_K \leqslant 10$ for the ATs and $m_K \leqslant 13$ for the UTs) and for detection ($m_K \leqslant 18$ on the ATs and $m_K \leqslant 22$ on the UTs), as well as suitable guiding and/or reference targets within the isoplanatic patch (F. Delplancke, Leveque et al., 2000).

Addendum

As PRIMA did not reach the expected limiting magnitude and astrometric precision, the scientific cases decreased significantly. Finally, with a very small niche of applications and due to the arrival of the more powerful second generation instruments, it was decided in 2014 to stop the PRIMA project and use the gathered experience for the benefit of GRAVITY.

Chapter 4

Estimation of visibilities with PRIMA

"Everything should be made as simple as possible, but not simpler."

— ALBERT EINSTEIN

Contents

ISOPLANATISM is a concept indicating that the transfer function of an optical system is independent of the angular FOV (Fried, 1976). Consequently, the *isoplanatic angle* or *patch* is characterised by spatial invariance within its limits. In contrast, *anisoplanatism* is the term used to indicate that wavefront errors are introduced over the angular FOV, mainly due to atmospheric turbulence. By corrugating the wavefront and, thus, introducing relative displacement between any two beams, turbulence implies that measured or computed quantities are dependent of anisoplanatic effects, as lateral and angular separation, chromatism and focusing of the beams (D'Arcio, 1999; Esposito, Riccardi and Femenìa, 2000; Hardy, 1998). Of those, angular anisoplanatism is of special interest in the domain of phase referencing, since there is no perfect coincidence of the atmospheric paths followed by the two wavefronts separated by a certain angular distance,

and, consequently, the determination of visibility amplitudes is affected by the position of the emitting source in the FOV.

The main purpose of this chapter, highly inspired in the work by Nuno Gomes, Schmid et al., (2012), is to describe the algorithm developed aiming at the estimation of visibility amplitudes from PRIMA data, and to present the results and conclusions of the application of this algorithm to on-sky astrometric data.

Visibility amplitude estimation from PRIMA data

When in the astrometric mode (see chapter 5, page 81), PRIMA can be used to estimate the visibilities of observed objects. Although the FSUs are optimised to measure the phase delay, this mode offers the possibility to calibrate visibilities and to study the dependence of the visibility on the *detector integration time* (DIT), on the separation between the stars, on the zenith distance, and on the physical conditions of temperature and seeing inside the light ducts. Measuring the variability of the visibility amplitude with the separation between two unresolved stars simultaneously observed by PRIMA allows to study the effects of the angular anisoplanatism on the power-spectra to be measured by auxiliary instruments, as AMBER. This problem is addressed in the following subsections.

Complex visibility amplitude and phase (ideal case)

The estimation of visibility amplitudes from FSUs data can be carried out by applying a variation of the ABCD method (Creath, 1988), already introduced in section 2.2.4, and by using the fact that the FSUs measure intensities at four points spaced by $\lambda/4$. The starting point is the relation

$$V = \frac{I_{\text{corr}}}{I_{\text{phot}}}, \tag{4.1}$$

where I_{corr} is the *correlated flux* and I_{phot} stands for the *photometric* or *total flux* (Schroeder, 1987).

In an ideal case, where the phase difference between the four beams emerging from the *polarising beam splitter* (PBS) is $\pi/2$, the raw intensities measured in each quadrant of the FSUs's PICNIC detector array are:

$$I_i(t) = I_0(t) + I_{\text{corr}}(t)\cos(\varphi_i), \tag{4.2}$$

where I_0 corresponds to the non-corrected photometric flux, $i = A,B,C,D$, and $\varphi_A = \varphi, \varphi_B = (\varphi + \frac{\pi}{2}), \varphi_C = (\varphi + \pi)$ and $\varphi_D = (\varphi + \frac{3}{2}\pi)$.

The raw intensities have to be corrected for bias introduced by the readout process — dark counts are removed and the flux is normalised by the photometric "flat" mean value (J. Sahlmann et al., 2009):

$$S_i(t) = \frac{I_i(t) - G_i}{P_i - 2G_i}, \tag{4.3}$$

where S_i stands for the corrected A, B, C and D intensities at time t, I_i accounts for the aforementioned instantaneous raw pixel intensities, G_i is the *dark mean value* for each quadrant and P_i the *photometric mean value* (sometimes referred as *flat* mean value) for each quadrant — the factor of 2 in the denominator arises from the fact that the photometric frames are taken in two steps, implying two detector integrations.[1] The denominator of eq. (4.3) is called *photometric factor* and, in fact, it corresponds to a photometric calibration. Since PRIMA does not use spacial filtering before the beam combination, it is acceptable to normalise the flux by using only one set of photometric frames acquired before the observation, taking into account the various transmissivities and sensitivities of the 4 channels of each FSU.

Applying the dark and photometric corrections to eq. (4.2),

$$A = \frac{I_A - G}{P - 2G} = \frac{I_0 - G}{P - 2G} + \frac{I_{corr}}{P - 2G}\cos\varphi \tag{4.4a}$$

$$B = \frac{I_B - G}{P - 2G} = \frac{I_0 - G}{P - 2G} - \frac{I_{corr}}{P - 2G}\sin\varphi \tag{4.4b}$$

$$C = \frac{I_C - G}{P - 2G} = \frac{I_0 - G}{P - 2G} - \frac{I_{corr}}{P - 2G}\cos\varphi \tag{4.4c}$$

$$D = \frac{I_D - G}{P - 2G} = \frac{I_0 - G}{P - 2G} + \frac{I_{corr}}{P - 2G}\sin\varphi. \tag{4.4d}$$

By construction,

$$I_0 - G_i \simeq P_i - 2G_i \simeq I_{\text{phot}}, \tag{4.5}$$

which will make the first term of equations (4.4) always close to 1. The final reduced fluxes are obtained by combining eqs. (4.3) to (4.5):

$$S_i = 1 + V\cos\varphi_i, \tag{4.6}$$

The amplitude of the visibility and the fringe phase can be estimated by means of the *fringe quadratures*, $X = A - C$ and $Y = B - D$, where X corresponds to the real part of the complex visibility and Y to the imaginary part:[2]

$$V = \frac{1}{2}\sqrt{X^2 + Y^2}, \tag{4.7}$$

$$\varphi = \arctan\frac{Y}{X}. \tag{4.8}$$

Phase Corrections

During real operations, existent imperfections in the system introduce non-ideal quadrature signals $X' = A' - C'$ and $Y' = B' - D'$, which can be accounted for by means of *phase shift errors a*,

[1] A different notation is adopted for the photometric frame (P instead of F) to avoid confusion with the *flat field* term, common amongst astronomers.

[2] There is a typo in J. Sahlmann et al., (2009) paper, where V is written as equal to $\sqrt{X^2 + Y^2}$.

b, c and d, defined as the difference between the real phase shifts and their ideal values, respectively of 0, $\frac{\pi}{2}$, π and $\frac{3}{2}\pi$ (J. Sahlmann et al., 2009):

$$A' = I_{phot} + I_{corr}\cos(\varphi + a) \tag{4.9a}$$
$$B' = I_{phot} - I_{corr}\sin(\varphi + b) \tag{4.9b}$$
$$C' = I_{phot} - I_{corr}\cos(\varphi + c) \tag{4.9c}$$
$$D' = I_{phot} + I_{corr}\sin(\varphi + d), \tag{4.9d}$$

where $a, b, c, d \in [0, \pi/2[$. Developing the trigonometrical identities and referencing the phase ($a = 0$), the ideal quadratures X and Y can be written as a function of the experimental ones (X' and Y'):

$$X = C(\gamma X' - \alpha Y') \tag{4.10a}$$
$$Y = C(\delta X' + \beta Y'), \tag{4.10b}$$

where $\alpha = \sin c$, $\beta = 1 + \cos c$, $\gamma = (\cos b + \cos d)$ and $\delta = (\sin b + \sin d)$ are the *phase shift error coefficients* and $C = \frac{2}{\beta\gamma - \alpha\delta}$.[3] The phase shift error coefficients can be retrieved from the header of the FITS file corresponding to the observation. For each FSU, they are stored in keywords which, in the specific case of the white pixel of the detector, are named KWPHAS.

The algorithm

The algorithm comprises two main steps: *data reduction* and *calculation of the visibility amplitude*. In the following, it is described the tasks involved in each of them, and it is explored the possibility of selecting part of the fluxes before the actual visibility estimation.

Data reduction

Firstly, A, B, C, D fluxes of the *dark frame* corresponding to the observation are averaged out for non-nil pixels — when the recording of a file takes longer than the exposure time, the remainder of the time stamps are removed (see fig. 4.1) — and for each quadrant of the detector of both FSUs. A representative dark mean value is thus obtained for each quadrant of the PICNIC detector.

Accompanying the observation file there are two *photometric calibration frames*[4] with imprinted fluxes for FSUA and FSUB. For each of these files and one quadrant at a time, the same aforementioned averaging procedure is applied and the averaged fluxes are added up, quadrant by quadrant, resulting in an averaged flux for each quadrant, for both FSUs. The mean dark values are then subtracted twice from the corresponding quadrants — see section 4.1.1. The result is a combined photometric flux value for each quadrant of FSUA and FSUB.

[3] Due to the typo pointed out in the previous footnote, an error was propagated in the equations by J. Sahlmann et al., (2009) paper, where $C = (\beta\gamma - \alpha\delta)^{-1}$.

[4] Known as *flat-fields* in the VLTI nomenclature.

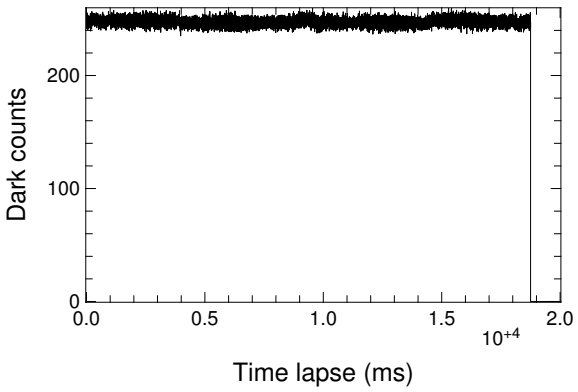

Figure 4.1: Dark counts for PICNIC_A present in a raw dark frame. It is visible that the exposure time is shorter than the recording time. The remainder of the time stamps are removed.

Finally, the calibrated fluxes are computed for each quadrant of the PICNIC detector, as described by eq. (4.3).

From this point, two approaches can be used to prepare the data before the calculation of the visibility amplitude: a subset of fluxes is selected from the histogram of the distribution prior to visibility calculations, or data is left "as is". In the former, a subset of values is selected from the histogram of the visibilities in order to compute the final averaged visibility amplitude, while in the latter, the visibility amplitude is computed directly from the set of fluxes.

Flux pre-selection *vs* visibility selection

After data reduction and before visibility estimation, a flux selection can be performed according to some criteria, aiming at the improvement of the quality of the results. For both FSUs, a mask is created for each quadrant of the detector in order to select fluxes within a certain interval, that can be defined as $[m_c - \sigma,\ m_c + \sigma]$ or as $[m_c + \sigma,\ +\infty[$, where m_c is a weighted arithmetic mean of the distribution with weight h_y, given by the equation

$$m_c = \frac{\sum(h_x \cdot h_y)}{\sum h_y}, \tag{4.11}$$

(h_x is the array of abscissae, in units of flux, and h_y is the array of histogram points) and σ is the standard deviation of the distribution — see fig. 4.2. The former case has the apparent advantage of eliminating less common points of the distribution, while the latter allows the selection of points with high flux values, which in principle would lead to a better SNR. However, two caveats became apparent from fig. 4.2: the shape of the distribution of fluxes is being modified and, specifically for the first case, sometimes not all the pixels with the most common flux values are selected (as can be seen in fig. 4.2b). In fact, a careful analysis leads to the conclusion that neither approach is good.

Figure 4.3 illustrates the fluxes relevant to each fringe quadrature, one versus the other, and fig. 4.4 depicts the ratio of those fluxes against time. The yellow ellipse encompasses the most common points (considering only fluxes A and C, or B and D), the magenta box contains the most bright pixels, and the green ellipses include points where one of the quadrants dominates in flux. Points within the green ellipses correspond to the peaks of fig. 4.4, where the flux was measured

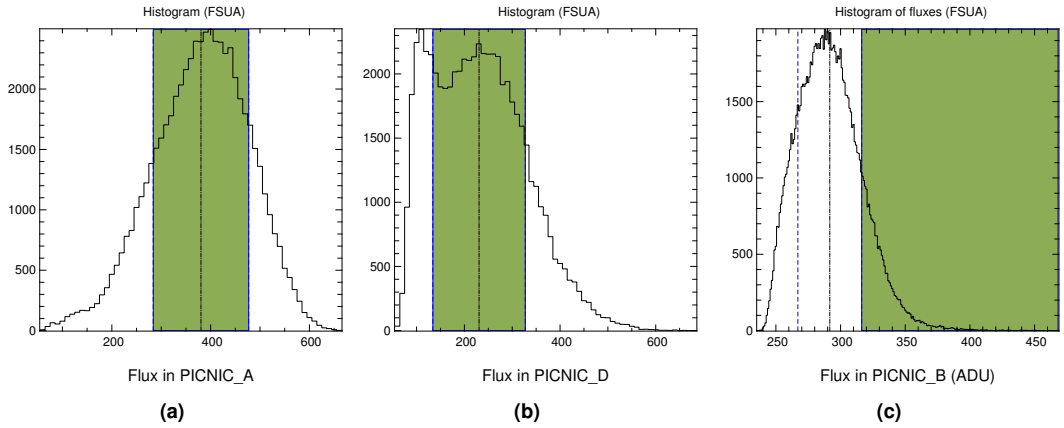

Figure 4.2: Histograms of fluxes in three quadrants of the FSUA's PICNIC detector, corresponding to the second (fig. 4.2a and fig. 4.2b) and fifteenth (fig. 4.2c) observations of the night 2008/11/26 from PRIMA commissioning #2. The object is, in this case, HD15520. In histograms (4.2a) and (4.2b), fluxes were picked around the mean value, while in histogram (4.2c), selected fluxes were larger than $m_c + \sigma$.

on the fringe (correlated flux), although some points inside the yellow ellipse might correspond to correlated flux as well. In fig. 4.4, values around 1 correspond to points of photometric flux, where correlated flux is very low or completely absent. Selecting the most common fluxes from the histogram corresponds to pick points within the yellow ellipse in fig. 4.3, while choosing the most bright fluxes is equivalent to take points within the magenta box in the same plot. Therefore, it is clear from these figures and eq. (4.6) that all points are relevant for the calculation of the visibility. Tests performed with the data set described in section 4.2.1 yielded visibility estimates roughly 70 % to 80 % inferior to what was expected if any flux selection would be made before computing the visibility arrays.

Therefore, none of the approaches is valid for a good estimation of the visibility amplitude and the latter should be computed directly from the reduced fluxes.

Computing the visibility amplitude

Using the quantities obtained from the data calibration, together with the phase shift error coefficients retrieved from the FITS header, eq. (4.7) is applied to create visibility arrays for both FSUs.

The visibility amplitude is then computed only for measurements on the fringe, *i.e.*, with either the OPDC and/or the DOPDC in tracking controlling state (*cf.* fig. 4.5), averaging out all points of the arrays. The averaging can be done using directly a bootstrapping technique or by selecting firstly the most common visibility points from the histogram of visibilities (*cf.* fig. 4.6), as they both produce similar results.

Comparing figs. 4.4 and 4.5a, it becomes apparent that the peaks in the latter correspond in fact to points of flux where the FSU was *fringe tracking* (FTK) and, thus, they are compatible to fluxes measured on the fringe.

Figure 4.7 is similar to fig. 4.3, but it depicts points of flux acquired during the first 4 seconds of recording, just before the fringe was found for the first time. As expected, the flux concentrates

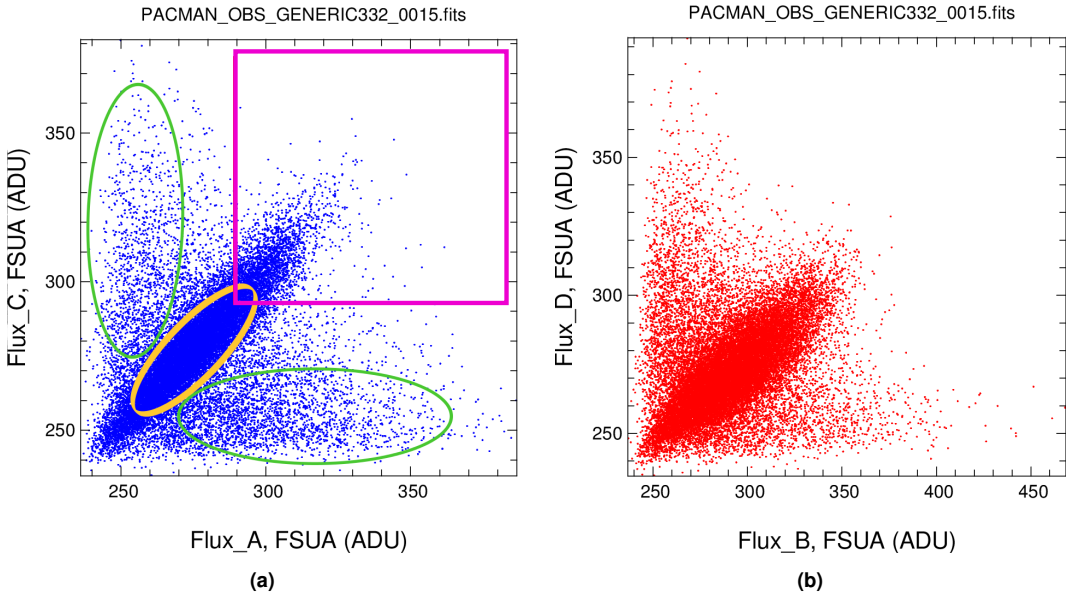

Figure 4.3: Plot of reduced fluxes C *vs* A (fig. 4.3a) and D *vs* B (fig. 4.3b). The yellow ellipse corresponds to points with the most common fluxes, the magenta box to points with the highest fluxes and the green ellipses encompass points with fluxes measured on the fringes.

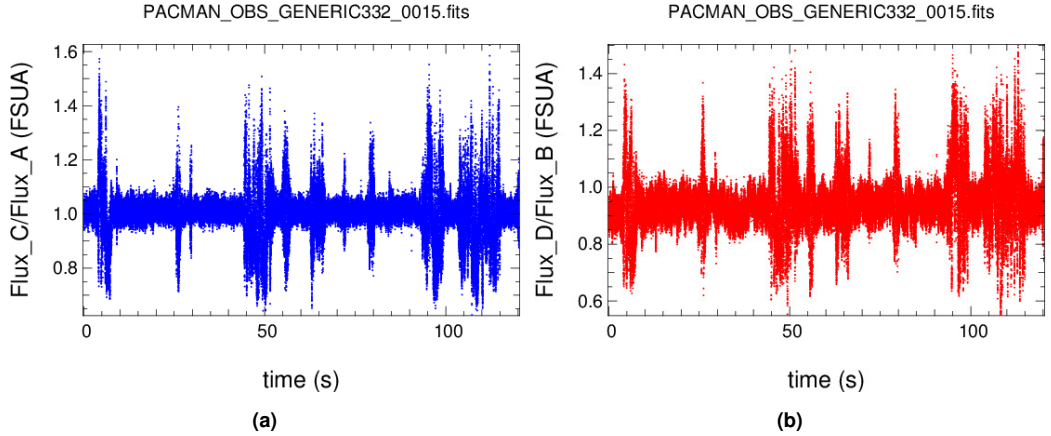

Figure 4.4: Plot of the ratio of the reduced fluxes C/A (fig. 4.4a) and D/B (fig. 4.4b) *vs* time. The peaks correspond to points of flux measured on the fringe (correlated flux) while values around 1 correspond to points of photometric flux or where the correlated flux is almost absent.

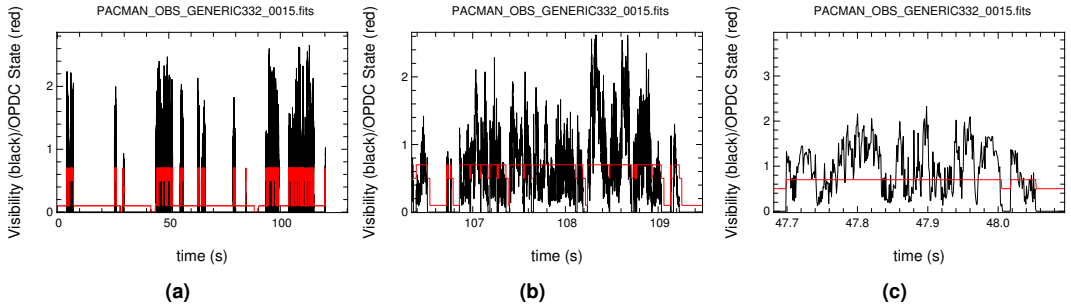

Figure 4.5: OPDC controlling state (red lines) over-plotted on the visibility array (black lines) *vs* time for the first observation set, corresponding to a total integration of 120 s on the object HD18829. fig. 4.5a represents the full visibility array after elimination of non-tracking points, while figs. 4.5b and 4.5c depict two different levels of zoom of the former. The OPDC state values were scaled down for clarity: 0.7 corresponds to *fringe tracking*, 0.5 to *system waiting* and 0.1 to *searching*. Clearly, the visibility points from fig. 4.5a match the peaks of flux of fig. 4.4, confirming that the latter correspond to points of flux measured on the fringe.

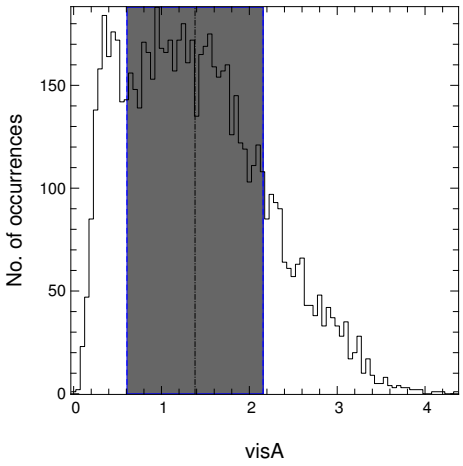

Figure 4.6: Example of histogram plotted for an array of visibilities. The grey shadow highlight the region $\pm\sigma$ around the mean value of the visibility. In this case, the computed visibility is roughly 1.4 with $\sigma \simeq 0.7$.

roughly in the line bisecting the graph, indicating that this is a photometric flux. As soon as the FTK begins, points near the axis start to be present, indicating fringes were found. This is consistent with fig. 4.5, where it is noticeable that the fringe was found for the first time around 4 s after the beginning of the recording.

It is notorious, from figs. 4.3b and 4.7b, that there is an imbalance of flux between quadrants B and D of FSUA, as the ratio of photometric fluxes is less than 1 — the slope $D/B \sim 0.9$. This situation was caused by a defective optical fibre in the cold optics of PRIMA. The fibre was promptly replaced and no imbalance was detected in data acquired subsequently.

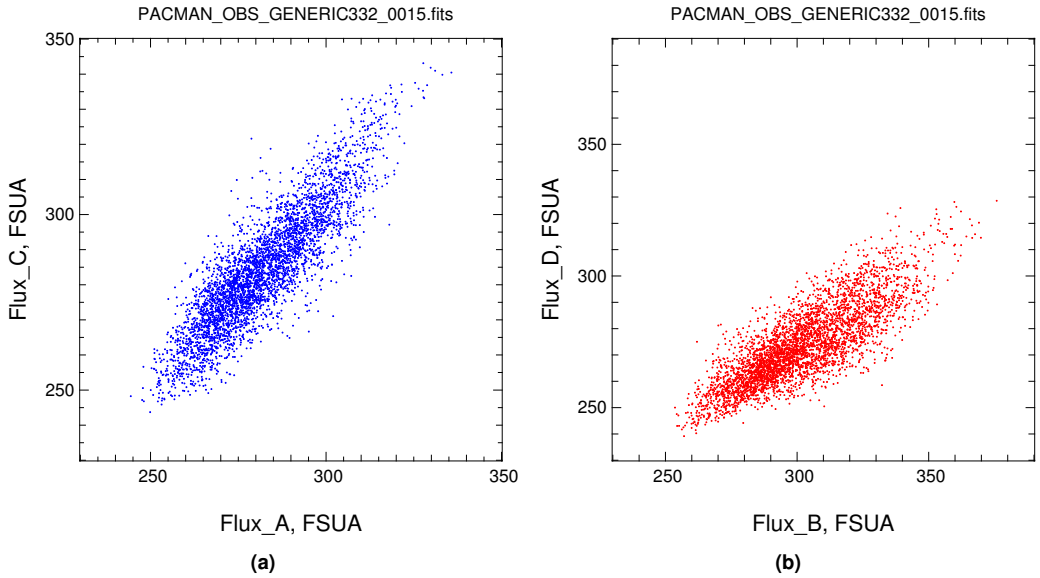

Figure 4.7: Similar to fig. 4.3, but only for the first 4 s of recording, just before the fringe was found for the first time. Only photometric flux is identified.

Applications to on-sky data

The commissioning runs of PRIMA produced enough data to test the algorithm described in the previous section. Two packages were developed aiming at the reduction of FSU data and the estimation of the visibility of objects observed with PRIMA, `VADER` and `PACMAN`. They were both written in `Yorick`,[5] and they are able to open any FITS file from ESO and to deal with non standard structures of the format.

Commissioning run #2 single-feed data (November 2008)

A set of 22 FSU data files, with respective dark and photometric frames, from the commissioning night of 2008/11/26 were analysed in order to compute the visibility amplitudes with `VADER` and `PACMAN`. The objects were two stars with similar coordinates and magnitudes (HD18829, $m_K = 4.2$, and HD15520, $m_K = 4.5$), always observed with the baseline G2–J2. For each observation, data was acquired for 120 s at a rate of 1 kHz in single-feed mode.

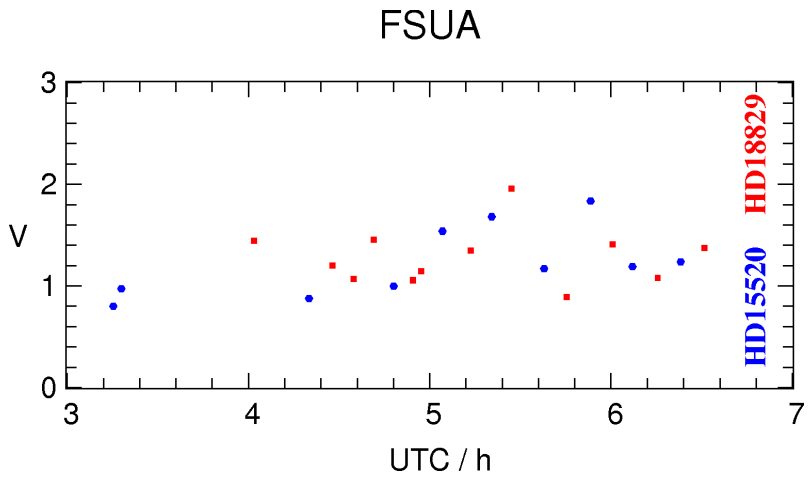

(a) Visibility points and respective error bars for HD18829 (red squares) and HD15520 (blue dots).

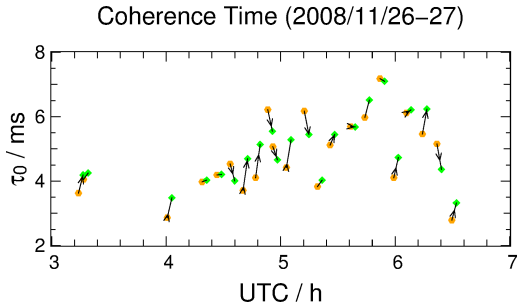

(b) Orange dots: τ_0 at the beginning of the observation; green diamonds: τ_0 at the end of the observation.

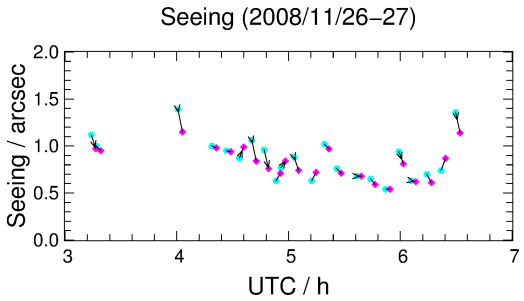

(c) Cyan dots: seeing at the beginning of the observation; magenta diamonds: seeing at the end of the observation.

Figure 4.8: Plots of the visibilities V *(top)*, coherence times τ_0 in ms *(bottom left)* and seeing in arcseconds *(bottom right) vs* hours of UTC for all valid set of data during the night run.

[5] http://yorick.sourceforge.net/

Figure 4.8a illustrates the calculated visibility points together with their error statistics. The latter correspond to the standard errors of the approximately normal distribution of the several thousand visibility estimates. Because of their tiny values, the error bars are not visible, lying inside the symbols used to represent the visibility amplitude points. This plot, globally in agreement with the results publish by J. Sahlmann et al., (2009), presents some discrepancies between the values of the visibility amplitude, that can be justified by differences in the algorithms and in the formulas used to compute the visibilities, as was previously mentioned. Moreover, there is a significant dispersion and many of the visibility amplitudes are larger than 1, which can be explained by the issue on the photometric calibration: since the photometry is done before tracking the fringes, some factors, such as seeing and air mass, can change between the photometric calibration and the measurements. This is why the FSUs are not really well suited to measure visibility amplitudes (they were not designed with that aim).

The visibilities for HD18829 and HD15520 are found to be respectively 1.3 ± 0.3 and 1.2 ± 0.3. The errors of the final averaged values for each star were estimated by means of the standard deviation of the mean visibility amplitudes set. Although higher than 1, these values are compatible with non-resolved objects (as expected) and with the results of J. Sahlmann et al., (ibid.). This outcome, which assumes a great relevance having in mind that the FSUs were designed to measure phases, not visibility amplitudes, opens the doors to study the effects of the angular anisoplanatism on the visibility measurements by the PRIMA FSUs, and is an indication of the robustness of the algorithm presented in the current section.

Relations between the visibility amplitude, the detector integration time and the light tunnel atmospheric conditions (temperature and seeing) would allow the extrapolation of the results to the PRIMA+AMBER case and to conclude on the advantages/disadvantages of combining both instruments using the FSU as an off-axis fringe tracker.

Figures 4.8b and 4.8c depict respectively the coherence times and seeing during the observations. There is an increasing of the coherence time and a corresponding decreasing of seeing around 6 h UTC, which seem to be related to the slightly larger values of the visibility amplitudes around 5.4 h to 5.8 h UTC. In order to check for this hypothetical correlation between the three quantities, the visibility was plotted against the coherence time (fig. 4.9a) and against the seeing (fig. 4.9b). From these pictures it is apparent that no correlation exists between them.

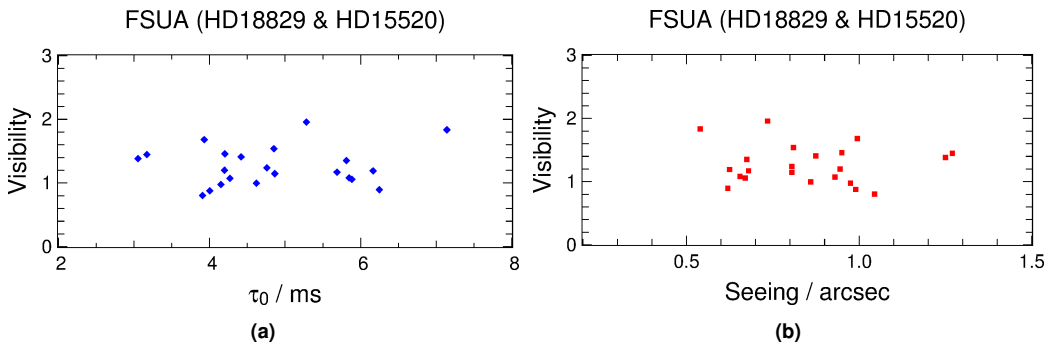

Figure 4.9: Plot of the visibility amplitudes *vs* the coherence time, in ms (fig. 4.9a), and *vs* the seeing, in arcseconds (fig. 4.9b). It is apparent from the graphs that no correlation exists between the quantities.

Regarding the data set of visibilities, the final values computed after the visibility histogram selection are the same as their counterparts calculated without previous visibility selection (*cf.* fig. 4.10). This indicates that previous histogram selection does not affect the estimation of the visibility and that the bootstrapping technique[6] is a powerful method to estimate statistical properties when sampling from approximated distributions.

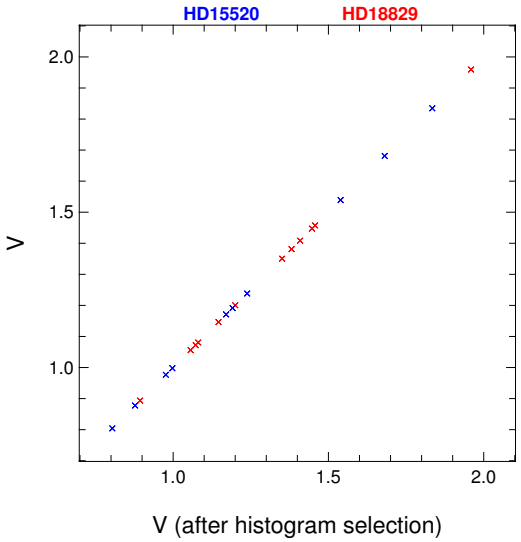

Figure 4.10: Plot of visibility amplitudes V *vs* visibility amplitudes computed after histogram selection V_{histo}. As in Figure 4.8a, red points correspond to HD18829 and blue ones to HD15520. $V \simeq V_{\mathrm{histo}}$ for all visibility points.

Commissioning run #14 dual-feed data (January 2011)

The so-called *dual DIT mode* of IRIS, for which the detector is run with different integration times accounting for the distinct flux levels of the two stars, was successfully implemented and tested on bright-bright pairs ($\Delta m_{\mathrm{H}} \lesssim 2$) during PRIMA commissioning run #12, in the fall of 2010 (Schmid et al., 2012).

During commissioning run #14 (between the 16$^{\mathrm{th}}$ of January and the 6$^{\mathrm{th}}$ of February 2011), the simultaneous use of both FSUs in the astrometric mode was tried in a target pair with a larger difference in brightness. The atmosphere was stabilised by using FSUB to track the fringes on HD87640, a $\mathrm{m_K} = 4.8$ star, while the integration time was systematically increased on FSUA up to one second, scanning through the fringes with the DDL on SAO221759, a $m_{\mathrm{K}} = 7.1$ star, 6.6″ distant. Availing of the excellent weather conditions (seeing of 0.87″ and coherence time of 10 ms), on the 5$^{\mathrm{th}}$ of February 2011 the team achieved a coherent exposure of the fringes on FSUA over a time span of more than 3 min, stabilising the white-light fringe during 180 one-second frames (ibid.). The resulting plot can be seen in fig. 4.11.

[6] *Bootstrapping* is the technique of estimating statistics, such as the mean or the variance, by measuring them over many randomly selected samples (of fixed size) of the population.

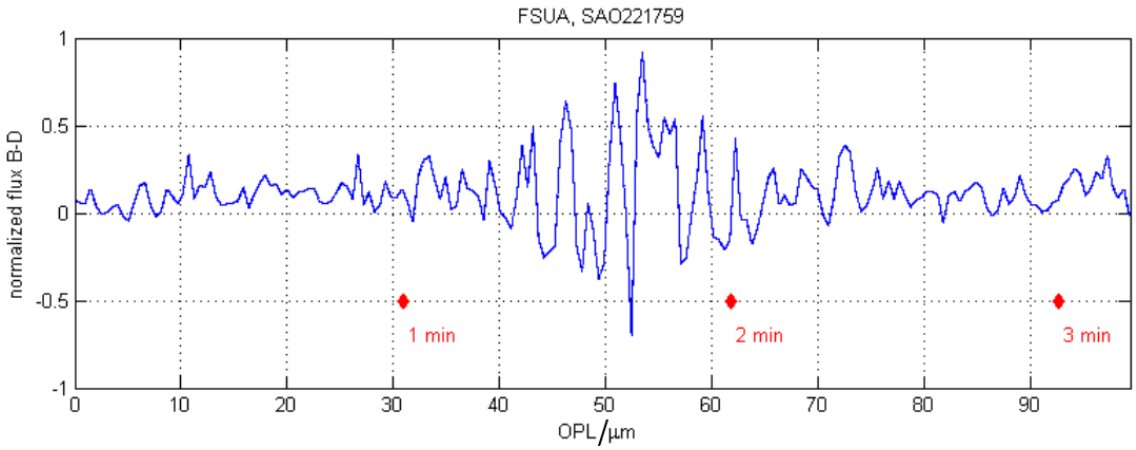

Figure 4.11: Plot of the SNR (blue dots) and interpolation curve (blue line) for the fringe packet measured with both FSUs on a pair of stars from a multiple system (HD87640 + SAO221759), during PRIMA commissioning run #14. Star SAO221759 ($m_K = 7.1$), tracked by FSUA, was stabilized by HD87640 ($m_K = 4.8$, 6.6″ apart) on FSUB (seeing: 0.87″; coherence time: 10 ms). Coherent data was integrated during more than 180 s, at a frequency of 1 Hz (Schmid et al., 2012). Plotting the flux difference $A - C$ (or $B - D$) or the flux ratio A/C (or B/D) for data collected at a very low frequency is a way to visualise the fringes that normally are not visible when the FSUs are fringe tracking, because, as pointed in section 2.3, a coaxial-combination scheme is used in PRIMA.

Commissioning runs #14-18 dual-feed data (2011–2012)

Eight sets of astrometric data files were collected between commissioning runs 14 to 18, between January 2011 and January 2012.[7] The data consisted in fluxes collected by PRIMA from 8 binary systems, whose stars, separated by angular distances θ in the range of approximately 7″ to 36″, are unresolved and were tracked simultaneously by FSUA and FSUB in the astrometric mode. The outcome of each observation was a set of FITS files with fluxes integrated during roughly 300 s, corresponding to fringe tracking data, and a set of calibration files (dark counts and "flat" files). The reference characteristics of the binaries and the dates when they were observed are compiled in table 4.1. Binary systems HD10360+HD10360J and HD66598+HD66598B were observed during more than one commissioning run, with a time span of several months (up to approximately one year in case of the latter).[8]

All data were reduced with `PACMAN`, according to the procedure described in section 4.1. The average values of the visibility amplitude for all integrations are plotted in fig. 4.12, following a chronological order. Each panel corresponds to one of the binary systems presented in table 4.1. Visibility points of the star tracked by FSUA are represented by the plus signs, while the ones estimated from FSUB data are indicated by the filled dots. Each point is obtained by averaging out several thousands of visibility estimates, by means of a bootstrapping algorithm. The error bars, smaller than the symbol size, were computed from the error on the mean. The five commissioning runs are highlighted in distinct colours.

Several aspects do spring to mind in fig. 4.12:

[7] Commissioning run 15, which was carried out in the summer of 2011, was the first on-sky PRIMA's astrometric commissioning run.

[8] Because PRIMA was still under development when the data were acquired, it is not guaranteed that the throughput of the instrument was constant during this period of time.

Table 4.1: PRIMA astrometric data, acquired in commissioning runs 14 to 18, between January 2011 and January 2012. The first on-sky astrometric run was commissioning run 15. The grey shaded columns correspond to dates belonging to the same commissioning run, whose number is indicated to the left of them.

PRIMA Astrometric Data							
θ / $''$	Objects	COMM #	Dates	θ / $''$	Objects	COMM #	Dates
7	HD202730 SAO246964	16	2011/08/23 2011/08/25 2011/08/28	8	HD100286J HD100286	18	2012/01/19
9	HD156274 LHS445	15	2011/07/18 2011/07/19	10	HD10360 HD10360J	15	2011/07/17
						16	2011/08/25
						17	2011/11/20 2011/11/23 2011/11/24 2011/11/25
11	HD18622 HD18623	18	2012/01/14 2012/01/16 2012/01/18	20	HD10268 HD10257	16	2011/08/28
35	HD65297 HIP38698	18	2012/01/18	36	HD66598 HD66598B	14	2011/01/30
						17	2011/11/23 2011/11/24
						18	2012/01/18

1. Regardless of the binary systems, in the presence of enough visibility points, the plots exhibit an oscillatory behaviour instead of remaining constantly close to 1.0 — the variations are greater than 0.5 and sometimes larger than unity — as if the coherent flux was periodically changing during the observation runs. A large scatter of visibility amplitude values on the same target has already been noted in the data of commissioning run #2 (*cf.* fig. 4.8a).
2. When a limited number of visibility amplitudes is available, such as in the cases for $\theta \sim 8''$, $11''$, $20''$ and $35''$, the points in the plots form small branches with positive or negative inclinations, that seem to fit in the aforementioned oscillatory behaviour in case more data were available.
3. Crossing the information of table 4.1 with panels of fig. 4.12, apparently there is a relation between the day on which the data was acquired with the "crests" and "valleys" seen when enough data points are available. This might be an indication of a correlation between the visibility amplitude determined with FSU data and the air mass.
4. A few points have amplitudes completely out of the range defined by the other points for the same object and, therefore, they can be safely considered as outliers and removed from the analysis (*cf.* panels for HD156274+LHS445 and HD10360+HD10360J).
5. During the same night of observation, it often occurs that the visibility amplitude difference

between data measured with FSUA and FSUB is not constant, suggesting the existence of other factors affecting the visibility amplitude estimation, such as the seeing.

6. Apart from outliers or bad data points, generally visibility arrays from different days and commissioning runs do not exhibit discontinuities when crossing the "date line", *i.e.*, when going from a day to the adjacent one in the plot (the exception is the case of HD156274+LHS445). They connect each other almost perfectly, along an imaginary continuous line, as if they were acquired during the same night or as if the observation conditions were frozen from one night to the following one.

Considering point 1., binaries HD10360+HD13060J and HD66598+HD66598B were both observed during commissioning run #17, and while the former exhibit an oscillatory pattern in the plot of the visibilities, the latter has a more constant behaviour. Since the same baseline and telescopes were used to observe both systems, assuming the FSUs are suitable instruments to measure visibility amplitudes and that their throughput is constant during the time span of one year between commissioning runs #14 to #18, the difference in the plots can only be explained either by the atmospheric conditions or by the separation between the stars (θ).

The visibility arrays were averaged out and their values plotted, with the corresponding error bars, as a function of the separation between the stars (see fig. 4.13). Since the mean visibility amplitude of the star tracked by FSUB, $V_{\mathrm{FSUB}} = V_{\mathrm{B}}$, is greater than that of FSUA, $V_{\mathrm{FSUA}} = V_{\mathrm{A}}$, it was assumed that the former was on-axis, where the greatest value is expected in face of anisoplanatic effects. All average values oscillate approximately between 0.5 and 0.9, never reaching 1.0, as would be expected for unresolved stars. Although no calibrator was used during the observations — hence, the visibility amplitude averages in the plots are not expected to be very close to 1.0 — and the FSUs are optimised to solely measure visibility phases, in face of the results obtained with the commissioning run #2 data, it would be reasonable to expect final average values of visibility amplitude closer to unity (*cf.* with section 4.2.1).

The differences between visibility amplitudes estimated on FSUA and FSUB data, ΔV, as a function of the angular separation between the stars, θ in arcsec, are illustrated in fig. 4.14. The black diamond highlight the only average value of V_{A} which is greater than the corresponding mean amplitude V_{B}. A quadratic polynomial was sought to fit the data, having the care of not including the visibility points for the binaries with separations $9''$ and $10''$ (marked with crosses in the graph), which were considered outliers. The second order polynomial is given by the equation

$$\Delta V = (0.009 \pm 0.014) + (0.0004 \pm 0.0017) \cdot \theta + (0.00003 \pm 0.00004) \cdot \theta^2. \tag{4.12}$$

The relative errors for all parameters, the standard deviations extracted from the fit, are always above unity. The quadratic polynomial points toward a slight increase of ΔV with θ, although not all the points have been included in the fit and the errors of the parameters are very large.

In order to investigate a hypothetical influence of the atmospheric conditions on the observed patterns of the plots, and in face of the previously listed considerations about fig. 4.12, the data reduction was refined, by the introduction of constraints in the air mass and seeing values. This

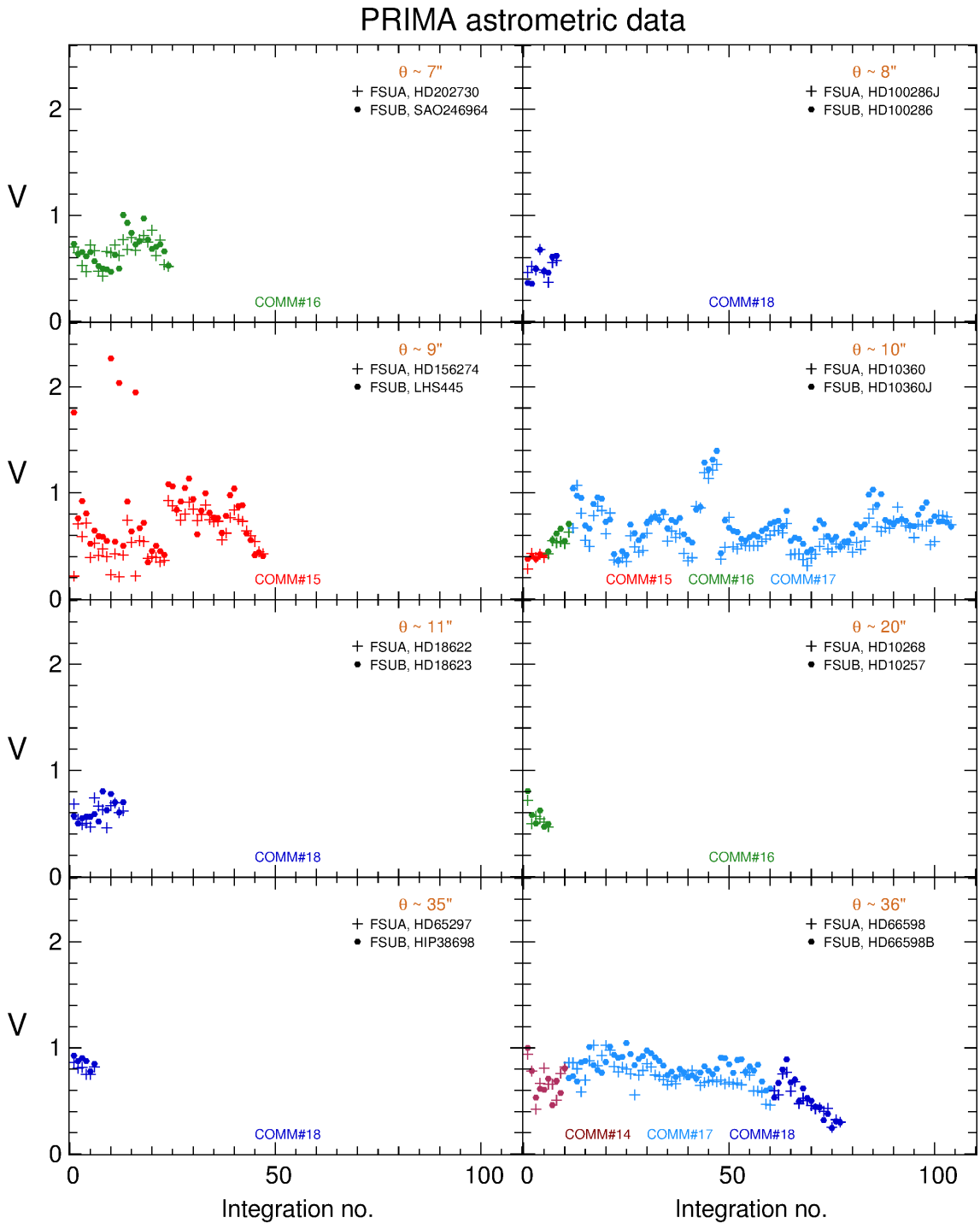

Figure 4.12: Observed visibility amplitudes computed from PRIMA's dual-feed data acquired during commissioning runs 14 to 18. Crosses (+) indicate visibility arrays from FSUA, whereas filled dots (•) visibility amplitudes from FSUB. The commissioning runs are highlighted in different colours.

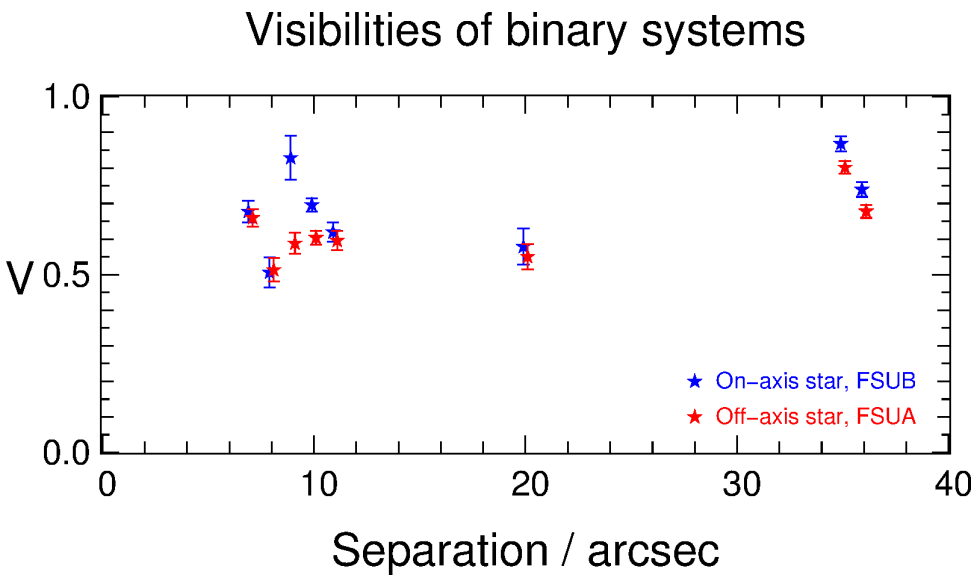

Figure 4.13: Averages of visibility amplitudes computed from PRIMA's dual-feed data acquired during commissioning run 14 and astrometric commissioning runs numbers 1 to 5. Red filled stars correspond to visibilities measured with FSUA (assumed off-axis), whereas blue filled stars are visibility points estimated from FSUB (assumed on-axis) data. For clarity, FSUA and FSUB points corresponding to the same binary were laterally displaced by a small amount. The error bars were obtained by computing the error on the mean of the visibility arrays.

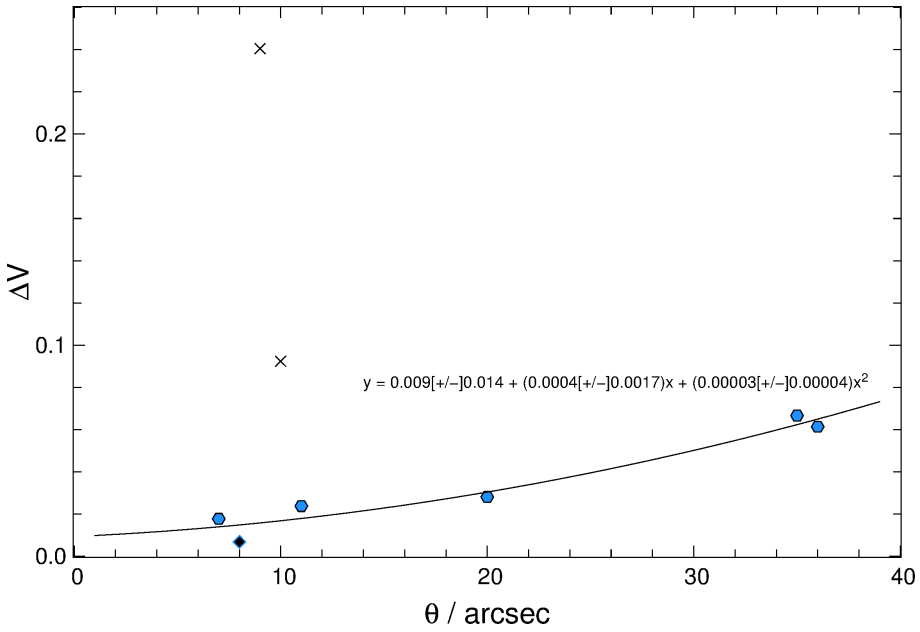

Figure 4.14: Visibility amplitude differences for binary stars as a function of angular separation between them, computed from PRIMA's dual-feed data acquired during commissioning run 14 and astrometric commissioning runs numbers 1 to 5. Dodger blue dots correspond to visibility differences in which the visibility amplitude estimated for the FSUB star is greater than that for FSUA. The black diamond indicates a visibility difference in which the opposite happens, *i.e.*, the visibility measured in FSUA is greater than that of FSUB. The crosses ($\times$) indicate points that were not used in the quadratic fit.

refinement also aimed at the identification of factors influencing the estimation of visibility amplitudes from FSU data, and the study of a possible correlation between the position of the stars in the FOV and the visibility amplitude measured for them (anisoplanatic effects).

Effects of anisoplanatism in visibility measurements

For a binary system composed of stars separated by the angle θ, considering, without loss of generality, that the angular separation between star A and the optical axis is θ_0, it can be written that

$$V_{\mathrm{obs,A}} = V_{\mathrm{T}} \cdot V_{\mathrm{atm}} \cdot V_{\mathrm{aniso,A}}(\theta_0) \cdot V_{\mathrm{A}}, \tag{4.13a}$$

$$V_{\mathrm{obs,B}} = V_{\mathrm{T}} \cdot V_{\mathrm{atm}} \cdot V_{\mathrm{aniso,B}}(\theta - \theta_0) \cdot V_{\mathrm{B}}, \tag{4.13b}$$

where V_{obs} is the *observed visibility*, V_{T} is the *transmission visibility factor*, introduced by the optical system, V_{atm} is the *atmospheric visibility factor*, due to atmospheric affects of first order above the telescopes, common to both stars (air mass, for instance), V_{aniso} is the *anisoplanatic visibility factor*, due to the angular anisoplanatism, and $V_{\mathrm{A,B}}$ is the *intrinsic visibility* for stars A and B. The anisoplanatic visibility factor $V_{\mathrm{aniso}}(\alpha)$ corresponds to the decrease in the visibility due to the angular distance α of the object from the optical axis. By definition, $V_{\mathrm{aniso}}(0) = 1$, and $0 \leqslant V_{\mathrm{aniso}}(\alpha) < 1$ for $\alpha \neq 0$.

If star A is on-axis, $V_{\mathrm{aniso,B}}(\theta - \theta_0) = V_{\mathrm{aniso}}(\theta)$. Considering that the atmospheric contribution is the same for both stars and the transmission factor is even in both arms of the interferometer,[9] eq. (4.13) simplifies to

$$\frac{V_{\mathrm{obs,A}}}{V_{\mathrm{obs,B}}} = \frac{V_{\mathrm{A}}}{V_{\mathrm{aniso}}(\theta) \cdot V_{\mathrm{B}}} \tag{4.14}$$

Since both stars are unresolved, *i.e.*, $V_{\mathrm{A}} = V_{\mathrm{B}} = 1$,

$$V_{\mathrm{aniso}}(\theta) = \frac{V_{\mathrm{obs,B}}}{V_{\mathrm{obs,A}}}. \tag{4.15}$$

In case none of the stars lies on the optical axis, the anisoplanatic factor is unknown for both stars, and eq. (4.15) becomes

$$\frac{V_{\mathrm{aniso,A}}(\theta_0)}{V_{\mathrm{aniso,B}}(\theta - \theta_0)} = \frac{V_{\mathrm{obs,A}}}{V_{\mathrm{obs,B}}}. \tag{4.16}$$

Of the two independent variables underlying eq. (4.16), to wit, θ and θ_0, the latter is the most important, because for a given angular separation between the stars, the ratio varies with θ_0, *i.e.*, with where the stars are placed in the FOV relative to the optical axis.

V_{aniso} can be estimated, in first approximation, by means of a linear relation:

$$V_{\mathrm{aniso}}(\alpha) = 1 - r \cdot \alpha, \tag{4.17}$$

[9] Or, at least, it is properly calibrated.

with r a positive number. This factor r can be found by measuring the visibility of an unresolved star when it is placed on the edge of the FOV, $V_{\text{aniso}}(\alpha_{\text{max}}) = V_{\text{min}}$. In that case,

$$r = \frac{1 - V_{\text{min}}}{\alpha_{\text{max}}}, \tag{4.18}$$

where $\alpha_{\text{max}} = \measuredangle(FOV)/2$. With this condition, eq. (4.17) becomes

$$V_{\text{aniso}}(\alpha) = 1 - \frac{1 - V_{\text{min}}}{\alpha_{\text{max}}} \cdot \alpha. \tag{4.19}$$

In order to estimate the anisoplanatic visibility for stars A and B, another possibility is to use a calibrator star C observed on the optical axis. In this situation, $V_{\text{aniso,C}} = 1$, and

$$V_{\text{aniso,A}}(\theta_0) = \frac{V_{\text{obs,A}}}{V_{\text{obs,C}}}, \tag{4.20a}$$

$$V_{\text{aniso,B}}(\theta - \theta_0) = \frac{V_{\text{obs,B}}}{V_{\text{obs,C}}}. \tag{4.20b}$$

Both equations are compliant with eq. (4.16). The *proper visibility ratio factor* q can be defined as

$$q(\theta, \theta_0) = \frac{V_{\text{obs,A}}}{V_{\text{obs,B}}}. \tag{4.21}$$

Plotting q *vs* θ when both stars are off-axis is only relevant if θ_0 is known. When $\theta_0 = 0$, q coincides with the anisoplanatic visibility factor, and

$$q(\theta, 0) = V_{\text{aniso}}(\theta) = \frac{V_{\text{obs,B}}}{V_{\text{obs,A}}}. \tag{4.22}$$

Air mass and seeing selection

It is not expected the air mass to substantially affect the ratio between the determined visibility amplitudes in a binary system, because its stars are, in first order, affected by the same value of X at a certain time. However, when the separation between the stars becomes larger, their light paths through the atmosphere will correspond to a distinct value of the airmass and, thus, the difference between the visibility amplitudes will not remain constant during the observation run.

For the current data set, there is no information about the evolution of the air mass during the data acquisition in addition to the values recorded at the beginning and at the end of the observation. Due to this limitation, to each estimated visibility amplitude point, it was associated a mean value of the air mass, computed by averaging the two aforementioned known values. It can be assumed that the *intrinsic visibility amplitude* of the source V_0 (as it could be measured above the atmosphere) decreases linearly with the distance travelled by light in the atmosphere, *i.e.*, with the air mass X, so that

$$V = V_0 - e_k \cdot X, \tag{4.23}$$

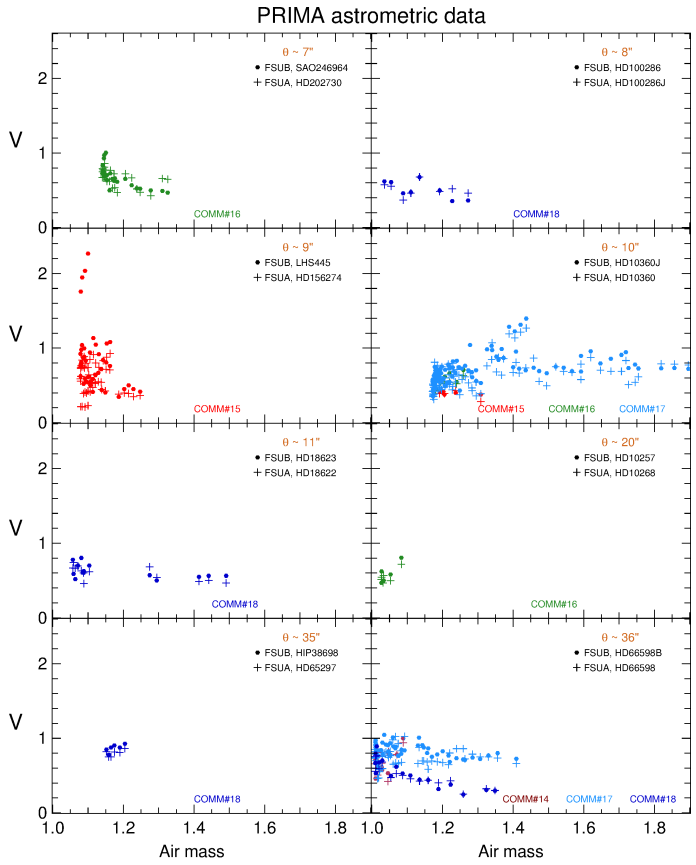

Figure 4.15: Visibility amplitudes of unresolved stars belonging to binary systems as a function of the mean air mass. Crosses (+) indicate visibility arrays from FSUA, whereas filled dots (•) visibility amplitudes from FSUB. The commissioning runs 14 to 18 are highlighted in different colours.

where V is the *observed visibility amplitude* and e_k is the *extinction coefficient*. Several observations of the source during the night, as wide a zenith distance range as possible, can be used to determine the extinction coefficient and the intrinsic visibility amplitude. Plotting the observed visibilities V against the air mass X, it is expected that the points lie in a straight line, whose (negative) slope will give $e_{\rm k}$ and the intersection of the line to $X = 1$ will yield V_0.[10]

The estimated visibility amplitudes V were plotted as a function of the mean air masses, for all observed binary systems. The resulting panels are illustrated in fig. 4.15. The majority of the panels exhibit a relatively high concentration of visibility points around low air mass values, specially those corresponding to the angular separations $7''$, $9''$, $10''$ and $36''$. This is an indication that there was a concern to perform the observations when the binaries were close to the meridian, trying to minimise the impact of the air mass in the quality of the data. Nevertheless, there are many visibility points with different amplitudes for the same values of the air mass, specially for $X \sim$1.0–1.2 — cases $\theta \sim 9''$ and $\theta \sim 36''$ are good examples of this. The sizeable variability of the amplitudes ($\Delta V \sim 1$) points to a considerable uncertainty in the determination of the visibilities with PRIMA FSUs. This might be an indication that V, when estimated by these instruments, is very sensitive to other observational factors, such as the seeing. Furthermore,

- To the low air mass values correspond the greatest number of visibility amplitudes, as can be

[10] Taking into account the transmission losses, how far is V_0 from 1 (for unresolved sources) can be used to test the affinity of the FSUs to estimate visibility amplitudes.

seen in the plots for $\theta \sim 7''$, $9''$, $10''$ and $36''$. This fact precludes selection of visibilities corresponding uniquely to the lowest air masses for each day and commissioning run. Although Nuno Gomes, Schmid et al., (2012) showed the opposite (*cf.* section 4.2.1), seeing presents itself as a candidate for the responsible for the high dispersion of the visibility amplitudes as a function of the air mass.

- It is very hard to fit a straight line to the data as it is — apparently, eq. (4.23) does not hold for these sets of data.
- For $\theta \sim 36''$, two straight lines with different slopes (hence, different extinction coefficients e_k) seem to coexist. Their points of intersection with the vertical axis (thus, the corresponding values of the visibility amplitude above the atmosphere, V_0) are apparently different, as well.
- For $\theta \sim 20''$ and $\theta \sim 35''$, the slopes are not even negative, as it would be expected.

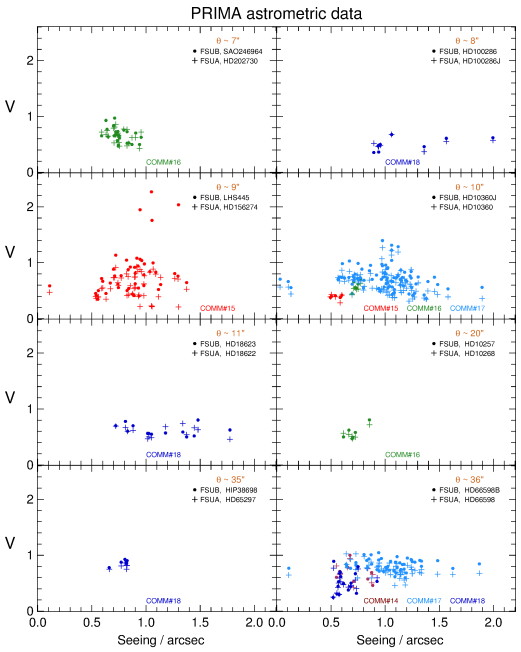

(a) Visibility amplitudes determined with PRIMA's FSUs as a function of the mean seeing (in arc-seconds) at Paranal.

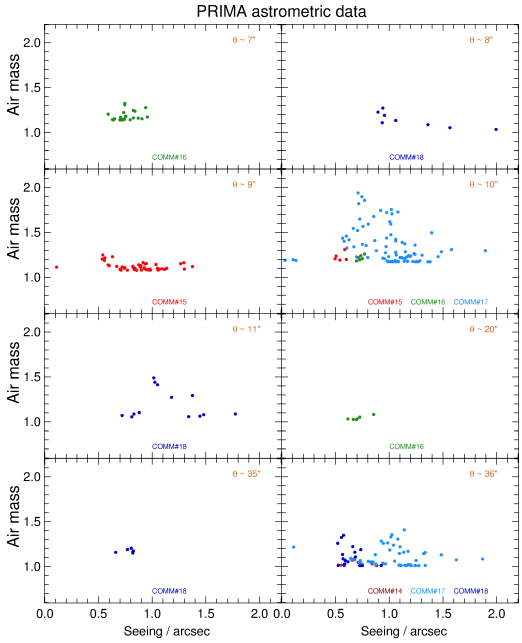

(b) Air mass as a function of the mean seeing (in arc-seconds) at Paranal.

Figure 4.16: Effects of seeing on the quality of observations performed with PRIMA's FSU's. In fig. 4.16a, crosses (+) indicate visibility arrays from FSUA, whereas filled dots (•) visibility amplitudes from FSUB. The commissioning runs 14 to 18 are highlighted in different colours. Refer to main text, for more details on the scatter plots.

The observed visibility amplitude V and the air mass X were plotted as a function of the seeing (see fig. 4.16), so as to investigate a possible correlation between these quantities. From fig. 4.16, it can be seen that, for some observation runs, a large number of data points was acquired under bad seeing conditions, well above the mean values at Paranal during the year of 2011 — approximately between $1.0''$ and $1.1''$ (see fig. 4.17). Moreover, a few bad data points (identifiable by the very low values of seeing, bellow $0.4''$) were registered in COMMS #15 and #17 and, thus, were considered outliers. A large dispersion is observed from the scatter plots, and no correlation is apparent between the visibility amplitudes and the seeing. Similarly, the panels illustrating the air masses as a function of the seeing (fig. 4.16b) indicate that there is no significant correlation between

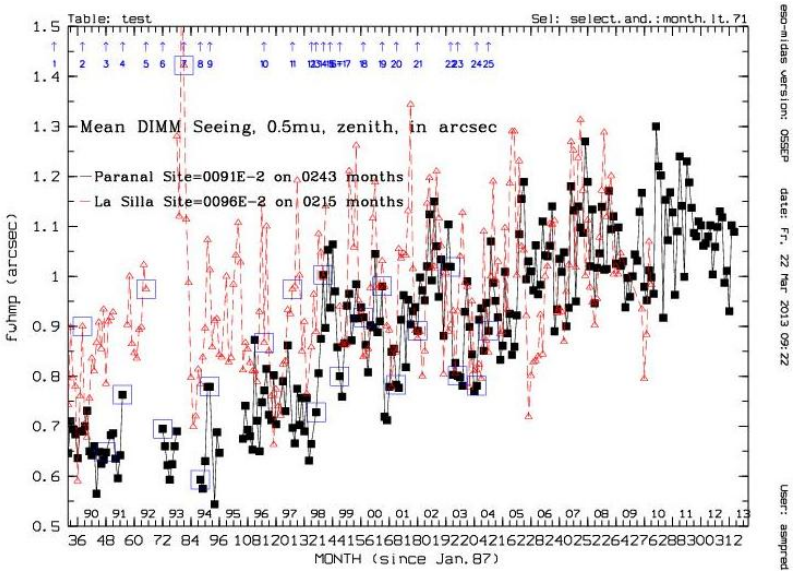

Figure 4.17: Mean DIMM seeing at Paranal in arcsec, measured at $\lambda = 500\,\mathrm{nm}$, on the zenith.

these quantities (as would be expected), in the sense that for the same value of the air mass, many different seeing values are registered over the course of one or more commissioning runs.

In order to refine the data reduction, the aforementioned outliers and bad data points were removed, and restrictions were introduced into the seeing and the air mass accepted values. Taking into account fig. 4.17, based on the fact that the mean seeing at Paranal in the years 2011 to 2013 oscillated between approximately $0.9''$ and $1.2''$ and that, on average, it was equal to $(1.085 \pm 0.014)''$, all points lying outside the interval $0.4'' \leqslant \mathit{seeing} \leqslant 1.1''$ were removed. As for the air mass, only points corresponding to a zenith distance less than about 40° ($X \leqslant 1.3$) were considered.

The scatter plots of figs. 4.18 to 4.20 illustrate the observed visibility amplitudes as a function of the seeing and air mass, as well as of the air mass as a function of the seeing,[11] after implementing these restrictions. With the stated conditions, all scatter plots became less populated and most of the outliers were removed. The most dramatic difference was in the panel for HD10360+HD10360J ($\theta \sim 10''$). Most of the points of COMM #17 disappeared, meaning that many of the observations carried out during this commissioning run were performed under bad seeing conditions and when the object was well away of the meridian. Furthermore, the temporal evolution of the visibility amplitudes in this panel lost its oscillatory shape, which does not happen for the scatter plots of other stellar separations (see fig. 4.18). There are still many values of seeing corresponding to a given value of the air mass — something to be expected, because the seeing is not constant over time — and, thus, the relation between these two quantities is approximately linear, except for the panels $\theta \sim 8''$ and $36''$, where the dispersion is large. In the $\theta \sim 9''$ case, while the visibility amplitudes $V_\mathrm{A} \sim 0.2$ and $V_\mathrm{B} \sim 1.8$ are removed by the constraints applied to the seeing and the airmass, the ones greater than that are not, which is an indication that the airmass and the seeing are not the only factors affecting the determination of the visibility amplitude from FSU data.

[11] This plot was done for testing purposes, since airmass as a function of DIMM seeing is meaningless.

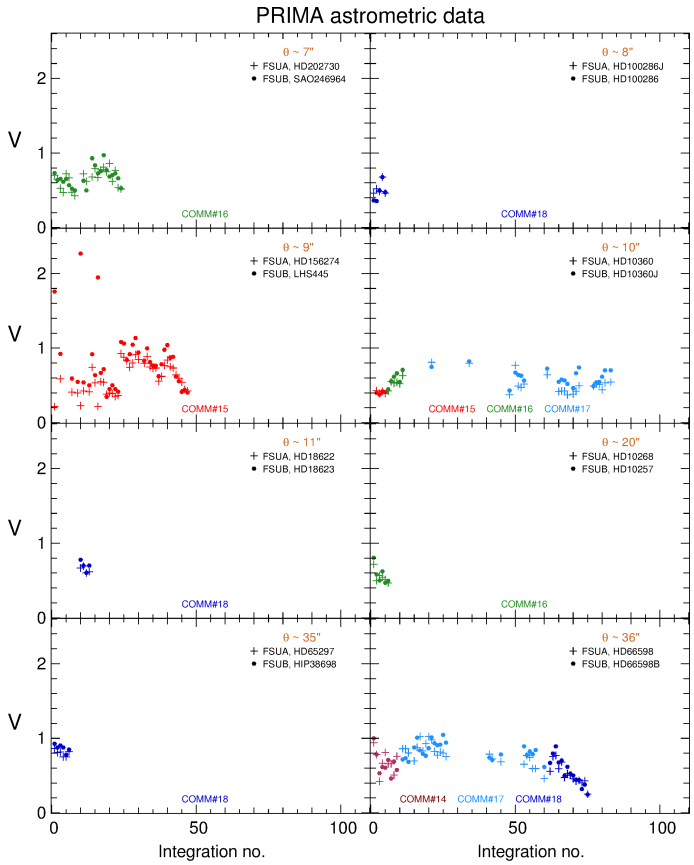

Figure 4.18: Reduced visibility amplitudes computed from PRIMA's dual-feed data acquired during commissioning runs 14 to 18. The conditions $X \leqslant 1.3$ and $0.4'' \leqslant \textit{seeing} \leqslant 1.1''$ were used as data filters. For more details, refer to the main text and fig. 4.12.

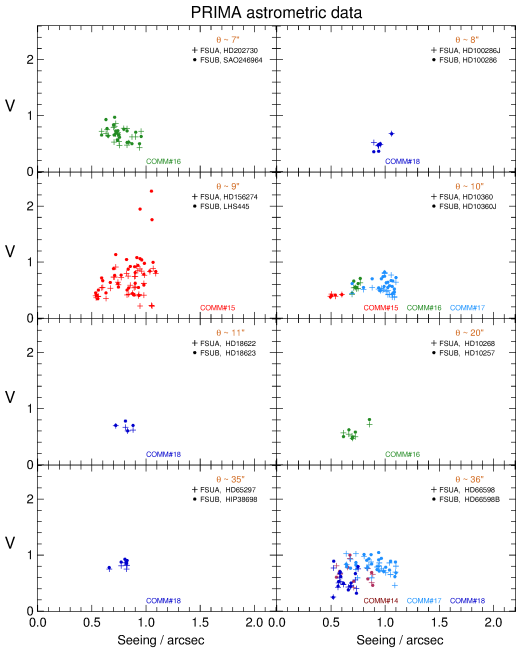

(a) Reduced visibility amplitudes determined with PRIMA's FSUs as a function of the mean seeing (in arc-seconds) at Paranal.

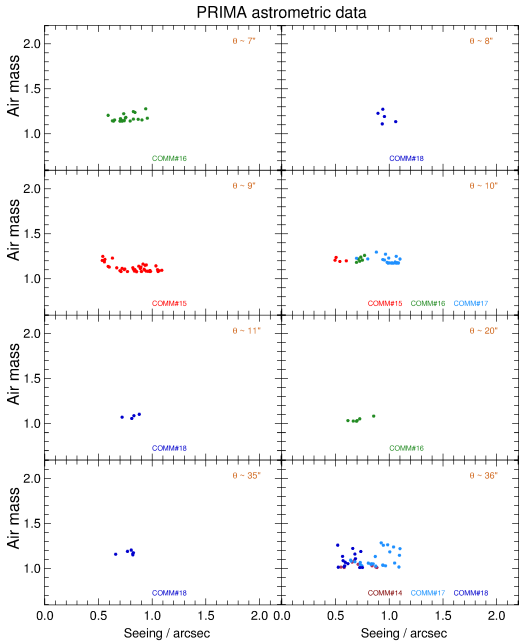

(b) Reduced air mass as a function of the mean seeing (in arc-seconds) at Paranal.

Figure 4.19: Same plots as in fig. 4.16, but with the conditions $X \leqslant 1.3$ and $0.4'' \leqslant \textit{seeing} \leqslant 1.1''$ used as data filters.

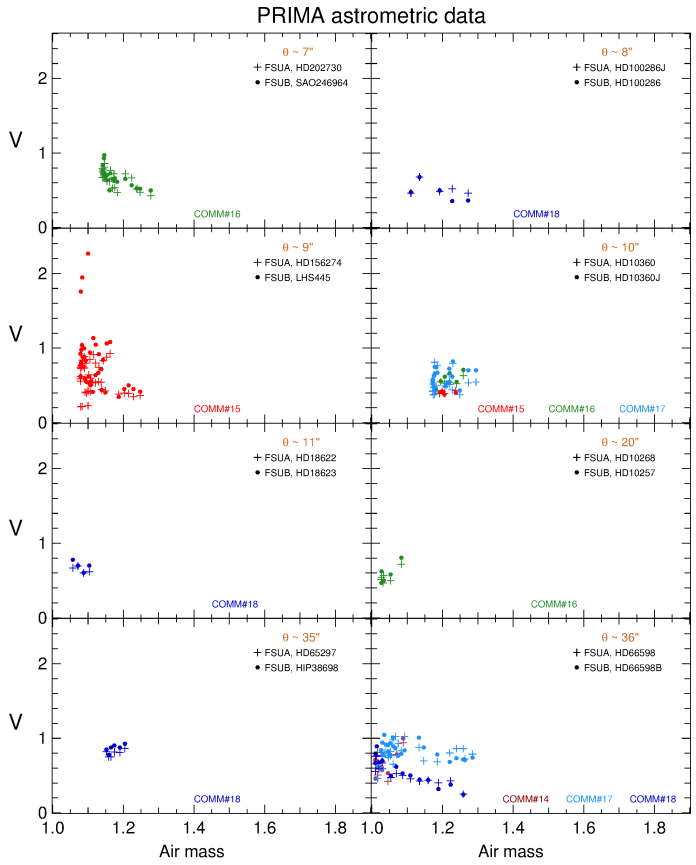

Figure 4.20: Reduced visibility amplitudes of unresolved stars belonging to binary systems as a function of the mean air mass, after imposing the data filters $X \leqslant 1.3$ and $0.4'' \leqslant$ *seeing* $\leqslant 1.1''$. For details on the scatter plots, refer to fig. 4.15.

Even with the imposed data filters, the plots of the visibility amplitude as a function of the seeing and the air mass register high levels of dispersion, specially for the panels $\theta \sim 7''$, $9''$, $10''$ and $36''$ and at low values of both quantities. This fact could be an evidence that the level of extinction at Paranal varies significantly over time, but that would contradict the results by, for example, Mason et al., (2008) and Lombardi et al., (2011), which point to extinction coefficients less than 0.1 mag/airmass in the NIR, at Paranal. A more plausible explanation is that the FSUs are not suitable instruments to estimate the visibility amplitude of unresolved emitting sources. In either case, from fig. 4.20 it becomes apparent that the air mass is not the responsible for the visibility variability, because to the lowest values of X, when light goes through the thinnest possible layer of the atmosphere for a given object, correspond many different amplitudes V, ranging approximately from 0.4 to 1.0 (see panels for $\theta \sim 7''$, $9''$, $10''$ and $36''$).

Straight lines illustrating the relation of eq. (4.23) were fit to the data and are plotted in fig. 4.21.[12] Due to their rounder shape and/or to the great dispersion of the visibility amplitudes, mainly at low air mass values (typically around 1.17), some linear approximations have positive slopes, such as those of panels $\theta \sim 10''$, $20''$ and $35''$. For these cases, eq. (4.23) has no physical meaning, since that would imply a lower visibility amplitude above the Earth atmosphere when compared to the observed one. The estimated values of V_0 for FSUA and FSUB in panel $\theta \sim 9''$ present the largest difference, because, on the one hand, the dispersion is large, and, on

[12] Due to their shape and typical intersections, these fits are nicknamed as "chopstick" plots.

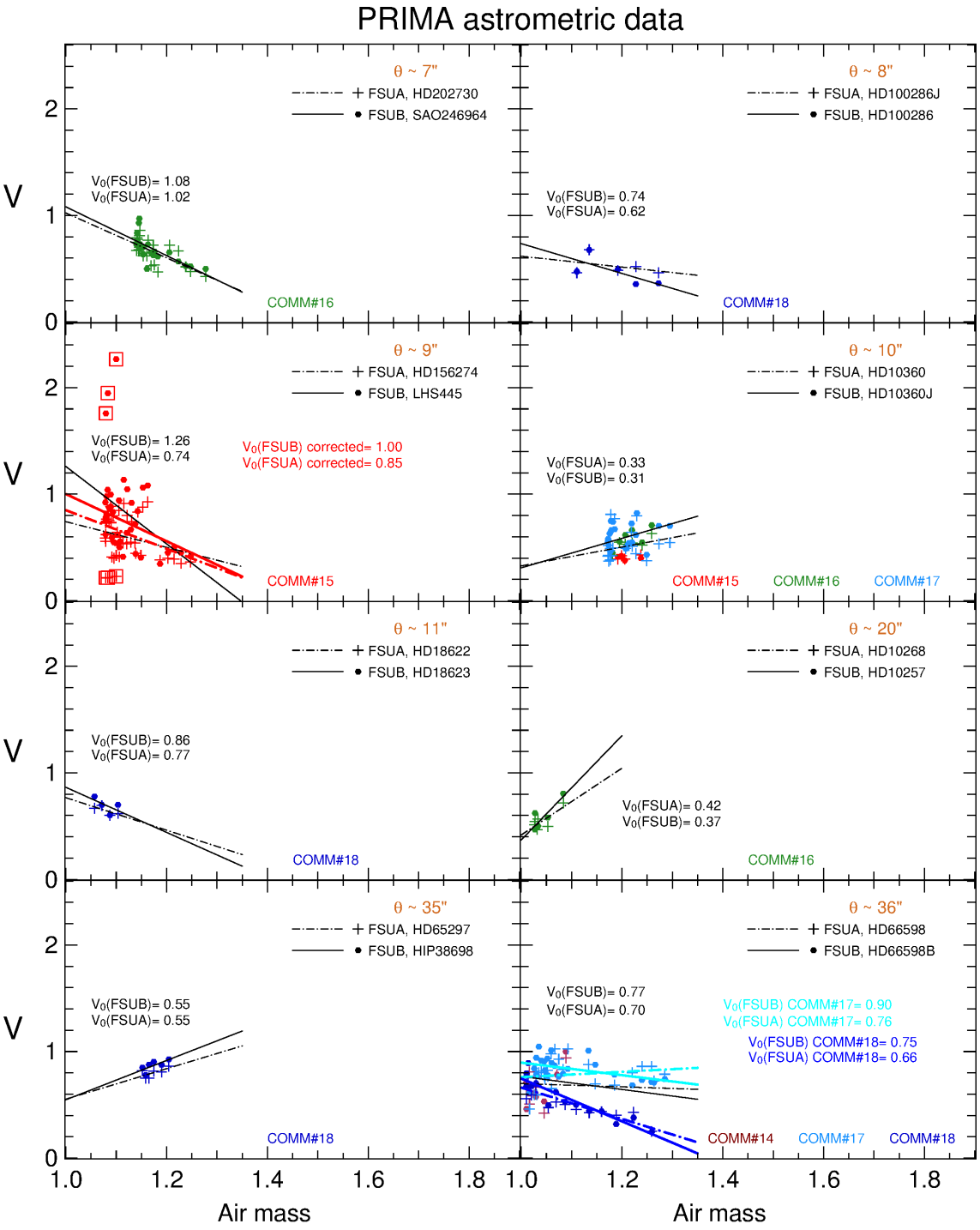

Figure 4.21: Observed visibility amplitudes V as a function of the air mass X and respective linear fits ("chopsticks" plots). For more details on the scatter plots, see the main text and fig. 4.20.

the other hand, the fitting lines for FSUA and FSUB are dominated by respectively three very low and very large visibility points (marked with red squares). These extreme visibility amplitudes (below 0.3 for FSUA and above 1.7 for FSUB) correspond to defective data, as the amplitude difference between them is much larger than for the other points (up to two orders of magnitude). Therefore, they are considered outliers. Removing them substantially improves the fit, bringing closer the intersection of the lines with the axis $X = 1.0$: $V^0_{\mathrm{FSUA}} = 0.8 \pm 0.2$ and $V^0_{\mathrm{FSUB}} = 1.0 \pm 0.3$ (red thicker lines), instead of the previous values of $V^0_{\mathrm{FSUA}} = 0.7 \pm 0.3$ and $V^0_{\mathrm{FSUB}} = 1.3 \pm 0.4$, (the thinner black lines).[13] Because panel $\theta \sim 36''$ display two branches of points, one corresponding to data acquired during commissioning run number 17 and another to visibility amplitudes from commissioning run 18, the data was divided into two corresponding subsets.[14] The subsets were fit to straight lines, each corresponding to different extinction coefficients of the Earth atmosphere, and leading to different values of the visibility amplitude V_0 above the atmosphere. It was found that, for COMM #17, $V^0_{\mathrm{FSUA}} = 0.8 \pm 0.5$ and $V^0_{\mathrm{FSUB}} = 0.90 \pm 0.16$, and for COMM #18, $V^0_{\mathrm{FSUA}} = 0.66 \pm 0.09$ and $V^0_{\mathrm{FSUB}} = 0.75 \pm 0.08$. The averages of these values yield $V^0_{\mathrm{FSUA}} = 0.7 \pm 0.3$ and $V^0_{\mathrm{FSUB}} = 0.82 \pm 0.12$, which are close to the average values of all data points, *i.e.*, considering the three commissioning runs (0.7 ± 0.3 for FSUA and 0.8 ± 0.2 for FSUB).

Results

Table 4.2 compiles the average visibility amplitudes for all above-mentioned cases. When eq. (4.23) could not be applied, the averages off all data set were used instead (cases of panels $\theta \sim 10''$, $20''$ and $35''$). It is assumed that the star with the highest visibility amplitude is on-axis (star tracked by FSUB in all cases).

Table 4.2: Average visibility amplitudes measured with FSUA and FSUB for the unresolved stars belonging to the observed binary systems, after imposing restrictions on the seeing and air mass values (see descriptions in main text for details). $V_{\mathrm{A/B}}$ respectively stands for V_{FSUA} and V_{FSUB}, $\Delta V = V_{\mathrm{B}} - V_{\mathrm{B}}$, and $V_{\mathrm{aniso}} = \frac{V_{\mathrm{A}}}{V_{\mathrm{B}}}$ is the anisoplanatic factor.

θ / $''$	V_{A}	V_{B}	ΔV	V_{aniso}
7	1.0 ± 0.2	1.08 ± 0.19	0.1 ± 0.3	0.9 ± 0.3
8	0.6 ± 0.5	0.7 ± 0.3	0.1 ± 0.6	0.8 ± 0.7
9	0.8 ± 0.2	1.0 ± 0.3	0.2 ± 0.4	0.8 ± 0.4
10	0.52 ± 0.02	0.609 ± 0.019	0.09 ± 0.03	0.85 ± 0.03
11	0.8 ± 0.4	0.9 ± 0.6	0.1 ± 0.7	0.9 ± 0.8
20	0.55 ± 0.04	0.58 ± 0.05	0.03 ± 0.06	0.95 ± 0.07
35	0.802 ± 0.018	0.87 ± 0.02	0.07 ± 0.03	0.92 ± 0.03
36	0.7 ± 0.3	0.82 ± 0.12	0.11 ± 0.03	0.9 ± 0.4

[13] $V^0_{\mathrm{FSUA/B}}$ indicates the intrinsic visibility amplitude estimated with FSUA/B data.

[14] Data acquired during commissioning run #14 were not considered in this refinement because they evidence large dispersion and did not fit any of the branches.

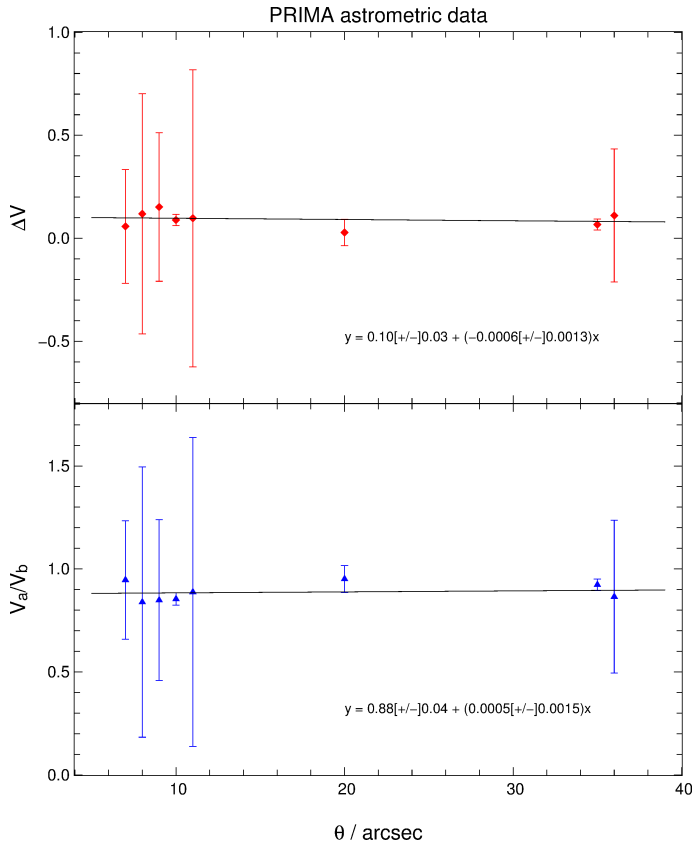

Figure 4.22: *Top panel:* $\Delta V = V_{\mathrm{FSUB}} - V_{\mathrm{FSUA}}$ as a function of the separation between the stars, θ (in arcsec). *Bottom panel:* anisoplanatic visibility factor, V_{aniso}, as a function of θ.

The plots illustrating the two rightmost columns of the table as a function of the angular separation between the stars are displayed in fig. 4.22. The top panel represents the visibility difference between the on-axis and off-axis stars, ΔV, as a function of the angular separation between them, θ (expressed in arcsec), and the bottom panel the anisoplanatic visibility factor, $V_{\mathrm{aniso}} = V_{\mathrm{FSUA}}/V_{\mathrm{FSUB}}$, as a function of θ. The equations that translate the best linear fit between the each of the quantities and θ are, respectively,

$$\Delta V = (0.10 \pm 0.03) - (0.0006 \pm 0.0013) \cdot \theta \tag{4.24}$$

and,

$$V_{\mathrm{aniso}} = (0.88 \pm 0.04) + (0.0005 \pm 0.0015) \cdot \theta. \tag{4.25}$$

Assuming that anisoplanatism affects the determination of the visibility amplitude, it would be expected that the latter decreases with the angular separation θ to the optical axis. In that case, the difference $\Delta V = V_{\mathrm{B}} - V_{\mathrm{A}}$ would increase with θ, whereas the anisoplanatic factor $V_{\mathrm{aniso}} = V_{\mathrm{A}}/V_{\mathrm{B}}$ would decrease with θ. However, this is not evinced by the plots of fig. 4.22: the error bars are too large, and there is not a physical support for these fits.

Conclusions

A large scatter was observed for the visibility amplitudes on all the targets. The results demonstrate that this variability cannot be attributed to air mass or seeing variations. It might be explained by effects not taken into account in the algorithm, such as the photon noise (*e.g.*, M. M. Colavita, 1999), and to limitations of PRIMA, such as the absence of a photometric channel and the monitoring of the dynamic differential injection in the ABCD fibres, both fundamental to a real-time correction of the visibility measurements (J. Sahlmann et al., 2009).

Other factors that might have influenced the accuracy on the estimation of the visibility amplitude are the integration time, polarisation effects that could impact on the contrast of the fringes and, thus, on their detection, and the defocus identified in AT3, which affected all the measurements performed during PRIMA's commissioning runs.

In order to study the effects of the former, it would be necessary to collect more data with different integration times on the same sources. As for polarisation effects, a careful investigation of all PRIMA's subsystems would have to be carried out in order to find possible flaws on the design and/or technical level of the instrument.

According to the available data and the performed analysis, there is no visible effect of the position of a star in the FOV on the estimation of the visibility amplitudes with PRIMA's FSUs, *i.e.*, the anisoplanatic visibility factor tends to be approximately constant with the angular separation between the object and the optical axis. Moreover, the visibility amplitude difference between the stars in FSUA and FSUB remains roughly constant along the sampled angular separations.

The large error bars in both ΔV and V_{aniso} are, however, an indication that these results might be biased,[15] and it is possible that, with more data and of better quality, an increase of ΔV and a decrease of V_{aniso} with θ could be observed.

Addendum

Since both stars are unresolved and the star tracked by FSUB is considered to be on-axis, its visibility V_{B} should be 1. Therefore, the observed visibilities were normalised by V_{B} and the difference $1-\overline{V}_{\text{A}} = 1-V_{\text{A}}/V_{\text{B}}$ was plotted against θ.[16] The results are compiled in table 4.3 and illustrated in fig. 4.23. A third order polynomial was sought to fit the data. Its equation is

$$\begin{aligned} \Delta V &= 1-\overline{V}_{\text{A}} \\ &= (-0.14\pm0.04)+(0.05\pm0.01)\cdot\theta+ \\ &\quad (-0.0027\pm0.0004)\cdot\theta^2+ \\ &\quad (0.000\,040\pm0.000\,006)\cdot\theta^3. \end{aligned} \tag{4.26}$$

[15] The errors associated to the panels $\theta\sim 10''$, $20''$ and $35''$ are typically an order of magnitude below the value of the corresponding quantity because the error on the mean was used to estimate them. The errors associated to the quantities for the other panels are larger, because they were computed directly from the parameters of the linear fits.

[16] This difference corresponds to the *isoplanatic* visibility factor, $1-V_{\text{aniso}}$.

Table 4.3: Normalised visibility amplitudes of the stars tracked by FSUA (V_B is the normalisation factor), and $\Delta V = 1 - \overline{V}_A = 1 - V_A/V_B$.

θ / $''$	V_A	ΔV
7	0.9 ± 0.3	0.053 ± 0.003
8	0.8 ± 0.6	0.2 ± 0.7
9	0.8 ± 0.4	0.2 ± 0.4
10	0.85 ± 0.03	0.15 ± 0.03
11	0.9 ± 0.8	0.1 ± 0.8
20	0.95 ± 0.07	0.05 ± 0.07
35	0.92 ± 0.03	0.08 ± 0.03
36	0.9 ± 0.4	0.1 ± 0.4

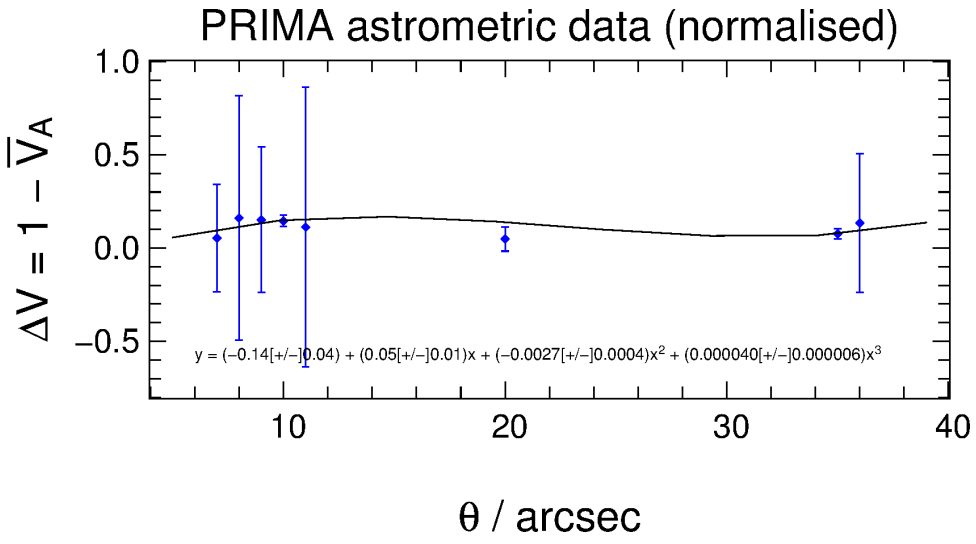

Figure 4.23: $\Delta V = 1 - V_{FSUA}$ as a function of the separation between the stars, θ (in arcsec). V_A is normalised by V_B, which is assumed to be on-axis.

The results do not bring any considerable improvement, mainly because the normalisation by V_B has the consequence of enlarging the error bars. Therefore, the conclusions of section 4.2.4 are still valid, *i.e.*, with the current data, one can only state that the effect of the anisoplanatism is of lower order of magnitude than the dispersion and error bars of the visibility amplitudes estimated with the FSUs.

Chapter 5

Faint science mode

"Everything we see hides another thing, we always want to see what is hidden by what we see."

— RENE MAGRITTE

Contents

IN THIS CHAPTER, it is discussed how PRIMA and AMBER could have been combined in the so-called *faint-object science mode*, a dual-beam operation mode where the pair of stellar beams from the bright reference object is tracked by one of the FSUs and the light coming from the faint science source is directly sent to AMBER. The faint-object science mode, which relies on the slow drift corrections applied to the stellar beams by the star separator, at the level of the telescopes, would allow for longer integration times on fainter objects. In order to work, it would be necessary that the drifts of the stellar beams, induced by mechanical vibrations and atmospheric conditions in the VLTI tunnels between the telescopes and the interferometric laboratory, be correlated. Therefore, this correlation was estimated through the position of the stellar beams on IRIS, one of the stabilisation subsystems of the VLTI. The method applied to calculate the correlation between the beams' offsets is presented in the following sections.

The infrared image sensor of the VLTI

The **I**nfra**R**ed **I**mage **S**ensor (IRIS) is the infrared field-stabiliser of the VLTI. It is used for *non-blind tracking*, by allowing real time corrections of the tip-tilt between the telescopes and the VLTI laboratory. IRIS aims at providing stable beams to interferometric instruments, such as AMBER or MIDI, combined or not with auxiliary fringe trackers, such as FINITO and PRIMA's FSUs, by correcting the stellar light beams offsets caused by atmospheric turbulence along the light tunnels of the VLTI and/or mechanical vibrations.

IRIS consists of a fast near-infrared camera, composed of a 256×256 PICNIC detector array, that collects up to four stellar beams simultaneously coming from the telescopes and performs field-stabilisation. These beams can either come from four telescopes collecting light from the same source or from two telescopes operating in dual-feed mode. Each of the beam images is projected onto one quadrant of the PICNIC detector, and its photo-centre is measured in real time. The low-frequency tip-tilt of the VLTI laboratory is thus estimated, allowing the correct alignment of the beams during the observations (Brillant, 2011).

IRIS can be operated in two modes: the **I**RIS **s**low-**g**uiding (ISG, also known as **I**RIS **l**ab-**g**uiding or ILG) and the **I**RIS **f**ast-**g**uiding (IFG). The former is used to correct the pointing of the telescopes, by sending the tip-tilt corrections to the Field Selector Mirror (FSM), at a frequency roughly of 5 Hz to 10 Hz; the latter is used for the FSUs, FINITO and AMBER: the tip-tilt corrections are sent to the ACUs of FINITO or the FSUs, at a rate of 100 Hz (ibid.).

In the K-band, the limiting magnitudes for IRIS are (ibid.):

- In slow-guiding mode:
  - $m_K = 8.0$ with the ATs;
  - $m_K = 11.5$ with the UTs.
- In fast-guiding mode:
  - $m_K = 5.0$ with the ATs;
  - $m_K = 8.5$ with the UTs.

When in operation with PRIMA, each quadrant of the PICNIC detector is scanned by a readout window, that has a fixed size and position within all quadrants (fig. 5.1).[1] Quadrants Q_1 and Q_2 usually collect light from FSUA, while the beams coming from FSUB strike quadrants Q_3 and Q_4. There are 8 input channels (IP) at the VLTI, which refer to the physical locations of the beams at the switchyard level (J. Sahlmann et al., 2013).[2]

It is not possible to define a single readout window for all observation cases, because the reference points do not have a fixed position within each quadrant. Consequently, an optimal readout window is defined each time the sensing loop is started, so that all reference points lie

[1] In dual-feed mode, the bright and faint spots are located at different regions within the quadrant (Gitton, Lévêque et al., 2004): for example, bright spots on the upper part and faint spots on the lower region of the quadrant. However, the details on how the PICNIC quadrants are swept in this mode are not relevant for the study under consideration.

[2] During PRIMA commissioning runs, the beams from AT3, IPs 1 and 2, were sent to quadrants Q_2 and Q_4, while the beams from AT4, IP3 and IP4, were sent to quadrants Q_1 and Q_3. AT3 was placed in station G2, and AT4 was located in station J2.

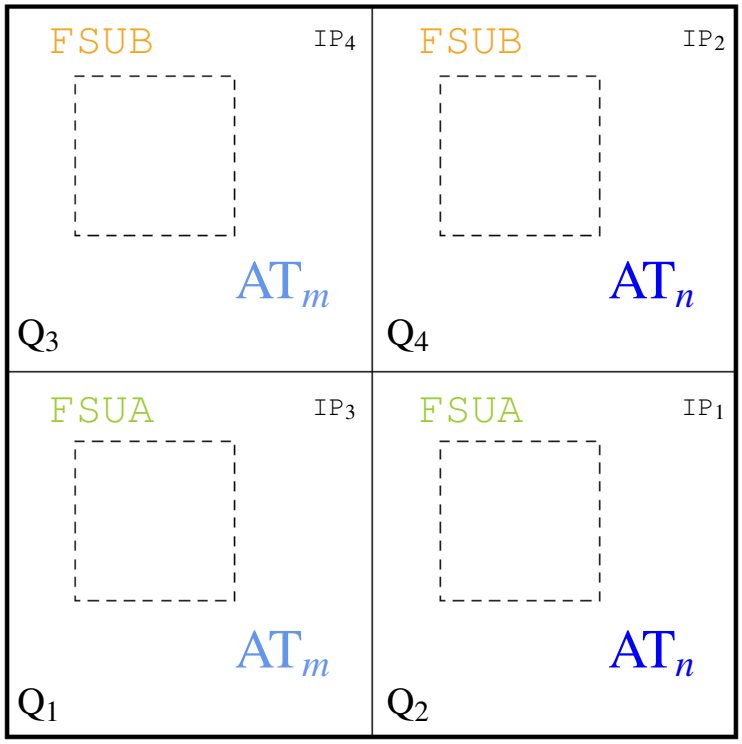

Figure 5.1: The four quadrants of IRIS PICNIC detector, 128×128 pixels each, and relative arrangement of the readout windows in each quadrant (dashed boxes). Q_1 and Q_3 receive beams from telescope m, and Q_2 and Q_4 collect beams from telescope n. Typically, beams from input channels IP1 and IP3 illuminate FSUA, while beams from IP2 and IP4 shine on FSUB (adapted from ibid.).

inside the window, and it can be kept unchanged during all the observation sequence without loosing track of any of those points. A virtual superposition of all quadrants with their readout window is illustrated in fig. 5.2.

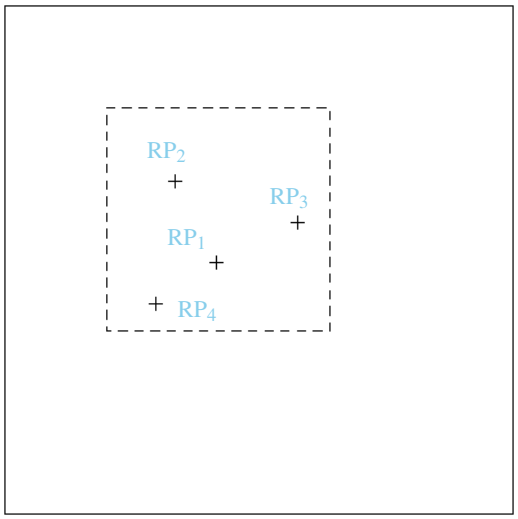

Figure 5.2: Definition of the PICNIC readout window as a function of the reference points (RPi, $i = 1,2,3,4$, marked with $+$). All active quadrants are virtually superimposed. The detector window (dashed box) is the same for all quadrants (adapted from ibid.).

Combining PRIMA and AMBER

Although the **st**ar **s**eparators (STS) and the FSUs are adapted to use both ISG and IFG, the **I**RIS **f**eeding **o**ptics to **A**MBER (IFOA) are not.[3] Both IFOA1 and IFOA2 have three positions:

- **Astrometric Position**: the mirrors reflect all the light to FSUA and IRIS (fig. 5.3).
- **AMBER Position**: the dichroic filters send the light to AMBER (in theory, the whole J and H bands and 70 % of the K-band) and to IRIS (30 % of the K-band). The 30 % of K-band light sent to IRIS is used by the latter for *fast-guiding* and *slow-guiding* (fig. 5.4). With the IFOAs in this position, PRIMA is said to be combined with AMBER in the so-called V^2 *imaging mode*.[4]
- **Free Position**: all the light is sent to AMBER, for alignment purposes.

When in the imaging mode, IFG and ISG would have to be provided both for the AMBER beams and for the FSUB beams simultaneously, in order to maximize the efficiency of AMBER. However, on the one side, IRIS has to be used in H-band because the full J- and K- bands are sent to FSUB, and, on the other hand, only part of the K-band coming from AMBER beams is sent to IRIS. Therefore, this mode is not compatible with the dichroic of IFOA. This is a consequence of the fact that no IFG for AMBER was originally foreseen in PRIMA plans and a new dichroic optimised for PRIMA+AMBER use would have to be designed and implemented within the space and optical constraints of the VLTI laboratory.

Both instruments could be combined in the so-called *faint-object science mode*. One of the FSUs would be used as a fringe tracker on the bright source, with the STS correcting the slow drifts of the beams between the telescopes and the laboratory, while the light-beam from the faint (science) source would be directly sent to AMBER. If the motions of the beams within the pairs IP1-IP2 and IP3-IP4 (*cf.* figs. 5.1 and 5.4) are correlated, the corrections inferred by the STS can be blindly sent to AMBER and it can be possible, at least in theory, to use this instrument to measure the visibility for longer integration times and reach deeper magnitudes.[5] This operation mode is addressed in the following section.

[3] The *feeding optics* are optical switches responsible for controlling the path of light, at the level of PRIMA, that can reach FSUA or AMBER.

[4] Combining PRIMA with AMBER in the V^2 imaging mode was one of the main objectives of this thesis. However, the original plan had to be changed after ESO's decision of postponing this combination mode, in April 2010 (Nuno Gomes, Schmid et al., 2012).

[5] Another possibility would consist in using the current dichroics to perform IFG. In principle, this would be feasible because the dichroics currently installed in the VLTI laboratory are not fully compliant with the specifications and reflect part of the H-band. However, since this mode was never tested during the commissioning time of PRIMA, it is not sure that the amount of photons sent to IRIS would be enough to perform the guiding.

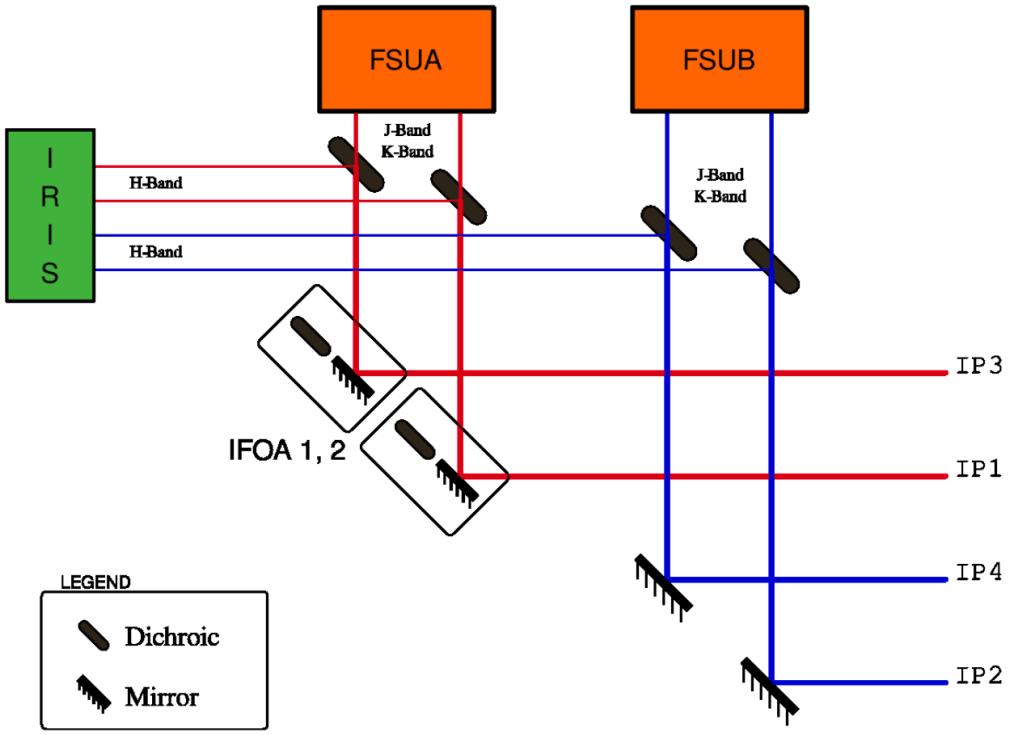

Figure 5.3: Feeding optics for the FSUs and IRIS in the astrometric mode of PRIMA, with the dichroic installed in IFOA 1 and 2, at the VLTI lab during PRIMA commissioning runs.

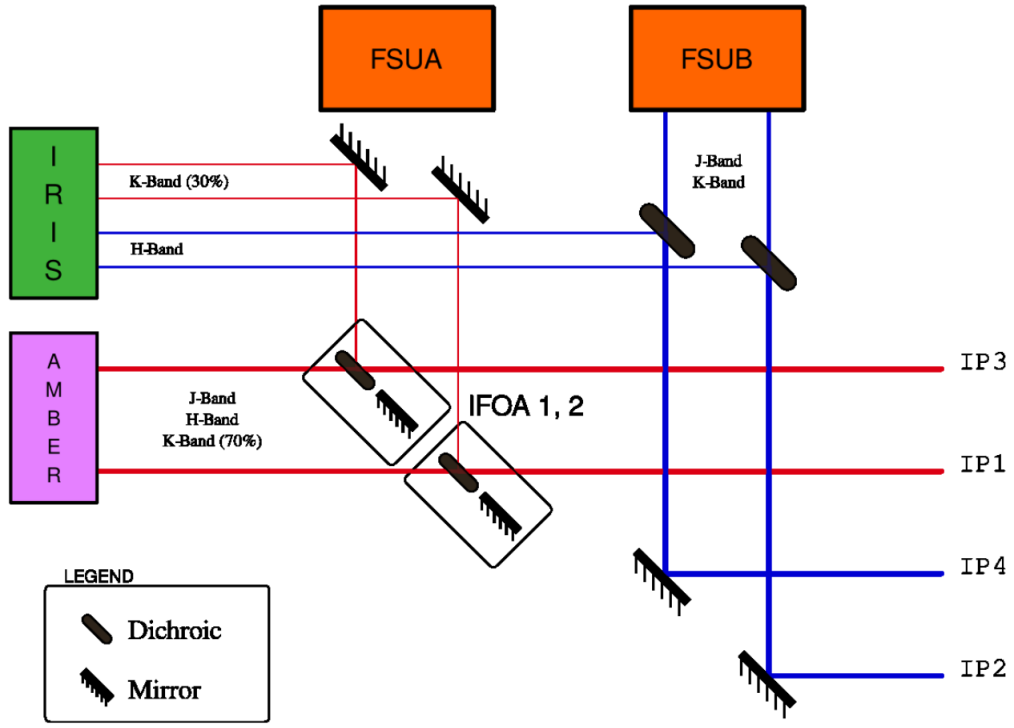

Figure 5.4: Feeding optics for the FSUs, IRIS and AMBER in the PRIMA+AMBER configuration, with the dichroic installed in IFOA 1 and 2 at the VLTI lab during PRIMA commissioning runs. This mode would not work as it stands, because IRIS would be receiving both K- and H- bands simultaneously. A proper dichroic, able to send part of the H-band to IRIS and to AMBER, would need to be provided.

Tip-tilt correlation in tunnel propagation

The IRIS infrared detector of PRIMA has four quadrants which, when in dual-feed mode, are paired in a way such that the beam coming from the bright reference star is going to one quadrant and the beam coming from the science object is going to the other quadrant, each pair being addressed to a telescope. Even if mechanical vibrations are disregarded, since the light ducts of the VLTI are not evacuated, the seeing inside them might affect the path of the light beams, having an impact on their positions in each quadrant of the PICNIC detector. IFG and, consequently, the V^2 imaging mode, are only possible on bright objects due to the IRIS limiting magnitude (*cf.* section 5.1, page 82). However, if the motion of both beams is correlated, PRIMA and AMBER can be combined for faint-object science, without tracking on the beam from the scientific (faint) source.

Therefore, it was important to address if the tip-tilts between the beams going to FSUB and AMBER were correlated at low frequencies. In case of correlation, the STS mirrors could be used to correct the slow drifts between the telescopes and the laboratory and send the beam coming from the faint (science) star to AMBER. The corrections would be calculated from the measurements done on the bright star, sent to FSUB and IFG. This procedure would correspond to a *blind correction*, extremely useful for observing *faint objects*[6] with AMBER.

Gitton, Puech et al., (2009) showed that the fast turbulence between the two beams *is not correlated*, but his study does not address the slow drifts. In order to seek for possible correlations between the beams offsets at low frequencies, the positions of the centroids of the beams in each pair of quadrants of IRIS were retrieved from engineering files and analysed.

Available data

A total of 102 engineering files (TXT and FITS), collected during PRIMA commissioning runs # 10, 11 and 12, were analysed. They consist on manually triggered logging files, executed during IRIS operations, where the centroids and pixel values of the incident beams were recorded. Out of the 102 files, 28 corresponded to sessions where the four PICNIC quadrants were active, of which 21 were in the TXT format. Examples of such files are illustrated in figs. 5.5 and 5.6

Methods and results

For each quadrant, the offsets in the X- and Y- directions were computed from the centroids of the beam images and the reference points. Then, the correlation of the movements of the beams was inferred from the offsets differences in each direction between the two quadrants corresponding to the same telescope (Q_1-Q_3 and Q_2-Q_4) and from the linear correlation coefficient between them. The results are illustrated in figs. 5.7 and 5.8.

[6] In this context, *faint objects* are those that are not detected by IRIS.

```
2010-02-19T03.11.14  FILT: 2  DIT: -1  BCK: 1  BADPIXMAP: 1  MINSAMP: 10  MAXSAMP: 15  (startX: 53  startY: 53   nx: 22  ny: 22) TEL: 4 3 4 3 STAT: 23 19 23 19

1266549073 587263   063.863  063.497  02804.00  -0001.00   063.672  066.942  02660.00  -0001.00   063.489  063.169  07774.00  -0001.00   063.996  066.881  01996.00  -0001.00
1266549073 637271   064.346  063.720  02892.00  -0001.00   063.262  066.675  03337.00  -0001.00   064.053  063.340  07924.00  -0001.00   063.750  065.963  02488.00  -0001.00
1266549073 687256   064.201  064.043  03225.00  -0001.00   063.157  067.100  03234.00  -0001.00   063.911  063.444  08687.00  -0001.00   063.077  066.611  02842.00  -0001.00
1266549073 737263   063.912  064.256  02579.00  -0001.00   063.341  067.414  03519.00  -0001.00   063.858  063.228  07892.00  -0001.00   062.516  066.670  02940.00  -0001.00
1266549073 787244   063.842  064.538  02004.00  -0001.00   063.606  067.486  03732.00  -0001.00   063.970  063.571  07111.00  -0001.00   063.172  066.352  02834.00  -0001.00
1266549073 837231   063.958  064.358  02551.00  -0001.00   063.949  066.997  03652.00  -0001.00   064.032  063.714  06581.00  -0001.00   063.902  064.898  02460.00  -0001.00
1266549073 887219   063.908  064.299  02544.00  -0001.00   063.766  066.595  03471.00  -0001.00   063.757  063.731  07176.00  -0001.00   063.883  064.432  02454.00  -0001.00
```

Figure 5.5: Example of an `irisCentroid*.txt` file, an IRIS log file manually triggered during IRIS operations. The header includes the starting time in the format YYYY-MM-DDTHH.MM.SS, IRIS filter used ($1 = \mathrm{J}$, $2 = \mathrm{H}$, $3 = \mathrm{K}$), the integration time used (dummy value is -1), the background removal status ($0 = \mathrm{NO}$, $1 = \mathrm{YES}$), the use of a bad pixel map ($0 = \mathrm{NO}$, $1 = \mathrm{YES}$), MINSAMP and MAXSAMP parameters (parameters that define the number of brightest pixels used for the calculation of the centroids), the readout window position and size, the telescopes numbers and the VLTI stations where they were located. The first two columns correspond to the absolute time with microseconds differential precision (seconds since 1900 + microseconds). For each quadrant, four columns are saved with data, of which the first two indicate the X- and Y- centroids in pixels with respect to the detector quadrant, and the two last columns respectively show the flux and the background in ADUs.

Select / All / Invert	TIME 1J usec Modify	Xoffset 1D um Modify	Yoffset 1D um Modify
1	-48649	-7.669230582660E-01	5.751357252925E-02
2	1350	-1.830851557150E+00	5.732639776189E-01
3	51386	-2.108312371771E+00	3.589887096335E-01
4	101433	-2.920236088003E+00	4.903509156240E-01
5	151492	-2.195838508422E+00	4.006949164335E-02
6	201487	-1.648400793087E+00	-9.297495516582E-01
7	251544	9.228619798255E-02	4.950746777086E-01

Figure 5.6: Example of a FITS file used to save IRIS data. The first column correspond to the time stamps in microseconds, and the second and third columns respectively to the X- and Y-offsets in micrometers.

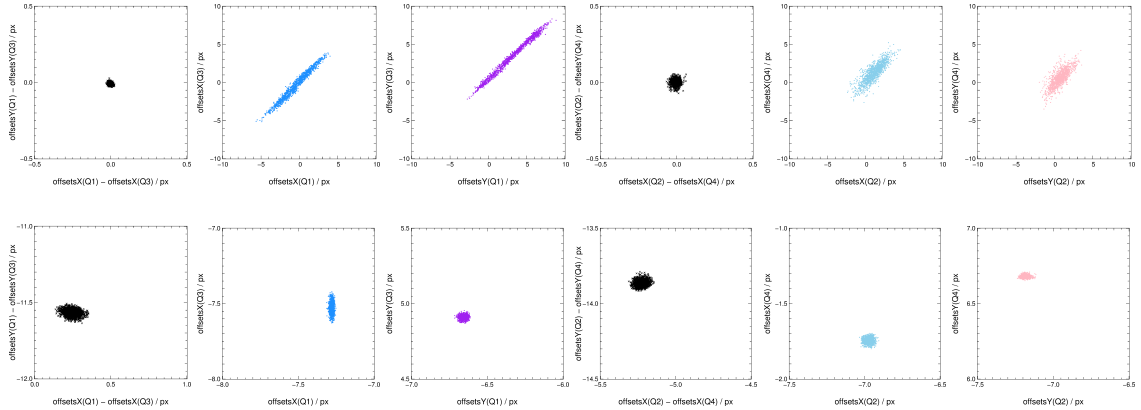

Figure 5.7: Offsets of beam positions in IRIS' quadrants Q_1-Q_3 and Q_2-Q_4. *Top-row*: example of high level of correlation (0.98 and 0.99 for Q_1-Q_3, and 0.91 and 0.82 for Q_2-Q_4, respectively in the X- and Y-direction) between two pairs of beams from the same telescope (either AT3 or AT4); *bottom-row*: same as the top-row, but for a case with very low level of correlation (0.01 and 0.03 for Q_1-Q_3, and 0.00 and 0.04 for Q_2-Q_4, respectively in the X- and Y-direction). Throughout all examined files, the correlation is typically larger between pairs Q_1-Q_3 than pairs Q_2-Q_4 (*cf.* fig. 5.8). The data were collected during PRIMA commissioning runs numbers 10 and 11 (2010).

Figure 5.7 illustrates two examples of data, with a high-level (top-row) and a low-level (bottom-row) correlation between the beams of the bright and faint sources arriving from the same telescope. The level of correlation is differently indicated by the panels of columns 1 and 4, and the ones of columns 2, 3, 5 and 6. While panels 1 and 4 indicate the correlation by measuring how well the differential in Y-offsets between paired quadrants as a function of the differential in X-offsets between the same quadrants is concentrated around the point $(0.0, 0.0)$, panels 2, 3, 4 and 5 measure the level of correlation by means of the linear relation between the offsets in Q_3 as a function of the offsets in Q_1 and the offsets in Q_4 against those of Q_2. The high level of correlation of the top-row example is apparent in the well concentrated points around $(0.0, 0.0)$ of panels of columns

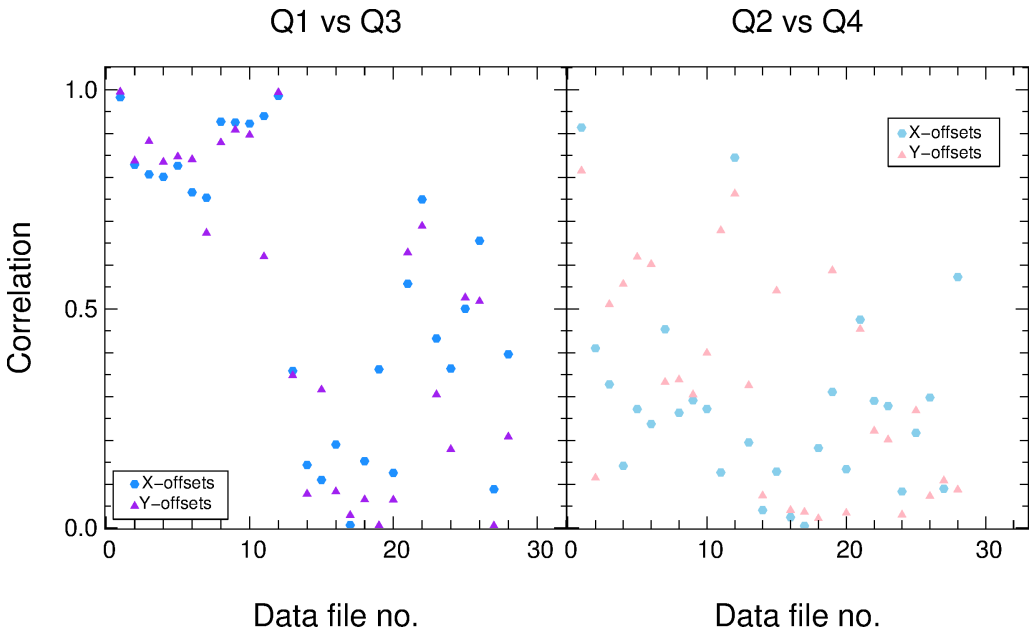

Figure 5.8: Level of correlation between the X- (blue and cyan circles) and Y-offsets (violet and pink triangles) for quadrants Q_1-Q_3 (*left*) and Q_2-Q_4 (*right*) in IRIS. The data were collected during PRIMA commissioning runs 10 and 11 (2010). The horizontal axis indicate the number of analysed files.

1 and 4, and in the approximately linear relation between the plots of panels 2, 3, 5, and 6. The low level of correlation of the bottom-row example is evinced by the less concentrated points in panels 1 and 4 (these points are also displaced in the X- and/or Y-direction by several pixels), and by the non-linear relation between the offsets of panels 2, 3, 5, and 6 — despite the drifts of the beams are not correlated, the offsets difference remains approximately constant throughout the acquisition run, with an amplitude less than the pixel length.

Figure 5.8 indicate the level of correlation for all analysed data. The correlation was estimated by means of the linear correlation coefficient between the offsets in one direction of pairing quadrants (Q_1-Q_3 or Q_2-Q_4). Blue (Q_1-Q_3) and cyan (Q_2-Q_4) filled circles represent the correlation between the drifts of the *reference* and *science* beams in the X-direction, while violet (Q_1-Q_3) and pink (Q_2-Q_4) triangles represent that correlation in the Y-direction.[7] Several aspects stand out from this figure:

- About 13 data files reflect a high level of correlation, above 70 %, specially between quadrants Q_1-Q_3.
- Typically, the correlation is larger between quadrants Q_1-Q_3 (corresponding to light from AT4) than between quadrants Q_2-Q_4 (beams from AT3). This corroborates what has been already detected in fig. 5.7, where panels 5 and 6 of the top-row point to a lower level of correlation between quadrants Q4 and Q2 when compared to the level of correlation between Q3 and Q1 (panels 2 and 3).
- For each data acquisition run, the correlation tends to be larger in either the X- or the

[7] The top and bottom rows of fig. 5.7 correspond respectively to the first and seventeenth points of the two panels of fig. 5.8.

Y-direction, indicating a predominance of the drifts' coupling in one of those directions. Between quadrants Q_1 and Q_3, the coupling was stronger in the X-direction in about 61 % of the cases, while between Q_2 and Q_4, the correlation was stronger in the Y-direction in about 57 % of the measurements.

The lower level of correlation between the beams coming from AT3 might be caused by *(a)* the seeing conditions inside the light ducts, between the telescope and the VLTI laboratory, and *(b)* the general and differential defocus identified in AT3 (Schmid et al., 2012).[8] The first reason seems not to be plausible, since, during all PRIMA commissioning runs under consideration, AT3 was placed in station G2, which is located on the North side of the platform (using the DL tunnel as reference), next to the VLTI lab, while AT4 was positioned in station J2, farther away, on the southern side of the platform (fig. 5.9). Although no atmospheric data inside the light ducts was available to study a possible correlation between the temperature/humidity/pressure values of the air in the tunnels and the slow drifts of the beams between the telescopes and the interferometric lab, it does not seem reasonable to think those factors are the main responsible for the lower correlation detected on AT3 beams when this telescope is closer to the lab than AT4. If that was the case, AT4 should exhibit the lowest correlation levels between the drifts of the beams in both directions, because a larger mass of air had to be crossed between the telescope and the lab. Therefore, the differential defocus identified in AT3 emerges as the most probable culprit for the lower correlations exhibited by the offsets of its beams when compared to those of AT4.

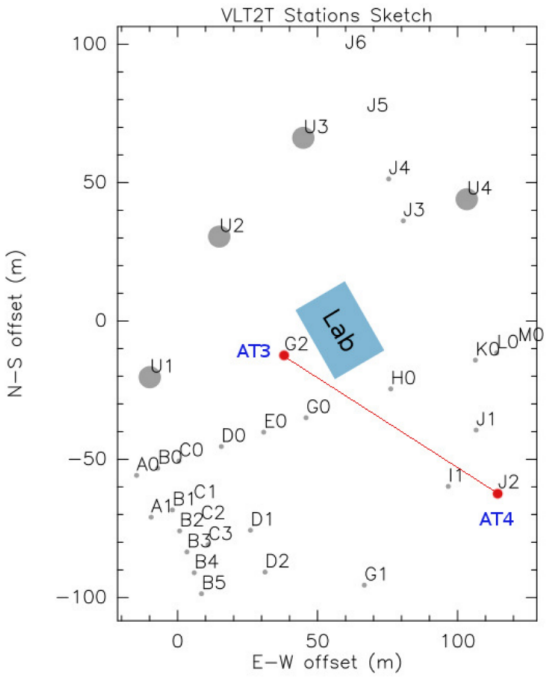

Figure 5.9: Configuration of the VLTI stations for PRIMA commissioning runs numbers 10, 11 and 12 (2010). Only telescopes AT3 and AT4 were used, and they were always positioned in stations G2 and J2, respectively, located on opposite North-South sides of the DL tunnel.

[8] A *global* defocus is common to both beams of a telescope, whereas a *differential* one corresponds to a defocus difference between two beams from the same telescope.

Conclusions

Generally, there is a high level of correlation between X- and Y-offsets for both pairs of IRIS' quadrants. Even when the correlation is very low or nonexistent, the offsets differences are always smaller than the width of the readout window (typically around 22 to 25 pixels). Since all data were acquired during commissioning time, and no information is available on the particular seeing conditions inside the light ducts when they were recorded, the examples of lowest correlation might have been due to technical problems, so typical during the acquisition of engineering data when an instrument is being tested and subsystems are being implemented and/or polished up. More data, recorded when images could be properly formed on IRIS and in controlled conditions of seeing inside the VLTI tunnels, would be however necessary in order to confirm that the highest correlation cases are the rule.

Since it was found a high level of correlation for a significant number of offsets both in X- and Y- directions, and considering that the differential defocus of AT3 or, at most, instrumentation problems that could be solved by way of technical interventions were the only factors contributing to the lower correlation in quadrants Q_2 and Q_4 and in all quadrants for some integration runs, these results paved the way for the implementation of the *faint-object science mode* of PRIMA, *i.e.*, the possibility to study objects too faint to be observed by IRIS.

Although the sought astrometric precision was never met, the development of the imaging and faint science modes would have made it possible to pursuit other scientific goals beyond exoplanet search, in the domain of the stellar and extra-galactic astrophysics (*cf.* section 3.3.7), and would have prevented the premature cancellation of the PRIMA project.

Nevertheless, reference stars have to be typically within $1'$ of the science object, and, therefore, one of the serious challenges faint science object interferometry has to deal with is the absence of natural guide stars in the immediate neighbourhood of scientifically interesting targets (A. Glindemann, 2011). A suitable solution to overcome this problem could be the generation of artificial guide stars unresolved to the observing configuration of the interferometer, by means of a laser beams system fired to a proper layer of the Earth's atmosphere (Gavel, Friedman and Olivier, 1998).

Lessons learned

PRIMA was an ambitious project, aiming at being the first common instrument capable of phase referencing observations. Some of the initial goals of this thesis were (*a*) to develop the imaging mode of PRIMA, combining it with AMBER, and to characterise the complex visibility of young stellar objects, namely to study the planet forming regions of pre-main sequence stars, and (*b*) to characterise the PRIMA on-sky astrometric performance, by measuring the separations of a sample of binaries.

Although at the end of 2008 PRIMA was starting its plan of commissioning runs, the moving from CAUP to ESO was anticipated by about seven months (February instead of July 2009), since

it was foreseen that the first set of data would be available in June 2009 and, by then, the project would had already made considerable progress. Unfortunately, the commissioning revealed to be slower than expected, and the imaging mode of PRIMA was postponed in 2010. The stay at ESO was extended one year, with the expectation of successful implementation of the instrument at Paranal, but that end up not to happen. Therefore, the first lesson learned is that when it comes to work on scientific instrumentation, one should never get as granted the success of a project without it being actually ready. The thesis had to be quickly adapted, and most of the work, which will be presented in the following chapters, was developed during the last year of the thesis, based at SIM/FEUP, in Portugal.

The participation on the PRIMA project was, however, very fruitful, from both the scientific and personal perspectives. Invaluable technical skills were acquired, such as the operation of interferometric facilities, the acquisition, reduction and analysis of VLTI data (FSU data, mainly), the conduction of simulations using `MiRA` reconstruction software to access the image quality of PRIMA+AMBER mode and compare it to phase closure imaging, just to mention a few.

It was also very important to be part of an international team of experts, which allowed the development of the ability to interact with different working environments and ways of thinking.

Part III

Interferometric Image Reconstruction

Chapter 6

Imaging

"To consult the rules of composition before making a picture is a little like consulting the law of gravitation before going for a walk."

— EDWARD WESTON (1886-1958)

Contents

LONG BASELINE OPTICAL INTERFEROMETRY (LBOI) paves the way for high angular resolution Astronomy in the visible and infrared (IR) ranges of the electromagnetic spectrum. However, no images of the emitting object can be directly produced from current interferometers, only a limited number of measurements of the complex visibility $\widetilde{V}$ of the source can. The type of observables depends on the instruments used, being the power-spectrum and the bi-spectrum/closure phase the most common up to date (*cf.* section 2.2). Employing model fitting, the object brightness distribution can be characterised and a new world of previously unreachable information about the light source becomes accessible. Notwithstanding the technique of model

fitting has already reached a high level of development, there are several astrophysical topics (*cf.* section 1.3) requiring high angular resolution model-independent imaging in order to be unequivocally clarified (J.-P. Berger, Malbet et al., 2012). A great advantage of IR and optical interferometers with imaging capabilities is the ability to circumvent ambiguities in the interpretation of visibility amplitudes and phases data. Therefore, the full potential of an interferometer cannot be exploited without image restoration methods.

This chapter concerns about the intricacies of the image reconstruction process in interferometry, and is built around the work by Éric Thiébaut (Éric Thiébaut, 2005, 2008, 2009; Éric Thiébaut and Giovannelli, 2010).

In section 6.1, it is explained that image reconstruction is regarded as an inverse problem, in the sense that it tries to build the brightness distribution of the object from the observed data. The image formation equation is presented and it is shown that directly back-Fourier transforming the measurements does not lead to a good image because of noise amplification.

Section 6.2 clarifies that the image reconstruction process is a ill-posed problem due to the holes in the spatial frequency space and to the lack of other information as the phase of the visibility. The most adopted method to tackle it — to wit the choice of a solution that minimises a penalty function under limiting conditions (such as positivity and normalisation) — is explained. The algorithm used for the image restorations produced during this thesis (`MiRA`) is described, as well as other algorithms already published and that had lead to notorious interferometric images and/or scientific results: CLEAN, in radio interferometry, and BSMEM, BBM, MACIM and WISARD, in the domain of IR interferometry.

The chapter ends with a brief description of the state of the art in the field of image reconstruction (section 6.5), where the most relevant interferometric images published so far are presented.

Principles of image reconstruction

Image formation equation

The *standard image formation equation* gives the observed image y of an incoherent source in a direction $\vec{s}$:

$$y(\vec{s}) = \int h(\vec{s} \mid \vec{s}')x(\vec{s}')\,\mathrm{d}\vec{s}' + n(\vec{s}), \tag{6.1}$$

where $x(\vec{s}')$ is the *source brightness distribution*, $h(\vec{s} \mid \vec{s}')$ is the *point spread function* (PSF), and $n(\vec{s})$ is the term estimating the noise due to both the object and the detector. The PSF $h(\vec{s} \mid \vec{s}')$ describes the response of the system (*i.e.*, it gives the brightness distribution) in a direction $\vec{s}$ to a point source situated in a direction $\vec{s}'$ (Éric Thiébaut, 2005).

When the FOV lies inside the *isoplanatic patch*, the PSF can be considered shift invariant, *i.e.*,

$$h(\vec{s} \mid \vec{s}') = h(\vec{s} - \vec{s}'). \tag{6.2}$$

Therefore, for small enough $\|\vec{s}-\vec{s}'\|$, the observed image is the true image convolved with the PSF plus some noise terms:

$$y(\vec{s}) = \int h(\vec{s}-\vec{s}')x(\vec{s}')\,\mathrm{d}\vec{s}' + n(\vec{s}). \tag{6.3}$$

Current detectors (*e.g.*, CCDs and CMOS in the NIR) transfer the continuous object brightness distribution into a discrete counterpart, typically a square array of pixels. Due to this *discretization* process, eq. (6.3) can be written in the matrix form:

$$\mathbf{y} = \mathbf{H}\cdot\mathbf{x} + \mathbf{n}, \tag{6.4}$$

where $\mathbf{H}$ is the *response matrix*, and $\mathbf{y}$, $\mathbf{x}$ and $\mathbf{n}$ are vectors representing respectively the data, the object brightness distribution and the noise (ibid.).

Since it is easier to compute products than convolutions, it is a common practice to work in the Fourier plane rather than in its imaging equivalent. Taking the Fourier transform (denoted by hats) in both members of eq. (6.3), one gets

$$\widehat{y}(\vec{u}) = \widehat{h}(\vec{u}) \times \widehat{x}(\vec{u}) + \widehat{n}(\vec{u}), \tag{6.5}$$

where $\vec{u}$ represents the spatial frequency related to the position $\vec{s}$. The Fourier transform of the PSF, $\widehat{h}(\vec{u})$, corresponds to the *Optical Transfer Function* (OTF), which determines the response of the system to an incident wavefront.[1] The modulus of the OTF is known as the *Modulation Transfer Function* (MTF), which is a measure of the contrast change between the emitting object and its image (Schroeder, 1987).

When the image is *discretized*, a discrete Fourier transform can be applied to eq. (6.4), and the image formation equation becomes

$$\widehat{y}_u = \widehat{h}_u \widehat{x}_u + \widehat{n}_u, \tag{6.6}$$

where the index u denotes the u^{th} spatial frequency $\vec{u}$ of the discrete Fourier transformed array (Éric Thiébaut, 2005).

Tentative direct inversion

A very appealing method to obtain the true brightness distribution of the source x is, while in the Fourier domain, to divide the data y by the MTF and, applying eq. (6.6), to solve for $\widehat{x}_u$ (*direct inversion*), and then to Fourier back transform to get the deconvolved image:

$$\widehat{x}_u^{(\text{direct})} = \frac{\widehat{y}_u}{\widehat{h}_u} = \widehat{x}_u + \frac{\widehat{n}_u}{\widehat{h}_u}. \tag{6.7}$$

However, the result is rather disappointing because the direct solution is corrupted by the noise term. At high spatial frequencies — to which small details in the image correspond — the noise

[1] The OTF can also be expressed as the magnitude of the normalised autocorrelation of the complex pupil function (J. W. Goodman, 2000).

dominates the signal and the MTF attains small values. This leads to noise amplification, which in turn introduces very large errors into the direct deconvolved image. Although the *instrumental transmission* (*i.e.*, the convolution with the PSF) smooths the image, the *noise amplification* associated to the deconvolution always deforms the direct solution, which is known as *ill-conditioning* in inverse problem theory (Éric Thiébaut, 2005).

Image reconstruction in interferometry

While a reflecting telescope is able to acquire a continuum of baselines and, thus, all available spatial frequencies up to its diffraction limit ($\sim \lambda/D$) in a single exposure,[2] an interferometer cannot produce more data than the corresponding to the spatial frequencies measurable in each baseline. Due to a limited number of measurements lying in the Fourier plane, an interferometer is unable to directly deliver an image, but the possibility of attaining high angular resolution imaging — sometimes with spectrum and polarisation analysis — can be achieved with the use of reconstruction algorithms (*e.g.*, J. M. Beckers, 1983; J.-P. Berger, Malbet et al., 2012). The process is feasible only because $\widetilde{V}$ relates to the brightness distribution by means of the van Cittert-Zernike theorem (*cf.* section 2.2.2).

The purpose of interferometric image reconstruction is to find a numerical solution that satisfactorily approximates the true brightness distribution of the emitting source, given the collected data (*e.g.*, Renard, Éric Thiébaut and Malbet, 2011; Éric Thiébaut, 2009). In order to account for the measurements, the Fourier transform of the image must contain the measured visibilities. This section describes methods to solve the problem of synthesising an image from interferometric data.

Model of the image

Due to the sparseness of the (u,v)-coverage and to the noise, it is impossible to restore exactly the true brightness distribution $I_\lambda(\vec{s}')$ of the emitting source. The common approach is to search for the best approximation $i(\vec{s}')$ of $I_\lambda(\vec{s})$, depending on a finite number of parameters (Éric Thiébaut, 2013). The *image*, which is thus a parametric representation of the source brightness distribution and that can be treated as a grid of square pixels (Renard, Éric Thiébaut and Malbet, 2011), is usually modelled by the linear relation (*e.g.*, Éric Thiébaut, 2013),

$$i(\theta) \doteq \sum_{n=1}^{N} x_n b_n(\theta) \approx I_\lambda(\theta), \tag{6.8}$$

being θ an angular direction, N the *total number of image parameters* (number of pixels of the image, and others), $x = \{x_n\}_{n=1}^{N} \in \mathbb{R}^N$ the set of parameters characterizing the sought solution (the pixel values of the image, for example), and $\{b(\theta) : \mathbb{R}^2 \mapsto \mathbb{R}\}_{n=1}^{N}$ a chosen basis of functions (such as the pixel response function). With this parametrisation, the image reconstruction process

[2] In that sense, a telescope can be seen as an interferometer with an infinite number of baselines with length up to its diameter.

is reduced to the estimation of the N parameters x that better fit the collected data (Renard, Éric Thiébaut and Malbet, 2011).

It is customary, for image reconstruction, to take a shift-invariant basis of functions equal to the *pixel shape*, $b(\theta)$, *i.e.*,

$$b_n(\theta) = b(\theta - \theta_n), \tag{6.9}$$

where $b(\theta) : \mathbb{R}^2 \mapsto \mathbb{R}$ is a single basis function and θ_n is the angular position of the n^{th} pixel. Given a grid of equispaced angular positions $\mathscr{G} = \{\theta_n \in \mathbb{R}^2\}_{n=1}^N$, the typical pixel representation of the image results from taking the pixel shape equal to a single *building block function*, $b(\Delta\theta)$.

This choice implies that x_n is proportional to the value of the n^{th} pixel of the sampled image,

$$x_n \doteq q\, i(\theta_n), \tag{6.10}$$

where $q > 0$ is chosen in order x to be normalised (ibid.).[3] From eqs. (6.8) and (6.9), the Fourier transform (FT) of the image is then

$$\widehat{i}(f) = \sum_{n=1}^{N} x_n \widehat{b}_n(f) = \widehat{b}(f) \sum_{n=1}^{N} x_n \, \mathrm{e}^{-\mathrm{i}2\pi\, \theta_n \cdot f}, \tag{6.11}$$

where $\widehat{b}_n(f)$ and $\widehat{b}(f)$ are respectively the FTs of the basis functions and of the pixel shape, and f is the spatial frequency, conjugate of the angular position θ.

Model of interferometric data

With the most common observables in optical interferometry, *i.e.*, the power-spectrum and the bi-spectrum, image reconstruction is highly multi-modal and, without proper regularisation, the solution tends to stall in local minima not corresponding to the best image. When the complex visibility is available, the joint criterion — comprising the likelihood term that enforces the fidelity to the data and the regularisation one that imposes the priors — is convex (*i.e.*, it has only one minimum). In this case, image reconstruction is relatively easy (provided enough spatial frequencies are measured with a good SNR) and the search for the solution amounts to a deconvolution problem (Éric Thiébaut, 2013).

If the instrument is able to record the complex visibilities $\widetilde{V}$ of the interference fringes between two telescopes,[4] its instantaneous output can be modelled by the following equation:

$$\widetilde{V}_{ij}(t) = g_i(t)^*(t) g_j \widehat{I}(f_{ij}(t)), \tag{6.12}$$

where $\widetilde{V}_{ij}(t)$ is the complex visibility measured at instant t between the telescopes i and j, $g_i(t)$ is the dimensionless *transmission gain* or *complex throughput* of the i^{th} telescope, $f_{ij}(t)$ is the spatial

[3] This condition is required by the OIFITS standard (*cf.* Pauls et al., 2005).

[4] It is less demanding, without loss of scope or generality, to start the analysis of the image reconstruction process by considering data composed uniquely of complex visibilities. The case of power-spectra and bi-spectra is treated afterwords.

frequency corresponding to the pair of telescopes (i, j), and $\widehat{I}(f_{ij}(t))$ is the Fourier transform of the source brightness distribution $I(\theta)$ (*cf.* sections 2.1 and 2.2; Éric Thiébaut, 2009).

Being complex quantities, the gains can be written as

$$g_i(t) = \tau_i(t)\,\mathrm{e}^{\mathrm{i}\phi_i(t)}, \tag{6.13}$$

where $\tau_i(t) = |g_i(t)|$ and $\phi_i(t)$ are respectively their amplitudes and phases. In the presence of photometric calibration, $\tau_i(t) \simeq 1$, and since the gain's phase arises from an OPD $\delta_i(t)$, which is telescope dependent, it can be written that $\phi_i(t) = 2\pi\,\delta_i(t)/\lambda$ (ibid.). This OPD has instrumental and atmospheric causes (*cf.* sections 3.2 and 3.3) and, therefore, it usually varies on the milli-second scale, requiring special techniques to be measured, like fringe tracking.

Assuming that the gains are known and stable, the measured complex visibilities can be written as

$$\widetilde{V}_{ij,m}^{\text{data}} = g_{i,m}^{*} g_{j,m} \widehat{I}(f_{ij,m}) + e_{ij,m} = \widetilde{V}_{ij,m} + e_{ij,m}, \tag{6.14}$$

where

$$f_{ij,m} = \frac{\vec{B}_{ij,m}^{\perp}}{\lambda} = \frac{(\vec{r}_{i,m} - \vec{r}_{j,m})^{\perp}}{\lambda} \tag{6.15}$$

is the m^{th} measured spatial frequency, sampled between telescopes i and j,[5] and e accounts for all the differences between the data and the model visibilities $\widetilde{V}_{ij,m}$, including the noise and modelling errors (ibid.). All quantities were averaged during the m^{th} exposure for a mean time $t_m = \langle t \rangle_m$. The function $G_m = \langle g_{i,m}^{*}(t_m)\, g_{j,m}(t_m) \rangle_m$ is known as the *transfer function*.[6]

For the set of M spatial frequencies $\Lambda = \{f_m\}_{m=1}^{M}$ sampled during the observations, the linear model of the complex visibilities are given by:

$$\widetilde{V}_m(x) = \widehat{I}_m = \widehat{I}(f_m) = \sum_{n=1}^{N} Q_{mn} x_n = (\mathbf{Q} \cdot x)_m\,, \tag{6.16}$$

where, for the *building block model* of eq. (6.11), the coefficients of the matrix $\mathbf{Q} \in \mathbb{C}^{M \times N}$ are given by

$$Q_{mn} = \widehat{b}_n(f_m) = \widehat{b}(f_m)\,\mathrm{e}^{-\mathrm{i}2\pi\,\theta_n \cdot f_m}. \tag{6.17}$$

From the linearity of eq. (6.16), the data in eq. (6.14) can be described by the affine equality

$$d = \mathbf{G} \cdot \mathbf{Q} \cdot x + e = \mathbf{M} \cdot x + e, \tag{6.18}$$

where $\mathbf{M} = \mathbf{G} \cdot \mathbf{Q}$ and $\mathbf{G}$ is a diagonal matrix containing the amplitude transmission gains $g_{i,m}^{*}\, g_{j,m}$. The coefficients of $\mathbf{G}$ are different from zero only when the spatial frequency m is measured. Equation (6.18) is the equivalent, in aperture synthesis, to eq. (6.5), commonly present in conventional

[5] $\vec{r}_{i,m}^{\perp}$ is the projected position on a plane perpendicular to the line of sight of the i^{th} telescope, and $\vec{B}_{ij,m}^{\perp}$ is the projected baseline on the same plane between telescopes i and j.

[6] For the same reasons as presented for the transmission gains (page 100), the transfer function is characterised by rapid variations due to the OPD between the interfering beams, mainly caused by the atmospheric turbulence, that induce a random phase delay.

imaging techniques. Consequently, the matrices $\mathbf{G}$ and $\mathbf{Q}$ correspond respectively to the OTF and to the FT operator (ibid.).[7]

The operation of the inverse Fourier transform (*i.e.*, the generalised inverse $\mathbf{Q}^{\dagger}$ of $\mathbf{Q}$) on the data yields the so called *dirty image*. Since the non measured visibilities are made equal to zero and, thus, only the measured complex visibilities contribute to the inverse Fourier transform, the quality of the dirty image is not satisfactory, since it presents several reconstruction features (not present in the original image) and there are regions where the intensity is negative (*cf.* fig. 6.1d).[8] The dirty image simply corresponds to the convolution of the specific brightness distribution by the *dirty beam*, which is equal to the FT of the *uv*-plane. Hence, the latter is the analogous to the PSF of optical systems in conventional imaging, but it is not a normalised and non-negative distribution (*e.g.*, Éric Thiébaut, 2013, *cf.* fig. 6.1b).[9] Therefore, image reconstruction from interferometric data is an inverse problem that can be seen (1) as a deconvolution issue between the dirty image and the dirty beam (easy case), or (2) as an interpolation problem between spatial frequencies to estimate the missing (u,v) points (harder approach). The easy case is, however, *ill-posed* because of the voids in the coverage of the (u,v)-plane and possibly due to the lack of other important knowledge (like phase information). Consequently, additional constraints to the data must be imposed to warrant the uniqueness of the solution (ibid.), inevitably leading one to the second and harder approach.

Choosing the field of view and the resolution of the image

When attempting the restoration of an image, the size of the pixel, $\delta\theta$, and the FOV (with width Ω) must be chosen carefully, taking into account the dimensions of the emitting source, the resolution of the interferometer (*e.g.*, Lannes, Anterrieu and Maréchal, 1997), the execution time, and computer memory limitations. The resolution of the image is fixed by the number of pixels, N, and the pixel size or *sampling step*, which are chosen to be the same in the two spatial dimensions of the image in order to avoid anisotropic effects (Éric Thiébaut, 2009). The *frequel* or *spatial frequency sampling step*, δf, is taken as the reciprocal of Ω:

$$\delta f = \frac{1}{\Omega} = \frac{1}{N\,\delta\theta}. \tag{6.19}$$

The *Shannon-Nyquist criterion* states that, in order to prevent under-sampling, the size of the pixel must be chosen smaller than the resolution of the interferometer, $\mathscr{R}$, which is imposed by the

[7] $\mathbf{Q}\cdot x$ corresponds to the FT of the object brightness distribution.

[8] A way of tackling this limitation consists in interpolating the non-measured spatial frequencies by means of FFTs, using the adjacent *frequels* (a *frequel* is a **freq**uency **el**ement from a grid of equally spaced spatial frequencies), an operation which is not consuming in terms of computation (Frigo and Johnson, 2005; Éric Thiébaut, 2009).

[9] The problem of effective PSF estimation in interferometric image reconstruction is addressed in section 7.7.4.1, page 181.

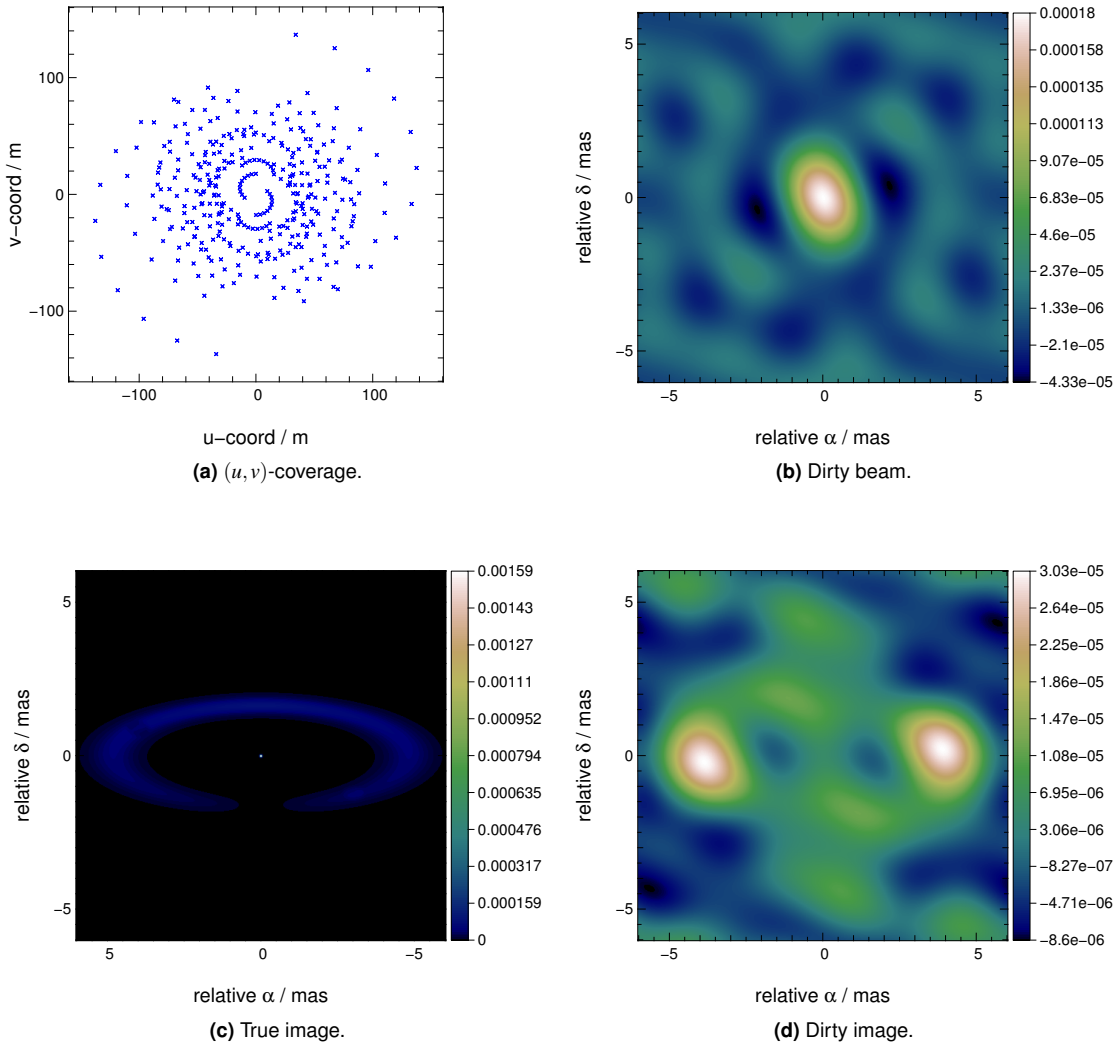

(a) (u,v)-coverage.

(b) Dirty beam.

(c) True image.

(d) Dirty image.

Figure 6.1: uv-coverage (*a*), dirty beam (*b*), true brightness distribution (*c*) and dirty image (*d*) corresponding to a YSO observed during 3 nights with the four ATs of the VLTI. The lack of high frequency (u,v)-points in the NNW-SSE direction is responsible for the elongated ellipse-shape of the dirty beam in that direction. Both the dirty beam and the dirty image present typical negative values/lobes. The object, a YSO, is described in detail in section 7.1 (*cf.* fig. 7.1b, page 118).

maximum projected baseline, $B_{\max}$:[10]

$$\delta\theta < \mathscr{R} = \frac{\lambda}{2B_{\max}} = \frac{1}{2f_c}, \tag{6.20}$$

where $f_c = \max|f| = \frac{B_{\max}}{\lambda}$ is the *Nyquist* or *cut frequency*, *i.e.*, the maximum frequency without *spatial aliasing* (*e.g.*, Voelz, 2011). A signal sampled at $2f_c$ is said to be *Nyquist sampled*. No information is lost if a signal is Nyquist sampled, and no additional information is gained by sampling faster than this rate. However, ignoring eq. (6.20) results in *aliasing*, in which different signals become indistinguishable (or aliases of one another) when sampled. Consequently, undersampled high-frequencies in the signal are misinterpreted as low-frequency content (ibid.)

As a rule of thumb, in order to avoid too much bias due to a pixelated image, the pixel size must be chosen such that

$$\delta\theta \leqslant \frac{\lambda}{4B_{\max}}. \tag{6.21}$$

Throughout this thesis it was adopted a *super-resolution factor* of 8,

$$\delta\theta \simeq \frac{\lambda}{8B_{\max}}, \tag{6.22}$$

in light of all the above considerations, and the fact that below this value the estimation of the effective PSF was harder due to lack of detail (the restored image of the PSF was too pixelated to allow for the determination of the orientation of the ellipse — *cf.* section 7.7.4.1).

Inverse problem approach

Image restoration from interferometric data is regarded as the search for a solution of an inverse problem (Tarantola, 2005; Éric Thiébaut, 2005). The path, however, is not straight and the process has to deal with several obstacles in order to find a satisfactory image (Éric Thiébaut, 2013):

- The major difficulty is the *sparse coverage of the uv-plane*. Aperture masking and multi-telescope interferometers operating in the optical can only offer a few scattered measurements of the complex visibility, because of the constraints imposed by the geometrical configuration of the array (number of combined telescopes and available delay lines).[11]
- The *atmospheric turbulence*, which implies the use of specific techniques to recover the phase information (like phase-referencing), or the use of non-linear data (power-spectra and/or bi-spectra) of more difficult fitting than the complex visibilities.
- *Missing phase data* when using only closure phases (very typical at optical wavelengths) — for instance, in a 3-telescopes case, $2/3$ of the phase information is missing.

[10] Shannon's version of the theorem states that if a function $s(\theta)$ contains no frequencies higher than W, it is completely determined by giving its ordinates at a series of points spaced by $1/(2W)$ (Shannon, 1984).

[11] The measurement of the interferometer response function for the whole (u,v)-plane at a single frequency would require a large number of telescopes to provide baselines at all possible orientations and separations, an expensive operation of very difficult implementation (Jackson, 2008).

- *Calibration problems* — due to the noise, it is expected some discrepancy between the measurements and their model — implying additional unknowns in the data.

Hence, an image can not be defined uniquely by the data alone, and the image reconstruction process is a *ill-posed problem*, in the sense that albeit there is a solution, that solution is not unique (there are more unknown pixels in the image than interferometric data). That is, the data alone is not enough to restrict the set of restored brightness distributions, that are solution to the restoration problem, to an unequivocal and stable image. Indeed, any image whose Fourier transform fits the measurements within the error bars in the least squared sense is a valid solution (J.-P. Berger, Malbet et al., 2012; Éric Thiébaut, 2009). Therefore, additional preceding information, known as *priors*, is required. Image restoration becomes, then, a trade-off between loyalty to the data and agreement with the priors.

The final reconstructed image is the most probable one, given the data and prior information (J.-P. Berger, Malbet et al., 2012). A common recipe to find the best restored brightness distribution (*e.g.*, Renard, Éric Thiébaut and Malbet, 2011; Éric Thiébaut, 2008) from a set Υ of possible images, consists in choosing the solution x^+ that minimises a *penalty function*, $f(x)$, under some restrictive conditions, such as *positivity* and *normalisation*:

$$x^+ = \arg\min_{x\in\Upsilon} f(x) \;\text{ s.t. } x \geqslant 0 \text{ and } \sum_n^N x_n = 1, \tag{6.23}$$

where x are the image parameters. The sought image x^+ is taken as a grid of square pixels. The penalty function depends on the data and on the prior information, and it is defined as

$$f(x) = f_{\text{data}}(x \mid d) + \mu f_{\text{prior}}(x), \tag{6.24}$$

where d is the data, the term $f_{\text{data}}(x)$, usually known as *likelihood term*, accounts for the difference between the measurements d and the model data x, the term $f_{\text{prior}}(x)$, commonly designated as *regularisation term*, measures the difference with the information available *a priori*, and μ is a positive hyper-parameter that balances the relative weight imposed by the real data and the priors — small values of μ enforces agreement with the measurements, while large values of the hyper-parameter amplify the priors (Renard, Éric Thiébaut and Malbet, 2011).

The two conditions in eq. (6.23), respectively the positivity and the normalisation of the brightness distribution, are always present: the former is a physical restriction (it must hold for the reconstructed image, as negative flux is meaningless in Astronomy), while the latter is required by the OIFITS data format (*cf.* Pauls et al., 2005).

The likelihood term, f_{data}, is usually built from an analytical model of the measurements and of the noise statistics, and it can result from the combination of different types of data, as complex visibilities, normalised power-spectra and/or bi-spectra/closure phases (J.-P. Berger, Malbet et al., 2012).

The regularisation term, f_{prior}, introduces the priori information into the minimisation process, and it allows to choose the image, from all the solutions compatible with the data, that is closer

to the a priori knowledge. The requirement for this term prevents the iterative process of image restoration to be automatic, in the sense that it is essential that the observer introduces all available knowledge about the brightness distribution to narrow the set of possible images. Although being a solution, the dirty image (*cf.* section 6.2.2, page 100) is not a satisfactory one, and the role of the regularisation is to drive the reconstruction process to a more acceptable restored image, trying to cope with the holes in the (u,v)-plane by means of continuous and smooth interpolations.

The most immediate and simple priors that can be included in the regularisation term are the aforementioned positiveness and normalisation, and the dimensions of the FOV. Other popular regularisations that introduce more restrictive conditions are (*e.g.*, J.-P. Berger, Malbet et al., 2012; Renard, Éric Thiébaut and Malbet, 2011; Éric Thiébaut, 2013):

- **Smoothness**, which smooths the image by avoiding unmeasured high spatial frequencies.[12] It is inserted in the regularisation term by means of the generic expression

$$f_{\text{prior}} = \|x - \mathbf{S}\cdot x\|^2, \tag{6.25}$$

  where $\mathbf{S}$ is a linear operator that smooths the image by a three-element convolution and defines the default solution, commonly called *floating prior*, $x_{\text{prior}} = \mathbf{S}\cdot x$ (Pichon and Éric Thiébaut, 1998; Éric Thiébaut, 2008, 2009).[13] This regularisation can be tuned in order to preserve some details in the brightness distribution, which is highly desirable for astronomical objects, typically having high frequency and high dynamical range content due to point-like sources or rapid variations close to sharp edges.
- **Compactness**, a quadratic prior,[14] which favours a compact and centred image, outside of which no flux is expected. It is implemented through the expression

$$f_{\text{prior}} = \sum_n w_n^{\text{prior}} x_n^2, \tag{6.27}$$

  where n is the pixel number, and the given weights w_n^{prior} are usually chosen positive and increasing with the distance to the centre of the image (for instance, $w_n^{\text{prior}} \propto \|\theta\|^\alpha$, being θ the angular direction and $\alpha > 0$). These conditions produce, in the Fourier space, the so-called *spectral smoothness*, which has been proven to be very effective in interpolating the typically sparse (u,v)-coverages of IR interferometric observations (Éric Thiébaut, 2013).
- **MEM**, which tries to find the smooth image most compatible with the data, using the minimum information possible and keeping high frequency information (Gull and Skilling,

[12] The process of smoothing usually requires the imposition of some level of correlation between neighbour pixels in the image solution (Éric Thiébaut, 2009).

[13] The floating prior is the image restored in the absence of data, that can be used as a starting point in the process of image reconstruction. A good initial guess is, for example, an image previously reconstructed using stronger restrictions or different kind of data.

[14] The general expression for a quadratic regularisation is

$$f_{\text{prior}}(x) = (\mathbf{A}_{\text{prior}}\cdot x - b_{\text{prior}})^{\mathrm{T}}\cdot \mathbf{W}_{\text{prior}}\cdot(\mathbf{A}_{\text{prior}}\cdot x - b_{\text{prior}}), \tag{6.26}$$

where any quadratic regularisation can be selected by properly adjusting the matrices $\mathbf{A}_{\text{prior}}$ and $\mathbf{W}_{\text{prior}}$ and the vector b_{prior} (Éric Thiébaut, 2008).

1984a,b; Narayan and Nityananda, 1986; Skilling and Bryan, 1984). The regularisation criterion is usually written in the form

$$f_{\text{prior}} = -\sum_n h(x_n \mid x_n^{\text{prior}}), \tag{6.28}$$

where the sum $\Sigma_n h$, known as the *entropy*, is a smoothness scalar estimator that measures the information content of the image. The entropy of the image can assume several definitions, some of which are:

$$h(x_n \mid x_n^{\text{prior}}) = \sqrt{x}, \tag{6.29a}$$

$$h(x_n \mid x_n^{\text{prior}}) = \log x, \tag{6.29b}$$

$$h(x_n \mid x_n^{\text{prior}}) = x - x^{\text{prior}} - x \log \frac{x}{x^{\text{prior}}}. \tag{6.29c}$$

MEM will always try to find the solution that best fits the measurements, while keeping the entropy maximum. This has been one of the most popular regularisations used in image reconstruction so far (J.-P. Berger, Malbet et al., 2012).

- **Non-linear smoothness**, which is introduced by the expression

$$f_{\text{prior}} = \sum_{n_1, n_2} \sqrt{\|\nabla x_{n_1, n_2}\| + \varepsilon^2}, \tag{6.30}$$

where

$$\|\nabla x_{n_1, n_2}\| = (x_{n_1+1, n_2} - x_{n_1, n_2})^2 + (x_{n_1, n_2+1} - x_{n_1, n_2})^2, \tag{6.31}$$

and $(n_1, n_2) \sim n$ are the indices of the n^{th} pixel in the two dimensions. When the threshold ε is strictly positive, eq. (6.30) originates the so-called *edge-preserving smoothness* penalty, which is similar to a quadratic smoothness regularisation in the regions of the image where the magnitude of its spatial gradient is smaller than ε and preserves the sharp edges in all the other regions (Éric Thiébaut, 2013).

- **Total Variation**, which seeks for the minimum of the image's total gradient (Rudin, Osher and Fatemi, 1992; Strong and Chan, 2003). The regularisation term, the so-called *total variation prior*, is defined as

$$f_{\text{prior}} = \sqrt{(x_{n_1+1, n_2} - x_{n_1, n_2})^2 + (x_{n_1, n_2+1} - x_{n_1, n_2})^2}. \tag{6.32}$$

It is obtained from eq. (6.30), when $\varepsilon \to 0$. It benefits uniform zones in the image, with fast intensity variations (stellar surfaces, for instance). Renard, Éric Thiébaut and Malbet, 2011 found that this is one of the best available regularisations to be used with different kinds of objects, being suitable to distinct morphologies, as point like sources and objects with uniform extended intensity. For this reason, this is the regularisation used in the image reconstructions performed throughout this thesis, which are presented in chapter 8.

Image reconstruction algorithms and their applications

When it comes to present the most significant algorithms for image reconstruction to date, two domains have to be differentiated: larger (radio) and shorter (optical) wavelengths.

In the radio, the procedure is more straightforward mainly because the visibility phase is known and the (u,v)-coverage is typically much larger. Phase variations during each exposure are small and since the gains can be figured out by calibration, the source brightness distribution can be estimated by direct deconvolution.[15]

In the optical (infrared and visible) domain, however, the observed quantities are not the same as in the radio regime. The model of the data is non-linear and a straight deconvolution leads to unsatisfactory results (*cf.* section 6.1.2). Several strategies have been developed to tackle the problem, resulting from adaptations from their radio counterparts or corresponding to completely new approaches, but they differentiate from each other mainly by the way the missing phase information is taken into account, by the way the statistics of the data is approximated, by the type of regularisation and by the paths followed for optimisation.

Radio domain

The CLEAN algorithm

Image reconstruction became a common practice amongst radio interferometers since the early 80's of the twentieth century, after the CLEAN algorithm (Högbom, 1974) and its variants, with or without self-calibration (Cornwell and Wilkinson, 1981), have been published.

CLEAN is an iterative algorithm that deconvolves the dirty beam from the *dirty map* of an observation done in the radio. It assumes that the FOV can be represented by a limited number of significant point sources, whose positions and intensities it tries to find. The restored image is the result of the convolution of these point-like *"CLEAN" sources* convolved with a *"CLEAN" beam*, a PSF usually of Gaussian shape and with size matching the resolution of the measurements — *i.e.*, the extension of the (u,v)-plane — a technique that usually allows the removal of spurious extrapolated high spatial frequency content. The employed method is the so-called *matching pursuit algorithm* (Mallat and Zhang, 1993), which can be summarised in the following three main steps:

[15] When it is not possible to calibrate the gains, the *self-calibration* method can be applied to simultaneously guess the transfer function of the system and the brightness distribution of the observed object. The inverse problem is described by the following equation:

$$(x,g) = \arg \min_{(x,g)\in(\Upsilon,\wp)} \{f_{\text{data}}(x,g) + \mu_{\text{img}} f^{\text{img}}_{\text{prior}}(x) + \mu_{\text{gain}} f^{\text{gain}}_{\text{prior}}(g)\}, \tag{6.33}$$

where Υ and $\wp$ are the sets of, respectively, possible images and possible gains, and $\mu_{\text{img}} f^{\text{img}}_{\text{prior}}(x)$ and $\mu_{\text{gain}} f^{\text{gain}}_{\text{prior}}(g)$ are the regularisation terms respectively for the image parameters and the complex gains. This method, originally proposed by Readhead and Wilkinson, (1978) and later improved by William Danchi Cotton, (1979), uses the current estimate of the image to calibrate the gains (hence the name). It can be used with any image reconstruction algorithm.

1. **Initialisation** of the *residual map* (matching it to the dirty map) and of the CLEAN components list (making it to a list of null elements);
2. **Iterative search** for the brightest CLEAN components that better match the data through the dirty map. As the components are found, they are subtracted from the residual map and are added to the CLEAN component list;
3. **Restoration** of the CLEAN map by (a) convolving the CLEAN component list with the CLEAN beam and (b) by adding the residual map.

The iterative process is repeated for the new residual map and is halted when the residue level is below some noise threshold, or when the maximum of the absolute value of the residual map is lower than a fraction of the maximum intensity of the original dirty map, or (in case the two preceding ones fail) when the total number of CLEAN components reaches an imposed limit. At this stage, most of the point sources have been removed, and the residual map is mainly composed of extended sources that are smooth enough to not be affected by the convolution with the CLEAN beam.

After restoration, the final image amounts to both compact (convolved with the CLEAN beam) and smooth extended sources.

The most relevant weak points of `CLEAN` are the instability of the CLEAN map in the object representation space, and the amplification of side lobes when the *spatial dynamic range* of the image, *i.e.*, the ratio between the largest and the smallest source structures, is large. However, provided the (u,v)-coverage is good, the image is not too large and the number of elements in the image is not greater than the number of measured visibilities (counting the real and imaginary parts separately, Schwarz, 1978, 1979), the method produces good results for point-like and extended sources, and it is a popular image reconstruction algorithm in the radio interferometry domain.

Other algorithms

Several methods have been developed to tackle the limitations of `CLEAN`. Some of the most relevant are:

- **Multi-Resolution `CLEAN`** (`MRC`, Wakker and Schwarz, 1988), a modification of `CLEAN`, able to restore images containing structures of different scales.
- **`WIPE`** (Lannes, Anterrieu and Maréchal, 1997), which is based on the concept of effective resolution of the image, introduces a global regularisation principle under constraints of positivity in order to fit the interferometric data.
- The **`Bi-Model`** method (Giovannelli and Coulais, 2005), which reconstructs images containing objects with two superimposed components: a set of points and an extended source.

Optical domain

Since the mid-90s of the twentieth century, several image synthesis algorithms have been developed from their radio counterparts or specifically designed to cope with optical interferometric data. The most relevant of these methods are presented in the following.

The BiSpectrum Maximum Entropy Method (BSMEM)

BSMEM (Baron and J. S. Young, 2008) implements the classic MEM method (*cf.* section 6.3, page 106) to find the most probable image given the data. It reconstructs an image from any type of optical interferometric measurements stored in an OIFITS file. BSMEM assumes independent Gaussian statistics for the amplitudes and phases and, as a regularisation criterion, it uses the entropy defined by Gull and Skilling, (1984a) — eq. (6.29c).[16] The initial guess is usually a centred Dirac delta, an uniform disc or a Gaussian. The minimisation of the regularisation weight relies on the comparison with the reference image, which can be updated during the iterative process. For the numerical optimiser, it uses MEMSYS, which implements the approach devised by Skilling and Bryan, (1984) to automatically find the best value for the hyper-parameter μ, by using a gradient-descent algorithm for maximising the posterior probability of the reconstructed image given the input data (David F. Buscher, 1994; Lawson, William Danchi Cotton et al., 2004).

One of the strongest principles behind BSMEM is the fact that it does not try to convert the bi-spectra into complex visibilities, thus allowing to load and use any type of data, even if they are not complete.

The Building Block Method (BBM)

The imaging code BBM, developed by Hofmann and Weigelt, 1993, resembles CLEAN in its approach, but it is able to restore images from bi-spectra (and, hence, closure phases). It follows an iterative process that aims to minimise the likelihood term, $f_{\text{data}}^{\text{bispec}}$. The minimisation is carried out by means of an algorithm of *matching pursuit* type, which imposes the less dense and more scattered solution (J.-P. Berger, Malbet et al., 2012).

The MArkov Chain IMager (MACIM)

MACIM, proposed by Ireland, J. D. Monnier and Thureau, 2006, is a Monte-Carlo Markov (MCM) chain algorithm that seeks for the global minimum of a regularised χ^2 statistic in the image space, while simultaneously characterising this minimum. It is able to handle any type of data, and, contrary to the precedent methods, it can operate with or without any kind of regularisations, searching for the best images in the Bayesian sense. It directly manipulates the *a posteriori* probability

$$\Pr(x \mid y) \propto \mathrm{e}^{-\frac{1}{2}\left(f_{\text{data}}+\mu f_{\text{prior}}\right)}, \tag{6.35}$$

trying to maximising it, thus providing a joint probability density of images consistent with the data.

[16] The image entropy (Skilling and Bryan, 1984),

$$h(x) = -\sum_{n=1}^{N} p_n \log p_n, \qquad p_n = \frac{x_n}{\sum x}, \tag{6.34}$$

is a measure of the smoothness in the image (J.-P. Berger, Malbet et al., 2012): low values of entropy will correspond to flat images, while large entropy values are typical of images having a great deal of contrast from one pixel to the next.

The code can also combine model-fitting and imaging, or use several regularisations based on *a priori* knowledge. Currently, two regularisations are encoded in `MACIM`: MEM (*cf.* section 6.3, page 106) and the *dark zone connectivity*, which favours large dark areas around bright regions (J.-P. Berger, Malbet et al., 2012).

The Maximum Entropy Method combined with Self-calibration

When combined, these two methods embark in an iterative process, that starts by guessing the phases of the visibility conformable with the closure phase measurements, and aims at converging to the image that is the most probable given the guessed phases. During the iteration, the atmospheric and instrumental errors are fitted, and the image is continuously remapped, while it is assured that the measured closure phases are respected (ibid.).

The Multi-aperture image Reconstruction Algorithm (MiRA)

`MiRA` (Éric Thiébaut, 2008) seeks the set of parameters characterising an image solution that minimises eq. (6.23), by means of a non-linear optimisation algorithm (Éric Thiébaut, 2002). The restored image depends on the image upon which the process is started because the method does not allow a global but a local optimisation. The main advantages of `MiRA` are:

1. It directly adjusts the interferometric observables without trying to explicitly rebuild the missing phases. Therefore, it can handle any type of optical interferometric data.
2. It already has encoded many different regularisations, and it can accept any type, thus offering the possibility to choose the most efficient for the planed image reconstruction.

The Weak-phase Interferometric Sample Alternating Reconstruction Device (WISARD)

The `WISARD` algorithm (Meimon, Mugnier and Le Besnerais, 2008) is an application of the self-calibration technique to the optical interferometry, to find the missing phases from the closure phases, and to reconstruct an image from the latter and the power-spectrum. It implicitly rebuilds the complex visibilities by adjusting the synthetic Fourier phases computed by self-calibration to the power-spectrum. Several regularisation terms are implemented while the synthesised complex visibilities are added to the process of image reconstruction.

The solution coming from the self-calibration is not strictly convex. Therefore, the process encompassing the inversion of the phases present several minima, being the global minimisation problem multi-modal, and, consequently, the final solution can depend on the initial image.

Summary of image reconstruction algorithms

Table 6.1 summarises the main features of each of the aforementioned image reconstruction methods. The performance of these algorithms has been put under scrutiny in the *Interferometric Imaging Beauty Contest*, which every two years since 2004 quantitatively compares the images synthesised from simulated optical interferometric data (Baron, William Danchi Cotton et al., 2012;

W. Cotton et al., 2008; Lawson, William Danchi Cotton et al., 2004; Lawson, William D. Cotton et al., 2006; Malbet et al., 2010). BSMEM won the competition in 2004, 2006 and 2010, MiRA won in 2008 and MACIM won in 2012, notwithstanding due to the system used for quantification of the quality of the images, to the winner of the last edition clearly did not correspond the best images (*cf.* Baron, William Danchi Cotton et al., 2012). During the 2010 *Beauty Contest*, a new algorithm, named SQUEEZE (Baron, J. D. Monnier and Kloppenborg, 2010), was presented. It is still under development and it is planned to be the successor of MACIM.

MiRA was the software used to restore the images presented in this thesis (*cf.* chapter 8). Other algorithms could have been used, like BSMEM or MACIM, since they tend to produce similar images, but the versatility of MiRA both on the type of data accepted, on the regularisation that can be input and on the easiness to read OIFITS files, prevailed over the other methods.

Table 6.1: Significant image reconstruction algorithms used in optical interferometry (Adapted from ibid.).

Name	Type of data	Regularisations	Optimisation
BSMEM	Any	Gull-Skilling entropy with given prior image, MEMSYS	Non-linear conjugate gradients with unsupervised hyper-parameter control
BBM	Bi-spectra	Positivity, sparseness	Matching pursuit
MACIM	Any	Any	Global optimisation by simulated annealing
MiRA	Any	Any	Limited memory quasi-Newton with boundary condition (positivity) and normalisation constraint
WISARD	Pseudo-complex visibilities computed from power-spectra and closure phases	Positivity, ℓ_2, $\ell_2 - \ell_1$[a]	Alternative minimisation and self-calibration

[a] Bohnenblust, (1940), Charbonnier et al., (1997) and Mugnier, Fusco and Conan, (2004)

State of the art of image reconstruction

This chapter finishes with a selection of significant interferometric images published in peer reviewed papers during the past two decades, which intend to illustrate the evolution in the field and the state of the art.

Figure 6.2, highly inspired in J.-P. Berger, Malbet et al., (2012), presents a grid of restored images in the IR by chronological order.

Panel 6.2a corresponds to one of the first attempts by A. Quirrenbach et al., (1994) to restore an image out of power-spectra measured with the Mark-III optical stellar interferometer. It illustrates the elongated emission of H_α around the B[e] shell star ζ Tauri. The image was reconstructed using the MEM method. Although the phase information was absent from the data, which is apparent

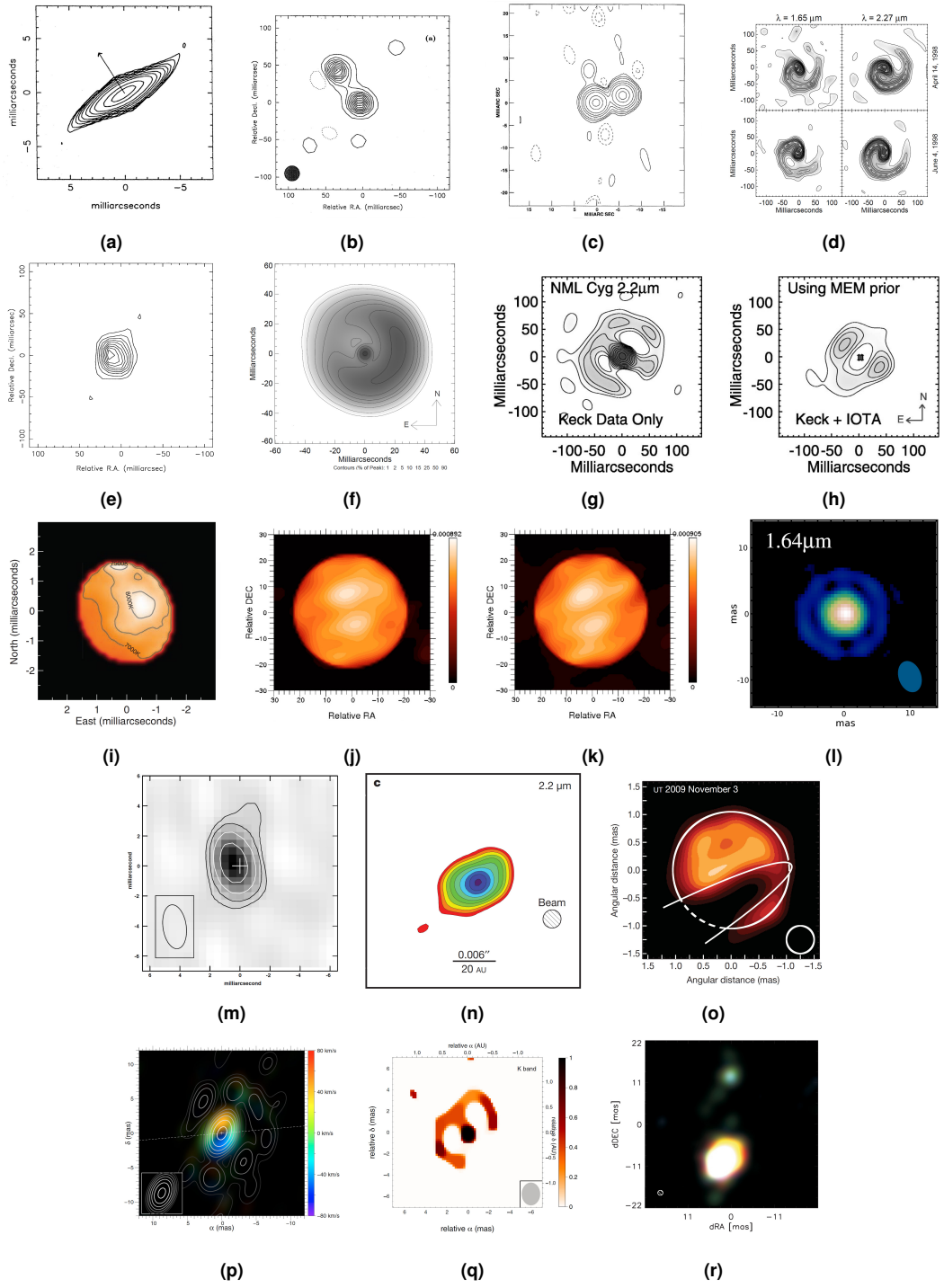

Figure 6.2: Examples of IR interferometric reconstructed images (see main text for details; adapted from J.-P. Berger, Malbet et al., 2012). Figure 6.2a A. Quirrenbach et al., (1994), fig. 6.2b J. E. Baldwin et al., (1996), fig. 6.2c Benson et al., (1997), fig. 6.2d Tuthill, J. D. Monnier and William C Danchi, (1999), fig. 6.2e J. S. Young et al., (2000), fig. 6.2f Tuthill, J. D. Monnier, W. C. Danchi et al., (2002), fig. 6.2g and fig. 6.2h J. D. Monnier, R. Millan-Gabet et al., (2004), fig. 6.2i J. D. Monnier, Zhao et al., (2007), fig. 6.2j and fig. 6.2k Haubois et al., (2009), fig. 6.2l Le Bouquin, Lacour et al., (2009), fig. 6.2m H. R. Schmitt et al., (2009), fig. 6.2n S. Kraus, Hofmann et al., (2010), fig. 6.2o Kloppenborg et al., (2010), fig. 6.2p Millour et al., (2011), fig. 6.2q Benisty et al., (2011), and fig. 6.2r S. Kraus, Calvet et al., (2012).

from the centre-symmetry of the emitting object, this image provided an important evidence for the equatorial disc model of the B[e] stars.

Panels 6.2b and 6.2c depict the first aperture synthesis maps of binary stars. The data corresponding to both images were normalised power-spectra and closure phases, but in the former they were collected in the COAST array (J. E. Baldwin et al., 1996), while in the latter they were acquired in the NPOI facility (Benson et al., 1997).[17] Image 6.2b shows the double-lined spectroscopic binary Capella (α Aurigae) at 830 nm, which was restored using self-calibration techniques within the Caltech VLBI mapping package. Figure 6.2c images the spectroscopic binary Mizar A (ζ Ursae Majoris) at 19 spectral channels (520–850 nm), and it was reconstructed using `AIPS`[18] associated to a CLEAN components self-calibration.

A reconstruction from high-resolution observations of WR 104[19] is illustrated in panel 6.2d. The data, collected at Keck using the aperture masking technique, consisted of power-spectra and bi-spectral information in the K and H bands, and acquired over 700 baselines and 7 000 closing triangles (Tuthill, J. D. Monnier and William C Danchi, 1999). The images were obtained from an algorithm based on MEM, and they are able to reveal details on the dust outflow around the WR star.

The surface of the red super-giant Betelgeuse (α Orionis) was imaged by J. S. Young et al., (2000), by means of a combination of MEM and the self-calibration methods (image 6.2e). The data consisted of IR (700 nm) interferometric measurements collected with the **W**illiam **H**erschel **T**elescope (WHT), using non-redundant aperture masking. A maximum resolution of ~ 39 mas was barely sufficient to resolve the surface of the star, which exhibits some asymmetry but no limb-darkening signatures.

Panel 6.2f shows an image reconstruction of the Herbig A[e]/B[e] star LkH$_\alpha$ 101, a pre-main-sequence or early main-sequence star surrounded by a massive circumstellar disc with a central hole or cavity caused by dust sublimation. The YSO was observed with the Keck telescope in the NIR, using non-redundant aperture masking. The data consisted of power-spectra and closure phases, enabling the image to be produced from a self-calibration method based on MEM (Tuthill, J. D. Monnier, W. C. Danchi et al., 2002).

Frames 6.2g and 6.2h correspond to the image restorations of the super-giant NML Cygni[20] circumstellar environment, where high-quality long-baseline data acquired with the IOTA and single-dish aperture masking Fourier measurements from Keck were combined to yield a well paved (u,v)-plane. Both images were produced by feeding an algorithm based on MEM with normalised power-spectra and closure phases, but in panel 6.2g the data came only from Keck, while in frame 6.2h data from Keck and IOTA was used. For the former, a uniform prior was used,

[17] Until November 2011, the observatory was known as Navy Prototype Optical Interferometer (NPOI). Subsequently, it was temporarily renamed to Navy Optical Interferometer (NOI, www.lowell.edu/news/2011/11/npoi-renamed-to-reflect-its-evolving-role-in-research), and now it is permanently known as the *Kenneth J. Johnston* Navy Precision Optical Interferometer (NPOI, www.public.navy.mil/fltfor/cnmoc/Pages/Johnston.aspx).

[18] **A**stronomical **I**mage **P**rocessing **S**ystem (Wells, 1985).

[19] A Wolf-Rayet (WR) star is an evolved luminous massive (over 20 solar masses initially) blue star which is rapidly loosing mass by means of a very strong stellar wind and which is thought to be in a stage immediately preceding the supernova phase (Tuthill, J. D. Monnier and William C Danchi, 1999).

[20] The acronym NML comes from the names of the three astronomers who, in 1965, discovered the star: Neugebauer, Martz and Leighton (Neugebauer, Martz and R. B. Leighton, 1965).

while for the latter, a MEM prior with 59 % of the flux in a 7 mas pixel was used instead (J. D. Monnier, R. Millan-Gabet et al., 2004).

Image 6.2i is an IR reconstruction of the rapidly rotating hot star Altair (α Aquilae) in the H-band, created with `MACIM`, using an uniform brightness elliptical prior and applying the MEM method (J. D. Monnier, Zhao et al., 2007). The data consisted of normalised power-spectra and closure phases from CHARA. The elliptical stellar photosphere is an indication of the strong effect of gravity darkening.

The surface of Betelgeuse was also imaged by Haubois et al., (2009) in the H-band, using power-spectra and closure phases acquired with IOTA. The image restorations, carried out using `MiRA` and `WISARD`, are illustrated in panels 6.2j and 6.2k, respectively. Both reconstructions led to similar results, exhibiting the same asymmetries (spatial variations of the photosphere, including its diameter, star spots, the limb darkening, and the surrounding brightness), confirming the conclusions taken by J. S. Young et al., (2000). In both algorithms, the same prior (a symmetric limb darkened disc), FOV, sampling, *a priori* image and quadratic regularisation were used.[21]

A model independent image reconstruction of the Mira star[22] T Leporis was carried out by Le Bouquin, Lacour et al., (2009) and is illustrated in panel 6.2l. The data (power-spectra and closure phases) were collected at the VLTI. The reconstruction was performed with `MiRA` in two steps, where a strong smoothness regularisation to restore the first step images was followed by a quadratic regularisation where the previous brightness distributions were used as a support.

Panel 6.2m represents the image reconstruction of the H_α emission around the interacting binary star β Lyrae using the *differential phase technique*.[23] The data, acquired at NPOI, consisted of visibility amplitudes and differential phases, and the image was produced using the `AIPS` package (H. R. Schmitt et al., 2009).

Image 6.2n depicts the NIR emission of a circumstellar disc around a massive YSO. The brightness distribution was restored using `BBM` from normalised power-spectra and closure phases acquired at the VLTI (S. Kraus, Hofmann et al., 2010).

Panel 6.2o shows the reconstructed image of the eclipsing binary star system ε Aurigae (Kloppenborg et al., 2010). The resulting figure confirmed the existence of a opaque disc moving in front of the F class star, tilted to the line of sight. The data, power-spectra and closure phases, were collected at CHARA, and the image was produced with `MACIM`.

[21] A quadratic regularisation has the effect of quadratically discriminate strong intensity gradients between the *a priori* image and the reconstructed one (Haubois et al., 2009).

[22] Mira stars are pulsating variable red giant stars, lying on the AGB, named after the star Mira (o Ceti), in the constellation of Cetus. They are evolving toward the planetary nebula and white dwarf phases, being characterised by low mass values ($1\,M_\odot$), an important mass-loss rate ($10\times10^{-7}-10\times10^{-6}\,M_\odot/\mathrm{yr}$), red colours, periods longer than 100 days, and varying amplitudes $\Delta V\approx 9$ (Le Bouquin, Lacour et al., 2009; Stahler and Palla, 2004).

[23] The differential phase technique, also known as *spectral phase referencing* or *self phased reference*, is a powerful self-calibration tool to measure small phase variations as a function of the wavelength, where line emission interferometric phases are compared to purely continuum emission. The procedure allows the removal of many systematic effects (instrumental and atmospheric) from the observed phases (R. L. Akeson, Swain and M. M. Colavita, 2000; Henrique R. Schmitt et al., 2006). Consequently, the image of the line-emitting source can be produced. In order to work, a sufficient spectral resolution is required (J.-P. Berger, Malbet et al., 2012).

The brightness distribution of the dust and gas surrounding the A[e] super-giant star HD 62623 is illustrated in panel 6.2p (Millour et al., 2011). The image was produced with `MiRA`, using power-spectra and closure phases from the VLTI, to which a self-calibration based on the differential phases technique was applied to retrieve absolute phases in the Br_γ line of the star. Due to the high spectral and spatial resolution of the measurements, the dust and gas emissions were disentangled, and the kinematics of the circumstellar disc was revealed.

Panel 6.2q illustrates the reconstruction of the circumstellar disc surrounding the Herbig A[e] star HR 5999 (Benisty et al., 2011). The image was reconstructed from normalised power-spectra and closure phases measured in the NIR at the VLTI, using the `MiRA` algorithm. The ring and the inner rim caused by dust sublimation are well resolved, while the central spot, corresponding to the star, is marginally resolved.

Image 6.2r illustrates the colour composite of high-resolution reconstructions in the NIR of the B[e] star V921 Scorpii (S. Kraus, Calvet et al., 2012). The multi-wavelength power-spectra and closure phases were collected at the VLTI, and the data set was subdivided in three wavelength bins. The corresponding model independent images were produced with the BBM algorithm, using MEM as regularisation and a smooth reconstruction (obtained without regularisation) as prior. It is possible to clearly identify the circumstellar material around V921 A and its unresolved companion, V921 B.

Images 6.2i, 6.2l and 6.2o are good representatives of the importance of image reconstruction in retrieving some features in an insufficient (u,v)-coverage, that can easily escape to traditional model-fitting techniques (J.-P. Berger, Malbet et al., 2012).

Figures 6.2f, 6.2n, 6.2q and 6.2r illustrate the best reconstructed maps of IR emissions of protoplanetary discs achieved so far. However, due to the sparse (u,v)-coverage characteristic of the VLTI, the images in the three last aforementioned panels exhibit a limited number of features.

Images 6.2d, 6.2g and 6.2h, on the contrary, exhibit the most complex morphologies of the selection displayed in fig. 6.2. This is due to the very well paved (u,v)-plane achieved with the 21 aperture mask of Keck. The drawback is the lower spatial resolution typical of aperture masking. These images emphasise the importance of complementing long-baseline interferometric measurements of extended sources with single-dish aperture masking data, in order to create a sufficient and well distributed (u,v)-coverage, at least at shorter spatial frequencies.

A final caveat: images 6.2j and 6.2k are limited in terms of dynamic range and resolution (the stellar spots are not well characterised), both due to the instrument's accuracy and its difficulty to detect fringes of low visibility (ibid.). Therefore, care should be taken when designing future interferometric instruments, to acquaint for reliable fringe trackers able to operate in scenarios of very low visibility amplitudes.

Chapter 7

Simulation toolbox

And now for something completely different...

— MONTY PYTHON

Contents

THIS CHAPTER pertains to the tools and set-up used to the simulations which led to the results presented in chapter 8. Section 7.1 describes the three objects used as image reference for image reconstructions: a group of stars, a stellar surface and a Young Stellar Object (YSO). In section 7.2, equations governing the transformations between the equatorial, horizontal and the astrometric coordinate systems are presented, and the (u, v) coordinates corresponding to the projected spacing are inferred. The synthetic of the observables are described in section 7.3. Section 7.4 presents the expressions need to compute the number of photo-electrons striking the top of the atmosphere, arriving at an interferometric array of telescopes and being recorded by a detector. Section 7.5 is the core of the current chapter, where the noise models used in the simulations, as well as others that have been published, are described. The main expressions for each model are presented, and their conditions of validity are explored. Section 7.6 describes how the different observations are simulated and how the data is created, taking into account the characteristics of the object, the *uv*-coverage, the noise model and the parameters used in `MiRA` for the image restoration procedure. Section 7.7 delineates the tools implemented to assess the quality of the restored images.

Object library

Three astrophysical objects (a cluster of stars, a YSO and a stellar surface), differing in morphology and structure scales, were synthesised (fig. 7.1).

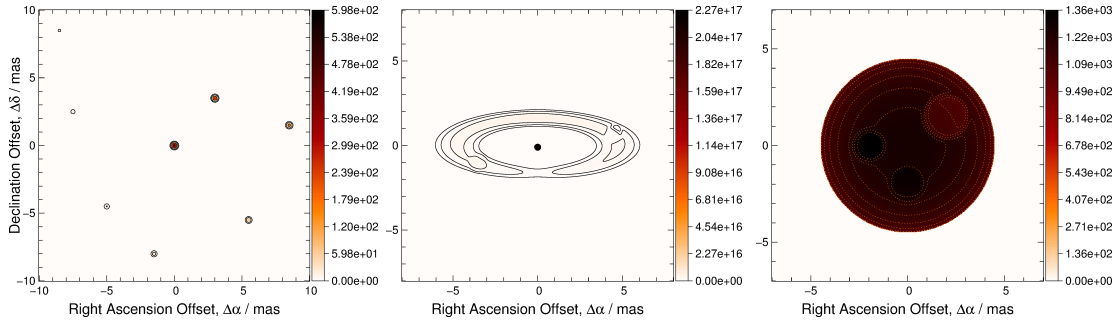

(a) Model image of a stellar cluster. Four intensity contours spaced at equal ratios from 3 to 598 are represented.

(b) Model image of a YSO. The image indicates 8 intensity contours spaced at equal ratios from 3×10^{14} to 2.27×10^{17}.

(c) Model image of a stellar photosphere. The image represents 13 intensity contours equally spaced from 900 to 1 360.

Figure 7.1: Model images used for the interferometric image reconstruction analysis of chapter 8. All images are normalised by the pixel area (the colour bars indicate surface intensities). In (*a*) the radii of the eight stars, which have Gaussian profile, is equal to 0.1 marcsec, and the amplitudes are spanning from 1 to 1/128 in powers of 2; in (*b*) there are two structures in the disc: one on its lower left, with positive amplitude, and one on its upper right, with negative amplitude, being the zero magnitude defined by the average of the disc's intensity in the surroundings; in (*c*) the upper right feature resembles a dark spot, while the remainder are hot spots. See figs. 7.2 and 7.4 for the intensity profiles respectively of the YSO and of the star.

Care was taken regarding the sizes of the objects and features they present, so that, on the one hand, they would be resolved by the interferometer, and, on the other hand, there would be enough

visibility amplitude values well above zero.[1]

The eight stars of fig. 7.1a were displaced in a spiral, with varying distances and orientations between them, in order to prevent hypothetical periodic features in the image restoration process due to the use of Fourier transforms. The magnitude difference between the brightest (the central star) and the faintest (top left) is approximately 5.3. The cluster spans a relative width of about 20 mas both in right ascension and declination.

The YSO depicted in fig. 7.1b is constituted by a central star and a disc, which discloses two structures: one characterized by a larger intensity profile than the surroundings, located at the lower left part of the disc, and another with a negative intensity profile, located at the upper right part. The intensity profiles are illustrated in fig. 7.2. A small local peak, with size beyond the limiting resolution of the interferometer, was added to the centre of the rightmost structure, for testing purposes.

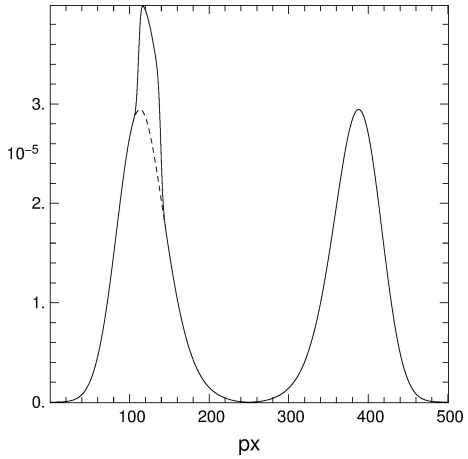

(a) Structure located at the lower left part of the disc.

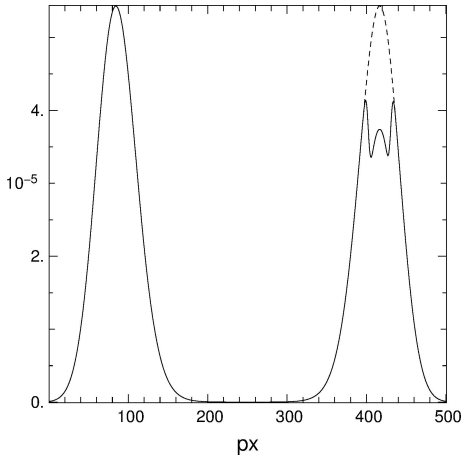

(b) Structure located at the upper right part of the disc.

Figure 7.2: Intensity profiles for the model YSO represented in fig. 7.1b. The structure located in the lower left part of the torus has an intensity about 25 % above the magnitude of the surroundings, and the one located on the upper right part of the disc presents an intensity about 30 % below that of the surroundings. The dashed curve represent the intensity of the disc in the absence of structures.

Figure 7.1c illustrates a simplified photosphere of a star. The surface intensity follows the limb darkening model

$$I(r) = I(0)\left[1 - l\left(1 - \sqrt{\frac{R^2 - r^2}{R^2}}\right)\right], \tag{7.1}$$

which was adapted from (Tatum, 2000) and (Cox, 2000).[2] R is the radius of the stellar disc, r the radial distance from the centre of the disc, l is the *limb darkening coefficient*, and $I(0)$ is the *specific intensity* at the centre of the disc. (fig. 7.3).

The photosphere presents several structures, simulating colder stellar spots close to the equator, and a dominant bright feature close to the northern pole of the star, which can be identified by

[1] In the configuration adopted for the study of chapter 8, the longest baseline is 144 m, implying a maximum resolution of about 1.6 mas in the K-band.

[2] Equation (7.1) is usually written in the form $I(r) = I(0)\,[1 - l\,(1 - \mu)]$, where $\mu = \cos\theta = \sqrt{\frac{R^2 - r^2}{R^2}}$.

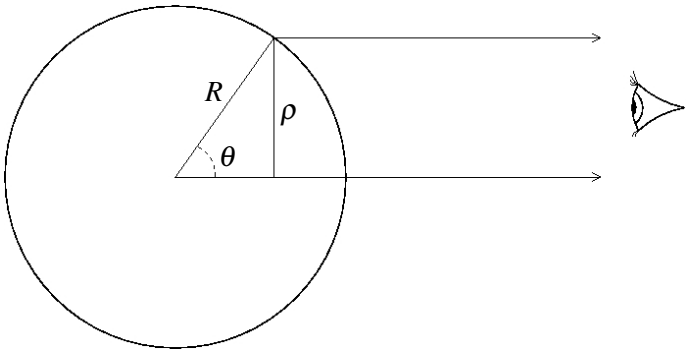

Figure 7.3: Representation of the quantities used in the limb darkening model of eq. (7.1).

a flare or by a brightness increasing due to the gravity darkening effect of a rapid rotator (J. D. Monnier, Zhao et al., 2007). The intensity profiles of the structures can be seen in fig. 7.4. While the prominent features have typical intensities of about 5 %–8 % above that of the photosphere's maximum, the dark spots present an intensity nearly 10 % below the star's brightness peak.

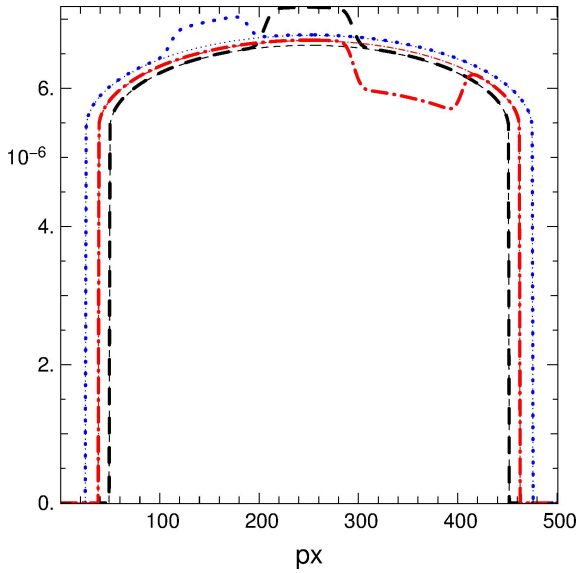

Figure 7.4: Intensity profiles for the model photosphere represented in fig. 7.1c. *Blue dotted line* and *Black dashed line* depict bright spots with intensities respectively about to 5 % and 8 % above that of the photosphere's maximum; *Red dashed-dotted line* indicate a dark spot with intensity about 10 % below that of the maximum. The corresponding thinner lines represent the intensities of the star surface in the absence of structures.

(u,v)-space generation

The sampled spatial frequencies (u,v) correspond to the conjugated of the (x,y) coordinates in the image plane, marking the loci where the visibilities are measured, in the so-called *uv-plane*. They are computed from the coordinates of the object in the sky, the separation between the apertures of the array and from the wavelength of the radiation used for the observation (*e.g.*, Fomalont and Wright, 1974, and Ségransan, 2007).

Recalling the definition of chapter 2, page 29, a vector $\vec{B}$ joining any two interferometer's apertures is known as a *baseline vector* (fig. 7.5). While spanning the *uv*-plane, an interferometer with two or more telescopes covers the spatial frequencies corresponding to the set of baselines

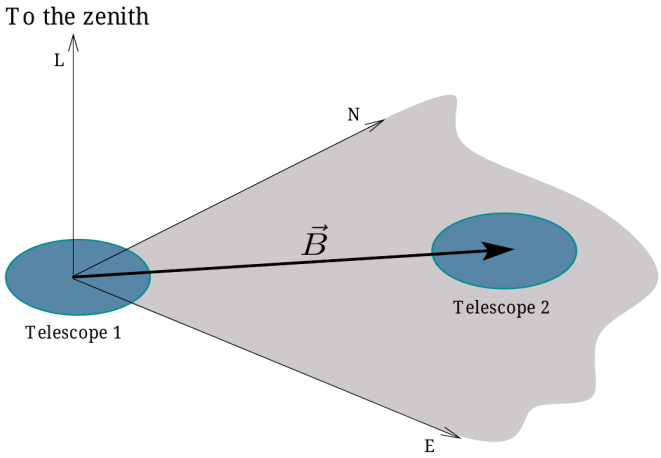

Figure 7.5: A representation of the baseline vector joining two telescopes of an interferometric array. The depicted axis correspond to the altitude-azimuthal system.

used for the observation. In a non-redundant array, the position of the telescopes is chosen so that each baseline is not repeated. The light coming from the apertures is combined in order to obtain Michelson interferograms, from which images can be restored by means of algorithms using visibility amplitude and phase information (Solf, 1993).

Using a formalism similar to the one presented by Fomalont and Wright, (1974) and A. R. Thompson, Moran and Swenson Jr., (2001), in what follows the baseline coordinates in the equatorial, horizontal and astrometric frames are calculated, and the equations for the spatial frequencies (u,v) in the Fourier plane are presented.

Figure 7.6 sketches out the coordinate systems more commonly used in interferometry. The *equatorial frame*, a right-handed Cartesian coordinate system, is based in a plane parallel to the Earth's equator, whose origin coincides with the centre of the Earth. The X axis is found by the interception between the equatorial and the meridian planes, Y points to the East and Z to the North celestial pole. The corresponding versors (unit vectors) are denoted by respectively $\widehat{x}$, $\widehat{y}$ and $\widehat{z}$.

In an *altazimuth (horizontal)* description of the observatory, the plane of reference is parallel to the horizon and passes through the observing point. The frame is defined by the axis E, N and L, pointing respectively to the east, to the north and to the zenith. It follows that the Y and E axis are always parallel.

The *astrometric system* is centred on the projection of the source on the sky and has axis U,V and W. U points to the east, V to the north and W to the source. The corresponding versors are respectively $\widehat{u}$, $\widehat{v}$ and $\widehat{w}$.

Equatorial and horizontal frames

The coordinates of the equatorial system can be expressed in terms of the horizontal ones, the *hour angle*, H, and the *declination*, δ. Figure 7.7 represents these two frames with the observer looking to the rotation from the Y direction. X is measured towards $H = 0$ and $\delta = 0$, Y towards $H = -6^h$ and $\delta = 0$ and Z towards $\delta = 90°$. For an observatory located at a mean latitude φ, the equatorial and horizontal systems are related by a rotation along the E axis (or, equivalently, along the Y axis), if the Earth's curvature is neglected (*i.e.*, if the apertures in the array are close enough,

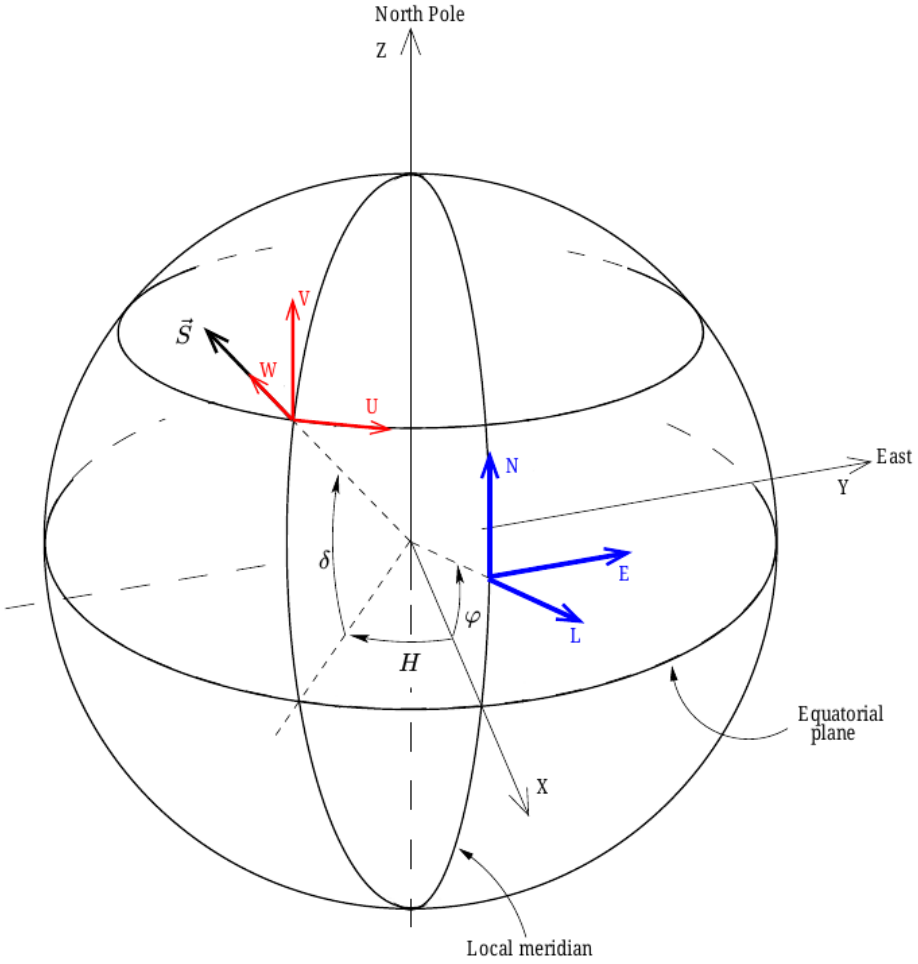

Figure 7.6: The equatorial, horizontal and astrometric coordinates systems used in interferometry. The axis YXZ form the equatorial system; ENL form the horizontal or altazimuthal frame; UVW belong to the astrometric coordinates system. $\vec{S}$ is pointing to the source (adapted from Fomalont and Wright, 1974).

all being at the same mean latitude). Rotating the ENL system counter-clock wise by an angle $-\varphi$, L will be parallel to X, E to Y and N to Z. This rotation can be expressed in matrix form by means of an arbitrary vector $\vec{V}$ with coordinates (V_X, V_Y, V_Z) and (V_E, V_N, V_L), respectively in the equatorial and horizontal systems (e.g., Arfken and Weber, 1995; Fomalont and Wright, 1974):

$$\begin{pmatrix} V_X \\ V_Y \\ V_Z \end{pmatrix} = \begin{pmatrix} \cos\varphi & 0 & -\sin\varphi \\ 0 & 1 & 0 \\ \sin\varphi & 0 & \cos\varphi \end{pmatrix} \begin{pmatrix} V_L \\ V_E \\ V_N \end{pmatrix}. \tag{7.2}$$

It is common to write a vector in the horizontal frame with components following the order north, east and zenith. Having this convention in mind, the previous equation can be rewritten as

$$\begin{pmatrix} V_X \\ V_Y \\ V_Z \end{pmatrix} = \begin{pmatrix} -\sin\varphi & 0 & \cos\varphi \\ 0 & 1 & 0 \\ \cos\varphi & 0 & \sin\varphi \end{pmatrix} \begin{pmatrix} V_N \\ V_E \\ V_L \end{pmatrix}, \tag{7.3}$$

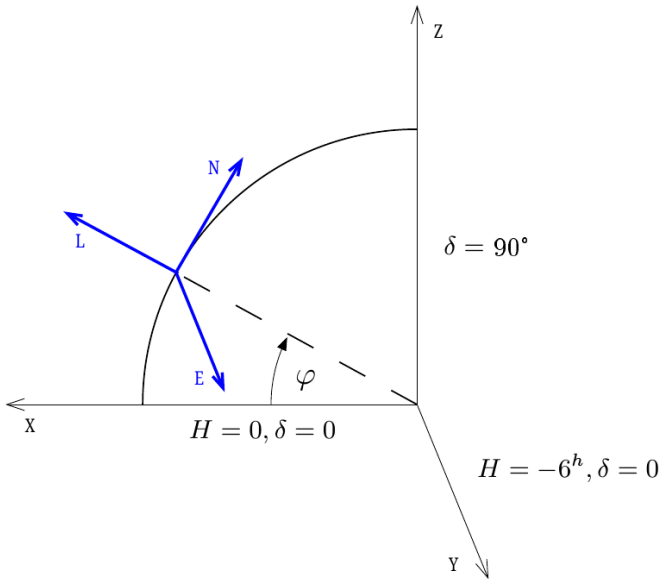

Figure 7.7: The equatorial and the horizontal frames viewed from the Y axis. The latitude of the observatory is marked by the angle φ.

where columns 1 and 3 in the rotation matrix were switched in order to keep valid the system of equations.

Astrometric and equatorial frames

A tracking interferometer is described by the astrometric system UVW (fig. 7.6). The versors $\hat{u}$, $\hat{v}$, $\hat{w}$ can be written as functions of $\hat{x}$, $\hat{y}$, $\hat{z}$, since the astrometric frame is similar to the equatorial system if the former is rotated around the U axis through an angle δ, followed by a rotation around the V axis through an angle H. Both rotations are counter-clockwise oriented, imagining the observer standing above the corresponding axis.

Using the example vector $\vec{V}$ introduced in the previous subsection, the coordinates (V_U, V_V, V_W) can be rearranged in order to match their equatorial counter-parts after the two aforementioned rotations:

$$\begin{pmatrix} V_X \\ V_Y \\ V_Z \end{pmatrix} = \begin{pmatrix} \cos H & -\sin H & 0 \\ \sin H & \cos H & 0 \\ 0 & 0 & 1 \end{pmatrix} \begin{pmatrix} \cos\delta & 0 & -\sin\delta \\ 0 & 1 & 0 \\ \sin\delta & 0 & \cos\delta \end{pmatrix} \begin{pmatrix} V_W \\ V_U \\ V_V \end{pmatrix}. \tag{7.4}$$

After simplification and inversion of the system of equations, eq. (7.4) yields

$$\begin{pmatrix} V_U \\ V_V \\ V_W \end{pmatrix} = \begin{pmatrix} -\sin H & \cos H & 0 \\ -\sin\delta\cos H & -\sin\delta\sin H & \cos\delta \\ \cos\delta\cos H & \cos\delta\sin H & \sin\delta \end{pmatrix} \begin{pmatrix} V_X \\ V_Y \\ V_Z \end{pmatrix} \tag{7.5}$$

Baseline vector and spatial frequencies

Considering the (u,v) coverage, the relevant quantity is the projected baseline $\vec{B}_p$ in the plane of the sky, as seen by the source, not $\vec{B}$ itself (Ségransan, 2007). $\vec{B}_p$ depends on the coordinates δ

and h of the object being observed and is related to the spatial frequencies by the following relation:

$$(u,v,w) = \frac{\vec{B}_p}{\lambda} = \frac{1}{\lambda}\left(B_u^p, B_v^p, B_w^p\right), \tag{7.6}$$

where λ is the wavelength of the radiation. The vector $\vec{b} = u\,\hat{u} + v\,\hat{v}$ is known as the *projected spacing* and $B_w = \vec{B}\cdot\hat{s}$ is the *optical delay*, where $\hat{s}$ is a versor pointing to the source. The combination of eqs. (7.3), (7.5) and (7.6) leads to

$$\begin{pmatrix} u \\ v \\ w \end{pmatrix} = \frac{1}{\lambda}\begin{pmatrix} \sin\varphi\sin H & \cos H & -\cos\varphi\sin H \\ \sin\varphi\sin\delta\cos H + \cos\varphi\cos\delta & -\sin\delta\sin H & -\cos\varphi\sin\delta\cos H + \sin\varphi\cos\delta \\ -\sin\varphi\cos\delta\cos H + \cos\varphi\sin\delta & \cos\delta\sin H & \cos\varphi\cos\delta\cos H + \sin\varphi\sin\delta \end{pmatrix}\begin{pmatrix} B_N \\ B_E \\ B_L \end{pmatrix}. \tag{7.7}$$

The so-called *uv-tracks* correspond to the paths of the projected baselines of a tracking interferometer in the spatial frequency plane, due to the rotation of the Earth — this is called *super-synthesis* (*e.g.*, Lawson, 2000; Éric Thiébaut, 2013). Over a 24 hour period, the path for a given baseline is given by an ellipse, whose equation can be obtained by eliminating the hour angle from eq. (7.7):

$$\frac{u^2}{a^2} + \frac{(v-v_0)^2}{b^2} = 1, \tag{7.8}$$

where $a = \sqrt{(B_x^2 + B_y^2)/\lambda^2}$, $b = a\sin\delta$ and $v_0 = (B_z/\lambda)\cos\delta$ (e.g., A. R. Thompson, Moran and Swenson Jr., 2001; Fomalont and Wright, 1974).

Figure 7.8 illustrates the *uv*-plane tracks for a two-telescope interferometer ($B_N = 50.837$ m and $B_E = 24.812$ m) located at ESO Paranal observatory ($\varphi = -24.62°$), observing in the K-band ($\lambda = 2.2\,\mu$m). Tracks for three different declinations of the source ($\delta = -10°, -30°, -60°$) were plotted, assuming the latter was observed 20 times during 9 hours equally split on either side of the meridian.

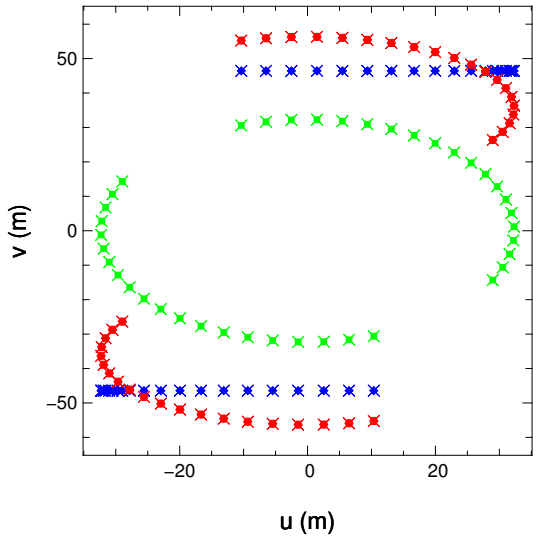

Figure 7.8: *uv*-tracks for an instrument operating with UT1 and UT2 of the VLTI (ESO), for sources at declinations equal to 0° (blue diamonds), –40° (red circles) and –90° (green squares). It is assumed that the interferometer tracks the sources over the range of hour angles $-4.5 \leq h \leq +4.5$.

Visibility quantities generation

Five interferometric quantities are synthetically generated in order to simulate the outcome of an interferometric observation, to wit, the *visibility amplitude*, V, the *visibility phase*, ϕ, the *normalised power-spectrum*, V^2, the *bi-spectrum*, B, and the *closure phase*, ϕ_c. `MiRA` package is used to generate the complex visibilities, from which all the other observables are computed. The procedure is described in detail in Renard, Éric Thiébaut and Malbet, (2011), Éric Thiébaut, (2008) and Éric Thiébaut and Giovannelli, (2010), but it is going to be outlined in the remainder of this subsection.

If

$$f_m \doteq \frac{B^{\perp}_{\mathrm{T}_{1,m},\mathrm{T}_{2,m}}(t_m)}{\lambda} \tag{7.9}$$

is the m^{th} spatial frequency, where $\mathrm{T}_{1,m}$ and $\mathrm{T}_{2,m}$ are telescopes 1 and 2 interfering in time t_m, and $B^{\perp}$ is the baseline projected on the sky, and if I is the object brightness distribution, than the m^{th} measure of the model complex visibility is given by

$$V_m = \mathscr{F}\{I(f_m)\} = \widehat{I}(f_m) = \sum_n A_{m,n} \cdot i^{\mathrm{p}}_n = (A \cdot i^p)_m, \tag{7.10}$$

where the complex coefficients $A_{m,n}$ are given by

$$A_{m,n} = \mathscr{F}\{s^{\mathrm{p}}_n(f_m)\} = \widehat{s^{\mathrm{p}}_n}(f_m) = \widehat{s^{\mathrm{p}}}(f_m)\mathrm{e}^{-2\pi \mathrm{i} x_n \cdot f_m}. \tag{7.11}$$

In eqs. (7.10) and (7.11), n represents the n^{th} pixel used to sample the image, i^{p}_n is the value of the n^{th} pixel, s^{p} is the *pixel shape*, and x_n is the position of the n^{th} pixel. The function s^{p} is also known as the *pixel response function*. It sets the effective resolution of the image, giving the usual "pixelated" image representation when the pixel size is fixed for the full set of image parameters (ibid.). The matrix multiplication in (7.10) corresponds to a linear operator between the model image and the "measured" complex visibilities, containing the Fourier transform, the pixel shape and the spatial frequencies of the sampled uv-plane. The remainder of the observables are computed from eq. (7.10), according to the definitions presented in chapters 2 and 6.

Computation of photoelectrons

Light, when interacting with matter, behaves as it is composed of particles, named *photons*, which carry energy and momentum. This interaction is essentially stochastic in nature (J. W. Goodman, 2000). Neglecting the fact that photons tend to group themselves in packets, it may be assumed that they are uncorrelated discrete entities. In this section photons are described as classical particles and the number of photons N_{phot} detected in an integration time t may be described by a Poisson distribution.

The ratio of the signal S to the noise N, that is, the *Signal to Noise Ratio* (SNR) is related to the number of photons arriving at the array of telescopes and subsequently being recorded by the detector. It is thus important to estimate this number in order to theoretically study the reconstruction of interferometric synthetic images.

If, in an observation, the source of noise[3] is dominated by the statistics of the number of arriving uncorrelated photons that are recorded, then the associated error is given by the standard deviation of the sample, *i.e.*, the square root of the number of photons in the mean sample. Hence, if $\dot{N}_{\text{phot}}$ is the mean number of photons detected per unit time, the standard deviation of N_{phot} is

$$\sigma(N_{\text{phot}}) = \sqrt{\langle \Delta N_{\text{phot}}^2 \rangle} = \sqrt{\dot{N}_{\text{phot}} \cdot t}. \tag{7.12}$$

For a Poisson process,

$$SNR = \frac{\dot{N}_{\text{phot}} \cdot t}{\sqrt{\dot{N}_{\text{phot}} \cdot t}} = \sqrt{\dot{N}_{\text{phot}} \cdot t} = \sigma(N_{\text{phot}}). \tag{7.13}$$

Radiometric quantities and astrophysical equivalents

This section introduces radiometric quantities and astrophysical equivalents important to compute the number of photons.

The *radiant flux*, F, measured in watts, is defined as the energy flow per unit time. When used to analyse the spectral content of the radiation, the radiant flux becomes the *spectral radiant flux*, F_ν (or F_λ), defined as the radiant flux emitted per unit frequency (or wavelength). In Astrophysics, these two quantities are known as *luminosity* (L) and *monochromatic* (or *spectral*) *luminosity* (L_ν or L_λ), respectively.

The *irradiance*, E, is the radiant flux per unit area. It has units W/m^2. The corresponding spectral quantity is the *spectral irradiance*, E_ν or E_λ, measured in W/(m^2 Hz) or W/(m^2 m), respectively. The astrophysical equivalents are the (*radiant*) *flux* (*density*) or "brightness", and the *monochromatic* (or *spectral*) *flux density* (Carroll and Ostlie, 2007). The latter is commonly denoted by F_ν or e_ν[4] (Léna et al., 2012; Sterken and Manfroid, 1992).

Flux of photons

The spectral flux density of a star is usually given in jansky. It is equivalent to 10^{26} W/(m^2 Hz):

$$1\,\text{Jy} = 10^{-26}\,\frac{\text{W}}{\text{m}^2\,\text{Hz}}\ (\text{SI}) = 10^{-23}\,\frac{\text{erg}}{\text{s}\,\text{cm}^2\,\text{Hz}}\ (\text{CGS})\ . \tag{7.14}$$

The radiant flux is related to the spectral flux density by

$$F = e_\nu \cdot \Delta S \cdot \Delta\nu = e^{(\text{J})} \cdot \Delta S \cdot \Delta\nu \times 1\,\text{Jy}\ , \tag{7.15}$$

[3] In the current study, *noise* is considered as the general degradation of the information carried by the radiation.

[4] The subscript ν is replaced by λ in the corresponding wavelength quantities.

where ΔS is the surface area in which the radiation is incident, $\Delta\nu$ is the frequency interval of the radiation and $e^{(\mathrm{J})}$ is the flux density in jansky.

However, $F = N_{\mathrm{phot}} h\nu/\Delta t$. So, the photon rate is

$$\dot{N}_{\mathrm{phot}} = \frac{N_{\mathrm{phot}}}{\Delta t} = \frac{F}{h\nu}. \tag{7.16}$$

It is very common to find in tables the jansky unit written as a function of the number of photons, as follows:

$$\frac{1\,\mathrm{Jy}}{h} = 1.51 \times 10^7 \frac{\mathrm{phot}}{\mathrm{s\,m^2}\left(\frac{\Delta\nu}{\nu}\right)}. \tag{7.17}$$

The combination of this result with eqs. (7.15) and (7.16) yields

$$\dot{N}_{\mathrm{phot}} = 1.51 \times 10^7 \cdot e^{(\mathrm{J})} \cdot \Delta S \left(\frac{\Delta\nu}{\nu}\right) \,(\mathrm{phot/s}) \tag{7.18a}$$

$$= 1.51 \times 10^7 \cdot e^{(\mathrm{J})} \cdot \Delta S \left(\frac{\Delta\lambda}{\lambda}\right) \,(\mathrm{phot/s})\,. \tag{7.18b}$$

Photon flux at the top of the atmosphere

Using photometric standards information (table 7.1), the number of photons incident on the top of the atmosphere can be estimated. The *monochromatic flux* of a source measured outside of the Earth's atmosphere is defined as

$$e_\lambda = e_0 \times 10^{-0.4 m_\lambda}, \tag{7.19}$$

where e_0 is the monochromatic flux at $m_\lambda = 0$ and m_λ the apparent magnitude of the source at the wavelength λ (Léna et al., 2012).[5]

From eq. (7.18b) and table 7.1, the number of photons per second per square centimetre per angstrom, in the V band ($\lambda = 0.55\,\mu\mathrm{m}$), delivered by Vega ($m_{\mathrm{V}} = 0.03$) to the top of the Earth's atmosphere is approximately equal to

$$\left(\frac{N_{\mathrm{phot}}}{\Delta t\,\Delta S\,\Delta\lambda}\right)_{m_{\mathrm{V}}=0.03} \approx 1\,000\ \frac{\mathrm{photons}}{\mathrm{s\,cm^2\,\mathring{A}}}. \tag{7.20}$$

This is a standard value, frequently used as a starting point for estimations. For a $m_{\mathrm{K}} = 0.0$ star, a similar calculation yields

$$\left(\frac{N_{\mathrm{phot}}}{\Delta t\,\Delta S\,\Delta\lambda}\right)_{m_{\mathrm{K}}=0.0} \approx 46\ \frac{\mathrm{photons}}{\mathrm{s\,cm^2\,\mathring{A}}}. \tag{7.21}$$

[5] In table 7.1, e_0 is presented both in Jy and in $\mathrm{W\,m^{-2}\,\mu m^{-1}}$. They are related by:

$$e = 10^{-32} \cdot \frac{c}{\lambda^2} \cdot e_0 \left(\frac{\mathrm{W}}{\mathrm{m^2\,\mu m}}\right). \tag{A}$$

Table 7.1: Table of standard photometry. eq. (A) (footnote 5) was used to convert the values between columns 4 and 5. Highlighted are the most used bands in IR interferometry. In the framework of this thesis, only K-band was used.

Band	λ_0 (µm)	$\frac{\Delta\lambda}{\lambda_0}$	$\mathbf{e_0}$ (Jy)	$\mathbf{e_0}$ (W m^{-2} µm^{-1})	**Name**	**Reference**
U	0.36	0.15	1810	4.19×10^{-8}	UV	Bessell, (1979)
B	0.44	0.22	4260	6.60×10^{-8}	Blue	Bessell, (ibid.)
V	0.55	0.16	3640	3.61×10^{-8}	Visible	Bessell, (ibid.)
R	0.64	0.23	3080	2.25×10^{-8}	Red	Bessell, (ibid.)
I	0.79	0.19	2550	1.22×10^{-8}	IR	Bessell, (ibid.)
J	1.26	0.16	1600	3.02×10^{-9}	IR	Campins, Rieke and Lebofsky, (1985)
H	1.60	0.23	1080	1.26×10^{-9}	IR	Campins, Rieke and Lebofsky, (ibid.)
K_s	2.16	0.32	667	4.30×10^{-10}	IR	Tokunaga, 2000
K	2.18	0.41	665	4.14×10^{-10}	IR	Tokunaga, (ibid.)
L	3.40	0.16	312	8.09×10^{-11}	IR	Léna et al., (2012)
M	5.0	0.06	183	2.19×10^{-11}	IR	Léna et al., (ibid.)
N	10.2	0.49	43	1.24×10^{-12}	IR	Léna et al., (ibid.)
Q	21.0	0.38	10	6.80×10^{-14}	IR	Léna et al., (ibid.)
g	0.52	0.14	3730	4.14×10^{-8}	Visible	Schneider, Gunn and Hoessel, (1983)
r	0.67	0.14	4490	3.00×10^{-8}	Red	Schneider, Gunn and Hoessel, (ibid.)
i	0.79	0.16	4760	2.29×10^{-8}	IR	Schneider, Gunn and Hoessel, (ibid.)
z	0.91	0.13	4810	1.74×10^{-8}	IR	Schneider, Gunn and Hoessel, (ibid.)

Photon flux recorded by a detector

The total number of photons N_{phot} recorded by a detector can be determined combining eqs. (7.16) and (7.19):

$$N_{\text{phot}} = \frac{\mathscr{E} \cdot e_\lambda \cdot \mathscr{A} \cdot t \cdot \Delta\lambda}{E_0}, \tag{7.22}$$

where $\mathscr{E}$ is the *total efficiency* or *throughput*, $\mathscr{A}$ is the *effective area* of the telescope, t is the total integration time and E_0 is the energy of a photon.

The total throughput is calculated multiplying the efficiencies of the several elements contributing to the absorption of light, i.e, taking into account the atmosphere, the telescope(s), the instrument and all the reflections/absorptions along the path through the light ducts and laboratory between the telescope(s) and the detector — *cf.* tables 7.2 to 7.4, which give the optical transmissions, respectively, for the atmosphere at Paranal, the VLTI and for four instruments with imaging capabilities already or soon to be installed at the VLTI.

The effective area sets the collecting area of a telescope, defined mainly by the sizes of the two first mirrors. For an AT, M_1 and M_2 have diameters of 1.82 m and 13.8 cm, respectively (ESO, 2014a).

Table 7.2: Average extinction coefficient for each broad band filter J, J_S, H and K_S in Paranal — (ibid.).

J band	**J_S band**	**H band**	**K_S band**
0.91 ± 0.01	0.95 ± 0.01	0.96 ± 0.01	0.94 ± 0.01

Table 7.3: Transmissions between the M_1 mirrors and the switch-yard of the VLTI for several configurations. To compute the stellar flux reaching an instrument, the transmittance/reflectivity of the dedicated feeding optics shall be taken into account and possibly the DDLs, if used. The DDL does not transmit in the L and N bands, except if the windows are removed, in which case the transmission is typically above 90% — (ibid.).

Configuration	V band	J band	H band	K band	L band	N band
UT SF	$\sim 0.2\%$	$> 13\%$	$> 27\%$	$> 34\%$	$> 33\%$	$> 38\%$
UT DF	$\sim 0.2\%$	$> 11\%$	$> 23\%$	$> 28\%$	$> 29\%$	$> 33\%$
AT SF	$\sim 0.2\%$	$> 19\%$	$> 27\%$	$> 35\%$	$> 38\%$	$> 42\%$
AT DF	$\sim 0.2\%$	$> 6\%$	$> 12\%$	$> 18\%$	$> 19\%$	$> 21\%$
DDL only	$\sim 25\%$	$> 82\%$	$> 84\%$	$> 85\%$	–	–

Transmittances of table 7.4 already include the average dynamic coupling loss in the optical fibres of the VLTI instruments, but those values can oscillate considerably according to the seeing conditions. Fibre transmissions of about 51 %, 37 % and 40 % were considered for AMBER (Robbe-Dubois et al., 2007), PRIMA (J. Sahlmann et al., 2009) and PIONIER, respectively. Because GRAVITY is fed by a high order AO system, an optimal fibre transmission was used.[6]

Table 7.4: Transmittances of four instruments (soon to be or already) installed in the VLTI.

Interferometer	Transmittance (%)	Installation	Reference
AMBER	4	2004	Robbe-Dubois et al., (2007)
GRAVITY	18	2015	GRAVITY Consortium (2011)
PIONIER	15	2010	PIONIER Consortium (2011)
PRIMA	18 ± 5	2009	J. Sahlmann et al., (2009)

Noise models

Until present date, the most common quantities in long baseline optical interferometry are the *square of the normalised visibility amplitude* (the *normalised power-spectrum*, usually denoted by V^2 or $V2$) and the *closure phase* (the phase of the *bi-spectrum*, having different denotations, such as ϕ_c, ϕ_{ijk}, or CP, just to name a few). While the visibility amplitude is related to the projected angular size of the source, the phase provides information on the location of the photo-centre of its brightness distribution (J.-P. Berger, Malbet et al., 2012). In fact, the spatial positioning information of the image is uniquely contained in the phase. One of the greatest advantages of

[6] As an example, considering an AT in DF, collecting light in the K-band, being recorded by PRIMA in the astrometric mode, the total throughput is about 3 %. For a m_K = 10.0 star, from eq. (7.21), the spectral density rate is 4.6×10^{-3} phot/(s cm^2 Å). The collecting area of an AT increases this number nearly to 120 phot/(s Å) and since a K filter has a passband of 510 nm wide (table 7.1), the total rate is increased to about 60 000 phot/s. The total throughput yields the final result of 1 800 phot/s, to which corresponds an SNR of about 130 for an integration time of 10 seconds.

having access to the complete visibility phase for image reconstruction is that solutions become convex.

The visibility function is degraded mainly by the refraction, and also by the absorption and scattering of the light by particles and different layers of moving gases in the turbulent atmosphere. Knowledge about the bias of the estimators and the noise statistics associated with the observables is fundamental to validate simulations of data and image reconstruction, and to understand the behaviour of the instruments under different observational conditions.

In order to account for the statistics of interferometric observables in mono-mode interferometers, models built upon the spatially continuous model of photo-detection introduced by J. W. Goodman, (1985) have been applied to estimate the noise associated to the power-spectrum and the closure phase — works developed by É. Tatulli and Chelli, (2005) and by Gordon and D. F. Buscher, (2012) — and to calculate the noise associated with the visibility amplitude and phase (see Renard, Éric Thiébaut and Malbet, 2011; É. Tatulli, Blind et al., 2010). The Simple noise model, which estimates the statistics of all the aforementioned observables, was also developed during this thesis.

This section describes each of the aforementioned noise models, highlighting the relevant equations, and the behaviour of the standard deviation and/or the SNR of the observables with each parameter on which they depend is analysed.

It is common to model the noise of interferometric observables as a combination of signal-dependent Poisson noise (*photon noise*, for example) and signal-independent Gaussian noise (*detector noise*, the readout noise resulting from the detector electronics, for example). The mixture of all the noise contributions for the detection process, including the photon noise, is commonly referred as *detection noise* (Gordon and D. F. Buscher, 2012). The relations between the SNR measured on the observables and the parameters upon which they rely are independently analysed on the light of each of these contributions (*photon rich*, *detection* and *photon starved* cases).

A particular nomenclature was adopted throughout the remainder of the section (tables 7.5 and 7.6). *Photon noise* is the regime where the signal terms have larger magnitude than the detector ones, while the opposite regime is denominated *detector noise* . When plotting the SNR *vs* any quantity on which depends the noise model, both regimes are identifiable by two branches separated by an “elbow” point (*cf.* plots of sections 7.5.3.2 and 7.5.3.3). Three cases were defined according to the magnitude of the source: the *photon rich* case, corresponding to bright sources, the *photon starved* case, related to faint sources, and the *detection* case, characterised by typically exhibiting the aforementioned “elbow” points.

Table 7.5: Nomenclature for noise regimes.

Regime	**Description**
Photon noise	$\lvert$signal/Poisson terms$\rvert > \lvert$detector terms$\rvert$
Detector noise	$\lvert$detector terms$\rvert > \lvert$signal/Poisson terms$\rvert$

Table 7.6: Noise cases characterised by the magnitude of the source.

Cases	Description
Photon rich	bright sources
Photon starved	faint sources
Detection	occupying intermediary position between the two other cases

Simple noise model for V, ϕ, V^2, B and ϕ_c

The *Simple noise model* was developed having in mind the analytical study of the relations between the visibility amplitude and phase, and their standard deviations. Recalling the notation introduced in chapter 2, page 28, the complex visibility $\widetilde{V}$ is written as

$$\widetilde{V} = V\mathrm{e}^{\mathrm{i}\phi} \tag{7.23a}$$

$$\widetilde{V} = \mathscr{R} + \mathrm{i}\mathscr{I}, \tag{7.23b}$$

where $\mathscr{R}$ and $\mathscr{I}$, which are assumed independent, are respectively the real and imaginary parts of $\widetilde{V}$. The visibility amplitude is denoted by V and the visibility phase by ϕ. Applying the *error propagation equation* (Bevington and Robinson, 2003, chapter 3)

$$\sigma_{\mathrm{f}}^2 \simeq \left(\frac{\partial \mathrm{f}}{\partial x}\right)^2 \sigma_x^2 + \left(\frac{\partial \mathrm{f}}{\partial y}\right)^2 \sigma_y^2, \tag{7.24}$$

to V, where x and y are assumed independent, it is straightforward to show that

$$\sigma(V) = \sigma_0 \tag{7.25}$$

if $\sigma_{\mathscr{R}} \simeq \sigma_{\mathscr{I}} = \sigma_0$ is the error in the real and imaginary parts of the complex visibility. Hence, assuming that the noise term is distributed randomly equally in the real and imaginary parts of the visibility, and that σ_0 is not varying with V, the error in the amplitude of the visibility should remain approximately constant with V and, consequently, the SNR measured in V should increase with the amplitude of the visibility. Noise models like É. Tatulli and Chelli, (2005, section 7.5.3) predict larger error bars for V near 1 than near 0. However, as will be shown in section 7.5.3.2, the SNR measured on the normalised power-spectrum, V^2, increases with V.

Concerning the phase, it is expected that its error decreases with V, scaling as $1/V^q$, with $q \in \mathbb{Q}^+$, a positive rational number, since the phase variations due to perturbations in the amplitude should be larger when the latter is small. Applying eq. (7.24) to ϕ yields

$$\sigma(\phi) = \frac{\sigma_0}{V}, \tag{7.26}$$

proving the result for $m = 1$.

The standard deviation of the visibility phase is thus defined by the following equation:

$$\sigma(\phi_n) = \begin{cases} \dfrac{\eta \langle V \rangle}{V_n}, & \text{if } V_n \neq 0 \quad (7.27a) \\ 10 \max\limits_{\forall m:\, V_m \neq 0} \{\sigma(\phi_m)\}, & \text{if } V_n = 0, \quad (7.27b) \end{cases}$$

where $\langle V \rangle$ is the mean value of the amplitudes of all measured visibilities, $\eta \in \mathbb{R}_0^+$ is a non-negative constant, and V_n is the amplitude of the n^{th} measure of the complex visibility.[7] Section 7.5.1 assures that the standard deviation of ϕ evolves as $1/V$, therefore respecting the theoretical prediction of eq. (7.26). The statistics for the visibility amplitude are obtained from eqs. (7.26) and (7.27):

$$\sigma(V_n) = \eta \langle V \rangle . \tag{7.28}$$

This equation is compatible with (7.25), where it was assumed the same error for the real and imaginary parts of the visibility. The η parameter, henceforth called the *noise-to-signal ratio* (NSR), can be viewed as a rough estimate of the inverse of the SNR measured on the visibility amplitude.

Figure 7.9a illustrates the theoretical behaviour of $\sigma(\phi)$ for V varying between 0 and 1 and for five NSR factors, which are compiled in table 7.7. In fig. 7.9b, the standard deviation of the

Table 7.7: NSR factors (η) and corresponding SNR regimes used in the Simple noise model.

η **(NSR)**	1	$\frac{1}{2}$	$\frac{1}{5}$	$\frac{1}{10}$	$\frac{1}{20}$
SNR	1	2	5	10	20
Regime	Very low	Very low	Low	Moderate	High

visibility phase is plotted against the visibility amplitude, for a simulated cluster of stars. Plot 7.9b illustrates the predicted behaviour of increasing phase noise when the amplitude is decreasing.

The normalised power-spectrum, V^2, is defined as the square of the normalised visibility amplitude. Hence, applying eq. (7.24) to V^2 and using eq. (7.28),

$$\sigma(V_n^2) = 2\,\eta\ \langle V \rangle\ V_n. \tag{7.29}$$

The standard deviation of the bi-spectrum amplitude is estimated as:

$$\sigma(B_{ijk}) = \sigma(V)\sqrt{(V_{ij}V_{jk})^2 + (V_{jk}V_{ik})^2 + (V_{ij}V_{ik})^2}, \tag{7.30}$$

where $\sigma(V)$ is defined by eq. (7.28). Assuming that the product of any two visibility amplitudes inside the closure remains approximately constant, eq. (7.30) can be simplified to

$$\sigma(B_m^{ijk}) \simeq \sqrt{3}\,\eta\ \langle V \rangle\ \left\langle V_m^2 \right\rangle , \tag{7.31}$$

[7] The error on the phase is mainly defined by eq. (7.27). Equation (7.27) is used to avoid divisions by zero. The maximum is taken over the set of values previously computed from eq. (7.27). The factor 10 was chosen so as to be one order of magnitude above the aforementioned maximum.

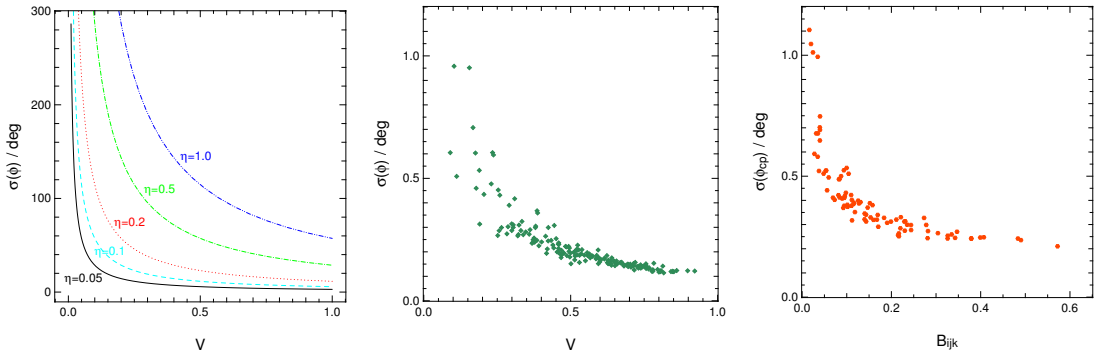

(a) Theoretical vales of the Simple Noise model for several values of NSR. From bottom to top: η =0.05, 0.1, 0.2, 0.5 and 1.0.

(b) Visibility phases *vs* amplitudes corresponding to a mock interferometric observation of a stellar cluster, using $\eta = 0.1$. The line represents theoretical values.

(c) Closure phases *vs* bi-spectra amplitudes (same configuration as in fig. 7.9b).

Figure 7.9: (*a*) Theoretical noise statistics for the visibility phase, ϕ, *vs* the amplitude of the visibility, V, for different NSR factors, η, in the Simple noise model; (*b*) standard deviation of ϕ *vs* V for a simulated cluster of stars mock observed with the VLTI (observing time of 9 h in the K-band, using 4 ATs in stations A0-B1-D2-J2, and integration time of 2 min). (*c*) standard deviation of ϕ_c *vs* B_{ijk} for the same simulated interferometric observation. In figs. 7.9b and 7.9c, η is equal to 0.1.

where $\langle V_m \rangle$ is the average value of the visibility amplitude inside the m^{th} closure, defined by telescopes i, j, and k. The closure phase, ϕ_c, corresponds to the phase of the bi-spectrum. Its statistics is given by

$$\sigma(\phi_c) = \sqrt{\sigma(\phi_{ij})^2 + \sigma(\phi_{jk})^2 + \sigma(\phi_{ik})^2}. \tag{7.32}$$

Considering that $\sigma(\phi_{ij}) \simeq \sigma(\phi_{jk}) \simeq \sigma(\phi_{ik}) \simeq \sigma(\phi)$, it can be approximated by

$$\sigma(\phi_c) \simeq \sqrt{3} \cdot \sigma(\phi). \tag{7.33}$$

For the m^{th} closure, one can take

$$\sigma\left(\phi_m^c\right) \simeq \sqrt{3}\eta \frac{\langle V \rangle}{\langle V_m \rangle}. \tag{7.34}$$

When no substantial changes occur in the visibility amplitude between different closures, the noise on the closure phase is expected to be roughly constant or, at least, constant by steps. This is evident if fig. 7.9c, which illustrates the variation of the closure phase with the bi-spectrum amplitude.

Taking the SNR measured on a phase ψ as the inverse of the error on ψ, the SNR measured on ϕ_c can be compared to the SNR measured on V:

$$\{\text{SNR on } \phi_c\} \sim \frac{1}{\sqrt{3}} \frac{\langle V_m \rangle}{V_n} \cdot \{\text{SNR on } V\}. \tag{7.35}$$

For an unresolved source, $\langle V_m \rangle \sim V_n \sim 1$, $\forall m,n$, and, hence,

$$\lim_{V_{m,n} \to 1} \{\text{SNR on } \phi_c\} \sim \frac{1}{\sqrt{3}} \cdot \{\text{SNR on } V\}. \tag{7.36}$$

Renard et al. 2011 noise model for V and ϕ

Renard, Éric Thiébaut and Malbet, (2011) introduced a simplified noise model partially based on the model by J. W. Goodman, (1985), in which the statistics is governed by an SNR factor, γ. It relates to the standard deviations of V and ϕ by the equations

$$\sigma(V_n) = \gamma \langle V_n \rangle \tag{7.37a}$$

$$\sigma(\phi_n) = \gamma, \tag{7.37b}$$

where, as in section 7.5.1, V_n and ϕ_n are respectively the amplitude and phase of the n^{th} measure of the complex visibility, and $\langle V_n \rangle$ is the expected value of he n^{th} amplitude that can be estimated from the complex visibility of the reference image.

Similarly to the η factor in the Simple noise model, γ gives an estimate of the inverse of the SNR, but now measured on both the visibility's amplitude and phase. Three values of γ were used by Renard, Éric Thiébaut and Malbet, (2011) in their analyses: 1 %, 5 % and 10 %, corresponding respectively to a very high, high and moderate SNR. This noise model assumes constant standard deviations for both amplitude and phase of the visibility.

A weak point of this model is the fact that the error in the phase does not decrease with the amplitude of the visibility, as physically expected and predicted by eq. (7.26).[8]

Tatulli & Chelli 2005 noise model for V^2 and ϕ_c

The model by (É. Tatulli and Chelli, 2005) presents estimators for the noise statistics associated to V^2 and ϕ. The signal is considered to be corrupted by three types of noise:

1. Signal **photon noise**, with a total number of detected photo-events $N_{\text{phot}}^{\text{tot}}$ (in all telescopes) split into τk photons in the photometric channel and $(1-\tau)N_{\text{phot}}^{\text{tot}}$ photons in the interferometric channel (τ is the fraction of light selected for photometry at the output of the beam splitter);
2. Additive **Gaussian noise** that results from the detector and from thermal emission;[9]
3. **Atmospheric** or **modal speckle noise**, which arises from the fluctuations in the coupling efficiency, due to the turbulence (É. Tatulli, Mège and Chelli, 2004).

It is assumed that the sources are not resolved by a single telescope,[10] such that the effect of spatial filtering by the fibres in the observables is entirely characterized by the instantaneous Strehl ratio statistics. Under this assumption and considering partial AO correction, the modal speckle noise can be neglected and one can concentrate only in the *photon noise* (Poisson) and *detector noise* (Gaussian) regimes (É. Tatulli and Chelli, 2005), or in the combination of both (*detection* noise).

[8] This limitation was one of the reasons for the development of the Simple noise model.
[9] The thermal emission is, however, less important for short integration times.
[10] Angular sizes typically below 250 mas for an AT at the VLTI.

The contributions of the correlation coefficients between the observables V^2 and ϕ_c are also omitted (ibid.). This approximation is justified by the fact that neglecting the correlation between the measurements leads to overestimating the SNR by a factor of $\sqrt{2}$ for the case of the power-spectrum and the closure phase. It is also assumed that the square of the visibilities and closure phases are uncorrelated, as they are observables of different nature (ibid.).

The quantities upon which the normalised power-spectrum and the closure phase depend are summarised in table 7.8.

Table 7.8: Quantities on which depend the statistics of the normalised power-spectrum and the closure phase needed for É. Tatulli and Chelli, (ibid.) noise model.

Symbol	Name	Remarks
N_{tel}	Number of telescopes	Telescopes in the array used for the observation.
$N_{\text{phot}}^{\text{tot}}$	Number of photons	Total number of photo-events coming from the array of apertures.
m_λ	Magnitude of the source	For the calculation of $N_{\text{phot}}^{\text{tot}}$ (not explicitly used in the noise model).
t	Integration time	For the calculation of $N_{\text{phot}}^{\text{tot}}$ (not explicitly used in the noise model). Unit: [s]
$\mathscr{E}$	Efficiency	Combined efficiency of the detector/instrument and the observatory (throughput). For the calculation of $N_{\text{phot}}^{\text{tot}}$ (not explicitly used in the noise model).
$V_\star$	Visibility	True visibility of the source. $V_\star = Ve^{i\phi}$.
$\mathscr{S}$	Long exposure Strehl ratio	
$\sigma_{\mathscr{S}}$	Error on the Strehl ratio	
ρ_0	Optimal coupling coefficient	Fixed by the fibre core design (mono-mode fibre coupling).
τ	Fraction of light for photometry	Selected at the output of the beam-splitter. Accounted for in $\sigma(V^2)$, but not in $\sigma(\phi_c)$.
N_{pix}	Number of pixels	Number of pixels in the detector used to sample the interferometric signal.
σ	Readout noise of the detector	Unit: $\left[\frac{e^-}{px}\right]$

The number of photons in the detector captured by a single aperture is given by eq. (7.22). Thus, the total number of photon-events arriving from the array of telescopes is equal to $N_{\text{phot}}^{\text{tot}} = N_{\text{phot}} \times N_{\text{tel}}$. Equation (7.22) was used to calculate the number of photons per second, per square metre of aperture and per micron of waveband, using Table 7.5 from Tokunaga, (2000) to test the results. The relative errors between both results are less than 1 %.

Equations for the statistics of the observables

The equations presented in this section were adapted from Tables 4, 5 and 6 of É. Tatulli and Chelli, (2005). As explained previously, it was asserted that no correlation exists between the coefficients of V^2 and ϕ_c and, therefore, only terms from the main diagonal of the covariance matrices were considered for the calculation of the variance of the observables. It is assumed that the transmissions and the level of corrections for the adaptive optics systems are the same for all apertures. Both photon and detector noise terms are taken into account. For the square of the visibility, these terms are combined in eq. (7.38), while for the closure phase, for clarity, they are separated into eq. (7.41).

The fraction of light selected for photometry at the output of the beam splitter, τ, is neglected in the calculation of the statistics of the closure phase — *cf.* eq. (7.41). The reasons why the authors excluded this parameter from the statistics of the closure phase are not clear, as it is at least expected that the error in the phase increases if the amount of light selected for photometry gets close to 100 %. This is considered a weak point of the model (section 7.5.3.3).

Noise on the square of the visibility's amplitude

The standard deviation of the normalised power-spectrum is

$$\sigma(V^2) = V_\star^2 \sqrt{\mathsf{V2D} + \mathsf{V2P}}\,, \tag{7.38}$$

where the terms inside the square root, V2D (terms for the normalised power-spectrum in the *detector noise* regime) and V2P (terms for the normalised power-spectrum in the *photon noise* regime), are given by:[11]

$$\begin{aligned}\mathsf{V2D} = &\left[\frac{2N_{\mathrm{pix}}\,\sigma^2}{(1-\tau)^2\left|V_\star(f_{ij})\right|^2\mathscr{S}^2}\right]\frac{N_{\mathrm{tel}}^2}{\rho_0^2 N_{\mathrm{tot}}^2}\\ &+\left[\frac{2N_{\mathrm{pix}}\,\sigma^2}{(1-\tau)^3\left|V_\star(f_{ij})\right|^4\mathscr{S}^3}\right]\frac{N_{\mathrm{tel}}^4}{\rho_0^3 N_{\mathrm{tot}}^3}\\ &+\left[\frac{N_{\mathrm{pix}}\,\sigma^4(3+N_{\mathrm{pix}})}{(1-\tau)^4\left|V_\star(f_{ij})\right|^4\mathscr{S}^4}\right]\frac{N_{\mathrm{tel}}^4}{\rho_0^4 N_{\mathrm{tot}}^4}.\end{aligned} \tag{7.39}$$

[11] To make the notation lighter, from now on the total number of photons in the array of telescopes will be denoted by N_{tot} and the number of photons striking one aperture will be represented by N_{phot}.

$$
\begin{aligned}
\mathsf{V2P} = & \left[\frac{4\sigma_{\mathscr{J}}^2 + 2N_{\mathrm{tel}}\mathscr{S}^2}{(1-\tau)\left|V_\star(f_{ij})\right|^2\mathscr{S}^3} + \frac{2(\sigma_{\mathscr{J}}^2+\mathscr{S}^2)}{\tau\mathscr{S}^3}\right]\frac{N_{\mathrm{tel}}}{\rho_0 N_{\mathrm{tot}}} \\
& + \left[\frac{2N_{\mathrm{tel}}\sigma_{\mathscr{J}}^2 + N_{\mathrm{tel}}^2\mathscr{S}^2}{(1-\tau)^2\left|V_\star(f_{\mathrm{if}})\right|^4\mathscr{S}^4} + \frac{4}{(1-\tau)^2\left|V_\star(f_{ij})\right|^2\mathscr{S}^2} + \frac{1}{\tau^2\mathscr{S}^2}\right]\frac{N_{\mathrm{tel}}^2}{\rho_0^2 N_{\mathrm{tot}}^2} \\
& + \frac{1}{(1-\tau)^3\left|V_\star(f_{ij})\right|^4\mathscr{S}^3}\cdot\frac{N_{\mathrm{tel}}^4}{\rho_0^3 N_{\mathrm{tot}}^3}
\end{aligned}
\tag{7.40}
$$

Noise on the closure phase

The standard deviation of the closure phase is

$$
\sigma(\phi_{\mathrm{c}}) = \sqrt{\mathsf{CPD} + \mathsf{CPP}}, \tag{7.41}
$$

where CPD (terms for the closure phase in the *detector noise* regime) and CPP (terms for the closure phase in the *photon noise* regime) are respectively given by

$$
\begin{aligned}
\mathsf{CPD} = & \frac{\left[|V_\star(f_{ij})|^4 + |V_\star(f_{jk})|^4 + |V_\star(f_{ik})|^4\right]\left(\mathscr{S}^4 + \sigma_{\mathscr{J}}^2\mathscr{S}^2\right)N_{\mathrm{pix}}\sigma^2}{2|V_\star(f_{ij})|^2|V_\star(f_{jk})|^2|V_\star(f_{ik})|^2\mathscr{S}^6}\cdot\frac{N_{\mathrm{tel}}^2}{\rho_0^2 N_{\mathrm{tot}}^2} \\
& + \frac{\left[|V_\star(f_{ij})|^2 + |V_\star(f_{jk})|^2 + |V_\star(f_{ik})|^2\right]\left(3+N_{\mathrm{pix}}\right)N_{\mathrm{pix}}\sigma^4\mathscr{S}^2}{2|V_\star(f_{ij})|^2|V_\star(f_{jk})|^2|V_\star(f_{ik})|^2\mathscr{S}^6}\cdot\frac{N_{\mathrm{tel}}^4}{\rho_0^4 N_{\mathrm{tot}}^4} \\
& + \frac{\left(3+N_{\mathrm{pix}}\right)N_{\mathrm{pix}}^2\sigma^6}{2|V_\star(f_{ij})|^2|V_\star(f_{jk})|^2|V_\star(f_{ik})|^2\mathscr{S}^6}\cdot\frac{N_{\mathrm{tel}}^6}{\rho_0^6 N_{\mathrm{tot}}^6}.
\end{aligned}
\tag{7.42}
$$

$$
\begin{aligned}
\mathrm{CPP} = \quad & \frac{|V_\star(f_{ij})|^2|V_\star(f_{jk})|^2 + |V_\star\left(f_{ik}\right)|^2(|V_\star(f_{ij})\,|^2 + |V_\star(f_{jk})|^2)}{2|V_\star(f_{ij})|^2|V_\star(f_{jk})|^2|V_\star(f_{ik})|^2\mathscr{S}^6} \\
& \times \left[N_{\mathrm{tel}}\mathscr{S}^5 + (N_{\mathrm{tel}}+4)\sigma_{\mathscr{S}}^2\mathscr{S}^3 + 2\sigma_{\mathscr{S}}^4\mathscr{S}\right] \cdot \frac{N_{\mathrm{tel}}}{\rho_0 N_{\mathrm{tot}}} \\
- & \frac{2V_\star(f_{ij})V_\star(f_{jk})V_\star^*(f_{ik})\left[|V_\star(f_{ij})|^2 + |V_\star(f_{jk})|^2 + |V_\star(f_{ik})|^2\right]}{2|V_\star(f_{ij})|^2|V_\star(f_{jk})|^2|V_\star(f_{ik})|^2\mathscr{S}^6} \\
& \times \left(\mathscr{S}^5 + 2\sigma_{\mathscr{S}}^2\mathscr{S}^3 + \sigma_{\mathscr{S}}^4\mathscr{S}\right) \cdot \frac{N_{\mathrm{tel}}}{\rho_0 N_{\mathrm{tot}}} \\
- & \frac{2\left[|V_\star(f_{ij})|^2|V_\star(f_{jk})|^2 + |V_\star(f_{ik})|^2\left(|V_\star(f_{ij})|^2 + |V_\star(f_{jk})|^2\right)\right]}{2|V_\star(f_{ij})|^2|V_\star(f_{jk})|^2|V_\star(f_{ik})|^2\mathscr{S}^6} \\
& \times \left(\mathscr{S}^4 + \sigma_{\mathscr{S}}^2\mathscr{S}^2\right) \cdot \frac{N_{\mathrm{tel}}^2}{\rho_0^2 N_{\mathrm{tot}}^2} \\
- & \frac{|V_\star(f_{ij})|^4 + |V_\star(f_{jk})|^4 + |V_\star(f_{ik})|^4}{2|V_\star(f_{ij})|^2|V_\star(f_{jk})|^2|V_\star(f_{ik})|^2\mathscr{S}^6} \cdot \left(\mathscr{S}^4 + 2\sigma_{\mathscr{S}}^2\mathscr{S}^2 + \sigma_{\mathscr{S}}^4\right) \cdot \frac{N_{\mathrm{tel}}^2}{\rho_0^2 N_{\mathrm{tot}}^2} \\
+ & \frac{|V_\star(f_{ij})|^2 + |V_\star(f_{jk})|^2 + |V_\star(f_{ik})|^2}{2|V_\star(f_{ij})|^2|V_\star(f_{jk})|^2|V_\star(f_{ik})|^2\mathscr{S}^6} \cdot \left(N_{\mathrm{tel}}^2\mathscr{S}^4 + N_{\mathrm{tel}}\sigma_{\mathscr{S}}^2\mathscr{S}^2 + 2\sigma_{\mathscr{S}}^4\right) \\
& \times \frac{N_{\mathrm{tel}}^2}{\rho_0^2 N_{\mathrm{tot}}^2} \\
+ & \frac{[N_{\mathrm{tel}}^3 - 2V_\star^*(f_{ij})V_\star^*(f_{jk})V_\star(f_{ik})]\mathscr{S}^3 + 3N_{\mathrm{tel}}^2\sigma_{\mathscr{S}}^2\mathscr{S}}{2|V_\star(f_{ij})|^2|V_\star(f_{jk})|^2|V_\star(f_{ik})|^2\mathscr{S}^6} \cdot \frac{N_{\mathrm{tel}}^3}{\rho_0^3 N_{\mathrm{tot}}^3}.
\end{aligned}
\tag{7.43}
$$

Dependence of the SNR measured on V^2 on the variables

In this subsection, the behaviour of the SNR measured on the square of the normalised visibility's amplitude with the parameters on which it depends, in the *photon rich*, *photon starved* and *detection* cases, is analysed. Table 7.9 presents the reference parameter values.[12]

Table 7.9: Values of the parameters used for the study of the dependence of the SNR measured on V^2 on the variables.

Test case	m_{K}	V	N_{tel}	t (ms)	$\mathscr{E}$	$\mathscr{A}$ (m^2)	$\mathscr{S}$	$\sigma_{\mathscr{S}}$	ρ_0	τ	N_{pix}	σ (e^- px^{-1})
Photon Rich	6.0	See								See		
Detection	11.0	Tabs.	4	20	0.15	2.53	0.5	0.2	0.8	Tab.	24	5.0
Photon Starved	16.0	7.10 and 7.11								7.11		

Three visibility amplitudes were assumed in this section, to wit, $V = 0.1$, $V = 0.5$ and $V = 1.0$, corresponding respectively to a *resolved*, *partially resolved* and *unresolved* source. The case $V = 1.0$ presents the advantage that the instantaneous modal visibility is equal to the object visibility (É. Tatulli, Mège and Chelli, 2004). For the sake of simplicity, this equality is assumed in the two

[12] The parameters have the same values in all test cases, except when explicitly stated.

Table 7.10: Elbow points of the graphs depicted in fig. 7.10.

	$t = 20\,\mathrm{ms}$			$t = 30\,\mathrm{s}$		
V	0.1	0.5	1.0	0.1	0.5	1.0
m_K	10.9	11.7	12.4	18.1	19.3	19.4
SNR	0.22	0.88	1.2	0.28	1.3	2.0
N_tot	2.05×10^3	1.08×10^3	7.45×10^2	4.88×10^3	1.77×10^3	1.62×10^3

other cases, *i.e.*, it is always supposed that there is no difference between the measured visibility, V, and the true visibility of the source, $V_\star$.

Taking into account the array configuration of current and future instruments — PIONIER (**Berger2010c**) and GRAVITY (Eisenhauer et al., 2005), in the case of the VLTI — 4 telescopes were used in the present study of the noise terms, but only ATs were considered, as movable apertures are more suitable with an imaging study with the VLTI.

The integration time was estimated using a typical coherence time of 20 ms in the K-band as a starting point, because this noise model does not take into account the noise statistics introduced by fringe trackers. However, integration times of 30 s would be attainable with optimal fringe trackers and justified by the fact that these are common instruments in current facilities dedicated to IR interferometry — FINITO (Corcione et al., 2003), PRIMA's FSU (J. Sahlmann et al., 2009) and CHAMP (D. H. Berger et al., 2008).

As for the efficiency, although it is not an explicit parameter of the formulas for the computation of the noise, it is fundamental for the estimation of the total number of photons striking the apertures. For the purpose of accounting for the impact of the efficiency on the SNR, it was used the combined values of the VLTI and PIONIER (table 7.4).

The area of $2.53\,\mathrm{m}^2$ corresponds to the effective surface of an AT. It was assumed a typical AO correction of $\mathscr{S} = 0.5$, with an associated error of 20 % ($\sigma_\mathscr{S} = 0.2$ which, according to É. Tatulli, Mège and Chelli, 2004, can produce visibility variations up to 10 %) and an optimum coupling coefficient of 0.8 (Shaklan, M. M. Colavita and M. Shao, 1992). The signal is sampled by $24\,\mathrm{px}$[13] in a detector with a readout noise of $5.0\,e^-\,\mathrm{px}^{-1}$ (Finger et al., 2012).

The magnitudes corresponding to each test case were chosen in order that the terms V2D and V2P of eq. (7.38) obey to the following relations:

- **Photon Starved case:** $\mathsf{V2P} \ll \mathsf{V2D}$;
- **Detection case:** $\mathsf{V2P} \simeq \mathsf{V2D}$;
- **Photon Rich case:** $\mathsf{V2P} \gg \mathsf{V2D}$.

The magnitude for the *detection* case was determined by investigating the "elbow" points in the plots of the SNR on V^2 *vs* m_K and the SNR on V^2 *vs* N_tot (table 7.10 and fig. 7.10). The elbow points indicate the values of the parameters where the V2D and the V2P terms from eq. (7.38) are equal.

[13] Cases, for instance, of PIONIER with no spectral dispersion (**Berger2010c**) or PRIMA (J. Sahlmann et al., 2009).

Table 7.11: Optimal values of τ for the SNR on V^2.

		$t = 20\,\mathrm{ms}$			$t = 30\,\mathrm{s}$		
Test case	$V =$	0.1	0.5	1.0	0.1	0.5	1.0
Photon Rich		0.050	0.20	0.34	0.049	0.21	0.34
Detection		0.020	0.11	0.14	0.049	0.21	0.34
Photon Starved		0.020	0.020	0.020	0.046	0.20	0.33

The elbow points depend on the visibility of the source and, because they are sensitive to the integration time as well as to the magnitude of the object, they also vary with the total number of photons reaching the detector. For $V \in [0.1, 1.0]$, the change in the slopes happens at points corresponding roughly to a difference of 1.5 magnitudes in the K-band, whether an efficient fringe tracker is present ($t = 30\,\mathrm{s}$) or not ($t = 20\,\mathrm{ms}$). When looking to the total number of photons, that difference is larger when no fringe tracker is used than when it is present: about 2 orders of magnitude for the former case and only about 5 times for the latter.

For bright sources, the SNR decreases with V, *i.e.*, it increases with the apparent projected size of the object, up to a point where the total number of photons reaching the array is not enough to allow the available baselines to match the full frequency content of the source. Then, the SNR increases with V, *i.e.*, it drops with the apparent projected size of the object. The degradation of the performance of the interferometer in terms of SNR and magnitude of the observed source is also related to the decrease of the coupling efficiency that happens for resolved objects (É. Tatulli, Mège and Chelli, 2004).

The elbow points are located around $m_\mathrm{K} = 9.0$ for the $t = 20\,\mathrm{ms}$ case and around $m_\mathrm{K} = 19.0$ for the $t = 30\,\mathrm{s}$ one. This noise model is clearly too optimistic in both cases. Regarding the variation of the SNR on V^2 with N_tot, the former should increase more slowly for the fringe tracker case because of the cumulative readout noise of the detector.

A typical value $N_\mathrm{tot} = 1\,000\,\mathrm{phot}$ can be drawn from table 7.10, above which the *photon noise* regime is roughly assured. The magnitude characterizing the *detection* case, $m_\mathrm{case} = 11.0$, was chosen from the data of table 7.10, as means to allow the analyses of the SNR corresponding to both partially resolved and unresolved sources.

The amount of light selected for photometry at the output of the beam splitter should be chosen having into account the visibility amplitude and the noise regime, for the purpose of maximizing the SNR on V^2. The value of τ that equalises the terms V2P and V2D, and the root of the derivative of eq. (7.38) in order to τ in the three test cases is presented in table 7.11 and fig. 7.11. For 20 ms of integration time, in the *photon starved* case, it was adopted a value $\tau = 20\,\%$ for the three visibility amplitudes, but only when $V = 1.0$ the derivative of $\sigma(V^2)$ has a root (*cf.* fig. 7.11). In this noise regime, when $V = 0.1$ and $V = 0.5$, the derivative is always positive, implying that the coupling efficiency is too low. For an unresolved source, however, it is found an optimal τ as low as 2 %.

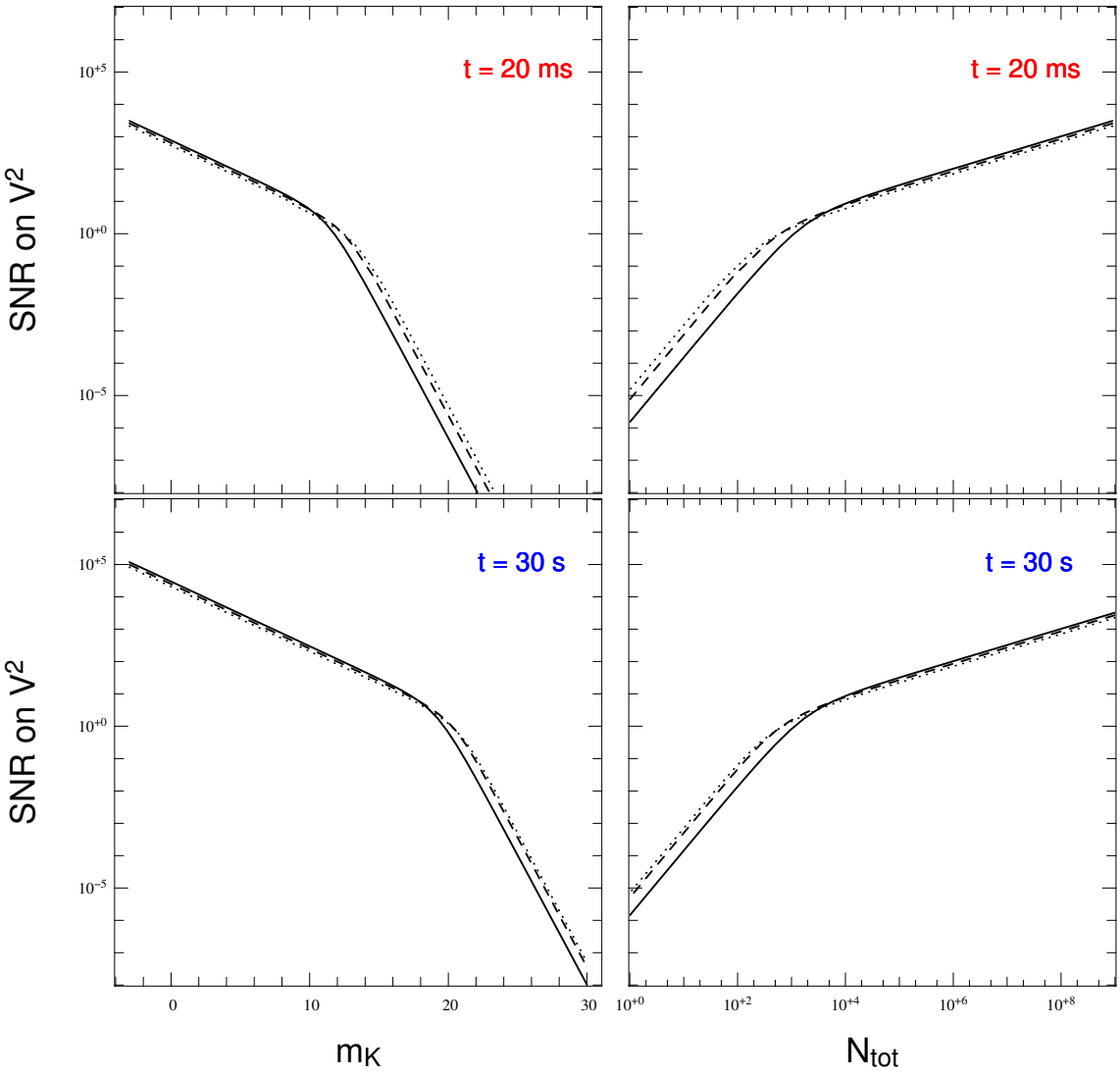

Figure 7.10: SNR measured on V^2 as a function of the magnitude of the source in the K-band, m_{K} (*left*), and SNR of V^2 as a function of the total number of photons in the detector, N_{tot} (*right*), for integrations times equal to 20 ms (*top*) and 30 s (*bottom*). The curves are calculated for different visibility amplitudes: $V = 0.1$ (solid line), $V = 0.5$ (dashed line) and $V = 1.0$ (dotted line).

For all test cases, the optimal τ increases with V because the noise on V^2 increases with V (*cf.* fig. 7.12a) and, thus, more light is needed for the photometric calibration.

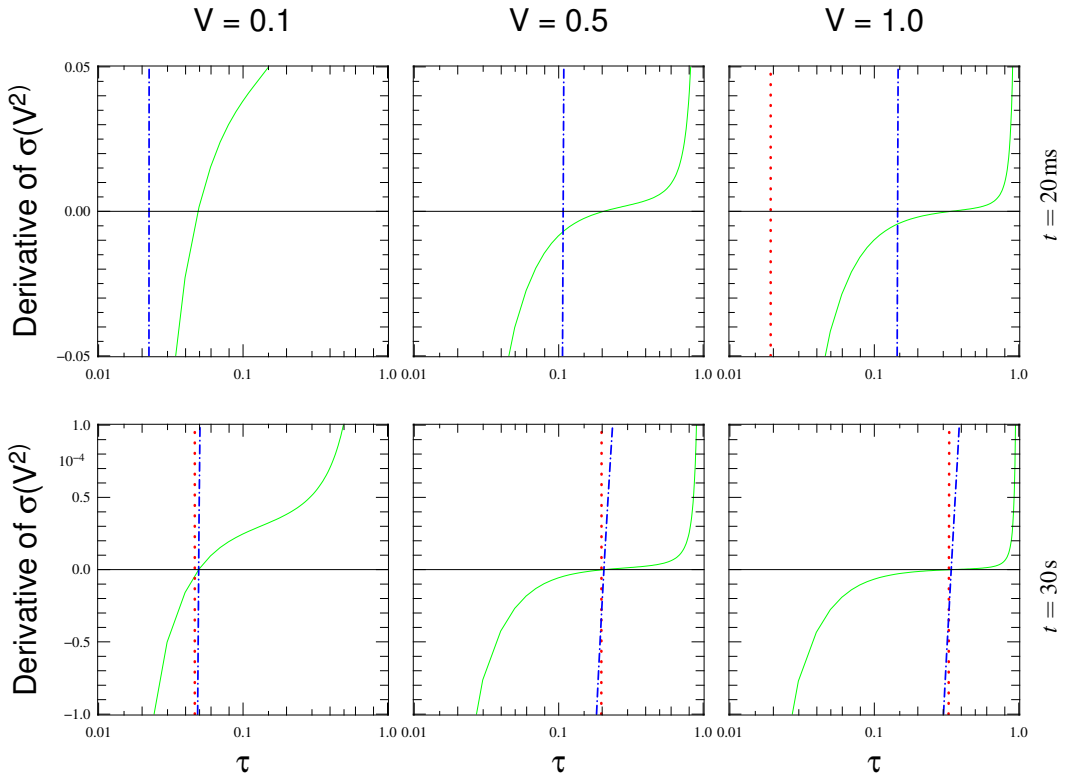

Figure 7.11: Derivative of eq. (7.38) in order to τ in the three test cases, for an integration time of 20 ms (*top*), and for an integration time of 30 s (*bottom*). The green solid line represents the *photon rich* case, the blue dashed-dotted line the *detection* case, and the red dotted line the *photon starved* case. For $V = 0.1$ and $V = 0.5$, when $t = 20$ ms, the derivative of $\sigma(V^2)$ in the *photon starved* case is always positive.

In the following paragraphs, the *photon rich* case is always represented by a green solid curve, the intermediate *detection* by a blue dashed-dotted curve, and the *photon starved* by a red dotted line. The three visibilities ($V = 0.1, 0.5, 1.0$) increase from the thinner to the thicker lines. If used, any other curve is described in the corresponding paragraph and/or figure.

SNR on V^2 *vs* V

Figure 7.12b illustrates the variation of the SNR calculated on V^2 with V. All parameters of eq. (7.38) are fixed according to tables 7.9 and 7.10, and only the visibility amplitude is varied.

The three test cases are differentiable by the magnitude of the SNR and by the inclination of the curves. In all cases, as expected, the SNR measured on V^2 increases with the visibility amplitude. Therefore, the SNR on the normalised power-spectrum decreases with the apparent projected size of the observed source, *i.e.*, as the object becomes increasingly resolved. This result is independent of the quantity the SNR on V^2 depends on, as it will be shown in the subsequent plots for the remainder of the parameters.

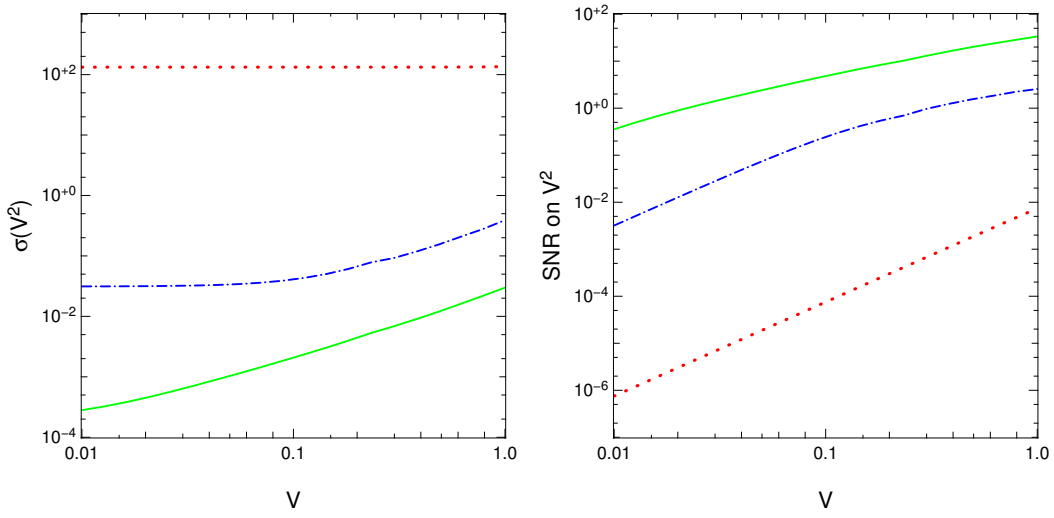

(a) Standard deviation of V^2 *vs* V. **(b)** SNR on V^2 *vs* V.

Figure 7.12: (*a*) $\sigma(V^2)$ *vs* V and (*b*) SNR on V^2 *vs* V. The green solid curves correspond to the *photon rich* case, the blue dashed-dotted curves to the *detection* case and the red dotted curves to the *photon starved* case.

The curve corresponding to the *photon rich* case presents good SNRs for resolved and unresolved sources. In the *photon starved* case, the SNR is meaningless. In the curve representing the *detection* case, it is identifiable an elbow point, which marks the separation between the two noise regimes: to the left, the steep straight line typical of the *detector noise* regime, and to the right, the less inclined and slightly concave curve of the *photon noise* regime. The SNR becomes greater than 1.0 for $V \gtrsim 0.3$, being always less than approximately 3.0.

In the Simple noise model, the SNR measured on V^2 is given by

$$\frac{V^2}{\sigma(V^2)} \sim \frac{V_n}{2\eta\langle V\rangle}. \tag{7.44}$$

Assuming that, for an even distribution of visibility amplitudes, $\langle V\rangle \sim 0.5$, the NSR factor can be estimated by

$$\eta \sim \frac{V_n}{\mathrm{SNR}_{V^2}}. \tag{7.45}$$

Therefore, the photon starved, detection and photon rich curves of fig. 7.12b approximately correspond to NSR factors equal to 100, 0.33 and 0.025 in the Simple noise model, respectively, which, in turn, can be roughly associated to SNRs on V of 0.01, 3 and 40.

SNR on V^2 *vs* N_{tel}

Figure 7.13 illustrates the behaviour of the SNR measured on V^2 with the number of telescopes.N_{tel} was varied from 2 (2 baselines) to 20 (190 baselines). The three aforementioned test scenarios are split into three visibility cases: *resolved source* ($V = 0.1$), *partially resolved source* ($V = 0.5$) and *unresolved source* ($V = 1.0$).

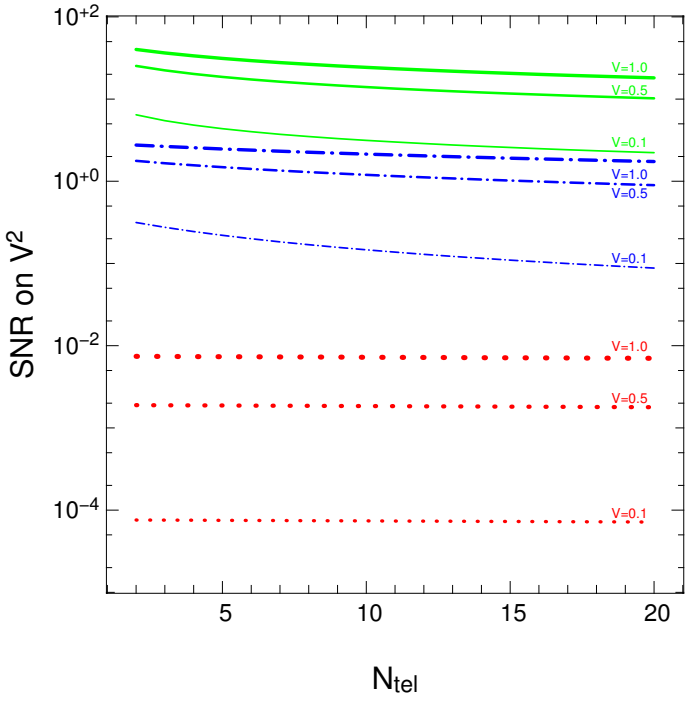

Figure 7.13: SNR on V^2 *vs* N_{tel}, with $N_{\text{tel}} = 1, 2, \ldots, 20$. The curves have the same meaning as in fig. 7.12. In each scenario, the visibility is increasing from the thinner to the thicker lines.

In the *photon rich* case, when comparing to an unresolved source, there is a decay of the SNR by approximately 40 % when observing a partially resolved source and about 85 % when observing a resolved object. In the *detection* case, this decrease scales approximately to 33 % and 90 % for less than 4 telescopes, and 47 % and 95 % above 4 telescopes. In the *photon starved* case, the SNR is too low to be meaningful. Therefore, as was foreseen in fig. 7.12b, there is a significant decrease in the SNR measured on V^2 for resolved sources.

In the *detection* scenario, it is visible the elbow point in the case of a resolved source, marking the separation between the *photon noise* and the *detector noise* regimes. This is the point where the terms V2D and V2P are equal, which, by construction and selection of the parameters for the current study, corresponds to $N_{\text{tel}} = 4$.

In all test cases presenting a meaningful SNR on V^2, the latter decreases with N_{tel}. In the *photon starved* scenario, the SNR measured on V^2 remains constant with N_{tel} because when the statistics are dominated by the detector, increasing the number of telescopes does not substantially affect the SNR. In the other two scenarios, due to the photon noise and the increasing of the detector noise, the SNR decreases with N_{tel}. The behaviour of the SNR on V^2 with N_{tel} can be deduced from eq. (7.38) if all quantities are replaced by the values of tables 7.9 and 7.10, taking, for instance, the *detection* scenario in the $V = 1.0$ case, and leaving N_{tel} as the free parameter. After simplification, the SNR on V^2 reduces to:

$$\left\{\text{SNR on } V^2\right\}_{\text{V=1.0}} \simeq \frac{3}{\sqrt{1 + \frac{N_{\text{tel}}}{10}}}. \tag{7.46}$$

For the case $V = 0.1$, the SNR simplifies to:

$$\left\{\text{SNR on } V^2\right\}_{\text{V}=0.1} \simeq \frac{0.45}{\sqrt{1+0.42N_{\text{tel}}\left(1+\frac{N_{\text{tel}}}{10}\right)}}. \tag{7.47}$$

The V2D and V2P terms leading to eq. (7.46) are the following:

$$\begin{aligned} \text{V2D} = &\quad 3.2\times10^{-2} + \quad 1.7\times10^{-4}N_{\text{tel}} \\ \text{V2P} = &\quad 7.8\times10^{-2} + \quad 1.0\times10^{-2}N_{\text{tel}} + \quad 2.7\times10^{-5}N_{\text{tel}}^2, \end{aligned} \tag{7.48}$$

while for eq. (7.47), these terms have the form:

$$\begin{aligned} \text{V2D} = &\quad 6.1 + \quad 1.7N_{\text{tel}} \\ \text{V2P} = &\quad 0.42 + \quad 1.1N_{\text{tel}} + \quad 0.27N_{\text{tel}}^2. \end{aligned} \tag{7.49}$$

Both 7.48 and 7.49 are plotted in fig. 7.14. It is apparent from this figure that, in the case $V = 1.0$, the term V2P prevails over the term V2D, while the latter remains practically constant. Hence, the shape of the curve in the *detection* scenario for $V = 1.0$ (fig. 7.13) is similar to the ones characterizing the *photon starved* scenario — it presents a slight decay for the biggest number of telescopes, when the term V2P is larger. In the $V = 0.1$ case, the V2D term prevails over the V2P one, but only up to approximately 4 telescopes. After that, the situation inverts and the SNR on V^2 becomes dominated by the V2P term. Since both terms increase with the number of telescopes, the decay in the SNR with N_{tel} is more prominent than in the $V = 1.0$ case. Due to the photometric calibration, the detector noise slightly increases with the number of telescopes.

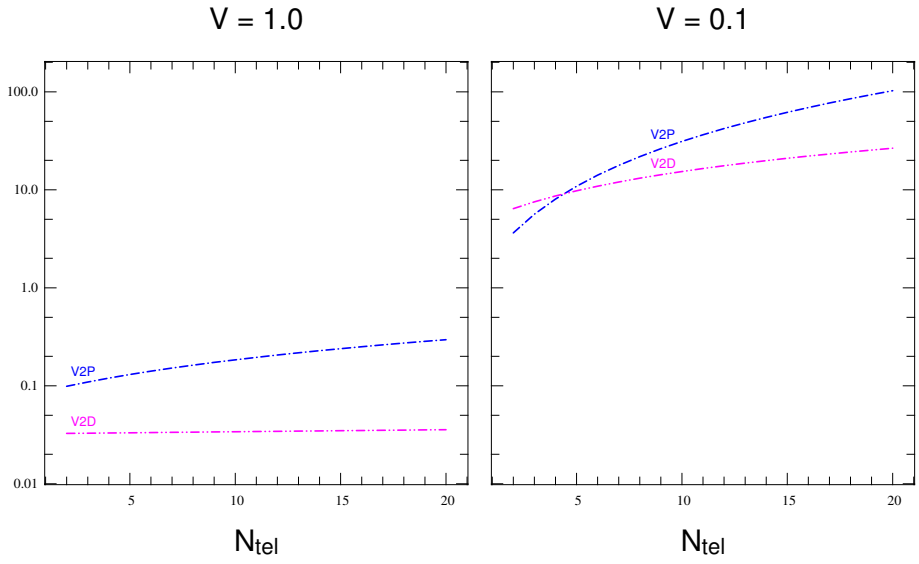

Figure 7.14: Terms V2D (*blue dashed-dotted curve*) and V2P (*magenta dashed-double-dotted curve*) of eq. (7.38) *vs* the number of telescopes used for the interferometric observation, N_{tel}. The curves correspond to points calculated using the quantities of tables 7.9 and 7.10. Two cases are depicted: unresolved ($V = 1.0$, *left*) and resolved ($V = 0.1$, *right*) source.

SNR on V^2 *vs* t

Figure 7.15 illustrates the behaviour of the SNR measured on V^2 with the integration time, which was varied from 10 ms to 2 min.

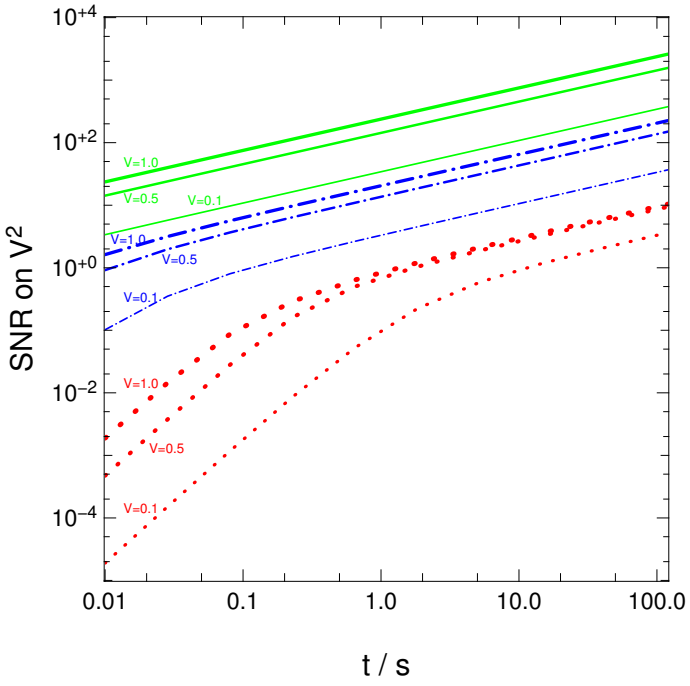

Figure 7.15: SNR on V^2 *vs* $t \in [0.01, 120.0]$ s. The green solid curves correspond to the *photon rich* case, the blue dashed-dotted curves to the *detection* case and the red dotted curves to the *photon starved* case.

For all test scenarios, the SNR increases significantly with the integration time. The curves representing the *photon starved* and *detection* cases present elbow points that separate a steeper part of the curve, corresponding to the *detector noise* regime of noise, from a less inclined part of the curve, which signalise the *photon noise* branch. While for the *photon starved* case the elbow points correspond to integration times roughly between a few hundreds of milliseconds to 1 second, in the *detection* case the *photon noise* branch is achieved after a few tens of milliseconds.

In the *photon rich* case, when compared to a measurement made on a unresolved source, the SNR decreases about 40 % when measured on a partially resolved source and about 85 % when measured on a resolved source. In the *detection* case, to the left of the elbow point (*detector noise* branch), the decrease is about 40 % to a partially resolved source and 90 % to a resolved source, and to the right of the elbow point (*photon noise* branch) it is respectively about 35 % and 85 %. In the *photon starved* case, the decrease scales respectively to 75 % and 99 % in the *detector noise* regime, and 10 % and 65 % in the *photon noise* branch. Thus, for faint sources, the difference in the SNR is less significant between unresolved and partially resolved objects if the *photon noise* regime is reached.

The plots indicate that in all cases, the *photon noise* regime is achieved after a few tens of milliseconds or, at most, after a few seconds of integration time. Varying the integration time from 1 s to 10 s increases the SNR by roughly 3 times. These results indicate that in order to achieve good SNRs with sources of large magnitude, efficient fringe trackers should be incorporated in night observations.

SNR on V^2 *vs* $\mathscr{E}$

Figure 7.16 illustrates the behaviour of the SNR measured on V^2 with the total combined efficiency of the observatory plus the instrument.

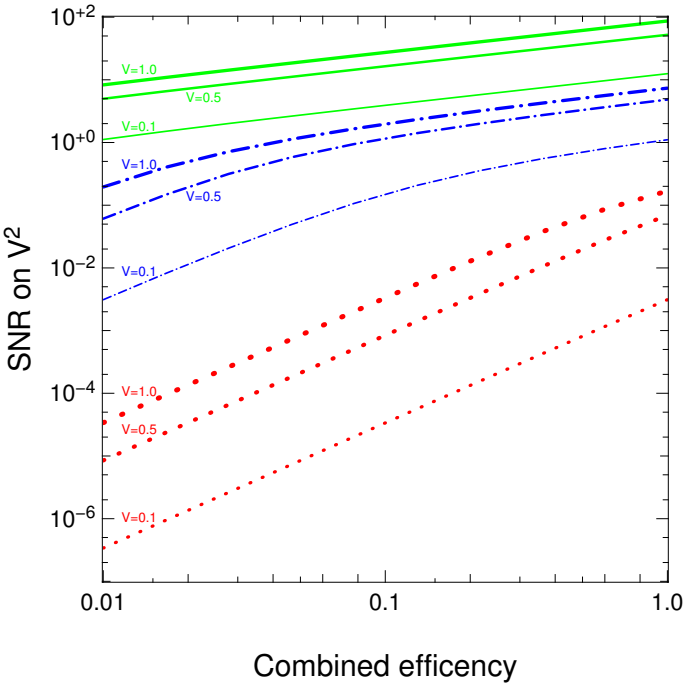

Figure 7.16: SNR on V^2 *vs* $\mathscr{E}$. The colour and shape of the curves have the same meaning as the ones in fig. 7.15.

In all test cases, the SNR increases with the combined efficiency. The *detection* scenario (blue dashed-dotted curve) is characterized for evidencing elbow points in all the three visibility cases. To the left of the elbow points, the curves have the typical slopes of the *detector noise* regime, while to the right of them, the curves are characterized for the slopes of the *photon noise* regime. The elbow point occurs approximately at $\mathscr{E} = 5\,\%$ for unresolved sources, $\mathscr{E} = 7\,\%$ for partially resolved objects and about $\mathscr{E} = 10\,\%$ for resolved sources. Thus, in the *detection* scenario, increasing the efficiency to 15 % brings the statistics of the normalised power-spectrum to the *photon noise* regime (with SNR greater than unity).

Varying $\mathscr{E}$ from 10 % to 20 %, leads to an increase roughly of 1.4 times in the *photon rich* case. Hence, if the *photon noise* regime is assured, the gain in SNR on V^2 is less significant than the impact of increasing significantly the integration time.[14]

SNR on V^2 *vs* $\mathscr{S}$

Figure 7.17a depicts the evolution of the SNR on V^2 with the long-exposure Strehl ratio.

The SNR increases with $\mathscr{S}$ for all noise regimes. In the *photon rich* case, increasing the Strehl from 0.1 to 0.5 leads to an increase in the SNR on V^2 of about 4 times. In the *detection* case, the same increase in $\mathscr{S}$ leads to an improvement of the SNR by roughly a factor of 5 for an unresolved

[14] However, image reconstruction simulations indicate that large SNRs on the interferometric observables are always important to achieve images of "good" quality and of "easy" reconstruction.

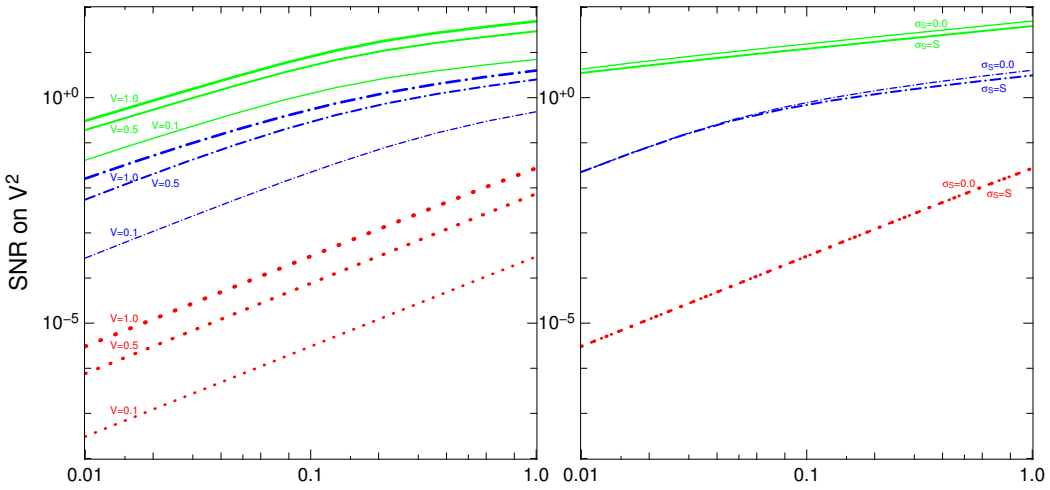

(a) SNR on V^2 *vs* $\mathscr{S}$. **(b)** SNR on V^2 *vs* $\mathscr{S}$ for $\sigma_{\mathscr{S}} = 0.0$ and $\sigma_{\mathscr{S}} = \mathscr{S}$.

Figure 7.17: (*a*) SNR on V^2 *vs* $\mathscr{S}$. The colour and shape of the curves have the same meaning as in fig. 7.16. (*b*) SNR on V^2 *vs* $\mathscr{S}$ for a pure turbulent case (lower curves, $\sigma_{\mathscr{S}} = \mathscr{S}$) and perfect AO correction (upper curves, $\sigma_{\mathscr{S}} = 0.0$). The colour and shape of the curves have the same meaning as in fig. 7.17a, although only the case $V = 1.0$ is illustrated.

object and by a factor of 11 for a resolved source. In the *photon starved* case, the improvement is even more dramatic (about 25 times), although the SNR values measured on V^2 are meaningless. Both *photon rich* and *detection* scenarios evidence elbow points, noting that it is important to have AO correction (at least 10 %) in order to safely be in the *photon noise* regime.

Figure 7.17b illustrates the evolution of the SNR on V^2 with $\mathscr{S}$ for an unresolved source in two different scenarios: a pure turbulent ($\sigma_{\mathscr{S}} = \mathscr{S}$) case and a fully AO corrected ($\sigma_{\mathscr{S}} = 0.0$) case. The improvement in the SNR is only visible in the *photon noise* regime and it roughly scales to a value 1.3 times better, indicating that when reducing the Strehl ratio error, the improvement in the SNR is not substantial.

In the *detector noise* regime, the green solid lines do not follow the behaviour of the curves of the *photon rich* case in fig. 7.17b. This phenomenon is explained by the fact that in the *detector noise* branch, the Strehl ratio is very small and, thus, the values for $\sigma_{\mathscr{S}}$ are very close to each other. Hence, the SNR is larger than in fig. 7.17b and the difference between the curves representing the cases $\sigma_{\mathscr{S}} = 0.0$ and $\sigma_{\mathscr{S}} = \mathscr{S}$ is small. In this sense, the graph of fig. 7.17a is pessimistic for all values $\mathscr{S} < 0.2$, since it was adopted a fixed value $\sigma_{\mathscr{S}} = 0.2$ for the error on the Strehl ratio (table 7.9).

SNR on V^2 *vs* τ

Figure 7.18 illustrates the dependence of the SNR measured on V^2 with the fraction of light selected for photometry.

In the *photon rich* case, the SNR increases with τ up to a maximum and then it decreases rapidly, while in the *photon starved* case, the SNR always decreases. In the latter, the decreasing of the SNR is slow up to a point where τ becomes so large that there is not enough coherent photons in

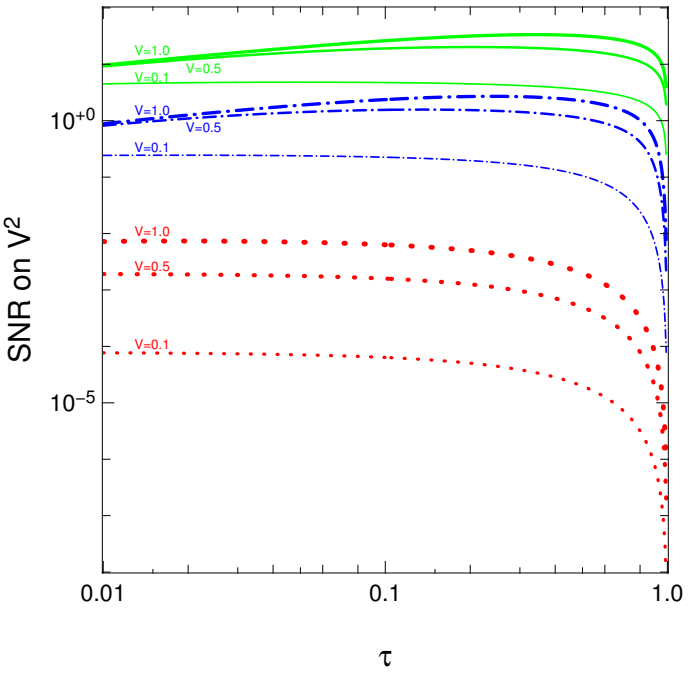

Figure 7.18: SNR on V^2 *vs* τ. The colour and shape of the curves have the same meaning as in fig. 7.17.

the fibre to produce fringes with a good SNR. After that point, the SNR on V^2 drops abruptly. This behaviour is seen in all scenarios. The optimal values of τ for each case were referred in table 7.11. For any particular observation, there is an optimal amount of light that should be directed to the photometric channel in order to minimize the error in the square of the visibility's amplitude.

The model assumes that there is always light in both interferometric and photometric channels, as it exhibits discontinuities in the limiting cases $\tau = 0.0$ and $\tau = 1.0$. Moreover, it does not take into account the influence of τ on the phase observables, including the closure phase, ϕ_c. It seems reasonable to think that, at least in the extreme case when no light is present in the detector, no phase should be possible to be measured.

SNR on V^2 *vs* N_{pix}

The number of pixels in the detector that are used to sample the interferometric signal is a quantity concerning only the *detector noise* regime. Figure 7.19a depicts the behaviour of the SNR measured on V^2 with N_{pix}, which was varied between 1 and 2 000.

When in the *detector noise* regime, the SNR on V^2 decreases with the number of pixels (in the *photon noise* regime it remains constant, as N_{pix} is a quantity affecting only the detector noise regime). The decay is more prominent in the *photon starved* case than in the *photon rich* case, because, in the former, the statistics are dominated by the Gaussian noise, arising from the readout noise of the detector and the thermal emission.

When there are enough photons reaching the detector, using more pixels to sample the signal does not affect significantly the SNR, since the statistics are dominated by the Poisson process associated to the signal. However, after a specific number of pixels, which depends on the test scenario, the term V2D of eq. (7.38) becomes predominant and the SNR on V^2 drops rapidly. In

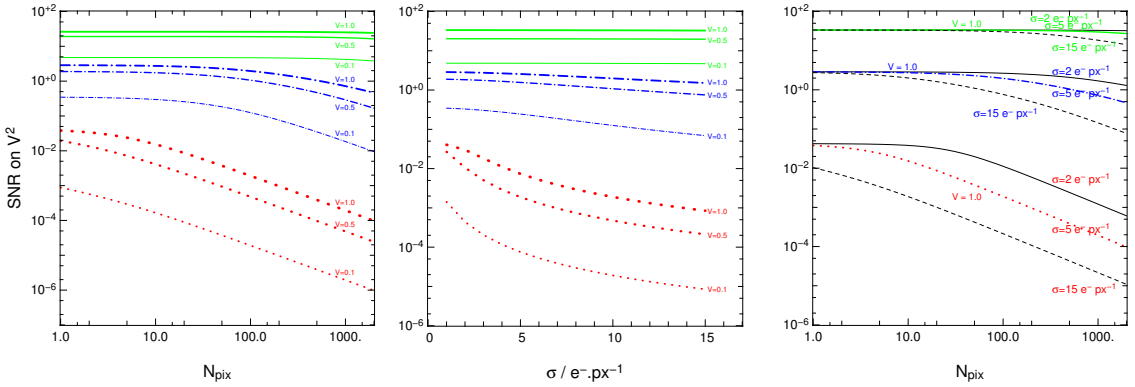

(a) SNR on V^2 *vs* N_{pix}. **(b)** SNR on V^2 *vs* σ. **(c)** SNR on V^2 *vs* N_{pix} for $\sigma = 2, 5, 15\,\text{e}^-\,\text{px}^{-1}$.

Figure 7.19: SNR on V^2 *vs* N_{pix} (*left*), *vs* the RON of the detector, σ (*centre*), and *vs* N_{pix} for three values of σ (*right*). In figs. 7.19a and 7.19c, $N_{\text{pix}} = 1, 2, \ldots, 2000$ and in fig. 7.19b, $\sigma \in [1, 15]$. The green solid curves correspond to the *photon rich* scenario, the blue dashed-dotted curves to the *detection* scenario and the red dotted curves to the *photon starved* scenario. In figs. 7.19a and 7.19b, in each case, the visibility is increasing from the thinner to the thicker lines. In fig. 7.19c, the black solid lines correspond to $\sigma = 2\,\text{e}^-\,\text{px}^{-1}$, the black dashed lines to $\sigma = 15\,\text{e}^-\,\text{px}^{-1}$ and the central colourful curves to $\sigma = 5\,\text{e}^-\,\text{px}^{-1}$.

that case, increasing 100 px induces a change in the SNR by a factor of 2 in the *photon starved* case (red dotted curves) and roughly by a factor of 1.4 in the *detection* case (blue dashed-dotted curves) — in the latter, the slope becomes more prominent as the number of pixels in the detector increases.

SNR on V^2 *vs* σ

The *readout noise* (RON), measured in $e^-\,\text{px}^{-1}$, is also a characteristic of the detector, only related to the *detector noise* regime. Figure 7.19b illustrates the behaviour of the SNR on V^2 with σ, which was varied from 1 to 15 $e^-\,\text{px}^{-1}$.

The SNR on V^2 decreases with σ, but only in the *detector noise* regime (blue dashed-dotted and red dotted curves). When the source is faint enough, there is a drop in the SNR after 1 or 2 $e^-\,\text{px}^{-1}$. The *photon noise* regime (green solid curves) is not affected by the RON since, in this case, the error on V^2 is dominated by the Poisson statistics associated to the photons striking the detector.

In fig. 7.19c it is depicted a combination of the two other graphs, but for unresolved sources. This figure allows one to understand the impact of the RON in the SNR on V^2 when the number of pixels used to sample the interferometric signal is increased. The *photon noise* regime is basically insensitive to the RON up to approximately 100 px. As the elbow points are approached, the SNR becomes increasingly more sensitive to the RON. In the *detection* scenario (blue dashed-dotted curve), the quality of the signal starts to degrade rapidly after 10 px if a detector with $\sigma = 15\,\text{e}^-\,\text{px}^{-1}$ is considered instead of a detector with $\sigma = 2\,\text{e}^-\,\text{px}^{-1}$.

Figures 7.19b and 7.19c show that efficient detectors are very important to achieve quality interferometric observations, especially when observing faint sources.

Dependence of the SNR measured on ϕ_c with the variables

The behaviour of the SNR measured on the closure phase, ϕ_c, with the variables on which it depends, is now analysed in the three noise regimes defined in section 7.5.3.2. Equations (7.41) to (7.43) are used to determine the statistics of ϕ_c in the *photon noise* and *detector noise* regimes.

The list of quantities on which depend $\sigma(\phi_c)$ and their respective values are organised in table 7.12. The parameters have the same values presented in table 7.9, except for the fraction of light selected for photometry at the output of the beam-splitter, τ, which is not present in eqs. (7.42) and (7.43). The description of the variables is compiled in table 7.8.

Table 7.12: Values of the parameters used for the study of the dependence of the SNR measured on ϕ_c on the variables.

Test case	m_K	V	N_{tel}	t (ms)	$\mathscr{E}$	$\mathscr{A}$ (m^2)	$\mathscr{S}$	$\sigma_{\mathscr{S}}$	ρ_0	N_{pix}	σ (e^- px^{-1})
Photon Rich	6.0	See									
Detection	11.0	Tab.	4	20	0.15	2.53	0.5	0.2	0.8	24	5.0
Photon Starved	16.0	7.13									

Similarly to section 7.5.3.2, the test cases were defined according to the relative values of CPD and CPP:

- **Photon Starved case:** CPP $\ll$ CPD;
- **Photon Rich case:** CPP $\gg$ CPD;
- **Detection case:** CPP $\simeq$ CPD.

The criterion used to select the magnitude characterising the *detection* scenario is the same as before: a magnitude in K-band that gives the same value of CPD and CPP in eqs. (7.42) and (7.43). As in section 7.5.3.2, it was adopted $m_K = 11.0$ for this case (*cf.* fig. 7.20 and table 7.13). In fig. 7.20, the diamonds indicate the points where CPP $\simeq$ CPD in each visibility case. It is apparent that these points do not coincide with the elbows of the curves for the $V = 0.5$ and $V = 1.0$ cases. The reason for that is related to the elbows that the photon and detector terms curves present themselves, and that are illustrated in fig. 7.21. When combined, as V increases, the terms produce curves with bigger elbows, displaced towards larger magnitudes. However, according to table 7.13 and the position of the diamonds in fig. 7.20, the magnitude characterizing the points where CPP $\simeq$ CPD decreases with V.[15] Moreover, the SNR measured on the closure phase increases with V in all noise regimes.

It is noteworthy that for $t = 30$ s the elbow points correspond to a magnitude around 20, which is unrealistic.Such an integration time is only attainable with fringe trackers, which are not taken under consideration by this noise model.

In fig. 7.22, the magnitudes and SNRs in tables 7.10 (page 139) and 7.13 were plotted against the corresponding visibility amplitudes for an integration time of 20 ms (no fringe-tracker case) and 30 s (fringe-tracker case).

[15] Although these points do not coincide with the "elbows" for $V > 0.1$, in what follows they will be referred as *elbow points*.

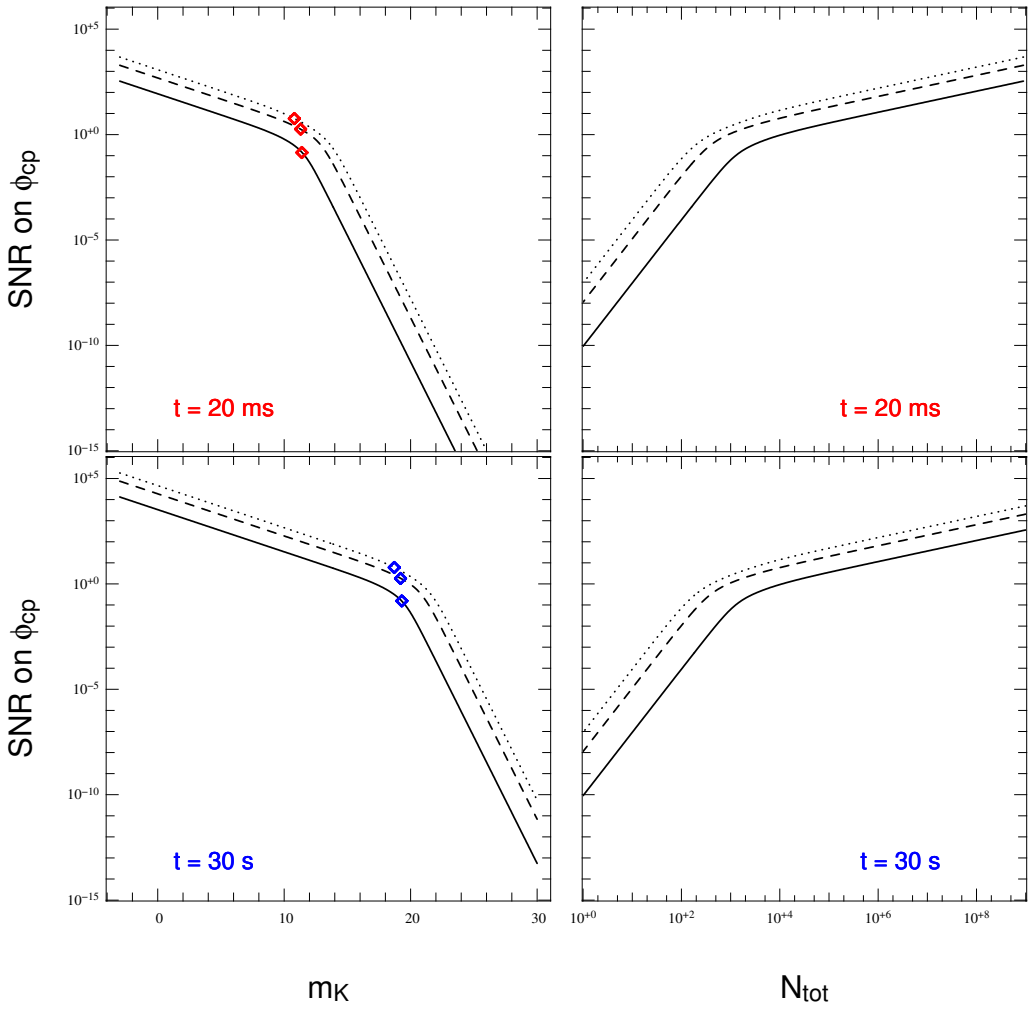

Figure 7.20: SNR measured on ϕ_c as a function of the magnitude of the source in the K-band, m_K (*left*), and SNR of ϕ_c as a function of the total number of photons in the detector, N_{tot} (*right*), for integrations times equal to 20 ms (*top*) and 30 s (*bottom*). The curves are calculated for different visibility amplitudes: $V = 0.1$ (solid line), $V = 0.5$ (dashed line) and $V = 1.0$ (dotted line). The red and blue diamonds mark the points where CPP $\simeq$ CPD. The elbow points depend on the visibility amplitude and on the total number of photons reaching the detector.

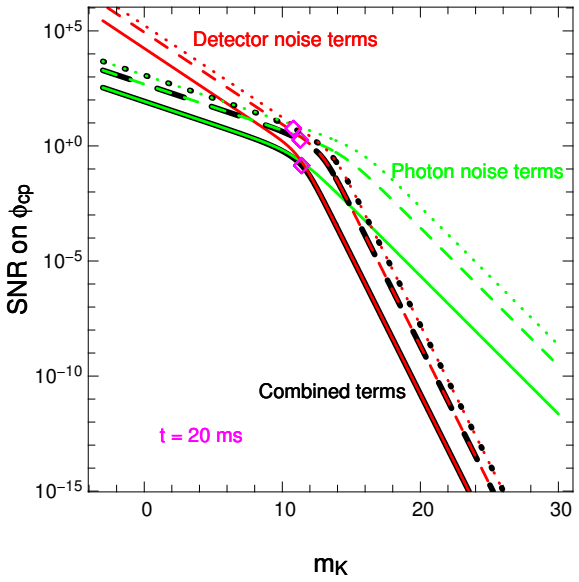

Figure 7.21: Same as in top left of fig. 7.20. The SNR for the *photon noise* and *detector noise* terms are over-plotted. The green and the red curves correspond respectively to the *photon noise* and the *detector noise* terms. The magenta diamonds mark the points where CPD $\simeq$ CPP. For the elbow points, m_K increases with V, while the magnitude of the points of equality between noise terms decreases with V.

Table 7.13: Elbow points of the graphs depicted in figs. 7.20 and 7.21.

	$t = 20\,\text{ms}$			$t = 30\,\text{s}$		
$V =$	0.1	0.5	1.0	0.1	0.5	1.0
m_K	11.4	11.3	10.8	19.3	19.2	18.7
SNR	0.14	1.8	5.8	0.15	1.9	6.0
N_tot	1.56×10^3	1.71×10^3	2.71×10^3	1.62×10^3	1.77×10^3	2.81×10^3

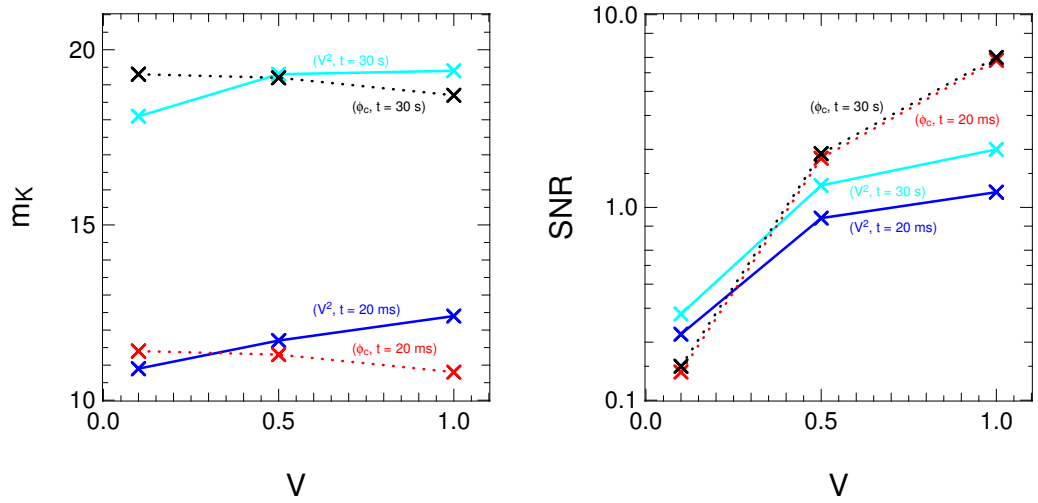

Figure 7.22: K-band magnitudes, m_K, for V^2 and ϕ_c (*left*), and SNR measured on V^2 and ϕ_c (*right*) as a function of the visibility amplitude of the source, V, for integration times equal to 20 ms and 30 s. The curves are calculated for $V = 0.1, 0.5, 1.0$. The K-magnitudes and SNR are measured in the elbow points, *i.e.*, the points where the photon noise terms are approximately equal to the detector noise terms.

For unresolved sources, the value of the magnitude in the K-band from which the statistics starts to become dominated by the photon noise is smaller in the case of the closure phase than in the normalised squared visibility amplitude. This means that, in the *photon noise* regime, brighter unresolved sources are needed to measure the closure phase than to measure the normalised power-spectrum. The situation inverts for resolved sources, *i.e.*, in order to be in the *photon noise* regime, brighter sources are needed for the measurement of V^2 than for the measurement of ϕ_c. This is expected, since for resolved sources less light can be sent to the photometric calibration in order to maximize the SNR on V^2. Both the SNRs measured on V^2 and on ϕ_c increase with the visibility amplitude, but it tends to be lower for the normalised power-spectrum than for the closure phase. For the latter, the SNR in the elbow points is approximately insensitive to the value of the integration time, which indicates that, for the closure phase, the quality of the measurements depends more on the nature of the source (resolved or unresolved) rather than on the integration time.

In the present study of the noise terms for the closure phase, it was assumed that, for a given integration time, the visibility has the same amplitude $V = 1.0$ in each of the three baselines of a given triangle of telescopes, except for the case when the variation of the SNR on ϕ_c with V was analysed.

Concerning τ, in order to determine the phase of the visibility in one baseline, it is necessary to measure the position of the fringes in some reference frame. However, the reading of the phase does not depend on the photometric calibration.In the detector noise regime, when a low number of photons is forming the fringe, it will be difficult to determine its position and, thus, the corresponding error on the phase should be large. In the borderline case when there is no light in the interferometric channel, it would be impossible to measure the phase and, consequently, the error associated to the closure phase should be infinite. These cases characterised by a low number of photons in the interferometric channel and large error bars associated to ϕ_c are not mathematically accounted for in this noise model. The fraction of light selected for photometry at the output of the beam-splitter thus should be taken into account when determining the standard deviation associated with the closure phase, $\sigma(\phi_c)$. As a rough estimate, N_{tot} can be replaced by $(1-\tau)N_{tot}$ in eqs. (7.42) and (7.43). For typical values of τ around 0.1 (table 7.10), the relative error associated with this substitution is less than 6 %, which does not affect significantly the results.

SNR on ϕ_c *vs* V

Figure 7.23 illustrates the variation of the SNR measured on the closure phase with the visibility amplitude. The SNR is defined as the inverse of the standard deviation of ϕ_c, *i.e.*, it is calculated for a standard angle of 1 rad.

In all test cases, the SNR measured on ϕ_c increases with V, which implies that the SNR on ϕ_c decreases towards more resolved sources.

In the *detection* scenario (blue dashed-dotted curve), an elbow point is present. The slope of the red dotted curve corresponding to the *photon starved* case is steeper than the slope of the green

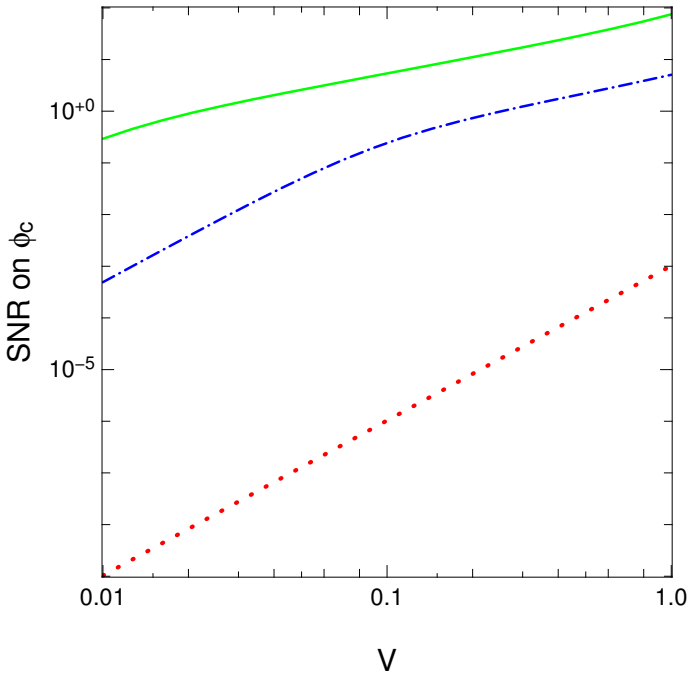

Figure 7.23: SNR measured on ϕ_c *vs* V. The green solid curve corresponds to the *photon rich* case, the blue dashed-dotted curve to the *detection* case and the red dotted curve to the *photon starved* case.

solid curve representing the *photon rich* case, although the SNR in the former is meaningless. This happens because the SNR on ϕ_c is more sensitive to visibility amplitude variations in a regime of a low number of photons. The SNR increases rapidly towards unresolved sources, as it is expectable to be easier to read the phase when V is close to 1, because the fringe is brighter and sharper.

The curve for the *photon rich* scenario crosses the line $\mathrm{SNR}_{\phi_c} = 1.0$ approximately for $V = 0.02$ and the SNR on ϕ_c is approximately equal to 5.4 for $V = 0.1$. Thus, good SNRs are achievable both for resolved and unresolved sources in this noise scenario. In the *detection* case, SNRs above 1.0 are attainable for amplitudes $V \gtrsim 0.25$ but the former does not overtake the value 5.1.

In fig. 7.24 it was plotted the SNR on ϕ_c and $1/\sqrt{3}$ of the SNR on V^2 to compare the behaviour of this noise model with the one predicted by the Simple noise model in eq. (7.36).[16] Clearly, according to É. Tatulli and Chelli, (2005) noise model, the equality between the SNR measured on ϕ_c and the SNR measured on V^2 rely on the magnitude of the source and on the visibility amplitude. For instance, in the *detection* scenario, the match happens for $V \simeq 0.04$. But it is fair to conclude the equality roughly holds in the *photon rich* and in the *detection* scenarios.

SNR on ϕ_c *vs* N_{tel}

In fig. 7.25 it is illustrated the variation of the SNR on ϕ_c with the number of telescopes used for the interferometric observations, which was varied from 1 to 20. There are two distinct behaviours of the curves according to whether the statistics are dominated by the photon or the detector noise terms, represented respectively by eqs. (7.42) and (7.43). When in the *photon noise* regime, the SNR measured on the closure phase decays with N_{tel}, while in the *detector noise* regime, the SNR

[16] The plot is done just for testing purposes, since É. Tatulli and Chelli, (2005) noise model estimates the statistics of the normalised power-spectrum, not of the visibility amplitude, as it is predicted by eq. (7.36).

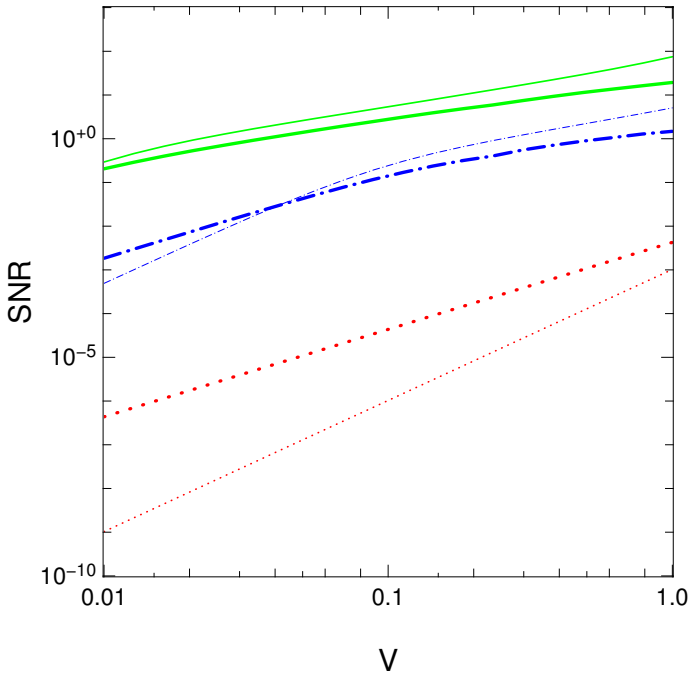

Figure 7.24: SNR measured on ϕ_c (thick lines) and $1/\sqrt{3}$ of the SNR measured on V^2 (thin lines) *vs* V.

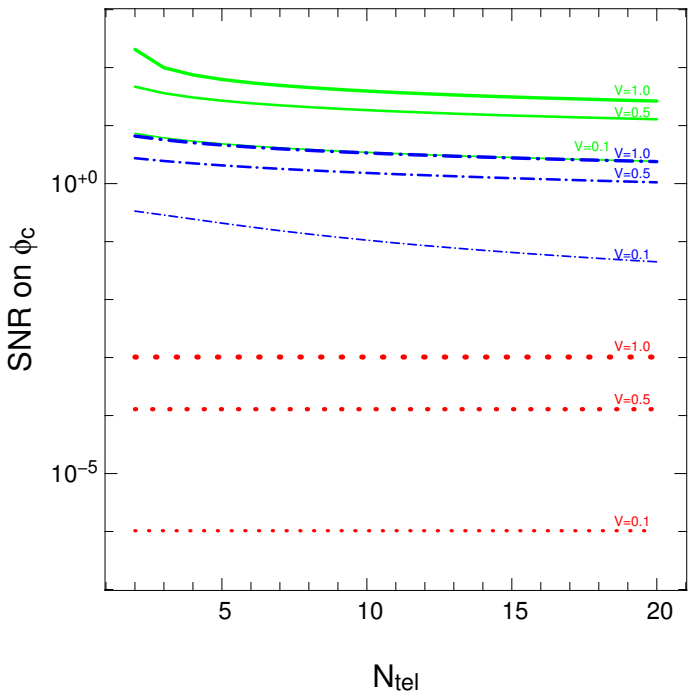

Figure 7.25: SNR measured on ϕ_c *vs* N_{tel}. The green solid curves correspond to the *photon rich* case, the blue dashed-dotted curves to the *detection* case and the red dotted curves to the *photon starved* case. In each scenario, the visibility is increasing from the thinner to the thicker lines.

remains constant with the number of telescopes. The behaviour in the latter is expected because if it is the detector that dominates the statistics, increasing the number of telescopes does not affect the SNR. The behaviour in the former can be understood combining eqs. (7.42) and (7.43) in the *detection* scenario ($m_K = 11.0$), while replacing all quantities by the values of table 7.12 and leaving N_{tel} as the free parameter. After simplification, for an unresolved source, the SNR on the closure phase becomes:

$$\{\text{SNR on } \phi_c\}_{V=1.0} \simeq \frac{11.6}{\sqrt{1+1.04N_{tel}}}. \tag{7.50}$$

When a resolved source is considered ($V = 0.1$), eq. (7.41) reduces to:

$$\{\text{SNR on } \phi_c\}_{V=0.1} \simeq \frac{0.42}{\sqrt{1+0.14N_{tel}\left(1+\frac{N_{tel}}{2.5}+\frac{N_{tel}^2}{18.1}\right)}}. \tag{7.51}$$

The CPD and CPP terms that lead to eq. (7.50) are:

$$\begin{aligned} \mathsf{CPD} = &\quad 0.021 \\ \mathsf{CPP} = &\quad -0.013 + \quad 0.007\,7N_{tel} + \quad 3.0\times10^{-5}N_{tel}^2 + \quad 4.4\times10^{-8}N_{tel}^3, \end{aligned} \tag{7.52}$$

while for eq. (7.51) these terms become:

$$\begin{aligned} \mathsf{CPD} = &\quad 5.4 \\ \mathsf{CPP} = &\quad 0.29 + \quad 0.82N_{tel} + \quad 0.32N_{tel}^2 + \quad 0.044N_{tel}^3. \end{aligned} \tag{7.53}$$

Equations (7.52) and (7.53) are plotted in fig. 7.26. Since no photometric calibration is necessary for the determination of the closure phase, the detector noise term remains constant with the number of telescopes in both resolved and unresolved cases. For unresolved sources, the CPD and CPP terms become equal when 4 telescopes are combined, while for resolved objects, the aforementioned terms attain the same magnitude for 3 telescopes. Therefore, in the condition of the present study and according to this noise model, 4 is the number of telescopes that marks the transition between the *detector noise* and the *photon noise* regimes, and, thus, from which the noise becomes dominated by the photon terms.

Figure 7.27 illustrates the evolution of the CPP and CPD terms when the visibility in one baseline of the triangle of telescopes is varied, while the other two visibilities remain constant and equal to 1.0. The dashed-double-dotted curves represent the CPP terms and the dotted ones the CPD terms. The $V = 1.0$ case is represented by the black solid and dashed lines. As expected, the noise increases as the visibility in the third baseline varies from 1.0 to 0.1.

SNR on ϕ_c *vs* t

The behaviour of the SNR measured on ϕ_c with the integration time is plotted in fig. 7.28.

For all test cases, the SNR notably increases with the integration time. The *detector noise* and *photon noise* regimes are identifiable by the two groups of slopes in the curves: a steeper one,

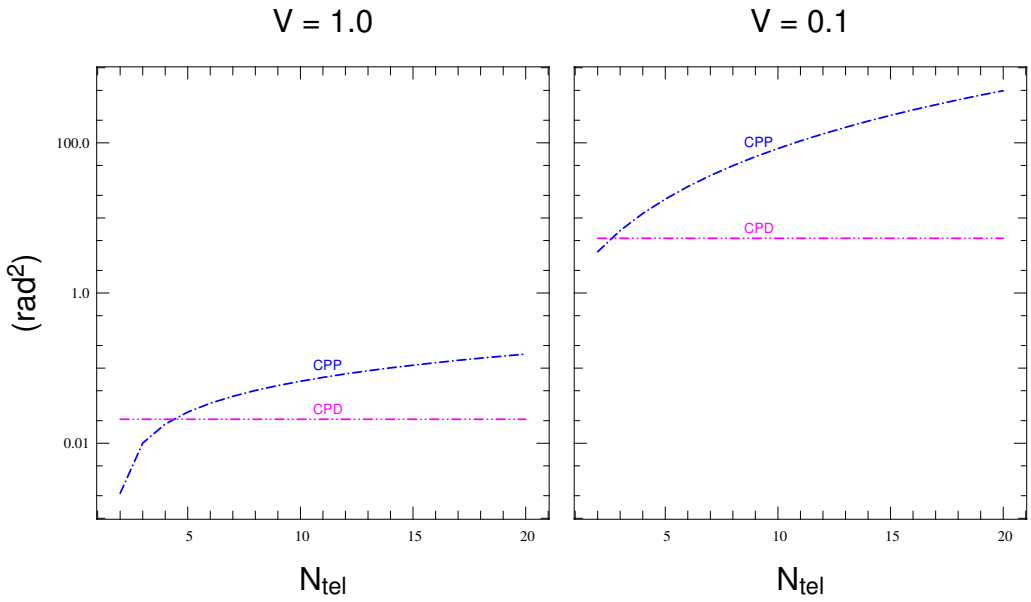

Figure 7.26: Terms CPP (*blue dashed-dotted curve*) and CPD (*magenta dashed-double-dotted curve*) of eqs. (7.42) and (7.43) *vs* $N_{\rm tel}$. The curves correspond to points calculated using the quantities of tables 7.12 and 7.13 in two cases: $V = 1.0$ (*left*) and $V = 0.1$ (*right*).

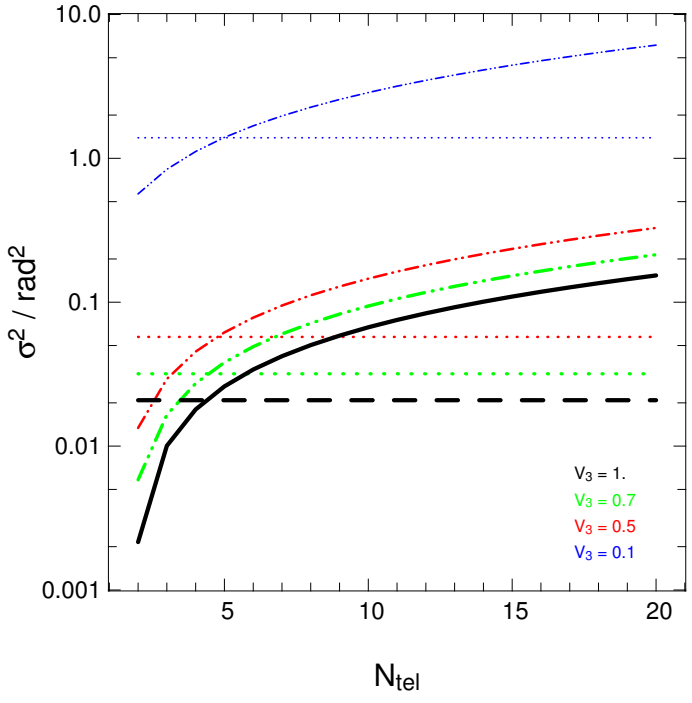

Figure 7.27: Terms CPD (*dashed-double-dotted curves*) and CPP (*dotted curves*) of eqs. (7.42) and (7.43) *vs* $N_{\rm tel}$, when the visibility in one of the baselines is changing while the other two remain constant and equal to 1.0. The black solid and dashed curves represent the case when all visibilities are equal to 1.0. The CPP and CPD terms are measured in rad^2.

corresponding to the former, which is visible to the left of the elbow points in the red dotted curves and blue dashed-dotted curves, and a less steeper slope, corresponding to the latter.

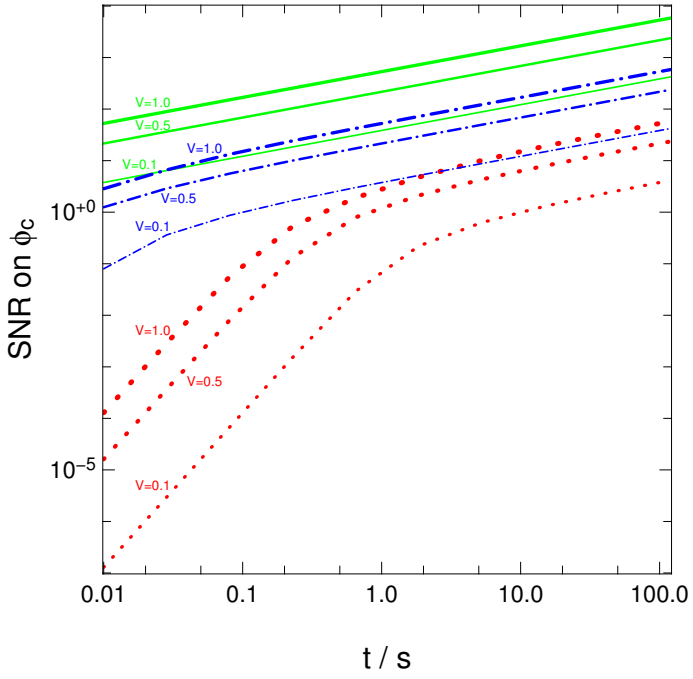

Figure 7.28: SNR measured on ϕ_c *vs* $t \in [0.01, 120.0]$s. The green solid curves correspond to the *photon rich* case, the blue dashed-dotted curves to the *detection* case and the red dotted curves to the *photon starved* case. In each scenario, the visibility is increasing from the thinner to the thicker lines.

The rapid increase of the *detector noise* regime reflects the sensitiveness of the SNR on ϕ_c with the integration time for faint sources. Although the values of SNR are too low in this case, increasing the integration time by a few hundreds of milliseconds results in an improvement of the SNR by two or three orders of magnitude.

Most of the points of the curves tagged as belonging to the *detection* case belong, in fact, to the *photon rich* scenario, as well as part of the points of the curves labelled as belonging to the *photon starved* case. In the *detection* scenario (blue dashed-dotted curves), the elbow point is observed after a few tens of milliseconds, while in the *photon starved* case (red dotted curves), depending on the visibility of the source, the *photon noise* regime can be achieved after a few hundreds of milliseconds or, at most after a few seconds of integration time. An unresolved source in the *photon starved* case attains higher values of SNR than a resolved object in the *detection* case after nearly 2.7 s of integration time, although both situations are in the *photon noise* branch. A similar situation happens between the *detection* and *photon rich* cases after an integration of about 26 ms. Therefore, independently of the test case, the *photon noise* regime is attainable from integration times of the order of the second.

Varying the integration time from 10 ms to 1 s can increase the magnitude of the SNR approximately 600 000 times for resolved sources and 20 000 times for unresolved objects in the *photon starved* scenario, about 50 times for resolved sources and 20 times for unresolved objects in the *detection* case, and around 100 times in the *photon rich* scenario. Similarly to the V^2 case, these results point to the necessity of providing interferometers with efficient fringe trackers in order to maximize the SNR during observations.

SNR on ϕ_c *vs* $\mathscr{E}$

In fig. 7.29 is illustrated the variation of the SNR measured on the closure phase with the total efficiency (throughput) of the interferometer.

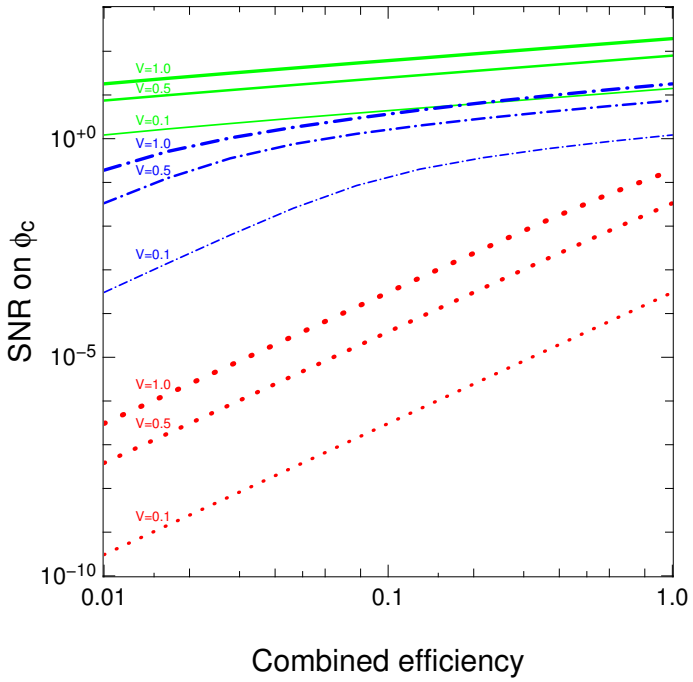

Figure 7.29: SNR measured on ϕ_c *vs* $\mathscr{E}$. The colour and shape of the curves have the same meaning as in fig. 7.28.

In all test cases, the SNR measured on the closure phase increases with the combined efficiency of the interferometer. The *detection* case (blue dashed-dotted lines) exhibits elbow points, marking the transition between the *photon noise* and the *detector noise* regimes. The latter is characterized by steeper increasing curves (red dotted lines and blue dashed-dotted lines to the left of the elbow points), while the former is identifiable by the less inclined straight curves (green solid and blue dashed-dotted lines to the right of the elbow points).

For $\mathscr{E} \gtrsim 19\,\%$, the curve corresponding to the $V = 1.0$ case in the *detection* scenario corresponds to a larger SNR than the $V = 0.1$ case in the *photon rich* scenario, indicating that it is possible to achieve larger SNRs for greater magnitudes if the source is unresolved. A visibility amplitude V close to 1 can be achieved, for instance, by selecting shorter baselines for the observation.

In the conditions of the present study, an efficiency $\mathscr{E} \gtrsim 15\,\%$ assures that, in the *detection* scenario, the CPP terms have larger magnitudes than the CPD ones. Varying $\mathscr{E}$ from 10 % to 20 % increases the SNR approximately by 1.3 and 7 times, respectively in the *photon rich/detection* and *photon starved* cases. Therefore, the combined efficiency of the interferometer only becomes an important parameter for the quality of the SNR in the *detector noise* regime.

SNR on ϕ_c *vs* $\mathscr{S}$

Figure 7.30a illustrates the behaviour of the SNR measured on ϕ_c with the average Strehl ratio, $\mathscr{S}$. The SNR increases with $\mathscr{S}$ in all test cases. Both *photon rich* and *photon starved* cases enter

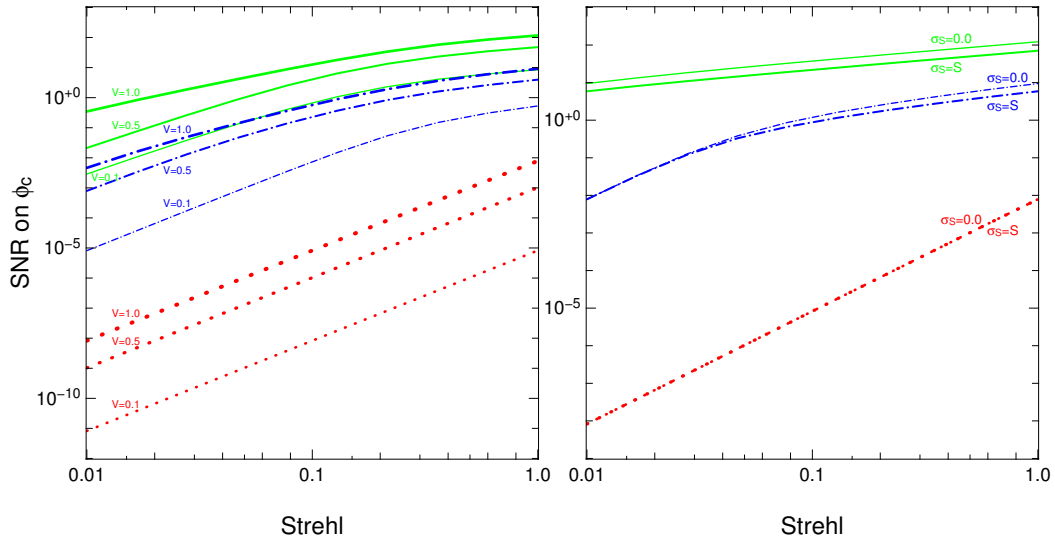

(a) SNR on ϕ_c *vs* $\mathscr{S}$. **(b)** SNR on ϕ_c *vs* $\mathscr{S}$ for $\sigma_{\mathscr{S}} = 0.0$ and $\sigma_{\mathscr{S}} = \mathscr{S}$.

Figure 7.30: (*a*) SNR on ϕ_c *vs* $\mathscr{S}$. The colour and shape of the curves have the same meaning as in fig. 7.29. (*b*) SNR on ϕ_c *vs* $\mathscr{S}$ for a pure turbulent case (lower curves, $\sigma_{\mathscr{S}} = \mathscr{S}$) and perfect AO correction (upper curves, $\sigma_{\mathscr{S}} = 0.0$). The colour and shape of the curves have the same meaning as in fig. 7.30a, although only the case $V = 1.0$ is illustrated.

the domain of the *photon noise* regime, *i.e.*, when the CPP term becomes larger than the CPD one, only for $\mathscr{S} \gtrsim 20\,\%$; hence, at least some level of AO correction is needed in order to achieve a good SNR in an interferometric observation.

In the *detection* and *photon rich* scenarios, increasing $\mathscr{S}$ from 0.1 to 0.5 fosters the SNR by roughly 8 and 7 times, respectively.[17] For an unresolved source, in the *detection* scenario, the improvement in the SNR is nearly equal to a factor of 30 for the same increase of $\mathscr{S}$.

Up to $\mathscr{S} \simeq 5\,\%$ and after $\mathscr{S} \simeq 65\,\%$, the SNR for an unresolved source in the *detection* case (blue dashed-dotted curve at the top) is larger than the SNR for a resolved object in the *photon rich* case (green solid line at the bottom).

In fig. 7.30b is depicted the evolution of the SNR on ϕ_c with $\mathscr{S}$ for an unresolved source in the case of a pure turbulent ($\sigma_{\mathscr{S}} = \mathscr{S}$) and a fully AO corrected ($\sigma_{\mathscr{S}} = 0.0$) observation.

Reducing $\sigma_{\mathscr{S}}$ brings an improvement in the SNR only when the *photon noise* regime is reached, *i.e.*, after $CPP > CPD$. In the *photon rich* case, the SNR increases by 1.8 times for a perfect corrected wave-front, while in the *detection* case, the enhancement of the SNR is about 1.8 times under the same conditions; thus, according to this noise model, the Strehl ratio error is not a fundamental parameter for the SNR measured on the closure phase.

SNR on ϕ_c *vs* N_{pix}

The number of pixels in the detector used to sample the coherent part of the flux, is a parameter affecting only the detector noise regime. The behaviour of the SNR measured on ϕ_c with N_{pix} is illustrated in fig. 7.31a.

[17] The *photon starved* case presents too low SNRs to be considered relevant.

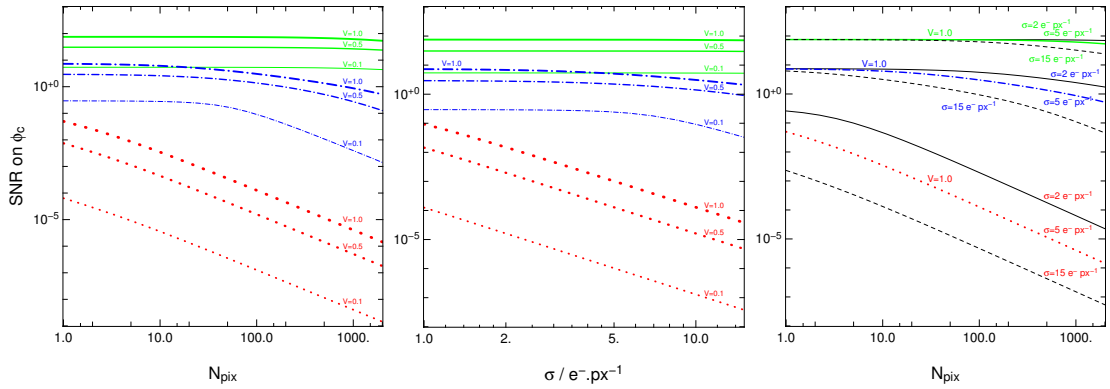

(a) SNR on ϕ_c *vs* N_{pix}. **(b)** SNR on ϕ_c *vs* σ. **(c)** SNR on ϕ_c *vs* N_{pix} for $\sigma = 2, 5, 15\,e^-\,px^{-1}$.

Figure 7.31: SNR on ϕ_c *vs* the number of pixels in the detector used to sample the interferometric signal, N_{pix} (*left*), *vs* the RON of the detector, σ (*centre*), and *vs* N_{pix} for three values of σ (*right*). In figs. 7.31a and 7.31c, $N_{pix} = \overline{1,2000}$, and in fig. 7.31b, $\sigma = \overline{1,15}\ e^-\ px^{-1}$. The green solid curves correspond to the *photon rich* scenario, the blue dashed-dotted curves to the *detection* scenario and the red dotted curves to the *photon starved* scenario. In figs. 7.31a and 7.31b, in each test case, the visibility is increasing from the thinner to the thicker lines. In fig. 7.31c, the black solid lines correspond to $\sigma = 2\,e^-\,px^{-1}$, the black dashed lines to $\sigma = 15\,e^-\,px^{-1}$ and the central colourful curves to $\sigma = 5\,e^-\,px^{-1}$.

In the *photon starved* case, the SNR decreases with N_{pix}. The SNR remains constant in the *photon rich* case, since the noise is dominated by the Poisson statistics and the number of pixels only affects the *detector noise* regime. When the CPD term overtakes CPP in magnitude, the SNR on ϕ_c decays rapidly. Adding 100 px for the sampling of the signal reduces the SNR approximately by a factor of 3 in the *photon starved* case (red dotted curves) and by a factor of 2 in the *detector noise* regime of the *detection* case (blue dashed-dotted lines to the right of the elbow points).[18]

SNR on ϕ_c *vs* σ

The RON is also uniquely related to the *detector noise* regime. The impact of the RON in the SNR is illustrated in fig. 7.31b, where σ was varied between 1 and $15\,e^-\,px^{-1}$. The plot is very similar to fig. 7.31a, exhibiting the same behaviour between unresolved sources in the *detection* case and resolved ones in the *photon rich* case. In the *detector noise* regime (red dotted curves and blue dashed-dotted lines to the right of the elbow), the SNR on ϕ_c decreases with σ, remaining constant in the *photon noise* regime (green solid lines and blue dashed-dotted curves to the left of the elbow), as the RON is a characteristic of the detector, not depending on the number of photons striking it. In the *photon rich* case (green solid lines) the noise is dominated by the Poisson statistics and, therefore, it is not affected by σ. The elbow, typical of the *detection* case, occurs around $\sigma = 6\,e^-\,px^{-1}$.

Figure 7.31c, which results from the combination of the previous two plots in the case of an unresolved source, illustrates the impact of the RON in the SNR measured on ϕ_c when the number of pixels in the detector is varied. The SNR measured on ϕ_c becomes more sensitive to the RON when the magnitude of the source increases. The *photon rich* case is insensitive to the RON up to

[18] The *detection* is characterised by too low SNRs to be meaningful.

about 75 px, while the *detection* case becomes visibly affected by the RON around 10 px and, in the *photon starved* case, the difference between the quality of the signal is larger than 2 orders of magnitude when comparing a $\sigma = 2\,e^-\,px^{-1}$ and a $\sigma = 15\,e^-\,px^{-1}$ detector.

Figure 7.31 points to the need of efficient detectors, especially for the observation of faint sources.

Tatulli et al. 2010 noise model for ϕ

É. Tatulli, Blind et al., (2010) introduce an estimator for the noise of the phase of the complex visibility. The phase error encompasses the photon, detector and atmospheric noises (already described in section 7.5.3) and it is computed for multi and single-mode interferometry. Similarly to section 7.5.3, only the single-mode case is analysed and the atmospheric noise is neglected (it is assumed that the sources are not resolved by a single telescope).

The model estimates the standard deviation of the visibility phase in a single baseline, joining two identical telescopes, described by the same pupil function, *i.e.*, with the same collecting area, but with different transmissions. It is taken into account the *Residual phase variance* in each telescope,[19] $\sigma^2_{\phi_r}$, which arises from an imperfect AO correction. For the first three corrected Zernike modes (piston and tip/tilt corrections), $\sigma^2_{\phi_r}$ has the form (Noll, 1976):

$$\sigma^2_{\phi_r} = 0.134 \left(\frac{D}{r_0}\right)^{5/3} \left[\text{rad}^2\right], \tag{7.54}$$

where D is the diameter of a single aperture and r_0 is the *Fried parameter*[20] The current study of the variables on which $\sigma(\phi)$ depends was performed simulating some typical conditions at the VLTI. Therefore, two AT telescopes were considered and the Fried parameter was estimated for the K-band by scaling the value of r_0 from $\lambda = 500\,\text{nm}$ to $\lambda = 2.2\,\text{nm}$. From Martin et al., (2000),

$$r_0(\lambda) = 0.98 \cdot \frac{\lambda}{\varepsilon}, \tag{7.55}$$

where $\varepsilon = 0.87''$ is the average *seeing* at Paranal ESO Observatory (Chile). Therefore, in the K-band ($\lambda = 2.179\,\mu\text{m}$), $r_0 = 0.68\,\text{m}$ and the corresponding *coherent energy associated to the Strehl ratio* is

$$e^{-\sigma^2_{\phi_r}} \simeq 51\,\%. \tag{7.56}$$

The first three corrected Zernike modes are concordant with the tip-tilt correction performed by the STRAP heads used in the ATs (Bonaccini et al., 1998).

[19] Also known as *Zernike-Kolmogoroff residual error* or *variance of the phase aberration across the pupil*.
[20] The Fried parameter is the size of an aperture over which the mean-square wavefront error is 1 rad^2).

Table 7.14: Quantities on which depend the statistics of the visibility amplitude, ϕ, in É. Tatulli, Blind et al., (2010) noise model.

Symbol	Name	Description and Observations
N_{phot}	Number of photons	Number of incoming photons in each aperture.
m_λ	Magnitude of the source	For the calculation of N_{phot} (not explicitly used in the noise model).
t	Integration time	For the calculation of N_{phot} (not explicitly used in the noise model). [s]
$\mathscr{E}$	Efficiency	Combined efficiency of the instrument and the observatory. For the calculation of N_{phot} (not explicitly used in the noise model).
V	Visibility	Visibility of the source.
$\mathscr{S}$	Long exposure Strehl ratio	
$\sigma^2_{\phi_r}$	Variance of the residual phase	In a single telescope.
ρ_0	Optimal coupling coefficient	Fixed by the fibre core design.
$\mathscr{T}_i$	Transmission in telescope i	Assumed to be 1.
N_{pix}	Number of pixels	Number of pixels in the detector used to sample the interferometric signal.
σ	Readout noise of the detector	$[\frac{e^-}{\text{px}}]$

The quantities on which the standard deviation of the visibility phase depends are compiled in table 7.14. The number of photons is determined by eq. (7.22).

Equations for the statistics of the observables

According to this noise model, the standard deviation of the visibility phase is given by

$$\sigma(\phi) = \sqrt{\mathsf{PP} + \mathsf{PD}}, \tag{7.57}$$

where PP represents the *variance of the residual phase in the photon regime of noise* and PD corresponds to the *variance of the residual phase in the detector noise regime*.[21] The PP and PD terms are respectively given by:[22]

$$\mathsf{PP} = \frac{\mathscr{S}}{\rho_0\, e^{-2\sigma^2_{\phi_r}} V^2 N_{\text{phot}}} \tag{7.58}$$

$$\mathsf{PD} = \frac{1}{2}\,\frac{N_{\text{pix}}\,\sigma^2}{\rho_0^2\, e^{-2\sigma^2_{\phi_r}} V^2 N^2_{\text{phot}}}. \tag{7.59}$$

[21] The atmospheric terms were disregarded, as mentioned before.

[22] Although the model takes into account different transmissions in the telescopes, it is assumed that $\mathscr{T}_1 = \mathscr{T}_2 = 1$ because the transmission is already included in the determination of N_{phot}.

Dependence of the SNR measured on ϕ upon the variables

This subsection concerns the analysis of the behaviour of the SNR measured on the visibility phase, ϕ, with the parameters on which it depends, in the *photon rich*, *photon starved* and *detection* cases. The values assumed for the quantities in all test cases are compiled in table 7.15.

Table 7.15: Values of the parameters used for the study of the dependence of the SNR measured on ϕ on the variables.

Test case	m_{K}	V	t (ms)	$\mathscr{E}$	$\mathscr{A}$ (m^2)	$\mathscr{S}$	$\sigma^2_{\phi_{\mathrm{r}}}$	ρ_0	N_{pix}	σ (e^- px^{-1})
Photon Rich	6.0	See								
Detection	11.0	Tab.	20	0.15	2.53	0.5	0.81	0.8	24	5.0
Photon Starved	16.0	7.16								

The magnitudes in each test case were chosen in order that the terms PD and PP obey to the following relations:

- **Photon Starved case:** PP $\ll$ PD;
- **Detection case:** PP $\simeq$ PD;
- **Photon Rich case:** PP $\gg$ PD.

As in sections 7.5.3.2 and 7.5.3.3, the magnitude for the *detection* case was determined by searching for the elbow points in the plots of the SNR measured on ϕ *vs* m_{K} and the SNR on ϕ *vs* the number of photons in each aperture, N_{phot} (*cf.* table 7.16 and fig. 7.32). The elbow points indicate the values of the parameters where the terms PP and PD of eq. (7.57) have identical magnitudes. Contrary to the closure phase case, the elbow points do not depend on the visibility amplitude, *i.e.*, for a given integration time, the magnitude where CP $\simeq$ CD is the same regardless V. Nevertheless, the position of the elbow points depends on the integration time. It was adopted the value $m_{\mathrm{K}} = 10.7$ ($t = 20\,\mathrm{ms}$).

The values for the remainder of the parameters were chosen according to the criteria presented in sections 7.5.3.2 and 7.5.3.3.

As in the model for the statistics of the closure phase, this noise model does not take into account the effects of the fraction of light selected for photometry.

SNR on ϕ *vs* V

In fig. 7.33, it is represented the variation of the SNR measured on ϕ with V. The SNR is

Table 7.16: Elbow points of the graphs depicted in fig. 7.32.

	$t = 20\,\mathrm{ms}$			$t = 30\,\mathrm{s}$		
$V =$	0.1	0.5	1.0	0.1	0.5	1.0
m_{K}	10.7	10.7	10.7	18.6	18.6	18.6
SNR	24.0	12.0	2.4	25.0	12.6	2.5
N_{phot}	7.42×10^2	7.42×10^2	7.42×10^2	7.70×10^2	7.70×10^2	7.70×10^2

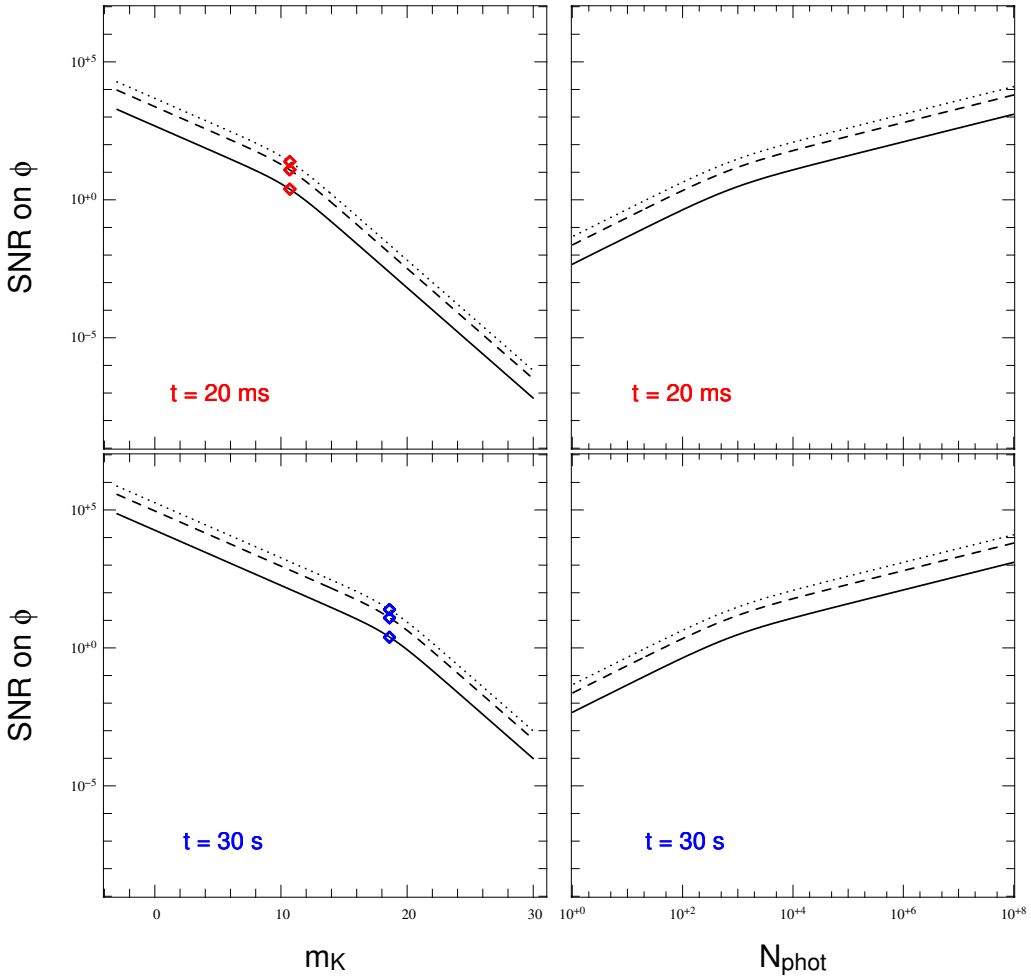

Figure 7.32: SNR measured on ϕ as a function of m_{K} (*left*), and SNR on ϕ as a function of the number of photons captured by a single aperture, N_{phot} (*right*), for integrations times equal to 20 ms (*top*) and 30 s (*bottom*). The curves are calculated for different visibility amplitudes: $V = 0.1$ (solid line), $V = 0.5$ (dashed line) and $V = 1.0$ (dotted line). The diamonds mark the points where CP $\simeq$ CD. The elbow points depend only on the total number of photons reaching the detector, not on the visibility amplitude.

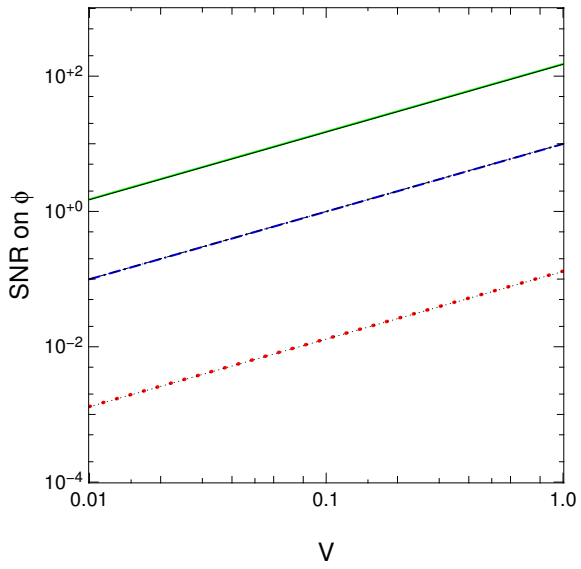

Figure 7.33: SNR measured on ϕ *vs* V. The green solid curve corresponds to the *photon rich* case, the blue dashed-dotted curve to the *detection* case and the red dotted curve to the *photon starved* case. The thin black curves represent the SNR on ϕ computed from the *Simple* noise model. $\eta =$ 0.017, 0.5, 50, respectively in the solid, dashed-dotted and dotted curves.

defined for a standard angle of 1 rad.

In all test cases, the SNR measured on ϕ monotonically increases with the visibility amplitude. Contrary to the closure phase case, the SNR on ϕ against V does not exhibit elbow points, indicating that there is no significant difference between the behaviour in the *photon noise* and the *detector noise* regimes, as expected from eqs. (7.58) and (7.59) In the *photon rich* scenario (green solid curve), the SNRs is always above 1, reaching a value around 150 for unresolved sources. The *detection* case (blue dashed-dotted curve) reaches SNRs above unity for $V \gtrsim 0.1$, thus starting with visibility amplitudes corresponding to unresolved sources. In the *photon starved* scenario (red dotted curve), the SNR is meaningless.

For comparison purposes, the SNR on ϕ computed from the *Simple* noise model (section 7.5.1, page 131) was over-plotted in the three aforementioned test cases (black thin curves). The SNR factor was chosen in order to have a match of the SNR for an unresolved source. There is a very good agreement between both noise models, being the difference between the SNR on ϕ always around or less than 1 %. This result supports the validity of the *Simple* noise model as a good estimator for the error on the phase.

SNR on ϕ *vs* t

Figure 7.34 illustrates the behaviour of the variation of the SNR measured on ϕ with the total integration time, which was varied between 10 ms and 2 min. In all test scenarios, the SNR

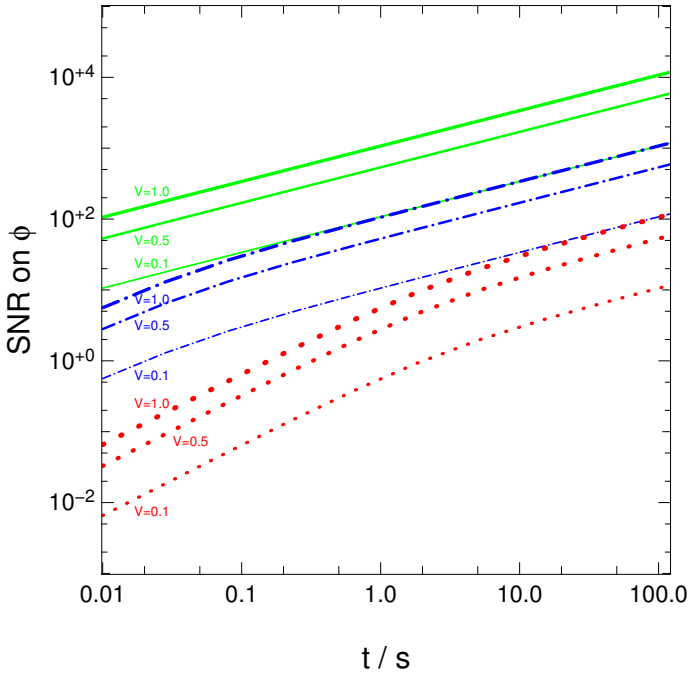

Figure 7.34: SNR measured on ϕ *vs* $t \in [0.01, 120]$ s. The green solid curves corresponds to the *photon rich* case, the blue dashed-dotted curves to the *detection* case and the red dotted curves to the *photon starved* case. In each scenario, the visibility amplitude increases from the thinner to the thicker lines.

increases with the integration time. The *photon noise* and *detector noise* regimes are identifiable in the *photon starved* and *detection* cases, respectively to the left and to the right of the elbow points present in the two test scenarios. While in the *photon starved* case, the elbow points correspond to

integration times of about 1 s, in the *detection* scenario the *photon noise* regime is achieved after about 50 ms. In all cases, to the *photon noise* regime corresponds an SNR on ϕ greater than 1.

Due to the increasing of the SNR on ϕ with the visibility amplitude, eventually some curves belonging to different test scenarios end up overlapping — a resolved source in the *photon rich* scenario and an unresolved object in the *detection* case in the *photon noise* branch, and a resolved source in the *detection* case and a unresolved object in the *photon starved* scenario.

Varying the integration time from 10 ms to 1 s increases the SNR by approximately 85 times in the *photon starved* case, by about 20 times in the *detection* case and by nearly 10 times in the *photon rich* scenario. Hence, as for V^2 and ϕ_c, efficient fringe trackers, allowing integration times of the order of the second, can push the SNR significantly forward.

SNR on ϕ *vs* $\mathscr{E}$

Figure 7.35 depicts the variation of the SNR measured on ϕ with the total efficiency of the interferometer.

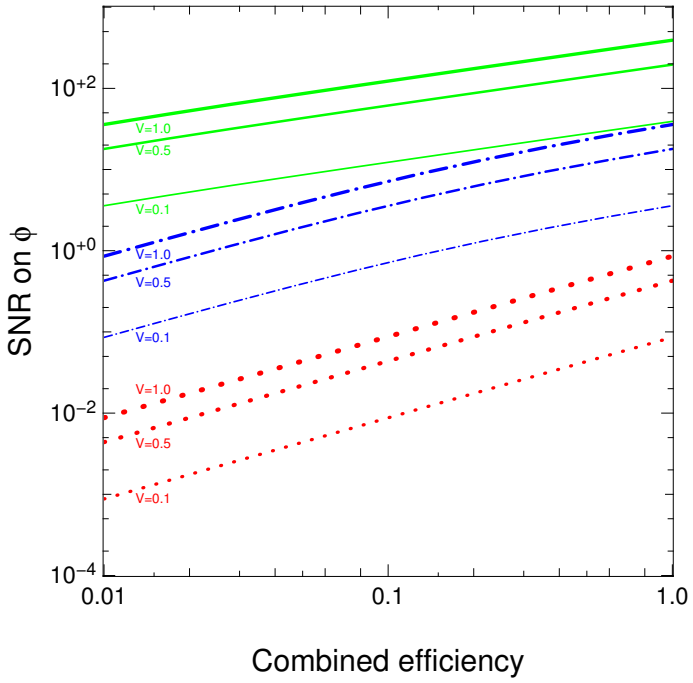

Figure 7.35: SNR measured on ϕ *vs* $\mathscr{E}$. The curves have the same meaning as in fig. 7.34.

In all test cases, the SNR measured on ϕ increases with the total efficiency of the interferometer. The transition between the *photon noise* and the *detector noise* regimes occurs in the *detection* scenario, for efficiencies around 10 %. The *photon rich* scenario is characterised by SNRs always above unity, reaching values as high as 120 and 60 respectively for unresolved and resolved sources when $\mathscr{E} = 10\,\%$, and respectively 174 and 17.5 when $\mathscr{E} = 20\,\%$. Varying $\mathscr{E}$ from 10 % to 20 % increases the SNR on ϕ by approximately 2 times in the *detection* and *photon starved* scenarios.

SNR on ϕ *vs* $\mathscr{S}$

Concerning the analysis of the impact of the average Strehl ratio on the SNR measured on ϕ, the *Maréchal approximation* (Born and E. Wolf, 2003; Brummelaar, Bagnuolo and Ridgway, 1995; Davies and Kasper, 2012) was used:

$$\mathscr{S} \simeq e^{-\sigma^2_{\phi_r}}. \tag{7.60}$$

Thus, eqs. (7.58) and (7.59) become:

$$\mathrm{PD} = \frac{1}{2}\frac{N_{\mathrm{pix}}\,\sigma^2}{\rho_0^2\,\mathscr{S}^2 V^2 N^2_{\mathrm{phot}}}. \tag{7.61}$$

$$\mathrm{PP} = \frac{1}{\rho_0\,\mathscr{S} V^2 N_{\mathrm{phot}}} \tag{7.62}$$

In fig. 7.36 it is represented the evolution of the SNR measured on ϕ with the average Strehl ratio. As expected, the SNR on ϕ increases with $\mathscr{S}$.

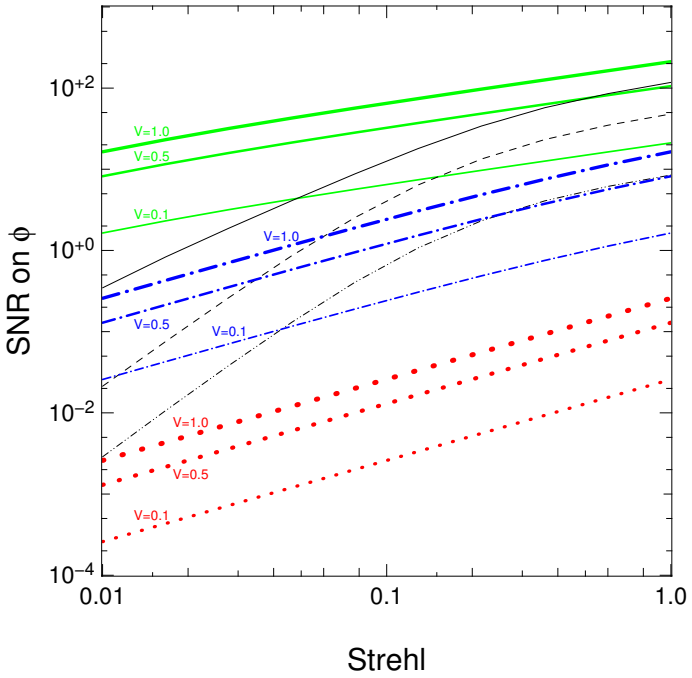

Figure 7.36: SNR measured on ϕ *vs* $\mathscr{S}$. The curves have the same meaning as in fig. 7.34. The black solid, dashed and dashed-double-dotted lines correspond respectively to the unresolved, partially resolved and resolved cases in the *photon rich* scenario for the closure phase.

In the *photon starved* case, the SNR on ϕ is meaningless and, therefore, it is disregarded in this analysis. The *photon rich* scenario exhibits a slight elbow point for $\mathscr{S} \sim 5\,\%$, indicating that the difference in SNR behaviour between the *photon noise* and *detector noise* regimes is unimportant. The SNR is always above unity, reaching values around 210 and 21, respectively for unresolved and resolved sources, when the Strehl ratio is equal to 100 %. For $\mathscr{S} = 50\,\%$, the SNR on ϕ is approximately equal to 150 and 15 respectively for $V = 1.0$ and $V = 0.1$. The curves representing the unresolved, partially resolved and resolved cases of the *photon rich* scenario for the closure phase were over-plotted in the graph of fig. 7.36 (thin black solid, dashed and dashed-double-dotted lines, respectively). Typically, the SNR on ϕ is greater than the SNR on ϕ_c. The visibility

phase exhibits a much better performance than the closure phase, in terms of SNR, when the AO correction is poor. For a high Strehl, the difference is not as large as in the previous case, but the SNR on ϕ is always greater than the SNR on ϕ_c by a factor that varies between 2 and 2.6 (it is larger for resolved sources).

The *detection* case presents values of SNR on ϕ above unity for $\mathscr{S} \gtrsim 4\,\%, 8\,\%$ and $50\,\%$ respectively for unresolved, partially resolved and resolved objects. This results indicates that, under the conditions of the current study, at least tip-tilt correction is necessary for observations of good quality for all kind of sources (resolved and unresolved).

SNR on ϕ *vs* N_{pix}

The behaviour of the SNR measured on ϕ with N_{pix} is illustrated in fig. 7.37a. N_{pix} is ranging from 1 to 2 000 px.[23]

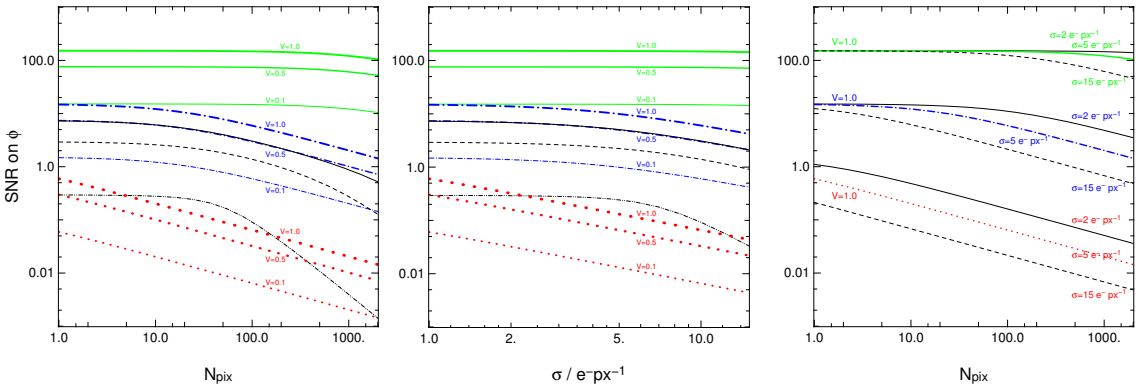

(a) SNR on ϕ *vs* N_{pix}. **(b)** SNR on ϕ *vs* σ. **(c)** SNR on ϕ *vs* N_{pix} for $\sigma = 2, 5, 15\,\text{e}^-\,\text{px}^{-1}$.

Figure 7.37: (*a*) SNR measured on ϕ *vs* $N_{\text{pix}} = 1, 2, \ldots, 2000$. (*b*) SNR on ϕ *vs* the RON of the detector, $\sigma = 1, 2, \ldots, 15\,\text{e}^-\,\text{px}^{-1}$. (*c*) SNR on ϕ *vs* N_{pix} for three values of σ. The curves have the same meaning as in fig. 7.34. In each scenario, the visibility amplitude increases from the thinner to the thicker lines. In figs. 7.37a and 7.37b, the thin black lines represent the SNR on ϕ_c in the *detection* case, while in fig. 7.37c the black solid lines correspond to $\sigma = 2\,\text{e}^-\,\text{px}^{-1}$, the black dashed lines to $\sigma = 15\,\text{e}^-\,\text{px}^{-1}$ and the central colourful curves to $\sigma = 5\,\text{e}^-\,\text{px}^{-1}$.

In all test cases, the SNR on ϕ decreases with N_{pix}. In the *photon rich* scenario (green solid curves), the SNR remains constant in the *photon noise* regime up to the elbow point, since the number of pixels is not a parameter affecting the statistics of the photons. When the *detector noise* regime is reached (at $N_{\text{pix}} \sim 1\,000\,\text{px}$ in the *photon rich* case, and at $N_{\text{pix}} \sim 10\,\text{px}$ in the *detection* scenario), the SNR decreases rapidly with the number of pixels used to sample the signal.

The behaviour of the SNR on the closure phase in the *detection* scenario (blue dashed-dotted curves), studied in section 7.5.3.3, page 161, was over-plotted and it is represented by the black solid (unresolved source), black dashed (partially resolved source) and black dashed-double-dotted (resolved source) curves. The line corresponding to the unresolved source for ϕ_c coincides with the $V = 0.5$ case for ϕ for most of the N_{pix} range and, therefore, is barely visible in the plot. Concerning the variation with N_{pix} and according to both noise models, the visibility phase presents better

[23] Although optical interferometry is currently more concerned with typically small numbers of photons in each spectral bin, a large number of pixels is needed when a great spectral resolution is required.

performance in terms of SNR than the closure phase. In the *detector noise* regime, the decrease of the SNR is more pronounced for the closure phase, especially for resolved sources. This behaviour is justified by the worst performance for resolved sources, in terms of SNR, of the closure phase case than the visibility phase case — *cf.* figs. 7.23 and 7.33, pages 155 and 166, respectively — probably due to the fact that less phase information is available for the former than for the latter. However, the elbow points in the ϕ_c curves are slightly shifted towards larger numbers of pixels, indicating that, for a given magnitude, the closure phase is less sensitive to the increment of N_{pix}.

SNR on ϕ *vs* σ

Figure 7.37b illustrates the behaviour of the SNR measured on ϕ with the RON, σ, which was varied between 1 and 15 e^- px^{-1}. The SNR on ϕ decreases with σ, remaining constant in the *photon noise* regime.

The *detection* case for the closure phase was over-plotted and it is indicated by the thin black lines (solid for the $V = 1.0$ case, dashed for the $V = 0.5$ branch and dashed-double-dotted for the $V = 0.1$ case). The black solid line for ϕ_c coincides with the blue dashed-dotted line in the $V = 0.5$ case for ϕ and, thus, it is hardly visible in the plot. The SNR on ϕ is always above 1, except when the source is resolved, for which the SNR goes bellow 1 for $\sigma \gtrsim 5\,\mathrm{e}^-\,\mathrm{px}^{-1}$. Nevertheless, the SNR on ϕ is always larger than the SNR on phi_c (it is typically at least twice larger), being the latter meaningless for resolved sources. Therefore, regarding uniquely the quantities related to the *detector noise* regime (N_{pix} and σ), the visibility phase seems to be an observable more suited for observations than the closure phase because the SNR on ϕ is typically larger than that on ϕ_c. More phase information per baseline in the phase referencing case than in the phase closure one seems to be the main reason for the discrepancy between the SNRs measured on ϕ and on ϕ_c when varying N_{pix} and σ.

Figure 7.37c stems from the combination of figs. 7.37a and 7.37b in the case of unresolved sources. It highlights the effect of the RON on the SNR measured on ϕ when the number of pixels used to sample the signal is varied. Similarly to the closure phase, the SNR on ϕ becomes more sensitive to the RON for fainter sources. In the *photon rich* case, the $\sigma = 15\,\mathrm{e}^-\,\mathrm{px}^{-1}$ branch starts to significantly detach from the other branches for $N_{pix} \gtrsim 55\,\mathrm{px}$; the $\sigma = 2\,\mathrm{e}^-\,\mathrm{px}^{-1}$ case is notably different from the central branch for $N_{pix} \gtrsim 450\,\mathrm{px}$. In the *detection* scenario, the difference in SNR between the extreme branches is about one order of magnitude for $N_{pix} \gtrsim 300\,\mathrm{px}$. A difference of one order of magnitude between the extreme branches is characteristic of the *photon starved* case for all tested values of N_{pix}, but the values of the SNR on ϕ are unimportant in this scenario.

Conclusions

The study of the noise terms of models from É. Tatulli and Chelli, 2005 for V^2 and ϕ_c and É. Tatulli, Blind et al., 2010 for ϕ, indicate that the parameter to which the SNR is the most sensitive is the integration time. Other parameters, like the efficiency of the interferometer or the Strehl ratio are also important, especially for faint sources. At least a combined efficiency above 10 % and

some level of AO correction (tip-tilt) should be guaranteed, but an efficient fringe tracker brings the highest gains when concerning the SNR of interferometric observables.

The results also indicate that when a photometric calibration is performed, care should be taken in order to find the optimum value of τ according to the characteristics of the source and of the observation (*cf.* table 7.10).

Clearly, the É. Tatulli and Chelli, 2005 and É. Tatulli, Blind et al., 2010 noise models are too optimistic in the sense that the balancing between the terms obeying to the Poisson statistics and the terms obeying to the Gaussian statistics happens for large magnitudes in the K-band.

The comparison between both noise models typically predicts better results for ϕ in terms of SNR.

Figure 7.33 reveals that the *Simple* noise model, although not as sophisticated as the ibid. one, it is in very good agreement with the latter in what concerns the dependency of the SNR on ϕ with the visibility amplitude.

Pipeline

Since no real data was used in the study undertaken in chapter 8, all "observations" were simulated by means of the **O**ptical **I**nterferometry **SIM**ulator (OI-SIM) code. Developed in the scope of the present thesis, the simulated sets of data depend on the characteristics of the model image, the (u,v) coverage and the chosen noise model.

In order to get an OIFITS file (Pauls et al., 2005) with all information necessary to feed MiRA and to perform image reconstruction, several steps need to be followed in sequence (*cf.* diagram of fig. 7.38).

1. Creation of a standard FITS file (Pence et al., 2010), containing the *model image* (*cf.* section 7.1 for details on the objects).
2. *Creation of a standard OIFITS file* containing all the observables and parameters of the interferometric observation.
   (a) *Station array configuration* for each night of observation. The number of configurations define the number of nights.
   (b) *Creation of observational data*, containing the following information: **names of the stations** used each night (previous item, *mandatory*), a hash-table containing the **names and coordinates of all the stations** (the VLTI stations are assumed by default), the **name of the array**, the **name of the instrument**, the **declination** of the object in degrees (*mandatory*), the **hour angles** in decimal hours when the observations where performed (*mandatory*), the **name of the observed object**, the **mean wavelength** in microns of the observations (*mandatory*), the **bandwidth** in microns (*mandatory*), the **integration time** in seconds (*mandatory*) and the **dates of the observations**.[24]
   (c) Selection and configuration of the *noise model* (*cf.* section 7.5 for details).
   (d) *Simulation of the interferometric data* — via *discrete Fourier transform* (DFT) from the model image — and *selection of the observables* to be recorded in the OIFITS file.
3. Usage of MiRA to *reconstruct the image*.
   (a) *Loading of the OIFITS* file previously created.
   (b) *Configuration of* MiRA, where the **dimensions of the image**, the **pixel size**, the **type of Fourier transform** (*exact* or *fast*) used as linear operator and the **regularisation** are indicated.
   (c) Execution of MiRA in an *iterative process*, where the **initial guess image**, the **total number of evaluations per iteration**, and the **strength of the hyper-parameter** μ (chapter 6) are indicated. The **normalisation** and the **positiveness** of the brightness distribution are always assured.

[24] Other parameters that can be configured are (see Pauls et al., 2005, for details): the *coordinate frame*, the *coordinates of the array centre*, the *names of the telescopes*, the *diameter* of the telescopes in metres, the *target number* as index, the *right ascension* at the mean equinox in degrees, the *equinox*, the *error in RA* at the mean equinox in degrees, the *error in DEC* at the mean equinox in degrees, the *systemic radial velocity* in m/s, the *reference for radial velocity*, the *definition of radial velocity*, the *PM in RA* expressed in deg/yr, the *PM in DEC* expressed in deg/yr, the *errors of the PMs in RA and DEC* in deg/yr, the *parallax* and its *error* expressed in degrees, the *object's spectral type*, and the *modified JD* at the start of the observations.

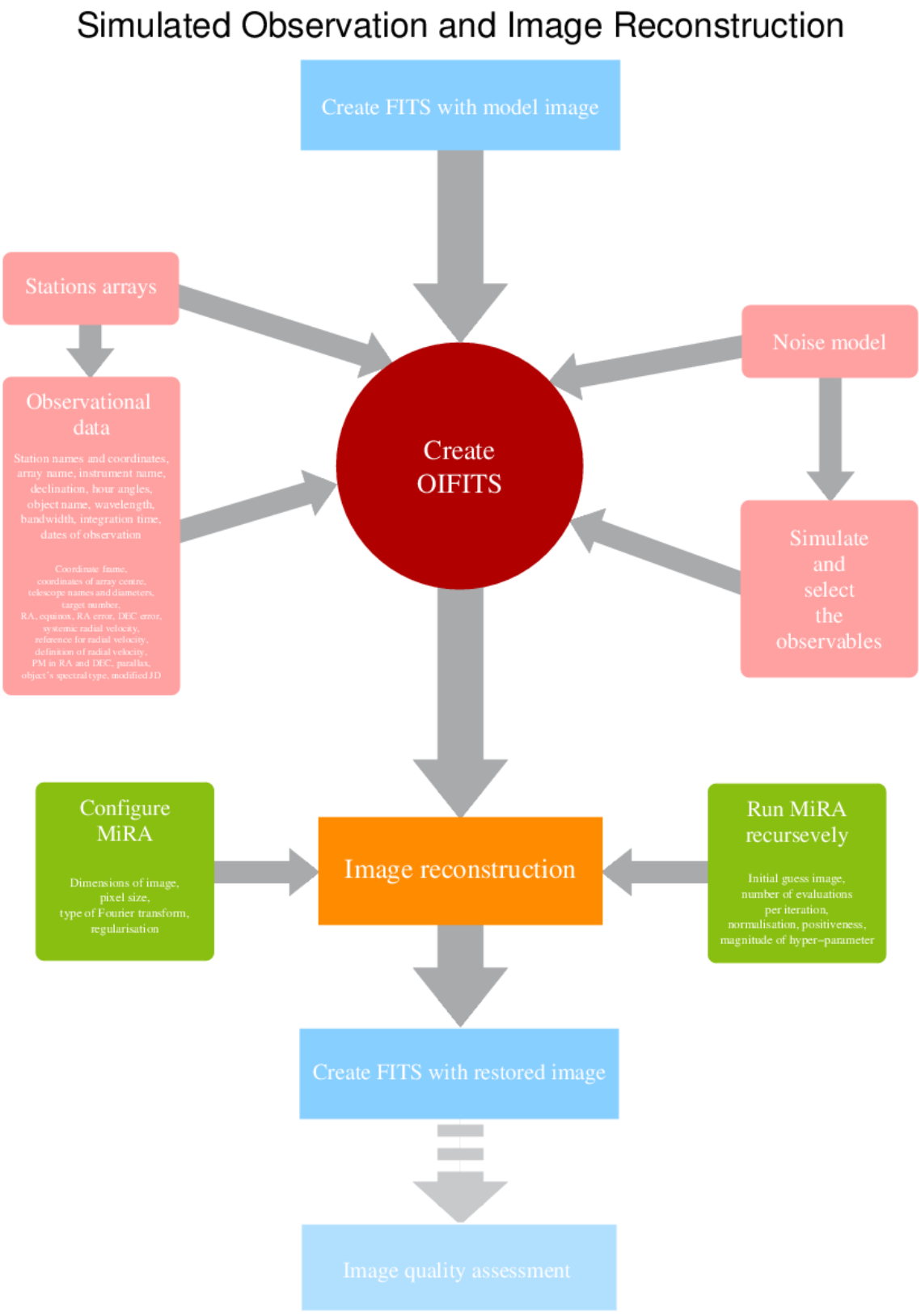

Figure 7.38: Diagram representing the simulation of the observation and the image reconstruction procedure.

(d) *Recording of the final image* in a standard FITS file.

When the true source brightness distribution is known, the quality of the restored image can be evaluated more easily. Some methods and procedures are described in the following section.

Image quality assessment

After restoration, the images must be compared with the ones from which they were originated, to assess the quality of the reconstruction process. The estimation of the quality of reconstructed images has been a concern since imaging started to be a goal amongst radio astronomers (John E. Baldwin and Haniff, 2002). The process is not straightforward, as, on the one hand, it depends on the science that is to be extracted from the data (Pety, Gueth and Guilloteau, 2001b), and, on the other hand, it relies on the kind of observables produced by the interferometer, especially the type of interferometric phase (visibility phases and/or closure phases). This section describes several approaches to the problem that have been implemented during the last decade and the one developed in the framework of the current thesis.

Fidelity estimators in ALMA

For practical reasons and to improve the indication of the overall quality of the observing process, several estimators of the image fidelity have been used to compare the quality of reconstructed images with the corresponding models in ALMA (Pety, Gueth and Guilloteau, 2001a).

Fidelity image

The *fidelity* is defined as the ratio of the input model to the difference between the original and the restored image:

$$\text{fidelity} = \frac{\text{model image}}{\max(\text{difference}, 0.7 \times \text{RMS}(\text{difference}))}. \tag{7.63}$$

The threshold to the lowest value of the difference image is imposed to avoid pixels that have exactly the same intensity as in the model image. These pixels, with high fidelity, are not accounted in the calculation because, according to the authors, they do not reflect the accuracy of an observation, which can only be estimated from a statistical point of view.

The highest the value of the fidelity, the better the image.

Histogram of cumulated fidelity

The *histogram of cumulated fidelity* is calculated with the aim of quantifying the visual impression given by the fidelity image. The outcome is the number of pixels in the image defined by eq. (7.63) whose values are larger than a given fidelity. A section in the graph with a rectangular shape is indication of a homogeneous fidelity.

Fidelity medians

Four *fidelity medians* are computed in order to improve the quantification of the comparison results. The medians are calculated in the pixels of the model image whose intensities are higher than 0.3, 1, 3.3 and 10 % of the maximum. These values were chosen in order to avoid medians to overweight the numerous pixels without signal, where the fidelity is low. By definition, the medians do not overweight points with high fidelity and they have the advantage that their inverse represents the inverse of the median of the relative error.

Fidelity range

The *fidelity range* is an estimator close to the dynamic range when the model image is for the most part made of point sources and close to the fidelity when the source is an extended object. It is defined as

$$\text{fidelity range} = \frac{\max\left(|\text{model}|\right)}{\text{RMS}(\text{difference})}. \tag{7.64}$$

RMS statistics in the Interferometry Imaging Beauty Contest

In the infra-red domain, the Optical/IR Interferometry Imaging Beauty Contest, taking place every two years, is a reference concerning the methods used to test the quality of restored images. The procedure adopted to compare the model and the reconstructed images slightly varies from contest to contest, but it is based on a best match to the model images (Baron, William Danchi Cotton et al., 2012; W. Cotton et al., 2008; Lawson, William Danchi Cotton et al., 2004; Lawson, William D. Cotton et al., 2006; Malbet et al., 2010). The model is convolved with a Gaussian to simulate the finite field of view and to account for the finite resolution of the data. Fiducial features in the objects are selected in order to align the images. Then, the reconstructed images are interpolated to the geometry of the model and the comparison is made over a normalization box defined on the reference image. The measurement of the quality of the reconstruction is a root mean squared about zero agreement, σ_{rms}, defined as

$$\sigma_{\text{rms}} = \sqrt{\frac{\sum_{j=1}^{N_{\text{pix}}} p_j^{\text{ref}} \cdot \left(p_j^{\text{ref}} - p_j^{\text{r}}\right)^2}{\sum_{j=1}^{N_{\text{pix}}} p_j^{\text{ref}}}}, \tag{7.65}$$

where N_{pix} is the total number of pixels, p_j^{ref} is a pixel in the reference image and p_j^{r} is the corresponding pixel in the restored image.

The lowest the value of σ_{rms}, the better the image.

The size and position of the normalization box varied according to the specifications of the objects under analysis and to the criteria adopted for the contest in a specific year. For example, in the first edition of the contest, the images were compared over a box defined on the model image containing all the emission (Lawson, William Danchi Cotton et al., 2004), while in 2008 and 2012, the box was defined in order to contain at least 90 % of the model flux density (Baron,

William Danchi Cotton et al., 2012; W. Cotton et al., 2008). In the two other editions of the contest, the coordinates of the boxes were specified, but no details were given about the flux inside of them.

In 2004 and 2012, the model images were used in their original form for the comparisons, but in the other editions the references were always firstly convolved with a Gaussian. The FWHM of the Gaussian depended on the criteria adopted for each edition of the contest. In 2006, the initial model was convolved with a 1 mas Gaussian, but no additional information is given regarding this choice (Lawson, William D. Cotton et al., 2006). In 2008, two convolutions were operated to the models: first, with a 15 mas FWHM Gaussian to simulate the finite field of view; then, with a Gaussian of FWHM equal to half (a quarter of) the fringe spacing on the longest baseline for the AGB — respectively, the AGN — model, to account for the finite resolution of the data while accommodating super-resolution in the imaging (W. Cotton et al., 2008). In 2010, the models were convolved by a 0.4 mas Gaussian to approximate the resolution to that of the reconstructed images (Malbet et al., 2010). In 2012, the authors suggested the pixel size and the FOV to the contestants, in order to prevent the rescaling or the convolution of the restored images to the pixel scale of the true image (Baron, William Danchi Cotton et al., 2012).

A drawback in the quality measurement σ_{rms} defined by eq. (7.65) resides in the fact that the flux comparison is weighted uniquely by the reference pixels. This means that a feature appearing in the reconstruction process that does not exist in the model image is not properly represented by the statistics, which leads to an inaccurate idea of the quality of the restored image.

The Accuracy function

General Case

The *accuracy function*, ζ^2, is based on a normalized weighted best-fit to the reference images, a method similar to the one used in the Interferometry Imaging Beauty Contests. It is defined as

$$\zeta^2 = \frac{\sum_{j=1}^{N_{\mathrm{pix}}} W_j \cdot \left(p_j^{\mathrm{ref}} - p_j^{\mathrm{r}}\right)^2}{\sum_{j=1}^{N_{\mathrm{pix}}} \left(p_j^{\mathrm{ref}} + p_j^{\mathrm{r}}\right)^2}, \tag{7.66}$$

where N_{pix}, p_j^{ref} and p_j^{r} are the same as in eq. (7.65). W is a normalised weighting function, a mask that eliminates all pixels where the reference and the restored images have intensities smaller than the dynamic range. On all non-negative pixels, W is equal to 1.0.

For the dynamic range, it was initially adopted the definition by John E. Baldwin and Haniff, 2002 and Haniff, 2007, where the dynamic range of an image reconstructed as the outcome of an interferometric observation can be estimated by multiplying the square root of the total number of baselines by the SNR per data point:

$$\text{dynamic range} = \sqrt{\frac{n}{\left(\frac{\delta V}{V}\right)^2 + (\delta\phi)^2}}, \tag{7.67}$$

where $\delta V/V$ is the relative error on the visibility amplitude, $\delta\phi$ is the phase error and n is the total number of measured visibility points. Although this expression corresponds to a limit for bright sources, it serves the purposes of establishing a selection criterion for the pixels to be accounted for the weighting function W. Later, and in the scope of the simulations of **??** and the work of N. Gomes, P. J. V. Garcia and É. Thiébaut, 2016, it was adopted a practical definition of the dynamic range, regarding it as a contrast ratio, *i.e.*, as the ratio between the brightest and faintest pixels of the image. The lowest brightness value of the image was estimated by the RMS of all pixels.

ζ^2 varies between 0 and 1 and the smaller it is, the better the quality of the restored image.

Particular case: stellar cluster

The efficiency of the accuracy function in determining the quality of a restored image was attested for the particular case of a source composed uniquely of unresolved structures. Nuno Gomes, Paulo J. V. Garcia, Éric Thiébaut et al., (2010) assessed the quality of reconstructed images of a stellar cluster by computing the individual photometry of the stars and the relative distances between the brightest and each other member of the cluster.[25] When using the accuracy function to measure the quality of those images, the results were similar to the ones found by (ibid.) This procedure also permitted to attest the photometric and astrometric accuracy of `MiRA`.

Implemented image comparison method

If visibility phase information is present, the comparison between the original and the restored image usually is quite straightforward. For instance, it can be done by means of a root mean squared of the difference between the images, because the absolute position of the source is contained within the phase information. However, when closure phases are the only phase information available, the position of the objects in the restored image are no longer absolute. Simply subtracting the model image from the reconstructed image would make the difference between them misleadingly large. Nevertheless, the absolute locus of the source in the FOV is not relevant,[26] as just the size of the object itself and the relative position of its structures matters. In this sense, it is important to recentre the image into a position that minimizes the difference between itself and the true image, in order to prevent closure phase data to always be in disadvantage when compared to visibility phase data.

Moreover, a reconstructed image will never have the same level of detail as the original one, since, on the one hand, the object brightness distribution behaves as if it is convolved with the *effective PSF* of the instrument and, on the other hand, the true image will potentially have an infinitely high resolution. The PSF, if estimated by the dirty beam (*cf.* section 6.2.2, page 100), is too pessimistic, in the sense that image reconstruction packages, by means of super-resolution, are able to restore images with finer details than the ones observed by the convolution of the original image

[25] The astrometric and photometric measurements were obtained with the `SExtractor` software package (Bertin and Arnouts, 1996).

[26] Provided the image is not cropped.

with the dirty beam. Hence, it is important to estimate the PSF by taking into account the effective resolution achievable by the instrument and the image reconstruction algorithm, and to convolve it with the original image prior to image quality assessment. Not doing so, the comparison will be unfair, because it will be carried out using as reference an unattainable brightness distribution (in terms of resolution). In that case, small displacements of sharp features would increase the metric differences between both images, while they would look very similar at lower and more realistic resolutions.

These considerations led to the development of a method of image comparison, which is based on the following steps (*cf.* diagram of fig. 7.39):

IMAGE COMPARISON STEPS in `OI-SIM`

1. *Effective PSF estimation*
2. *Data creation*
3. *Recording of simulated data* $\longrightarrow$ *OIFITS*
4. *Restoration of image from interferometric data*
5. *Saving of restored image* $\longrightarrow$ *FITS*
6. *Resampling of restored image* $\longrightarrow \mathscr{R}$
7. *Adjustment of PSF position + Convolution of best PSF* ($\mathscr{G}$) *with original image* ($\mathscr{O}$) $\longrightarrow \mathscr{O} * \mathscr{G}$
8. *Image comparison* $\longrightarrow \mathscr{O} * \mathscr{G} \ominus \mathscr{R}$

In the box IMAGE COMPARISON STEPS IN `OI-SIM`, steps from 2. to 8. are used for execution of step 1. The principle behind the latter resides in the fact that the effective PSF should correspond to the response of the interferometric system to an unresolved source — the method is described in more detail in section 7.7.4.1.[27]

All simulated interferometric data are recorded in standard OIFITS files, which can always be used as input to image restoration packages.

For image reconstruction, the initial guess should ideally correspond to an image quickly restored using visibility complex phase data, in order to keep (as much as possible) the right orientation and absolute position of the source. In the absence of complex visibility data, and working in a *blind* reconstruction scenario (*i.e.*, without previous information about the source brightness distribution), a good initial estimate can be obtained by performing a quick restoration without phase information (only visibility amplitudes are kept). The resulting image $\mathscr{R}$ is saved in a standard FITS file.

Before **image comparison**, the original image $\mathscr{O}$ is convolved with the previously estimated PSF $\mathscr{G}$, and an iterative process is initiated with the aim of optimising the position of $\mathscr{G}$, *i.e.*, to find

[27] In the work by N. Gomes, P. J. V. Garcia and É. Thiébaut, 2016, the first step was removed, and the estimation of the effective PSF was incorporated in step 7, by finding simultaneously the best position and width of the PSF that lead to the least difference between the images being compared.

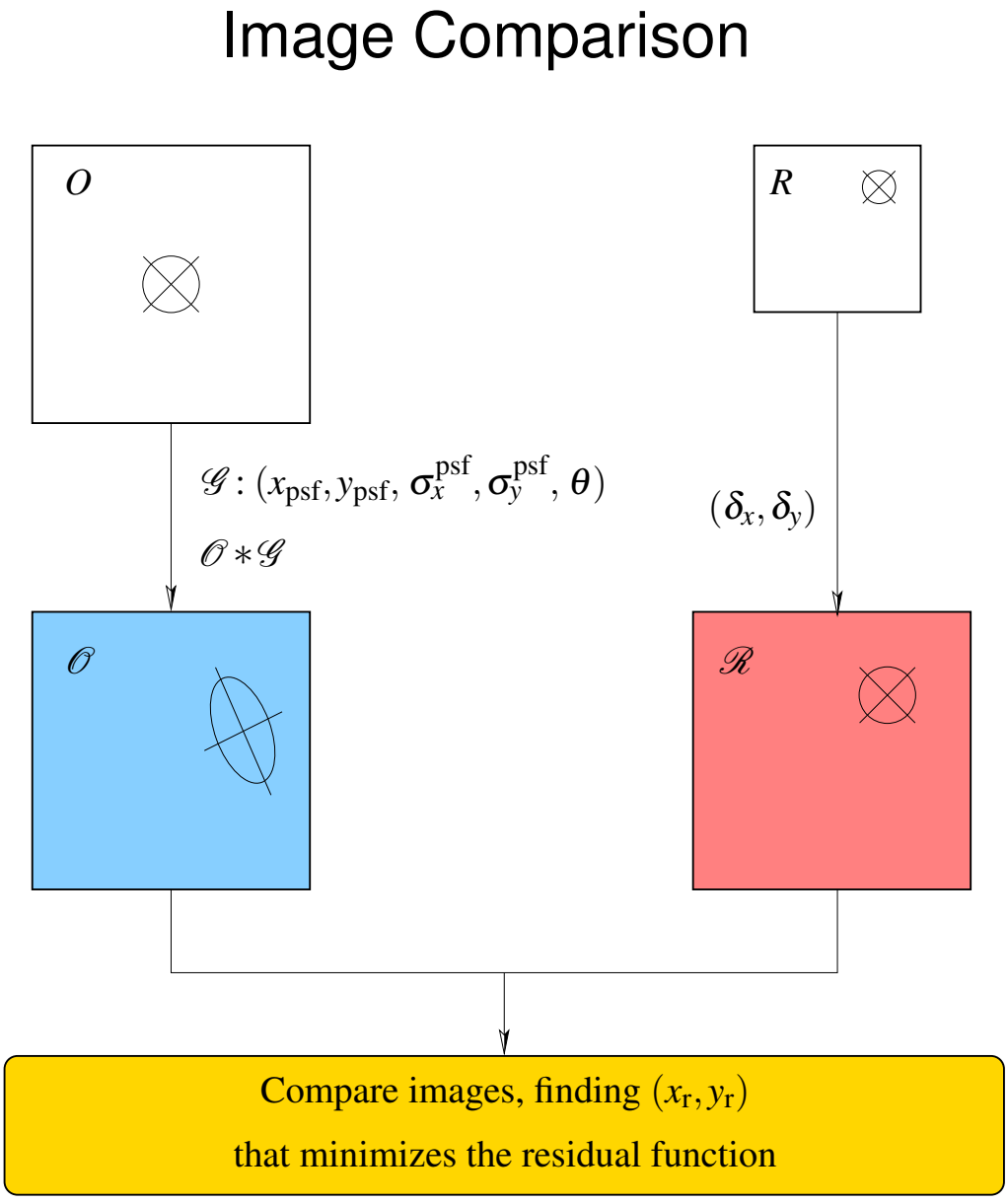

Figure 7.39: Diagram representing the image comparison process adopted in the frame of the current thesis.

the values of $(x_{\rm psf}, y_{\rm psf})$ that minimise the difference between $\mathscr{O} * \mathscr{G}$ and $\mathscr{R}$.[28] This step is essential when an image is restored from data containing uniquely closure phases, as the bi-spectrum is not able to keep the absolute position of a source within the FOV.

When the optimal values of $(x_{\rm psf}, y_{\rm psf})$ are found, the comparison between $\mathscr{O} * \mathscr{G}$ and $\mathscr{R}$ is made by means of *residual functions*, three of which were implemented in `OI-SIM`: the *fidelity* function of eq. (7.63), the *RMS-sigma* function of eq. (7.65) and the *accuracy* function of eq. (7.66).[29]

Effective PSF estimation algorithm

An effective PSF is the elliptical Gaussian that when convolved with a reference model image minimises the residuals between the resultant convolution and the restored image. It is assumed that its shape is defined by the parameters $(\sigma_x^{\rm psf}, \sigma_y^{\rm psf}, \theta_{\rm psf})$, respectively the standard deviations in the X- and Y- directions, and the anticlockwise rotation angle. The process relies on the reconstruction of a reference image, $\mathscr{O}_{\rm psf}$, composed of unresolved sources, having the same intensity and size, and spread in the FOV. Data is created using identical conditions to this "scientific" image: same *uv*-coverage (equal number of apertures, occupying the same stations of the interferometer), object located at the same declination angle, with unaltered transit and integration time, observed at the same central wavelength, and with similar level of noise. The restoration of $\mathscr{O}_{\rm psf}$ is carried out aiming at the best figure of merit. After reconstruction, the image is resampled to the dimensions of $\mathscr{O}_{\rm psf}$, yielding $\mathscr{R}_{\rm psf}$ (*cf.* fig. 7.40c). Finally, to estimate the best PSF, an iterative process is executed, where $\mathscr{O}_{\rm psf}$ is convolved with the current elliptical Gaussian and the resulting image is compared with $\mathscr{R}_{\rm psf}$. The parameters of the tentative effective PSF — displacement vector $(x_{\rm psf},\ y_{\rm psf})$, standard deviations $\sigma_x^{\rm psf}$ and $\sigma_y^{\rm psf}$, and rotation angle $0 \leqslant \theta_{\rm psf} \leqslant \pi/2$ in the direct sense, relative to the X-axis — are eventually pulled out in each iterative step.[30] With the first iteration, only the position $(x_{\rm psf}, y_{\rm psf})$ is granted with good accuracy, by a non-linear least squares fit to a function of five parameters.[31] In the second iteration, $x_{\rm psf}$ and $y_{\rm psf}$ previously found are kept fixed, while the three other degrees of freedom are tuned by the non-linear fit. The best PSF is sought by confining $\sigma_x^{\rm psf}$, $\sigma_y^{\rm psf}$ and $\theta_{\rm psf}$ to a cube of n^3 points (n is arbitrarily chosen, typically of order 10^3), with $\theta_{\rm psf}$ varying between 0° and 89°. During the last iteration, $\sigma_x^{\rm psf}$ and $\sigma_y^{\rm psf}$ are also kept unaltered, and the rotation angle is fine tuned by directly comparing $\mathscr{O}_{\rm psf} * \mathscr{G}$ and $\mathscr{R}_{\rm psf}$ when $\theta_{\rm psf}$ is varied inside the interval $[\theta_{\rm psf} - 5^\circ, \theta_{\rm psf} + 5^\circ]$ for an array of 100 points. If the image $\mathscr{O}_{\rm psf} * \mathscr{G}$ yields a better comparison, *i.e.*, smaller residuals computed by the simple quadratic difference $\sum(\mathscr{O}_{\rm psf} * \mathscr{G} - \mathscr{R}_{\rm psf})^2$, the newest parameters are saved and returned. For each *uv*-coverage and observing configuration, the estimation of the elliptical Gaussian is performed

[28] $A * B$ denotes the *convolution* between A and B. $A \ominus B$ represents any residual function used to estimate the differences between A and B. During the **iterations** of the algorithm, the comparison between $\mathscr{O} * \mathscr{G}$ and $\mathscr{R}$ are done by means of simple residuals, *i.e.*, the quadratic difference between both images.

[29] Also thoroughly used by the image comparison algorithm in `OI-SIM` in intermediary steps is a *simple residuals* function $\sigma_0^2 = \sum(\mathscr{O} * \mathscr{G} - \mathscr{R})^2$, where $\mathscr{O}$, $\mathscr{G}$ and $\mathscr{R}$ are as described before.

[30] A good initial guess for the parameters of the elliptical Gaussian is $(x_{\rm psf}^0, y_{\rm psf}^0) = (0.0, 0.0)$, $\sigma_{\rm psf}^0 = \sigma_x^{\rm psf} = \sigma_y^{\rm psf} = {\rm FWHM}/(2\sqrt{2\log 2})$, where ${\rm FWHM} \sim \lambda / B_{\rm max}$ and $B_{\rm max}$ is the length of the largest baseline, and $\theta_0 = 0^\circ$.

[31] It was used an implementation of the Levenberg-Marquardt method (Levenberg, 1944; Marquardt, 1963).

a statistically meaningful number of times (typically 12 times), and the parameters are averaged out to get the ultimate solution for the effective PSF. This final solution is kept fixed, except if the phase information is contained uniquely in closure phases — in this case, an extra displacement of the image needs to be carried out because the absolute position of the object is not contained within the phase of the bi-spectrum.

Figure 7.40 illustrates the main steps of effective PSF estimation: selection of the (u,v)-space (fig. 7.40a), *reference spotty image* $\mathscr{O}_{\text{psf}}$ (fig. 7.40b), corresponding restored image $\mathscr{R}_{\text{psf}}$ (fig. 7.40c), and estimated effective PSF (fig. 7.40d). An example of an effective PSF, obtained for an *uv*-

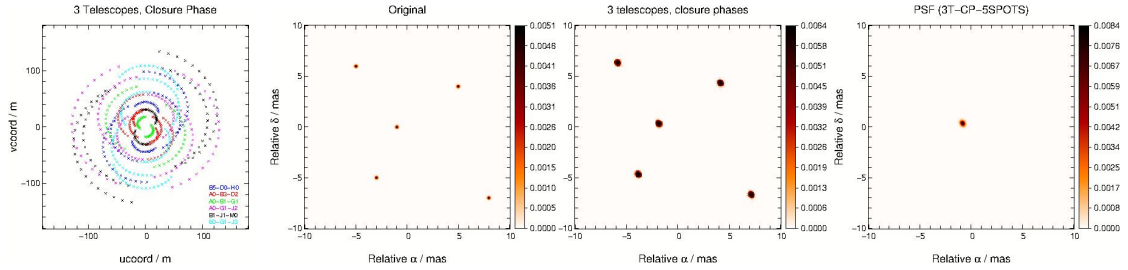

(a) *uv*-coverage. **(b)** Model reference image. **(c)** Restored image. **(d)** Estimated effective PSF.

Figure 7.40: Example of effective PSF estimation, stemming from the combination of 3 ATs used during 6 nights of observation, and the usage of an AMBER-like instrument collecting power-spectra and bi-spectra only. (*a*) *uv*-coverage; (*b*) reference model image; (*c*) restored model image; (*d*) actual estimated effective PSF.

coverage built with 6 telescopes, and using uniquely closure phases to retrieve the phase information of the complex visibility, is illustrated in fig. 7.41.

Concerning $\mathscr{O}_{\text{psf}}$, the FWHMs of the spots should always be smaller than the resolution of the interferometer, so to grant that the reconstruction corresponds to that of point-like sources. Choosing spots with different intensities is not an option, since the brightest spots tend to become rounder than the others when restored, dominating the shape of the ellipse. The number of sources must be kept low in order to assure, on the one hand, a successful image reconstruction (due to the nature of the image, the amplitudes and phases vary quickly, as there are many very contrasted fringes in the (u,v)-plane[32]) and, on the other hand, to avoid anisoplanatic effects, especially for badly paved (u,v)-spaces.[33]

To achieve a correct estimation of the parameters of the ellipse, $\mathscr{O}_{\text{psf}}$ must be wisely chosen according to the *uv*-coverage and the width of the FOV. In a *generous uv*-coverage, *i.e.*, a (u,v)-space paved with a great number of spatial frequencies, a good reference image consists of 5 non-resolved Gaussian spots disposed as in the face of a dice. The advantage of using 5 spots instead of just 1 centred in the FOV is that, on the one hand, more points will contribute to the final average of the Gaussian parameters, and, on the other hand, the convergence to the higher spatial frequencies is easier in the former than in the latter during image restorations, especially if closure

[32] Using too many point sources makes it very difficult to get rid of the numerous strong degeneracies of the problem, as the brute force approach used by `MiRA` (*i.e.*, local minimisation from the starting solution) is not able, in this particular case, to travel to a near-global minimum. Another optimisation strategy could be developed, especially when many point-like sources are used — a possible method might be a Monte-Carlo greedy algorithm (*i.e.*, `CLEAN` with a random search).

[33] *Anisoplanatic* means that the PSF is position dependent.

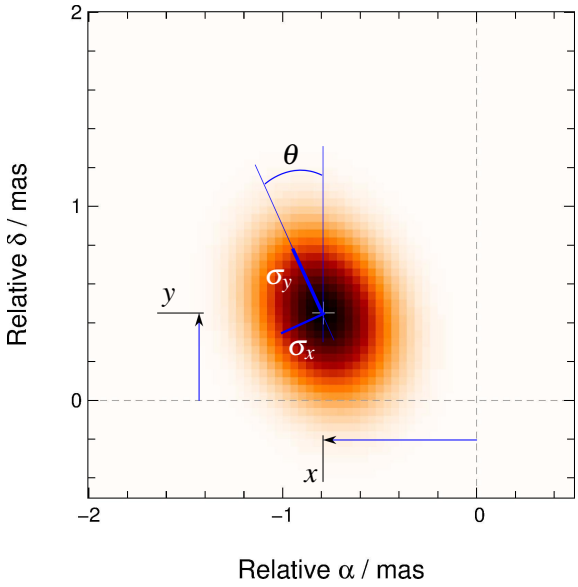

Figure 7.41: Estimated effective PSF for 6 telescopes, using uniquely closure phases. The corresponding (u,v)-space is depicted in fig. 8.7i. In this example, $x = -0.79$ mas, $y = 0.45$ mas, $\sigma_x = 0.19$ mas, $\sigma_y = 0.25$ mas, and $\theta = 21.2°$. This is the effective PSF that, when convolved with the original image, minimises the differences between the latter and the restored image.

phases are present in the data. As a result, the estimated Gaussian tends to become more compact, meaning the flux is more concentrated in a smaller FWHM. Moreover, displacing the spots in a grid instead of having them randomly spread in the FOV prevents situations of spots lying very close to each other and, consequently, their restored images becoming deformed, affecting the estimation of the PSF. It is important to have a non-resolved spot in the centre of the image, as this is the one that will have the best chances of being properly restored, due to the absence of boundary effects (notorious in a sparse *uv*-coverage and when approximate Fourier transforms are used).

Therefore, if the (u,v)-space is well enough paved, having some extra spots in the FOV will help in the estimation of the parameters of the Gaussian, since more elements are contributing to their statistics. However, in a *sparse uv*-coverage, *i.e.*, composed of a small number of, or badly distributed, spatial frequencies, as the one depicted in fig. 8.1a of page 189, the reference image must be composed of a single centred spot (fig. 7.42). Extra spots beyond the central one will most probably be badly restored due to anisoplanatic effects and, thus, will negatively affect the estimation of the effective PSF. Examples of that situation are illustrated in figs. 7.42d and 7.42e. These images, reconstructed in a *sparse uv*-coverage environment, stem from phase referencing data, using exact Fourier transforms. In the former, it is clear that only the central spot was duly restored to a (correct) circular Gaussian. The remaining spots present different FWHMs in X- and Y- directions, and non-constant rotation angles, which will yield an erroneous effective PSF. The situation is worse in the latter: in addition to several deceptive spots, non of the genuine points is properly restored, and at least two pairs of them appear blended (one of which encompasses the central spot). The estimated effective PSF, illustrated in fig. 7.42f, does not represent the *uv*-coverage to which it corresponds: it should be rounder, as the spatial frequencies are symmetrically distributed in the (u,v)-space, and more compact.

With respect to the noise, for a given SNR, the process of estimating the effective PSF does not depend on the noise model. In fact, the effective PSF does not noticeably change if the *Simple* or *Tatulli's* models are used, for example. Nevertheless, it is important that the level of noise is

judiciously chosen, so as to find the right parameters of the Gaussian that faithfully translate the distribution of the spatial frequencies in the (u,v)-space. Any visibility amplitudes with levels of SNR above 20 yield fine results.

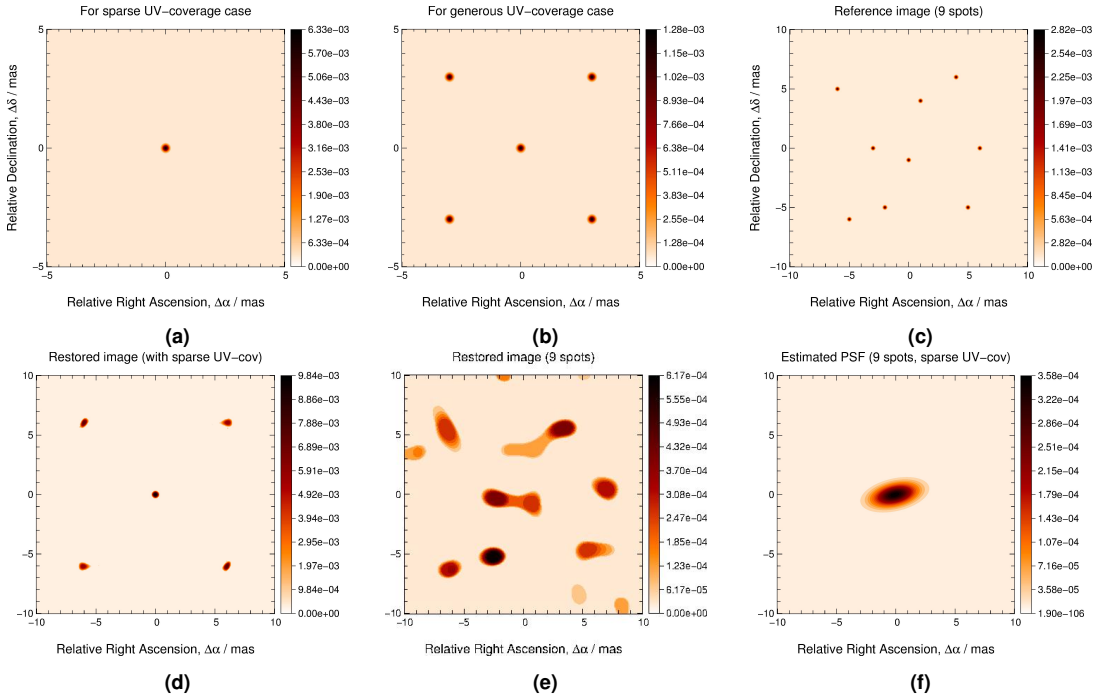

Figure 7.42: Examples of reference images used for effective PSF estimation. (*a*) Unresolved central spot used for a badly paved (u,v)-space; (*b*) five unresolved spots used for a generous uv-coverage; (*c*) example of reconstruction of (*b*), using phase referencing in the sparse uv-coverage of fig. 8.1a. Only the central spot is correctly restored. The other points, due to extended semi-major axis and incorrect rotation angles, will give rise to an erroneous effective PSF. (*d*) Nine unresolved spots randomly spread in the FOV. This image must be avoided when the (u,v)-space is badly paved; (*e*) reconstruction of (*d*) using phase referencing in the sparse uv-coverage of fig. 8.1a. In addition to spurious features, two pairs of spots are blended (including the central one) and all spots present different sizes and orientations. (*f*) Effective PSF estimated from fig. 7.42e. Clearly, it does not correctly translate the distribution of the spatial frequencies in the (u,v)-space of fig. 8.1a.

The value of the hyper-parameter μ is varied during the reconstruction, aiming at the fastest convergence for the solution, and the best possible match between `MiRA`'s and experimental spatial frequencies. Typically, when the algorithm is already converging for the global minimum, the value of μ is reduced by one or two orders of magnitude, so that the high spatial frequencies of `MiRA` converge to the corresponding experimental ones.

`OI-SIM` is a useful tool to estimate the effective PSF for any uv-coverage. It is only necessary to simulate a spotted image with unresolved sources, to input the coordinates of the stations used for observations, the declination of the source, the hour angles when data was collected, and the effective wavelength of the radiation used during data acquisition. Image reconstructions can be performed using phase referencing, closure phase or the combination of both techniques. When more than one set of data is available (*i.e.*, different realisations of the mock observation), all results can then be aggregated to produce a final and robust estimation of the effective PSF.

An important caveat regarding this method is that it is fundamental to accurately estimate the effective PSF, especially the standard deviations and rotation angle of the ellipses. Otherwise,

images can be wrongly classified depending on their qualities (the merit values yielded by the adopted metric for image quality assessment).

Addendum

The procedure to estimate the PSF described in the previous section was only used in the simulations of section 8.2.1. In section 8.4 and in N. Gomes, P. J. V. Garcia and É. Thiébaut, 2016, the process was shortened, by removing the restorations of unresolved sources. In this new approach, the parameters of the effective PSF are simultaneously sought by minimising some merit function (the accuracy function, for instance) using a numerical optimisation algorithm, such as the Levenberg-Marquardt method (Levenberg, 1944; Marquardt, 1963) or `NEWUOA` (Powell, 2006). The final parameters are the ones that minimize the difference between the reference image convolved with the PSF and the restored image resampled to the grid of the reference one.

Assessing the quality of restored images

Assessing the quality of recovered images is important for the scientific outcome of optical/IR interferometric observations, to benchmark image reconstruction algorithms, and for the design/upgrade of new/existing interferometers. A study was conducted to find the best metric to assess the quality of a reconstructed image, and the results were published in a peer reviewed paper (N. Gomes, P. J. V. Garcia and É. Thiébaut, 2016).

Several merit functions were considered: the metric of the Interferometric Imaging Beauty Contest (IBC), the ℓ_2-norm (L2N), the Mean Squared Error (MSE), the Peak Signal to Noise Ratio (PSNR), the Universal Image Quality Index (Q), Image Structural Similarity (SSIM), the Accuracy function (ACC), the ℓ_1-norm (L1N), the Fidelity function of ALMA (FID), and the Kullback-Leibler Divergence (KL) — *cf.* appendix A. Of them, only L2N, IBC, L1N and ACC, were used to evaluate the quality of interferometric restored images in the work of (ibid.), because (*a*) MSE and PSNR are equivalent to the Euclidean norm (L2N) of the pixel-wise difference between the images being compared (although expressed in different units), (*b*) SSIM and Q are not insensitive to the background level (not appropriate in the astrophysical context, where images of compact objects on a constant background are always considered), and (*c*) KL is not able to distinguish between two different images with pixels equal to zero if those are non-zero pixels in the reference image.

IBC is clearly not a good merit function because, on the one hand, it discards pixels of the reconstructed image where the reference image is zero (a very common situation for a compact astronomical source on a dark background) and, on the other hand, it overemphasises the brighter regions of the image. This metric was nevertheless kept in the study, because of historical reasons.

`MiRA` was used to recover all images, and the aforementioned selected metrics were scrutinised. It was found that:

1. It is fundamental to convolve the true image with an effective PSF before image comparison, taking into account the resolution of the instrument and the super-resolution achieved by the image reconstruction algorithm;
2. The width of the PSF is significantly smaller than an equivalent Rayleigh-like criterion based on the maximum baseline;
3. Of all considered merit functions, L1N is the most robust and the only one that paves the way for automatic image reconstruction and quality assessment.

The full details of this study are presented in appendix A, page 235.

Chapter 8

Phase referencing *versus* phase closure imaging

"To know ahead of time what you're looking for means you're then only imaging your own preconceptions, which is very limiting, and often false."

— DOROTHEA LANGE (1895-1965; ADAPTED)

Contents

THIS CHAPTER is dedicated to address certain problems related to the impact of the nature of visibility phase variables on the quality of interferometric image reconstruction. Section 8.1 introduces three major questions pertaining the dichotomy *phase referencing/phase closure vs image reconstruction quality*, to wit: (*a*) which set of phase variables leads to better image restorations under the same observational conditions: *square of the visibility plus baseline (total visibility) phase* (*e.g.*, PRIMA+AMBER or GRAVITY like cases) or *square of the visibility together with closure phases* (*e.g.*, AMBER or PIONIER like cases), (*b*) what is the impact, if any, of increasing the number of telescopes in the quality of images, and (*c*) which scenario should be chosen for a fixed number of observed nights: phase referencing with less baselines or phase closure with more telescopes. These questions are analysed in sections 8.2 to 8.4.

Statement of the problem

Interferometric image reconstruction at mas has become routine, thanks to instruments that are capable of combining several apertures, such as AMBER and PIONIER at VLTI (Kluska et al., 2014; Le Bouquin, J.-P. Berger et al., 2011; Mérand, Stefl et al., 2010; Petrov et al., 2007), and the Michigan InfraRed Combiner (MIRC) at CHARA (J. D. Monnier, J.-P. Berger et al., 2004; J. D. Monnier, Pedretti et al., 2012). These instruments measure power- and bi-spectra, from which interferometric images can be restored. Current and future instruments, such as PRIMA and GRAVITY at the VLTI, are or will be able to provide the full visibility phase of objects by means of phase referencing.

While there has long been discussions concerning the use of phase closure or phase referencing as the main technique to retrieve visibility phase information and, thus, to support image reconstruction, the subject became a matter of hot debate during the last decade, especially every time a new beam combiner or image restoration algorithm was under discussion.[1]

The impact of increasing the number of telescopes on the quality of images is also still an open question. This issue was already partially addressed in section 7.5.3.3, when analysing the behaviour of the SNR measured on V^2 and on ϕ_c with N_{tel}, but no images were produced to test the conclusions that came out of that study.

Supported by comparison methods, such as the unbiased functions capable to evaluate the similarities and differences between the restored and original images (described in sections 7.6 and 7.7, page 143), sections 8.2 and 8.3 are devoted to the evaluation of the strength of each type of phase variables and to the analyses of the impact of the number of telescopes in the quality of image reconstruction, respectively.

These discussions arouse the urge to solve an important problem, fundamental in the framework of image reconstruction, to wit:

> *What is the best approach for image reconstruction for a given number of available nights: to use an instrument that combines less telescopes but is able to perform phase referencing, or to choose phase closure with an instrument capable of dealing with more baselines?*

This question becomes relevant at a time when new interferometers are being devised, such as MROI (D. F. Buscher et al., 2013). The answer to the former is not straightforward, because the disadvantage of less phase information can be filled in with more available baselines. This problem is the subject of section 8.4, the last of the current chapter.

[1] As an illustrative example, a debate of this kind spontaneously arouse at the SPIE conference *Optical and Infrared Interferometry II* in 2010, after a talk about the SQUEEZE restoration software (Baron, J. D. Monnier and Kloppenborg, 2010), with some specialists tenaciously defending that phase referencing simply does not work, while others supporting the idea that closure phases are very hard to handle within the context of image reconstruction.

Phase referencing *vs* phase closure

Current interferometric facilities are able to deliver two different sets of data which are fundamental for imaging: *power-spectrum* (square of the visibility) + *closure phase data* (hereafter referred as *phase closure* case) and *power-spectrum* + *visibility phase data* (hereafter identified as *phase referencing* case).

In the framework of image reconstruction, it may appear obvious that for a given *uv*-coverage, phase referencing is preferable to phase closure, simply because more phase information is available. This statement is strengthened under limited observing conditions, such as when it is not possible to sample many (u,v)-points, or when the SNR is low — the improved performance of phase referencing over phase closure under low SNR conditions was attested by Nuno Gomes, Paulo J. V. Garcia, Éric Thiébaut et al., (2010), for a stellar cluster.

However, when the number of sampled *uv*-points grows to be large, the amount of phase information enclosed by closure phases becomes comparable to that of phase referencing (J. D. Monnier, 2007). Hence, one should expect images of similar quality restored either by phase referencing or phase closure cases when the (u,v)-space is well paved.

In order to test the veracity of this claim, the three case study objects described in section 7.1 were mock observed and restored under four scenarios, obtained by crossing two subsets of conditions: [**sparse** and **generous** ***uv*-coverage**] *vs* [phase information provided by **baseline visibilities (phase referencing) only**, or by **closure phases only**]. The sparse *uv*-coverage was built with 18 unique calibrated measurements selected from a 4-nights configuration available for PIONIER. The generous case is based in a test case for the VSI instrument (Renard, Malbet et al., 2008), corresponding to a 6-nights configuration of 3 ATs, with two calibrated points measured each hour, per baseline. The two *uv*-coverages are illustrated in fig. 8.1.

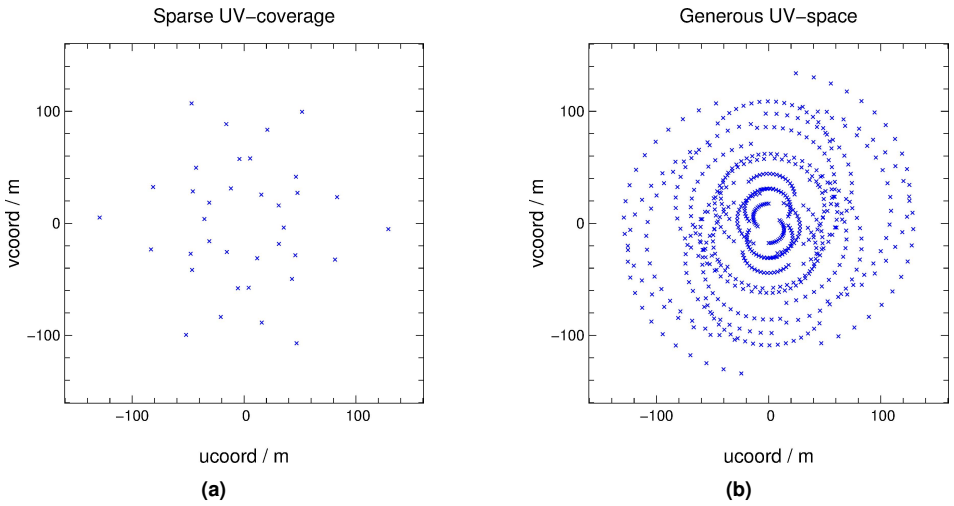

Figure 8.1: Sparse (*a*) and generous (*b*) *uv*-coverages used to compare the phase referencing and the phase closure cases. 18 and 323 unique spatial frequencies were sampled respectively in the sparse and generous pavements. Restored images of objects observed with these coverages are depicted in figs. 8.4 and 8.5. The parameters of the corresponding effective PSFs, estimated for all used FOVs, are compiled in table 8.1.

All sources were assumed to be located at a fixed 60° declination angle, and to be observed in the K-band, for an entire transit for 9 hours, during 2 min with the aid of a fringe tracker. Data were simulated using the *Simple Noise Model*, with an SNR of order 100, measured on V. For each simulation, an OIFITS file with mock observational data was generated. The file was subsequently loaded into `MiRA` and an image was restored.

Effective PSF estimation

Following the method described in section 7.7.4.1, effective PSFs were estimated for the two configurations of the *uv*-plane depicted in fig. 8.1.

Table 8.1: Average PSF parameters for image quality assessment. In all parameters, the used measure of dispersion was the standard error of the mean. All effective PSFs are assumed to be Gaussian ellipses displaced from the centre of the FOV by (x,y), with semi-major and semi-minor axis equal to (σ_x,σ_y), anticlockwise rotated by θ°. The FOVs of 20 mas, 12 mas and 10 mas correspond to the stellar cluster, the YSO, and the stellar photosphere, respectively. The original images are convolved with the respective effective PSF, prior to image comparison with the restored maps of figs. 8.4 and 8.5.

	Sparse *uv*-coverage			Filled *uv*-coverage		
	20 mas	12 mas	10 mas	20 mas	12 mas	10 mas
$x\,(\times10^{-2}\,\text{mas})$	2.56 ± 0.04	$2.06\ \pm0.05$	$0.9\ \pm0.1$	2.23 ± 0.07	$1.7\ \pm0.1$	$1.0\ \pm0.3$
$y\,(\times10^{-2}\,\text{mas})$	1.93 ± 0.01	$0.68\ \pm0.05$	0.59 ± 0.03	1.93 ± 0.05	$0.85\ \pm0.03$	$1.1\ \pm0.2$
$\sigma_x\,(\times10^{-1}\,\text{mas})$	0.80 ± 0.03	$1.97\ \pm0.02$	1.46 ± 0.01	0.46 ± 0.03	$2.05\ \pm0.06$	2.73 ± 0.04
$\sigma_y\,(\times10^{-1}\,\text{mas})$	0.99 ± 0.03	$1.97\ \pm0.03$	1.02 ± 0.02	0.92 ± 0.10	$0.91\ \pm0.04$	1.33 ± 0.04
$\theta\,(^\circ)$	$27.3\ \pm0.8$	$0.0\ \pm0.1$	$28\ \pm2$	$57\ \pm6$	$0.0\ \pm0.1$	$0.0\ \pm0.1$

Both reference images were adapted for the three FOVs under scrutiny, while keeping fixed the size of the spots (standard deviations in X- and Y- directions equal to 0.2 mas).[2]

Only the phase referencing case was used to simulate data during the effective PSF estimation, because in the presence of closure phases, the reconstruction becomes slower and harder, in the sense that it is more difficult to make `MiRA`'s high spatial frequencies converge to the corresponding experimental ones. Consequently, PSFs estimated using closure phases tend to be wider (*i.e.*, the flux becomes less concentrated, in Gaussian ellipses with larger semi-major axes) than PSFs assessed in the pure phase referencing case. Better results are achieved with less effort and in a shorter amount of time if data are composed uniquely of baseline visibilities;[3] accordingly, during image comparison (see next subsection), the effective PSF parameters were not varied between the phase referencing and the phase closure scenarios.

[2]For the baselines present in the current section, the corresponding resolution was always equal to or less than 3.4 mas in the K-band.

[3]Good estimations of effective PSFs, *i.e.*, ellipses whose shape and size are compliant with the *uv*-coverage, can be achieved with data containing only bi-spectra and closure phases, or in the phase referencing + phase closure case (*i.e.*, OIFITS files encompassing complete visibility phases and bi-spectra). However, the process is more laborious, and it delivers adequate results only when the (u,v)-space is well paved. Examples of those are presented in the next subsection.

The simulated data for the effective PSFs estimated in the frame of this subsection were created using the *Simple noise model*, with an SNR around 100, estimated on V.

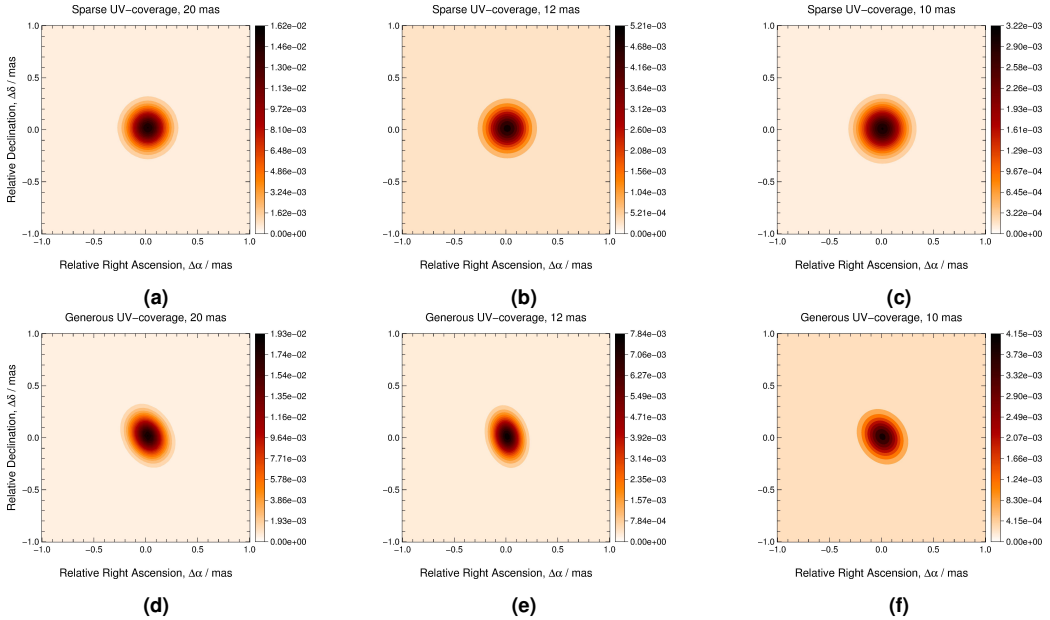

Figure 8.2: Effective PSFs estimated for the sparse (*a, b, c*) and generous (*d, e, f*) uv-coverages. (*a*) and (*d*) correspond to an effective PSF in a FOV of 20 mas (stellar cluster), (*b*) and (*e*), to a FOV of 12 mas (YSO), and (*c*) and (*f*), to a FOV of 10 mas (stellar surface). Both pavements of the (u, v)-space are correctly represented by all Gaussian ellipses: a round effective PSF translating the symmetrical sparse uv-coverage, and a slightly elongated ellipsis in the direction NNW-SSE (where the density of spatial frequencies is lower), representing the generous uv-coverage. The parameters of the ellipses are compiled in table 8.1.

All images were restored under the same conditions as the corresponding scientific objects. During `MiRA` configuration, the size of the pixel was chosen in accordance to the number of pixels, so as to match the FOVs of the original and restored images, and to thus maintain the physical sizes of the objects.[4]

An estimated angle of a simulation was very different from the values which resulted from the rest of the estimations for about 5 % of the tries. The reason behind this resides in the fact that, in those cases, the Gaussian was "too circular" (its standard deviations in X- and Y- directions were very similar), and the algorithm could hardly find the correct rotation angle. Although the resultant Gaussian was very similar to the other resulting from the remaining of the trials, these particular values of rotation angles affected the average and error statistics of the sought parameters. Therefore, they were usually classified as outliers, and removed from the data prior to computation of the statistics.

The resulting parameters, compiled in table 8.1 and illustrated in fig. 8.2, together with the normalised intensity profiles of fig. 8.3, demonstrate that the width of the FOV is not relevant for effective PSF assessment. That is predictable since, on the one hand, the physical sizes of the spots used for PSF estimation were kept fixed when the widths of the FOVs were varied, and, on the other hand, and as a principle, the shape of the effective PSF should rely solely on the uv-coverage. As

[4] Ergo, the spots are not depicted by the same number of pixels in different FOVs.

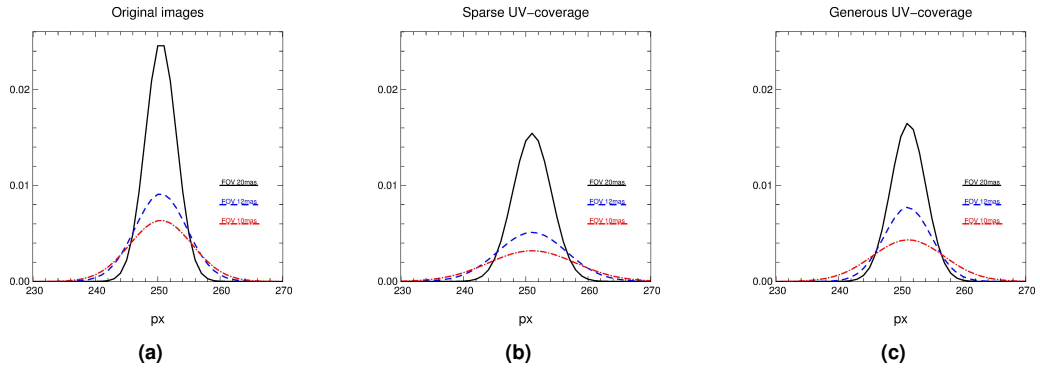

Figure 8.3: Normalised intensity profiles in FOVs of 10 mas, 12 mas and 20 mas for (*a*) a spot centred in the image, (*b*) the estimated effective PSF in the sparse uv-coverage of fig. 8.1a, and (*c*) the estimated effective PSF in the generous uv-coverage of fig. 8.1b. In the original images, the widths of the central spots extend respectively for about 5 px, 8.3 px and 10 px. These values are reasonably respected in the estimated PSFs. The differences in the fluxes stem from the fact that the total fluxes of the images are concentrated in Gaussian profiles of different FWHMs.

expected, the FWHMs are about the same size (0.2 mas) for all estimated effective PSFs, spanning a row containing approximately the same number of pixels as in the corresponding original images.

All results presented in the current subsection emphasise the robustness of the method described in section 7.7.4.1, for the estimation of the effective PSF associated to an imaging interferometric instrument.

Results and conlusions

For image reconstruction, an isotropic total variation regularisation (in agreement with Renard, Éric Thiébaut and Malbet, 2011) was used, as well as exact Fourier transforms, and a factor of about 8 in super-resolution. The best image possible was sought, corresponding to the minimum number of steps until stabilisation of the former. The hyper-parameter μ was always chosen so that the restored images would have the best figure of merit. The smallest value of μ used for PSF estimation served as a starting point for reconstruction of the images of the science objects, and proved to be a good estimate of the optimal value of the hyper-parameter. Most of the times, images stabilised and attained the best figure of merit using this optimal value of μ, previously found when estimating the effective PSF.

Examples of restorations are depicted in figs. 8.4 and 8.5. The first column corresponds to image restorations of the stellar cluster of fig. 7.1a, while the middle column to images of the stellar photosphere of fig. 7.1c, and the rightmost column to images of the YSO of fig. 7.1b (these objects are reproduced in the first row of both figures, for easier reference). Rows two and three show images restored with the sparse uv-coverage of fig. 8.1a and with the generous (u,v)-space of fig. 8.1b, respectively in figs. 8.4 and 8.5 — in each set of rows, the phase referencing images are located in line 1, while the phase closure bitmaps appear on the second line.

For each scenario, 12 realisations were carried out and the corresponding quality values were computed. The averages and standard deviations of the latter are summarised in the captions of figs. 8.4 and 8.5 (*cf.* section 7.7, page 175, for details on these functions).

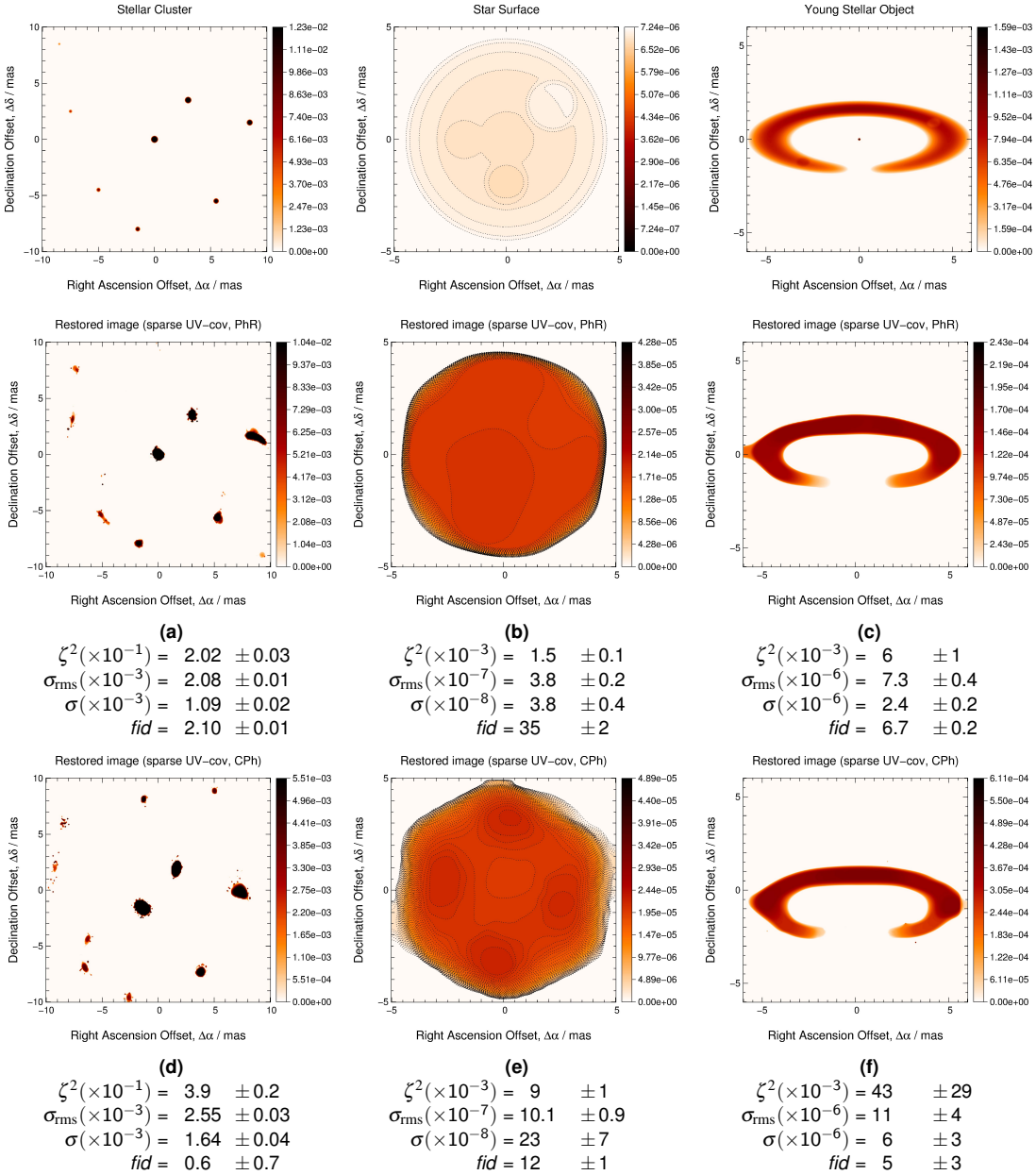

(a)
$\zeta^2(\times10^{-1}) = 2.02 \pm 0.03$
$\sigma_{\rm rms}(\times10^{-3}) = 2.08 \pm 0.01$
$\sigma(\times10^{-3}) = 1.09 \pm 0.02$
fid = 2.10 ±0.01

(b)
$\zeta^2(\times10^{-3}) = 1.5 \pm 0.1$
$\sigma_{\rm rms}(\times10^{-7}) = 3.8 \pm 0.2$
$\sigma(\times10^{-8}) = 3.8 \pm 0.4$
fid = 35 ±2

(c)
$\zeta^2(\times10^{-3}) = 6 \pm 1$
$\sigma_{\rm rms}(\times10^{-6}) = 7.3 \pm 0.4$
$\sigma(\times10^{-6}) = 2.4 \pm 0.2$
fid = 6.7 ±0.2

(d)
$\zeta^2(\times10^{-1}) = 3.9 \pm 0.2$
$\sigma_{\rm rms}(\times10^{-3}) = 2.55 \pm 0.03$
$\sigma(\times10^{-3}) = 1.64 \pm 0.04$
fid = 0.6 ±0.7

(e)
$\zeta^2(\times10^{-3}) = 9 \pm 1$
$\sigma_{\rm rms}(\times10^{-7}) = 10.1 \pm 0.9$
$\sigma(\times10^{-8}) = 23 \pm 7$
fid = 12 ±1

(f)
$\zeta^2(\times10^{-3}) = 43 \pm 29$
$\sigma_{\rm rms}(\times10^{-6}) = 11 \pm 4$
$\sigma(\times10^{-6}) = 6 \pm 3$
fid = 5 ±3

Figure 8.4: Examples of image reconstructions in the phase referencing and phase closure scenarios, for a sparse uv-coverage. **first row**: model/reference images; **second row**: phase referencing; **third row**: phase closure; **Leftmost column**: stellar cluster; **centre column**: photosphere; **rightmost column**: YSO. The average values and standard errors of the mean of the quality functions for all scenarios are presented in the captions of the corresponding image. ζ^2: accuracy function; $\sigma_{\rm rms}$: RMS statistics; σ: simple residuals; *fid*: fidelity function (*cf.* section 7.7).

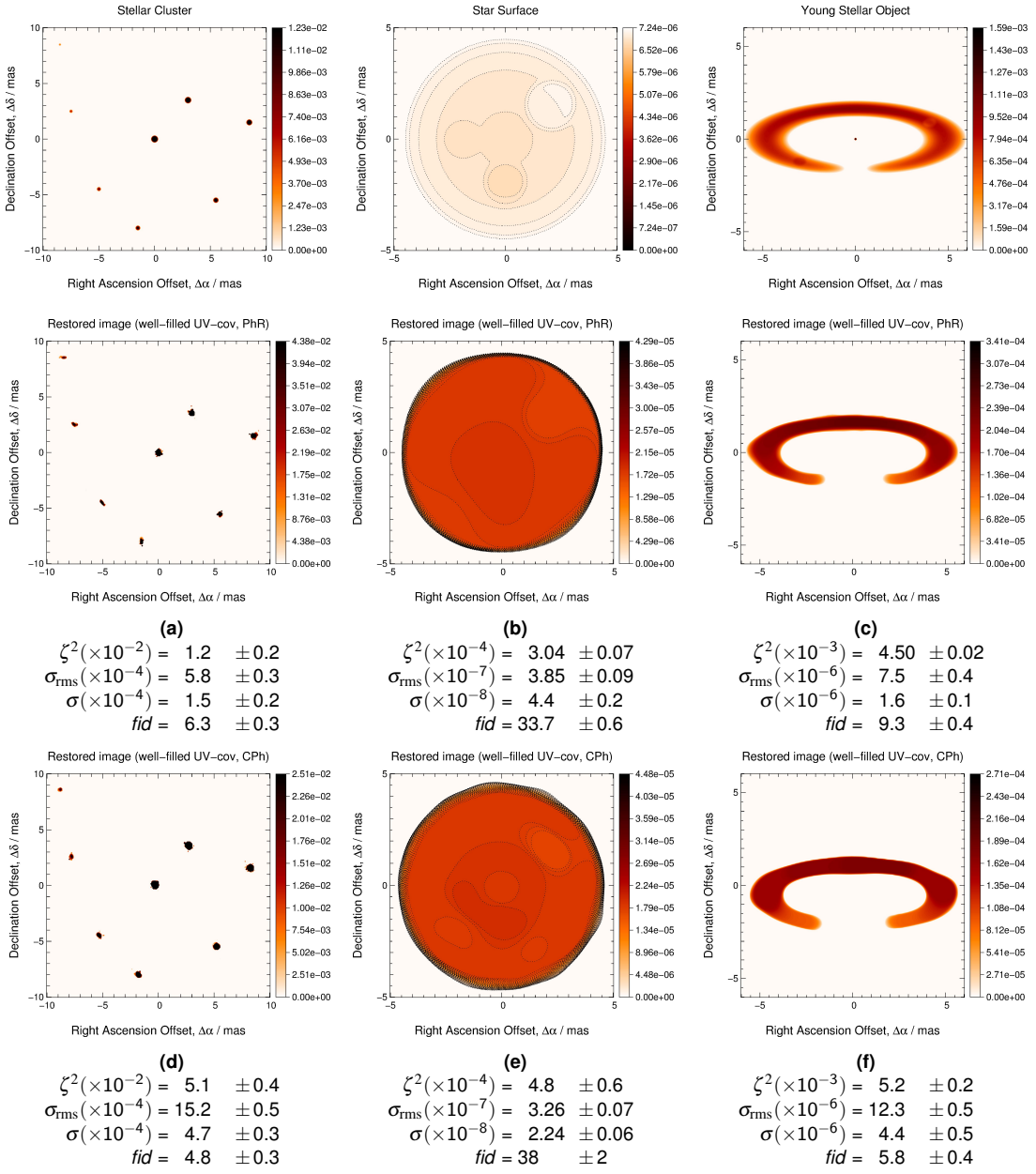

(a)
$\zeta^2(\times 10^{-2}) = 1.2 \pm 0.2$
$\sigma_{\rm rms}(\times 10^{-4}) = 5.8 \pm 0.3$
$\sigma(\times 10^{-4}) = 1.5 \pm 0.2$
fid = 6.3 ±0.3

(b)
$\zeta^2(\times 10^{-4}) = 3.04 \pm 0.07$
$\sigma_{\rm rms}(\times 10^{-7}) = 3.85 \pm 0.09$
$\sigma(\times 10^{-8}) = 4.4 \pm 0.2$
fid = 33.7 ±0.6

(c)
$\zeta^2(\times 10^{-3}) = 4.50 \pm 0.02$
$\sigma_{\rm rms}(\times 10^{-6}) = 7.5 \pm 0.4$
$\sigma(\times 10^{-6}) = 1.6 \pm 0.1$
fid = 9.3 ±0.4

(d)
$\zeta^2(\times 10^{-2}) = 5.1 \pm 0.4$
$\sigma_{\rm rms}(\times 10^{-4}) = 15.2 \pm 0.5$
$\sigma(\times 10^{-4}) = 4.7 \pm 0.3$
fid = 4.8 ±0.3

(e)
$\zeta^2(\times 10^{-4}) = 4.8 \pm 0.6$
$\sigma_{\rm rms}(\times 10^{-7}) = 3.26 \pm 0.07$
$\sigma(\times 10^{-8}) = 2.24 \pm 0.06$
fid = 38 ±2

(f)
$\zeta^2(\times 10^{-3}) = 5.2 \pm 0.2$
$\sigma_{\rm rms}(\times 10^{-6}) = 12.3 \pm 0.5$
$\sigma(\times 10^{-6}) = 4.4 \pm 0.5$
fid = 5.8 ±0.4

Figure 8.5: Same as in fig. 8.4, but for a generous uv-coverage.

During the simulations under scrutiny, some advantages of image reconstruction in the pure phase referencing case, *i.e.*, when only baseline visibility phases are available, were identified. These include: (*a*) with `MiRA` there is no need of using an initial guess in order to find the right path to the solution, (*b*) less steps are necessary for image stabilisation, (*c*) the iterations are performed more quickly, and (*d*) the absolute positions of the sources are preserved. Preservation of absolute positions favours image reconstruction because a smaller FOV can be selected without the risk of loosing information and, therefore, less unknowns (pixels) are to be sought. Moreover, photometry is more accurate in the phase referencing case, because light is more concentrated in each spot/star.

Overall, and as expected, for the three tested objects, *phase referencing leads to better results than phase closure when the uv-coverage is sparse*, whilst *both scenarios yield similar images when the* (u,v)*-space is filled*. Phase referencing behaved fairly in the sparse *uv*-coverage case, and greatly in the generous case; in turn, phase closure respectively behaved poorly and quite well in the same cases. The differences in quality were more notorious for the stellar cluster and the photosphere (surprisingly, the YSO was satisfactorily restored in all scenarios). In the badly paved *uv*-coverage, only the first four brighter stars were fairly restored in the phase closure case, with the image presenting several spurious features that do not belong to the original image. The stellar surface did not have a rounded shape, either. In turn, phase referencing was able to detect all 8 stars of the first model image, and the stellar photosphere was decently reconstructed. In the generous case, the quality values of phase referencing and phase closure were of the same order of magnitude. No central star and none of the structures in the YSO were detected in any scenario, because their sizes lied bellow the interferometer resolution, and/or were too faint to be detected.

When using uniquely closure phases to restore images in a sparse *uv*-coverage, the solution highly relies on the initial guess, namely in its brightness distribution and position of features. A displacement of the initial image by a few pixels, both in the horizontal or vertical positions, can dictate the success or not of the reconstruction. The initial guess for the phase closure case was created by performing a quick restoration of 500 iterative steps without any phase information (*i.e.*, only visibility amplitudes were used).[5] It was decided not to use any model resembling the original image, in order to put the simulation in a blind scenario, where not much is know about the source brightness distribution apart from the boundary conditions (positivity, normalisation, and regularisation). In addition to the 180° uncertainty in the orientation of this initial image, it often happened that the guess was converging to a local minimum, which translates in a very different image from the sought cluster, star or YSO.[6] A good initial guess is thus mandatory when closure phases are contained in the data, even if complete visibility information is present as well. In this sense, closure phases can act as an obstacle because they increase the amount of steps necessary

[5] In order to create a good initial guessing image without phase information, it is fundamental to give enough iterative steps for the first round of the reconstruction process. With too few steps, the image might not converge for the best solution. For example, when seeking the effective PSF, the estimated ellipse becomes too large if less than 200 iterative steps is applied during guess estimation. Typically, a number in the range 300 to 500 is enough to obtain a nice initial guess.

[6] This effect was frequently observed with extended, partially or completely resolved objects.

for the stabilisation of the solution.

To convolve the original image with the effective PSF before comparison becomes particularly relevant in a face-to-face between phase referencing and phase closure, especially for non-resolved sources. In fact, point-like objects tend to become rounder when restored with data composed only of closure phases in a generous (u,v)-space, leading to an erroneously rounded effective PSF, and, consequently, to misleading quality values for phase closure images. This is apparent in the restored images of the generous case, especially for the fainter and smaller stars of the cluster, and for the stellar surface.

Increasing the number of telescopes

The number of telescopes currently used for interferometric observations remains very limited ($2 \leqslant N_{\text{tel}} \leqslant 6$) and, therefore, the *uv*-coverage is typically very sparse and uneven (Éric Thiébaut, 2013, *cf.* fig. 8.6).

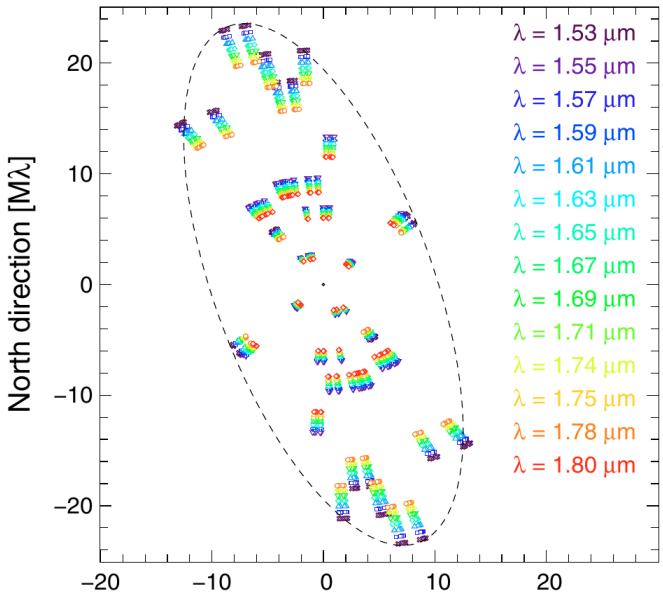

Figure 8.6: *uv*-coverage with IOTA 3-telescope interferometer in the H-band (ibid.).

The problem of increasing the number of telescopes for data acquisition is intimately related with the total number of sampled points in the *uv*-space. If, on the one hand, using more apertures leads, in theory, to better interferometric images because more visibility information is available for the algorithms, on the other hand adding more telescopes becomes effective only if the spatial frequencies are well spread in the (u,v)-space, and not concentrated in some privileged directions. If this condition is met, then increasing the number of telescopes will lead to better interferometric images, because the excess in visibility amplitude and phase information compensates the decrease of the SNR on V^2 with N_{tel}. As shown in section 7.5.3.3 (page 156), the SNR measured on ϕ_{c} decreases with the number of telescopes, similarly to what happens to V^2. However, in the

framework of image reconstruction another quantity becomes important in the estimation of the SNR, to wit, the number of baselines used for the observations, $n_{\rm bas}$. To each baseline corresponds one spatial frequency and, hence, one point of measurements. This allows to increase the *effective* SNR, which can be estimated by $n_{\rm bas}/\sigma(V^2,\phi_{\rm c})$, where $\sigma(V^2,\phi_{\rm c})$ is the standard deviation of V^2 or that of $\phi_{\rm c}$. Since $n_{\rm bas} = N_{\rm tel}(N_{\rm tel}-1)/2$ and $\sigma(V^2,\phi_{\rm c}) \propto N_{\rm tel}^{\alpha}$, with $\alpha < 2.0$, the *effective* SNR will also increase with the number of telescopes, leading to better restored images.

Phase referencing *vs* phase closure revisited: best observing set-ups

This subsection addresses the question presented in the box of page 188: for a given number of planned observing nights, should one choose (*a*) *a phase referencing configuration*, with less baselines but more phase information per (u,v)-point, or (*b*) *a phase closure scenario*, with more available collecting apertures but less phase information per sampled spatial frequency?

Simulations and discussion

In face of the configurations currently available for the VLTI, as well as others accessible in a near future or already foreseen, three scenarios were put under scrutiny:

1. *Two telescopes in phase referencing* (hereafter **2TPhR**, PRIMA+AMBER like) *vs three telescopes in phase closure* (from now on **3TCPh**, AMBER like) during 6 nights of observation;[7]
2. *Three telescopes in phase referencing* (henceforth **3TPhR**, GRAVITY like) *vs four telescopes in closures* (henceforward **4TCPh**, PIONIER like) during 3 nights;
3. *Four telescopes in phase referencing* (hereafter **4TPhR**, GRAVITY like) *vs six telescopes in closures* (henceforth **6TCPh**, VSI[8] or MIRC like).

The synthetic emitting sources of fig. 7.1 were imported to `OI-SIM`, using typical magnitudes to generate noisy data by means of the Simple model of section 7.5.1 (page 132), and the models from Tatulli & Chelli 2005 and Tatulli & Chelli 2010 (sections 7.5.3 and 7.5.4, pages 134 and 163, respectively).

All sources were assumed to be observed in the K-band, for an entire transit of 9 hours, and at a fixed -60° declination angle. In every hour, two calibrated (u,v)-points were obtained per baseline, assuming an on-source integration time of 120 s and 1 s, respectively for the *Simple* and *Tatulli et. al* noise models, aided by a fringe tracker (the remainder of the time is supposed to be needed for overheads).[9] An OIFITS file was generated for each observation, comprising all nights spent for data acquisition. The OIFITS were imported to `MiRA`, and images were restored using

[7] PhR stands for **Ph**ase **R**eferencing, while CPh corresponds to **C**losure **Ph**ase.

[8] J.-P. Berger, Malbet et al., 2012.

[9] It is important to assure that an image is restored for all *uv*-coverages. Therefore, regardless of the noise model, low noise regimes were always adopted in the current subsection.

a *total variation* regularisation, exact Fourier transforms, a factor of about 8 in super-resolution, and a minimum number of steps until stabilisation of images. For each case, μ was chosen so as to have the best figure of merit possible for the restored images (see section 8.2.1, page 183, for more details). The restored images were then imported to `OI-SIM` and compared to the corresponding synthetic ones. The results of the image comparisons for the two aforementioned noise models are presented respectively in sections 8.4.1.3 and 8.4.1.4.

Fine-tuning the *uv*-plane for phase referencing

The fact that the ATs can be reallocated every day, but not during the night, imposes limitations to the way the (u,v)-space is paved, because the telescopes are kept fixed during an observation run. Swapping between baselines is possible, but not the simultaneous combination of different sets of baselines, since that would demand the presence of at least two beam-combiners and two star-separators. While considering these limitations of the VLTI, but not bearing in mind details such as shadowing or real object observability, the set-ups were chosen in order to optimise the spatial frequencies plane.

In the *phase referencing case*, two classes of *uv*-coverages were used for the simulations: *standard* and *improved*.[10] In both of them, the *uv*-coverage is filled using the stations available for the *phase closure case* to which comparisons are being made, always aiming at the best paving of the spatial frequency space, *i.e.*, (u,v)-points spread in the best possible way in the full range of spatial frequencies, trying to avoid holes in all directions. However, while in the *standard class* the measurements are carried out along full *uv*-tracks spanning the whole night of observation, in the *improved class* the measurements are selectively performed over different baselines during the night, by means of *baseline-switching*, while keeping constant the total number of measured spatial frequencies. With this technique, instead of being fixed to a single set of baselines during the full night, different combinations of telescopes can be used by alternatively swapping between them, aiming at the uniform distribution of the spatial frequencies in the (u,v)-space (Nuno Gomes, Paulo J. V. Garcia and Éric Thiébaut, 2014).[11]

The *uv*-coverages used in the simulations are illustrated in fig. 8.7. Left column represents standard phase referencing configurations, middle column stands for improved phase referencing configurations, and right column corresponds to phase closure configurations. The sets of spatial frequencies depicted in the top row were collected during 6 nights of observation, while the sets of the centre row were obtained after 3 nights of observation, and the ones in the bottom row were acquired during a single observing night.

[10] A distinction should be made between *improved* and *well-paved uv*-coverages. The former corresponds to the best coverage possible with the available baselines; the latter, to a coverage where no holes are present in the whole range of spatial frequencies, being the (u,v)-coordinates evenly separated by a distance roughly equal to the smallest baseline.

[11] Although this is a study on imaging with the VLTI, the UTs were not considered in the simulations because, on the one hand, the ATs can be reallocated, and, on the other hand, currently the UTs cannot be simultaneously combined with the ATs — notwithstanding, this hybrid mode has been foreseen and successfully tested, and it might be available in the future (Haguenauer et al., 2012).

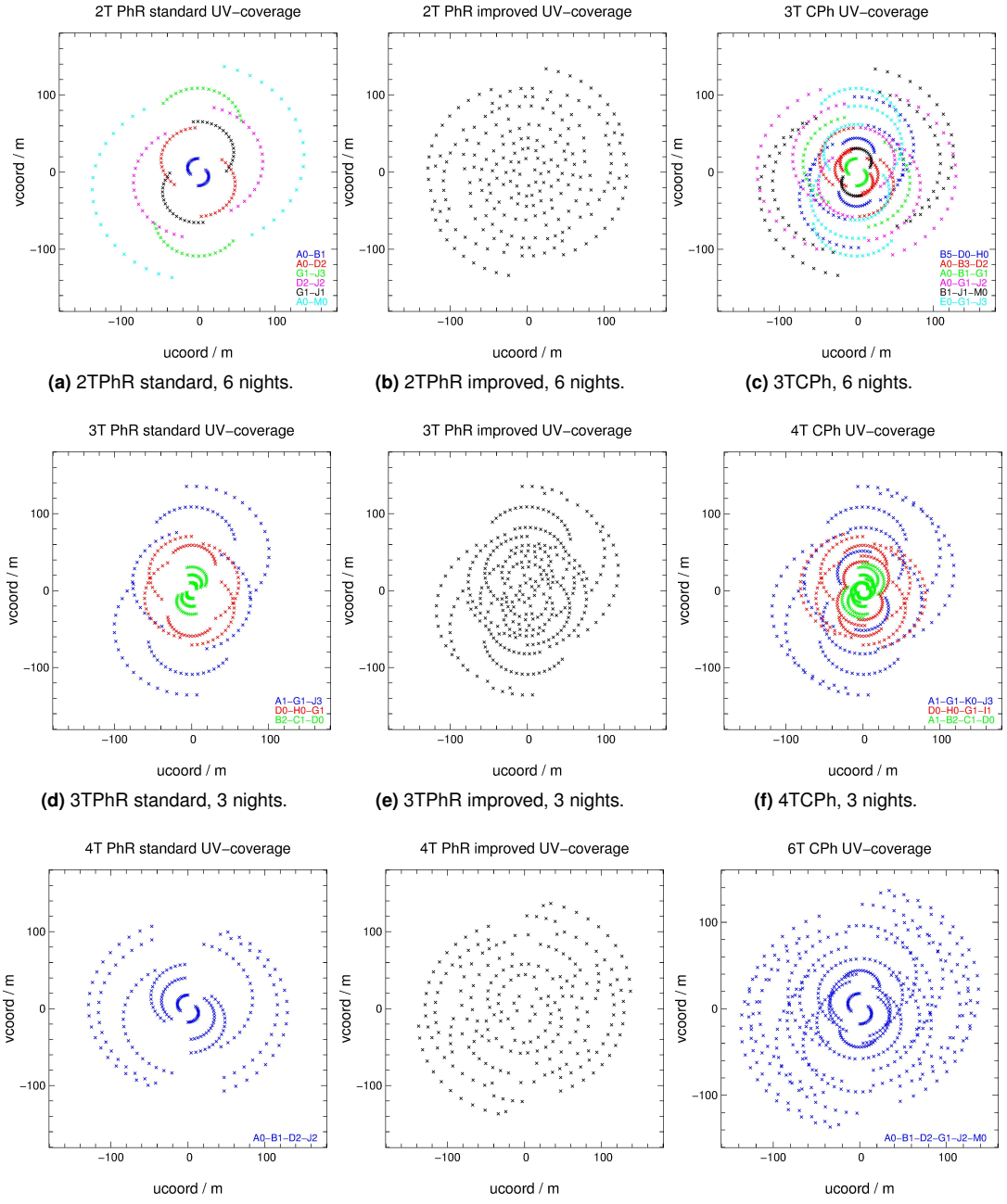

(a) 2TPhR standard, 6 nights. **(b)** 2TPhR improved, 6 nights. **(c)** 3TCPh, 6 nights.

(d) 3TPhR standard, 3 nights. **(e)** 3TPhR improved, 3 nights. **(f)** 4TCPh, 3 nights.

(g) 4TPhR standard, 1 night. **(h)** 4TPhR improved, 1 night. **(i)** 6TCPh, 1 night.

Figure 8.7: uv-coverages used for simulations. **Let column**: phase referencing, standard uv-coverage; **Centre column**: phase referencing, improved uv-coverage; **Right column**: phase closure. **Top row**: 6 nights of observation; **Middle row**: 3 nights of observation; **Bottom row**: 1 night of observation. For the left and centre columns, the total number of sampled frequencies is the same in each row. All configurations are for an object assumed at -60° declination. The VLTI stations are indicated for the standard phase referencing and phase closure configurations.

Effective PSF estimation

Effective PSFs were estimated for each configuration represented in fig. 8.7. Their net experimental parameters are compiled in tables 8.2 and 8.3, where the used measure of dispersion was the standard error of the mean.

Table 8.2: Averaged effective PSF parameters for phase referencing configurations used in the current study. For each parameter, the second figure corresponds to the standard error of the mean. "std" and "imp" stand respectively for *standard* and *improved* uv-coverage (see text for details). The PSFs are assumed to be Gaussian ellipses displaced from the centre of the FOV by (x,y), with semi-major and semi-minor axis equal to (σ_x,σ_y), anticlockwise rotated by θ°. The original images were convolved with the corresponding PSF prior to image comparison.

	2TPhR		3TPhR		4TPhR	
	std	imp	std	imp	std	imp
$x\,(\times10^{-2}\,\mathrm{mas})$	1.47 ± 0.08	$1.35\ \pm0.09$	$1.7\ \pm0.1$	$1.33\ \pm0.09$	$1.6\ \pm0.1$	$1.36\ \pm0.09$
$y\,(\times10^{-2}\,\mathrm{mas})$	1.12 ± 0.05	$1.18\ \pm0.08$	1.02 ± 0.09	$1.18\ \pm0.08$	1.20 ± 0.08	$1.20\ \pm0.08$
$\sigma_x\,(\times10^{-1}\,\mathrm{mas})$	1.46 ± 0.09	$1.9\ \pm0.1$	$1.8\ \pm0.2$	$2.1\ \pm0.1$	1.04 ± 0.07	$1.8\ \pm0.1$
$\sigma_y\,(\times10^{-1}\,\mathrm{mas})$	$2.1\ \pm0.1$	$2.3\ \pm0.1$	$1.9\ \pm0.2$	$2.9\ \pm0.2$	$1.5\ \pm0.1$	$2.2\ \pm0.1$
$\theta\,(^\circ)$	$21\ \pm2$	$5\ \pm1$	$30\ \pm4$	$49\ \pm3$	$12\ \pm3$	$3.6\ \pm0.9$

Table 8.3: Averaged effective PSF parameters for the phase closure configurations used in the current study (see description of the parameters in table 8.2).

	3TCPh	4TCPh	6TCPh
$x\,(\times10^{-1}\,\mathrm{mas})$	$-2.0\ \pm0.2$	$-2.0\ \pm0.2$	$-2.1\ \pm0.2$
$y\,(\times10^{-1}\,\mathrm{mas})$	$1.2\ \pm0.2$	$1.0\ \pm0.1$	$1.1\ \pm0.1$
$\sigma_x\,(\times10^{-1}\,\mathrm{mas})$	1.62 ± 0.06	$1.55\ \pm0.07$	1.35 ± 0.05
$\sigma_y\,(\times10^{-1}\,\mathrm{mas})$	1.87 ± 0.06	$2.01\ \pm0.09$	1.78 ± 0.07
$\theta\,(^\circ)$	$15\ \pm1$	$49\ \pm2$	$9.4\ \pm0.7$

A single spot was used as reference to estimate the effective PSF in the sparse uv-coverages. The restoration was more effective than when using several spots under a scenario of a poor paved (u,v)-space, and the convergence of the image reconstruction to the full set of spatial frequencies was not affected. As a general rule, in case of dubious results when employing a model image with several spots, a unique (large enough but unresolved) spot will guarantee a good estimation of the effective PSF.

Apart from the fact that the effective PSFs thus obtained are "super-resolved" when compared to their dirty beams (*cf.* fig. 6.1, page 102), their shape and orientations are in good agreement with the uv-coverages depicted in fig. 8.7, in the sense that the ellipses are more elongated in the direction with lower density of (u,v)-points. The shapes of the corresponding phase referencing and phase closure scenarios are identical, but in the latter the flux is more concentrated because of the inherent greater resolution of the interferometer.

All effective PSFs estimated exclusively with phase referencing data have lower displacements shifts when compared to those computed uniquely with closure phase data. In the aforementioned

tables, they are about one order of magnitude less, but that happens only because re-centring techniques were used during the restoration of phase closure images. Otherwise, the difference would account for several orders of magnitude. The displacements in phase referencing data, approximately equal to 0.01 mas in the X- and Y- directions, lie well inside the size of the pixel, which is of 0.1 mas, 0.06 mas and 0.05 mas, respectively for the FOV of 20 mas, 12 mas and 10 mas. This attests the accuracy of phase referencing and supports the decision of introducing an extra shift prior to image comparison for images restored exclusively with closure phase data, as described in section 7.7.4, page 181.

Nevertheless, it is interesting to note that the displacements of the PSF in the phase referencing case are systematic, in the sense that they always point to the same direction, by roughly the same amount. The reasons behind them might be related to the sampling, the image reconstruction algorithm, or even the nature (shape and size) of the object used to estimate the PSF, but further investigation is needed to address this question.

When estimating PSFs, it was found that the hyper-parameter μ (*cf.* section 6.3) should be small enough (*i.e.*, it should not be given too much weight to the *a priori* information) in order to make all spatial frequencies of `MiRA` converge to the sampled ones. Otherwise, the point-like sources become too round and the rotation angles cannot be estimated correctly. This effect is most noticeable when only closure phase information is used, because unresolved sources tend to become larger after reconstruction. However, μ cannot be taken too small or, in that case, point-like sources become tiny, well below the interferometer resolution, thus invalidating the estimation of the effective PSF.

It was found that the optimal value of μ for effective PSF estimation, *i.e.*, the lowest value used during reconstruction of the model image, is an accurate reference for the reconstruction of the scientific object. It typically leads to the best figure of merit for the restored images of the corresponding science cases. A rule of thumb is to start with a value of μ greater than the optimal value found during effective PSF estimation, in order to assure the convergence of the lower spatial frequencies. Progressively, this value is lowered one order of magnitude in each step, so as to bring `MiRA`'s and sampled high spatial frequencies to convergence. Usually, the image stabilises at the best solution when the optimal value of μ — or, at most, a value one order of magnitude lower — is used during the last step of the reconstruction. This practice was applied in all simulations, always leading to restored images with the best figure of merit. This optimal value of μ can be particularly useful when the original image of the emitting source is unknown.

Simple noise model

Aiming at a low noise regime, an SNR of 20 (measured on the visibility amplitude) was adopted. This value is supported by several contemporary observations, where SNRs are typically in the range 10 to 20 and some data points attain SNRs above 20 (*e.g.*, Defrère et al., 2012; P. J. V. Garcia et al., 2013; Sana et al., 2013).

Cluster of stars

Examples of reconstructed stellar clusters are illustrated in fig. 8.8. The positions of the restored images match the corresponding *uv*-coverages depicted in fig. 8.7.

It is notorious that the shapes of the spots reflect the *uv*-coverage, and that the quality of restorations become better when going from the standard classes (left column) to the improved ones (centre column). In fact, the spots become rounder and better defined, and the phase referencing reconstructed images become very similar to their phase closure counterparts. The reconstructions are quantified by means of the quality functions, compiled in table 8.4.

Table 8.4: Mean values of the quality functions for the synthesised stellar cluster (*Simple* noise model). Except for the fidelity function, the smaller the value, the better the reconstruction (the best value in each phase referencing *vs* phase closure configuration is highlighted in bold). These values were obtained by computing the statistics for at least 12 realisations in each scenario. The second figures correspond to the standard error of the mean.

	2TPhR		3TCPh	3TPhR		4TCPh
	std	imp		std	imp	
$\zeta^2(\times 10^{-2})$	15.8 $\pm$0.4	**2.21 $\pm$ 0.01**	3.0 $\pm$0.2	11.7 $\pm$0.4	**1.86 $\pm$ 0.05**	3.7 $\pm$0.2
fid	2.12 $\pm$ 0.02	**5.78 $\pm$ 0.02**	5.68 $\pm$ 0.09	2.45 $\pm$ 0.03	**6.40 $\pm$ 0.02**	5.5 $\pm$0.1
$\sigma_{\rm rms}(\times 10^{-4})$	15.0 $\pm$0.3	**2.34 $\pm$ 0.01**	4.5 $\pm$0.1	11.1 $\pm$0.3	**1.91 $\pm$ 0.03**	2.88 $\pm$ 0.04
$\sigma(\times 10^{-5})$	119 $\pm$4	**6.29 $\pm$ 0.03**	11.8 $\pm$0.5	77 $\pm$3	**4.32 $\pm$ 0.08**	8.1 $\pm$0.3

	4TPhR		6TCPh
	std	imp	
$\zeta^2(\times 10^{-2})$	12.1 $\pm$0.4	**2.26 $\pm$ 0.01**	2.27 $\pm$ 0.07
fid	2.36 $\pm$ 0.03	**5.69 $\pm$ 0.02**	5.5 $\pm$0.7
$\sigma_{\rm rms}(\times 10^{-4})$	13.1 $\pm$0.4	**2.64 $\pm$ 0.01**	3.20 $\pm$ 0.07
$\sigma(\times 10^{-5})$	91 $\pm$4	**7.03 $\pm$ 0.03**	8.0 $\pm$0.3

Since in the phase closure scenario, (*a*) the adopted initial guess was an image reconstructed wiping all phase information and giving a substantial weight to the data, (*b*) there is an uncertainty of π in the orientation of the image when only visibility amplitudes are used for the reconstruction, (*c*) the phase information is uniquely contained within closure phases, thus loosing the absolute position of objects, (*d*) the restoration process was intended to be automatic, without human intervention, and (*e*) the FOV is not big enough to ensure that the image will lay well inside it after `MiRA` photometric re-centring, a special procedure to properly re-orient and re-centre phase closure images was necessary, such as the ones represented in the rightmost column of fig. 8.7.[12] The algorithm consisted of overlapping the original ($\mathscr{O}$) and restored ($\mathscr{A}$) images on their maxima (the brightest star), to create the inverse of the restored image ($\mathscr{B}$), and to compare $\mathscr{A}$ and $\mathscr{B}$ to

[12] Otherwise, the faintest stars, located close to the top left boundary of the image, would have been wiped out most of the times, negatively affecting the quality of the image.

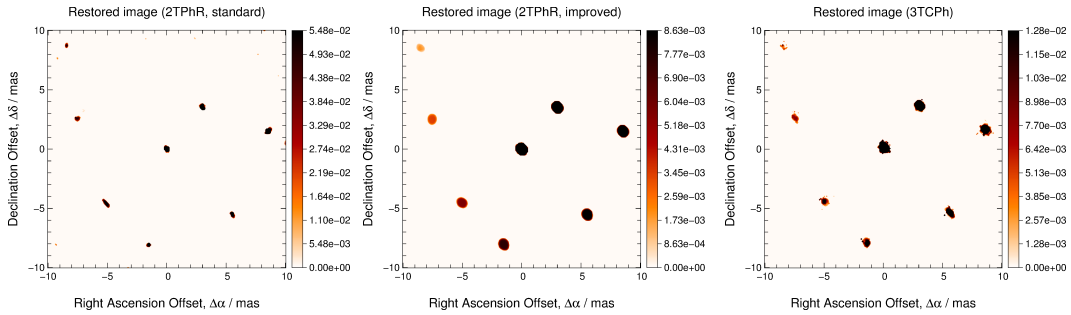

(a) Phase referencing, standard uv-coverage, 2 telescopes.

(b) Phase referencing, improved uv-coverage, 2 telescopes.

(c) Phase closure, 3 telescopes.

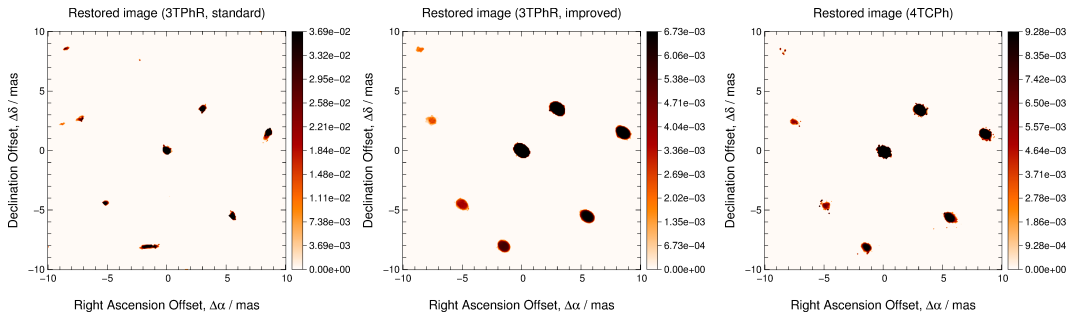

(d) Phase referencing, standard uv-coverage, 3 telescopes.

(e) Phase referencing, improved uv-coverage, 4 telescopes.

(f) Phase closure, 4 telescopes.

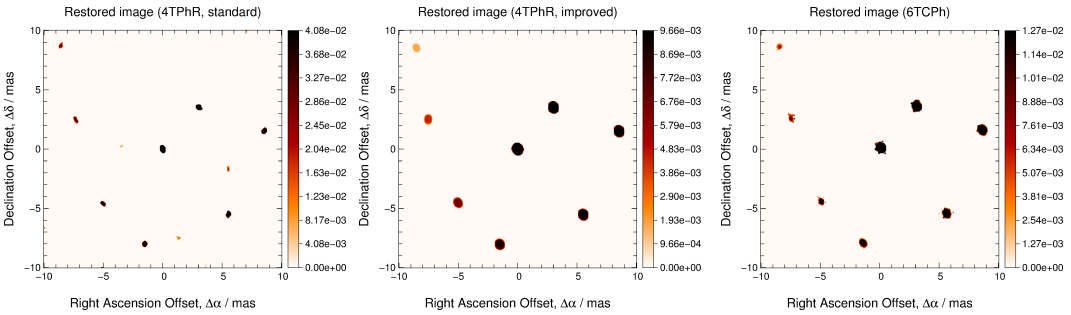

(g) Phase referencing, standard uv-coverage, 4 telescopes.

(h) Phase referencing, improved uv-coverage, 4 telescopes.

(i) Phase closure, 6 telescopes.

Figure 8.8: Examples of restorations of the cluster for data simulated with the *Simple* noise model. The first and second columns correspond respectively to a standard and an improved uv-coverage in the phase referencing case, and the third column stems for the phase closure scenario. The position of the images in the grid match their correspondent uv-coverages of fig. 8.7.

$\mathscr{O}$. The one which yielded the smallest residuals ($\mathscr{A}$ or $\mathscr{B}$) was kept for the remaining iterations of the reconstruction process.[13]

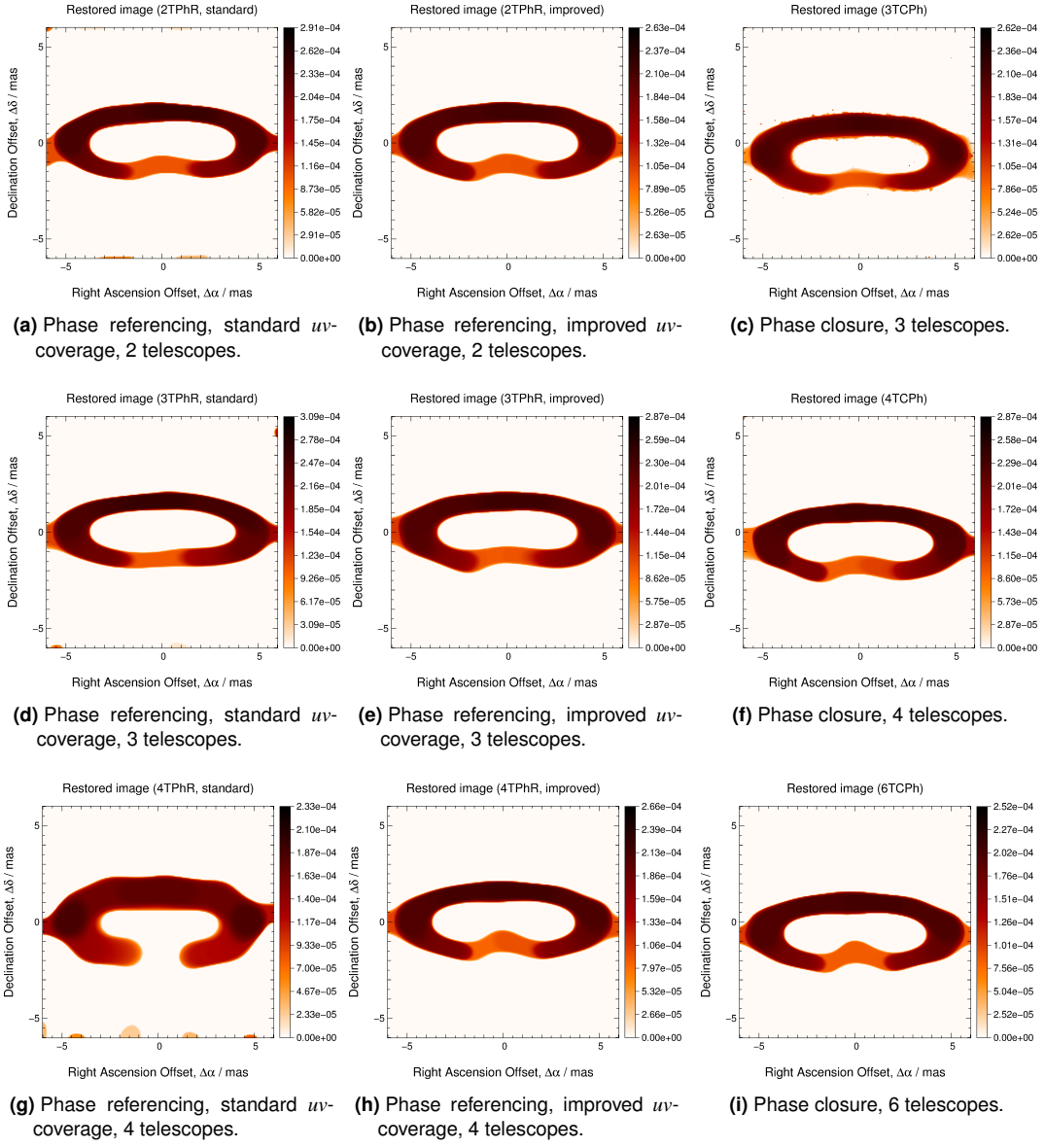

(a) Phase referencing, standard uv-coverage, 2 telescopes.

(b) Phase referencing, improved uv-coverage, 2 telescopes.

(c) Phase closure, 3 telescopes.

(d) Phase referencing, standard uv-coverage, 3 telescopes.

(e) Phase referencing, improved uv-coverage, 3 telescopes.

(f) Phase closure, 4 telescopes.

(g) Phase referencing, standard uv-coverage, 4 telescopes.

(h) Phase referencing, improved uv-coverage, 4 telescopes.

(i) Phase closure, 6 telescopes.

Figure 8.9: Examples of restorations of the YSO for all comparing configurations. The first and second columns correspond respectively to a standard and an improved uv-coverage in the phase referencing case, and the third column stems for the phase closure scenario.

The restorations are sensitive to the holes and asymmetries in the (u,v)-space, as it can be observed in the standard cases (*cf.* figs. 8.7a and 8.8a, figs. 8.7d and 8.8d, and figs. 8.7g and 8.8g, respectively). Several intertwined factors related to the distribution of the spatial frequencies in the

[13] Other solutions could involve (*i*) the dilation of the FOV, keeping at least half the size of the object on each side of it, and (*ii*) the generation of an extra OIFITS file containing phase referencing data, that could be used to carry out a quick image reconstruction. The latter, in turn, could be used as initial guess — that way, the absolute position of the source would be well preserved when restoring the image.

(u,v)-space, such as the minimum number of baselines necessary for proper image reconstruction, and the shape of the spectrum of spatial frequencies, affect the quality of image reconstruction.

Young stellar object

Figure 8.9 illustrates examples of reconstructions of the YSO. The mean values of the quality functions are compiled in table 8.5.

As in the previous object, all improved *uv*-configurations led to restored images with better quality than their standard counterparts. Except for the 4TPhR standard case, all images were fairly restored. The disc is very well formed and although it is closed on the bottom (contrarily to the original image), there is a notch bending inwards, indicating the presence of an "invisible" structure — the central unresolved star of the synthesised model image. It is interesting to note that the star is not restored, even though its intensity is about 35 times greater than the disc's surface brightness maximum. The reason for that is related to the fact that the size of the star (about 0.1 mas) is well bellow the resolution of the interferometer (approximately 3 mas).

Table 8.5: Mean values and corresponding standard errors of the mean of the quality functions for the synthesised YSO in every simulation. Except for the fidelity function, the smaller the value, the better the reconstruction (the best value in each phase referencing *vs* phase closure configuration is highlighted in bold). These values were obtained by computing the statistics for 12 realisations in each scenario.

	2TPhR		3TCPh	3TPhR		4TCPh
	std	imp		std	imp	
$\zeta^2(\times10^{-2})$	2.53 ± 0.03	$\mathbf{1.36\pm0.04}$	$1.4\ \pm0.2$	1.58 ± 0.02	$\mathbf{1.60\pm0.01}$	1.68 ± 0.02
fid	6.22 ± 0.03	$\mathbf{8.70\pm0.08}$	7.92 ± 0.03	6.32 ± 0.04	$\mathbf{7.23\pm0.03}$	6.62 ± 0.03
$\sigma_{\rm rms}(\times10^{-6})$	9.92 ± 0.06	$\mathbf{5.98\pm0.08}$	5.99 ± 0.04	7.74 ± 0.05	$\mathbf{6.14\pm0.02}$	7.09 ± 0.02
$\sigma(\times10^{-6})$	3.25 ± 0.03	$\mathbf{1.24\pm0.05}$	1.54 ± 0.02	2.73 ± 0.04	$\mathbf{1.85\pm0.01}$	2.35 ± 0.02

	4TPhR		6TCPh
	std	imp	
$\zeta^2(\times10^{-2})$	$7.9\ \pm0.1$	$\mathbf{1.90\pm0.01}$	1.92 ± 0.01
fid	3.65 ± 0.03	$\mathbf{6.75\pm0.01}$	6.74 ± 0.01
$\sigma_{\rm rms}(\times10^{-6})$	$16.3\ \pm0.1$	$\mathbf{7.16\pm0.01}$	7.19 ± 0.01
$\sigma(\times10^{-6})$	$8.5\ \pm0.1$	$\mathbf{2.18\pm0.01}$	2.24 ± 0.01

The 4TPhR standard configuration did not behave as well when compared with the other scenarios, as it is attested by the quality values of table 8.5. Although the disc is visible, it is thicker and rougher than its counterparts, and there is no concavity on the bottom indicating the presence of a central non-restored structure. The worst observed quality value of this image is a clear indication that more sampled spatial frequencies is not *per se* a guarantee of better image reconstruction. A well-paved *uv*-coverage is essential, even with less (u,v)-points.

Stellar photosphere

Examples of restored stellar surfaces are depicted in fig. 8.10. The mean values of the quality functions applied to all reconstructions of the stellar surface are summarised in table 8.6.

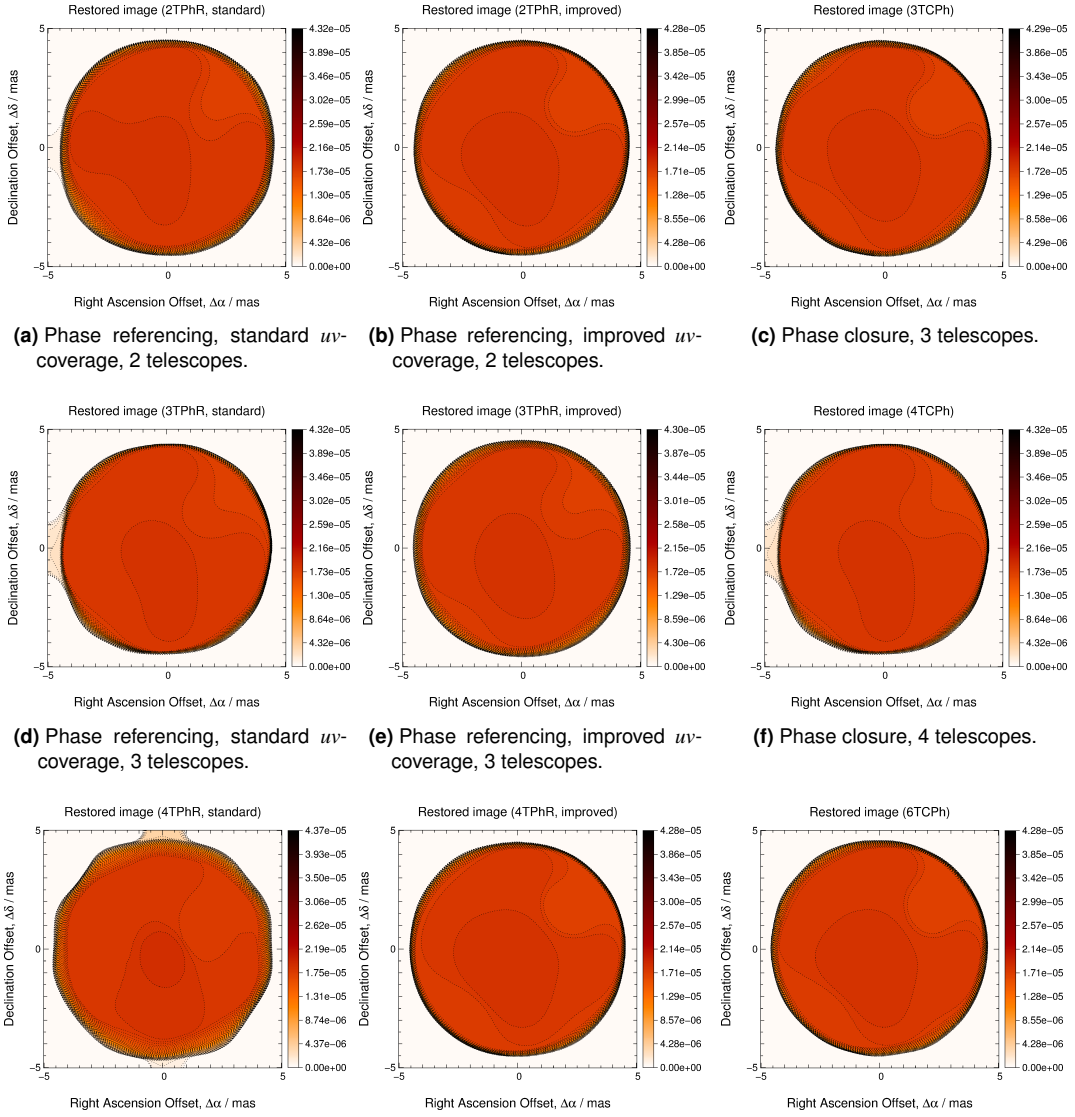

(a) Phase referencing, standard *uv*-coverage, 2 telescopes.

(b) Phase referencing, improved *uv*-coverage, 2 telescopes.

(c) Phase closure, 3 telescopes.

(d) Phase referencing, standard *uv*-coverage, 3 telescopes.

(e) Phase referencing, improved *uv*-coverage, 3 telescopes.

(f) Phase closure, 4 telescopes.

(g) Phase referencing, standard *uv*-coverage, 4 telescopes.

(h) Phase referencing, improved *uv*-coverage, 4 telescopes.

(i) Phase closure, 6 telescopes.

Figure 8.10: Examples of restorations of the stellar photosphere for all comparing configurations. The first and second columns correspond respectively to a standard and an improved *uv*-coverage in the phase referencing case, and the third column stems for the phase closure scenario.

As in the previous case, the stellar photosphere was satisfactorily reconstructed, except in the 4TPhR standard configuration. None of the three structures was clearly restored but, in the PhR improved and CPh cases, there are evidences of the brightest spot on the north-east side of the star, as well as of the two faintest spots (a valley and a crest), restored as one large structure, on the south-west part of the photosphere (*cf.* figs. 7.1c and 7.4). In the 4TPhR standard configuration, the star exhibits a rougher shape and the structures in the south-west part are not seen.

Table 8.6: Mean values of the quality functions for the synthesised stellar photosphere in every simulation. Except for the fidelity function, the smaller the value, the better the reconstruction (the best value in each phase referencing *vs* phase closure configuration is highlighted in bold). These values were obtained by computing the statistics for at least 12 realisations in each scenario. The measures of dispersion are the standard error of the mean.

	2TPhR		3TCPh	3TPhR		4TCPh
	std	imp		std	imp	
$\zeta^2(\times10^{-3})$	1.17 ± 0.04	$\mathbf{1.13\pm0.01}$	1.50 ± 0.03	$6.1\ \pm0.4$	$\mathbf{1.05\pm0.01}$	1.08 ± 0.02
fid	$36.3\ \pm0.6$	$\mathbf{37.50\pm0.07}$	$30.9\ \pm0.4$	$26.7\ \pm0.5$	$\mathbf{30.98\pm0.05}$	28.15 ± 0.04
$\sigma_{\text{rms}}(\times10^{-7})$	3.67 ± 0.06	$\mathbf{3.17\pm0.01}$	3.64 ± 0.06	$4.7\ \pm0.1$	$\mathbf{3.10\pm0.01}$	3.86 ± 0.03
$\sigma(\times10^{-8})$	$3.5\ \pm0.1$	$\mathbf{2.89\pm0.02}$	3.82 ± 0.01	$6.3\ \pm0.3$	$\mathbf{2.71\pm0.02}$	4.29 ± 0.06

	4TPhR		6TCPh
	std	imp	
$\zeta^2(\times10^{-3})$	0.41 ± 0.02	$\mathbf{0.24\pm0.03}$	0.26 ± 0.02
fid	$28.1\ \pm0.5$	$\mathbf{36.72\pm0.01}$	$35.7\ \pm0.4$
$\sigma_{\text{rms}}(\times10^{-7})$	4.09 ± 0.02	$\mathbf{3.30\pm0.01}$	3.62 ± 0.03
$\sigma(\times10^{-8})$	4.40 ± 0.04	$\mathbf{3.17\pm0.02}$	3.78 ± 0.04

Since the noise on the visibility amplitude relies on the average of all sampled visibilities (*cf.* eq. (7.28), page 132) and the stellar photosphere is a resolved object, it might happen that the noise level on the visibility amplitude attains very low values, which could explain the satisfactory quality of all restored images. Figure 8.11 depicts the average values of the square of the visibility amplitudes measured for the stellar photosphere in all observed configurations. Typically, the star is more resolved in the PhR improved scenarios, and the power-spectrum attains its lowest value (around 0.05) for the 4TPhR improved case. It corresponds to a visibility amplitude of about 0.22, which is well above zero for a resolved object, and perfectly acceptable in the framework of noise estimation.

Tatulli & Chelli 2005 + Tatulli & et al. 2010 noise models

When using *Tatulli & Chelli 2005* model for computing the noise on the power-spectrum and on the bi-spectrum, and *Tatulli et al.* model for the noise associated to the phase of the complex visibility, the following parameters were assumed:[14]

- $D_{\text{M1}} = 1.8\,\text{m}$ (diameter of main mirror);
- $D_{\text{M2}} = 0.136\,\text{m}$ (diameter of secondary mirror);
- $m_{\text{K}} = 10$ (magnitude of the source);
- $t = 1\,\text{s}$ (integration time);
- $\mathscr{E} = 0.15$ (efficiency);
- $\mathscr{S} = 0.5$ (long exposure Strehl ratio);

[14] Recall tables 7.9, 7.12 and 7.15, pages 138, 151 and 165 respectively.

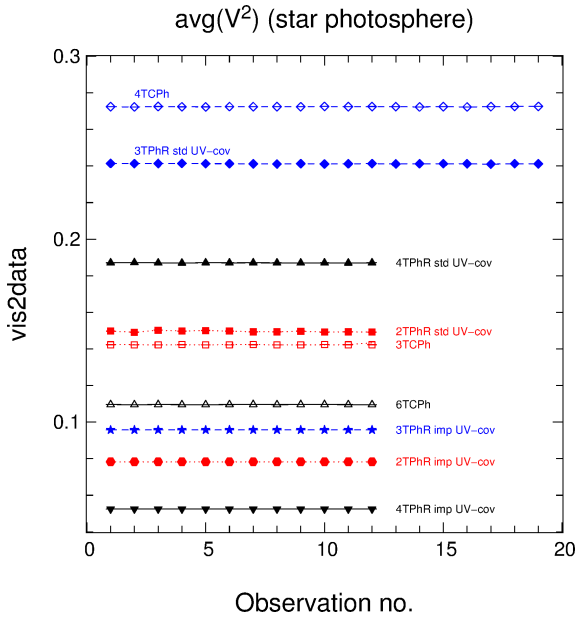

Figure 8.11: Average values of the power-spectrum for the stellar photosphere, for data simulated with the *Simple* noise model. Red squares and circles joined by a dotted line correspond to the 2Tx3T case, blue diamonds and stars, linked by a dashed line, to the 3Tx4T scenario, while the 4Tx6T case is represented by the black triangles connected by the solid line.

- $\sigma_{\mathscr{S}} = 0.2$ (error on the Strehl ratio);
- $\rho_0 = 0.8$ (optimal coupling coefficient);
- $\tau = 0.2$ (fraction of light for photometry);
- $N_{\text{pix}} = 24$ (detector pixels number);
- $\sigma_{\text{det}} = 5.0$ (readout noise of the detector);
- $\sigma^2_{\phi\text{r}} = 0.81$ (variance of the residual phase);
- $\mathscr{T}_i = 1.0$ (transmission in telescope i).

This set of parameters led to an SNR measured on the visibility amplitude of about 40, a value above the SNR used with the *Simple* noise model, but within the same order of magnitude and with a greater variance due to the nature of the model.

Concerning image reconstruction, exactly the same principles regarding effective PSF estimation (optimal μ parameter, and admeasure of the quality of images) were applied, being all described in the previous subsections. The results are presented in what follows.

Cluster of stars

The values of the quality functions computed for the reconstructions carried out with the stellar cluster are compiled in table 8.7, and examples of restored images are illustrated in fig. 8.12.

Table 8.7: Mean values of the quality functions for the synthesised cluster (*Tatulli et al.* noise model). A better reconstruction is indicated by a smaller quality value, except for the *fidelity* function (the best value in each phase referencing *vs* phase closure configuration is highlighted in bold). These values were obtained by computing the statistics for at least 12 realisations in each scenario. The second figures correspond to the standard error of the mean.

	2TPhR		3TCPh	3TPhR		4TCPh
	std	imp		std	imp	
$\zeta^2(\times10^{-2})$	45.4 ±0.4	**1.2 ±0.1**	2.4 ±0.3	49.8 ±0.6	**0.94±0.06**	2.5 ±0.1
fid	1.39±0.01	5.9 ±0.2	**6.4 ±0.2**	1.35±0.01	**6.3 ±0.1**	6.06±0.07
$\sigma_{\text{rms}}(\times10^{-4})$	13.3 ±0.3	**0.85±0.01**	9.1 ±0.5	9.6 ±0.1	**0.56±0.02**	8.6 ±0.2
$\sigma(\times10^{-5})$	218 ±4	**2.3 ±0.2**	21 ±2	176 ±4	**1.5 ±0.1**	20.6 ±0.7

	4TPhR		6TCPh
	std	imp	
$\zeta^2(\times10^{-2})$	11.51±0.04	8.18±0.01	**4.52±0.02**
fid	2.42±0.02	7.3 ±0.2	**9.08±0.02**
$\sigma_{\text{rms}}(\times10^{-4})$	12.3 ±0.3	8.10±0.01	**2.71±0.02**
$\sigma(\times10^{-5})$	84.8 ±0.4	24.9 ±0.5	**14.3 ±0.1**

The first thing that stands out from the images depicted in fig. 8.12 is the smaller smoothness of the spots, especially in the phase referencing case. This was already evident from the results presented in table 8.7, where the quality values are lower than the ones presented in table 8.4 for the *Simple* noise model. At a first glance, it is surprising to note that a different noise model, even with a greater SNR measured on the visibility amplitude, can have such an impact in the quality of the images. However, the graphs of fig. 8.13, illustrating several visibility quantities plotted against each other, show that the profiles of the error on the visibility amplitude, the error on the amplitude of the bi-spectrum, and the error on the closure phase are not similar in both noise models. While for the *Simple* noise model, $\sigma(V)$ remains constant with V, the former exhibit a minimum for low visibility amplitudes. Moreover, the closure phase, when plotted against the amplitude of the bi-spectrum, has a smoother drop in the *Simple* than in the *Tatulli et al.* noise model, while the error on the amplitude of the bi-spectrum, when plotted against B_{ijk} (the amplitude of the bi-spectrum), remains approximately constant in the *Tatulli et al.* noise model, and logarithmically increases in the *Simple* model of noise. These differences can explain the roughness exhibited by the reconstructions with data simulated with the *Tatulli et al.* noise model: or a more realistic noise model proves that phase referencing leads to worse images than phase closure (not plausible), or there is an error in the code which generates phase referencing data using the *Tatulli et al.* noise model (more likely). Further investigation is needed to address this question.

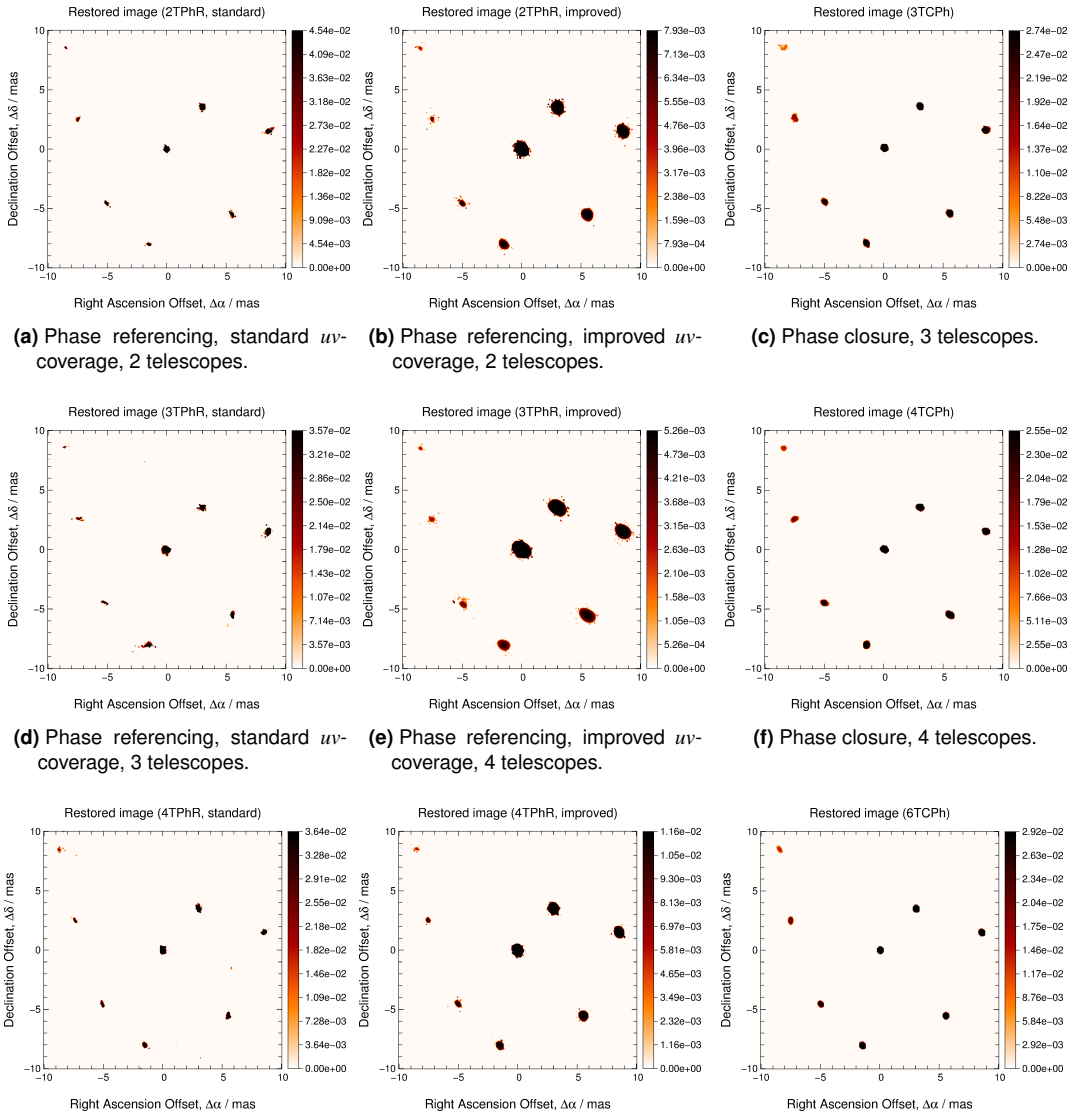

(a) Phase referencing, standard uv-coverage, 2 telescopes.

(b) Phase referencing, improved uv-coverage, 2 telescopes.

(c) Phase closure, 3 telescopes.

(d) Phase referencing, standard uv-coverage, 3 telescopes.

(e) Phase referencing, improved uv-coverage, 4 telescopes.

(f) Phase closure, 4 telescopes.

(g) Phase referencing, standard uv-coverage, 4 telescopes.

(h) Phase referencing, improved uv-coverage, 4 telescopes.

(i) Phase closure, 6 telescopes.

Figure 8.12: Examples of restorations of the cluster when the *Tatulli et al.* noise model was employed. The first and second columns correspond respectively to a standard and an improved uv-coverage in the phase referencing case, and the third column stems for the phase closure scenario. As for the previous examples with the *Simple* noise model, the position of the images in the grid match their correspondent uv-coverages of fig. 8.7.

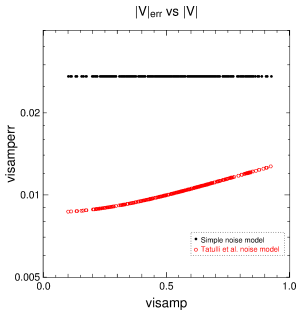

(a) Phase referencing, standard *uv*-coverage, 2 telescopes.

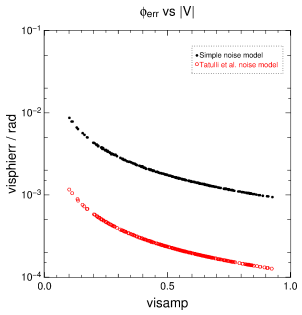

(b) Phase referencing, improved *uv*-coverage, 2 telescopes.

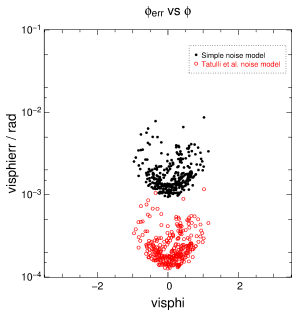

(c) Closure phase, 3 telescopes.

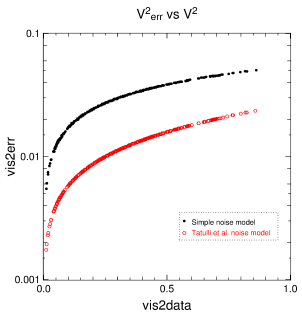

(d) Phase referencing, standard *uv*-coverage, 3 telescopes.

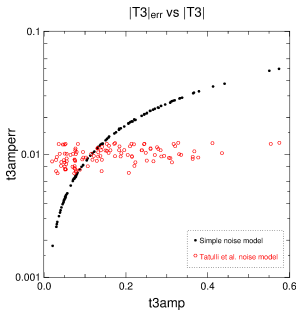

(e) Phase referencing, improved *uv*-coverage, 4 telescopes.

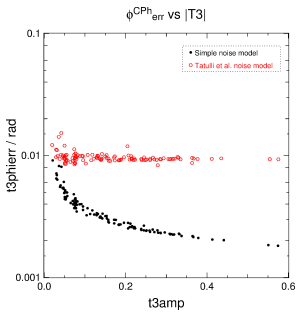

(f) Closure phase, 4 telescopes.

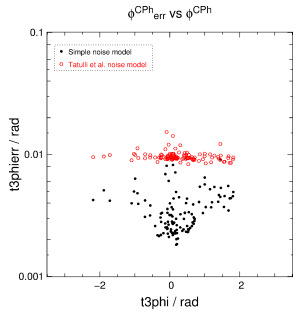

(g) Phase referencing, standard *uv*-coverage, 4 telescopes.

Figure 8.13: Visibility quantities for data simulated with the stellar cluster, with a configuration of 3 telescopes, and employing the *Simple* and *Tatulli et al.* noise models. The black filled dots correspond to data built upon the *Simple* noise model, while the red shallow circles represent data points simulated with the *Tatulli et al.* model.

Conclusions

From the results compiled in section 8.4.1.3, it becomes evident that if the *uv*-coverage is judiciously chosen (for instance by means of baseline switching) with the aim of spreading all spatial frequencies in the (u,v)-space, (a) the quality of reconstructed images is improved in the phase referencing case, and (b) both phase referencing with less telescopes and phase closure with more telescopes cases yield similar reconstructed images.

These results point to the need of making more efficient observations, in order to allow baseline switching between calibrated measurements, and thus to achieve an improved (u,v)-space, which in turn leads to better image reconstructions.

The outcome of section 8.4.1.4 indicate a better performance of phase closure than phase referencing. However, in face of the great difference in quality between the two sets of data, most likely these results are due to errors on the code when generating the visibility phase data using the *Tatulli et al.* noise model.

Part IV

Conclusions and Perspectives

Chapter 9

Conclusions and prospects

"What makes the Universe so hard to comprehend is that there's nothing to compare it with."

— ASHLEIGH BRILLIANT

Contents

THIS THESIS, entitled "Imaging with the VLTI", reports the work developed under the "Programa Doutoral em Astronomia" of FCUP. On the one hand, it presents the results of data reduction procedures and visibility amplitude computations carried out within the framework of PRIMA, the Phase Referenced Imaging and Micro-Arcsecond Astrometry dual-feed facility of ESO. On the other hand, it describes the results obtained within the study of optical interferometric image reconstruction, where two cases (*phase referencing* and *phase closure*) were put under scrutiny and the quality of images was quantified and compared.

PRIMA

In the astrometric operation mode, where both fringe trackers (FSUs) are operated simultaneously to determine the angular separation between two stars, PRIMA can be used to measure the visibility amplitude of the observed objects. The algorithm utilised to estimate the amplitude of visibilities was explained and tested against unresolved objects observed during PRIMA's commissioning run #2. The values of visibility amplitude obtained for stars HD15520 and HD18829, respectively 1.2 ± 0.3 and 1.3 ± 0.3, are compliant with point-like sources and previously published values of visibilities for the same objects. The results demonstrate that, although the FSUs

have been designed to uniquely measure the phase delay, they can also be safely used to infer the visibility amplitude of the emitting sources.

The feasibility of the faint-science mode was also attested, where light coming from the bright reference star is sent to FSUB, and light from the faint science object is directly sent to AMBER, the Astronomical Multi-Beam Combiner of the VLTI. The correlation between the centroids of the two beams striking the infrared detector IRIS of PRIMA was estimated, by plotting the relative positions in X- and Y- directions. The results indicate a high level of correlation (although some uncorrelated points have been exhibited due to the defocus on the Auxiliary Telescope 3, used during most of PRIMA's commissioning runs), validating the possibility of using PRIMA and AMBER to observe objects of high magnitude, which otherwise would be impossible to study due to the magnitude limitations of IRIS.

Prospects

In June 2014, ESO decided to cancel the PRIMA project (ESPRI, 2014). Consequently, to propose future tasks is to some extent an empty gesture. Nevertheless, work regarding the estimation of visibility amplitudes with the FSUs has been conducted, with science to be extracted from it that can be useful for future dual-feed instruments. For this reason, prospects are presented, addressed at the phase referencing technique and not PRIMA *per se*.

The first follow-up task should be the completion of the work presented in chapter 4, *i.e.*, the study of the dependence of the visibility amplitude with the separation between unresolved objects. Other pairs of binary stars, already observed during PRIMA commissioning time, can be used for that study. The aim is to determine the effects of the angular anisoplanatism in the estimation of visibilities, and how much their amplitudes vary with the position of the source in the FOV. The results would be relevant for the imaging mode of PRIMA, where the instrument is combined with AMBER — the latter computes the visibility amplitude of the source, while the former stabilises the fringes and reads the complex visibility phase (baseline phase). A paper on this subject is being prepared.

Other topics of interest which can be studied with the tools developed in this part of the thesis are the analysis of the dependence of the visibility, both with the detector integration time, and with the physical conditions of temperature and seeing inside the light ducts. The outcome will be helpful for a faint-science mode similar to PRIMA's, which may be developed in the future at the VLTI or at any other interferometer using light ducts where vacuum has not been created.

In conclusion, anisoplanatic effects and beam correlation studies would be critical for the astrophysical exploration of PRIMA in imaging and faint-object science mode. The developed work presents essential tools to endeavour important tasks such as the effects of angular anisoplanatism in the visibility amplitude determination, and the correlation of the positions on IRIS between the bright reference beam and the faint-science one. Although PRIMA is no longer operational, this work is relevant for the operation of future similar instruments and interferometric facilities.

Image reconstruction

The greatest advantage of carrying out image reconstructions in the domain of optical interferometry is the possibility of getting brightness distributions of emitting sources without knowing exactly what their shapes are or what kind of structures they exhibit. Currently, the quality of restored images is limited by the typically poorly-paved (u,v)-spaces produced by nowadays facilities. These images need to be properly analysed in order to extract valid physical information from them, even when they are supported by *a priori* models.

Two main cases were compared during this thesis: *phase referencing* and *phase closure*. While the former yields complete complex visibility information, the latter only delivers part of the phase, but its implementation is technically easier. For the comparison, three distinct objects (a stellar cluster, a young stellar object and a stellar photosphere) were mock observed with the VLTI. The statistics of the observables were estimated with the *Simple* noise model, which was developed aiming at the simplicity of its implementation and at the correct dependence of the visibility phase error bars on the visibility amplitude.

The results demonstrate that under the same observational conditions, both cases produce images of similar quality, provided that the *uv*-coverage is *good*, *i.e.*, the (u,v) points are evenly distributed over the full range of spatial frequencies. When the (u,v)-space is badly paved, that is, with a small number of sampled spatial frequencies or exhibiting pronounced holes in their coverage, phase referencing produces better images than phase closure. This outcome emphasises the importance of using phase referencing instruments with the UTs (such as GRAVITY), where the *uv*-coverage is very limited.

When less telescopes are employed for phase referencing than for phase closure, both scenarios yield images of similar quality on the condition that the (u,v)-space for the former is improved by means of baseline selection. When that condition is assured, even with less sampled spatial frequencies, the quality of images restored in phase referencing becomes comparable to that of images reconstructed in the phase closure case. Therefore, *uv*-selection is very important to maximize the efficiency of an observation and the quality of an image reconstruction. When restoring images is one of the primary objectives of the research, all available telescopes should be used during the observation. This is an indication that in VLTI and in other imaging facilities, algorithms allowing fast baseline switching should be developed, and their infrastructures should be improved to allow for a quick recombination of the telescopes (assuming the latter are movable), or adding for additional stations.

An important result for automatic image reconstruction was also achieved within the scope of this thesis, by relating the optimal μ hyper-parameter (which regulates the weight given to the data and to the *a priori* information for image reconstruction) to the best μ used when the effective PSF is being estimated. In order to create a blind guess of the image, the reconstruction should start without phase information and using a value of μ some orders of magnitude (typically 2 or 3) above the optimal value of μ found when the effective PSF was determined. Then, μ should gradually be reduced during the restoration until the convergence of the solution is verified. Typically, the

image with the best figure of merit is reached when the aforementioned optimal value of μ (the PSF μ) is finally used as a parameter of the reconstruction and a few hundreds of iterative steps are executed.

Prospects

As a first follow-up activity, the phase referencing and phase closure cases should be again compared, although this time with data simulated employing *Tatulli et al.* noise model, or any other model producing estimates of the error bars of the observables relying on more physical parameters, such as the characteristics of the interferometer and of the detector. It is fundamental to attest that the results are not dependent on the model used to mock the data. A paper on this matter is currently under preparation.

Automatic image reconstruction is fundamental for the VLTI scientific exploration and the quality assessment of the data. Therefore, the algorithmic estimation of the μ hyper-parameter should be further explored. It is important to analyse the impact of the nature of the visibility phase variable (baseline phase information or closure phases), as well as of the regularisation and the essential characteristics of the source brightness distribution on the evolution of μ during the reconstruction. A paper on this subject will be prepared.

In order to restore an image with a given structure and dynamic range, it would be also important to determine the minimum number of sampled spatial frequencies. At least four scenarios should be devised to study the influence of the type of the *uv*-coverage on the ability to produce an image or not:

1. The number of (u,v)-points is increased from the centre to the outskirts of the (u,v)-space;
2. Spatial frequencies are kept concentrated in the centre of the (u,v)-space;
3. A hole is kept in the centre, and the number of (u,v)-points is increased in the outskirts;
4. Spatial frequencies are removed from two opposing slices of the (u,v)-space, lying in one direction.

The results coming out of this work will allow for a better planing of interferometric observations aimed at the production of images.

In conclusion, image reconstruction is a fundamental area for the astrophysical exploration of the VLTI. The results obtained in the thesis, namely that *phase referencing* is superior to *phase closure* in the situation of a small number of telescopes, present for the first time a clear justification for the rational of imaging with GRAVITY using the UTs. Faint objects not within reach of the ATs can be observed with the UTs array. Secondly, although the technical development of optical interferometry is still very far of that of sub-millimetre interferometry, the evolution towards automatic images, such as those delivered by ALMA, is of strategic importance for the scientific success of the VLTI and other facilities, including those under study, such as the *Planet Formation Imager* (J. D. Monnier, S. Kraus et al., 2014).

Bibliography

Akeson, R. L. et al. (2005). 'Keck Interferometer Observations of Classical and Weak-line T Tauri Stars'. In: *The Astrophysical Journal* 635, pp. 1173–1181.

Akeson, Rachel L., Mark R. Swain and M. Mark Colavita (2000). 'Differential phase technique with the Keck Interferometer'. In: *Interferometry in Optical Astronomy*. Ed. by Pierre J. Lena and Andreas Quirrenbach. Vol. 2. Munich, Germany, pp. 321–327. URL: http://proceedings.spiedigitallibrary.org/proceeding.aspx?articleid=898086.

Arfken, George B. and Hans J. Weber (1995). 'Determinants and Matrices'. In: *Mathematical Methods for Physicists*. 4th. London, United Kingdom: Academic Press. Chap. 3, pp. 156–222. ISBN: 978-0120598151.

Armstrong, J. T. et al. (1998). 'The Navy Prototype Optical Interferometer'. In: *The Astrophysical Journal* 496.1, pp. 550–571. ISSN: 0004-637X. URL: http://stacks.iop.org/0004-637X/496/i=1/a=550.

Baldwin, J. E. et al. (1996). 'The first images from an optical aperture synthesis array: mapping of Capella with COAST at two epochs'. In: *Astronomy and Astrophysics* 306, p. L13.

Baldwin, John E. and Christopher A. Haniff (2002). 'The application of interferometry to optical astronomical imaging.' In: *Philosophical transactions. Series A, Mathematical, physical, and engineering sciences* 360.1794, pp. 969–86. ISSN: 1364-503X. URL: http://www.ncbi.nlm.nih.gov/pubmed/12804289.

Baron, Fabien, William Danchi Cotton et al. (2012). 'The 2012 Interferometric Imaging Beauty Contest'. In: *Optical and Infrared Interferometry III*. Ed. by Françoise Delplancke, Jayadev K. Rajagopal and Fabien Malbet. Amsterdam, The Netherlands: SPIE, p. 14.

Baron, Fabien, John D. Monnier and Brian Kloppenborg (2010). 'A novel image reconstruction software for optical/infrared interferometry'. In: *Optical and Infrared Interferometry II*. Ed. by William C. Danchi, Françoise Delplancke and Jayadev K. Rajagopal. Vol. 7734. 1. San Diego, California, USA: SPIE, pp. 77342I–77342I–8. URL: http://proceedings.spiedigitallibrary.org/proceeding.aspx?articleid=750592.

Baron, Fabien and John S. Young (2008). 'Image reconstruction at Cambridge University'. In: *Optical and Infrared Interferometry*. Ed. by Markus Schöller, William C. Danchi and Françoise Delplancke, pp. 70133X–70133X–11. URL: http://proceedings.spiedigitallibrary.org/proceeding.aspx?articleid=788969.

Beckers, J. M. (1990a). 'Instrumental factors affecting the fringe contrast in optical interferometers'. In: *Astrophysics and Space Science* 171, pp. 333–339.

— (1990b). 'The VLT interferometer. II - Factors affecting on-axis operation'. In: *Advanced Technology Optical Telescopes IV*. Ed. by L. D. Barr. Vol. 1236. Society of Photo-Optical Instrumentation Engineers (SPIE) Conference Series, pp. 364–371.

Beckers, Jacques M. (1983). *MMTO Technical Report Nr. 14 - Interferometric Imaging With The NNTT*. Tech. rep. European Southern Observatory (ESO), p. 59.

— (2005). *Interferometric Imaging in Astronomy: A Personal Retrospective*. URL: http://www.ctio.noao.edu/diroff/TALKS%5C_PDF/Beckers%5C_ctio%20Lecture.pdf.

Belle, Gerard T. van (2010). *PRIMA Startup Procedure & Other Useful Operational Information*. Garching.

Benisty, Myriam et al. (2011). 'A low optical depth region in the inner disk of the Herbig Ae star HR 5999'. In: *Astronomy & Astrophysics* 531, A84. ISSN: 0004-6361. URL: http://www.aanda.org/10.1051/0004-6361/201016091.

Benson, James A. et al. (1997). 'Multichannel optical aperture synthesis imaging of zeta1 URSAE majoris with the Navy prototype optical interferometer.' In: *The Astronomical Journal* 114, p. 1221. ISSN: 00046256. URL: http://adsabs.harvard.edu/cgi-bin/bib%5C_query?1997AJ....114.1221B.

Berger, David H. et al. (2008). 'CHARA Michigan phase-tracker (CHAMP): a preliminary performance report'. In: *Optical and Infrared Interferometry*. Ed. by Markus Schöller, William C. Danchi and Françoise Delplancke. Vol. 7013. San Diego, California, USA: SPIE, pp. 701319–701319–10. URL: http://spiedigitallibrary.org/proceeding.aspx?doi=10.1117/12.790168.

Berger, Jean-Philippe, Fabien Malbet et al. (2012). 'Imaging the heart of astrophysical objects with optical long-baseline interferometry'. In: *The Astronomy and Astrophysics Review* 20.1, p. 53. ISSN: 0935-4956. URL: http://www.springerlink.com/index/10.1007/s00159-012-0053-0.

Berger, Jean-Philippe, Gérard Zins et al. (2010). 'PIONIER: a visitor instrument for the VLTI'. In: *Optical and Infrared Interferometry II*. Ed. by William C. Danchi, Françoise Delplancke and Jayadev K Rajagopal. Society of PhotoOptical Instrumentation Engineers SPIE Conference Series, pp. 773435–773435–14. URL: http://link.aip.org/link/PSISDG/v7734/i1/p773435/s1%5C&Agg=doi.

Bergh, Sidney van den (2011). 'The Curious Case of Lemaître's Equation No. 24'. In: *Journal of the Royal Astronomical Society of Canada* 105, p. 151.

Bertin, E. and S. Arnouts (1996). 'SExtractor: Software for source extraction'. In: *Astronomy and Astrophysics Supplement* 117, pp. 393–404.

Bessell, M. S. (1979). 'UBVRI photometry. II - The Cousins VRI system, its temperature and absolute flux calibration, and relevance for two-dimensional photometry'. In: *Publications of the Astronomical Society of the Pacific* 91, p. 589. ISSN: 0004-6280. URL: http://ucp.uchicago.edu/cgi-bin/resolve?id=doi:10.1086/130542.

Bevington, Philip R. and D. Keith Robinson (2003). *Data reduction and error analysis for the physical sciences*. Ed. by ESO. Third. ESO. ISBN: 0-07-247227-8.

Boden, A. F., M. J. Creech-Eakman and D. Queloz (2000). 'The Visual Orbit and Evolutionary State of 12 Bootis'. In: *The Astrophysical Journal* 536, pp. 880–890.

Bohnenblust, F. (1940). 'An axiomatic characterization of L_p-spaces'. In: *Duke Mathematical Journal* 6.3, pp. 627–640. ISSN: 0012-7094. URL: http://projecteuclid.org/euclid.dmj/1077492067%20http://projecteuclid.org/Dienst/getRecord?id=euclid.dmj/1077492067/.

Bonaccini, Domenico et al. (1998). 'Adaptive Optics for ESO VLT-Interferometer'. In: *Adaptive Optical System Technologies*. Ed. by Domenico Bonaccini and Robert K. Tyson. Vol. 3353. March. SPIE, pp. 224–232.

Born, Max and Emil Wolf (2003). *Principles of Optics*. Ed. by Cambridge University Press. 7 (Expande, p. 988. ISBN: 978-0521642224.

Brillant, Stéphane (2011). *VLTI User Manual*. Garching bei München, Germany. URL: http://www.eso.org/sci/facilities/paranal/telescopes/vlti/documents/VLT-MAN-ESO-15000-4552%5C_v88.pdf.

Brummelaar, Theo A. ten, W. G. Jr. Bagnuolo and S. T. Ridgway (1995). 'Strehl ratio and visibility in long-baseline stellar interferometry.' In: *Optics letters* 20.6, pp. 521–3. ISSN: 0146-9592. URL: http://www.ncbi.nlm.nih.gov/pubmed/19859242.

Buenzli, E. et al. (2010). 'Dissecting the Moth: discovery of an off-centered ring in the HD 61005 debris disk with high-resolution imaging'. In: *Astronomy and Astrophysics* 524, L1, p. L1.

Buscher, D. F. et al. (2013). 'The conceptual design of the Magdalena ridge Observatory Interferometer'. In: *Journal of Astronomical Instrumentation* 02.02, p. 1340001. ISSN: 2251-1717. URL: http://www.worldscientific.com/doi/abs/10.1142/S2251171713400011.

Buscher, David F. (1994). 'Direct maximum-entropy image reconstruction from the bispectrum'. In: *Very high angular resolution imaging*. Ed. by J. G. Robertson and William J. Tango. Sydney, Australia, p. 91.

Campins, H., G. H. Rieke and M. J. Lebofsky (1985). 'Absolute calibration of photometry at 1 through 5 microns'. In: *The Astronomical Journal* 90, p. 896. ISSN: 00046256. URL: http://adsabs.harvard.edu/cgi-bin/bib%5C_query?1985AJ.....90..896C.

Carroll, B.W. and D.A. Ostlie (2007). *An Introduction to Modern Astrophysics*. Pearson Addison-Wesley. ISBN: 9780805304022. URL: http://books.google.pt/books?id=M8wPAQAAMAAJ.

Charbonnier, P. et al. (1997). 'Deterministic edge-preserving regularization in computed imaging.' In: *IEEE transactions on image processing : a publication of the IEEE Signal Processing Society*. Vol. 6. 2, pp. 298–311. URL: http://www.ncbi.nlm.nih.gov/pubmed/18282924.

Cittert, Pieter Hendrik van (1934). 'Die Wahrscheinliche Schwingungsverteilung in Einer von Einer Lichtquelle Direkt Oder Mittels Einer Linse Beleuchteten Ebene'. In: *Physica* 1.1-6, pp. 201–210. ISSN: 00318914. URL: http://linkinghub.elsevier.com/retrieve/pii/S0031891434900264.

Colavita, M. M. (1999). 'Fringe Visibility Estimators for the Palomar Testbed Interferometer'. In: *Publications of the Astronomical Society of the Pacific* 111, pp. 111–117.

Corcione, L. et al. (2003). 'FINITO: Fringe tracking Instrument of NIce and Torino for VLTI'. In: *GENIE - DARWIN Workshop - Hunting for Planets*. Ed. by H. Lacoste. Leiden, The Netherlands.

Cornwell, Tim J. and P. N. Wilkinson (1981). 'A new method for making maps with unstable radio interferometers'. In: *Monthly Notices of the Royal Astronomical Society* 196.Sep. 1981, pp. 1067–1086. URL: http://adsabs.harvard.edu/abs/1981MNRAS.196.1067C.

Cotton, William Danchi (1979). 'A method of mapping compact structure in radio sources using VLBI observations'. In: *The Astronomical Journal* 84, p. 1122. ISSN: 00046256. URL: http://adsabs.harvard.edu/cgi-bin/bib%5C_query?1979AJ.....84.1122C.

Cotton, William et al. (2008). '2008 imaging beauty contest'. In: *Optical and Infrared Interferometry*. Ed. by Markus Schöller, William C. Danchi and Françoise Delplancke. Vol. 7013. SPIE, 70131N–70131N–14. URL: http://proceedings.spiedigitallibrary.org/proceeding.aspx?articleid=788830.

Cox, Arthur N. (2000). *Allen's Astrophysical Quantities*. Ed. by Arthur N. Cox. 4th. Vol. 53. 10. London, United Kingdom: Springer, p. 719. ISBN: 978-0387987460. URL: http://link.aip.org/link/PHTOAD/v53/i10/p77/s2%5C&Agg=doi.

Creath, Katherine (1988). 'Phase-measurement interferometry techniques'. In: *Progress in optics* 26.26, pp. 349–393.

D'Arcio, Luigi Arsenio (1999). 'Selected aspects of wide-field stellar interferometry'. Ph.D. Thesis. TU Delft University, p. 238.

Davies, Richard and Markus E. Kasper (2012). 'Adaptive Optics for Astronomy'. In: *Annual Review of Astronomy and Astrophysics* 50.1, pp. 305–351. ISSN: 0066-4146. URL: http://www.annualreviews.org/doi/abs/10.1146/annurev-astro-081811-125447.

Davis, J. et al. (2005). 'Orbital parameters, masses and distance to β Centauri determined with the Sydney University Stellar Interferometer and high-resolution spectroscopy'. In: *Monthly Notices of the Royal Astronomical Society* 356, pp. 1362–1370.

Defrère, D. et al. (2012). 'Hot circumstellar material resolved around β Pic with VLTI/PIONIER'. In: *Astronomy & Astrophysics* 546, p. L9. ISSN: 0004-6361. URL: http://www.aanda.org/10.1051/0004-6361/201220287.

Delplancke, F., F. Derie et al. (2006). 'PRIMA for the VLTI: a status report'. In: *Society of Photo-Optical Instrumentation Engineers (SPIE) Conference Series*. Vol. 6268. Society of Photo-Optical Instrumentation Engineers (SPIE) Conference Series,

Delplancke, F., S. A. Leveque et al. (2000). 'Phase-referenced imaging and micro-arcsecond astrometry with the VLTI'. In: *Interferometry in Optical Astronomy*. Ed. by P. Léna and A. Quirrenbach. Vol. 4006. Society of Photo-Optical Instrumentation Engineers (SPIE) Conference Series, pp. 365–376.

Delplancke, Françoise (2008). 'The PRIMA facility phase-referenced imaging and micro-arcsecond astrometry'. In: *New Astronomy Reviews* 52.2-5, pp. 199–207. ISSN: 13876473. URL: http://linkinghub.elsevier.com/retrieve/pii/S1387647308000444.

Delplancke, Françoise et al. (2003). 'PRIMA for the VLTI – Science'. In: *Astrophysics and Space Science* 286.1, pp. 99–104.

Eisenhauer, Frank et al. (2005). 'GRAVITY, The AO-Assisted, Two-Object Beam-Combiner Instrument for the VLTI'. In: *Astronomische Nachrichten* 326, p. 12. URL: http://arxiv.org/abs/astro-ph/0508607.

Eisner, J. A., L. A. Hillenbrand et al. (2007). 'Near-Infrared Interferometric, Spectroscopic, and Photometric Monitoring of T Tauri Inner Disks'. In: *The Astrophysical Journal* 669, pp. 1072–1084.

Eisner, J. A., J. D. Monnier et al. (2010). 'Spatially and Spectrally Resolved Hydrogen Gas within 0.1 AU of T Tauri and Herbig Ae/Be Stars'. In: *The Astrophysical Journal* 718, pp. 774–794.

ESO, European Southern Observatory (2014a). *Auxiliary Telescopes*. URL: https://www.eso.org/public/teles-instr/vlt/auxiliarytelescopes/.

— (2014b). *Revolutionary ALMA Image Reveals Planetary Genesis*. URL: http://www.eso.org/public/news/eso1436/.

Esposito, Simone, Armando Riccardi and Bruno Femenìa (2000). 'Differential piston angular anisoplanatism for astronomical optical interferometers'. In: *Astronomy and Astrophysics* 353, pp. L29–L32.

ESPRI, Exoplanet Search with PRIma (2014). *ESPRI News: ESO decides to cancel the PRIMA project*. URL: http://www.mpia-hd.mpg.de/PRIMA-DDL/news.php.

Feynman, Richard P., Robert B. Leighton and Matthew Sands (2013). *The Feynman Lectures on Physics, Desktop Edition*. v. 1. Basic Books. ISBN: 9780465072934. URL: http://books.google.pt/books?id=kNRFAgAAQBAJ.

Finger, Gert et al. (2012). 'Evaluation and optimization of NIR Evaluation and optimization of NIR HgCdTe avalanche photodiode arrays for adaptive optics and interferometry'. In: *High Energy, Optical, and Infrared Detectors for Astronomy V*. Amsterdam, The Netherlands: SPIE, 84530T–84530T–16. URL: http://proceedings.spiedigitallibrary.org/proceeding.aspx?articleid=1363321.

Fizeau, Hippolyte (1851). 'The Hypotheses Relating to the Luminous Aether'. In: *Philosophical Magazine and Journal of Science* 2.4, pp. 568–573.

— (1868). 'Prix Bordin: rapport sur le concours de lánnée 1867'. In: *Comptes rendus de l'Académie des sciences* 66.06, pp. 932–934.

Fomalont, Edward B. and Melvyn C. H. Wright (1974). 'Interferometry and Aperture Synthesis'. In: *Galactic and Extra-Galactic Radio Astronomy*. Ed. by Gerrit L. Verschuur and Kenneth I. Kellermann. First. Vol. 297. 3. New York, USA: Springer-Verlag Berlin Heidelberg New York. Chap. 10, pp. 256–290. ISBN: 978-0387065045. URL: http://doi.wiley.com/10.1002/asna.19762970315.

Fresnel, Augustin Jean (1866). *Œuvres complètes d'Augustin Fresnel: Théorie de la lumière*. Ed. by Henry Hureau de Sénarmont, Émile Verdet and L'eonor François Fresnel. 1st ed. Paris: Imprimerie impériale, pp. I–XCIX, 1–805. URL: http://books.google.pt/books/about/%5C%C5%5C%92uvres%5C_compl%5C%C3%5C%A8tes%5C_d%5C_Augustin%5C_Fresnel%5C_Th.html?id=3QgAAAAAMAAJ%5C&redir%5C_esc=y.

Fried, David L. (1976). 'Varieties Of Isoplanatism'. In: SPIE.

Frieden, B R (1972). 'Restoring with maximum likelihood and maximum entropy.' In: *Journal of the Optical Society of America* 62.4, pp. 511–518. ISSN: 0030-3941.

Frigo, M. and S.G. Johnson (2005). 'The Design and Implementation of FFTW3'. In: *Proceedings of the IEEE* 93.2, pp. 216–231. ISSN: 0018-9219. URL: http://ieeexplore.ieee.org/lpdocs/epic03/wrapper.htm?arnumber=1386650.

Garcia, P. J. V. et al. (2013). 'Pre-main-sequence binaries with tidally disrupted discs: the Br in HD 104237'. In: *Monthly Notices of the Royal Astronomical Society* 430.3, pp. 1839–1853. ISSN: 0035-8711. URL: http://mnras.oxfordjournals.org/cgi/doi/10.1093/mnras/stt005.

Gaskill, Jack D. (1978). *Linear Systems, Fourier Transforms, and Optics*. Illustrate. Wiley, p. 554. ISBN: 0471292885.

Gautschy, A. and H. Saio (1996). 'Stellar Pulsations Across the HR Diagram: Part 2'. In: *Annual Review of Astronomy and Astrophysics* 34, pp. 551–606.

Gavel, D. T., H. W. Friedman and S. S. Olivier (1998). 'Wide-baseline optical interferometry with laser guide stars'. In: *Astronomical Interferometry*. Ed. by R. D. Reasenberg. Vol. 3350. Society of Photo-Optical Instrumentation Engineers (SPIE) Conference Series, pp. 793–799.

Giovannelli, Jean-François and A. Coulais (2005). 'Positive deconvolution for superimposed extended source and point sources'. In: *Astronomy and Astrophysics* 439.1, pp. 401–412. ISSN: 0004-6361. URL: http://www.edpsciences.org/10.1051/0004-6361:20047011.

Gitton, Philippe B. (2009). *Statistical analysis of residual tip-tilt jitter as measured in the VLTI laboratory*. Tech. rep. November 2008. ESO, pp. 1–13.

Gitton, Philippe B., Françoise Delplancke et al. (2007). *Description of the algorithms used for IRIS*. Tech. rep. Garching bei München, Germany: European Southern Observatory, p. 24. URL: http://www.eso.org/sci/facilities/develop/detectors/optdet/CCDtestbench/doc/VLT-PRO-ESO-13600-4686%5C_i1.pdf.

Gitton, Philippe B., Samuel Lévêque et al. (2004). 'IRIS: an infrared tilt sensor for the VLTI'. In: *Proceedings of SPIE* 5491, pp. 944–953. ISSN: 0277786X. URL: http://link.aip.org/link/?PSI/5491/944/1%5C&Agg=doi.

Gitton, Philippe B., Florence Puech et al. (2009). *Interface Control Document between VLTI and its Instruments (Part I)*. Tech. rep. 6. ESO, p. 64.

Glindemann, Andreas (2011). *Principles of Stellar Interferometry*. Astronomy. Astronomy and Astrophysics Library. Berlin, Heidelberg: Springer Berlin Heidelberg New York, p. 342. ISBN: 978-3-642-15027-2. URL: http://www.springerlink.com/index/10.1007/978-3-642-15028-9.

Glindemann, Andreas et al. (2002). 'The VLTI and its Subsystems'. In: *GENIE - DARWIN Workshop - Hunting for Planets (ESA SP-522)*. Ed. by H. Lacoste. Leiden, The Netherlands, pp. 1–16.

Glindemann, A. et al. (2004). 'VLTI technical advances: present and future'. In: *New Frontiers in Stellar Interferometry*. Ed. by W. A. Traub. Vol. 5491. Society of Photo-Optical Instrumentation Engineers (SPIE) Conference Series, p. 447.

Gomes, N., P. J. V. Garcia and É. Thiébaut (2016). 'Assessing the quality of restored images in optical long-baseline Interferometry (submitted)'. In: *Monthly Notices of the Royal Astronomical Society*.

Gomes, Nuno, Paulo J. V. Garcia and Éric Thiébaut (2014). 'Two, three, four, or six telescopes with phase referencing or closure phase relations: the best tactics for interferometric image reconstruction'. In: *SPIE Astronomical Telescopes + Instrumentation91462M-91462M-10*. Ed. by Jayadev K. Rajagopal, Michelle J. Creech-Eakman and Fabien Malbet. Montreal, Canada: SPIE, p. 91462M. URL: http://proceedings.spiedigitallibrary.org/proceeding.aspx?doi=10.1117/12.2056545.

Gomes, Nuno, Paulo J. V. Garcia, Éric Thiébaut et al. (2010). 'Comparison between closure phase and phase referenced interferometric image reconstructions'. In: *Optical and Infrared Interferometry II*. Ed. by William C. Danchi, Françoise Delplancke and Jayadev K. Rajagopal. Vol. 7734. San Diego, California, USA: SPIE, pp. 773438–773438–13. URL: http://link.aip.org/link/PSISDG/v7734/i1/p773438/s1%5C&Agg=doi.

Gomes, Nuno, Christian Schmid et al. (2012). 'Estimating visibility amplitudes with the PRIMA fringe trackers'. In: *Optical and Infrared Interferometry III*. 1. Amsterdam, , Netherlands: SPIE.

Goodman, Douglas S. (1994). 'Geometric Optics'. In: *Handbook of Optics: Fundamentals, techniques, and design, Volume 1*. Ed. by Michael Bass and Optical Society of America (OSA). 2nd ed. New York, USA: McGraw-Hill. Chap. 1, p. 1664. ISBN: 0070479747, 9780070479746. URL: http://photonics.intec.ugent.be/education/IVPV/res%5C_handbook/v1ch01.pdf.

Goodman, Joseph W. (1985). *Statistical Optics*. New York: John Wiley and Sons, p. 567. ISBN: 0471399167.

— (1996). *Introduction to Fourier Optics*. Vol. 8. 5. McGraw-Hill, p. 491. ISBN: 0070242542. URL: http://stacks.iop.org/1355-5111/8/i=5/a=014?key=crossref.ad20ea108e8f625cb0486bf680f74198.

— (2000). *Statistical Optics*. 1st ed. Wiley Classics Library, p. 572. ISBN: 978-0-471-39916-2.

Gordon, J. A. and D. F. Buscher (2012). 'Detection noise bias and variance in the power spectrum and bispectrum in optical interferometry'. In: *Astronomy & Astrophysics* 541, A46. ISSN: 0004-6361. URL: http://www.aanda.org/10.1051/0004-6361/201117335.

Gull, S. F. and J. Skilling (1984a). 'Maximum entropy method in image processing'. In: *IEE Proceedings F Communications, Radar and Signal Processing* 131.6, pp. 646–659. ISSN: 01437070. URL: http://digital-library.theiet.org/content/journals/10.1049/ip-f-1.1984.0099.

— (1984b). 'The Maximum Entropy Method'. In: *Indirect Imaging: Measurement and Processing for Indirect Imaging*. Ed. by J. A. Roberts. Sydney, Australia: Cambridge University Press, p. 267.

Haguenauer, Pierre et al. (2012). 'The Very Large Telescope Interferometer v2012+'. In: ed. by Françoise Delplancke, Jayadev K. Rajagopal and Fabien Malbet. Vol. 8445, pp. 84450D–84450D–10. URL: http://proceedings.spiedigitallibrary.org/proceeding.aspx?articleid=1357049.

Hanbury Brown, R. and R. Q. Twiss (1956). 'A Test of a New Type of Stellar Interferometer on Sirius'. In: *Nature* 178.4541, pp. 1046–1048. ISSN: 0028-0836. URL: http://www.nature.com/doifinder/10.1038/1781046a0.

Haniff, Christopher A. (2007). 'An introduction to the theory of interferometry'. In: *New Astronomy Reviews* 51.8-9, pp. 565–575. ISSN: 13876473. URL: http://linkinghub.elsevier.com/retrieve/pii/S1387647307000619.

Hardy, John W. (1998). *Adaptive Optics for Astronomical Telescopes*. 1st ed. Oxford University Press, pp. 1–448. ISBN: 9780195090192.

Haubois, X. et al. (2009). 'Imaging the spotty surface of Betelgeuse in the H band'. In: *Astronomy and Astrophysics* 508.2, pp. 923–932. ISSN: 0004-6361. URL: http://www.aanda.org/10.1051/0004-6361/200912927.

Hofmann, Karl-Heinz and Gerd P. Weigelt (1993). 'Iterative image reconstruction from the bispectrum'. In: *Astronomy and Astrophysics* 278.1, pp. 328–339.

Högbom, Jan A. (1974). 'Aperture Synthesis with a Non-Regular Distribution of Interferometer Baselines'. In: *Astronomy and Astrophysics Supplement* 15, p. 417.

Hubble, Edwin Powell (1929). 'A Relation between Distance and Radial Velocity among Extra-Galactic Nebulae'. In: *Proceedings of the National Academy of Science* 15, pp. 168–173.

— (1937). *The observational approach to cosmology*. Clarendon Press Oxford.

Hutter, Donald J. (2012). 'Ground-based optical interferometry'. In: *Scholarpedia* 7.6, p. 10586. ISSN: 1941-6016. URL: http://www.scholarpedia.org/article/Ground-based%5C_optical%5C_interferometry.

Ireland, Michael J., John D. Monnier and Nathalie D. Thureau (2006). 'Monte-Carlo imaging for optical interferometry'. In: *Advances in Stellar Interferometry*. Ed. by John D. Monnier, Markus Schöller and William C. Danchi. 1, 62681T–62681T–8. URL: http://proceedings.spiedigitallibrary.org/proceeding.aspx?articleid=1288308.

Isella, A. et al. (2008). 'Gas and dust in the inner disk of the Herbig Ae star MWC 758'. In: *Astronomy and Astrophysics* 483, pp. L13–L16.

Jackson, Neal (2008). 'Principles of Interferometry'. In: *Jets from Young Stars II, Lecture Notes in Physics, Volume 742*. Springer-Verlag Berlin Heidelberg, pp. 193–219.

Jennison, R C (1958). 'A phase sensitive interferometer technique for the measurement of the Fourier transforms of spatial brightness distributions of small angular extent'. In: *Monthly Notices of the Royal Astronomical Society* 118, pp. 276–284. ISSN: 0035-8711. URL: http://articles.adsabs.harvard.edu/full/1958MNRAS.118..276J%5C&data%5C_type=PDF%5C_HIGH%5C&whole%5C_paper=YES%5C&type=PRINTER%5C&filetype=.pdf.

Kaler, J. B. (2006). *The Cambridge Encyclopedia of Stars*. Cambridge University Press. ISBN: 978-0521818032.

Kervella, P. (2006). 'Cepheid distances from interferometry .' In: *Memorie della Società Astronomica Italiana* 77, p. 227.

Kervella, P. et al. (2004). 'Cepheid distances from infrared long-baseline interferometry. III. Calibration of the surface brightness-color relations'. In: *Astronomy and Astrophysics* 428, pp. 587–593.

Kloppenborg, Brian et al. (2010). 'Infrared images of the transiting disk in the epsilon Aurigae system.' In: *Nature* 464.7290, pp. 870–2. ISSN: 1476-4687. URL: http://www.ncbi.nlm.nih.gov/pubmed/20376144.

Kluska, J. et al. (2014). 'First images from the PIONIER/VLTI optical interferometry imaging survey of Herbig Ae/Be stars'. In: *Proceedings of the International Astronomical Union*. Vol. 8. S299, pp. 117–118. URL: http://www.journals.cambridge.org/abstract%5C_S1743921313008065.

Konacki, M. et al. (2010). 'High-precision Orbital and Physical Parameters of Double-lined Spectroscopic Binary Stars — HD78418, HD123999, HD160922, HD200077, and HD210027'. In: *The Astrophysical Journal* 719, pp. 1293–1314.

Kragh, Helge (1999). *Cosmology and Controversy: The Historical Development of Two Theories of the Universe*. Princeton University Press. ISBN: 9780691005461. URL: http://books.google.pt/books?id=eq7TfxZOzSEC.

Kraus, Stefan, Nuria Calvet et al. (2012). 'On the Nature of the Herbig B[e] Star Binary System V921 Scorpii: Discovery of a Close Companion and Relation to the Large-scale Bipolar Nebula'. In: *The Astrophysical Journal* 746.1, p. L2. ISSN: 2041-8205. URL: http://stacks.iop.org/2041-8205/746/i=1/a=L2?key=crossref.576047e915ca8eb5587ccf8bc6121bbc.

Kraus, Stefan, Karl-Heinz Hofmann et al. (2010). 'A hot compact dust disk around a massive young stellar object.' In: *Nature* 466.7304, pp. 339–42. ISSN: 1476-4687. URL: http://www.ncbi.nlm.nih.gov/pubmed/20631793.

Kraus, S. et al. (2008). 'The origin of hydrogen line emission for five Herbig Ae/Be stars spatially resolved by VLTI/AMBER spectro-interferometry'. In: *Astronomy and Astrophysics* 489, pp. 1157–1173.

Lacour, S. et al. (2008). 'The limb-darkened Arcturus: imaging with the IOTA/IONIC interferometer'. In: *Astronomy and Astrophysics* 485.2, pp. 561–570. ISSN: 0004-6361. URL: http://www.aanda.org/10.1051/0004-6361:200809611.

Lagrange, A.-M. et al. (2009). 'A probable giant planet imaged in the β Pictoris disk. VLT/NaCo deep L'-band imaging'. In: *Astronomy and Astrophysics* 493, pp. L21–L25.

Lane, Benjamin F. and M. Mark Colavita (2003). 'Phase-referenced Stellar Interferometry at the Palomar Testbed Interferometer'. In: *The Astronomical Journal* 125.3, pp. 1623–1628. ISSN: 00046256. URL: http://stacks.iop.org/1538-3881/125/i=3/a=1623.

Lannes, A., E. Anterrieu and P. Maréchal (1997). 'CLEAN and WIPE'. In: *Astronomy and Astrophysics Supplement Series* 123.1, pp. 183–198. ISSN: 0365-0138. URL: http://www.edpsciences.org/10.1051/aas:1997312.

Lawson, Peter R. (2000). *Principles of Long Baseline Stellar Interferometry*. Ed. by Peter R. Lawson. Pasadena, Californa, USa: JPL, p. 352. URL: http://olbin.jpl.nasa.gov/iss1999/coursenotes.html.

Lawson, Peter R., William Danchi Cotton et al. (2004). 'An Interferometry Imaging Beauty Contest'. In: *New Frontiers in Stellar Interferometry*. Ed. by Wesley A. Traub. Vol. 1. 818. Bellingham, WA, U.S.A.: The International Society for Optical Engineering, p. 886.

Lawson, Peter R., William D. Cotton et al. (2006). '2006 interferometry imaging beauty contest'. In: *Advances in Stellar Interferometry*. Ed. by John D. Monnier, Markus Schöller and William C. Danchi. Vol. 6268. 818. SPIE, 62681U–62681U–12. URL: http://proceedings.spiedigitallibrary.org/proceeding.aspx?articleid=1288309.

Lazorenko, P. F. et al. (2009). 'Precision multi-epoch astrometry with VLT cameras FORS1/2'. In: *Astronomy and Astrophysics* 505, pp. 903–918.

Le Bouquin, Jean-Baptiste, Jean-Philippe Berger et al. (2011). 'PIONIER: a 4-telescope visitor instrument at VLTI'. In: *Astronomy & Astrophysics* 535, A67. ISSN: 0004-6361. URL: http://www.aanda.org/10.1051/0004-6361/201117586.

Le Bouquin, Jean-Baptiste, S. Lacour et al. (2009). 'Pre-maximum spectro-imaging of the Mira star T Leporis with AMBER/VLTI'. In: *Astronomy and Astrophysics* 496.1, pp. L1–L4. ISSN: 0004-6361. URL: http://www.aanda.org/10.1051/0004-6361/200811579.

Lemaître, Georges (1927). 'Un Univers homogène de masse constante et de rayon croissant rendant compte de la vitesse radiale des nébuleuses extra-galactiques'. In: *Annales de la Société Scientifique de Bruxelles* 47, pp. 49–59.

— (1931). 'A Homogeneous Universe of Constant Mass and Increasing Radius accounting for the Radial Velocity of Extra-galactic Nebulæ'. In: *Monthly Notices of the Royal Astronomical Society* 91.5, pp. 483–490. URL: http://mnras.oxfordjournals.org/content/91/5/483.short.

Léna, Pierre et al. (2012). *Observational Astrophysics*. 3rd. Astronomy and Astrophysics Library. Berlin, Heidelberg: Springer Berlin Heidelberg, pp. XV + 719. ISBN: 978-3-642-21814-9. URL: http://www.springerlink.com/index/10.1007/978-3-642-21815-6.

Levenberg, Kenneth (1944). 'A Method for the Solution of Certain Non-linear Problems in Least-Squares'. In: *Quarterly of Applied Mathematics* 2.2, pp. 164–168.

Lévêque, Samuel (2003). *Design Description of the PRIMA Metrology System*. Tech. rep. VLT-TRE-ESO-15730-3000. European Southern Observatory.

Lindegren, L. (1980). 'Atmospheric limitations of narrow-field optical astrometry'. In: *Astronomy and Astrophysics* 89, pp. 41–47.

Livio, Mario (2011). 'Lost in translation: Mystery of the missing text solved'. In: *Nature* 479, pp. 171–173.

Lombardi, G. et al. (2011). 'A study of NIR atmospheric properties at Paranal Observatory'. In: *Astronomy and Astrophysics* 528, A43, A43.

Lopez, B. et al. (2014). 'An Overview of the MATISSE Instrument — Science, Concept and Current Status'. In: *The Messenger* 157, pp. 5–12.

Malbet, Fabien et al. (2010). 'The 2010 interferometric imaging beauty contest'. In: *Optical and Infrared Interferometry II*. Ed. by William C. Danchi, Françoise Delplancke and Jayadev K. Rajagopal. Vol. 7734. San Diego, California, USA: SPIE, 77342N–77342N–12. URL: http://proceedings.spiedigitallibrary.org/proceeding.aspx?articleid=750597.

Mallat, Stéphane G. and Zhifeng Zhang (1993). 'Matching pursuits with time-frequency dictionaries'. In: *IEEE Transactions on Signal Processing*. Vol. 41. 12. IEEE Signal Processing Society, pp. 3397–3415. URL: http://ieeexplore.ieee.org/lpdocs/epic03/wrapper.htm?arnumber=258082.

Marquardt, Donald W. (1963). 'An Algorithm for Least-Squares Estimation of Nonlinear Parameters'. In: *Journal of Society for Industrial and Applied Mathematics* 11.2, pp. 431–441.

Martin, F. et al. (2000). 'Optical parameters relevant for High Angular Resolution at Paranal from GSM instrument and surface layer contribution'. In: *Astronomy and Astrophysics Supplement Series* 144.1, pp. 39–44. ISSN: 0365-0138. URL: http://www.edpsciences.org/10.1051/aas:2000197.

Mason, E. et al. (2008). 'NIR Extinction Coefficients in Paranal'. In: *The 2007 ESO Instrument Calibration Workshop*. Berlin, Heidelberg: Springer-Verlag Berlin Heidelberg, pp. 439–442.

McCabe, C., G. Duchêne and A. M. Ghez (2003). 'The First Detection of Spatially Resolved Mid-Infrared Scattered Light from a Protoplanetary Disk'. In: *The Astrophysical Journal* 588, pp. L113–L116.

Meimon, Serge C., Laurent M. Mugnier and Guy Le Besnerais (2008). 'Self-calibration approach for optical long-baseline interferometry imaging'. In: *Journal of the Optical Society of America A* 26.1, p. 108. ISSN: 1084-7529. URL: http://www.opticsinfobase.org/abstract.cfm?URI=josaa-26-1-108.

Mérand, Antoine (2015). *VLTI User Manual*. Garching bei München, Germany. URL: http://www.eso.org/sci/facilities/paranal/telescopes/vlti/documents/VLT-MAN-ESO-15000-4552%5C_v96.pdf.

Mérand, Antoine, Pierre Kervella, Vicent Coudé du Foresto et al. (2005). 'The projection factor of δ Cephei. A calibration of the Baade-Wesselink method using the CHARA Array'. In: *Astronomy and Astrophysics* 438.1, pp. L9–L12. ISSN: 0004-6361. URL: http://www.edpsciences.org/10.1051/0004-6361:200500139.

Mérand, Antoine, Pierre Kervella and Alexandre Gallenne (2009). 'What we learned from interferometric observations of Cepheids'. In: *AIP Conference Proceedings*. Vol. 79. 1. American

Institute of Physics, pp. 79–82. ISBN: 9780735407077. URL: http://link.aip.org/link/APCPCS/v1170/i1/p79/s1%5C&Agg=doi.

Mérand, Antoine, Stan Stefl et al. (2010). 'Perspectives for the AMBER Beam Combiner'. In: *Optical and Infrared Interferometry II*. Ed. by William C. Danchi, Françoise Delplancke and Jayadev K. Rajagopal. San Diego, California, USA: SPIE, 77340S–77340S–8. URL: http://proceedings.spiedigitallibrary.org/proceeding.aspx?articleid=1346431.

Michelson, Albert Abraham (1920). 'On the Application of Interference Methods to Astronomical Measurements'. In: *The Astrophysical Journal* 51, p. 257. ISSN: 0004-637X. URL: http://adsabs.harvard.edu/doi/10.1086/142550.

Michelson, Albert Abraham and Edward W. Morley (1887). 'On the Relative Motion of the Earth and the Luminiferous Ether'. In: *The American Journal of Science* 34.203, pp. 333–345. URL: http://www.aip.org/history/gap/PDF/michelson.pdf.

Michelson, Albert Abraham and Francis G. Pease (1921). 'Measurement of the diameter of alpha Orionis with the interferometer.' In: *The Astrophysical Journal* 53, p. 249. ISSN: 0004-637X. URL: http://adsabs.harvard.edu/doi/10.1086/142603.

Millour, Florentin et al. (2011). 'Images of unclassified and supergiant B[e] stars disks with interferometry'. In: *Proceedings of the International Astronomical Union* 6.S272, pp. 410–411. ISSN: 1743-9213. URL: http://www.journals.cambridge.org/abstract%5C_S1743921311010969.

Monnier, J. D., J.-P. Berger et al. (2006). 'Few Skewed Disks Found in First Closure-Phase Survey of Herbig Ae/Be Stars'. In: *The Astrophysical Journal* 647, pp. 444–463.

Monnier, J. D., R. Millan-Gabet et al. (2005). 'The Near-Infrared Size-Luminosity Relations for Herbig Ae/Be Disks'. In: *The Astrophysical Journal* 624, pp. 832–840.

Monnier, John D. (2003). 'Optical interferometry in astronomy'. In: *Reports on Progress in Physics* 66.5, pp. 789–857. ISSN: 0034-4885. URL: http://stacks.iop.org/0034-4885/66/i=5/a=203?key=crossref.c1b6e5c01042f7bcbfcac736c3de1a50.

— (2007). 'Phases in interferometry'. In: *New Astronomy Reviews* 51.8-9, pp. 604–616. ISSN: 13876473. URL: http://linkinghub.elsevier.com/retrieve/pii/S1387647307000656.

Monnier, John D., Jean-Philippe Berger et al. (2004). 'The Michigan Infrared Combiner (MIRC): IR imaging with the CHARA Array'. In: *New Frontiers in Stellar Interferometry*. Ed. by Wesley A. Traub. Bellingham, WA: The International Society for Optical Engineering, pp. 1370–1377.

Monnier, John D., Stefan Kraus et al. (2014). 'Planet formation imager (PFI): introduction and technical considerations'. In: *SPIE Astronomical Telescopes + Instrumentation*. URL: http://proceedings.spiedigitallibrary.org/proceeding.aspx?articleid=1891923.

Monnier, John D., Rafaël Millan-Gabet et al. (2004). 'High-Resolution Imaging of Dust Shells by Using Keck Aperture Masking and the IOTA Interferometer'. In: *The Astrophysical Journal* 605.1, pp. 436–461. ISSN: 0004-637X. URL: http://stacks.iop.org/0004-637X/605/i=1/a=436.

Monnier, John D., Ettore Pedretti et al. (2012). 'Five years of imaging at CHARA with MIRC'. In: *Optical and Infrared Interferometry III*. Ed. by Françoise Delplancke, Jayadev K. Rajagopal and Fabien Malbet. Vol. 8445. Amsterdam, Netherlands: SPIE, 84450Y. 7pp. URL: http://proceedings.spiedigitallibrary.org/proceeding.aspx?doi=10.1117/12.926433.

Monnier, John D., Ming Zhao et al. (2007). 'Imaging the Surface of Altair'. In: *Sciences-New York* 317.5836, pp. 342–365.

Mugnier, Laurent M., Thierry Fusco and Jean-Marc Conan (2004). 'MISTRAL: a myopic edge-preserving image restoration method, with application to astronomical adaptive-optics-corrected long-exposure images'. In: *Journal of the Optical Society of America A* 21.10, p. 1841. ISSN: 1084-7529. URL: http://www.ncbi.nlm.nih.gov/pubmed/15497412%20http://www.opticsinfobase.org/abstract.cfm?URI=josaa-21-10-1841.

Narayan, R. and R. Nityananda (1986). 'Maximum Entropy Image Restoration in Astronomy'. In: *Annual Review of Astronomy and Astrophysics* 24.1, pp. 127–170. ISSN: 0066-4146. URL: http://www.annualreviews.org/doi/abs/10.1146/annurev.aa.24.090186.001015.

Neugebauer, G., D. E. Martz and R. B. Leighton (1965). 'Observations of Extremely Cool Stars.' In: *The Astrophysical Journal* 142, p. 399. ISSN: 0004-637X. URL: http://adsabs.harvard.edu/doi/10.1086/148300.

Nijenhuis, J. et al. (2008). 'Simultaneous observation of two stars using the PRIMA Star Separator'. In: *Society of Photo-Optical Instrumentation Engineers (SPIE) Conference Series*. Vol. 7013. Society of Photo-Optical Instrumentation Engineers (SPIE) Conference Series, p. 3.

Noll, Robert J. (1976). 'Zernike polynomials and atmospheric turbulence'. In: *Journal of the Optical Society of America.* 66, pp. 207–211. ISSN: 1084-7529. URL: http://dx.doi.org/10.1364/JOSA.66.000207.

Paresce, Francesco (2002). 'The VLTI: challenges for the future'. In: *The unsolved universe: challenges for the future*. Ed. by Mário J. P. F. G. Monteiro. Porto, Portugal: Kluwer Academic Publishers, pp. 119–131. ISBN: 1-4020-1673-5.

Paresce, F. et al. (1996). 'A new start for the VLTI.' In: *The Messenger* 83, pp. 14–21.

Pauls, Thomas A. et al. (2005). 'A data exchange standard for optical (visible/IR) interferometry'. In: *The Publications of the Astronomical Society of the Pacific* 117.837, pp. 1255–1262. ISSN: 0277786X. URL: http://link.aip.org/link/?PSI/5491/1231/1%5C&Agg=doi.

Pence, W. D. et al. (2010). 'Definition of the Flexible Image Transport System (FITS), version 3.0'. In: *Astronomy & Astrophysics* 524, A42. ISSN: 0004-6361. URL: http://www.aanda.org/10.1051/0004-6361/201015362.

Penzias, Arno A. and Robert W. Wilson (1965). 'A Measurement of Excess Antenna Temperature at 4080 Mc/s.' In: *The Astrophysical Journal* 142, pp. 419–421.

Pepe, F. et al. (2008). 'The ESPRI Project: differential delay lines for PRIMA'. In: *Society of Photo-Optical Instrumentation Engineers (SPIE) Conference Series*. Vol. 7013. Society of Photo-Optical Instrumentation Engineers (SPIE) Conference Series,

Petrov, Romain G. et al. (2007). 'AMBER, the near-infrared spectro-interferometric three-telescope VLTI instrument'. In: *Astronomy and Astrophysics* 464.1, pp. 1–12. ISSN: 0004-6361. URL: http://www.aanda.org/10.1051/0004-6361:20066496.

Pety, J., F. Gueth and S. Guilloteau (2001a). *ALMA Memo 386 - ALMA+ACA Simulation Tool*. Tech. rep. Saint Martin d'Hères, France: IRAM, Institut de Radio Astronomie Millimétrique, p. 10.

— (2001b). *ALMA Memo 387 - ALMA+ACA Simulation Results*. Tech. rep. Grenoble, France: IRAM, Institut de Radio Astronomie Millimétrique, p. 16.

Pichon, C. and Éric Thiébaut (1998). 'Non-parametric reconstruction of distribution functions from observed galactic discs'. In: *Monthly Notices of the Royal Astronomical Society* 301.2, pp. 419–434. ISSN: 0035-8711. URL: http://mnras.oxfordjournals.org/cgi/doi/10.1046/j.1365-8711.1998.02026.x.

Powell, M.J.D. (2006). *The NEWUOA software for unconstrained minimization without derivatives*. Ed. by G. Di Pillo and M. Roma. Springer, pp. 255–297.

Quirrenbach, Andreas et al. (1994). 'Maximum-entropy maps of the Be shell star zeta Tauri from optical long-baseline interferometry'. In: *Astronomy and Astrophysics* 283.2, pp. L13–L16.

Quirrenbach, A. et al. (1998). 'PRIMA: study for a dual-beam instrument for the VLT Interferometer'. In: *Astronomical Interferometry*. Ed. by R. D. Reasenberg. Vol. 3350. Society of Photo-Optical Instrumentation Engineers (SPIE) Conference Series, pp. 807–817.

Ragland, S. et al. (2006). 'First Surface-resolved Results with the Infrared Optical Telescope Array Imaging Interferometer: Detection of Asymmetries in Asymptotic Giant Branch Stars'. In: *The Astrophysical Journal* 652, pp. 650–660.

Readhead, A. C. S. and P. N. Wilkinson (1978). 'The mapping of compact radio sources from VLBI data'. In: *The Astrophysical Journal* 223, p. 25. ISSN: 0004-637X. URL: http://adsabs.harvard.edu/doi/10.1086/156232.

Reich, Eugenie Samuel (2011). 'Edwin Hubble in translation trouble'. In: *Nature*.

Renard, Stéphanie, Fabien Malbet et al. (2008). 'Imaging reconstruction for infrared interferometry: first images of YSOs environment'. In: *Optical and Infrared Interferometry*. Ed. by Markus Schöller, William C. Danchi and Françoise Delplancke. SPIE, pp. 70131L–70131L–10. ISBN: 9780819472236. URL: http://arxiv.org/abs/0807.3020%20http://proceedings.spiedigitallibrary.org/proceeding.aspx?articleid=788825.

Renard, Stéphanie, Éric Thiébaut and Fabien Malbet (2011). 'Image reconstruction in optical interferometry: benchmarking the regularization'. In: *Astronomy & Astrophysics* 533, A64. ISSN: 0004-6361. URL: http://www.aanda.org/10.1051/0004-6361/201016263.

Richardson, N. D. et al. (2013). 'The H-band Emitting Region of the Luminous Blue Variable P Cygni: Spectrophotometry and Interferometry of the Wind'. In: *The Astrophysical Journal* 769, 118, p. 118.

Richichi, Andrea, Andreas Glindemann and Markus Schöller (2002). 'The VLTI and its instrumentation'. In: *The Origin of Stars and Planets: The VLT View*. Ed. by J. F. Alves and M. J. McCaughrean. Garching bei München: Springer-Verlag, p. 416.

Robbe-Dubois, Sylvie et al. (2007). 'Optical configuration and analysis of the AMBER/VLTI instrument'. In: *Astronomy and Astrophysics* 464.1, pp. 13–27. ISSN: 0004-6361. URL: http://www.aanda.org/10.1051/0004-6361:20065432.

Roy, A. E. and D. Clarke (2003). *Astronomy: Principles and practice*. 4th. CRC Press. ISBN: 978-0750309172.

Rudin, Leonid I., Stanley Osher and Emad Fatemi (1992). 'Nonlinear total variation based noise removal algorithms'. In: *Physica D: Nonlinear Phenomena* 60.1-4, pp. 259–268. ISSN: 01672789. URL: http://linkinghub.elsevier.com/retrieve/pii/016727899290242F.

Saha, Swapan Kumar (2011). *Aperture Synthesis - Methods and Applications to Optical Astronomy*. Astronomy and Astrophysics Library. New York, NY: Springer New York, pp. XXIII, 466. ISBN: 978-1-4419-5709-2. URL: http://www.springerlink.com/index/10.1007/978-1-4419-5710-8.

Sahlmann, Johannes et al. (2009). 'The PRIMA fringe sensor unit'. In: *Astronomy and Astrophysics* 507.3, pp. 1739–1757. ISSN: 0004-6361. URL: http://www.aanda.org/10.1051/0004-6361/200912271.

Sahlmann, J. et al. (2013). 'The ESPRI project: astrometric exoplanet search with PRIMA. I. Instrument description and performance of first light observations'. In: *Astronomy and Astrophysics* 551, A52, A52.

Sana, H. et al. (2013). 'Three-dimensional orbits of the triple-O stellar system HD 150136'. In: *Astronomy & Astrophysics* 553, A131. ISSN: 0004-6361. URL: http://arxiv.org/abs/1304.3457%20http://www.aanda.org/10.1051/0004-6361/201321189.

Schmid, Christian (2009). *SNR Thresholds setting*. Garching.

Schmid, Christian et al. (2012). 'Status of PRIMA for the VLTI – heading to astrometry'. In: SPIE.

Schmitt, H. R. et al. (2009). 'Navy Prototype Optical Interferometer Imaging of Line Emission Regions of β Lyrae Using Differential Phase Referencing'. In: *The Astrophysical Journal*

691.2, pp. 984–996. ISSN: 0004-637X. URL: http://stacks.iop.org/0004-637X/691/i=2/a=984?key=crossref.6209be1505335e5158061ae6a978b6e8.

Schmitt, Henrique R. et al. (2006). 'Using differential phases in optical interferometry'. In: *Advances in Stellar Interferometry*. Ed. by John D. Monnier, Markus Schöller and William C. Danchi. Vol. 6268. 06. Orlando, Florida, USA, 62683B–62683B–8. URL: http://proceedings.spiedigitallibrary.org/proceeding.aspx?articleid=1327107.

Schneider, D. P., J. E. Gunn and J. G. Hoessel (1983). 'CCD photometry of Abell clusters. I - Magnitudes and redshifts for 84 brightest cluster galaxies'. In: *The Astrophysical Journal* 264, p. 337. ISSN: 0004-637X. URL: http://adsabs.harvard.edu/doi/10.1086/160602.

Schöller, Markus (2000). 'Fizeau beam combination with optical interferometers: some ideas for second-generation VLTI instrumentation'. In: *Society of Photo-Optical Instrumentation Engineers (SPIE) Conference Series*. Ed. by P Léna and A Quirrenbach. Vol. 4006. Society of Photo-Optical Instrumentation Engineers (SPIE) Conference Series, pp. 116–123.

Schroeder, Daniel J. (1987). *Astronomical Optics*. San Diego, California, USA: Academic Press, pp. 1–364.

Schwarz, U. J. (1978). 'Mathematical-statistical Description of the Iterative Beam Removing Technique (Method CLEAN)'. In: *Astronomy and Astrophysics* 65, p. 345.

— (1979). 'The Method 'Clean' — Use, Misuse and Variations'. In: *The Formation of Images from Spatial Coherence Functions in Astronomy*. Ed. by Cornelis Van Schooneveld. Springer Netherlands, pp. 261–275.

Ségransan, Damien (2007). 'Observability and UV coverage'. In: *New Astronomy Reviews* 51.8-9, pp. 597–603. ISSN: 13876473. URL: http://linkinghub.elsevier.com/retrieve/pii/S1387647307000644.

Shaklan, S. B., M. Mark Colavita and Michael Shao (1992). 'Visibility calibration using single mode fibers in a long-baseline interferometer'. In: *ESO Conference on High Resolution Imaging by Interferometry, Part II*. Ed. by ESO. Garching bei München: ESO, pp. 1271–1283.

Shannon, Claude E. (1984). 'Editorial note on "Communication in the presence of noise"'. In: *Proceedings of the IEEE* 72.12, pp. 1713–1713. ISSN: 0018-9219. URL: http://ieeexplore.ieee.org/lpdocs/epic03/wrapper.htm?arnumber=659497%20http://ieeexplore.ieee.org/lpdocs/epic03/wrapper.htm?arnumber=1457347.

Shao, M. and M. M. Colavita (1992). 'Potential of long-baseline infrared interferometry for narrow-angle astrometry'. In: *Astronomy and Astrophysics* 262, pp. 353–358.

Shao, Michael and David H. Staelin (1977). 'Long- baseline optical interferometer for astrometry'. In: *Journal of the Optical Society of America* 67.1, p. 81. ISSN: 0030-3941. URL: http://www.opticsinfobase.org/abstract.cfm?URI=josa-67-1-81.

Skilling, J. and R. K. Bryan (1984). 'Maximum Entropy Image Reconstruction - General Algorithm'. In: *Monthly Notices of the Royal Astronomical Society* 211.1, p. 111.

Solf, J. (1993). 'Optical high-resolution methods'. In: *Landolt-Börnstein - Group VI Astronomy and Astrophysics - Volume 3*. Ed. by H. H. Voigt. Berlin: Springer Berlin Heidelberg. Chap. Instrument, pp. 36–38. ISBN: 978-3-540-31380-9.

Stahler, Steven W. and Francesco Palla (2004). *The Formation of Stars*. Ed. by Steven W. Stahler and Francesco Palla. Weinheim, Germany: Wiley-VCH Verlag GmbH, p. 865. ISBN: 9783527618675. URL: http://doi.wiley.com/10.1002/9783527618675.

Sterken, Christiaan and Jean Manfroid (1992). *Astronomical Photometry, A Guide*. Berlin, Heidelberg: Springer-Verlag Berlin Heidelberg, p. 288. ISBN: 0-7923-1653-3.

Strong, David and Tony Chan (2003). 'Edge-preserving and scale-dependent properties of total variation regularization'. In: *Inverse Problems* 19.6, S165–S187. ISSN: 0266-

5611. URL: http : / / stacks . iop . org / 0266 - 5611 / 19 / i = 6 / a = 059 ? key = crossref . de29564b123774dc23aaf2d408ab1582.

Tarantola, Albert (2005). *Inverse Problem Theory and Methods for Model Parameter Estimation*. SIAM, p. 342. ISBN: 0898717922. URL: http://www.ipgp.fr/~tarantola/Files/Professional/Books/InverseProblemTheory.pdf.

Tatulli, Éric, Nicolas Blind et al. (2010). 'Estimating the phase in ground-based interferometry: performance comparison between single-mode and multimode schemes'. In: *Astronomy & Astrophysics* 524, p. 9. ISSN: 0004-6361. URL: http://arxiv.org/abs/1009.1797.

Tatulli, Éric and Alain Chelli (2005). 'Fiber optic interferometry: statistics of visibility and closure phase'. In: *Journal of the Optical Society of America A* 22.8, p. 1589. ISSN: 1084-7529. URL: http://www.opticsinfobase.org/abstract.cfm?URI=JOSAA-22-8-1589.

Tatulli, Éric, Pierre Mège and Alain Chelli (2004). 'Single-Mode versus multimode interferometry: a performance study'. In: *Astronomy and Astrophysics* 418.3, p. 13. ISSN: 0004-6361. URL: http://arxiv.org/abs/astro-ph/0402330.

Tatulli, E. et al. (2008). 'Spatially resolving the hot CO around the young Be star 51 Ophiuchi'. In: *Astronomy and Astrophysics* 489, pp. 1151–1155.

Tatum, J. B. (2000). *Physics Topics*. Ed. by J. B. Tatum. URL: http://orca.phys.uvic.ca/~tatum/index.html.

ten Brummelaar, Theo A., Hal McAlister et al. (2005). 'First Results from the CHARA Array. II. A Description of the Instrument'. In: *The Astrophysical Journal* 628.1, pp. 453–465. ISSN: 0004-637X. URL: http://stacks.iop.org/0004-637X/628/i=1/a=453.

ten Brummelaar, Theo A., Peter G. Tuthill and Gerard T. van Belle (2013). 'Introduction to the special issue on optical and infrared interferometry'. In: *Journal of Astronomical Instrumentation* 02.02, p. 1303001. ISSN: 2251-1717. URL: http://www.worldscientific.com/doi/abs/10.1142/S2251171713030013.

Thiébaut, Éric (2002). 'Optimization issues in blind deconvolution algorithms'. In: *Astronomical Data Analysis II*. Ed. by Fionn D. Starck, Jean-Luc; Murtagh. Waikoloa, HI, USA: SPIE, pp. 174–183.

— (2005). 'Introduction To Image Reconstruction And Inverse Problems'. In: *Optics in astrophysics: Proceedings of the NATO Advanced Study Institute on Optics in Astrophysics*. Ed. by R. Foy and F.-C. Foy. Cargese, France: Springer, Dordrecht, The Netherlands, pp. 397–421.

— (2008). 'MIRA: an effective imaging algorithm for optical interferometry'. In: *Proceedings of SPIE* 7013.3, pp. 70131I–70131I–12. ISSN: 0277786X. URL: http://link.aip.org/link/PSISDG/v7013/i1/p70131I/s1%5C&Agg=doi.

— (2009). 'Image reconstruction with optical interferometers'. In: *New Astronomy Reviews* 53.11-12, pp. 312–328. ISSN: 13876473. URL: http://linkinghub.elsevier.com/retrieve/pii/S1387647310000126.

— (2013). 'Principles of Image Reconstruction in Interferometry'. In: *EAS Publications Series* 59. Ed. by D. Mary, C. Theys and C. Aime, pp. 157–187. ISSN: 1633-4760. URL: http://www.eas-journal.org/10.1051/eas/1359009.

Thiébaut, Éric and Jean-François Giovannelli (2010). 'Image reconstruction in optical interferometry'. In: *IEEE Signal Processing Magazine* 27.1, pp. 97–109. ISSN: 1053-5888. URL: http://ieeexplore.ieee.org/lpdocs/epic03/wrapper.htm?arnumber=5355500.

Thompson, A. R., J. M. Moran and G. W. Swenson Jr. (2001). *Interferometry and Synthesis in Radio Astronomy*. 2 Edition. Wiley-VCH, p. 715. ISBN: 978-0471254928.

Thompson, L. A. (1994). 'Adaptive optics in astronomy.' In: *Physics Today* 47, pp. 24–31.

Tokunaga, A. T. (2000). 'Infrared Astronomy'. In: *Allen's astrophysical quantities*. Ed. by Arthur N. Cox. 4th. New York, USA: AIP Press, Springer. Chap. 7, pp. 143–168. ISBN: 0-387-98746-0.

Traub, Wesley A. (2000). 'Beam Combination and Fringe Measurement'. In: *Principles of Long Baseline Stellar Interferometry*. Ed. by Peter R. Lawson. California Institute of Technology, Pasadena, CA: National Aeronautics and Space Administration, Jet Propulsion Laboratory. Chap. 3, pp. 31–58.

Tuthill, Peter G., John D. Monnier, W. C. Danchi et al. (2002). 'Imaging the Disk around the Luminous Young Star LkHα 101 with Infrared Interferometry'. In: *The Astrophysical Journal* 577.2, pp. 826–838. ISSN: 0004-637X. URL: http://stacks.iop.org/0004-637X/577/i=2/a=826.

Tuthill, Peter G., John D. Monnier and William C Danchi (1999). 'A dusty pinwheel nebula around the massive star WR 104'. In: p. 7. URL: http://arxiv.org/abs/astro-ph/9904092.

Vinković, D. and T. Jurkić (2007). 'Relation between the Luminosity of Young Stellar Objects and Their Circumstellar Environment'. In: *The Astrophysical Journal* 658, pp. 462–479.

Voelz, David G. (2011). *Computational Fourier Optics - A MATLAB Tutorial*. SPIE Press, p. 250. ISBN: 9780819482044. URL: http://www.ece.nmsu.edu/~davvoelz/cfo/.

Wakker, B. P. and U. J. Schwarz (1988). 'The Multi-Resolution CLEAN and its application to the short-spacing problem in interferometry'. In: *Astronomy and Astrophysics* 200, pp. 312–322.

Wells, D. C. (1985). 'NRAO's Astronomical Image Processing System (AIPS)'. In: *Data Analysis in Astronomy*. Ed. by V. Di Gesù et al. Erice, Italy: Springer US, pp. 195–209.

Wilhelm, Rainer, B. Köhler and Philippe B. Gitton (2002). *Functional Description of the VLTI*. Tech. rep. 089. Garching bei München, Germany: European Southern Observatory (ESO), pp. 1–114.

Woillez, J. et al. (2014). 'Improving the astrometric performance of VLTI-PRIMA'. In: p. 12. ISSN: 1996756X. URL: http://arxiv.org/abs/1407.0470.

Wolf, Sebastian et al. (2012). 'Circumstellar disks and planets'. In: *The Astronomy and Astrophysics Review* 20.1, pp. 1–83. ISSN: 0935-4956. URL: http://www.springerlink.com/index/10.1007/s00159-012-0052-1.

Wyant, J. C. (1975). 'Use of an ac heterodyne lateral shear interferometer with real-time wavefront correction systems'. In: *Applied Optics* 14, pp. 2622–2626.

Young, John S. et al. (2000). 'New views of Betelgeuse: multi-wavelength surface imaging and implications for models of hotspot generation'. In: *Monthly Notices of the Royal Astronomical Society* 315.3, pp. 635–645. ISSN: 0035-8711. URL: http://mnras.oxfordjournals.org/cgi/doi/10.1046/j.1365-8711.2000.03438.x.

Young, Thomas (1804). 'The Bakerian Lecture: Experiments and Calculations Relative to Physical Optics'. In: *Philosophical Transactions of the Royal Society of London* 94.January, pp. 1–16. ISSN: 0261-0523. URL: http://rstl.royalsocietypublishing.org/cgi/doi/10.1098/rstl.1804.0001.

— (1807). *A course of lectures on natural philosophy and the mechanical arts, Volume 1*. 1st ed. London, United Kingdom: Joseph Johnson, p. 826. URL: http://books.google.pt/books?id=YPRZAAAAYAAJ%5C&pg=PA464%5C&lpg=PA464%5C&dq=Supposing+the+light+of+any+given+colour+to+consist+of+undulations+of+a+given+breadth,+or+of+a+given+frequency%5C&source=bl%5C&ots=YQ6u%5C_CfNDk%5C&sig=wZ0bxDkygEraxVXV7j0DaS7o%5C_d0%5C&hl=en%5C&ei=T6CjTtDSIsqgtwfb552dBQ%5C&sa=X%5C&oi=book%5C_result%5C&ct=result%5C&redir%5C_esc=y%5C#v=onepage%5C&q%5C&f=false.

Zernike, Frits (1938). 'The concept of degree of coherence and its application to optical problems'. In: *Physica* 5.8, pp. 785–795. ISSN: 00318914. URL: http://linkinghub.elsevier.com/retrieve/pii/S0031891438802032.

Appendix A

Peer reviewed papers

"In any case, as usual, a lot more work is necessary."

— FULLER ALBRIGHT

THIS APPENDIX includes a copy of the paper "Assessing the quality of restored images in optical long-baseline interferometry", submitted to the journal Monthly Notices of the Royal Astronomical Society (MNRAS). Figure A.1 illustrates the front page automatically generated by the ScholarOne Manuscripts website upon submission. The results of this work provide the tools to publish a second peer reviewed paper (under preparation) on the subject of comparing the phase referencing and phase closure techniques within the scope of image reconstruction.

Assessing the quality of restored images in optical long-baseline interferometry

Journal:	*Monthly Notices of the Royal Astronomical Society*
Manuscript ID	Draft
Manuscript type:	Main Journal
Date Submitted by the Author:	n/a
Complete List of Authors:	Gomes, Nuno; Universidade do Porto Departamento de Fisica e Astronomia, Física e Astronomia; Universidade do Porto Faculdade de Engenharia, Engenharia Física Thiebaut, Eric; Centre de Recherche Astrophysique de Lyon, AiRi Garcia, Paulo; Universidade do Port, Faculdade de Engenharia
Keywords:	techniques: high angular resolution < Astronomical instrumentation, methods, and techniques, techniques: interferometric < Astronomical instrumentation, methods, and techniques, techniques: image processing < Astronomical instrumentation, methods, and techniques, instrumentation: high angular resolution < Astronomical instrumentation, methods, and techniques, instrumentation: interferometers < Astronomical instrumentation, methods, and techniques

SCHOLARONE™
Manuscripts

Figure A.1: Front page of the refereed paper, automatically generated by the website, upon submission.

Mon. Not. R. Astron. Soc. **000**, 1–16 (2016) Printed 20th July 2016 (MN LATEX style file v2.2)

Assessing the quality of restored images in optical long-baseline interferometry

Nuno Gomes[1,2,3⋆], Paulo J. V. Garcia[1,2] and Éric Thiébaut[4]
[1] *Universidade do Porto - Faculdade de Engenharia, Rua Dr. Roberto Frias, 4200-465 Porto, Portugal*
[2] *CENTRA, Instituto Superior Técnico, Av. Rovisco Pais, 1049-001 Lisboa, Portugal*
[3] *Universidade do Porto - Faculdade de Ciências, Rua do Campo Alegre, 4169-007 Porto, Portugal*
[4] *Centre de Recherche Astrophysique de Lyon/Obvservatoire de Lyon, 9, Avenue Charles André, 69561 Saint-Genis Laval Cédex, France*

Accepted year month day. Received year month day; in original form year month day

ABSTRACT
Assessing the quality of aperture synthesis maps is relevant for benchmarking image reconstruction algorithms, for the scientific exploitation of imaging data from optical long-baseline interferometers, and for the design/upgrade of new/existing interferometric imaging facilities. Although metrics have been proposed in these contexts, no systematic study has been conducted on the selection of a robust metric for quality assessment.

This article addresses the question: what is the best metric to assess the quality of a reconstructed image?

It starts by considering several metrics, and selecting a few based on general properties. Then, a variety of image reconstruction cases is considered. The observational scenarios are phase closure and phase referencing at the Very Large Telescope Interferometer (VLTI), for a combination of 2, 3, 4 and 6 telescopes. They are realistic and reflect existing/planed instrumentation such as *PIONIER*, *GRAVITY*, or *MATISSE*. End-to-end image reconstruction is accomplished with the MiRA software, and then several merit functions are put to test.

It is found that convolution by an effective point spread function is required for proper image quality assessment. The effective angular resolution of the images is superior to naive expectation based on the maximum frequency sampled by the array. This is due to the prior information used in the aperture synthesis algorithm and to the nature of the objects considered.

The ℓ_1-norm is the most robust of all the metrics considered, because being a linear metric it is less sensitive to image smoothing by high regularisation levels. For the cases considered, this metric allows the implementation of automatic quality assessment of reconstructed images, with a performance similar to human selection.

Key words: techniques: high angular resolution – techniques: interferometric – techniques: image processing – instrumentation: high angular resolution – instrumentation: interferometers.

1 INTRODUCTION

Existing optical long-baseline interferometers provide information at angular scales a factor of 10 smaller than any existing or planed single aperture telescope. This is achieved by measuring interference fringes from pairs of telescopes. The fringes' contrast and position at the detector can be related to the spatial coherence of the incoming electromagnetic field, which in turn contains information on the object image (cf. e.g., Buscher 2015; Glindemann 2011). This makes an imaging interferometer very different from an imaging camera. The first difference is related to the information content. A camera generates an image from a continuous sampled pupil, while an interferometer only obtains information at a much smaller number of specific locations of an effective "meta-pupil" – the so-called *uv*-coverage of the data. A second difference is that, while in a camera all the information is obtained simultaneously, in an interferometer data is taken from diverse array combinations separated in time. Finally, for an interferometer an algorithm must be used to synthesise an image.

In optical long-baseline interferometry, phase inform-

⋆ E-mail: nunogomes@fe.up.pt

© 2016 RAS

ation degradation by atmospheric turbulence is normally overcome by phase closure triangulation (e.g., Jennison 1958; Monnier 2007), at the expense of further reducing the information content of the measurement. It is therefore not surprising that the first optical long-baseline images were of binaries (morphological simple objects) and were first obtained with three telescopes (Baldwin et al. 1996; Benson et al. 1997). Since the publication of the first relevant results, the technique of image reconstruction of long-baseline interferometric data in the optical/infrared (O/IR, 0.4–20 µm) regime has evolved and it is nowadays well established. A major breakthrough in optical long-baseline interferometry was the availability of the CHARA and VLTI arrays (ten Brummelaar et al. 2005; Schöller 2007) coupled to the control of atmospheric effects with spatial filtering (Coudé du Foresto et al. 1997; Tatulli et al. 2010) and adaptive optics (e.g., Arsenault et al. 2003). By combining 3 or more telescopes and reasonable *uv*-coverages, the information content allowed to overcome the binary barrier and enter into more complex morphologies such as stellar surfaces and discs (e.g., Benisty et al. 2011; Che et al. 2011; Hillen et al. 2016; Kloppenborg et al. 2015; Le Bouquin et al. 2009; Millour et al. 2011; Mourard et al. 2015).

Because of the low information content of interferometric data, the generation of images is an ill-posed problem with more unknowns than available data. Therefore, images are reconstructed by minimizing a cost function that includes both the data and some prior information on the object (e.g., Thiébaut 2013). To overcome the effects of the turbulence, optical long-baseline interferometry data traditionally relies on the closure phase (and not on the baseline phase). The non-convex nature of the problem makes image reconstruction a difficult task, and algorithms are still matter of active research (cf. Berger et al. 2012 for a recent review). The availability of dispersed fringes increased the information content of interferometry data, enabling spectral self-calibration (e.g., Millour et al. 2011; Schutz et al. 2014). Other developments are algorithms joining imaging and parametric descriptions of the astronomical objects (e.g., Kluska et al. 2014), or compressed sensing (Baron et al. 2014).

With the advent of *GRAVITY* at ESO, the first common instrument allowing phase referencing observations (Eisenhauer et al. 2008), most of the aperture synthesis algorithms may be simplified, because when a reference source is available, the phase closure is no longer required to remove atmospheric effects and the baseline phase becomes accessible. Standard radio interferometry approaches have proved successfully with simulated data in this context (e.g., Vincent et al. 2011).

The large variety of aperture synthesis methods naturally leads to the question on which is the best approach. In 2001, the Working Group on Optical Interferometry of the International Astronomical Union (IAU) decided to compare and promote the development of different algorithms to restore O/IR interferometric images, on a regular basis. Starting in 2004, an "Imaging Beauty Contest" has been held by SPIE every two years (Lawson et al. 2004, 2006; Cotton et al. 2008; Malbet et al. 2010; Baron et al. 2012; Monnier et al. 2014), where contestants present blindly restored images from synthetic or observational data provided by the organisation of the contest. They are also asked to interpret the results, indicating what is believed to be real features and what are the potential artefacts of the imaging process. Subsequently, the restored images obtained from the different software are compared to their corresponding reference images by means of a best-fit method. This method typically comprises a resampling of the restored image to the grid of the reference one, the normalisation of the restored image to its peak brightness, and the comparison with the reference image convolved with the effective PSF of the interferometer, using a root-mean-square agreement. However this approach is limited, because a particular metric might favour a special algorithm for a specific object morphology. This is a pertinent objection which, to our knowledge, is not addressed in the literature.

The work presented here addresses this very question: how can we equitably measure the quality of an image obtained in aperture synthesis? This is a question of relevance not only for algorithms, but also to the scientific exploitation of aperture synthesis, and for any future infrastructure relying on aperture synthesis imaging, such as the Planet Formation Imager (Monnier et al. 2014; Kraus et al. 2014).

This article is structured as follows. In Section 2, we review merit functions used for image quality assessment, and we select a few for further analysis. It is underlined that image convolution with an effective point spread function (PSF) is mandatory. In Section 3, we present the methods we used to recover the interferometric images, explaining how we generate the observables and respective noise, how we restored the images, and how we assess their quality. Important aspects of this approach are (*a*) both phase closure and phase referencing techniques are addressed, and (*b*) the array configurations are selected from available stations at the VLTI, particularly the case for 4 telescopes using phase closure, where the configurations are the ones used with the *PIONIER* instrument. Section 4 concerns about the reconstructed images and the analysis of the behaviour of the selected merit functions. We discuss the results and provide a summary of our findings. The most surprising outcome is that the metric used in the "Imaging Beauty Contest" is biased, but it can be replaced by a simple metric. A side bonus of our approach is that it paves the way for image quality assessment without human intervention. In Section 5 we conclude and present directions for future developments.

2 IMAGE QUALITY

The quality of an image has to be assessed by an objective quantitative criterion. What is the best criterion also largely depends on the context. Here we will assume that the *metric* $\Theta(x, y)$ is used to estimate the discrepancy between a reconstructed image x and a reference image y. To simplify the discussion, we also assume that the lower $\Theta(x, y)$ the better the agreement between x and y. In other words, $\Theta(x, y)$ can be thought as a measure of the distance between x and y.

When assessing image quality it is important that the result does not depend on irrelevant changes. This however depends on the type of images and on the context. For instance, for object detection or recognition, the image metric should be insensitive to the background level, to a geometrical transform (translation, rotation, magnification, etc.) or to a multiplication of the brightness by some positive factor

which does not affect the shape of the object. In cases where image reconstruction has underdeterminations, these should not have any incidence on the metric. For optical interferometry and when only power-spectrum and closure phase data are available, the images to be compared may have to be shifted for best matching. In general, the metric should be minimized with respect to the undetermined parameters.

When comparing a true image z (with potentially an infinitely high resolution) to a restored image x, the effective resolution achievable by the instrument and the image restoration process must be taken into account. Otherwise and because image metrics are in general based on pixel-wise comparisons, the slightest displacement of sharp features would lead to large loss of quality (according to the metric) whereas the images may look very similar at a lower and more realistic resolution. The easiest solution is then to define the reference image y to be the true image z blurred by an effective PSF $h_{\rm ref}$, whose shape corresponds to the effective resolution

$$y = h_{\rm ref} * z, \tag{1}$$

where symbol $*$ denotes the convolution. The choice of the effective resolution is then a parameter of the metric.

To summarise and to be specific, using the distance $\Theta(x, y)$ between the restored image x and the reference image y, the discrepancy between x and the true image z would be given by:

$$d(x, z) = \min_{\alpha,\beta,\sigma,t} \Theta\big(\alpha\, h_{\sigma,t} * x + \beta, h_{\rm ref} * z\big), \tag{2}$$

with α a brightness scale, β a background, and $h_{\sigma,t}$ an effective PSF of width parameter[1] $\sigma > 0$ and centred at position t. Note that the merit function should be minimized with respect to the width σ of the PSF in order to estimate the effective resolution achieved by a given restored image. Our choice to assigning the translation to the PSF is to avoid relying on some particular method to perform sub-pixel interpolation (of x, y or z) for fine tuning the position. Not doing so would add another ingredient to the metric. When dealing with images with different pixel sizes, the resampling of the images at a given common resolution can be implemented by a linear operator which performs at the same time the resampling, the fine shifting and the blurring by the effective PSF.

In the following subsections, we first review the most common metrics found in the literature and argue whether they are appropriate or not in the context of optical interferometry. We then propose a family of suitable metrics.

2.1 Merit functions

2.1.1 Quadratic metrics

Quadratic merit functions are probably the most widely used ones, for they are easy to manipulate and can be made insensitive to various effects, such as an affine change in the image levels (see Section 2.1.2). Even though it is not always obvious, they are, in fact, related to various metrics proposed for comparing images. Compared to the Kullback-Leibler divergence (see Section 2.1.7), quadratic merit functions amount to assuming a simple distribution of the differences between two images (that is to say, independent and Gaussian). The most general expression of a quadratic metric to measure the discrepancy between two images x and y takes the form of a weighted (squared) ℓ_2-norm:

$$\mathrm{WL2N}(x, y; W) = \|x - y\|_W^2,$$

where we denote by $\|q\|_W^2 = q^{\rm T}\, W\, q$ the weighted squared Euclidean norm, with W a positive (semi-)definite weighting operator. Using a diagonal weighting operator $W = \mathrm{diag}(w)$ yields:

$$\mathrm{WL2N}(x, y; w) = \sum_i w_i\, (x_i - y_i)^2, \tag{3}$$

where the sum is carried out for all pixels of the images and where the $w_i \geqslant 0$ is the weight of pixel i.

By choosing specific weights, it is possible to mimic a number of commonly used metrics. For instance, the metric of the *Interferometric Imaging Beauty Contest* (Lawson et al. 2004) is

$$\begin{aligned}\mathrm{IBC}(x, y) &= \sqrt{\mathrm{WL2N}(x, y; w = y/\textstyle\sum_i y_i)} \\ &= \left[\frac{\sum_i y_i\, (x_i - y_i)^2}{\sum_i y_i}\right]^{1/2},\end{aligned} \tag{4}$$

which amounts to taking the weights as being proportional to the reference image: $w = y/\sum_i y_i$. The main drawbacks of this merit function are that it overemphasises the brighter regions of the image and discards pixels where the reference image y is zero, which occurs for many pixels for a compact astronomical source on a dark background. For these reasons, we anticipate that IBC may not be the best metric.

The most simple quadratic metric is the squared ℓ_2-norm (also known as the *squared Euclidean norm*) of the pixel-wise differences between the images:

$$\begin{aligned}\mathrm{L2N}(x, y) &= \|x - y\|_2^2 \\ &= \sum_i (x_i - y_i)^2,\end{aligned} \tag{5}$$

which is WL2N when $w = 1$. The *Mean Squared Error* (MSE) is directly derived from the Euclidean norm by taking $w = 1/N_{\rm pix}$, with $N_{\rm pix}$ the number of pixels:

$$\mathrm{MSE}(x, y) = \frac{1}{N_{\rm pix}}\, \|x - y\|_2^2. \tag{6}$$

The MSE was used by Renard et al. (2011) to benchmark the effects of the regularisation in the image reconstruction from interferometric data. For all the metrics presented so far, the smaller the merit value, the more similar are the images.

Some other commonly used metrics are also based on the Euclidean norm of the differences. For instance, the *Peak Signal to Noise Ratio* (PSNR) is

$$\mathrm{PSNR}(x, y) = 10 \times \log_{10}\left(\frac{\big[\max(y) - \min(y)\big]^2}{\mathrm{MSE}(x, y)}\right). \tag{7}$$

Here, $\min(y)$ and $\max(y)$ correspond respectively to the minimum and maximum possible pixel value of the reference image y. The PSNR is given in decibel (db) units and the higher the PSNR, the more similar are the images.

[1] In this paper we took σ to be the standard deviation of the PSF profile.

Clearly, MSE and PSNR are the squared Euclidean norm of the pixel-wise difference between the images (L2N) but expressed in different units. They can be used interchangeably and we will only consider IBC and L2N in what follows.

2.1.2 Minimizing the discrepancy with respect to the brightness distortion

In order to make a formal link between different metrics, it is worth investigating what happens when the minimization with respect to the brightness distortion parameters α and β is carried on. As we will show, this minimization has a closed form solution with a quadratic metric:

$$\|\alpha\, x + \beta\, \mathbb{1} - y\|_W^2,$$

with x and y the images to compare, $\alpha \in \mathbb{R}^+$ a positive factor, $\beta \in \mathbb{R}$ a constant background, and $\mathbb{1}$ an image where all pixels are equal to 1.

Let us first consider the constant background correction. Introducing $r = y - \alpha\, x$, we want to minimize $\|r - \beta\, \mathbb{1}\|_W^2$ with respect to β. Expanding the quadratic norm yields

$$\|r - \beta \mathbb{1}\|_W^2 = \|r\|_W^2 - 2\,(\mathbb{1}^{\mathrm{T}}\, W\, r)\,\beta + \|\mathbb{1}\|_W^2\, \beta^2.$$

This is a simple 2nd order polynomial in β and the minimum is achieved for the optimal background

$$\beta^\star = \frac{\mathbb{1}^{\mathrm{T}}\, W\, r}{\mathbb{1}^{\mathrm{T}}\, W\, \mathbb{1}}, \tag{8}$$

which can be seen as a weighted averaging of r. Thus,

$$\min_\beta \|r - \beta\, \mathbb{1}\|_W^2 = \|r - \beta^\star\, \mathbb{1}\|_W^2 = \|C\, r\|_W^2, \tag{9}$$

where the linear operator C is given by

$$C = I - \mathbb{1}\, \frac{\mathbb{1}^{\mathrm{T}}\, W}{\mathbb{1}^{\mathrm{T}}\, W\, \mathbb{1}}, \tag{10}$$

and I is the identity. The linear operator C has the effect of removing the weighted average of its argument. Replacing r by $y - \alpha\, x$ yields:

$$\min_\beta \|\alpha\, x + \beta\, \mathbb{1} - y\|_W^2 = \|\alpha\, C\, x - C\, y\|_W^2, \tag{11}$$

which amounts to comparing the weighted average subtracted images.

The expansion

$$\|\alpha\, x - y\|_W^2 = \|y\|_W^2 - 2\,(y^{\mathrm{T}}\, W\, x)\,\alpha + \|x\|_W^2\, \alpha^2,$$

readily shows that the optimal factor α is

$$\arg\min_\alpha \|\alpha\, x - y\|_W^2 = \frac{y^{\mathrm{T}}\, W\, x}{x^{\mathrm{T}}\, W\, x},$$

and, after trivial simplifications, that

$$\min_\alpha \|\alpha\, x - y\|_W^2 = \|y\|_W^2 - \frac{(y^{\mathrm{T}}\, W\, x)^2}{\|x\|_W^2}.$$

Putting all together we have shown that

$$\min_{\alpha,\beta} \|\alpha\, x + \beta\, \mathbb{1} - y\|_W^2 = \|C\, y\|_W^2 - \frac{(y^{\mathrm{T}}\, C^{\mathrm{T}}\, W\, C\, x)^2}{\|C\, x\|_W^2}, \tag{12}$$

where the linear operator C is given in equation (10). If no bias correction is wanted, it is sufficient to take $C = I$. The above expression can be divided by $\|C\, y\|_W^2$ to obtain a symmetric distance between x and y and which is independent of an affine transform of the brightness of any of the two images

$$d(x, y) = 1 - \mathrm{Corr}(x, y)^2\,, \tag{13}$$

with

$$\mathrm{Corr}(x, y) = \frac{y^{\mathrm{T}}\, C^{\mathrm{T}}\, W\, C\, x}{\|C\, x\|_W\, \|C\, y\|_W} \tag{14}$$

the (weighted) correlation between the two images x and y. If $W \propto I$, then the usual definition of the correlation, given in equation (16), is retrieved.

The distance $d(x, y)$ takes values in the range $[0, 1]$, the smaller it is the better is the agreement. Conversely, the better the agreement the larger the absolute value of the (weighted) correlation. It is therefore clear now that comparing images by mean of their (weighted) correlation coefficient is equivalent to using a quadratic norm minimized with respect to an affine transform of the image intensity.

2.1.3 Universal Image Quality Index and Image Structural Similarity

The *universal image quality index* was proposed by Wang et al. (2002) to overcome MSE and PSNR, which were found to be very poor estimators of the image quality for common brightness distortions and image corruptions (like salt-and-pepper noise, lossy compression artefacts, etc.). The universal image quality index is defined as

$$\mathrm{Q}(x, y) = \frac{4\,\mathrm{Avg}(x)\,\mathrm{Avg}(y)\,\mathrm{Cov}(x, y)}{\big(\mathrm{Avg}(x)^2 + \mathrm{Avg}(y)^2\big)\,\big(\mathrm{Var}(x) + \mathrm{Var}(y)\big)}, \tag{15}$$

where $\mathrm{Avg}(x)$, $\mathrm{Var}(x)$ and $\mathrm{Cov}(x, y)$ are respectively the empirical average, variance and covariance of x and y, given by:

$$\begin{aligned}
\mathrm{Avg}(x) &= \frac{1}{N_{\mathrm{pix}}} \sum_i x_i\,,\\
\mathrm{Var}(x) &= \mathrm{Cov}(x, x)\,,\\
\mathrm{Cov}(x, y) &= \frac{1}{N_{\mathrm{pix}} - 1} \sum_i \big(x_i - \mathrm{Avg}(x)\big)\,\big(y_i - \mathrm{Avg}(y)\big)\,.
\end{aligned}$$

The universal image quality index takes values in the range $[-1, 1]$. $Q(x, y)$ is maximal for the best agreement, which occurs when $y = \alpha\, x + \beta$, and minimal when $y = -\alpha\, x + \beta$, for any $\alpha > 0$ and any β. Although the universal image quality index was designed to cope with brightness distortions such as mean shift or dynamic shrinkage, this indicator is not exactly insensitive to any affine transform of the intensity as is (see the demonstration in Section 2.1.2) the correlation coefficient:

$$\mathrm{Corr}(x, y) = \frac{\mathrm{Cov}(x, y)}{\sqrt{\mathrm{Var}(x)\,\mathrm{Var}(y)}}. \tag{16}$$

In order to improve over the universal image quality index, Wang et al. (2004) introduced the *image Structural SIMilarity* (SSIM):

$$\begin{aligned}
\mathrm{SSIM}(x, y) = &\frac{2\,\mathrm{Avg}(x)\,\mathrm{Avg}(y) + \varepsilon_1}{\mathrm{Avg}(x)^2 + \mathrm{Avg}(y)^2 + \varepsilon_1}\\
&\times \frac{2\,\mathrm{Cov}(x, y) + \varepsilon_2}{\mathrm{Var}(x) + \mathrm{Var}(y) + \varepsilon_2},
\end{aligned} \tag{17}$$

where $\varepsilon_1 > 0$ and $\varepsilon_2 > 0$ are small values introduced to avoid divisions by zero. Note that with $\varepsilon_1 = 0$ and $\varepsilon_2 = 0$, the SSIM is just the image quality index defined in equation (15). The higher the SSIM, the better the agreement. In principle SSIM and the quality index should be used *locally*, that is on small regions of the images.

2.1.4 Accuracy function

Similarly to the IBC metric, the *accuracy function* (ACC, Gomes 2016) is based on a normalised weighted quadratic difference between the reconstructed image x and the reference image y:

$$\mathrm{ACC}(x,y) = \frac{\sum_i w_i\,(x_i - y_i)^2}{\sum_i (x_i + y_i)^2}. \tag{18}$$

Here w is a normalised weighting function, a mask that eliminates all pixels where the reference and the restored images have intensities smaller than the image's dynamic range. On all non-negligible pixels, w is equal to 1.

ACC varies between 0 and 1 and the smaller it is, the greater the resemblance between both images. Note that the accuracy function is neither quadratic in x nor in y.

2.1.5 Sum of absolute differences

One of the drawback of quadratic metrics is that they strongly emphasize the largest differences. To avoid this, an ℓ_p-norm can be used with an exponent $p < 2$. For instance, the *sum of absolute differences* or ℓ_1-norm is given by:

$$\begin{aligned}\mathrm{L1N}(x,y) &= \|x - y\|_1 \\ &= \sum_i |x_i - y_i|.\end{aligned} \tag{19}$$

2.1.6 Fidelity function

The *fidelity function* was introduced by Pety et al. (2001) in the context of image reconstruction for ALMA. It is defined as the ratio of the total flux of the reference y to the difference between the restored image x and the reference one:

$$\mathrm{FID}(x,y) = \frac{\sum_i y_i}{\sum_i \max\{\eta, |y_i - x_i|\}}, \tag{20}$$

where η is some non-negative threshold. The higher the fidelity value, the better the agreement.

Choosing $\eta > 0$ avoids divisions by zero, and Pety et al. (2001) took $\eta = 0.7\,\mathrm{RMS}(x - y)$, where RMS(...) yields the root mean squared value of its argument. We note that with $\eta > 0$, all differences smaller than η have the same incidence on the total cost and are therefore irrelevant. To avoid this, one has to take $\eta = 0$, in which case the reciprocal of the fidelity function is then just the ℓ_1-norm defined in equation (19) times some constant factor which only depends on the reference y. As the fidelity function would then yield the same results as the ℓ_1-norm, we only consider the latter in our study.

2.1.7 Kullback-Leibler divergence

Being non-negative everywhere and normalised, the images can be thought as distributions (over the pixels). The *Kullback-Leibler divergence* measures the similarity between two distributions. When applied to our (normalised), images it writes

$$\mathrm{KL}(x,y) = \sum_i y_i\,\log(x_i/y_i). \tag{21}$$

A restriction for the Kullback-Leibler divergence is that x and y must be strictly positive everywhere. It is however possible to account for non-negative distributions by modifying the definition of the Kullback-Leibler divergence as follows:

$$\mathrm{KL}(x,y) = \sum_i c_{\mathrm{KL}}(x_i, y_i),$$

where $c_{\mathrm{KL}}(q,r)$ extends $r\log(q/r)$ by continuity:

$$c_{\mathrm{KL}}(q,r) = \begin{cases} 0 & \text{if } q = r, \text{ or } q > 0 \text{ and } r = 0, \\ -\infty & \text{if } q = 0 \text{ and } r > 0, \\ r\log(q/r) & \text{otherwise.} \end{cases}$$

Note that the Kullback-Leibler divergence is not symmetric, i.e., $\mathrm{KL}(x,y) \neq \mathrm{KL}(y,x)$. The Kullback-Leibler divergence is less or equal to zero. The lower the Kullback-Leibler divergence the worse is the agreement between x and y. The maximal value of the Kullback-Leibler divergence is equal to zero and is achieved when $x = y$.

Like the IBC metric, the Kullback-Leibler divergence disregards x_i where $y_i = 0$. In addition, any image x with at least one pixel, say i_0, such that $x_{i_0} = 0$ while $y_{i_0} > 0$ yields $\mathrm{KL}(x,y) = -\infty$, which corresponds to the maximum possible discrepancy. These are serious drawbacks for using the Kullback-Leibler divergence as an image metric, because it could not make a distinction between restored images such that $x_{i_0} = 0$, whatever the values of the other pixels.

2.1.8 Designing the metric

We want to derive an image metric that is adapted to our particular case: we consider images of compact objects (i.e., with finite size support) over a constant background, and which may be shifted by an arbitrary translation.

We assume that $d(x,y,t)$ yields the discrepancy between the image x and the image y shifted by a translation t. Quite naturally, we require that the following properties hold:

(i) The metric does not change if the images are extended with pixels set with the background level; likewise, the metric does not change if the images are truncated provided that the values of the removed pixels equal the background level;
(ii) The metric is non-negative and equal to zero if the two images are the same (for a given relative translation); in particular $d(x,x,0) = 0$, whatever the image x;
(iii) The metric is *stationary* in the sense that whatever the images x and y and the translations t, t' and t'',

$$d\big(s(x,t), s(y,t'), t''\big) = d(x, y, t + t'' - t'), \tag{22}$$

where $s(x,t)$ yields image x shifted by translation t:

$$s(x,t)_i = x_{i-t}.$$

A last requirement, although optional, could be:

(iv) The metric is *symmetric* in the sense that

$$d(y, x, -t) = d(x, y, t), \tag{23}$$

whatever the images x and y and the translation t.

To limit the number of possibilities, we consider that the metric is the sum of a pixel-wise cost. Then, accounting for property (i),

$$d(x, y, t) = \sum_{i \in \mathbb{Z}^n} c(\widetilde{x}_i, \widetilde{y}_{i-t}), \tag{24}$$

where n is the number of dimensions of the images x and y (in our case, $n = 2$), $\mathbb{Z}$ is the set of integers, $t \in \mathbb{Z}^n$ is the considered translation, $c(q, r)$ is the pixel-wise cost, and $\widetilde{x}$ (resp. $\widetilde{y}$) is the image x (resp. y) infinitely extended with the background level β:

$$\widetilde{x}_i = \begin{cases} x_i & \text{if } i \in \mathbb{X}; \\ \beta & \text{else,} \end{cases} \tag{25}$$

with $\mathbb{X} \subset \mathbb{Z}^n$ (resp. $\mathbb{Y} \subset \mathbb{Z}^n$) the support of the image x (resp. y). We note that property (ii) implies that $c(q, q) = 0$ whatever $q \in \mathbb{R}$, and also that the background level must be the same for the two images. We also note that property (iv) implies that the pixel-wise cost be a symmetric function, i.e., $c(q, r) = c(r, q)$ whatever $(q, r) \in \mathbb{R}^2$. Finally, property (iii) holds because the same pixel-wise cost is used whatever the index i.

As $c(\beta, \beta) = 0$, the sum over the infinite set $\mathbb{Z}^n$ in equation (24) simplifies to sums over three finite (and possibly empty) subsets:

$$d(x, y, t) = \sum_{i \in \mathbb{X} \cap \mathbb{Y}_t} c(x_i, y_{i-t}) + \sum_{i \in \mathbb{X} \setminus \mathbb{Y}_t} c(x_i, \beta) + \sum_{i \in \mathbb{Y} \setminus \mathbb{X}_t} c(y_i, \beta), \tag{26}$$

where $\mathbb{A} \setminus \mathbb{B}$ denotes the set of elements of $\mathbb{A}$ which do not belong to $\mathbb{B}$, and

$$\mathbb{X}_t = \{i \in \mathbb{Z}^n \mid i - t \in \mathbb{X}\},$$

is the set of indices i such that $i - t$ belongs to the support of x. An efficient implementation of the metric may be achieved with:

$$d(x, y, t) = \gamma + \sum_{i \in \mathbb{X} \cap \mathbb{Y}_t} \big[c(x_i, y_{i-t}) - c(x_i, \beta) - c(y_{i-t}, \beta)\big], \tag{27}$$

where $c(x_i, \beta)$ (resp. $c(y_i, \beta)$) can be pre-computed for all $i \in \mathbb{X}$ (resp. for all $i \in \mathbb{Y}$) and:

$$\gamma = \sum_{i \in \mathbb{X}} c(x_i, \beta) + \sum_{i \in \mathbb{Y}} c(y_i, \beta)\,.$$

Finally, it remains to choose the pixel-wise cost $c(q, r)$. A whole family of merit functions can be derived with the following pixel-wise cost

$$c(q, r) = \big|\Gamma(a) - \Gamma(r)\big|^p \tag{28}$$

where $p > 0$ is a chosen exponent and Γ is a function used to emphasise the discrepancy in the low/high range of the brightness distribution. For example, taking

$$\Gamma(q) = \operatorname{sign}(q)\,|q|^\gamma, \tag{29}$$

with $\gamma \in]0, 1[$, it amounts to paying more attention to the least bright part of the images. Taking $p = 2$ and $\gamma = 1$ yields the ℓ_2-norm (L2N); while taking the quadratic merit $p = 1$ and $\gamma = 1$ yields the ℓ_1-norm (L1N). Incidently, this shows that the required aforementioned properties (including the symmetry) do hold for these norms.

2.1.9 *Choice of the candidates*

We already mentioned that not all merit functions reviewed in this paper are appropriate for comparing synthetic aperture images. For example, we disregarded the Kullback-Leibler divergence (see Section 2.1.7) because of its inability to distinguish between very different images which have pixels equal to zero while they are non-zero in the reference image. In our context, the background level is known (i.e., $\beta = 0$ which corresponds to the positivity constraint) and should not have to be adjusted when comparing images. The Universal Quality Index and Image Structural Similarity described in Section 2.1.3 are therefore not appropriate for our needs. The brightness scale α may have to be tuned so as to minimize the discrepancy between the images because, on the one hand, they may have different normalization constraints and, on the other hand, they may have been interpolated to cope with different pixel sizes. As we have shown in Section 2.1.2, minimizing a quadratic cost function in α would be equivalent to use the correlation of the images as a metric.

To summarize, we will compare images using the ℓ_2-norm (L2N), the ℓ_1-norm (L1N), the metric used in the past Interferometric Beauty Contests (IBC) and the accuracy function (ACC).

3 METHODS

3.1 Synthetic image library

The true images (z) used in the study are presented in Fig. 1. They span representative science cases of interferometric imaging (cf. e.g., Berger et al. 2012): compact clusters/multiple stellar systems, young stellar objects and stellar surfaces. We fixed the size of the images to ease the interpretation of the results. The width of the pixel is 0.04 mas. The images cover a wide range of visibilities, from the very sharp cluster to the over-resolved stellar photosphere. The cluster consists of 8 stars "randomly" spread in the FOV, with a Gaussian profile of standard deviation 0.1 mas, whose intensities decrease in factors of 2. The typical separation between neighbouring stars is 5 mas. The young stellar object (YSO) consists of a central star and a circumstellar disc, with a total flux ratio of 10 to 1. The disc has two features: a dark spot on the first quadrant and a bright spot in the third quadrant. The stellar surface has two bright spots in the third quadrant, and a dark spot on the first quadrant.

3.2 UV-space generation

We used realistic uv-coverages for the VLTI station positions.[2] Six observational configurations are considered, corresponding to 1, 3 and 6 nights of observation, and to phase

[2] Available at https://www.eso.org/observing/etc/doc/viscalc/vltistations.html.

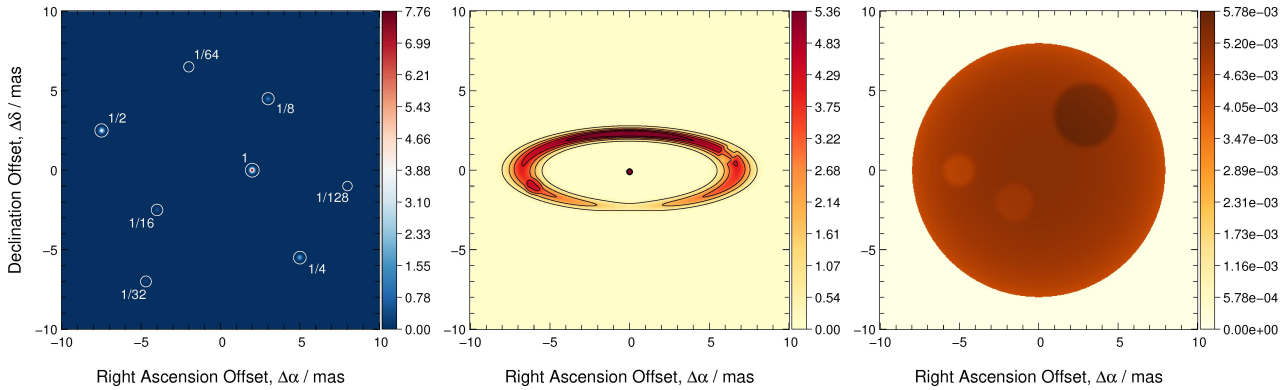

Figure 1. True images (z) used for the image reconstruction study: stellar cluster (*left*), young stellar object (*centre*), and stellar photosphere (*right*). The images are normalised by their total flux. The colour bars indicate surface flux. The stars of the cluster have relative intensities as indicated in the figure. The circles point the position of the stars. All colour maps are sequential, and they have been chosen in order to maximize the contrast of the features in each image.

referencing (PhR) and phase closure (PhC) data. The stations configurations are inspired in previous imaging studies (Filho et al. 2008a,b), and are representative of several instruments: *PRIMA* (2TPhR, Delplancke 2008), *AMBER* (3TPhC, Petrov et al. 2007), *GRAVITY* (3T-4TPhR, Eisenhauer et al. 2011), *PIONIER* (4TPhC, Le Bouquin et al. 2011; Eisenhauer et al. 2011), and *VSI* (6TPhC, Malbet et al. 2006). To compute the uv-tracks, which depend on the object position, observatory location, station positions and hour-angle of the observations (Thompson, Moran & Swenson 1986), the following assumptions were made: (i) object declination of $-60°$, (ii) a full uv-track corresponding to 19 instantaneous and evenly sampled data points, during a 9 h transit, and (iii) station configurations fixed during each night. The corresponding uv-coverages are presented in Fig. 2.

3.3 Noise model

The observables used in this study are the visibility amplitude V, the baseline visibility phase ϕ, the squared visibility V^2, the bi-spectrum $\mathcal{B}$, and the closure phase ϕ_c. A synthetic observable o_s is generated by,

$$o_s \sim \mathcal{N}(\mathrm{E}\{o\}, \mathrm{Var}\{o\}),$$

where the expected value of the observable ($\mathrm{E}\{o\}$) is computed by interpolating the reference image at the angular frequencies of the observations,[3] using the MiRA package.[4] We adopted the *Simple Noise Model* (Gomes 2016), which is Gaussian and described by one free parameter, the *noise-to-signal ratio* factor $\eta = 1/\mathrm{SNR}$. It is assumed to be $\mathrm{SNR} = 20$, a value typical of good quality interferometric observations. The variance of the noise for the n^{th} visibility amplitude is defined as

$$\mathrm{Var}\{V_n\} = (\eta\langle V\rangle)^2 = \left(\frac{\langle V\rangle}{\mathrm{SNR}}\right)^2, \qquad (30)$$

where $\langle V\rangle$ is the average of all visibility amplitudes for a given uv-coverage (cf. Table 1).

In order to derive the noise for the baseline phase, we assume that the complex visibility has independent real and imaginary parts, with the same Gaussian noise (Goodman approximation, Goodman 1985). The variance of the noise for the n^{th} baseline phase becomes

$$\mathrm{Var}\{\phi_n\} = \frac{\mathrm{Var}\{V_n\}}{V_n^2}. \qquad (31)$$

The noise for the remaining observables can be determined by error propagation.

The simple noise model is in contrast with the one used by Renard et al. (2011), since it initially sets the noise in the visibility amplitude instead of the phase, making the noise in the phase increase with decreasing visibility amplitude. It also qualitatively agrees with Tatulli & Chelli (2005), where the visibility signal-to-noise ratio increases with the visibility amplitude.

3.4 Image reconstruction with MiRA

The noisy data generated is saved in an OIFITS file (Pauls et al. 2005) and used as input for the MiRA image reconstruction software, assuming monochromatic data. As the goal of the study is to find the best metric for image reconstruction, the actual algorithm is not relevant, as long as it remains the same for all metrics. The MiRA software and its principles are described in detail by Thiébaut (2008, 2013). To summarize, MiRA searches for the image x^+ which minimizes the 2-term penalty criterion:

$$x^+ = \arg\min_x \Big\{ f(x) = f_{\mathrm{data}}(x|d) + \mu\, f_{\mathrm{prior}}(x) \Big\}. \qquad (32)$$

The term $f_{\mathrm{data}}(x|d)$, usually known as the *likelihood term*, measures the discrepancy between the actual data d (e.g., squared visibilities V^2, visibility amplitudes V, baseline phases ϕ, and closure phases ϕ_c) and their model, given the image, x. The term $f_{\mathrm{prior}}(x)$, commonly designated as the *regularisation term*, is a penalty which enforces additional priors, and it is required to avoid artefacts. It is needed because the data alone cannot unambiguously yield a

[3] The observing wavelength is taken at the centre of the K-band: 2.179 µm.
[4] Available for download at http://cral.univ-lyon1.fr/labo/perso/eric.thiebaut/?Software/MiRA.

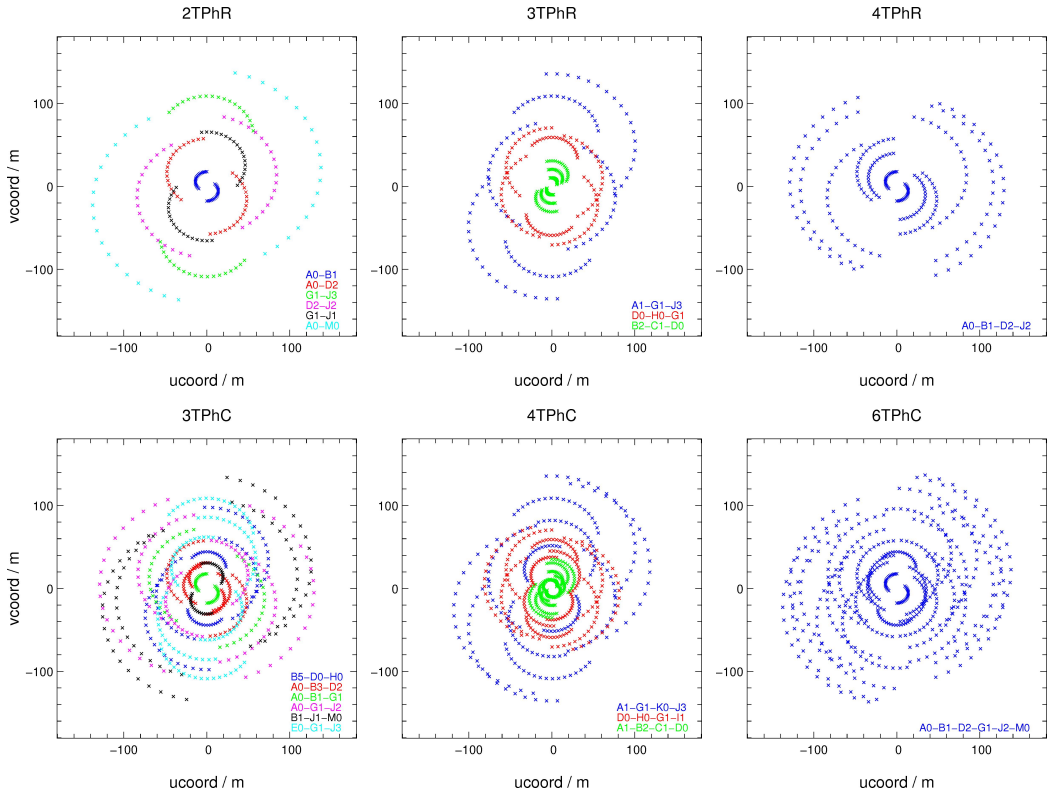

Figure 2. *UV*-coverages of the observational configurations used in the study. PhR stands for phase referencing and PhC for phase closure. The observing nights are fixed for each column and are as follows: 6 nights left column, 3 nights central column and 1 night right column. The stations used in each configuration are indicated.

Table 1. Mean values of the visibility amplitudes for the objects in each *uv*-configuration. The figures between parenthesis correspond to the standard error of the mean of the last digit.

Object	2TPhR	3TPhC	3TPhR	4TPhC	4TPhR	6TPhC
Stellar Cluster	0.60064(5)	0.63110(7)	0.6307(2)	0.62139(3)	0.5854(1)	0.57993(1)
Young Stellar Object	0.36905(10)	0.34055(3)	0.4849(1)	0.47229(1)	0.37082(8)	0.30223(9)
Stellar Photosphere	0.28246(2)	0.20076(1)	0.36520(4)	0.37313(5)	0.28580(8)	0.18560(1)

unique image. The so-called *level of regularisation* or *hyper-parameter* $\mu > 0$ is adjusted to set the relative weight of the priors. In addition to minimising the cost $f(x)$, the sought image x^+ is strictly constrained to be non-negative and normalised (the sum of the pixels being equal to 1).

For the regularisation term, we chose a relaxed version of the total variation criterion (Rudin et al. 1992; Strong & Chan 2003), which enforces edge-preserving smoothness (Charbonnier et al. 1997), and that was found by Renard et al. (2011) to be the most effective for a large variety of astronomical objects:

$$f_{\text{prior}}(x) = \sum_{i,j} \sqrt{(x_{i+1,j} - x_{i,j})^2 + (x_{i,j+1} - x_{i,j})^2 + \varepsilon^2}, \tag{33}$$

with x the image and i, j the pixel indexes ($\varepsilon > 0$ is a small value to have a differentiable prior term).

3.4.1 *Practical implementation*

Once the regularisation is defined, MiRA takes as input (*i*) the data, (*ii*) an optional initial estimate for the image – assumed a square of $N \times N$ pixels – (*iii*) the pixel size $\delta\theta$, (*iv*) the hyper-parameter μ, and (*v*) the maximum number of iterations. MiRA stops once the convergence criterion is fulfilled or the maximum number of iterations is reached. It then outputs a reconstructed image.

The image lateral size is $\Omega = N\,\delta\theta$. It provides a strict constraint which limits the support of the restored object and strongly impacts on the reconstruction process. As we want to have as few constraints as possible for the reconstruction, we chose an image size significantly larger than that of the object. In the present work, Ω was set to be 40 mas, roughly 2.5 times the object size. The pixel size should sample the maximum angular resolution in the Nyquist-Shannon sense, i.e., $\delta\theta < \lambda/(2\,B_{\max})$, with $B_{\max}$ the maximum projected baseline length. However, it was found that to make image comparison of point-like structures reliable, a much smaller value had to be used: $\delta\theta \simeq \lambda/(12\,B_{\max})$.

By combining the above constrains and taking into account that the maximum baseline of the configurations in Figure 2 is $B_{\max} = 144\,\mathrm{m}$, we adopted $N = 160$ and $\delta\theta = 0.25\,\mathrm{mas}$.

The only remaining parameters in the reconstruction are the (optional) initial image estimate, the number of iterations, and the value of the hyper-parameter. Their joint management is described in the following subsection.

3.4.2 Tuning the hyper-parameter μ

For the phase referencing reconstructions, MiRA is called without an initial image estimate, which amounts to starting with a random guessing image whose pixels are drawn following an independent uniform law. For the phase closure restorations, the initial image was a quick reconstruction from the corresponding phase referencing observation[5] with a large value of μ. Because of the strong level of regularisation, this image is a highly blurred version of the true image z. Other procedures could be devised to obtain the starting image for phase closure, such as a short image recover without any phase information, but this aspect is not important for the goal of this study, to wit, devise a method to assess the quality of final reconstructed images. The first restoration step (with or without initial guess) is performed for 300 iterations.

The image reconstruction process then follows a cascade of calls[6] to MiRA, where μ is reduced by a constant factor in each call. The intermediary restored image output in each step is used as the image estimate for the next call. The total number of calls in the cascade is 5 and 7, respectively for PhR and PhC.[7] MiRA normally achieves convergence before the maximum number of iterations is reached. In the PhC case, the guess image for the next MiRA call was obtained by soft-thresholding the output of the previous call at 5% of its maximum[8].

A limitation of the previous method is that convergence can be achieved for different values of μ. Furthermore, no objective criterion for setting μ is available. In this work two approaches were followed to identify the best μ. Initially, reconstructions were conducted for different values of μ, spanning logarithmically from 10^4 to 10^{-3}. In the first approach, a human panel was asked to select the reconstructed image that most resembled the true image z, therefore determining the value of μ. In the second approach, the metrics selected in Section 2.1.9 were used. The PSF h was taken as a Gaussian characterized by its standard deviation, σ. The restored image x is resampled to the grid of the reference image y. Then, each metric was evaluated in the 2D parameter space (μ, σ), with σ spanning from 0 to 0.5 mas.[9] The minimum of the metric would then determine μ.

4 RESULTS AND DISCUSSION

4.1 Reconstructed images

We produced 18 mock observations of the three reference images of Fig. 1 in all aforementioned array and phase scenarios. Images were restored from the corresponding interferometric data, stopping at 15 different levels of regularisation, logarithmically ranging between 10^4 and 10^{-3}. Some examples of the 270 restored images are illustrated in Fig. 3. The full set of restored images is available at the JMMC website.[10]

The top two rows correspond to restored images of the stellar cluster, the following three rows to the YSO, and the bottom three rows to the stellar photosphere. For the former, the first row lists images obtained when $\mu = 10^4$, and the second row to $\mu = 300$; for the YSO, the first row corresponds to $\mu = 10^4$, the second row to $\mu = 3$, and the last row to $\mu = 10^{-3}$; finally, for the stellar photosphere, $\mu = 10^4$ in the first row, $\mu = 300$ in the middle row, and $\mu = 10^{-3}$ in the last row. The columns are organized as follows: the phase cases alternate between PhR and PhC, and the number of telescopes increases from left to right – 2, 3, 4, and 6 telescopes (respectively 2T, 3T, 4T, and 6T) – so as to get the scenarios 2TPhR, 3TPhC, 3TPhR, 4TPhC, 4TPhR, and 6TPhC.

4.2 Observational scenarios

The quality of the images changes according to the observational scenarios considered (2T, 3T, 4T and 6T, and PhR or PhC) and their respective *uv*-coverages. This is essentially related to the *uv*-coverage of the data and the amount of phase information. It is not the goal of the present study to compare phase referencing with phase closure (and the data presented does not allow to draw conclusions), but to present a wide variety of situations in image reconstruction to successfully test merit functions.

4.3 Effect of the level of regularisation on the image reconstruction

Concerning the reconstructions and levels of regularisation (Fig. 3), it is noticeable that all restored images become sharper as the level of regularisation is decreased, that is, as more weight is given to the data. However, below a certain level of μ – which depends on the object and telescopes+phase configuration – no visible effect on the shape and surface flux of the stellar cluster is seen, because the

[5] 2TPhR for 3TPhC, 3TPhR for 4TPhC, and 4TPhR for 6TPhC.
[6] Each using 1000 iterations.
[7] The two extra steps in the PhC case are necessary for better convergence and to properly centre the image in the FOV.
[8] $x_{k+1} = \max(0,\, x_k - 0.05 \cdot \max(x_k))$, with x_k the recovered image in step k. This approach was required because of the non-convex nature of PhC image reconstruction. The algorithm frequently converges to local minima.
[9] For $\sigma = 0$, the image is only shifted as expected from the analytic convolution. Because PhC does not keep the absolute position of the objects (Monnier 2007), the PSF included a positional displacement $t = (t_1, t_2)$. This displacement was found by an iterative process that minimized the metric as a function of the displacement.
[10] Available at `http://apps.jmmc.fr/oidata/shared/ngomes/` (tbd).

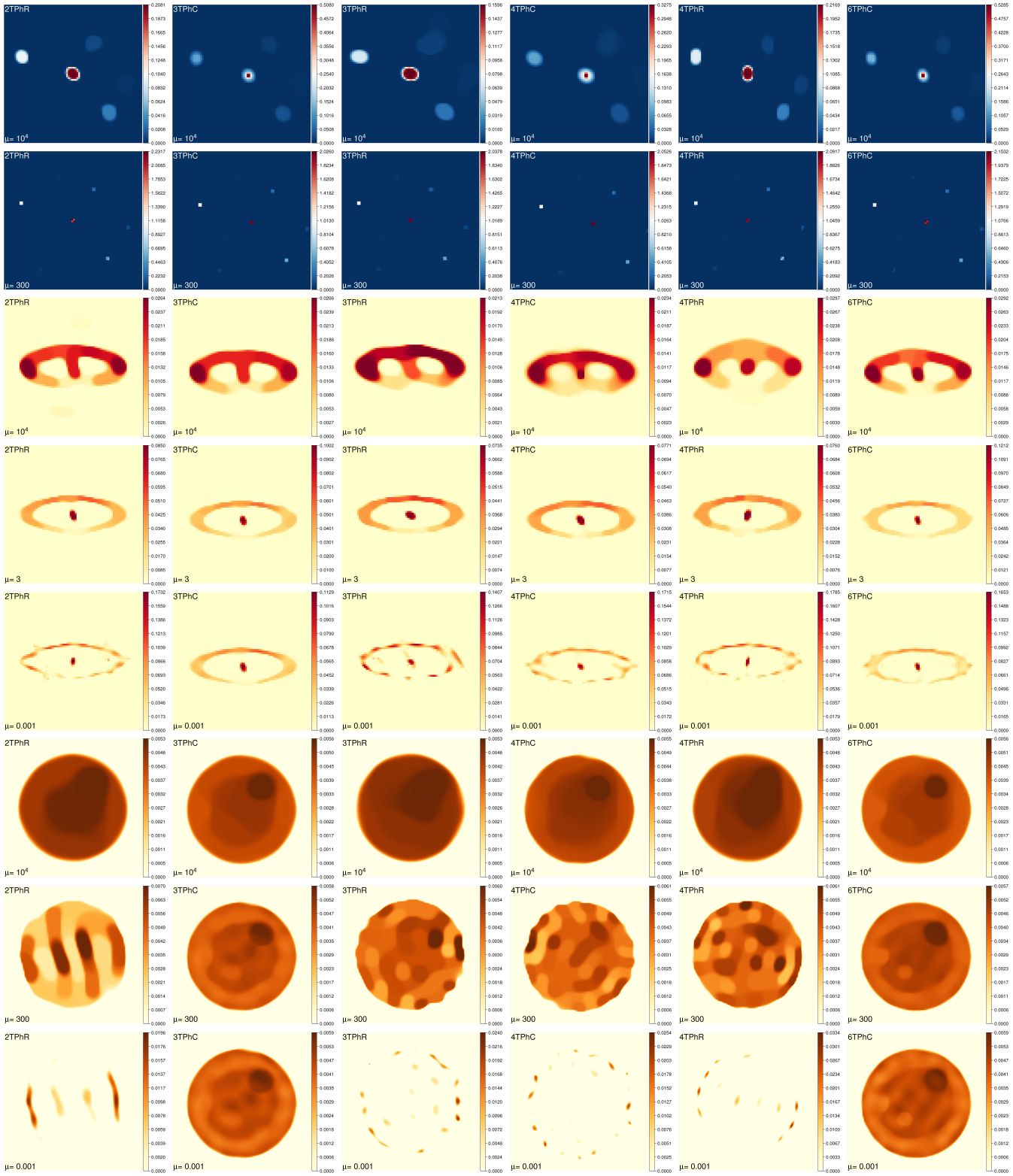

Figure 3. Examples of image reconstructions for the three reference objects: stellar cluster (first two rows), young stellar object (three middle rows), and stellar photosphere (three last rows). Each column matches a different configuration of the synthetic observations, and every row corresponds to a different level of regularisation. For all objects, the lateral image size is 20 mas.

stars (point-like unresolved source objects) become confined to one pixel. This is not the case for objects with extended/resolved structures, such as the YSO and the stellar photosphere, where reducing the regularisation below a certain level introduces reconstruction artefacts and noticeably degrades the quality of the image. For instance, in the YSO, for the highest tested level of regularisation ($\mu = 10^4$) all images are blurred, with the central star attached to the disc. When $\mu = 3$, the disc is nicely restored in all configurations, with the central star separated from it. For $\mu = 10^{-3}$, only the 3TPhC configuration yields a well restored image. The configurations 2TPhR, 3TPhR, 4TPhC and 4TPhR exhibit disrupted discs, full of artefacts coming out of the reconstruction process, and the 6TPhC scenario produces an image where the disc, although intact, is very irregular. In the stellar photosphere, when $\mu = 10^4$, only the phase closure cases produce well enough restored images, with the most prominent spot visible. When $\mu = 300$, the 3TPhC and the 6TPhC cases yield images where the 3 spots are identifiable, but all other configurations produce discs full of restoration artefacts. For $\mu = 10^{-3}$, the 3TPhC and 6TPhC produce well enough restored images, with 2 and 3 spots identifiable respectively in the former and the latter configurations. In the remainder of the scenarios, the image is not properly restored – the disc is not produced, and the algorithm gives rise solely to restoration artefacts distributed in a circular configuration.

4.4 Human determination of the hyper-parameter

Table 2 presents the average and standard deviation of the regularisation hyper-parameter μ determined by the human panel, for each object and configuration. The value of μ for the stellar photosphere is much larger than for the stellar cluster, which in turn is larger than that for the YSO. For a given object, μ varies across configurations, without any specific pattern.

The values of μ determined by human selection correspond to images that were fed to selected merit functions (see Section 2.1). The PSF width is a remaining free parameter. We present in Table 3 the values of the Gaussian PSF σ that minimize the metric for the human determined μ. These values were obtained by computing the statistics for 12 realisations in each object and observational scenario. The σ values are of the order of 0.2 mas, which corresponds to a FWHM of about 0.5 mas. This should be compared to the angular resolution of the interferometer, which is around 3 mas, and to the reference images pixel size of 0.25 mas. Clearly the image reconstruction achieves a significant level of super-resolution, which is limited by the pixel size of the reconstructed images. This result might appear puzzling at first sight, but angular resolution is a sophisticated concept than cannot be fully enclosed in a simple Rayleigh-like criterion (e.g., den Dekker & van den Bos 1997). Because we have prior information (enforced by the regularisation and positivity of the solution), a reasonable SNR and relatively smooth objects, it is expected that the image reconstruction achieves significant super-resolution.

In order to check the robustness of Figs. 4 to 6 to different realisations of the data, we carried out 12 simulations of the 18 synthetic observations. The statistics of the minima for the human determined μ are presented in Table 4 (the errors in Table 3 were computed from this same dataset). The standard error of the mean is very small, supporting the robustness of the results to the noise in the dataset.

4.5 Benchmarking the metrics

As explained in Section 3.4, a reconstructed image is a function of the final chosen μ. Furthermore, the application of a given metric requires the convolution by a PSF whose width is characterized by σ. In this subsection we present and discuss the results for the behaviour of the merit functions.

Table 4, where μ is determined by human selection, provides an initial benchmark. The values of the quality functions show that IBC mimics the behaviour of L2N in most objects and configurations. On the one hand, this is explained by the quadratic nature of both metrics and, on the other hand, by the fact that the weighting function of IBC is the reference image itself, which makes the metric disregard pixels where the latter is zero. The failure of ACC in properly characterizing the quality of restored images in some scenarios is related to the fact that it applies a mask to the reference image before comparison, thus eliminating parts containing reconstruction artefacts that are important to determine the quality of the image. This however could be an interesting merit function when we are focused on certain parts of the image and want to eliminate others that we safely identify as artefacts of the reconstruction. For all objects and configurations, the L1N metric appears to properly characterize the quality of the restored images.

We also conducted a systematic study of the metric behaviour as a function of μ and σ. We varied μ logarithmically between 10^4 and 10^{-3}, and σ between 0 and 0.5 mas. The values of the merit functions versus μ and σ are plotted in Fig. 4 (for the stellar cluster), Fig. 5 (for the YSO) and Fig. 6 (for the stellar photosphere). The top, middle and bottom rows present the results for the quality functions L1N, L2N and IBC, respectively. The columns are organized as in Fig. 3. The colour palette is inverted, such that the minima (darker colours) indicate a better agreement between the restored images and the references. All merit functions exhibit regions of minima, which is also verified in the ACC metric (not depicted). The red crossed circles point to the global minima of the panels. The pink stars are located at the position of the aforementioned values of μ determined by human selection. The position of the corresponding σ was obtained by minimizing the merit function for the fixed μ, using the NEWUOA algorithm (Powell 2006).

The first result is that, generally, the merit functions are reasonably convex (i.e., they depict regions with a clear minima). Overall, the effective resolution worsens with the hyper-parameter μ, as expected (i.e., the dark regions bend towards larger values of σ and μ). This is expected because increasing μ amounts to smooth the image.

The shape of the minima regions of Figs. 4 to 6 depends on the object. In the case of the stellar cluster (Fig. 4), the minima regions exhibit an horizontal branch up to a certain level of regularisation. This is compatible with the aforementioned limiting value of regularisation, below which restored images present no noticeable differences in quality and the (super-)resolution becomes limited by the size of the pixel. A single pixel encompasses the totality of the flux emanating from a restored unresolved star lying inside of it. The value

Table 2. Value of the hyper-parameter μ obtained by the human panel. The values are computed by $10^{\mathrm{avg}(\log_{10}\mu_i)}$. The digits between brackets correspond to the standard deviation of the human panel distribution.

Object	2TPhR	3TPhC	3TPhR	4TPhC	4TPhR	6TPhC
Stellar Cluster	12(7)	16(12)	8(6)	7(15)	17(6)	27(7)
Young Stellar Object	1(2)	0(32)	4(2)	2(2)	2(3)	7(3)
Stellar Photosphere	594(3)	30(3)	413(5)	691(3)	440(3)	74(9)

Table 3. Mean values of the PSF σ for the synthesised objects, observational scenarios and merit functions. The numbers between parenthesis correspond to the standard error of the mean on the last digit.

	σ / mas					
Metric	2TPhR	3TPhC	3TPhR	4TPhC	4TPhR	6TPhC
Stellar Cluster						
ACC	0.14612(3)	0.1484(3)	0.1481(2)	0.1472(2)	0.1587(9)	0.1481(1)
L1N	0.14373(7)	0.1483(4)	0.1464(4)	0.1458(3)	0.1625(9)	0.1498(3)
L2N	0.14985(3)	0.1522(3)	0.1518(2)	0.1508(2)	0.1629(9)	0.1520(1)
IBC	0.15437(3)	0.1560(3)	0.1560(2)	0.1550(1)	0.1648(8)	0.15547(9)
Young Stellar Object						
ACC	0.281(2)	0.273(4)	0.294(2)	0.281(2)	0.320(2)	0.263(2)
L1N	0.204(2)	0.191(5)	0.198(2)	0.216(4)	0.259(4)	0.207(2)
L2N	0.306(3)	0.298(4)	0.320(1)	0.301(2)	0.347(2)	0.282(2)
IBC	0.343(4)	0.333(4)	0.367(2)	0.334(2)	0.384(2)	0.305(3)
Stellar Photosphere						
ACC	0.293(2)	0.216(3)	0.270(2)	0.255(2)	0.242(2)	0.189(4)
L1N	0.274(2)	0.198(3)	0.239(2)	0.232(2)	0.219(2)	0.166(4)
L2N	0.269(2)	0.198(2)	0.245(2)	0.233(2)	0.221(2)	0.170(3)
IBC	0.277(2)	0.201(3)	0.251(2)	0.239(3)	0.226(2)	0.173(4)

of $\sigma \sim 0.15$ mas indicated by the branch is compatible with the pixel size of 0.25 mas. For sources with extended emission, the branch is not visible because the image degrades rapidly below a certain level of regularisation (cf. Fig. 3 for some examples). Nevertheless, regions of minima are also evident, the position of which largely depends on the merit function.

4.5.1 L1N as the most robust metric

For L1N, the global minima typically[11] lie well inside the limits defined by the plots. That is not the case for many L2N and IBC observations (especially for the cluster and YSO), suggesting that if the study was extended to larger values of σ and μ, the global minima would point to more blurred images. The minima valley oriented in the direction of increasing μ and σ is less pronounced for L1N than for L2N and IBC. For L2N and IBC, this would indicate a better agreement between the restored and the reference images in those extreme regions of the plots, where the restored images is more blurred. This clearly shows that these metrics are biased and are not robust to over-smoothing by large values of the μ hyper-parameter. They will consider that an image with lower "angular resolution" is a better image than one with higher "angular resolution". These results support L1N as the most robust of the merit functions used for the variety of cases considered.

The morphology of the object has some impact on the behaviour of the metrics. The quality of extended resolved objects can be more easily assessed than that of unresolved sources. When the emitting source combines both type of objects (resolved and unresolved), the studied merit functions seem to have a harder job to evaluate the quality of the restored images. The great imbalance in intensity between the central star and the surrounding disc might explain the differences in quality.

4.6 Automatic image quality assessment

The distance between the pink stars (minima obtained from human selection) and the circled red crosses (global minima) in Figs. 4 to 6 indicate how well a given merit function translates the human perception of a "good" restored image.

[11] Except for the 3TPhC stellar photosphere and 4TPhC YSO cases.

Table 4. Mean values of the merit functions at the positions of μ determined by human selection (pink stars in Figs. 4, 5 and 6). The scores were obtained by computing the statistics for at least 12 realisations in each scenario. The smaller the values, the better the agreement. The numbers between parenthesis correspond to the standard error of the mean of the last digit.

	2TPhR	3TPhC	3TPhR	4TPhC	4TPhR	6TPhC
Stellar Cluster						
ACC	0.03760(9)	0.0364(2)	0.065(5)	0.060(4)	0.066(4)	0.063(3)
L1N	0.239(1)	0.231(2)	0.19(1)	0.199(9)	0.191(8)	0.195(7)
L2N	$6.08(1) \times 10^{-8}$	$5.73(6) \times 10^{-8}$	$2.3(3) \times 10^{-8}$	$2.7(2) \times 10^{-8}$	$2.0(2) \times 10^{-8}$	$2.3(2) \times 10^{-8}$
IBC	$4.76(1) \times 10^{-5}$	$4.49(4) \times 10^{-5}$	$2.0(2) \times 10^{-5}$	$2.3(2) \times 10^{-5}$	$1.8(1) \times 10^{-5}$	$2.0(1) \times 10^{-5}$
Young Stellar Object						
ACC	0.064(7)	0.092(7)	0.067(4)	0.077(4)	0.066(3)	0.072(3)
L1N	0.254(6)	0.274(5)	0.207(9)	0.220(8)	0.200(7)	0.208(7)
L2N	$4.3(4) \times 10^{-8}$	$2.9(3) \times 10^{-8}$	$2.5(2) \times 10^{-8}$	$2.2(2) \times 10^{-8}$	$2.2(2) \times 10^{-8}$	$2.0(2) \times 10^{-8}$
IBC	$3.5(2) \times 10^{-5}$	$2.5(2) \times 10^{-5}$	$2.2(2) \times 10^{-5}$	$2.0(1) \times 10^{-5}$	$2.0(1) \times 10^{-5}$	$1.8(1) \times 10^{-5}$
Stellar Photosphere						
ACC	0.083(6)	0.068(5)	0.074(4)	0.068(4)	0.070(3)	0.066(3)
L1N	0.24(1)	0.19(1)	0.208(8)	0.187(8)	0.201(7)	0.187(7)
L2N	$2.5(3) \times 10^{-8}$	$1.9(3) \times 10^{-8}$	$2.0(2) \times 10^{-8}$	$1.8(2) \times 10^{-8}$	$2.0(2) \times 10^{-8}$	$1.8(1) \times 10^{-8}$
IBC	$2.2(2) \times 10^{-5}$	$1.7(2) \times 10^{-5}$	$1.8(1) \times 10^{-5}$	$1.6(1) \times 10^{-5}$	$1.8(1) \times 10^{-5}$	$1.6(1) \times 10^{-5}$

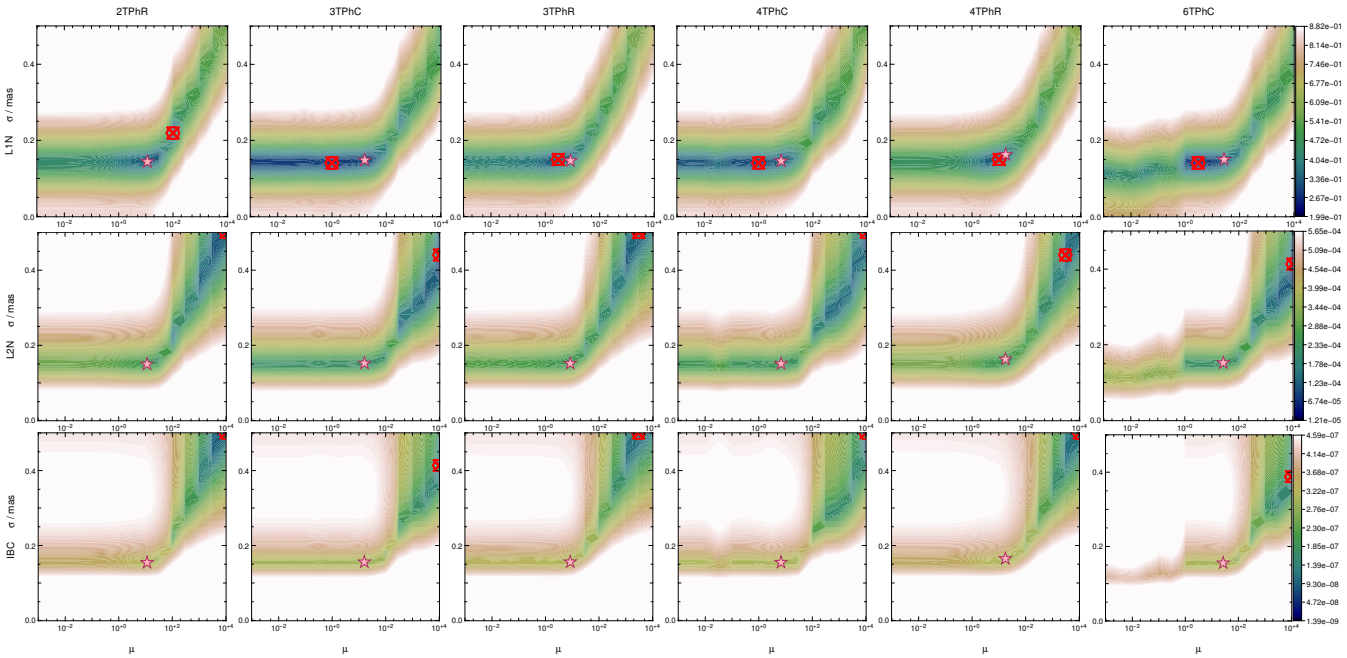

Figure 4. Scores of the metrics L1N (*top row*), L2N (*central row*) and IBC (*bottom row*) as function of the standard deviation σ of the PSF and the level of regularisation μ. The object is the stellar cluster of Fig. 1. From left to right, the panels are organized as follows: 2TPhR, 3TPhC, 3TPhR, 4TPhC, 4TPhR, and 6TPhC. The red crossed circles correspond to global minima, while the pink stars are positioned at the human determined value of μ and the value of σ that minimizes the merit function.

In this regard, L1N is clearly the best of all studied metrics, as it is the only one where both beacons lie close together for the typology of objects and most of the configurations.

This is not as well verified as with the other metrics, being IBC the less robust of the tested merit functions. In the case of the stellar photosphere (Fig. 6), all metrics behave similarly.

Since we are truncating the intervals of σ and μ, those distances most probably would increase in the cases where the global minima lie at extreme points of the plots.

These results open the possibility of automatic image

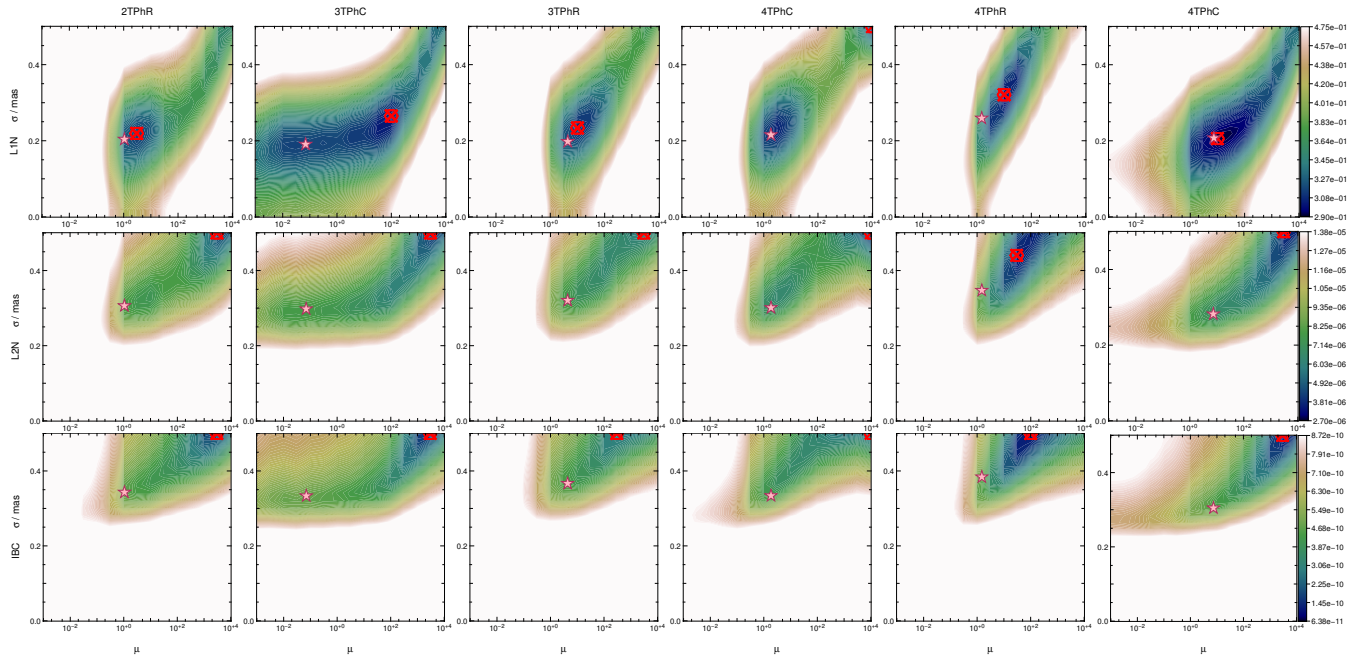

Figure 5. Same as in Fig. 4, but for the young stellar cluster.

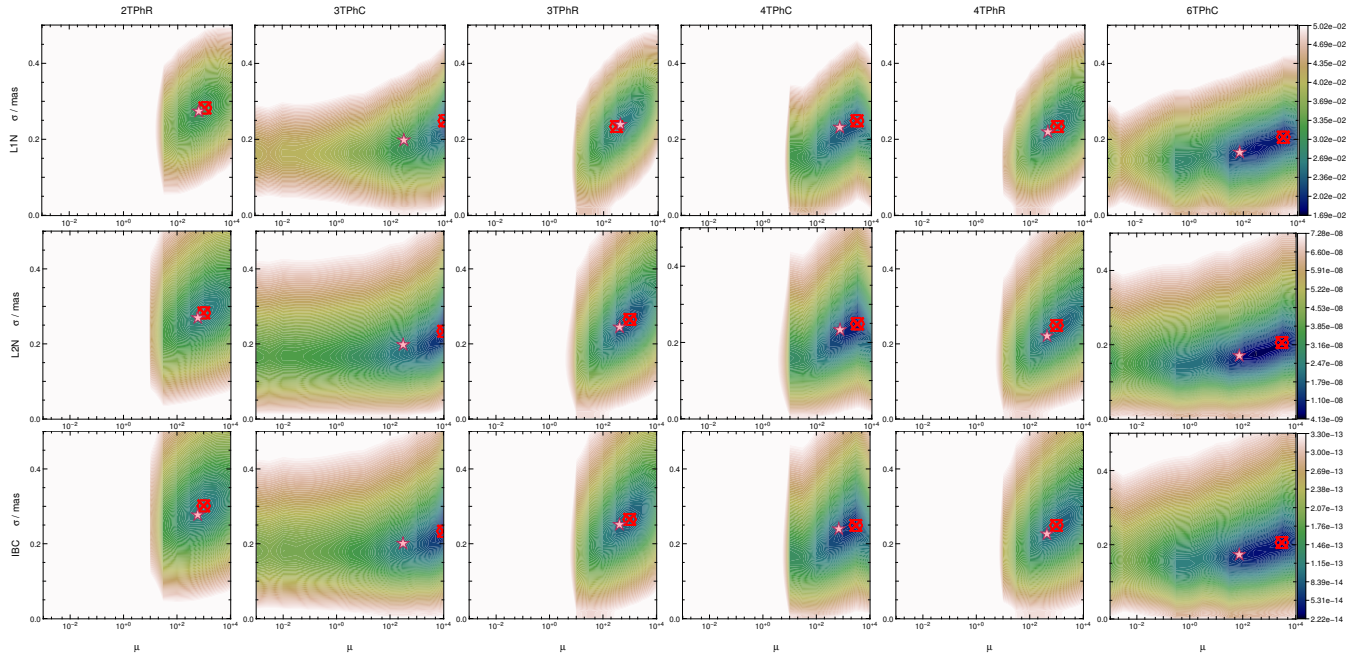

Figure 6. Same as in Fig. 4, but for the stellar photosphere.

quality assessment thus removing human intervention in the process.

5 CONCLUSIONS AND FUTURE DEVELOPMENTS

This article addresses the question: what is the best metric to assess the quality of a reconstructed image?

Several merit functions are considered in the realistic context of the Very Large Telescope Interferometer and using the MiRA image reconstruction software.

A semi-automatic pipeline is developed to reconstruct images, with the only human intervention being the determination of the final value of the hyper-parameter μ. It is found that the image reconstruction process outputs images with an effective angular resolution, characterized by a Gaussian σ, with a value significantly smaller than an equivalent Rayleigh-like criterion, based on the maximum baseline.

Convolution by an effective point spread function is mandatory for proper image quality assessment.

Of all the merit functions considered, the ℓ_1-norm is the most robust. The commonly used Interferometric Imaging Beauty Contest quadratic metric is biased, considering as best images those with higher smoothing (or hyperparameter μ), and not fully exploiting the effective angular resolution of the data and image reconstruction process.

By minimizing the ℓ_1-norm over the μ and σ parameter space, it is possible to implement automated image quality assessment.

Based on the this work, several developments are foreseen, the most obvious of which being algorithm comparison with the ℓ_1-norm and proper convolution. The most ambitious is automated image reconstruction. To achieve this goal, two aspects must be addressed: (*i*) the determination of an initial image for the reconstruction algorithm (for phase closure only), and (*ii*) the determination of the final μ in the reconstruction. The second aspect is clearly the most difficult. It opens the requirements for image reconstruction algorithms to output tables of images for different levels of regularisation, allowing the end-user to determine the final values of μ.

An important aspect is to identify the situations where phase referencing or phase closure are the best options for imaging. This choice is now possible with the *GRAVITY* and *PIONIER* instruments. Its study requires the inclusion of other ingredients not addressed in the present article, such as (*i*) compatible *uv*-coverages, (*ii*) noise models taking into account photon and detector statistics (e.g., Tatulli & Chelli 2005) or light splitting between telescopes (e.g., Gordon & Buscher 2012), and (*iii*) a span of signal-to-noise ratios.

ACKNOWLEDGEMENTS

The research leading to these results has received funding from the European Community's Seventh Framework Programme, under Grant Agreements 226604 and 312430 (OPTICON), as well as from Fundação para a Ciência e Tecnologia grants SRFH/BD/44282/2008, PTDC/CTEAST/116561/2010 and COMPETE FCOMP-01-0124-FEDER-019965. This research has made use of the Jean-Marie Mariotti Center Aspro service [12]. All the analysis was done with YORICK, a free interactive data processing language written by David Munro[13].

The authors would like to thank Paulo Andrade, Narsireddy Anugu, Joana Ascenso, Paul Berlioz-Arthaud, Maud Langlois, Jonathan Léger, Magali Loupias, Matthew Ozon, Eliana Pinho, Manuel Silva, Michel Tallon, Isabelle Tallon-Bosc, and Nicolas Verrier, for their valuable contribution in the poll aiming at determining the best levels of regularisation for image reconstruction.

References

Arsenault, R., Alonso, J., Bonnet, H., et al. 2003, SPIE PROC SER, 4839, 174
Baldwin, J. E., Beckett, M. G., Boysen, R. C., et al. 1996, A&A, 306, L13
Baldwin, J. E., Christopher A. H. 2002, Philosophical transactions, 360.1794, 969–86
Baron, F., Cotton, W. D., Lawson, P. R. et al. 2012, SPIE PROC SER, 8445, 84451E
Baron, F., Monnier, J. D., Kiss, L. L., et al. 2014, ApJ, 785, 46
Benisty, M., Renard, S., Natta, A. et al. 2011, A&A, 531
Benson, J. A., Hutter, D. J., Elias, N. M. et al. 1997, AJ, 114
Berger, J.-P., Zins, G., Lazareff, B., et al. 2010, SPIE PROC SER, 7734, 773435
Berger, J.-P., Malbet, F., Baron, F., et al. 2012, A&ARv, 20(1), 53
Buscher, D. F. 2015, Practical Optical Interferometry, b, Cambridge, UK: Cambridge University Press
Charbonnier, P., Blanc-Féraud, L., Aubert, G., & Barlaud, M., 1997, IEEE Trans. Im. Proc. 6, 298
Che, X., Monnier, J. D., Zhao., M., et al. 2011, ApJ, 732
Coudé du Foresto, V., Ridgway, S., & Mariotti, J.-M. 1997, A&A, 121, 379
Cotton, W., Monnier, J. D., Baron, F., et al. 2008, SPIE PROC SER 7013, 70131N
den Dekker, A. J., & van den Bos, A. 1997, JOSA A, 14, 547
Delplancke, F. 2008, NewAR, 52, 199
Eisenhauer, F., Perrin, G. Brandner, W., et al. 2008, SPIE PROC SER 7013, 70132A
Eisenhauer, F., Perrin, G., Brandner, W., et al. 2011, The Messenger, 143, 16
Filho, M. E., Garcia, P., Duvert, G., et al. 2008, SPIE PROC SER, 7013, 70131F
Filho, M. E., Renard, S., Garcia, P., et al. 2008, SPIE PROC SER, 7013, 70133Z
Glindemann, A. 2011, Principles of Stellar Interferometry, Springer Berlin Heidelberg
Gomes, N. 2016, Imaging with the VLTI, PhD Thesis
Goodman, J. W. 1985, Statistical Optics. Methods, New York: John Wiley and Sons
Gordon, J. A., & Buscher, D. F. 2012, A&A, 541, A46
Hanniff, C. A. 2007, NewARv, 51
Hillen, M., Kluska, J., Le Bouquin, J.-B. 2016, A&A, 588
Jennison, R. C. 1958, MNRAS, 118, 256
Kluska, J. Malbet, F., Berger, J.-P., et al. 2014, A&A, 564
Kloppenborg, B. K., Stencel, R. E., Monnier, J. D., et al. 2015, ApJS, 220, 14
Kraus, S. Buscher, D. F., Monnier, J. D., et al. 2014, EPSC, 2014-765
Lawson, P. R., Cotton, W. D., Hummel, C. A., et al. 2004, SPIE PROC SER 5491, 886
Lawson, P. R., Cotton, W. D. Hummel, C. A., et al. 2006, SPIE PROC SER 6268, 62681U
Le Bouquin, J.-B., Lacour, S., Renard, S., et al. 2009, A&A, 496
Le Bouquin, J.-B., Berger, J.-P., Lazareff, B., et al. 2011, A&A, 535, A67
Malbet, F., Kern, P. Y., Berger, J.-P., 2006, SPIE PROC SER 62680Y
Malbet, F. Cotton, W. Duvert, G., et al. 2010, SPIE PROC SER 7734, 77342N
Millour, F., Meilland, A., Chesneau, O., et al. 2011, A&A,

[12] Available at http://www.jmmc.fr/aspro
[13] Available at http://yorick.sourceforge.net/

526
Monnier, J. D. 2007, NEW ASTRON REV, 604–616
Monnier, J. D., Pedretti, E., Thureau, N. D., et al. 2012, SPIE PROC SER 8445, 84450Y
Monnier, J. D., Berger, J.-P., Le Bouquin, J.-B., et al. 2014, SPIE PROC SER 9146, 91461Q
Monnier, J. D., Kraus, S., Buscher, D., et al. 2014, SPIE PROC SER 9146, 914610
Mourard, D., Monnier, J. D., Meilland, A., et al. 2015, A&A, 577
Pauls, T. A., Young, J. S., Cotton, W. D., et al. 2005
Pence, W. D., Chiappetti, L., Page, C. G., et al. 2010, A&A, 524
Petrov, R. G., Malbet, F., Weigelt, G., et al. 2007, A&A, 464, 1
Pety, J., Gueth, F., Guilloteau, S. 2001a, Tech. rep., 16
Pety, J., Gueth, F., Guilloteau, S. 2001b, ALMA Memo 398
Powell, M. J. D. 2006, Large-Scale Nonlinear Optimization, 255–297
Renard, S., Thiébaut, É., Malbet, F. 2011, A&A, 533
Rudin, L. I., Osher, S., Fatemi, E. 1992, PhysD, 60(1-4), 259–268
Schutz, A., Vannier, M., Mary, D., et al. 2014, A&A, 565
Schöller, M. 2007, NewAR, 51, 628
Strong, D., Chan, T. 2003, Inverse Problems, 19(6), S165–S187
Tatulli, É., & Chelli, A. 2005, J OPT SOC AM A, 22(8), 1589
Tatulli, É., Blind, N., Berger, J. P., et al. 2010, A&A, 524, A65
ten Brummelaar, T. A., McAlister, H. A., Ridgway, S. T., et al. 2005, ApJ, 628, 453
Thiébaut, É. 2008, SPIE PROC SER, 7013(3), 70131I–70131I–12
Thiébaut, É. 2013, EAS PUBLICATIONS, 59, 157–187
Thompson, A. R., Moran, J. M., Swenson, G. W. 1986, Wiley
Vincent, F. H., Paumard, T., Perrin, G., et al. 2011, MNRAS, 412
Wang, Z., Bovik, A. C. 2002, IEEE SIGNAL PROC LET, 9(3), 81–84
Wang, Z., Bovik, A. C., Sheikh, H. R., et al. 2004, IEEE T IMAGE PROCESS, 13(4), 600-612

This paper has been typeset from a TEX/ LATEX file prepared by the author.

Appendix B

Number of linearly independent triangles in an array of telescopes

"I ran into Isosceles. He had a great idea for a new triangle!"

— WOODY ALLEN

IN THIS APPENDIX, it is established by means of mathematical induction that, in an array of n telescopes, no more than $(n-1)(n-2)/2$ *linear independent triangles* can be set up with the apertures. One should remind that with n dots, $\binom{n}{3} = \frac{n(n-1)(n-2)}{6}$ triangles can be drawn. What is claimed is that not all of these triangles are linearly independent and, thus, some of them can be built from the others.

Theorem 1. *The number of independent triangles formed by an array of n telescopes is equal to*

$$P(n) = \binom{n-1}{2} = \frac{(n-1)(n-2)}{2},$$

with $n \in \mathbb{N}_3$.[1]

One can look at the problem by thinking that after fixing one telescope, there are $\binom{n-1}{2}$ ways of combining the remaining $n-1$ telescopes in pairs, in order to build a triangle with the fixed one. This idea is used in the following proof.

Proof. (mathematical induction for all natural numbers greater than 2)

Base case

For $n = 3$, on the one hand, only one (independent) triangle can be drawn with the telescopes and, on the other hand, $P(3) = \frac{(3-1)(3-2)}{2} = 1$. Therefore, the condition is satisfied.

Inductive step

Inductive hypothesis: assuming that the condition is valid for k telescopes, *i.e.*, $P(k) = \binom{k-1}{2} = \frac{(k-1)(k-2)}{2}$, for $k \in \ltimes_3$...

[1] $\mathbb{N}_3 = 3,4,5,6,...$, *i.e.*, the set of all integers starting from 3.

Thesis: than, for $(k+1)$ telescopes, $P(k+1) = \frac{k(k-1)}{2}$ should hold as well.

Lets suppose there are k telescopes in the array. Fixing one telescope, there are $\binom{k-1}{2} = \frac{(k-1)(k-2)}{2}$ linear independent ways of combining the remaining $(k-1)$ telescopes 2-by-2 with the fixed one. Adding one more telescope and keeping this and the previous one fixed, these two telescopes can be combined with the other $(k-1)$ telescopes in $(k-1)$ ways to build linear independent triangles.

Now, by hypothesis, from the $(k-1)$ telescopes $P(k) = \binom{k-1}{2}$ linear independent triangles can be set up and, thus, the total number of linear independent triangles that can be built from the $(k+1)$ telescopes is

$$(k-1) + \frac{(k-1)(k-2)}{2} = \frac{k(k-1)}{2}. \qquad \square$$

Appendix C

Beam Combiner Phase-Shifts

"No one has ever been able to define the difference between interference and diffraction satisfactorily. It is just a question of usage, and there is no specific, important physical difference between them."

— RICHARD FEYNMAN, *The Feynman Lectures on Physics*

THIS APPENDIX pertains to the proof that the phase difference between the two beams propagated inside the FSU and emerging from the BC is π. This, combined with the K-prism, which introduces an additional $\pi/2$ phase, eventually translates itself into a phase difference of $\pi/2$ between each of the four beams striking the PICNIC detector of the FSU.

Beams I (B_I) and II (B_{II}), respectively coming from telescopes I and II, are directed to the BC, where they interfere coherently (*cf.* fig. C.1). Before combination, B_I experiences a $\pi/2$ retardation between *p*- and *s*- polarisation components, by traversing a phase shifter. After interference in the BC and reflection on the fixed mirrors M4, both beams emerge parallel and propagate in direction to the PBSs, which separate the combined beams into a total of four beams de-phased by $\pi/2$.[1]

Assuming that, for a wavefront reflected in the BC, the relative amplitude is r with phase shift δ_r and, similarly, for a transmitted wavefront, the relative amplitude is t with phase shift δ_t. It is also considered, without loss of generality, that both incoming beams have amplitude $A_0 = 1$ and that a phase shift of ϕ is introduced into B_I prior to beam combination.

Upon arriving to the BC, each incident beam is divided into a transmitted and a reflected complex amplitude, and a part is also absorbed by the splitter plate. These amplitudes are denoted respectively by $re^{i\delta_r}$, $te^{i\delta_t}$ and a. The corresponding relative intensities, *transmittance*, *reflectance* and *absorptance*, are denoted by $T = |t|^2$, $R = |r|^2$ and $A_a = |a|^2$.[2]

Adding the transmitted component from B_I and the reflected part of B_{II}, A_1 can be written as:

$$A_1 = te^{i(\delta_t+\phi)} + re^{i\delta_r}. \tag{C.1}$$

[1] For more details, *cf.* **Sahlmann2009a**

[2] It is adopted, in this section, a similar notation to Traub, 2000.

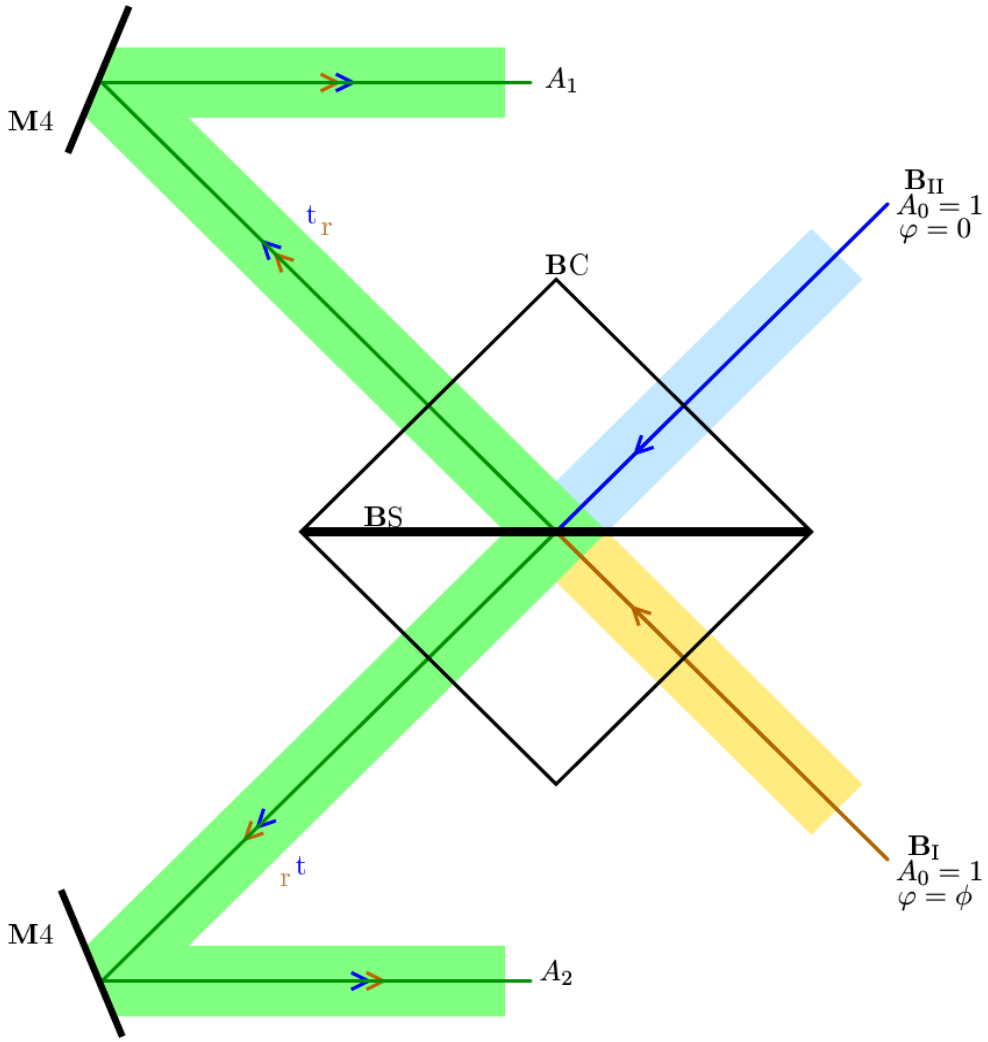

Figure C.1: Schematics of the FSU BC. Beams I and II, having hypothetical amplitudes $A_0 = 1$, are superimposed in the splitter plate (BS). Beam I has previously passed through an achromatic p-s-retarder and, therefore, its p- and s- polarisations are shifted by $\pi/2$ in phase. After being reflected in mirrors M4, both beams emerge parallel, with amplitudes A_1 and A_2. They eventually meet polarisation beam splitters, which divide the combined beams into four new beams de-phased by $\pi/2$.

Similarly, for A_2:

$$A_2 = re^{i(\delta_r+\phi)} + te^{i\delta_t}. \tag{C.2}$$

The intensities of the emerging beams are given by:

$$I_1 = A_1 A_1^* \tag{C.3a}$$

$$= T + R + 2\sqrt{TR}\cos(\delta_t - \delta_r + \phi) \tag{C.3b}$$

and

$$I_2 = A_2 A_2^* \tag{C.4a}$$

$$= T + R + 2\sqrt{TR}\cos(\delta_r - \delta_t + \phi). \tag{C.4b}$$

It is known that if $T = R$, the phase difference between the reflected and transmitted parts of a beam striking a splitter is $\pi/2$ (*cf. e.g.*, Traub, 2000), *i.e.*, $|\delta_t - \delta_r| = \pi/2$. Assuming, without loss of generality, that $\delta_r - \delta_t = \pi/2$, from eqs. (C.3) and (C.4) it is straightforward to conclude that the phase difference $\Delta\delta$ between the emerging beams 2 and 1 is equal to π.

Appendix D

FSU FTK engineering manual

"Any product that needs a manual to work is broken."

— ELON MUSK

Contents

THIS APPENDIX presents the *FSU fringe tracker engineering manual* written by Nuno Gomes and Christian Schmid during PRIMA's commissioning runs that were carried out between June 2009 and August 2011. The document started as a compilation of simple notes taken by Gomes during his first participation in PRIMA commissionings, and quickly evolved to an illustrated document, with several sections describing the calibration and operation of the FSUs. The manual was often requested by the VLTI team and used during PRIMA operations. Several versions were created during the aforementioned time span. The following sections correspond to a transcription of the last update of the document (version 3.0.2, dated 2012/02/10), adapted to the format of this thesis.

Abstract

This "document" (appendix) presents the steps needed to operate the PRIMA FSUs, both in single-feed and dual-feed modes. It starts with a checklist, helpful to the user who already has some experience with the FSU but needs a guideline for the operations, and goes through sections which detail the set-up of the workspace, as well as the operations in the laboratory and on sky. The lab operation section describes the FSU health check (cold camera check and warm fibre co-alignment) and the calibration (FSU-response). The section about the night operation covers the flux optimisation, the sky calibration (VLTI-response) and details how to find and track fringes.

In the appendices we present information that can be useful during PRIMA operations, namely a troubleshooting section, a reference table of panels and a table with the correct (D)OPDC settings for fringe tracking.

Task	Section	Page
☐ Start-up of VLTI		
☐ Setting up ISS		
☐ Target's preset		
☐ Optimise the star light beam		
☐ Start lab guiding with IRIS		
☐ **Set-up the workspace**	D.3	
☐ **Check names of working areas**		266
☐ **Open fundamental panels for operation**		266–268
☐ **Prepare PRIMET (if needed)**		269
☐ **Activate PRIMET interlock (if needed)**		271
☐ **Optimise the Flux in the FSU**	D.3.7	273
☐ **Perform a sky calibration (*flats* and *darks*)**	D.5.3	280
☐ **Find the fringes**	D.5.4	281
☐ **Record the VLTI response**	D.3.2; D.5.4	268; 283
☐ **Track the fringes**	D.5.5	284

Checklist

In order to operate PRIMA, you need to follow the black steps (steps 6–11). **Grey steps** refer to all the subsystems that need to be online for PRIMA operations and, therefore, are not covered in this manual.

Introduction

In the context of interferometry, the purpose of **F**ringe **T**rac**K**ing (FTK) is to find and track fringes. This technique is the equivalent to the adaptive optics systems used in conventional single telescope observations, to reduce the blur created by the atmosphere.

The FSU is the heart of PRIMA, providing fringe sensing and tracking both on- and off-axis. PRIMA has two twins FSU, *FSUA* and *FSUB*, that can be used simultaneously in the *astrometric* mode. If PRIMA is operated in its V^2 *science* mode, one FSU (typically FSUB) is combined with AMBER or MIDI instruments and used as an off-axis fringe tracker.[1]

This document concerns only about the FTK process and all the set-up needed. Therefore, no other instruments besides PRIMA are focused.

It starts with a checklist of all the major steps (start-up, optimisation and sky operations), useful for the user who already operated the FSU but needs to revive the general procedures. A list of preliminary steps are listed in grey colour, indicating that although it does not correspond to operations with the FSU (these steps are not, therefore, covered in this manual), it is necessary to be checked for the proper functioning of PRIMA.

The document then comprises three essential chapters (D.3, D.4 and D.5), which cover the preparation of the systems before going to action, the operation of the FSU in the laboratory (cold camera check, co-alignment check of the warm fibres[2] and calibration) and operation on sky (flux optimisation, sky calibration and find and track fringes).

We also included small appendices at the end with information that, although not essential, can be helpful during PRIMA operations. appendix D.6 compiles a series of solutions to potential problems that can arise during FSU operations. appendix D.7 presents a reference table with the most common panels available to the user. appendix D.8 is probably the most useful of them all. It gives the correct (D)OPDC settings for FTK with PRIMA. appendix D.9 gives a short description of the thresholds necessary for FTK. appendix D.10 explains how to configure ISS for operations in the laboratory. appendix D.11 describes how to stop the metrology. Finally, appendix D.12 briefly explains how to load an OB stored in P2PP.

The first version of this tutorial was born during commissioning runs 5 and 8 of PRIMA, at Paranal, while the calibration procedures or the *preset*[3] of objects where taking place. Version 2 appeared after commissioning runs 11 and 12, when the STS became available, together with the respective changes in the panels. Subsequent versions have been written/updated during or after commissioning runs and this is supposed to be an ongoing updated document, to include other modes of operation and future changes in the panels. Current version reflects the state of PRIMA and its subsystems as of commissioning run number 16 (astrometric commissioning run number 3, August/September 2011).

[1] The combined mode with AMBER is on hold, for the moment. Changes both in the warm optics and in the templates are needed in order to combine the two interferometers for phase referencing.

[2] The *cold camera check* and the *co-alignment check of the warm fibres* correspond to the **health check**.

[3] This is the ESO's expression for "pointing the telescope".

Since this is an engineering manual, aimed for lower level operations, a mixture of high and low level panels is presented for the moment. As PRIMA approaches the end of its commissioning runs and becomes available to the community, another document describing only the high level panels will be available to the public. By then, it is hopped that the setting up of the panels will be handled by scripts and the OPDC operation will be automatic. In a near future, this document is intended to make part of a larger collection of user manuals of the VLTI instruments, available at the ESO Intranet.

Please remember this is still a draft document, written during commissioning operations, that probably is going to suffer changes both in form and content in the future. In case you have comments, suggestions or updates (which are all very welcome), please contact the authors (`ngomes@eso.org` and `cschmid@eso.org`).

Modus Operandi

During 2010 commissioning runs, a concept for the operation of the FSU with regard to the fringe search has been proven to be successful. It consists of a fast OPL scan (across the fringe) using the tracking (D)DL. While the scan is performed, a file is recorded and the resulting data is subsequently analysed by a MATLAB® script. This method has two main advantages: firstly, it allows to find the fringes in a comparably low amount of time (scan of 1 cm takes about 1 minute) even if there is no OPD model or it is insufficient; secondly, it allows to get a good starting set of SNR thresholds for fringe tracking. After all, scanning many times across the fringe allows one to take interesting data even in conditions in which fringe tracking is very difficult or impossible.

In order to simplify the fringe scanning method for the operator, two algorithms were implemented in the OPDC as well as the DOPDC, which are described in the following.

The OPDC and DOPDC auxiliary algorithms

The algorithms are called SimpleScan and FringeScan. SimpleScan applies a triangular sawtooth trajectory to the (D)DL with period *Scan period* and amplitude *Scan amplitude*, starting at *ZPDoffset* (see fig. D.1). FringeScan applies the same kind of triangular sawtooth trajectory. However, it does not start at *ZPDoffset*, but it starts at the position where it detects the fringe according to the specified SNR detection level. Before the detection, it will apply the normal *ZPD search* trapezium like trajectory.

Finding the Fringe:

SimpleScan is also employed to find the fringe by one single scan across a specified range of the (D)DL. To this end, the first rising edge of the sawtooth is used. In parallel, a file is recorded (see fig. D.2). Post processing of this file by the MATLAB® script *evalFringeScan.m*[4] yields the

[4] All *.m* scripts mentioned in this tutorial are written in MATLAB® (this information will be omitted from here on).

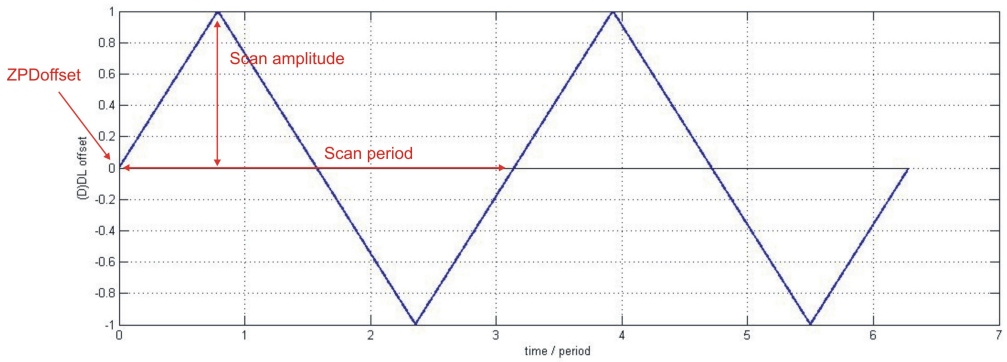

Figure D.1: The search pattern of the auxiliary algorithms. The *ZPDoffset* is the offset with respect to the zero position. When the fringe is found, it corresponds to the value in the $y-$axis of the search panel. In the presence of a good OPD model, the *ZPD offset* is small.

fringe position that can be entered in the OPDC GUI as *ZPDoffset*. The evaluation of the file yields also a first starting set of SNR thresholds. The parameters for the scan can be retrieved from the script *scanparameter.m*.

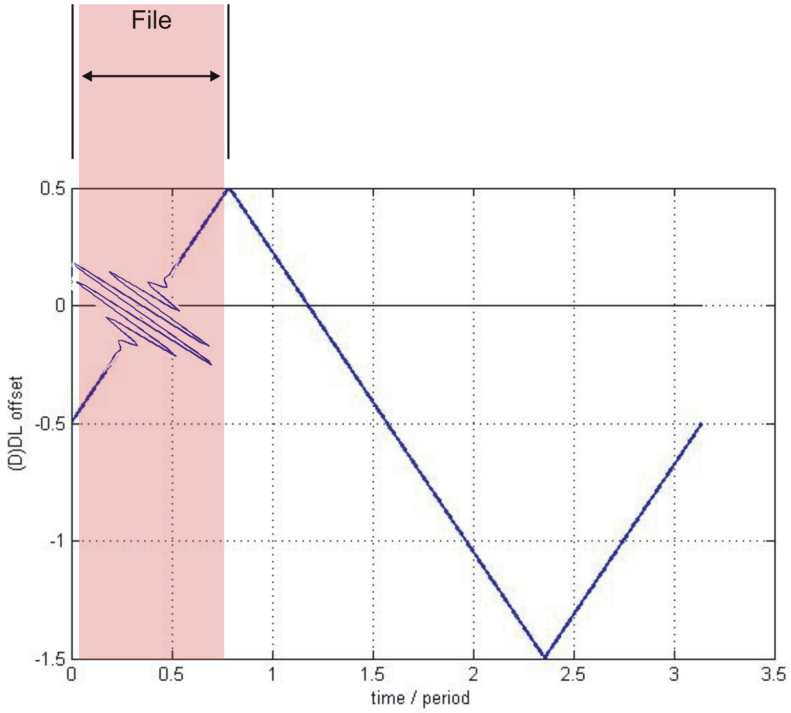

Figure D.2: The first rising edge of the SimpleScan can be used for a single scan across the fringe.

Note:

Actually, the scan can start with a *rising* edge but also with a *falling* edge, depending on the (D)DL sign. However, this will be taken into account if the scan parameters are determined with the script *scanparameter.m*.

Preparation and General Steps

Most of the panels used during the operation of the system are the same for night operation on sky and day operation in the lab. Hence, this section applies equally well to both activities and describes the necessary steps to open all panels and bring the system online. Further, it details steps that are common to day and night operations.

- Login to a terminal as *prima* and enter the usual password.

You will find that the working area is divided in six desktops: **PACMAN**, **FSU-A**, **FSU-B**, **Metrology**, **Logs** (or **DOPDC**) and **Engineering** (or **MATLAB**)[5]. As the number of GUI involved in the operation is large, keeping a tidy and well organized workspace is of major importance. Therefore, we recommend to open each panel in the corresponding desktop. Moreover, the usage of a terminal with two screens is highly recommended. For night operation the usage of two terminals is even preferable.

Preparing the FSUs

All actions and panels are symmetric for both FSU.

- Click on the **FSU-A** desktop.
  - Mouse **middle** click on an open area of the desktop[6] and select FSUA Control. If needed, you can also open the panels FSUA ACU Tip/Tilt[7] and FSUA Motors[8].

[5] You can change the name of any workspace for a more convenient one, if you prefer, although it is advisable to keep these names.

[6] In case the mouse middle click is not available, start the panels from `Xterm` (see appendix D.7, page 288, for a reference table of panels).

[7] The FSUA ACU Tip/Tilt panel is no longer needed for normal operations.

[8] This panel allows one to move the LMOT and set it manually on the fringe. Normally, this procedure is not necessary. Open the panel only if you think you are really going to need it.

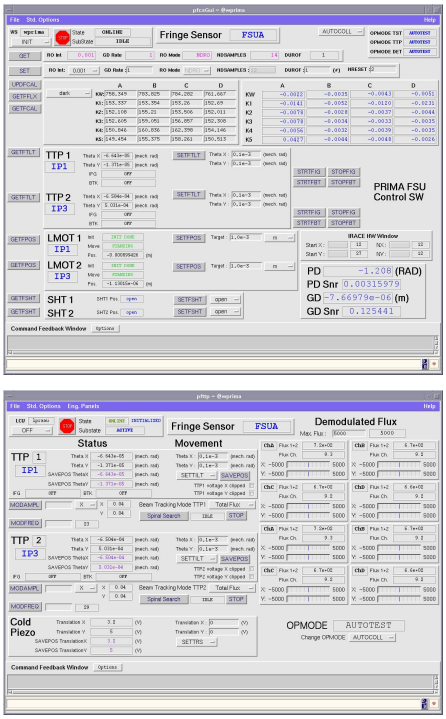

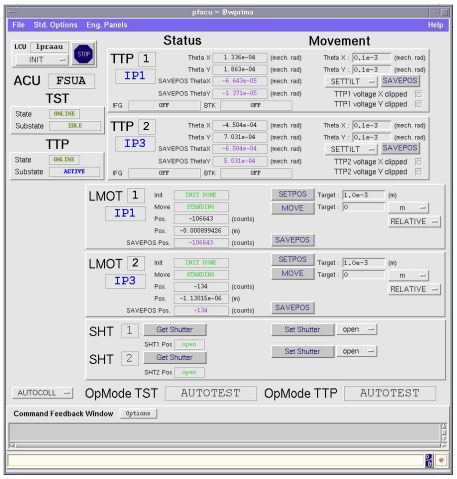

- Click on the **FSU-B** desktop.
  - Mouse **middle** click and open FSUB Control. If needed, open also FSUB ACU Tip/Tilt and FSUB Motors[9].
- In FSU*x* Control, select in the drop-down menu the desired mode for both FSUs: SCIENTIFIC, AUTOTEST or AUTOCOLL. AUTOTEST shall be used during the day or for calibration purposes; SCIENTIFIC, for night operations; AUTOCOLL can be used to debug problems, but it is not available yet.
- Bring the FSUs online.
  - Mouse **middle** click the desktop and select OSF Starter.
  - Enter your name.
  - Open the file *priosfFSUAStart.osf* and run it (i.e., press Start).
  - Open the file *priosfFSUBStart.osf* and run it.

FSUAStart asks whether *PMTEMP* should be brought on-line, activating the *autrep* logging of the FSU temperature sensors. There have been some problems with the F200 temperature measurement device in the past. In case of new occurrence, this device needs to be reset or power-cycled. If it is not possible to fulfil this procedure, the Bring PMTEMP online step shall be skipped during the startup.

[9] If you have two computers available for operation, it is advisable to open FSU*x* Control and FSU*x* ACU Tip/Tilt on separate machines (each panel on the left screen of each computer).

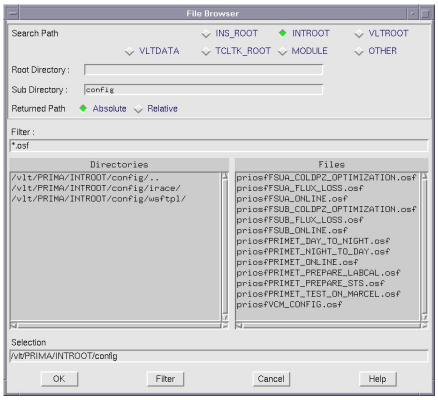

In case of **FSU online osf-scripts failure**, see appendix D.6 (Troubleshooting, appendix D.6.1, page 286).

Preparing for file recording

- Click on the **PACMAN** desktop.
  - Mouse left click and select PACMAN > Bob.

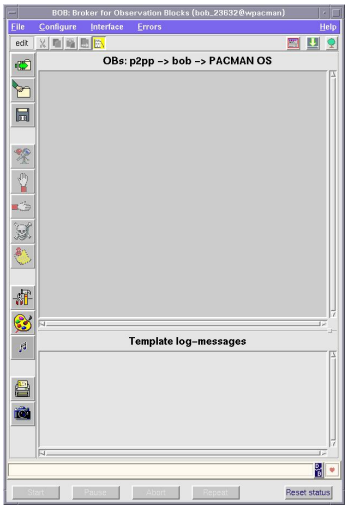

  - Select Engineering on the Interface menu.
  - Open and edit the template that is going to be used before running it.

Preparing the Scope

- On the right monitor, mouse middle click and select RTD Scope.

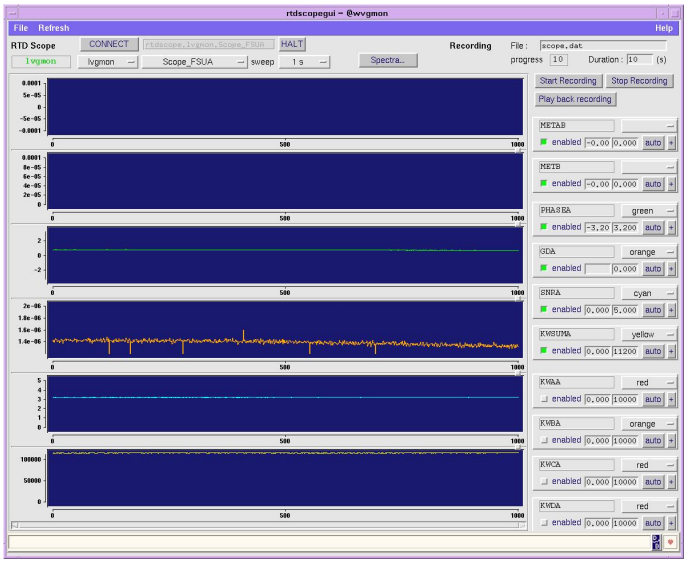

- Check that the scope is correctly connected. If not, select a probe block and press CONNECT.
- Select the proper Scope_*xxxx* from the drop-down menu, depending on what is going to be done.

In case of **problems with the RTD Scope**, see appendix D.6 (Troubleshooting, appendix D.6.2, page 286).

Preparing PRIMET

The **PRI**MA **MET**rology (PRIMET) system is required for the lab calibration (FSU-response), sky calibration (VLTI-response) and astrometric observations.

- Click on the **Metrology** desktop.
- Mouse **middle** click and open Laser Stab. System and Metrology Phase Meter.

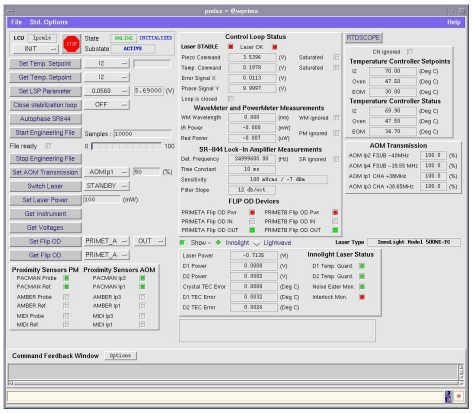

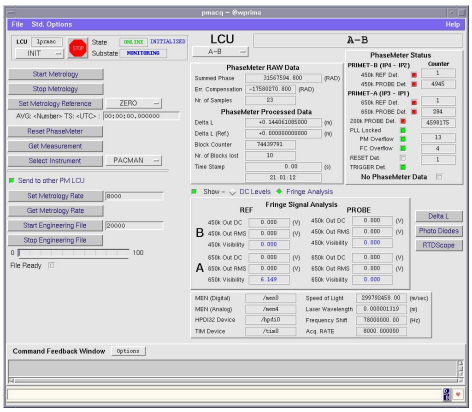

- Check the interlock status in the Laser Stab. System panel: Interlock Mon. should be **green**.
- If the interlock is not activated, switch it on (see appendix D.3.6, page 271).
- Bring PRIMET online: mouse middle click the desktop and select OSF Starter.
  - Enter your name.

– Open the proper ***.osf** script (to be specified)[10] and run it by pressing Start .

If the **PRIMET osf-scripts fail**, see appendix D.6 (Troubleshooting, appendix D.6.3, page 287).

Miscellaneous

MATLAB and data evaluation

MATLAB® is installed on PACMAN and the packages written in this language have been proven very useful for on-the-fly data evaluation. A package of useful functions (starting with `xp···.m`) is installed which allows the processing of the FSU FITS files. Each MATLAB® function is briefly described in its own header.

- Click on the **Engineering/MATLAB** desktop.
  - Mouse right click on `Xterm` and log on PACMAN.

```
wprima prima:~ > ssh -X pacman@wpacman
```

  - Open MATLAB®.

```
wpacman pacman:~ > matlab &
```

Writing logs

It is very important to document the work that is done. To this end, it has become common practice to write log-files directly on the **PRICS twiki page**.

- Click on the **Logs/DOPDC** desktop.
  - Mouse right click on `Xterm` and log on Odyssey3.

```
wprima prima:~ > ssh -X vltitec@odyssey3
```

  - Open `Mozilla` web browser and go to the twiki page.

```
odyssey3 vltitec:~ > mozilla &
```

`https://websqa.hq.eso.org/sdd/bin/view/PRICS/PRICSDailyLogs`

Copying data

Data taken with the templates can be found on PACMAN in the folder `/rmnrec`. It should be copied to Odyssey3 in order to be stored and to make it accessible from Garching.

- Mouse right click `Xterm` and log on Odyssey3.

```
wprima prima:~ > ssh -X vltitec@odyssey3
```

  - Go to `/home/vltitec/VLTITec/PRIMA/`.

[10] E.g., priosfPRIMET_PREPARE_LABCAL.osf for lab calibration.

  - Go to the directory `COMM`*nn*. If it does not exist yet, create it.
  - Go to the directory `yyyymmdd`. If it does not exist yet, create one for the date on which the files were taken.

    ```
    odyssey3 vltitec:~ > cd /home/vltitec/VLTITec/PRIMA/
    COMMnn/yyyymmdd/
    ```

  - Finally, entering `pwd` should yield `/home/vltitec/VLTITec/PRIMA/COMMnn/yyyymmdd`.

- Mouse right click on the desktop, select `Xterm` and log on PACMAN.

  ```
  wprima prima:~ > ssh -X pacman@wpacman
  ```

- Go to `/rmnrec`.

  ```
  wpacman pacman:~ > cd /rmnrec
  ```

  - Copy the files that have been taken to the aforementioned directory. This can be done, e.g., by

    ```
    wpacman pacman:~ > scp -p *nnn*.fits vltitec@odyssey3:
    /home/vltitec/VLTITec/PRIMA/COMMmm/yyyymmdd/
    ```

    The *nnn* stands for the running file number of the day;[11] the option `-p` preserves the file dates.

- Go to the `Xterm` on Odyssey3 and check that the files have been successfully copied.
- Go to the `Xterm` on **PACMAN** and keep the `/rmnrec` folder clean. If the files should not be deleted yet, copy them at least in a dedicated subdirectory (to be created, if necessary).

Activation of PRIMET Interlock

This description was taken from:
http://www.pl.eso.org/vlti/wiki/index.php/PRIMET_interlock.

- Go to the G2 pit (via the VLTI computer room).
  - Close the door behind you.
  - Check that nobody, or only authorized people wearing safety goggles, are inside the pit.
  - Push the ACK IL button on the control box (no sound or light will be emitted).
  - Then, push the Door Override button (again, no sound or light are emitted).
  - Go out and close the door behind you (you have 10 s to do it after pressing the Door override button).

[11] All the files are of the form `*nnn_nnnn.fits`, with `nnnn` being the running file number within a day.

- Go to the VLTI laboratory and repeat the same actions, using the control box which is located at the left of the door when entering the lab (to your right if you are facing the door from inside the lab).
- Go to the storage room.
  - Close the door.
  - On the control box near the interlock panel (see figure in next page), press Acknowledge IL: all the lights on the panel should go off and not be blinking.
    Note: IC104 corresponds to the storage room and IC108 corresponds to the emergency exit door of the VLTI laboratory (the main access of the VLTI lab is labelled *Antechamber*).

  - Press Laser IL System OFF button (the Laser Off lamp on the interlock panel should become green).
  - Press Laser IL System ON (the Laser On lamp on the interlock panel should become green). Actually, the laser will still be off, but the interlock is now activated.

– Press the Door Override button next to the door, go out from the storage room and close the door behind you. All the red lights above the doors of the protected rooms should be flashing.

Optimise flux in FSUs

Whenever we want to use the FSUs, we have to check that there is light reaching them and we have to optimise the corresponding fluxes. The optimisation of the flux is the same for FSUA and FSUB, as well as for day and night operation. The procedure has been reduced to a simple execution of a script.

- Go to the BOB panel (appendix D.3.2, page 268) and load the script PACMAN_gen_tec_getReady.
- Check that both FSUA and FSUB are set to **T**.[12]
- Run the script.

In case you need to perform the flux optimisation manually in any of the FSUs, perform the following steps.

- Go to the FSU*x* Control GUI (see appendix D.3.1, page 266) and make sure that OPMODE is selected to be AUTOTEST for day operation or SCIENTIFIC for night operation.

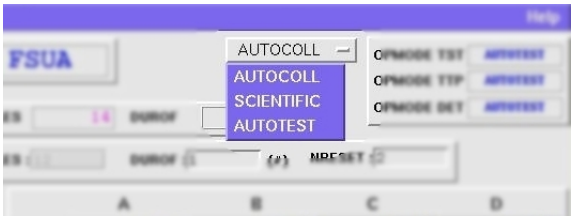

- Select the integration time RO Int you want (usually, 0.001 s) to use and press SET.

[12] In case you need to skip the test in any FSU, put it to **F**.

- On the RTD Scope (appendix D.3.3, page 268), select Scope_FLX*x* and make sure that at least KWSUMA is enabled.
- Go to the FSU*x* ACU Tip/Tilt GUI (see appendix D.3.1, page 266).
  - Check that Beam Tracking Mode TTP1 and Beam Tracking Mode TTP2 are set to **Total Flux**. If not, set them by selecting it from the drop-down menu.

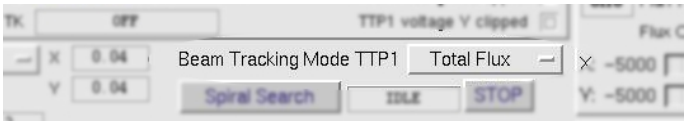

  - Go with TTP1 and TTP2 **ONPOS** and then **OFFPOS** (select these commands from the drop-down menu).
  - Start with the first beam and bring it **ONPOS**. The flux on the RTD Scope should increase. **If not**, see Appendix A (Troubleshooting) (appendix D.6.4, page 288).
  - Enable beam tracking (select **ENABTK**) and observe the flux, which should at least not decrease. In the ideal case, see it increasing and wait until the beam tracking has converged. Criterion for the convergence is that the second harmonic of the modulation frequency appears in the flux on the RTD Scope and that the **Demodulated Flux** values are becoming small (on Flux Ch. A, B, C, D, something like ~ 0.014). Another criterion is that the Theta X/Y values are not changing significantly any more. **Note:** The appearance of the second harmonic can usually not be seen on sky due to turbulence.
  - After convergence of beam tracking, disable it (select **DISBTK**), press SAVEPOS and go with the beam **ONPOS** and then **OFFPOS**.
  - Repeat the same procedure for the other beam.
  - Repeat the same procedure for the other FSU.
  - Do not forget to set all beams **ONPOS** at the end!
- If the procedure was successful, KWSUM should be between 80 000 and 100 000 ADUs for both beams on position (ONPOS), when using MARCEL. On sky, the number of ADU depends naturally on the K magnitude of the star. In this case, a good check is that at least the fluxes of TTP1 and TTP2 are similar. This can be verified by putting both beams separately **ONPOS** and **OFFPOS**.

If **no flux can be found** and wrong configuration or other reasons have been excluded, see appendix D.6 (Troubleshooting, appendix D.6.5, page 288).

Operation in the laboratory

The lab operation during the day comprises two major steps: the health check (cold camera check and co-alignment check of the warm fibres) and the calibration of the FSUs with the artificial light source MARCEL (FSU-response).

Health Check

Cold camera check

Inside the cryostat, the light of each of the four FSU fibres is dispersed along five pixels. By moving with a piezoelectric, it can be controlled on which $4 \times 5 = 20$ pixels of the detector the light is shining. These 20 pixels on which the light falls have to be the same pixels which are read by the software. Overall, the piezo should be aligned such that the flux loss, due to light falling on pixels which are not read, should be minimized. It is important to check the cold camera piezo alignment, and the procedure to do that is described in the following.

- Here, it is assumed that ISS was correctly configured for PACMAN AUTOTEST and that two (four) beams of MARCEL are arriving at the FSU(s).
- The workspace is set up as described in appendix D.3, page 266.
- Optimise the flux in the FSUs as described in appendix D.3.7, page 273.
- Check the flux loss.
  - Mouse **middle** click on the desired **FSU-** desktop and select OSF Starter.
  - Enter your name.
  - Open the script `priosfFSUx_FLUX_LOSS.osf`.
  - Run it by pressing Start.
  - If the message "– Pls. confirm that ARAL and MARCEL are set up correctly" appears in the **Script log-messages**, click on the white box next to the **turquoise arrow** of the current task on the **Check List** area. The execution of the script resumes.

Co-alignment check of the warm fibres

In the FSUs, after the beam combination, the two beams are further split by two polarizing beam splitters. The resulting four beams are coupled in to four single mode fibres. It is important that these fibres are co-aligned with respect to each other, which needs to be checked by the procedure described in the following.

- Here, it is assumed that ISS was correctly configured for PACMAN AUTOTEST and that two (four) beams of MARCEL are arriving at the FSU(s).
- The workspace is set up as described in appendix D.3, page 266.
- Optimise the flux in the FSUs as described in appendix D.3.7, page 273.
- Go to **PACMAN** desktop and open the OB[13] PACMAN_tec_Lab_WarmCoalign.obd (see appendix D.3.2, page 268).
  - Open all drop-down menus, by left clicking on the arrows preceding them.
  - Mouse **middle** click and edit PACMAN_tec_Lab_Coalign – FSU Coalign Calibration > FSU.LIST for the FSU that is used (A, B or ALL).

[13] Remember that in order to perform this operation, the Interface menu must be in Engineering mode.

  - Keep one FSU.ID equal to A and the other equal to B in the PACMAN_cal_Lab_COA... fields.
  - If the complete ISS is correctly configured, keep ISS.MODE.CHECK = T and press Start .
  - If ISS is not correctly configured but is at least online, PRIMA is online and the lab, i.e., ARAL, is configured correctly. In this case, edit ISS.MODE.CHECK to F and press Start .
- When this template is finished, load the template PACMAN_cal_Lab_COAPlot.obd.
- Open all drop-down menus by left clicking, as mentioned before.
- Mouse **middle** click and edit FSU.ID to the FSU you want to use (A or B).
- Press Start .
- When the MATLAB® figures appear (see Figure D.3), **save them**!
- When the message "`Dump processing log?`" appears, press Yes .
- Repeat the last four steps for the other FSU.
- Copy the files
  `FSU`*x*`Calibration_Coalign.dat`,
  `PACMAN_LAB_COALIGN_`*xxx_xxxx*`.fits`
  and the MATLAB® figures to Odyssey3 (see appendix D.3.5.3, page 270).

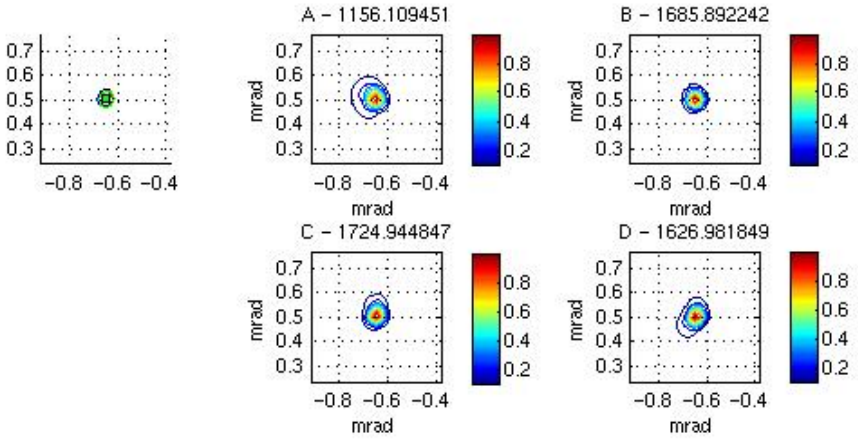

Figure D.3: An example of a MATLAB® set of plots resulting from the cold camera check.

Calibration (FSU-response)

The main aims of the **Lab Calibration**[14] are: 1) to determine the wavelength of the light falling on each of the dispersed pixels and 2) to determine the offset phases of the FSU, i.e., the deviation of the ideal phase shifts in the channels A, B, C, D.

The calibration procedure relies on PRIMET. Therefore, we have to make sure that PRIMET is running and properly configured. The wavelengths of the pixels are needed for the evaluation of

[14]This procedure is referred as "Fringe Calibration" by **Sahlmann2009a**

the group delay, and the offset phases are part and parcel of the algorithms for the phase delay, the fringe amplitude, etc. The successful Lab Calibration results in the production of three data-files: one containing the *detector dark counts*, one containing the so-called *flats* (i.e., flux seen by the detector outside of the fringe), and one containing an OPD-scan across the fringes. Post processing of these files yields the values for the wavelength and offset phases.

NOTE: The (differential) Delay Line system and the telescopes are not involved in the Lab Calibration. Therefore, and in order to avoid disturbances with/from other subsystems, we recommend to ignore these systems – in the VLTI Status panel (issguiObsStatus – see Appendix D.7, page 288), put ignore flags on all telescopes, DDLs and DLCS.

- Here it is assumed that ISS was correctly configured for PACMAN AUTOTEST and that two (four) beams of MARCEL are arriving at the FSU(s).
- The workspace is set up as described in appendix D.3, page 266.
- Optimise the flux in the FSUs as described in appendix D.3.7, page 273.
- Make sure that PRIMET is running and working – load and run the script priosfPRIMET_PREPARE_LABCAL.osf (see appendix D.3.4, page 269).
- Select the SNR, the group delay, the phase, the metrology and the total flux in the RTD Scope.
- Make sure that the LMOTs are set correctly to be on the fringe.
  - Open the template PACMAN_tec_Lab_CenterFringes.obd in BOB (see appendix D.3.2, page 268).
  - Open all drop-down menus.
  - Mouse **middle** click and edit the FSU.LIST for the FSU that should be calibrated. Note that the first part of the template can be run for both FSUs at the same time (ALL). However, the second part, concerning the processing, can be run only for one FSU at a time.
  - Mouse **middle** click and edit the FSU.ID for the FSU that should be calibrated.
  - If ISS is correctly configured, keep ISS.MODE.CHECK = T and press Start .
  - If ISS is not correctly configured but is at least online, PRIMA is online and the lab, i.e.,ARAL is configured correctly. In this case, edit ISS.MODE.CHECK to F and press Start .
  - Watch the RTD Scope. Fringes should pass by during the scanning process. If not, try to increase the value in the template for FSU.LTS.FULLRANGE.
  - If the template was successful, the LMOTs should be on the fringe now. Check this by looking on the RTD Scope at the SNR and the group delay signals; the SNR should be high (around 3) and the group delay should be very small (around 0).
- Open the template PACMAN_cal_Lab_Calibrate.obd[15] in BOB (see appendix D.3.2, page 268).
  - Open all drop-down menus.

[15] This template requires PRIMET to be active and running correctly! See appendix D.3.4, page 269.

  - The lab calibration can be done for both FSUs simultaneously: in each pull down section, mouse **middle** click on FSU.LIST and type ALL.
  - If the lab calibration should be done only for one FSU, make FSU.LIST either A or B in each pull down section.
  - To save time, keep only the integration time you want to have: in each pull down section, mouse **middle** click on FSUx.DIT.LIST and keep only one integration time. Make sure that the value is the same as the one which was selected in the FSUs Control GUI (pfcsGui) for RO Int.
  - Make sure that in each pull down section the value for FSUx.DIT.UPDRTC is the same as the one selected for FSUx.DIT.LIST. In case FSUx.DIT.LIST has more values, ensure the value of FSUx.DIT.UPDRTC is contained.
  - If needed/wanted, in each pull down section increase the value of AVG.DIT. However, make sure that it is not bigger than PCR.DIT.
  - The sections PACMAN_cal_Lab_LQC and PACMAN_cal_Lab_FTS contain quality ch-ecks that can be sent to the database. If you want to update the database after the quality checks, type "Yes" in the LQC.UPDFCAL field.
  - If the complete ISS is correctly configured, keep ISS.MODE.CHECK = T.
  - If ISS is not correctly configured but is at least online, PRIMA is online and the lab, i.e., ARAL is configured correctly. In this case, edit ISS.MODE.CHECK to F.
  - Run the template by pressing Start.
  - The quality control parameter should ideally all be +1. 0 means still acceptable, -1 means that the lab calibration did not go well and -2 that it was not measured (it can be disregarded).
- Check the results of the template PACMAN_cal_Lab_Calibrate.obd. If the phase shifts and wavelengths are OK[16], the data base can be updated. To this end, run the last section of the template again.
  - Disable all sections before PACMAN_cal_Lab_FTS by mouse right clicking once on them (thumb down).
  - Mouse **middle** click on FTS.UPDFCAL and edit it to YES. This option updates the database with the parameters got from the Lab Calibration.
  - Press Start.
  - Do it for each of the FSUs.
  - The files are saved in the PACMAN machine, in the folder `$INS_ROOT/SYSTEM/DETDATA`.

[16]The calibration angles check is not still meaningful, except if the majority of the values is -1. If it is not the case, accept the results as correct.

Operation on sky

The operation during the night comprises several major steps, which are listed and described in detail in the following:

1. Start-up of VLTI.
2. Setting up ISS.
3. Preset a target.
4. Optimize the star light beam (pupil, focus, etc.).
5. Start lab guiding with IRIS.
6. Optimize the Flux in the FSUs.
7. Do a sky calibration (*flats* and *darks*) – VLTI-response.
8. Find the fringes.
9. Record the VLTI response.
10. Track fringes.

Steps 1 to 5 are not part of this manual, i.e., in the following it is assumed that ISS was started and that VLTI is correctly configured, the star (double/single) is preset, IRIS is lab guiding and (at least some) light is coming in to the FSUs.

Step 7. is referred as "Night Calibration" by **Sahlmann2009a** It consists of measuring the sky background and the source's photometry, and to recompute the visibility noise. Step 9. will comprise a fringe calibration on the observed source and will account for the transmission of the VLTI. However, since it is not available yet, this topic is not included in this tutorial for now.

Preparation

See appendix D.3, page 266.

- Check that all PRIMA systems are online.
  - Mouse right click on the desktop, select `Xterm` and open the PRIMA CONTROL SYSTEM panel.

```
wprima prima:~ > priguiStatus &
```

  - If everything is online, prepare for observation (see the following sections).

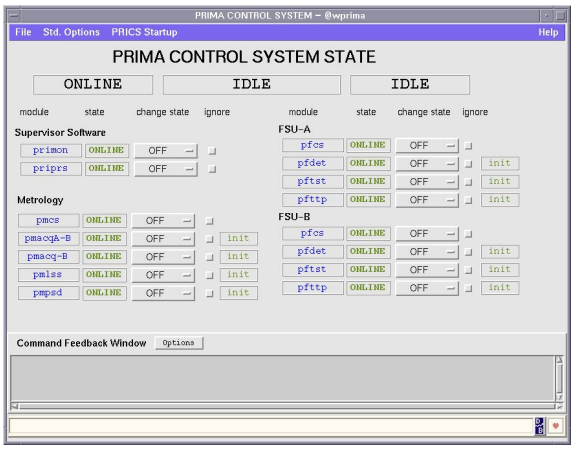

Flux optimisation

- Optimise the flux on FSUs (this is the same for FSUA and FSUB) – see appendix D.3.7, page 273.

Sky calibration (VLTI-response)

- It is convenient to open two BOB in the **PACMAN** desktop (see appendix D.3.2, page 268), one for the sky calibration and other for the recording of fringe tracking data.
  - Select Engineering on the menu Interface.
  - Open the file PACMAN_cal_Sky_Calibrate.obd for the sky calibration.[17]
  - Open file PACMAN_obs_Generic.obd for recording FTK data.[18]
- Do a sky calibration running the PACMAN_cal_Sky_Calibrate.obd.
  - The sky calibration can be done for both FSUs simultaneously: in each pull down section, mouse middle click on FSU.LIST and type ALL.
  - If the sky calibration has to be done only for one FSU, make FSU.LIST either A or B in each pull down section.
  - To save time, keep only the integration time you want to have: in each pull down section, mouse middle click on FSU*x*.DIT.LIST and keep only one integration time. Make sure that the value is the same as the one which was selected in the FSUs Control GUI for RO Int.
  - Make sure that in each pull down section the value for FSU*x*.DIT.UPDRTC is the same as the one selected for FSU*x*.DIT.LIST. In case FSU*x*.DIT.LIST has more values, ensure that the value of FSU*x*.DIT.UPDRTC is contained.

[17] Alternatively, you can load the more general template PACMAN_obs_Astrometry.obd. The advantage of using this file is that the integration time is read directly from the system, as it was passed by the OB. Enter the names of the primary and secondary stars in the fields PS.ID and SS.ID, respectively, and enter F for the fields SKY.ASTEXP, SKY.DSWAP and SKY.METRO. Then, run the template.

[18] If you need to record metrology data, use the template PACMAN_obs_Astrogen.obd instead.

- If needed/wanted, in each pull down section increase the value of AVG.DIT. However, make sure that it is not bigger than PCR.DIT.
- The last section PACMAN_cal_Sky_SQC can be run only for one FSU at a time! Therefore, make sure that FSU.ID is A or B there. If wanted, this section can be run for the other FSU after the template has finished. To this end, change the value of the FSU, disable all sections before by one time mouse **right** click on them (thumb down) and run the template again.
- Run the template by pressing Start.
- The quality control parameter should ideally all be +1. 0 means still acceptable, −1 means that the fringe tracking is very likely to fail or no fringes will be observed at all and −2 that the value was not measured.

Finding fringes

- Open the GUI for OPDC and DOPDC.
  - Log on to a terminal as *prima*.
  - Mouse right click on the desktop and select `Xterm`. Type the following:

```
wprima prima:~ > ssh -X dl@wdline
```

  - Start the OPDC GUI.

```
wdline dl:~ > opdcgui &
```

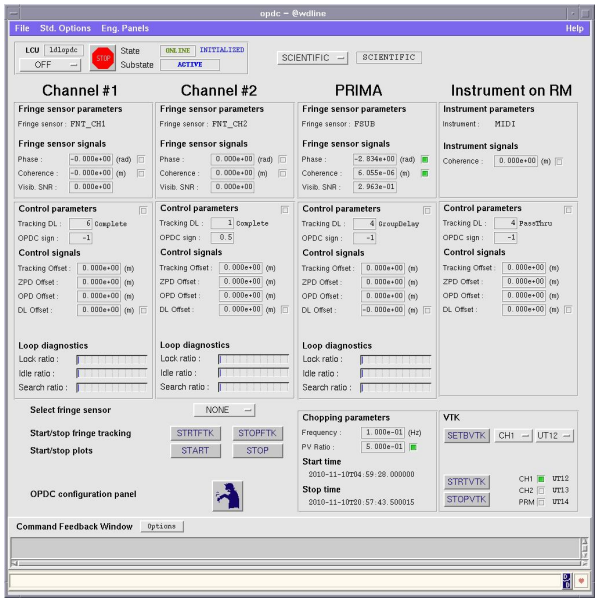

  - Mouse right click on the desktop and select `Xterm`. Type the following:

```
wprima prima:~ > ssh -X ddl@wddl
```

  - Start the DOPDC GUI.

```
wddl ddl:~ > ddopdcgui &
```

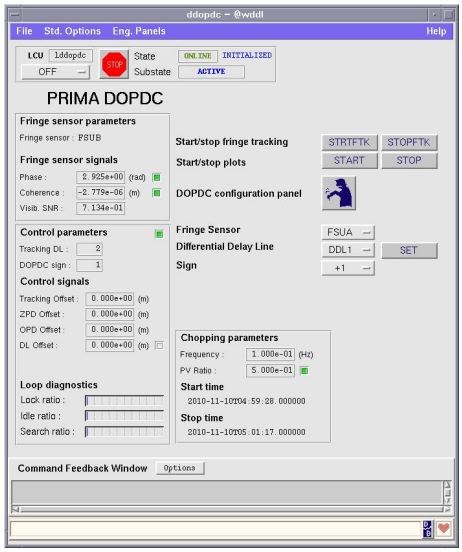

- On the RTD Scope select the right Scope_FTK*x*, depending on which FSU(s) FTK should be done.
  - Make sure that at least the STATE, the SNR and the flux are enabled (PHASE and GD are also useful).
  - Fix the scale for the STATE to $0-22$ for fringe scanning and to $0-8$ for FTK.
  - Fix the scale of the SNR from $0-8$ (even higer, if required).
- In the PACMAN workspace (see appendix D.3.5.1, page 270), load the script *scanparameter.m* (located in `/home/pacmamgr/newscript/`). Put there the desired input parameter. The *scanrange* is, in principle, arbitrary, but 0.01 might be a good starting value. *Offset* is in principle arbitrary, but start where the fringes are supposed to appear, usually at 0. *Dlsign* has to be read from the OPDC GUI or the DOPDC GUI, respectively. Run the script.
  - Go to (D)OPDC GUIand click on the (D)OPDC Configuration Panel. To open the configuration panel press the square button with the strange man on it (man with thumbs down).

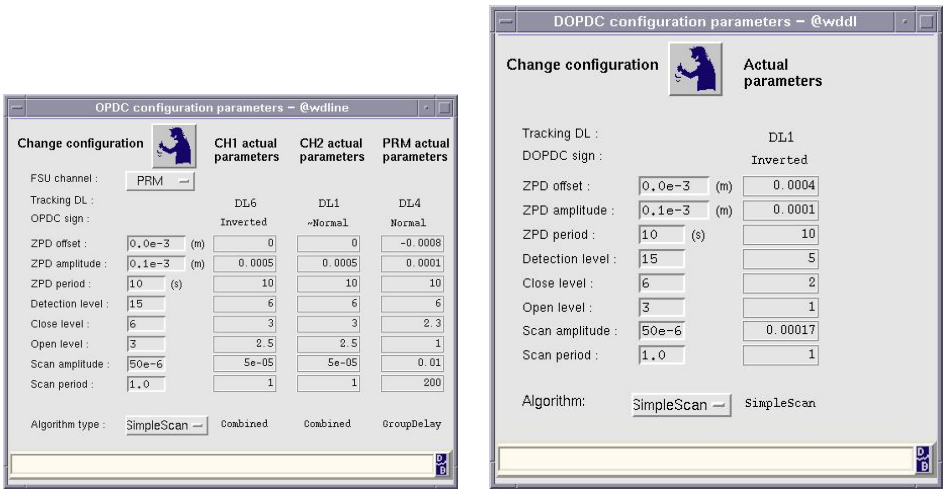

– Put in the (D)OPDC configuration panel the output values of the MATLAB® script for ZPD offset and Scan period. Put in Scan amplitude what was selected as scan range in the script.

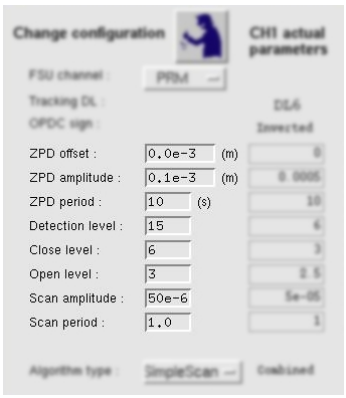

– Select SimpleScan for algorithm type.[19]
– In the OPDC Configuration panel, change also the FSU Channel to PRM.
– Press the change configuration button (man with thumbs up).

- Visit the template PACMAN_obs_Generic.obd.
- Put the output of the script *scanparameter.m* for file length in the field DIT (**middle** mouse click it to edit).
- Start the template by pressing Start.
- Watch the "Template log-messages".
  – When "Recording started. Waiting *nnnnn* ms..." appears, go to the (D)OPDC GUI and press STRTFTK. Press also STOP and START to get the plots.
  – Wait until the template has finished.

[19] You can also choose GroupDelay for Algorithm type. The fringes are within ±1mm and it is faster to find them.

- Go to MATLAB® and open the script *evalFringeScan.m* (located in `/home/pacmamgr/newscript/`).
  - Specify the **Filename**,[20] the **FSUid**, the **OPDCid** and run the script.
  - Look at the plots and decide whether you see the fringes or not.
  - If fringes were found, the position of the maximum SNR can be put as ZPDoffset in the (D)OPDC configuration panel. **Be careful: the value has to be multiplied by the (D)DL sign!** See appendix D.8, page 289, for the correct (D)OPDC settings for FTK.
  - SNR threshold values recommendation still needs to be improved, but it might be used as a starting point.
  - Now everything is ready for fringe tracking.

Tracking fringes

- When attempting to track fringes with both FSUs, concentrate first on one FSU only; preferably the primary sensor, associated with the main DL.
  - Try to find the fringes with the scan method – see appendix D.5.4, page 281.
  - Allow the FSU to track and leave it that way. Then, forget about it and concentrate on the second FSU. Just keep an eye on the primary FSU from time to time, checking that it does not lose the fringe position completely and wanders away.
  - The quality of the tracking (lock ratio) is not important at this stage.
  - Then, try to find the fringes on the second FSU with the above described scan method (see appendix D.5.4, page 281).
  - Once fringes are found, decide whether they should be tracked or scanned.
- Put the value of the full-offset at which the maximum SNR was found by the *evalFringeScan.m* routine as ZPD offset in the (D)OPDC configuration panel. However, **do not forget to multiply it with the (D)DL sign!** Put in also the values for the ZPD amplitude[21] and ZPD period[22] (the default parameters of 0.1 mm in 10 s usually work fine).
- Set the SNR thresholds. As rough rules, you can put the *Detection level* equal to the mean value of the SNR in the fringe, the *Close level* equal to the value of the SNR at the overlapping region between inside and outside of the fringe, and the *Open level* equal to the mean value of the SNR outside of the fringe. For more information about these thresholds, consult appendix D.9, page 289.
- Select the algorithm GroupDelay for tracking.
- Record a file using the PACMAN_obs_Generic.obd template.
- Press STRTFTK for tracking and then STOP followed by START for the plots.

[20] The filename, you can look up on PACMAN in `/rmnrec`. It should be the most recent file and it is of the form PACMAN_OBS_GENERIC*nnn_nnnn*.fits.

[21] The *ZPD amplitude* is the amplitude of the search spiral (see appendix D.2.1, page 264).

[22] The *ZPD period* is the period of the search spiral, i.e., the time the search spiral takes to go up, down and up again until the starting point (see appendix D.2.1, page 264).

- When the first file is finished, it can be quickly evaluated with the script *checkFSU.m* (located in `/home/pacmamgr/newscript/`). This script gives a better estimation on the SNR threshold, which can be used for refinement and possible improvement of the tracking.
- In case of multiple scans across the fringe (assumable on the secondary star), either algorithm SimpleScan or FringeScan can be used. The former, preferably in case the fringe position is known very well and stable. The latter, preferably when the fringes might have strongly drifted since the first scan to find the fringe. For the FringeScan, the SNR detection value has to be set correctly!
  - Recorded files of multiple scans across the fringe can be evaluated with the script *checkBlindTraj3.m* (located in `/home/pacmamgr/newscript/`).
    Beware: this script is not yet fully developed and might crash for particular files!
- If (D)OPDC repeatedly finds the fringes, jumps into fringe lock, but gets kicked out immediately afterwards, i.e., does not stay in state tracking, this might indicate that the (D)DL sign is set wrongly. In order to change the sign, consult table D.1 in appendix D.8, page 289.
  - Stop FTK first, by pressing STOPFTK.
  - For OPDC, open the OPDC GUI DL on wdline.

```
wdline dl:~ > opdcguiDL &
```

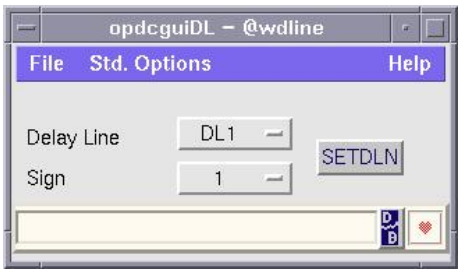

  - Select the tracking delay line, select the desired sign and press SETDLN.
  - Start fringe tracking again, but **before change the sign of the** ZPD offset **in the configuration panel!**
  - Press  .
  - Press STRTFTK.
  - For DOPDC, the procedure is the same but the option to change the DDL sign is included in the DOPDC GUI.

REMARK 1: The (D)DL sign has to be reset after each preset.

REMARK 2: If you intend to record a file with metrology data for post-processing, make Scan amplitude approximately equal to 160×10^{-6} m and Scan period around 2 s (if the weather is not too bad, 3 s is also good).

Troubleshooting

Failure of the FSU online osf-scripts

In case the FSU online osf-scripts fail, do the following:

- Bring IRACE online manually for FSUA and FSUB.
  - Mouse **middle** click the workspace and open FSU IRACE for FSUA and FSUB.

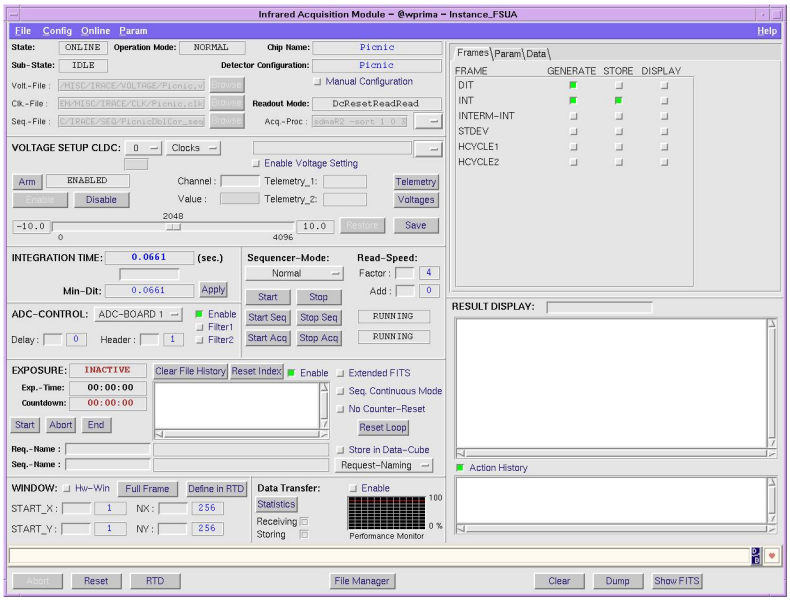

  - Go to the Config menu and select Load Detector Config.
  - Make sure the path under Selection is `/data/PRIMA/INS_ROOT/SYSTEM/MISC/DET`, select the file Picnic6ch.dcf and press OK.
  - Go online: Online > online.
  - Check that External Trigger is selected in the drop-down menu of **Sequencer-Mode:** and press Arm, Enable, Apply (Min-Dit:) and Start.

RTD Scope stuck

In case the RTD Scope is completely stuck, i.e., no signal, nothing changing, try to reboot.

- Log on `wvgvlti` as *mon*.[23]

```
wprima prima:~ > ssh -X mon@wvgvlti
```

- Reboot LCU and wait (this can take some time).

```
wvgvlti mon:~ > lccBoot lvgmon
```

- When finished, open `tacgui` and select the correct configuration.

```
wvgvlti mon:~ > tacgui &
```

[23] In order to enable a trusted X11 forwarding, use `-Y` instead. You can also use a combination of both, i.e., `-XY`.

- Select INIT in the drop-down menu located left to the STOP button.
- Type, as configuration file, rmnmon.tac and select CONFIG from the drop-down menu on the left.
- Go ONLINE (on the first drop-down menu).

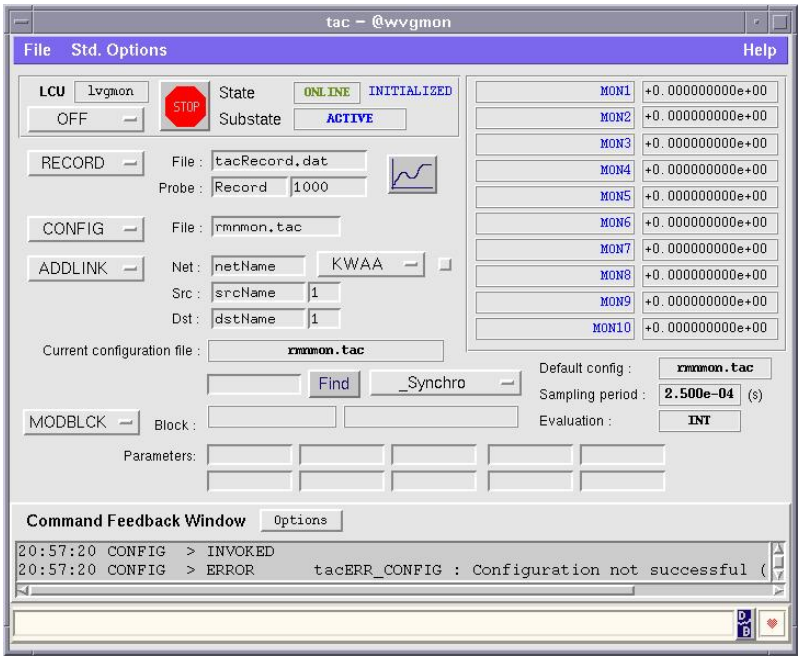

Failure of the PRIMET osf-scripts

In case the PRIMET osf-scripts fail, perform each of the following steps one by one, until the problem is solved.

- Check the PRIMA status at the VLTI Status panel. If the status is STANDBY, go to the Prima Control System panel (see appendix D.7, page 288) and bring everything online.
- Switch on the laser by hand: go to the Laser Stab. System panel.
  - In the drop-down menu next to Switch Laser, select ON and press Switch Laser.
  - In the drop-down menu next to Set LSP Parameter, select the highest value (for lab calibration) and press Set LSP Parameter.
  - In the drop-down menu next to Close stabilization loop, select ON and press Close stabilization loop.
  - Check that AOM transmission is set to 100%.
  - For operation in the lab with MARCEL, select OUT in the drop-down menu next to Set Flip OD and press this button; for operation on sky, select IN from the same drop-down menu and press the aforementioned button.
- Go to the Metrology Phase Meter panel.
  - Select -B from the LCU drop-down menu.
  - In the field next to Set Metrology Rate, type 8000 and press this button.

– Press Stop Metrology and then Start Metrology.
– Execute the same steps for LCU A-B.

No increase of flux in the RTD Scope

If during the flux optimisation procedure you realise the flux on the RTD Scope does not increase when each beam is brought in to position separately, try the following:

- Verify if the hardware window for the cold camera is correct – see appendix D.4.1.1, page 275.
- For *day operation*: check the lab configuration and that the shutters[24] of the FSUs are open.
- For *night operation*: check IRIS lab guiding, correct reference pixels, focus of the telescope and pupil of the beam on ARAL.

No flux found

If no flux is found and wrong configuration or other reasons have been excluded (see appendix D.6.4, above), try a *spiral search*.
Note: Try the spiral search on sky only for bright sources ($m_K \leq 2$).

- In the FSU*x* Control GUI (see appendix D.3.1, 266), go with TTP1 and TTP2 **ONPOS** and then **OFFPOS**.
- Start with the first beam, bring it **ONPOS**, press Spiral Search, wait and watch the RTD Scope.
- If the spiral search has finished and flux was found, press SAVEPOS.
- Repeat the beam tracking procedure.
- Do it for all the beams.

Reference table of panels

In this appendix, a reference table containing all the panels needed to operate PRIMA is presented. The first column gives the "official" name of the panel; the second one, the name figured in the title-bar of the window; the third, the command that can be issued to start the panel (not needed in most of the cases, as the command is already available from one of the mouse menus); the fourth column tells in which machine the panel runs.

Some commands present an underscore as suffix (pfttpgui_, for e.g.). In those cases, the underscore must be replaced by "a" or "b", whether you are going to load the panel for FSUA or FSUB, respectively. Similarly, some panel names contain an *x*, which corresponds to an "a" or a "b", depending if the panel refers to FSUA or FSUB, respectively.

[24] The shutters can be checked in the FSU*x* Motors panel – see appendix D.3.1, page 266.

PRIMA Panels			
Name	Name in title-bar	Command	Machine
BOB	BOB: Broker for Observation Blocks	bob	wpacman
OPDC GUI DDL	opdcguiDDL	ddopdcgui	wddl
FSU*x* ACU Tip/Tilt	pfttp	pfttpgui_	wprima
FSU*x* Control	pfcsGui	pfcsgui_	wprima
FSU*x* IRACE	Infrared Acquisition Module	iracqFSU_	wprima
FSU*x* Motors	pfacu	pfacugui_	wprima
Laser Stab. System	pmlss	pmlssgui	wprima
Metrology Control Software	Metrology Control SW (pmcsGui)	pmcsgui	wprima
Metrology Phase Meter	pmacq	pmacqguiab	wprima
OPDC	opdc	opdcgui	wdline
OPDC GUI DL	opdcguiDL	opdcguiDL	wdline
OSF Starter	Start/Shutdown Telescope	osfStarter	wprima
PRIMA States	Prima Control System	priguiStatus	wprima
	tac	tacgui	wvgmon

Correct (D)OPDC Signs for PRIMA

Table D.1: Correct OPDC and DOPDC settings for FTK with PRIMA (current as of July 2011).

Magic Table (to switch signs)

Mode	OPDC Sensor	TRK DL	Sign	DOPDC Sensor	TRK DDL	Sign
NORMAL	FSUB	2	−1	FSUA	1	−1
SWAPPED	FSUA	2	−1	FSUB	2	−1
NORMAL	FSUB	4	1	FSUA	1	−1
SWAPPED	FSUA	4	1	FSUB	2	−1

In order to change the sign, use the OPDC GUI DL and DOPDC GUI DDL panels (see appendix D.5.5, page 285.)

FTK thresholds

Currently, the process of fringe tracking with PRIMA can be described by five states: 1, 5, 7, 20 and 21. *State 1* is equivalent to "*searching*", *State 5* means the system is "*waiting*" and *State 7* is equivalent to "*fringe tracking*". *States 20* and *21* correspond to an "upwards" and a "downwards" scanning, respectively.

There are three fundamental thresholds that have to be passed to the FSUs for the process of fringe tracking: the *Detection Level*, the *Close Level* and the *Open Level*.

The *Detection Level* depends on the star magnitude and defines the point where the signal is locked. As long as the SNR is between the *Detection Level* and the *Close Level*, the fringes are being tracked (*State 7*).

If the SNR goes below the *Close Level*, the loop freezes and no corrections are sent to the delay line for a maximum duration of 20 ms, while the system is trying to get back the signal (*State 5*). Thereafter, the loop opens.

When the SNR goes under the *Open Level*, that means the FSU completely lost the signal and starts to search for it again (*State 1*).

For more information about the FTK thresholds, see the "SNR thresholds setting" memorandum by Schmid, 2009.

ISS configuration for Lab Calibration

Having ISS correctly configured is mandatory for PRIMA operations. Therefore, if you need to perform a lab calibration during day time (the so called *FSU Response*, before going on sky for observations), you will have to go through these steps. For more details, please consult the "PRIMA Startup Procedure & other useful operational information" manual from Belle, 2010.

- Log on to a `wvgvlti` machine as *iss*.

```
wprima prima:~ > ssh -X iss@wvgvlti
```

- Start the following panels.

```
wvgvlti iss:~ > issguiConfig &
```

```
wvgvlti iss:~ > issguiObsMain &
```

```
wvgvlti iss:~ > issguiObsStatus &
```

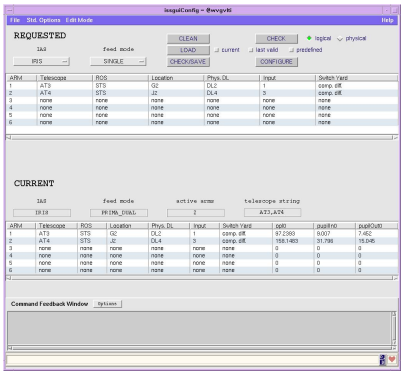
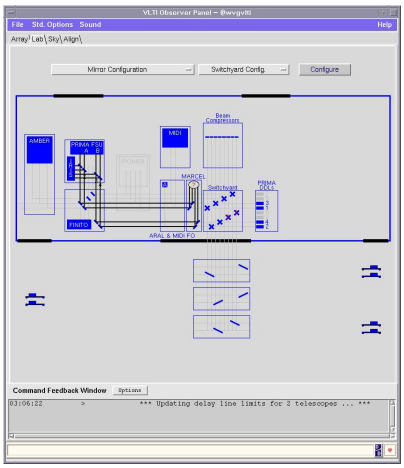
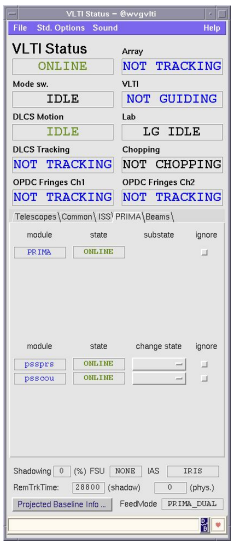

Start in the VLTI Status panel.

- In a lab calibration we do not need the telescopes.
  - Go to the Telescopes tab and press the radio button left to "Disable all telescopes"[25].
- Visit the Common tab and check if all the systems are ONLINE. Some systems are not needed for lab calibration, though, like the (D)DLs.
  - Press the "ignore" radio buttons in front of DLCS and DDL.
- Visit the ISS tab and check if all ISS modules are ONLINE. If not, change state accordingly, by selecting ONLINE from the corresponding drop-down menu.
- Go to PRIMA tab and check if all the modules are ONLINE. Deselect any "ignore" button and, in case PRIMA is on STANDBY, go to a PRIMA machine, load the PRIMA Control System panel (See appendix D.7, 288) and check what is wrong.

Now, go to the issguiConfig panel.

- Select Expert Mode from the Edit Mode menu.
- In the `feed mode` drop-down menu, select PRIMA_DUAL.
- On the upper right side of the panel, press CHECK for both options (logical and physical).
- Now, click on CONFIGURE to set-up PRIMA.

These configurations performed so far are up to the switch-yard. However, we also need to configure the laboratory. To achieve that, visit the VLTI Observer Panel (see appendix D.7, page 288), where we can see how the VLTI is configured.

- Go to the Lab tab and select PACMAN AUTOTEST from the drop-down menu.
- Make sure the drop-down menu in the centre is set to Switchyard Config. and press Configure.

Starting/Stopping the metrology

In order to start the metrology, go to the OSF Starter (see appendix D.3.1, page 266) and run the script priosfPRIMET_DAY_TO_NIGHT.

[25] You can also ignore the telescopes one-by-one, pressing the "ignore" button in front of them.

To stop the metrology, run instead the script priosfPRIMET_NIGHT_TO_DAY.osf.

Note: Do not forget to enter your name before running the scripts.

In case you need to manually start the metrology, desktop **middle** click and select the Metrology Control Software panel (see appendix D.7, page 288).

- Bring it ONLINE and press the button Start Freq. Stabilization. The SubState goes from ERROR to STABILIZING and then to STABLE_NOTGUIDING.
- Press Start Pupil Tracking. After a while, the SubState goes to STABLE_GUIDING.
- Press Start Metrology and wait until SubState goes to STABLE_RECORDING (that is where we want to be). The wavelength of the laser must be around 1 319 nm.

Preset an OB from P2PP

In order to preset an OB, go to BOB and fetch the OB by clicking on the first button on the left vertical tool bar (if you hover it, you see a bubble with the description "Fetch an OB from OH"). The OB which is selected in P2PP is automatically loaded.

Decide at what frequency you are going to run the FSUs and change the integration times accordingly in the FSU*x*.DT.LIST fields under PACMAN_acq_Preset – PACMAN Acquisition > SEQ. You can ignore the third section, by right clicking on the arrow preceding it (you get a "thumbs down"), before hitting Start.

Acknowledgements

The authors acknowledge useful inputs by Johannes Sahlmann, Roberto Abuter, Gerard van Belle, Ettore Pedretti, Jean-Baptiste Le Bouquin, Samuel Lévêque and André Müller.

List of Abbreviations & Acronyms

The following abbreviations and acronyms are used in this document:

ACU **A**lignment **C**ontrol **U**nit

ADU **A**nalogue-to-**D**igital **U**nit

AMBER **A**stronomical **M**ulti-**BE**am Combine**R**

ARAL **AR**tificial Source and **AL**ignment Unit

BOB **B**roker for **O**bservation **B**locks

DDL **D**ifferential **D**elay **L**ine

DL **D**elay **L**ine

DOPDC **d**ifferential **O**ptical **P**ath **D**ifference **C**ontroller

ESO **E**uropean **S**outhern **O**bservatory

FITS **F**lexible **I**mage **T**ransport **S**ystem

FSU **F**ringe **S**ensor **U**nit

FTK **F**ringe **T**rac**K**ing

GUI **G**raphical **U**ser **I**nterface

IRIS **I**nfra**R**ed **I**mage **S**ensor

ISS **I**nterferometer **S**upervisor **S**oftware

LCU **L**ocal **C**ontrol **U**nit

LMOT **L**inear **MOT**or

MARCEL **M**ulti-beam **A**lignment **R**eference and **C**alibration IR **E**mitter for the VLTI **L**aboratory

MIDI **MID**-Infrared **I**nterferometric Instrument

OB **O**bservation **B**lock

OPD **O**ptical **P**ath **D**ifference

OPDC **O**ptical **P**ath **D**ifference **C**ontroller

OPDC GUI **O**ptical **P**ath **D**ifference **C**ontroller **GUI**

OPDC GUI DL **OPDC GUI D**elay **L**ine

OPL **O**ptical **P**ath **L**ength

P2PP **P**hase **II** **P**roposal **P**reparation

PACMAN **P**RIMA **A**strometric **C**amera for **M**icro-arcsecond **A**stro**N**omy

pfcsGui **P**RIMA **F**SU **C**ontrol **S**oftware **GUI**

PRIMA **P**hase **R**eferenced **I**maging and **M**icro **A**rcsecond **A**strometry

PRIMET **PRI**MA **MET**rology

RTD Scope **R**eal **T**ime **D**isplay **SCOP**e **GUI**

SNR **S**ignal to **N**oise **R**atio

STS **ST**ar **S**eparator

TRK **TR**a**K**ing

VLTI **V**ery **L**arge **T**elescope **I**nterferometer

ZPD **Z**ero **P**ath **D**ifference

Appendix E

Outreach: the GalileoMobile programme

"Eppur si muove..."

— GALILEO GALILEI, 1633

GALILEOMOBILE is a non-profit, pure volunteering, itinerant science outreach initiative that brings Astronomy closer to young people in areas with little or no access to outreach programmes. The team performs astronomy-related activities in schools and communities, encouraging follow-up activities through teacher training workshops and the donation of telescopes and other educational resources. GalileoMobile also extends its impact to a worldwide audience through deliverable products. The effort is shared worldwide through the production of documentaries, books and a wide range of Internet resources (Official Website and Blog, Facebook page, Google+,Twitter, Youtube and Vimeo).

GalileoMobile is an unprecedented initiative promoting science knowledge and the interaction beyond borders through Astronomy, while raising awareness for the diversity of human cultures,

conveying the message of "unity under the same sky".

The aims of GalileoMobile are:

- To encourage a will of learning in young people residing in areas where Science outreach programmes are a rare opportunity.
- To provide schools and teachers the tools and knowledge to run the activities independently, to facilitate the long-term continuation of the programme locally and promote sustainable development in the communities visited.
- To foster a cultural exchange by exploring, alongside modern Scientific views, traditional Astronomical understandings of the Sky and the Cosmos of the communities visited, hence promoting a message of peace and mutual understanding.
- To inspire young people over other parts of the world by the grandeur of the cosmos and encourage them to undertake similar initiatives.

GalileoMobile is composed of 13 volunteer team members and more than 30 collaborators from different countries. Several of the expeditions were initially motivated by the desire of one of the volunteers to bring GalileoMobile to his/her country of origin, in communities where s/he had witnessed first-hand the lack of access to science outreach programmes. Since its creation in 2008, GalileoMobile has organised expeditions in Chile, Bolivia and Peru (2009), Bolivia (2012), India (2012), and Uganda (2013), and extended actions in Portugal (2012, 2013), Nepal (2013), Guatemala (2013), Dominican Republic (2013), and the United States (2013), reaching over 11 000 students 1 000 teachers and 1 300 community persons (fig. E.1).[1] The efforts and activities have been shared with the public in over 80 conferences and talks, including a TEDx talk (fig. E.1l). Currently, the team counts on the support of *Universe Awareness* (UNAWE, http://www.unawe.org/), and the collaboration of the *Galileo Teacher Training Program* (GTTP, http://galileoteachers.org/) and *A Touch of the Universe* (ATU, http://astrokit.uv.es/).

[1] For more information, please visit the Internet page http://www.galileo-mobile.org/galileomobile-about-us/galileomobile-in-numbers.

Figure E.1: Examples of activities developed by the GalileoMobile team. From figs. E.1a to E.1c: 2009 expedition in South America; from figs. E.1d to E.1g: 2012 expedition in India; from figs. E.1h to E.1j: 2013 expedition in Uganda. fig. E.1k: hands-on activity for visually impaired children (Portugal, 2013). fig. E.1l: talk by Nuno Gomes at TEDx Youth@Leiria, in November 2013.

Index